

ICMAR' 98



Novosibirsk, Russia

Proceedings

Part I

DISTRIBUTION STATEMENT A

Approved for public release;
Distribution Unlimited

REPORT DOCUMENTATION PAGE

Form Approved OMB No. 0704-0188

Public reporting burden for this collection of information is estimated to average 1 hour per response, including the time for reviewing instructions, searching existing data sources, gathering and maintaining the data needed, and completing and reviewing the collection of information. Send comments regarding this burden estimate or any other aspect of this collection of information, including suggestions for reducing this burden to Washington Headquarters Services, Directorate for Information Operations and Reports, 1215 Jefferson Davis Highway, Suite 1204, Arlington, VA 22202-4302, and to the Office of Management and Budget, Paperwork Reduction Project (0704-0188), Washington, DC 20503.

1. AGENCY USE ONLY (Leave blank)		2. REPORT DATE 1998	3. REPORT TYPE AND DATES COVERED Conference Proceedings	
4. TITLE AND SUBTITLE International Conference on the Methods of Aerophysical Research 98 "ICMAR 98"			5. FUNDING NUMBERS F61775-98-WE002	
6. AUTHOR(S) Conference Committee				
7. PERFORMING ORGANIZATION NAME(S) AND ADDRESS(ES) Institute of Theoretical and Applied Mechanics Novosibirsk 630090 Russia			8. PERFORMING ORGANIZATION REPORT NUMBER N/A	
9. SPONSORING/MONITORING AGENCY NAME(S) AND ADDRESS(ES) EOARD PSC 802 BOX 14 FPO 09499-0200			10. SPONSORING/MONITORING AGENCY REPORT NUMBER CSP 98-1025	
11. SUPPLEMENTARY NOTES				
12a. DISTRIBUTION/AVAILABILITY STATEMENT Approved for public release; distribution is unlimited.			12b. DISTRIBUTION CODE A	
13. ABSTRACT (Maximum 200 words) The Final Proceedings for International Conference on Methods of Aerophysical Research (ICMAR'98), 29 June 1998 - 3 July 1998 This is an interdisciplinary conference. Topics include: Problems of Modeling at sub/trans/super/hypersonic velocities; Methods of flow diagnostics; Instrumentation for aerophysical experiments; Verification of CFD models and methods.				
14. SUBJECT TERMS Aerodynamics, Flow Diagnostics, Computational Fluid Dynamics			15. NUMBER OF PAGES 258	
			16. PRICE CODE N/A	
17. SECURITY CLASSIFICATION OF REPORT UNCLASSIFIED	18. SECURITY CLASSIFICATION OF THIS PAGE UNCLASSIFIED	19. SECURITY CLASSIFICATION OF ABSTRACT UNCLASSIFIED	20. LIMITATION OF ABSTRACT UL	

NSN 7540-01-280-5500

Standard Form 298 (Rev. 2-89)
Prescribed by ANSI Std. Z39-18
298-102

**RUSSIAN ACADEMY OF SCIENCES SIBERIAN DIVISION
RUSSIAN NATIONAL COMMITTEE
ON THEORETICAL AND APPLIED MECHANICS
INSTITUTE OF THEORETICAL AND APPLIED MECHANICS
INTERNATIONAL CENTER OF AEROPHYSICAL RESEARCH**

**INTERNATIONAL CONFERENCE
ON THE METHODS OF AEROPHYSICAL RESEARCH**

29 June - 3 July, 1998, Novosibirsk, Russia

**Proceedings
Part I**

**Novosibirsk
1998**

19980805 105

AQ F98-11-2175

ICMAR'98 PROGRAM COMMITTEE

Prof. V.M. FOMIN (Russia) - Co-Chairman

Prof. A.M. KHARITONOV (Russia) - Co-Chairman

Prof. V.A. LEBIGA (Russia) - Scientific Secretary

Prof. N.A. ANFIMOV (Russia)

Prof. S. BOGDONOFF (USA)

Prof. V.N. GUSEV (Russia)

Dr. Ph.E. CASSADY (USA)

Prof. J. COUSTEIX (France)

Prof. M.S. IVANOV (Russia)

Dr. R.A. KILGORE (USA)

Dr. G. KOPPENWALLNER (Germany)

Prof. V.V. KOZLOV (Russia)

Prof. E. KRAUSE (Germany)

Dr. G. LARUELLE (France)

Prof. A.A. MASLOV (Russia)

Prof. G.E.A. MEIER (Germany)

Dr. A.S. RUDAKOV (Russia)

Prof. J. SCHETZ (USA)

Prof. A.F. SIDOROV (Russia)

Prof. A.V. ZABRODIN (Russia)

**The papers are printed by direct reproduction from the authors' originals.
The authors are responsible for possible misprints and the quality of translations.**

ICMAR'98 is sponsored by:

- **Russian National Committee on Theoretical and Applied Mechanics**
- **Russian Foundation for Basic Research (RFBR)**
- **American Institute of Aeronautics and Astronautics (AIAA)**

We wish to thank

**The United States Air Force European Office
of Aerospace Research and Development (EOARD)**

for its contribution to the success of the Conference



We thank the Novosibirsk
Branch of TOKOBANK
for its financial support

6 Lavrent'eva av., 630090, Novosibirsk, Russia, Phone:(3832) 35-23-62, Fax: (3832) 32-41-46

The ICMAR'98 Organizing Committee Office is equipped with
computers of FRACTAL Company:



*Institutskaya 4, Building 18
630090, Novosibirsk, RUSSIA*

*Phone: (3832) 35-75-15
(3832) 39-75-15*

Fax: (3832) 35-65-15

HTTP: // www.fractal.ru

**THE STUDY OF SCHEME VISCOSITY EFFECT ON THE STREAM
STRUCTURE IN THE PARTICLE-IN-CELL METHOD
BY THE EXAMPLE OF THE PERFECT GAS FLOW
AROUND A CYLINDER IN A PLANE CHANNEL**

S.M.Aulchenko, A.F.Latypov, and Yu.V.Nikulichev

Institute of Theoretical and Applied Mechanics SB RAS,
Novosibirsk, Russia

It is known that the mechanism of energy dissipation is always inherent in homogeneous difference schemes. In the particle-in-cell method, this is the approximation viscosity generated by the structure of difference equations [1]. Viscous effects lead to flow stall and formation of vortex zones, especially in flow simulation around bluff bodies, i.e., to obtaining solutions which do not result from solving the evolution problem for the initial system of Euler equations. An important element in implementation of these schemes, therefore, is the algorithms of generating the computational grids, which are based on this or that principle and allow one to affect the approximation viscosity coefficient [2]. A principle of generating such a grid is suggested in the present paper. This grid is formed in a single process of solution of an unsteady problem, whose solution is most close to potential. The results of comparative calculations of the subsonic flow of perfect gas around a cylinder in a plane channel on fixed and flexible grids are presented.

Problem formulation. The flow around a cylinder with diameter D in the channel with length L and width H is simulated. The left and right ends of the channel, L_1, L_2 , are connected with infinite chambers containing the gas with parameters p_1, ρ_1, J_1 and p_2, ρ_2, J_2 , respectively. Here p is the pressure, ρ is the density, J is the internal energy. The jump of gas parameters in the channel is set by its abscissa - x_0 . The cylinder is located in the chamber with gas 1. A system of unsteady Euler equations with a closing equation of state is used. The boundary conditions for this system are p_1 - the pressure at the left end of the channel, the free stream conditions at the right end of the channel (the pressure there is assumed equal to the flow pressure), and the no-slip condition on the body and channel walls.

Method of solution. The particle-in-cell method on a non-uniform grid is used for solving the problem. The realization of conditions on the curvilinear boundary reduces to the formation of gas parameters in fictitious cells inside the body under the condition $w_n \sim O(h^2)$ at the intersection point of the contour with the normal to it, which passes through the center of the fictitious cell. w_n is the projection of velocity vector \vec{w} onto this normal.

Computational grid. The grid is formed by setting the nodes $\{x_i\}, i=1, \overline{N_{x1}}, \{x_i\}, i=1, \overline{N_{x2}}$ in the sections from the left boundary of the domain to the cylinder center and from the cylinder center to the right boundary, and $\{y_j\}, j=1, \overline{N_{y1}}$ from the lower boundary of the domain to the symmetry plane with subsequent symmetric reflection onto the upper part of the domain.

The values of physical nodes are calculated in terms of non-dimensional parameters λ using the formulas

$$S_i = \prod_{k=1}^i \left(\frac{1}{\lambda_k} - 1 \right), \quad x_1 = x_0 + \frac{x_N - x_0}{1 + \sum_{i=1}^N S_i},$$

$$x_i = x_{i-1} + (x_{i-1} - x_{i-2}) \left(\frac{1}{\lambda_{i-1}} - 1 \right),$$

where x_0, x_N are the domain boundaries, N is the number of intervals on this section. The parameters λ_i are calculated from the formula

$$\lambda_i = a + (b - a)z + c4z(1 - z),$$

$$z = i/N, \quad \lambda_{\min} \leq \lambda_i \leq \lambda_{\max}, \quad 0 < \lambda_{\min} < \lambda_{\max} < 1,$$

$0 < a < 1, 0 < b < 1, c \in \mathbb{R}$ are prescribed quantities.

Algorithm. The problem is solved in the following way. At each time step Δt_n , having calculated all flow parameters in the computational cells of the domain from the formulas of the particle-in-cell method, we find the value of the functional

$$F^n = q_1 (dP + d\bar{P}) + q_2 (f_{kp}^2 + f_{nv}^2) / \varepsilon_2^2 + q_3 f_m^2 / \varepsilon_3^2.$$

Here $dP, d\bar{P}$ are the maximum and mean values of residual of the total mechanical energy in the region Ω , calculated from the formula

$$dP_{ij} = \int_{\omega_{ij}} \left(\bar{w} \rho \frac{d\bar{w}}{dt} + \bar{w} \text{grad } p \right)^2 d\omega, \quad \bigcup_{ij} \omega_{ij} = \Omega.$$

The second term ensures the number of boundary cells on the body equal or greater than specified:

$$f_{kp} = f_k + f_p, \quad f_{nv} = f_n + f_v,$$

$$f_k = \frac{1}{2} [(x_k - x_{ik}) + |x_k - x_{ik}|],$$

$$f_p = \frac{1}{2} [(x_{ip} - x_p) + |x_{ip} - x_p|],$$

$$f_n = \frac{1}{2} [(y_n - y_{jn}) + |y_n - y_{jn}|],$$

$$f_v = \frac{1}{2} [(y_{jv} - y_v) + |y_{jv} - y_v|],$$

x_k, x_p, y_n, y_v are the minimum and maximum values of the body coordinates, ip, ik, jv, jn are the prescribed node numbers. The last term in the functional is an algorithm restriction on the minimum size of the cell:

$$f_m = \frac{1}{2} [(h_m - dh_m) + |h_m - dh_m|],$$

dh_m is the minimum cell size, h_m is a prescribed quantity,

q_1, q_2, q_3 are the weight coefficients, $\varepsilon_2, \varepsilon_3$ are the accuracies of restriction fulfillment.

If $F^n \leq F^{n-1}$, the next step is made on the same grid, otherwise, one of the coefficients responsible for λ distribution is varied. Each time, the varied parameter is randomly chosen on the basis of a uniform law. Then the fields of flow parameters are recalculated from the cells of the old grid to the cells of the new one, using the following approximation formula:

$$\varphi(\xi, \eta) = k_0 + k_1 \xi + k_2 \eta + k_3 \xi \eta,$$

where k_0, k_1, k_2, k_3 are determined from the conditions

$$\varphi(0,0) = \varphi_{i-1,j-1}, \quad \varphi(1,0) = \varphi_{i,j-1},$$

$$\varphi(0,1) = \varphi_{i-1,j}, \quad \varphi(1,1) = \varphi_{i,j}.$$

Here φ_{ij} is the value of φ in the center of the (i,j)-th cell, $\varphi = (u, v, \rho, E)$, u, v are the components of velocity vector \vec{w} , E is the total energy.

$$\xi = \frac{x - x_{i-1}}{x_i - x_{i-1}}, \quad \eta = \frac{y - y_{j-1}}{y_j - y_{j-1}}.$$

After that, a step Δt_n is made. The functional \tilde{F}^n is calculated. If $\tilde{F}^n < F^n$, the next iteration is performed on a new grid, otherwise, a step Δt_{n+1} is made on the old grid.

As a result, beginning from some time moment T , we obtain a solution of the problem of flow with the number of cells at the body surface equal or greater than a prescribed value (satisfaction of this condition provides the second term in the functional relation), which realizes the minimum energy dissipation.

Results. The flow around a cylinder was calculated for the following parameters:

$$D=1, \quad L=17, \quad H=9, \quad L_1=-8, \quad L_2=9, \quad x_c=-2.8.$$

The gas parameters in the channel are normalized to the corresponding parameters of gas 1, the linear dimensions are normalized to the cylinder diameter.

The following initial conditions were used:

$$p_1=0.73, \quad p_2=0.44, \quad \rho_1=1, \quad \rho_2=0.6, \quad J_1=J_2=2.0, \quad N_{x1}=35, \quad N_{x2}=55, \quad N_{y1}=45$$

A total of 8100 cells were used. The number of nodes on the body for a fixed grid was taken equal to their number obtained by solving the problem on a variable grid. The splitting is piecewise-uniform.

For the same time moments the fixed and variable grids are presented in Figs. 1 and 2. Figure 3 and 4 show the corresponding Mach number distributions. The grid is shown in the vicinity of the body, while the Mach number is presented for the entire computational domain. Two vortices formed as a result of flow separation from the cylinder surface are seen in Fig. 3. The separation region length on the cylinder is $\sim 20\%$ of its diameter. $\Delta P_f \sim 1$ on the body, and $\Delta \overline{P_f} \sim 10^{-3}$ in the domain. The calculations on a variable grid yield $\Delta P_v \sim 10^{-2}$, $\Delta \overline{P_v} \sim 10^{-4}$. It is seen in Fig. 4 that there are no large-scale vortices, and the separation region length is less than 10% of the cylinder diameter. The residuals of the mass and energy conservation laws in both calculations for a time moment T are

$$d\overline{m}_f = 7.10^{-3}, \quad d\overline{E}_f = 4.10^{-2}, \quad d\overline{m}_v = 1.10^{-3}, \quad d\overline{E}_v = 8.10^{-3}$$

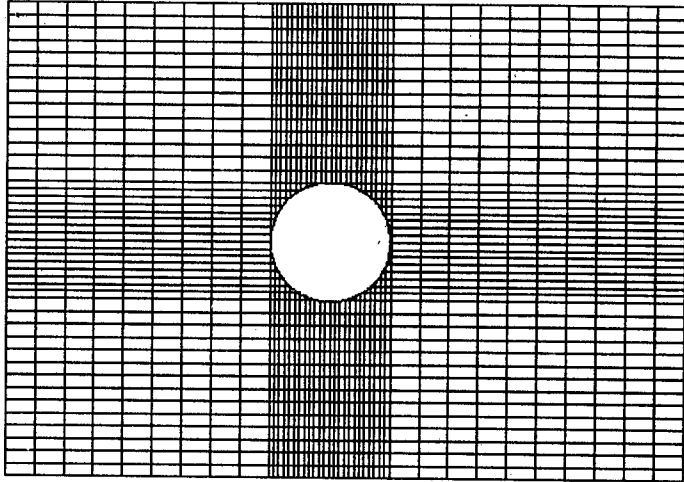


FIG. 1

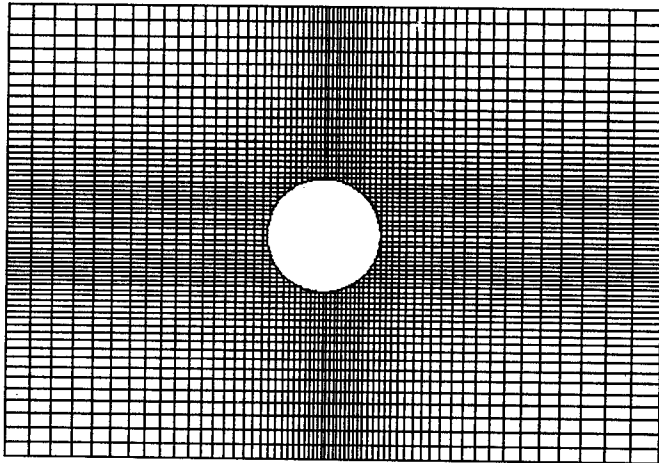


FIG. 2

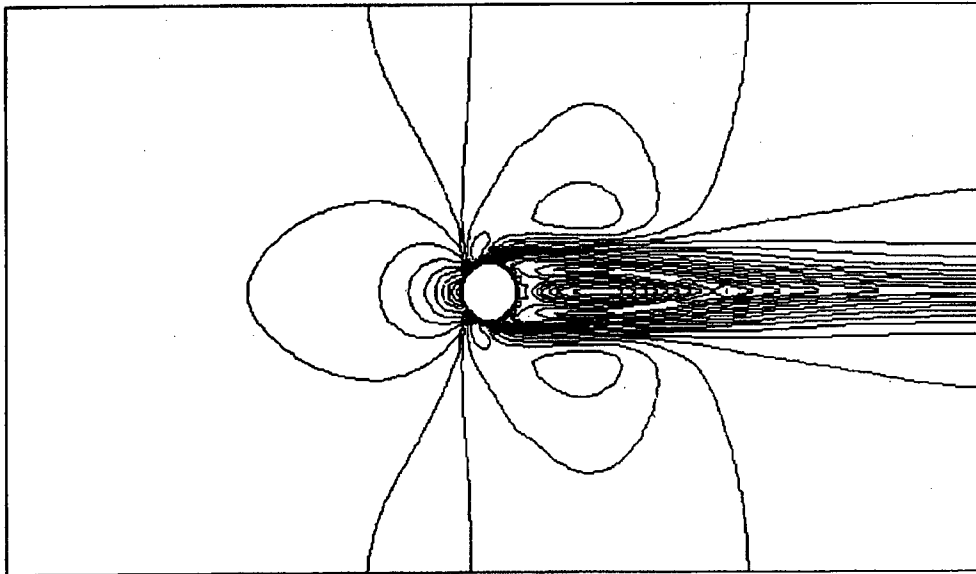


Fig. 3

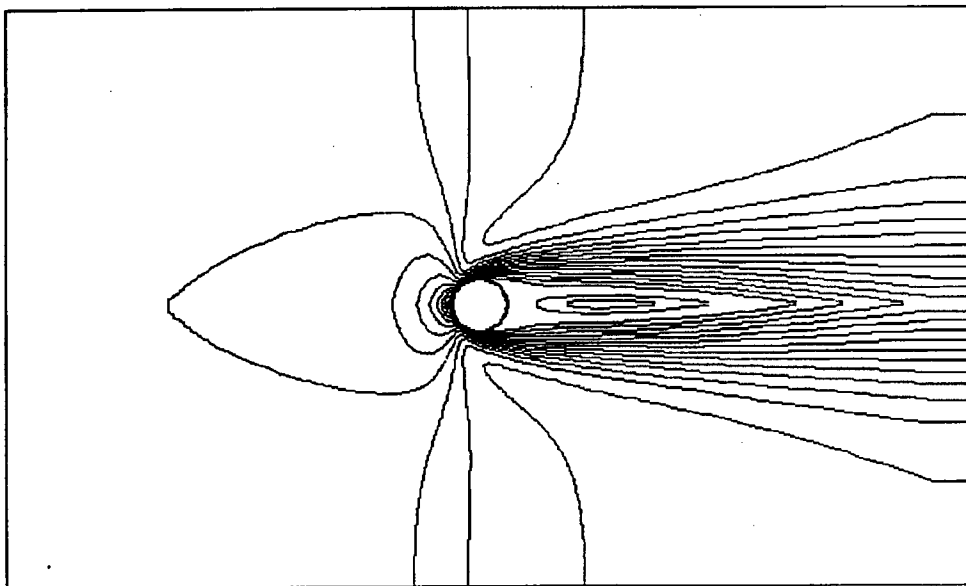


Fig. 4

on fixed and variable grids, respectively. The value of T being set, the time spent for computing the problem on a variable grid is approximately three times larger than that for the problem on a fixed grid.

The researches described in this publication was made possible in part by Grant № 96-01-01548, from the Russian Foundation of Fundamental Researches.

References

1. O.M.Belotserkovsky and Yu.M.Davydov. Method of Coarse Particles in Gas Dynamics. Moscow: Nauka, 1982. 331 p.
2. J.F.Thompson, Z.U.A.Wars and C.W.Mastin. Numerical Grid Generation Foundations and Applications. Amsterdam: North-Holland, 1985. 483 p.

AN EXPERIMENTAL STUDY OF THE STREAKY STRUCTURES INTERACTION WITH THE HIGH-FREQUENCY DISTURBANCES

A.A. Bakchinov, G.R. Grek, M.M. Katasonov & V.V. Kozlov

Institute of Theoretical and Applied Mechanics SB RAS,
630090, Novosibirsk, Russia

INTRODUCTION

Smoke-visualization of the laminar-turbulent transition at high freestream turbulence (HFST) for so-called natural conditions demonstrates that a boundary layer is modulated in transverse direction by some longitudinal localized structures which start to develop from the leading edge of model [1-3]. These structures are identified as the "streaky structures" in a scientific literature [2]. Downstream development of the streaky structures leads up to the turbulent spots origination. Mechanism of the streaky structures appearance, their development characteristics and a role of these disturbances for the turbulent spots generation are so far not clear from information obtained in the experiments under "natural" conditions. In these studies were obtained data indicating of existence the disturbances with the development characteristics which are different from the characteristics of Tollmien-Schlichting (T-S) waves [4]. The general conclusion of these investigations is the laminar-turbulent transition at HFST ($\epsilon \geq 1\%$) and low free stream turbulence (LFST) ($\epsilon \leq 0,04\%$) are differed in principle. Professor M.V. Morkovin claim that at HFST levels above 1%, T-S waves play no role in transition, and suggest that some other, as yet unknown, mechanism is at work, termed to them "by-pass" mechanism [5]. However, the usefulness of this concept is limited, since that can not to explain many phenomena observed in this case and, as wrote Professor E. Reshotko [6], "...Unfortunately, at higher freestream disturbance levels the boundary layer transition process is not very well understood..."

A few new data about the HFST transition were obtained by generating controlled "model" disturbances. Experiments [7,8] were demonstrated that T-S waves can exist, develop in a similar way as in an LFST and influence on the transition both in a flat plate and to 2-D gradient boundary layer up to $\epsilon = 4\%$. The localized longitudinal structures were artificially generated into the flat plate boundary layer by means of their excitation by impulsive "injection or suction" of air both on the flat plate wall and from freestream. The latter case reproduced the localized disturbances from a HFST. Qualitative and quantitative characteristics of these disturbances ("puffs"- streaky structures) were studied [8,9].

Interaction mechanism of the localized disturbances with the T-S waves result in appearance of the increasing wave packets which developed into the turbulent spots downstream was studied in [8]. Smoke-visualization of the localized disturbances introducing in a boundary layer both from the wall [3] and freestream [2] demonstrated that ones can be identified as streaky structures observed in a "natural" transition at the $\epsilon \geq 1\%$. On the other hand, visualization pictures clear showed the high-frequency wave packets existence on the streaky structures [2]. The same picture is observed for case, when the artificially T-S wave was introduced into a disturbed boundary layer [3]. Waves interacted with the streaky

structures and this process led to high-frequency wave packets origination, which transformed downstream into the turbulent spots.

Therefore, we can suggest that present modelling of a transition mechanism at the high freestream turbulence, which is connected with the transformation of outer localized disturbances into the specific longitudinal structures of a boundary layer and appearance on their high-frequency wave packets developed in the turbulent spots reflects the real processes observed at a natural transition under HFST.

The main aim of a present work is the investigation of an interaction between longitudinal localized structures with a high-frequency disturbances and reception of detailed information about structure and development characteristics of disturbances originated in this situation.

1. Experimental set-up and measurement technique

The experiments were performed in the MT-324 wind tunnel at the Institute of Theoretical and Applied Mechanics (ITPM), Novosibirsk, Russia. It is closed return tunnel, with a 800 mm long test section of 200×200 mm cross-section, preceded by a contraction with ratio 17:1.

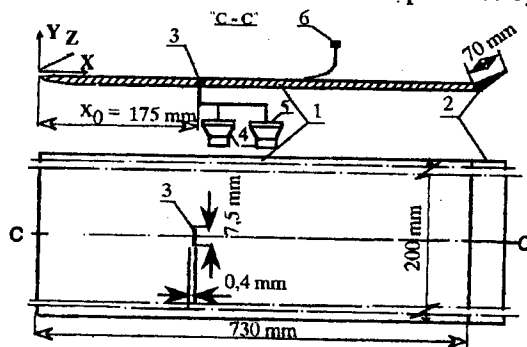


Figure 1. Experimental set-up.

A general sketch of the set-up is shown in figure 1. The experiments were carried out on a 730 mm long flat plate (1) with a 70 mm long flap (2) for adjustment of the stagnation line. The streamwise, wall-normal and spanwise directions are denoted X, Y and Z respectively. Measurements were undertaken in the region between 200 and 550 mm from the leading edge ($X=0$), at free stream speed ($U_{\infty}=6,6$ m/s). Localized disturbances ($f=1\div 2$ Hz) were excited by introducing a short duration jet through a narrow transverse slit (3) by means of dynamic loudspeaker (4), as shown in figure 1. High frequency periodic waves ($f=205$ Hz) were excited by similar method but by means of dynamic loudspeaker (5), as shown in figure 1. Disturbances can be introduced both separately and simultaneously through the same a narrow transverse slit (3), positioned at $X_0=175$ mm. The same function generator was used both for the high frequency periodic waves generation and the triggering of the localized disturbance, giving a definite phase relation between the two disturbances.

The streamwise velocities were measured with constant-temperature hot-wire anemometer, using a single probe (6). In the present paper the structure of the disturbances is presented as contour plots showing (Z-t) plane at the $X=335$ mm, i.e. measured in the spanwise direction (Z) and with time (t) as the second variable. The distributions show the streamwise disturbance velocity, which is defined as the deviation from the local mean velocity in the undisturbed flow. Since the study is focussed on the behaviour of the deterministic part of the

signal, ensemble averaging was carried out at each measurement point. The measured (Z-t)-distributions were decomposed by temporal and spatial Fourier transforms. Spanwise wave number $\beta (=1/\lambda_z)$ is normalized by boundary layer thickness (δ). The mean velocity profiles in the undisturbed flow are close to the Blasius distribution, which can be observed already at $X=25$ mm. The zero pressure gradient was observed in the region of present measurements.

2. Results of measurements

As observed in oscilloscope traces of the present work the amplitude of the localized disturbance is decaying downstream, although the initial amplitude is high ($\approx 5\% U_\infty$). Also the high frequency wave is continuously damped, but it has the low initial amplitude ($\approx 0,5\% U_\infty$). However, when the two disturbances are generated simultaneously, the total disturbance amplitude is increased as the interaction of these disturbances leads to increasing wave packet origination. Further downstream the evolution of the wave packet becomes more stochastic and it evolve into the turbulent spot.

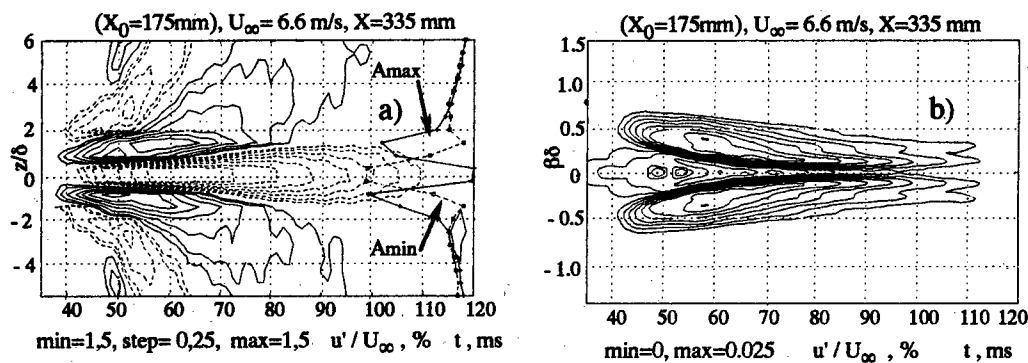


Figure 2. Contour diagrams of constant velocity fluctuation for localized disturbance presented in z/δ - t - (a) and $\beta\delta$ - t - (b) planes at $X=335$ mm ($Y=Y(u'_{max})$)

Figure 2 shows the downstream development of the localized disturbance at $X=335$ mm that obtained for the case of air injection. The spanwise u' -distribution are measured at Y -position corresponding to the maximum perturbation amplitude on the centerline. The aim of this part experiment was to generate a localized disturbance similar with characteristics resembling the streamwise streaks which can be observed at HFST. The structure of disturbances is a negative streak on the centerline surrounded by two positive regions. The spectrum shown in figure 2(b) are obtained from Fourier transformation of the corresponding velocity distributions in figure 2(a). In the initial X -position the two specific scales are detected with different periodically along spanwise direction. The first scale is $\beta\delta = \pm 0,5$ at $t = 40$ - 60 ms and second scale is $\beta\delta = \pm 0,2$ at $t=75$ - 110 ms. Numerical work [10], where the evolution of the localized disturbance was studied, shows that a $\beta\delta = 0,5$ correspond to the streaky structures and a $\beta\delta=0,2$ correspond to the oblique waves. Therefore, the disturbances with the periodically ($\beta\delta=\pm 0,5$) are streaky structures and disturbances with the periodically ($\beta\delta = \pm 0,2$) are oblique waves. The oblique waves are generated by the streaky structures when they propagate downstream. Oblique waves can be observed in figure 2(a) as the few positive contours located at outside of the streaky structures (from $z/\delta = \pm 2$ to $z/\delta = \pm 6$). It is known, that Λ -structures [11] or turbulent spots [12] generate the oblique waves. Probably, the present situation reflects the same phenomenon.

Figure 3 shows that is obtained when the high-frequency wave interacts with the localized disturbances at the same X-position. It is seen, that structure of the disturbance is strong changed. Maximum value of the disturbance amplitude (38%) increased more than ten times in comparison with the same parameter for the streaky structures in the absence of the high-frequency wave (3%). The disturbance localization in spanwise direction increases that is seen both from figure 3(a) ($z/\delta \approx \pm 0,65$ in comparison with $z/\delta \approx \pm 0,9$ in figure 2(a)) and from distribution $\beta\delta=f(t)$ in figure 3(b) ($\beta\delta = \pm 0,6$ in comparison with $\beta\delta = \pm 0,5$ in figure 2(b)).

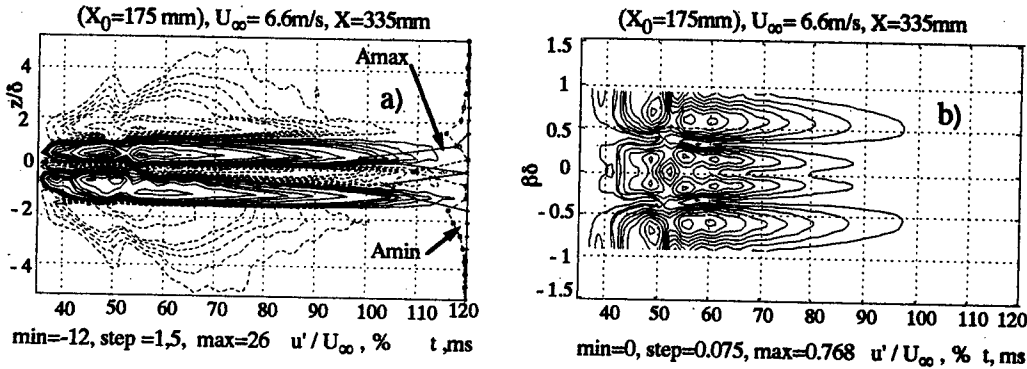


Figure 3. Contour diagrams of constant velocity fluctuation for the localized disturbance interacted with the high-frequency waves presented in z/δ - t - (a) and $\beta\delta$ - t (b) planes at $X=335\text{mm}$ ($Y=Y(u'_{\text{max}})$)

The wave packet generating by disturbances interaction develops on the streaky structures. It is clear seen in figure 3(a) and especially in figure 4, where the spatial-temporal surface - $u'=f(z/\delta, t)$ obtained from figure 3(a) is presented. Presence of the wave packet with frequency of about 170 Hz reflects the toothed view of plot in region of the disturbance amplitude maximum (a few peaks on the streaky structures in figure 4). Intensity maximum location of the high-frequency disturbances coincided with a position of the velocity gradient maximum along spanwise direction ($\partial u/\partial z$). Position of velocity gradient maximum in spanwise direction (see in figure 2(a)) and intensity maximum location (see in figure 3(a)) are coincided at $z/\delta \approx \pm 0,6$. The intensity growth of secondary high-frequency disturbances in region at maximum velocity gradient ($\partial u/\partial z$) for the flow modulated by stationary vortices was demonstrated in work [13].

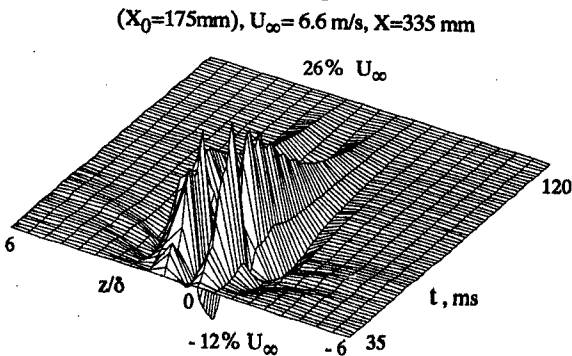


Figure 4. Spatial-temporal picture of $u'=f(z/\delta, t)$ for the interacted disturbances at $X=335\text{mm}$.

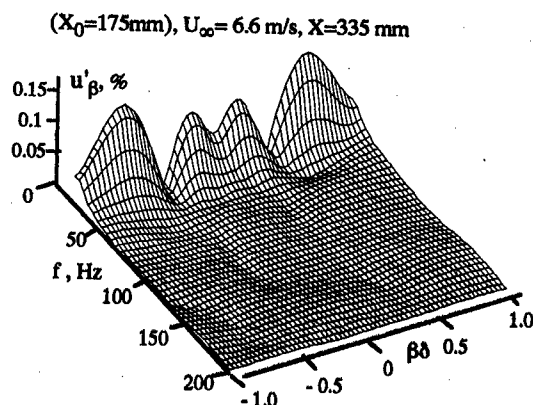


Figure 5. Spectral decomposition $u'_{\beta} = F(f, \beta\delta)$ of the spanwise distribution for the interacted disturbances at $X=335\text{mm}$

Distribution of $u'\beta = F(\beta\delta, f)$ shows that the highest amplitudes of disturbance occurs within a low frequency range ($f \approx 0 \div 25\text{Hz}$) especially for the disturbances with a periodically along spanwise direction, which is $\beta\delta = \pm 0,6$ and it characterizes the streaky structures (see figure 5.). Hence, the spatial-temporal Fourier-analyse demonstrates that the high-frequency disturbances in a process of interaction result in transfer of mean flow energy to the low-frequency streaky structures. The redistribution of energy to lower frequencies is seen more clearly in figures 3 and 4, which shows a large increase in the low-frequency disturbances (streaky structures) intensity and development of the high-frequency wave packet on them. Namely, the high-frequency wave packet developed in region of the leading edge of the streaky structures transforms into the turbulent spot downstream.

CONCLUSIONS

The above observations can be summarized as follows:

1. Interaction of the decreasing localized disturbance and high-frequency wave leads to the generation the high-frequency wave packet which is transformed into the turbulent spot downstream.
2. Mechanism of the disturbances interaction results in increase of the streaky structures transverse localization ($\beta\delta = \pm 0,6$), increase their intensity and downstream duration and the high-frequency fluctuations appearance in region their leading edge.
3. The redistribution of mean flow energy to lower frequencies by means of high-frequency disturbance results in large growth of the streaky structures intensity.

These experiments were made possible by the financial support of the Russian Foundation for Fundamental Researches under Grants 96-01-01892 and 96-15-96310.

REFERENCES

1. Gulyaev, A.N., Kozlov, V.E., Kuznetsov, V.R., Mineev, B.I., & Secundov, A.N. Interaction of a laminar boundary layer with external turbulence // *Izv. Akad.Nauk SSSR, Mekh. Zhid. i Gaza* №5, P. 55-65 (English transl. *Fluid Dyn.*-1990. -V.24(5).- P. 700-710).
2. Alfredsson P.H., Bakchinov A.A., Kozlov V.V. & Matsubara M. Laminar-turbulent transition structures at a high level of a free stream turbulence // *IUTAM Symposium on Nonlinear Instability and Transition in Three-Dimensional Boundary Layers: Proc. Manchester, U.K.,(Ed. P.W. Duck), July, 1995. -P. 423-436.*
3. Matsubara M., Kozlov V.V., Alfredsson P.H., Bakchinov A.A. & Westin K.J.A. On flat plate boundary layer perturbations at high free stream turbulence level // *Int. Conf. on the Methods of Aerophysical Research: Proc. Novosibirsk, 1996. Pt. 1, -P. 174-179.*
4. Kosorygin, V.S., Polyakov N.Ph., Suprun, T.T. & Epic E.Ya. Development of disturbances in the laminar boundary layer on a plate at high level of free stream turbulence.// *In Instability of Subsonic and Supersonic Flows, -P. 85-92. Institute of Theoretical and Applied Mechanics, Siberian Branch of USSR Academy of Sciences, Novosibirsk, 1982 (in Russian).*
5. Morkovin M.V. Bypass transition to turbulence and research desiderata // *Transition in Turbines. NASA Conf. Publ. 2386. 1984. -P. 161-204.*

6. Suder K.L., O'Brien J.E., Reshotko E. Experimental study of bypass transition in a boundary layer // NACA Rep. 100 913, 1988. -P. 189.
7. Grek, G.R., Kozlov. V.V. & Ramasanov, M.P. Laminar-turbulent transition in the presence of high level of free stream turbulence // Preprint No, 8-87, USSR Academy of Sciences, Institute of Theor. and Appl. Mechanics, Novosibirsk, 1987 (English transl. Fluid Dyn. -1988.- V.6 (23). - P. 829-834).
8. Grek, G.R., Kozlov. V.V. & Ramasanov, M.P. Laminar-turbulent transition in the presence of high level of free stream turbulence: Review // Izv.Sib. Otdel. Akad.Nauk SSSR, Ser. Tehn. Nauk. 1991. №6. -P. 106-137 (in Russian).
9. Bakchinov, A.A., Grek, G.R., Katasonov, M.M & Kozlov. V.V. 1997a. Experimental study of the process of localized disturbances development and structure in a boundary layer on a flat plate // Preprint No. 1-97, ITAM, Russian Academy of Sciences Novosibirsk, Russia. (in Russian).
10. Breuer K. S., Landahl M.T. The evolution of a localized disturbance in a laminar boundary layer. Pt. 2. Strong disturbances // J. Fluid Mech. -1990. -V.220. -P. 595-621.
11. Grek, G.R., Kozlov. V.V. & Ramasanov, M.P. Modelling of turbulent spot origination from nonlinear wave packet // Modelling in Mechanics. T. 3(20). No. 1. -Novosibirsk: ITPM i VC SOAN SSSR. 1989. -P.46-60. (in Russian).
12. Wignansky I., Haritonidis J.H., Kaplan R.E. On a Tollmien-Schlichting wave packet produced by a turbulent spot // J. Fluid Mech. -1979. -No. 92. -P. 505-528.
13. Bakchinov, A.A., Grek, H.R., Klingmann, B.G.B. & Kozlov, V.V. Transition experiments in a boundary layer with embedded streamwise vortices // Phys. Fluids.-1995. -V.7(4). - P. 820-832.

A METHOD OF EXPERIMENTAL STUDY OF VIBRATIONAL RECEPTIVITY OF A BOUNDARY LAYER ON A CURVED WALL

S. Bake¹, A.V. Ivanov², Y.S. Kachanov², H.H. Fernholz¹

1) Hermann-Föttinger Institut, Berlin Technical University, Berlin, Germany

2) Institute of Theoretical and Applied Mechanics, Novosibirsk, Russia.

1. INTRODUCTION

The problem of the boundary-layer receptivity to external perturbations represents a very important aspect of a more general problem of the turbulence onset (see for review [1,2]). The data available at present give possibility to suggest that the following external perturbations can be regarded as the most dangerous ones for the laminar boundary layer transition: (i) free-stream vortices, (ii) acoustic waves, (iii) surface vibrations, (iv) steady surface non-uniformities, and (v) steady free-stream non-uniformities. The unsteady perturbations (i) to (iii) can be equally important in both the 2D and 3D boundary layers, while the steady disturbances (iv) and (v) are important mainly in 3D boundary layers. The present paper is devoted to a study of the aspect (iii) of the problem, namely — the problem of generation of the 3D instability waves by localized surface vibrations in the 2D boundary layer on a concave (in the spanwise direction) wall. The flow under investigation is very close to the Blasius boundary layer but it has a weak favorable streamwise pressure gradient and a spanwise curvature of the surface.

The problem of the Blasius boundary layer receptivity to 2D surface vibrations was studied experimentally [3] and theoretically [4,5] (see also for review [6]). At the same time, there are still few experimental studies of the boundary layer receptivity to *three-dimensional* disturbances. Such investigations have been started relatively recently and their results give usually a qualitative information which, as a rule, can not be used for a direct comparison with theoretical approaches and for a validation of the methods of the receptivity calculations. First quantitative experimental study of the 2D boundary layer receptivity to 3D perturbations was performed in [7] where the receptivity of the flat-plate boundary layer to surface vibrations was investigated. The goal of the present study was to carry out similar experiments but in another wind tunnel and in presence of the spanwise wall curvature. In the present paper we concentrate on a method of this study that was significantly improved as compared to the previous experiments. The new method gives possibility to obtain a necessary experimental information in a more reliable way.

2. EXPERIMENTAL PROCEDURE AND MEAN-FLOW STRUCTURE

2.1. Experimental set-up and basic flow. The experiments were carried out at low-turbulence wind-tunnel 'LaWiKa' at the Hermann-Föttinger Institute of Berlin Technical University (Fig. 1). The wind-tunnel test section is axisymmetric and made of Plexiglas tubes with an inner diameter of 441 mm and a total length of 6000 mm. The wind-tunnel has a nozzle contraction-ratio 18:1 over a length of 2 m and the boundary-layer of the nozzle is sucking out in the beginning of the test section. The experiments were conducted in the laminar boundary-layer that starts at an elliptic leading edge of the test section and develops downstream on its inner wall (see Fig. 1). The free-stream velocity U_0 was equal to 7.4 m/s.

Shown in Fig. 2 is a set of the mean-flow velocity profiles measured in the boundary-layer by a hot-wire anemometer at different streamwise positions. These distributions are seen to be very close to the Blasius profile (also shown in Fig. 2) despite a presence of a very weak favorable streamwise pressure gradient observed in the potential flow and conditioned by a growth of the boundary-layer on the test-section walls. Under the conditions of the present experiment the free-stream turbulence level in the test section was below 0.08% in a frequency range between 0.1 and 1000 Hz.

2.2. Disturbance excitation. The investigation of the boundary layer receptivity was performed under controlled disturbance conditions. In contrast to previous experiment [7], two

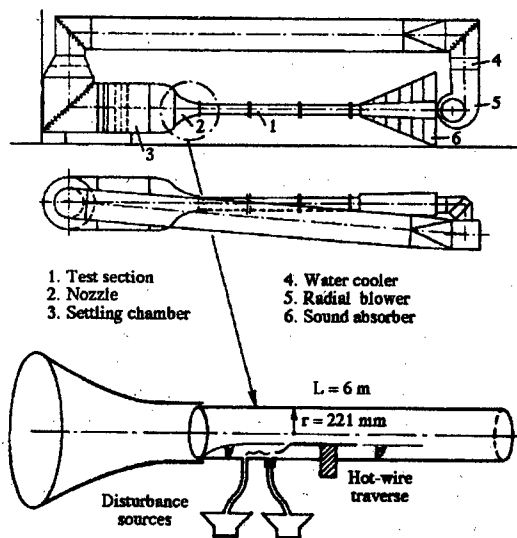


Fig. 1. Wind-tunnel 'LaWiKa' and sketch of measurements.

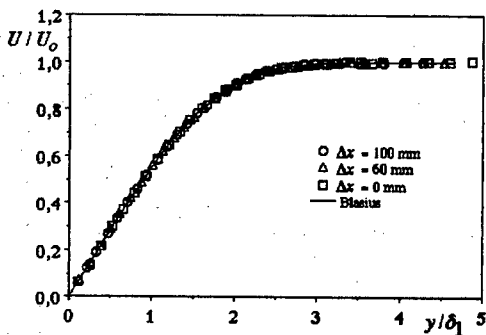


Fig. 2. Mean velocity profiles in boundary layer.

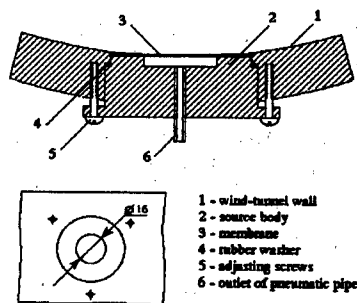


Fig. 3. Sketch of the main source (surface vibrator).

disturbance sources were used in the present study. The first (the main) sources represented a surface vibrator 16 mm in diameter mounted flush with the wall (Fig. 3) at a spanwise position $z = 0$ and a streamwise position $x = x_{s1} = 647$ mm from the leading edge. The second (an additional) disturbance source was a slit generator [8] that worked in a 'point-source' regime. It was positioned at the same spanwise coordinate ($z = 0$) but 100 mm upstream from the first one at a streamwise coordinate $x = x_{s2} = 547$ mm. By means of plastic pipes the two sources were connected with loudspeakers that were excited by signals produced by a computer, D/A converters, and power amplifiers.

The sources were used one after another and excited in the flow wave-trains (consisted of the boundary-layer instability waves), i.e. harmonic in time and localized in span perturbations. Three different disturbance frequencies were investigated $f_1 = 37.8$ Hz, $f_2 = 55.7$ Hz, and $f_3 = 75.0$ Hz which corresponded to the values of the non-dimensional frequency parameter $F = 2\pi f\nu/U_0^2$ of $F_1 = 66.2 \cdot 10^{-6}$, $F_2 = 97.9 \cdot 10^{-6}$, and $F_3 = 131.7 \cdot 10^{-6}$ respectively. At the position of the main source the boundary layer displacement thickness δ_1 was equal to 1.84 mm and the local Reynolds number $Re = U_0\delta_1/\nu = 890$.

2.3. Procedure of measurements. In the present experiments there were two kinds of measurements: (a) in the flow measurements and (b) a study of the vibrator shape.

All measurements in the flow were conducted by means of a constant-temperature hot-wire anemometer with a linearizer. A single-wire probe measured the streamwise component of the time-mean and fluctuation velocities of the flow. The probe with the wire of 5 μ m diameter and

1 mm active length was mounted on an x - y traverse. The spanwise displacement was provided by rotation of the inserts with the disturbance sources around the wind-tunnel axis. The hot-wire signal was sampled and analyzed with a Tektronix Fourier analyzer. In each spatial point the following values were documented: (i) the mean flow velocity, (ii) the r.m.s. disturbance amplitude, and (iii) the disturbance phase.

The shape of oscillations of the vibrator (the main source) was investigated carefully. In contrast to the previous experiments [7] a field of the membrane displacements was measured directly by means of the laser vibrometer "Polytec OFV 1102" without a procedure of an integration of spatial distributions of the surface inclination angle used in [7]. The membrane shape was studied at various amplitudes and frequencies of excitation. During the wind-tunnel tests the amplitude and phase of the vibrations were under a permanent control.

The experiments were carried out in the following order. After the calibration of the vibrator this source was used for the main receptivity measurements (similar to experiment [7]) performed for all three disturbance frequencies. During these measurements three sets of spanwise distributions of the disturbance amplitudes and phases were documented for each fixed frequency at several streamwise positions downstream the vibrator (starting with $\Delta x = x - x_{s1} = 60$ mm). The measurements were performed at a fixed non-dimensional distance to the wall $y/\delta_1 = 0.86$ ($U/U_o = 0.435$) that was close to the amplitude maxima in the instability-wave y -profiles. After Fourier decomposition of the wave trains the information on the downstream behaviour of the normal-mode amplitudes and phases was obtained for each studied value of the frequency and the spanwise wavenumber (or the wave propagation angle). The procedure of the decomposition is described in [9].

After the measurements with the main source the second source was used. With the help of it information about the stability behaviour of the normal oblique modes in the near-field of the main source was obtained. The matter is that to determine the receptivity coefficients it is necessary to know the initial spectra of the Tollmien-Schlichting (T-S) modes at the position of the main source (the vibrator). It is impossible to obtain this data directly from measurements with the main source because of a presence of other modes in the near-field of the vibrator (like the continuous-spectrum instability modes and the bounded fluctuations produced by the surface vibrations). In previous experiment [7] the initial spectra of the T-S waves were 'reconstructed' at the source position by means of an upstream extrapolation of the spectra obtained downstream from the vibrator. An accuracy of such extrapolation is not very good. That is why in the present experiment instead of the extrapolation an experimental information about the downstream growth of the normal-mode amplitudes and phases in the vicinity of the main source was used. This information was obtained after measurements of sets of spanwise distributions of the disturbance amplitude and phases generated by the second source. The measurements were performed for each studied frequency at several streamwise positions including the position of the main source. Some of these positions overlapped with those used in the measurements with the main source.

3. RESULTS OF MEASUREMENTS

3.1. Properties of surface vibrator. The measurements of the shape of oscillations of the surface vibrator (the main source) have shown that the amplitude (A_m) and phase of the oscillations are independent for this vibrator on both the frequency and the amplitude of excitation (in the range studied). A three-dimensional shape of oscillations of the main source is presented in Fig. 4 in (x, z, A_m) -space. The shape turned out to be axisymmetric in practice. The experimentally measured distributions of the vibrational amplitude along the source radius $A_m(\rho)$ were approximated with an eight order polynomial. The coefficients of this polynomial were used for determining the 2D wavenumber spectrum of the surface vibrations the amplitude part of which is shown in Fig. 5. The spectral phase (not shown) is constant within the central cupola and the every ring but jumps by π when crossing the circles of the amplitude minima. This spectrum is necessary for determining the vibrational receptivity coefficients.

3.2. Normal-to-wall disturbance profiles. A set of the y -profiles of the flow-velocity disturbance amplitudes and phases measured at the frequency $f = 37.8$ Hz are shown in Fig. 6 for different streamwise distances Δx from the main source along the wave-train axis.

These profiles were obtained at the boundary-layer excitation by means of the main or the second source. It is seen that the profiles measured at $\Delta x = 60$ and 100 mm are qualitatively similar to each other and correspond to a superposition of the eigenfunctions of different normal oblique T-S waves. [Note, that the profiles measured for two different disturbance sources should not coincide with each other because of different spanwise-wavenumber spectra generated by these sources.] At the same time, the profile measured in the near-field of the main

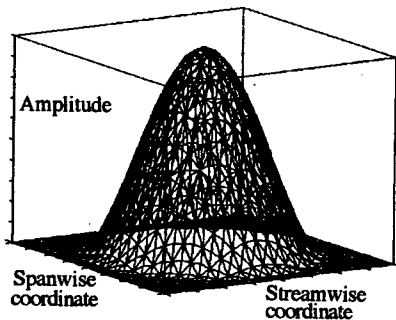


Fig. 4. Shape of vibrator oscillations.

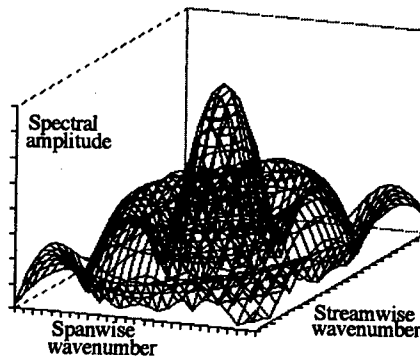


Fig. 5. Wavenumber spectrum of vibrator shape.

source is significantly different from the others because of an admixture in this case of the continuous-spectrum modes and bounded perturbations generated by the surface displacements. This fact shows that it is really impossible to determine directly the initial spectrum of the instability waves and a kind of an upstream extrapolation of the data obtained far enough from the vibrator is necessary. The profiles shown in Fig. 6 demonstrate also that the non-dimensional distance to the wall chosen for the main receptivity measurement ($y/\delta_1 = 0.86$) is really close to the disturbance amplitude maxima. Similar results were obtained of two other disturbance frequencies.

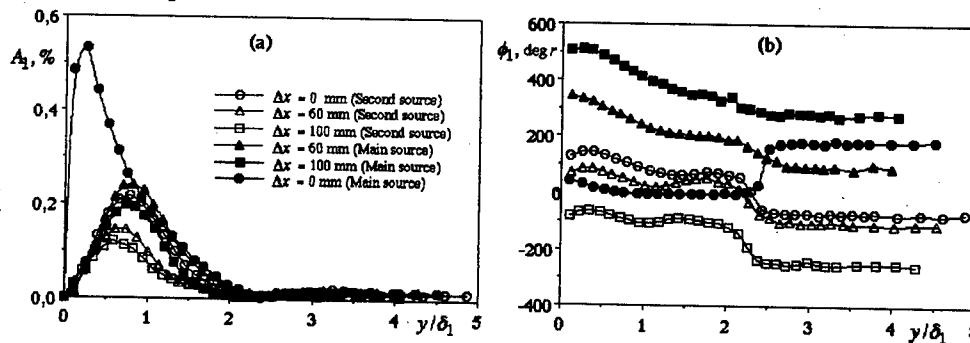


Fig. 6. Normal-to-wall profiles of disturbance amplitude (a) and phase (b) for frequency $f = 37.8$ Hz.

3.3. Spanwise distributions. An example of a result of the main receptivity measurements is presented in Fig. 7 where three spanwise distributions of the disturbance amplitudes and phases are shown for the frequency 37.8 Hz for three streamwise positions. These distributions are obtained for the wave-train generated by the main source (the vibrator). Similar spanwise distributions were measured for the other frequencies and for the wave trains generated by the second source. After Fourier decompositions of these distributions the spanwise wavenumber spectra of the disturbances were obtained (not shown) for all studied regimes of excitation.

3.4. Initial disturbance spectra. As was mentioned above, a determination of the initial spectra of the disturbances generated by the vibrator represents one of the most difficult methodological problem. A new solution of it used in the present experiments is illustrated by Figs. 8 and 9. Shown in Fig. 8 are two examples of the streamwise distributions of the spectral

amplitudes obtained for two normal oblique T-S modes with the frequency $f = 75.0$ Hz and the non-dimensional spanwise wavenumber $\beta\delta_{1s} = 0.09$ and 0.18 . The results obtained for the main source provide the absolute values of the normal-mode amplitudes generated by the vibrator, while the results obtained by means of the second source (positioned upstream from

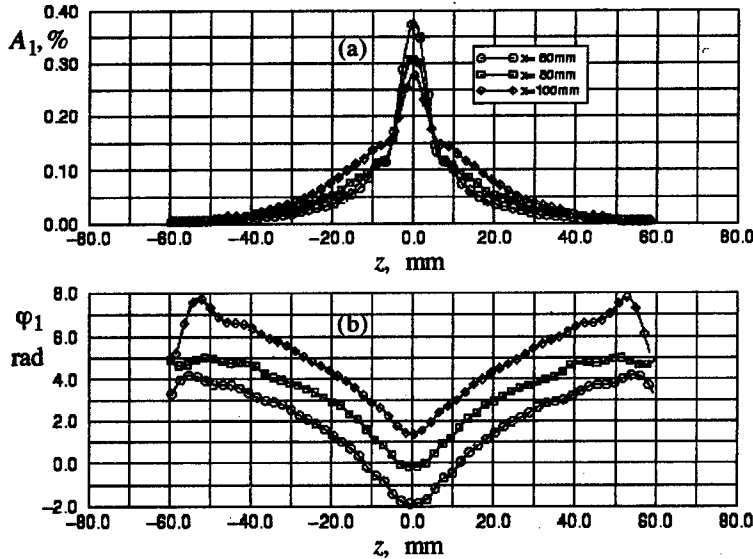


Fig. 7. Spanwise distributions of the disturbance amplitudes (a) and phases (b) in the wave-train generated by the main source at frequency $f = 37.8$ Hz for $\Delta x = 60, 80,$ and 100 mm.

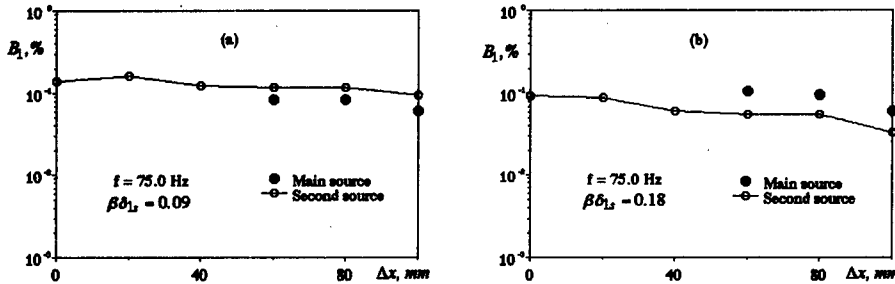


Fig. 8. Streamwise distributions of spectral amplitudes obtained for two normal oblique modes.

the main one) give an information about the streamwise evolution of amplitudes of the same normal modes, including the near-field of the main source around $\Delta x = 0$. It is clear that the absolute values of the spectral amplitudes generated by different sources should not coincide with each other. Meanwhile, and this is of the most importance, the laws of the downstream evolution of the normal modes must be the same for the two sources because they are independent of the method of excitation and depend only on the stability properties of the boundary layer. Using this circumstance we rescale the amplitudes obtained for the second source by means of multiplying them by coefficients $k = k(f, \beta) = B_{1mm}(f, \beta) / B_{1sm}(f, \beta)$, where $B_{1ma}(f, \beta)$ and $B_{1sa}(f, \beta)$ are averaged amplitudes obtained in the range $\Delta x = 60$ to 80 mm for the main and second sources respectively. Such rescaling gives possibility to determine the initial spectral amplitudes generated by the vibrator in a way illustrated in Fig. 9 where the streamwise distributions of the normal-mode amplitudes obtained for the main source are plotted for the two spectral modes (Figs. 9a and 9b, respectively) together with rescaled distributions obtained for the second source.

The initial phased of the normal oblique modes are determined in a similar way. The only difference is that the "rescaling" of the phases of the modes obtained for the second source is

reduced to simple shifts of them by a value $\Delta\phi = \Delta\phi(f, \beta) = \phi_{1mm}(f, \beta) - \phi_{1sm}(f, \beta)$, where $\phi_{1mm}(f, \beta)$ and $\phi_{1sm}(f, \beta)$ are averaged phases obtained in the range $\Delta x = 60$ to 80 mm for the main and second sources respectively.

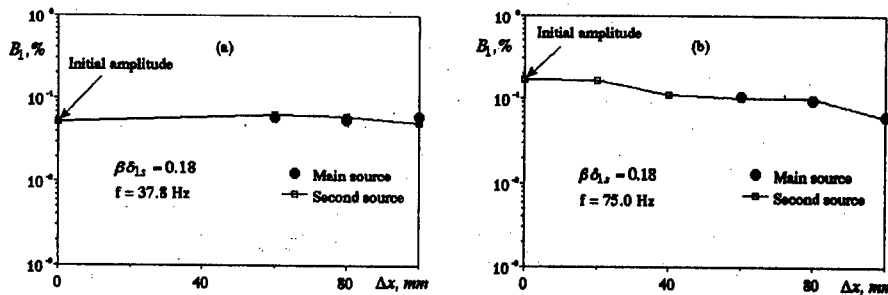


Fig. 9. Procedure of determining the initial normal-mode amplitudes.

3.5. Subsequent analysis of data. Subsequent procedure of the experimental data analysis is similar to that used in previous study [7]. The analysis of the streamwise distributions of the normal-mode phases give possibility to determine the dispersion curves, i.e. the dependences of the streamwise wavenumber on the spanwise wavenumber (for each frequency studied). These curves give possibility to select from the spectrum of the vibrator shape (see Fig. 5) the resonance spectral modes which have the same values of the streamwise and the spanwise wavenumbers as the 3D T-S waves. Finally, the ratio of the initial wavenumber spectrum of the instability modes and the resonant spectrum of the surface vibrations represent a spectrum of the receptivity coefficients that depends on the disturbance frequency and the spanwise wavenumber (or the wave propagation angle).

Conclusion

Thus, the advanced method described above represents an effective tool for the experimental study of the 3D vibrational receptivity of the boundary-layer flow. In contrast to the previously developed methods it gives possibility to increase an experimental accuracy and to avoid uncertainties conditioned by the upstream extrapolation of the experimental data used in the previous studies.

This work is supported by RFBR (grant 98-01-04090) and DFG (grant FE-43/42-1).

References

1. Kachanov Y.S., Kozlov V.V., Levchenko V.Y. Origin of Turbulence in Boundary Layers. - Novosibirsk: Nauka, 1982.
2. Zhigulyov V. N., Tumin A. M. Origin of Turbulence. Dynamic Theory of Generation and Development of Instabilities in Boundary Layers. - Novosibirsk: Nauka, 1987.
3. Gilyov V.M., Kozlov V.V. Excitation of Tollmien-Schlichting waves in the boundary layer on a vibrator / Preprint No 19-83. - Novosibirsk: Inst. Theor. & Appl. Mech., 1983.
4. Terentyev E.D. Linear problem on a vibrator in subsonic boundary layer // PMM. - 1981. - Vol.45, No 6. - P. 1049-1055 (in Russian).
5. Tumin A.M., Fyodorov A.V. Excitation of instability waves by a localized vibrator in a boundary layer // Zhurn. Prikl. Mekh. i Tekh. Fiziki. - 1984. - No 6. - P. 65-72.
6. Kozlov V.V., Ryzhov O.S. Receptivity of boundary layers: asymptotic theory and experiment // Proc. Roy. Soc. London. - 1990. - V. A429. - P. 341-373.
7. Ivanov A.V., Kachanov Y. S., Obolentseva T.G. Experimental investigation of flat-plate boundary-layer receptivity to 3D surface vibrations // Stability and Transition of Boundary-Layer Flows. EUROMECH Colloquium 359. Collection of Abstracts. Stuttgart: Universitat Stuttgart, March 10-13, 1997.
8. Bake S., Kachanov Y.S., Fernholz H.H. Subharmonic K-regime of boundary-layer breakdown // Transitional Boundary Layers in Aeronautics. - Amsterdam: North-Holland. - 1996. - P. 81-88.
9. Kachanov Y.S., Michalke A. Three-dimensional instability of flat-plate boundary layers: Theory and experiment // Eur. J. Mech., B/Fluids. - 1994. - V. 13, No 4. - P. 401-422.

NUMERICAL SIMULATION OF SUPERSONIC TURBULENT SEPARATED FLOWS USING VARIOUS HIGH-RESOLUTION SCHEMES

Bedarev I.A., Fedorova N.N.

Institute of Theoretical and Applied Mechanics SB RAS,
630090, Novosibirsk, Russia

The increasing role of mathematical modeling as an instrument for investigating into complex gas flows imposes more stringent requirements upon numerical algorithm used, which must ensure a solution to be obtained with a guaranteed accuracy in minimum consumed computer time. The primary emphases here is placed upon that the numerical solution be robust. To this end the algorithm properties are investigated on special tests built up either on an exact solutions or on experimental data.

Problems on the boundary layer separation caused by a shock wave interacting with the boundary layer, are the most difficult ones for mathematical simulation. The boundary layer separation is formed as a result of the nonlinear interaction between viscous and nonviscous forces, and, hence, both the mathematical model and numerical algorithm should properly describe the balance between the convection and viscous mechanisms of a physical flow under consideration. The final result depends on how exactly the flowfield structure is resolved, that is determined by the way the convective terms are approximated, as well as on what turbulence model is used to close the averaged equations of gas motion, because it is turbulence which contribute markedly to the viscous forces of the flows under study.

In the paper, the influence of the convective terms approximation method is studied on the capability of algorithm to predict the parameters of supersonic turbulent separated flows. For comparison purposes, several Euler high-resolution finite-difference schemes have been chosen built on different Flux Vector Splitting methods, namely splitting according to physical processes [1], Steger-Warming [2] and Van Leer [3] methods.

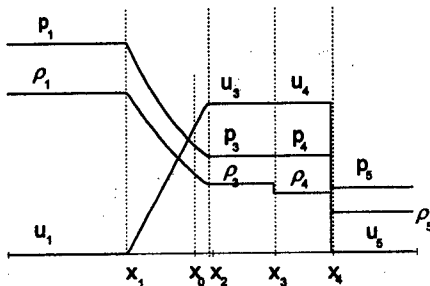


Fig. 1 Sod shock tube test problem.

The properties of algorithms mentioned above were studied first on the Sod shock tube test problem [4]. Two different gas states ($\rho_1=1.0$, $p_1=1.0$, $u_1=0$ and $\rho_3=0.125$, $p_3=0.1$, $u_3=0$) are separated from one another by a diaphragm placed at $x_0=0$. At the moment $t=0$ the diaphragm breaks and a solution gets realized in the shock tube which is plotted in Fig.1. In this Figure, points x_1 and x_2 represent the location of the head and the tail of the rarefaction wave spreading to the left. Point x_3 marks the position of contact discontinuity;

point x_4 is the shock wave location. The following values of parameters correspond to the initial data chosen: $u_3=0.926$, $p_3=0.303$, $\rho_3=0.427$; $u_4=0.926$, $p_4=0.303$, $\rho_4=0.265$. The approximate solution was determined on a uniform finite-difference grid with $\Delta x=0.04$.

Schemes of different orders were used to approximate on the spatial and time variables. Time approximation was conducted within the framework of Runge-Kutta methods, allowing to easily get a required order of accuracy. To improve the space-variable accuracy, the upwind TVD high order approximations were used [5].

The calculations performed have shown that each scheme has its own features, which reveal themselves at the points where discontinuities in the solution or in its derivatives take

place. Figure 2 presents the charts of the exact solution (solid line) and the solutions computed using two different first-order approximation schemes (markers) at time $t=0.8$. It can be seen that the scheme based on the splitting according to physical processes (curve 1) resolves the shock better as well as the rarefaction fan tail, while the Van Leer scheme (curve 2) better predicts the head of the rarefaction fan.

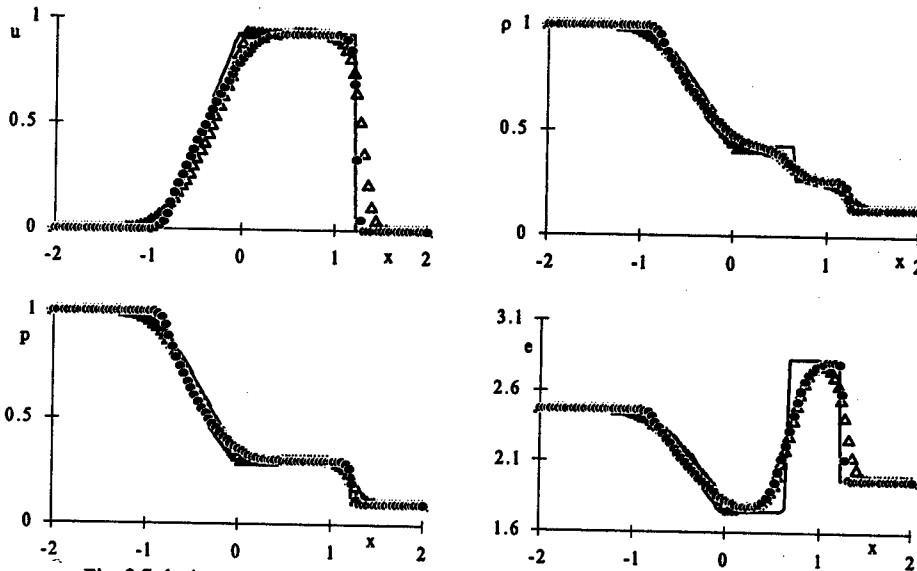


Fig. 2 Solutions computed using two different first-order approximation schemes.
 • — 1, Δ — 2

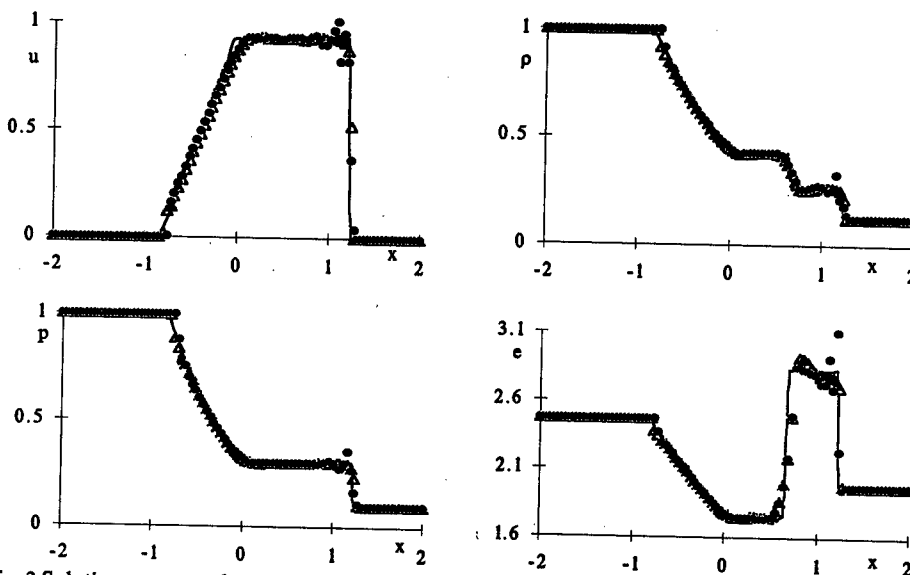


Fig. 3 Solutions computed using second-order space approximation and first- and second-order time approximation.
 • — 1, Δ — 2

Figure 3 presents the results which have been obtained using method [1] of the second-order space approximation and of the first- (1) and the second- (2) order time approximation, respectively. Using a spatial approximation of the second order enables one to properly describe the discontinuities whereas improving the time accuracy makes the scheme more stable.

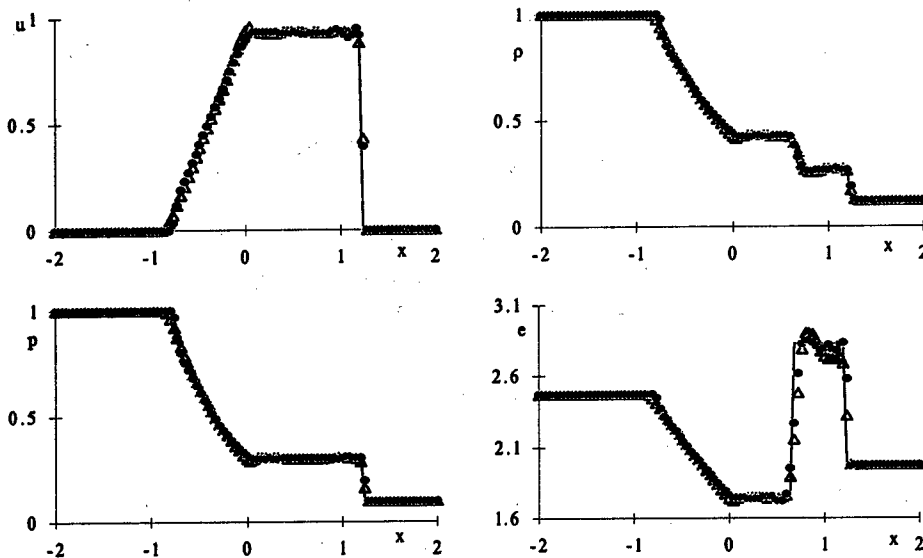


Fig. 4 Solutions computed using the different flux vector splitting with first-order time and third-order space approximation schemes. • — 1, Δ — 2

Figure 4 shows the results obtained with the third-order space and first-order time approximation schemes using different flux vector splitting: 1 and 2 denote methods [1] and [3], respectively. This Figure shows some advantage of scheme [1] over scheme [3] from the viewpoint of shock and contact discontinuity resolution, as well as energy level prediction in the region between the shock wave and the contact discontinuity. The solution obtained with method [3] has slight overshoots at the expansion fan tail. Results of calculations obtained with scheme [2] are omitted, since they lie much close to those of the Van Leer scheme. A drawback of scheme [1] is that, as the Curant number increases, the numerical solution acquires nonmonotonic behaviour near the shock.

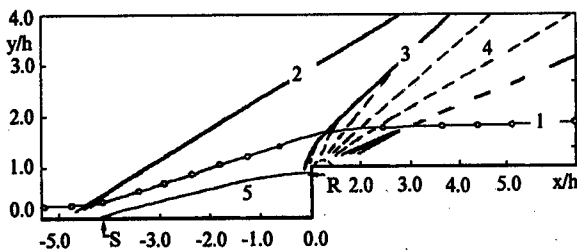


Fig. 5 Experimental flowfield pattern.

The methods tested on the 1-D problem were applied to the approximation of convective terms of the Favre-averaged Navier-Stokes equations and used for numerical simulation of the 2-D problem on the supersonic flow over a forward-facing right step. The calculations were conducted for the conditions of physical experiment [6,7]. Figure 5

represents the experimental flowfield structures, in which 1 is the boundary layer edge, 2 is the separating shock, 3 is the reattachment shock, 4 is the expansion fan formed when flowing around the upper corner of the step, 5 is the large-scale separation zone lying between the separation (*S*) and reattachment (*R*) points.

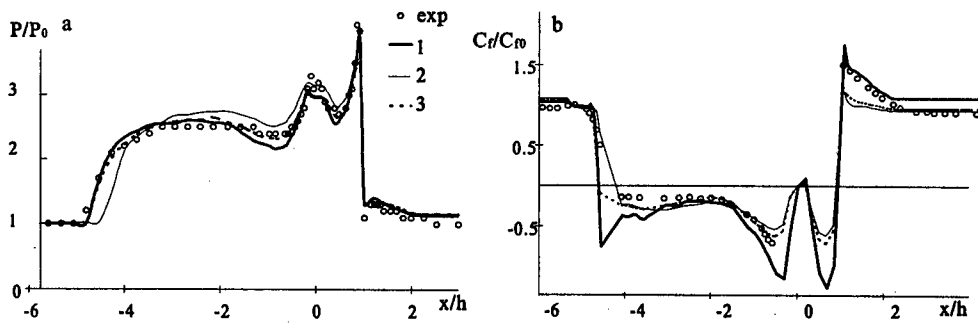


Fig. 6 Experimental and computed static pressure and skin friction distributions (second-order space approximation, $\omega_b=0.38$).

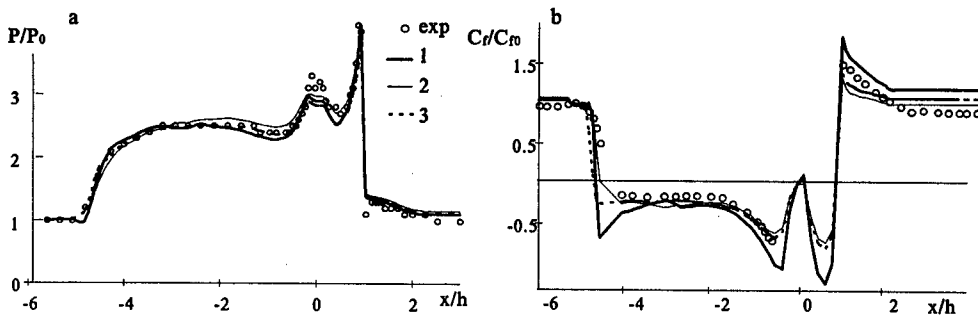


Fig. 7 Experimental and computed static pressure and skin friction distributions (third-order space approximation, $\omega_b=0.27$).

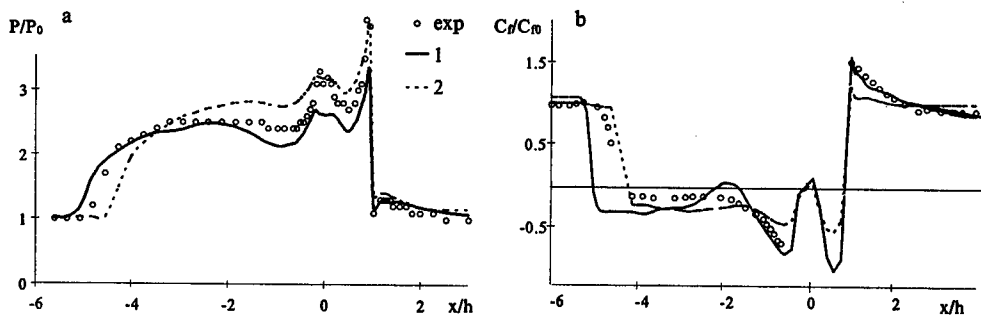


Fig. 8 Experimental and computed static pressure and skin friction distributions (1- third-order space approximation, $\omega_0=0.38$; 2- second-order, $\omega_0=0.27$).

The detailed description of the governing equations, numerical algorithm and results obtained using the scheme [1] is given in [8], where it is demonstrated also that the results of computations depend strongly on the algorithm resolution. In particular, it has been shown

there that the use of the first-order accuracy schemes for the convective terms approximation, brings about a smearing of the separating shock, which in its turn results in the substantially underestimated separation zone scales and, thus, in poorly reproduced flowfield parameters.

Modeling of viscous stresses for developed turbulent flows is determined to a considerable extent by the turbulence model used to close the governing equations. In this paper, the $k-\omega$ turbulence model was used [9]. One of the particularities of usage of this model in calculations is the necessity to apply some limiter to the values of the second turbulent parameter, the specific turbulent kinetic energy dissipation rate $\omega = \epsilon/k$. In this paper, the following condition was used: $\omega \geq \omega_0$. Since in the given turbulence model the relationship $\mu_t \sim k/\omega$ is valid, the limitation of ω values brings about a reduction in the μ_t level in the regions where the turbulent layer interacts with the shock waves and expansion fans. Calculations show that the introduction of the limiter and variation of its value greatly affects the turbulent viscosity distribution and exerts an influence upon the solution behavior.

In Figure 6a,b, the experimental and the second-order scheme computation results are presented on the surface pressure and skin friction distributions for $\omega_0 = 0.38$. Markers show experimental data [6,7], curves 1-3 correspond to the calculations employing different inviscid vector flux splitting methods [1-3]. The axis x is directed along the body surface including the step face, the point $x/h=0$ corresponds to the compression corner, $x/h=1$ is the expansion corner. Figure 6 shows that for the given ω_0 all the schemes used provide a good prediction of the pressure and skin friction distributions. It is necessary to note that the scheme [2] (curve 2) predicts later position of pressure growing and higher level of its plateau. Curve 1 in the C_f plot (Fig. 6,b), which corresponds to the scheme [1], exhibits a local minimum near the separation point not-observable in the experiment. The experimental level of C_f behind the reattachment point ($x/h > 1$) is best predicted by calculations according to scheme [1].

The results presented in Fig. 7 a,b demonstrate a good agreement between the experiment and the calculation results obtained with the third-order approximation schemes. The results of different schemes lie close together, however, the tendencies being retained noted in the preceding Figure. For the third-order schemes, having, as our 1-D test problem calculations have shown, the best resolution capabilities, the agreement with the experiment was achieved upon assuming a smaller value of ω_0 , namely $\omega_0 = 0.27$, which results in higher values of turbulent viscosity than those obtained for $\omega_0 = 0.38$. This can be explained by that the sharp shock wave can separate a more viscous layer, and, vice versa, in order to get a separation in a calculation with the smeared shock, the turbulent viscosity level in the interaction region must be lowered. It is also confirmed by Fig. 8, which presents the results obtained with the third-order scheme [1] calculation for the value $\omega_0 = 0.38$ providing the best agreement with experiment for the second-order scheme, and those obtained with the second-order scheme [3] calculations for $\omega_0 = 0.27$ (curve 2). The second-order scheme smears the shock more strongly, which explains the later onset of pressure growing and higher pressure plateau level. The third-order scheme showing a better resolution capability yields a sharper shock, which, when interacting with a less viscous layer, brings about the formation of a more extent, as compared to experiment, separation zone.

The positive pressure gradient at $x/h < 1$ is a concomitant one for the reverse flow directed from the step face to the separation point. Under its influence, the reverse flow gets relaminarized, i.e. near the rigid wall there arises a zone with low turbulent viscosity level. An intensive recirculative eddy forms inside the separation zone, of that the pressure fall under its core is indicative. The pressure fall under the eddy core is unfavorable for the reverse flow,

and the low-turbulent reverse flow can separate once again when interacting with it. The not-established experimentally the reversed flow secondary separation can be observed in the C_f plot (curve 2) at $x/h=2$.

Figure 9 presents the mean velocity profiles at different cross-sections. Markers show experimental data, curves denoted by 1 are calculated using the scheme [1] of the second order for $\omega_0=0.38$, and 2 denotes the third-order accuracy calculations for $\omega_0=0.27$. Having noted fairly good agreement with the experiment of both sets of the computed curves, let us point the fact, that the third-order scheme calculations yield a reversed flow velocity maximum in the immediate vicinity of the plate surface, which is indicative of more turbulent flow than that observed in the experiment (see also [10]).

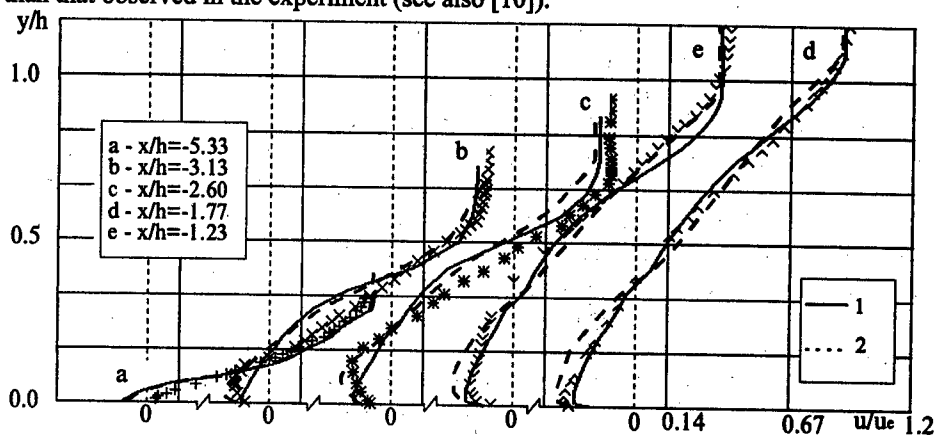


Fig. 9 Mean velocity profiles at different cross-sections.
(1 - third-order space approximation, $\omega_0 = 0.38$; 2 - second-order, $\omega_0 = 0.27$).

Thus, the studies performed have shown a strong dependence of the separated flow calculation results on the numerical algorithm characteristics as well as on the turbulence model parameter which governs the processes of turbulence kinetic energy generation and dissipation. The mechanism influencing the turbulence model, by means of which one can control the separated flow parameters, is found. Varying the ω_0 parameter, it is possible to control the turbulent viscosity level both in the separating shock and recirculation regions. However, it is worth noting that although the described method seems to be useful in explaining many unsuccessful attempts to adequately calculate the turbulent separated flow, it is by no means not universal. Further joint experimental and computational investigations which would invoke the comparison on different flow parameters, including turbulent ones, are required to arrive to final conclusions on the problem.

This work was supported by Russian Foundation for Fundamental Research, grants No. 96-01-01777 and No. 97-01-00885.

REFERENCES

1. Kovenia V.M., Yanenko N.N. Method of splitting in the gas dynamics problems. - Novosibirsk: Nauka, 1981.
2. Steger J.L., Warming R.F. Flux Vector Splitting of the inviscid gasdynamic equations with application to finite difference methods // J. of Comput. Phys. - 1981. - Vol. 40. - P. 263-293.
3. Van Leer B. Flux-Vector Splitting for the Euler equations: ICASE Technical Report 82-30, 1982.

4. Sod G.A. A survey of several finite difference methods for systems of nonlinear hyperbolic conservation laws // *J. of Comput. Physics.* - 1978. - Vol. 27. - P. 1-31.
5. Chakravathy S.R. A new class of high accuracy TVD schemes for hyperbolic conservation laws. AIAA Paper 85-0363, 1985.
6. Zheltovodov A.A and Pavlov A.A. A study of the flow in supersonic separation region in front of step. Novosibirsk, 1979, 50 p. - (Preprint / Inst. of Theor. and Appl. Mechanics SD SSSR AS; N 1) (In Russian).
7. Borisov A.V., Vorontsov S.S., Zheltovodov A.A., Pavlov A.A., Shpak S.I. Development of experimental and computational facilities for supersonic separated flow studies. - Novosibirsk, 1993. - 45 p. - (Preprint / Inst. of Theor. and Appl. Mechanics SD SSSR AS; N 9-93) (In Russian).
8. Borisov A.V., Fedorova N.N. Numerical simulation of turbulent flows near forward-facing steps // *Thermophysics and Aeromechanics.* -1996. -Vol. 3, No. 1. -P.69-84.
9. Wilcox D.C. Turbulence modeling for CFD - La Cañada, California: DCW Industries, Inc, 1993. - 460 p.
10. Borisov A.V., Zheltovodov A.A., Maksimov A.I., Fedorova N.N., Shpak S.I. Verification of turbulence models and computational methods of separated flows // *Int. Conf. on the Methods of Aerophys. Research: Proc. Pt. 1* - Novosibirsk, 1996 - P. 54-61.

SUPERSONIC TURBULENT SEPARATED FLOWS NUMERICAL MODEL VERIFICATION

I.A.Bedarev, A.A.Zheltovodov, N.N.Fedorova

Institute of Theoretical and Applied Mechanics
SD RAS, 630090 Novosibirsk, Russia

The shock wave/turbulent boundary layer interaction and the boundary layer separation prediction is one of the classical problems of high-speed fluid dynamics. A full understanding of these phenomena is important for efficient aerodynamic and propulsion design. Recent advances in the physical understanding of such complex turbulent flows on a basis of experimental studies as well as a continuing rapid rate of growth of computer performance has enabled more accurate simulation. Nevertheless, a comparison of computed and experimental results for a wide variety of compressible turbulent flows has demonstrated the difficulties of some principal features prediction with reasonable accuracy for the large-scale separation [1–3]. Say, the surface heat transfer can not be accurately predicted for 2-D and 3-D shock wave/turbulent boundary layer interactions. The computations and experimental data also diverge, for example, for the case of large-scale separation in the vicinity of forward-facing steps with the Mach number increasing [4]. Development and improvement of numerical computations for different types of separated flows on a basis of the Reynolds-averaged Navier–Stokes (RANS) equations with turbulence incorporated using different two-equation turbulence models is important from an engineering standpoint [3].

The experimental study [5] and RANS computations [6] employing the $k-\omega$ turbulence model have demonstrated a possibility of the reverse flow relaminarization in the 2-D turbulent separation zone upstream of a forward facing step. The experimental [7, 8] and numerical [9, 10] works have demonstrated that a 3-D separation zone in the vicinity of fin mounted on a flat plate contains simultaneously turbulent external shear layer in the primary vortex and almost laminar region between the reattachment line and the secondary vortex. In accordance with the experiments [7, 8] the secondary separation behavior is related to laminar, transitional and then turbulent reverse flow state in the swept separation bubble at different shock wave strengths conditions. All these studies offered a very interesting and important way to explain the failure of some turbulence models and many computations on the considered flows by the necessity of correct reverse flows state modeling in the turbulent separated zones. Our attention herein is focused on this question and application of the RANS and $k-\omega$ turbulence model to the 2-D separated flows computations.

The computations of separated flows in the vicinity of forward facing steps carried out previously in [6, 11] on a basis of the RANS and $k-\omega$ turbulence model [12] have demonstrated good agreement with the experimental data for surface pressure, skin friction distributions and velocity profiles at the Mach number $M = 2,9$. The additional studies have been performed to verify an application of such an approach at different Mach numbers as well as for analysis of a possibility of correct heat transfer prediction in the shock wave and expansion fans/turbulent boundary layer interaction regions.

The level of the specific turbulence kinetic energy dissipation rate ω was limited by some minimal value $\omega_e \sim 10^{-3} \omega_0$ in the framework of the $k-\omega$ turbulence model to obtain the turbulence production and dissipation balance modeling correctness. (ω_0 is the maximum ω value on the wall). The ω_e value variation changes substantially the turbulent viscosity μ

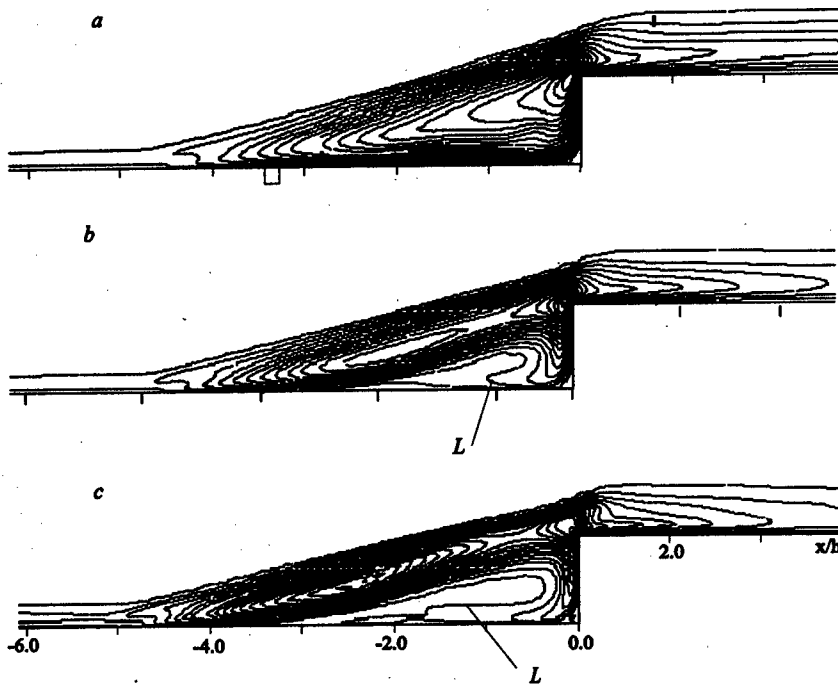


Fig. 1. Equal μ_t value lines in the vicinity of normal forward facing step at $M = 2,9$, $Re_1 = 30 \cdot 10^6 m^{-1}$, $h/\delta = 2,84$: $\omega_e = 0,15$ (a), $\omega_e = 0,27$ (b), $\omega_e = 0,37$ (c)

distribution and influences the general flowfield structure. These effects are confirmed by Fig. 1, in which the lines of equal μ_t values are shown for various ω_e levels in the vicinity of a normal forward facing step with a height $h = 6$ mm at the Mach number $M = 2,9$ and the Reynolds number $Re_1 = 30 \cdot 10^6 m^{-1}$. The step height to undisturbed boundary layer thickness ratio was $h/\delta = 2,84$. The computations have been performed using the third-order approximation numerical algorithm for the spatial variables described in details in [13]. It is seen from the figure that the μ_t level is high in the separated shear layer and ω_e increasing stimulates an appearance of reverse flow region L close to the laminar where μ_t tends to zero in the separated zone upstream of the step.

A comparison of the computations with experimental data on surface pressure [5] and skin friction [6] distributions is represented in Fig. 2 for the same ω_e values. Excessively high values of the turbulent viscosity μ_t have been realized in the separated zone at $\omega_e = 0,15$ and this stimulated the discrepancies of the surface pressure computations with experimental data at $-0,5 \leq x/h \leq -1,5$ and $-4,5 \leq x/h \leq -2,5$ (Fig. 2, a). The turbulence has been suppressed excessively in the separated zone at the used maximal value $\omega_e = 0,37$ and this stimulated substantial discrepancy of the computed surface pressure with the data in the region under the vortex core upstream of the step ($x/h \approx -1$) and on its face ($0 \leq x/h \leq 1$). The secondary separation and following reattachment of a reverse flow have appeared in the points $x/h \approx -1,7$ and $x/h \approx -2,1$, where $C_f = 0$ in the computations at such conditions (Fig. 2, b). Such phenomena were not registered in the experiments. The best agreement of surface pressure

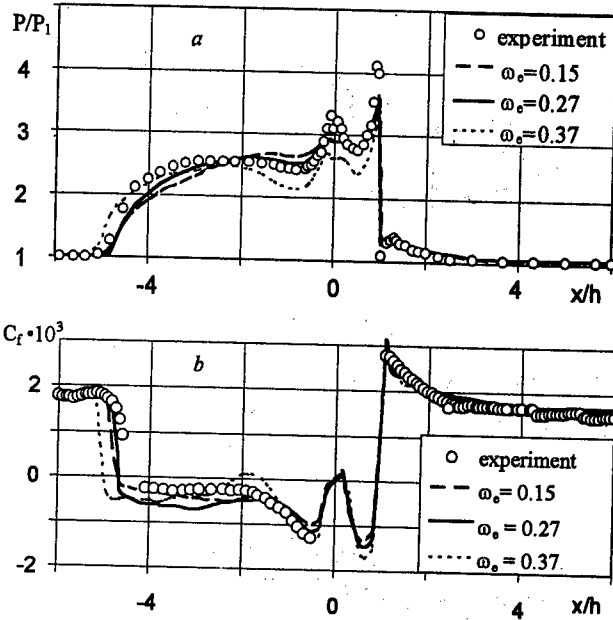


Fig. 2. Influence of ω_s variation on surface pressure and skin friction prediction in the vicinity of normal forward facing step with $h/\delta=2,84$ at $M=2,9$

and skin friction computations with experimental data has been achieved at $\omega_s=0,27$. This conclusion is additionally confirmed by good agreement of computed and experimental [5] velocity profiles for a normal forward facing step with a height $h=15$ mm at Mach number $M=2,9$ (Fig. 3).

Substantiated optimal values $\omega_s=0,25-0,27$ have been used for the computations of separated flows in the vicinity of forward facing step with a

height $h=10$ mm at different Mach and Reynolds numbers (Fig. 4). The computed surface pressure distribution (3) is in the limits of the experimental data (1) [5] and (2) [14] discrepancy at $M=2$, $Re_1=30 \cdot 10^6 \text{ m}^{-1}$ (Fig. 4, a). It is important that good agreement of computations with data is also retained at higher values of the Mach and Reynolds numbers: $M=2,5$, $Re_1=50 \cdot 10^6 \text{ m}^{-1}$ (Fig. 4, b) and $M=4$, $Re_1=48 \cdot 10^6 \text{ m}^{-1}$ (Fig. 4, c).

As it was noted above it is not sufficient now to predict reliably the heat transfer distribution in the shock wave/turbulent boundary interaction regions. The heat transfer computations have been performed in the vicinity of a forward facing step with a face angle $\beta=25^\circ$ and a height $h=6$ mm at the Mach number $M=4$ and the Reynolds number $Re_1=40 \cdot 10^6 \text{ m}^{-1}$ to verify the capability of considered numerical algorithm and turbulence model. This turbulent separated flow has been experimentally studied in [15, 16] at close to adiabatic wall conditions. Some flowfield features of such flow are illustrated in Fig. 5, a which shows previously obtained experimental qualitative scheme and computed equal static pressure lines. An interaction of the turbulent boundary layer with successive shock waves and expansion fan with an appearance of local separated zone in the vicinity of compression corner is realized in this situation. It is seen from the computation that the secondary expansion fan (its boundaries are shown by dotted lines) penetrates to the top step surface from the triple point of the λ -shock wave structure.

Taking into account the demonstrated substantial influence of

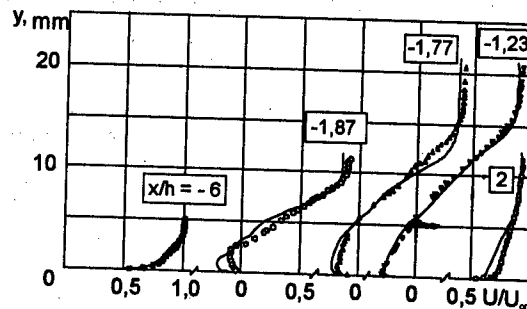


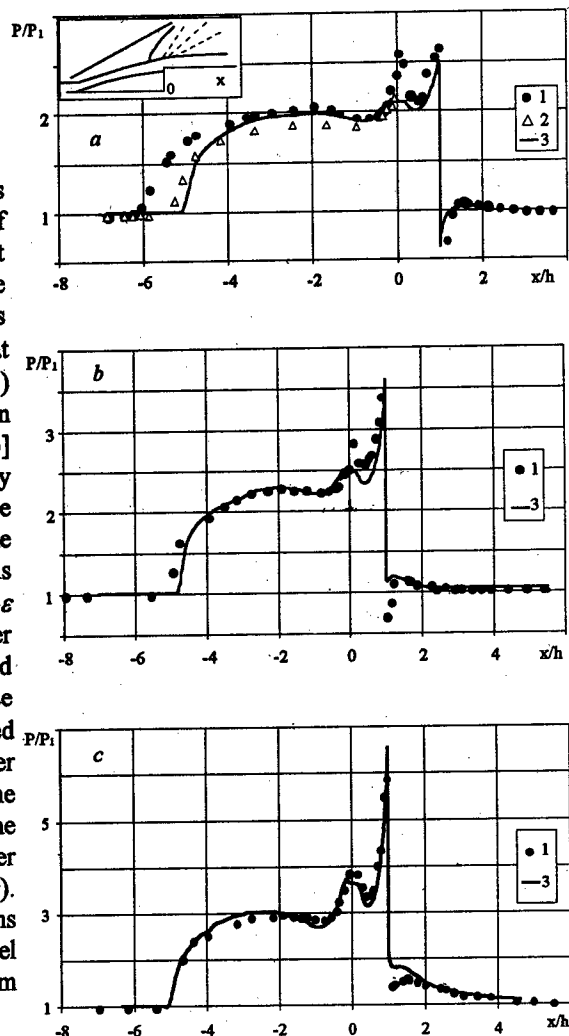
Fig. 3. Velocity profiles in the vicinity of normal forward facing step with $h/\delta=2,84$ at $M=2,9$, $Re_1=33 \cdot 10^6 \text{ m}^{-1}$

Fig. 4. Surface pressure distributions in the vicinity of normal forward facing step with $h = 10$ mm: $M = 2$, $h/\delta = 2,3$ (a); $M = 2,5$, $h/\delta = 2,6$ (b) $M = 4$, $h/\delta = 2,5$ (c)

the ω_e level on various performances of the computed flows, analysis of this parameter influence on the heat transfer prediction is interesting. The computations performed on a basis of the $k-\omega$ turbulence model at different ω_0 and ω_e values (lines 1-3) are shown in Fig. 5, b in comparison with the experimental data [15, 16] for surface heat transfer intensity coefficient C_h . C_{h1} is the value upstream of the interaction. The previous computations [1] of this flow with the Jones-Launder $k-\epsilon$ turbulence model and its two-layer modification by Rodi are represented in Fig. 5, c. It is obvious that the use of the $k-\omega$ model (Fig. 5, b) allowed one to predict better the heat transfer in the separated zone upstream of the compression corner and on the corner face comparing with other turbulence models (Fig. 5, c). Nevertheless all the computations underpredict the heat transfer level on the top step surface downstream of an expansion fan.

A more detailed analysis of the data represented in Fig. 5, b allows one to characterize the ω_0 and ω_e influence on the heat transfer modeling at such conditions. Say, at the same value $\omega_e = 0,15$ some increasing of ω_0 (line 1) leads to the heat transfer increasing in the separated zone, on the compression corner and top step surfaces comparing with the computations at lower value of ω_0 (2). These results demonstrate the dissipation effects influence on the process of the turbulence energy to heat transformation close to the wall. Solutions 2 and 3 have been obtained at the same ω_0 value and different ω_e values (0,15 and 0,27 respectively). It is seen that the turbulence suppression in the external flow stimulates the heat transfer decreasing on the step face.

As it is seen from Fig. 5, a the secondary expansion fan penetrating to the top step surface from the triple point may be one of the reasons which lead to the heat transfer decreasing found in the experiments at $x/h > 8$. The influence of such secondary fan is also displayed in the computations at $x/h = 6-8$, nevertheless $C_h/C_{h1}(x/h)$ distribution differs from the



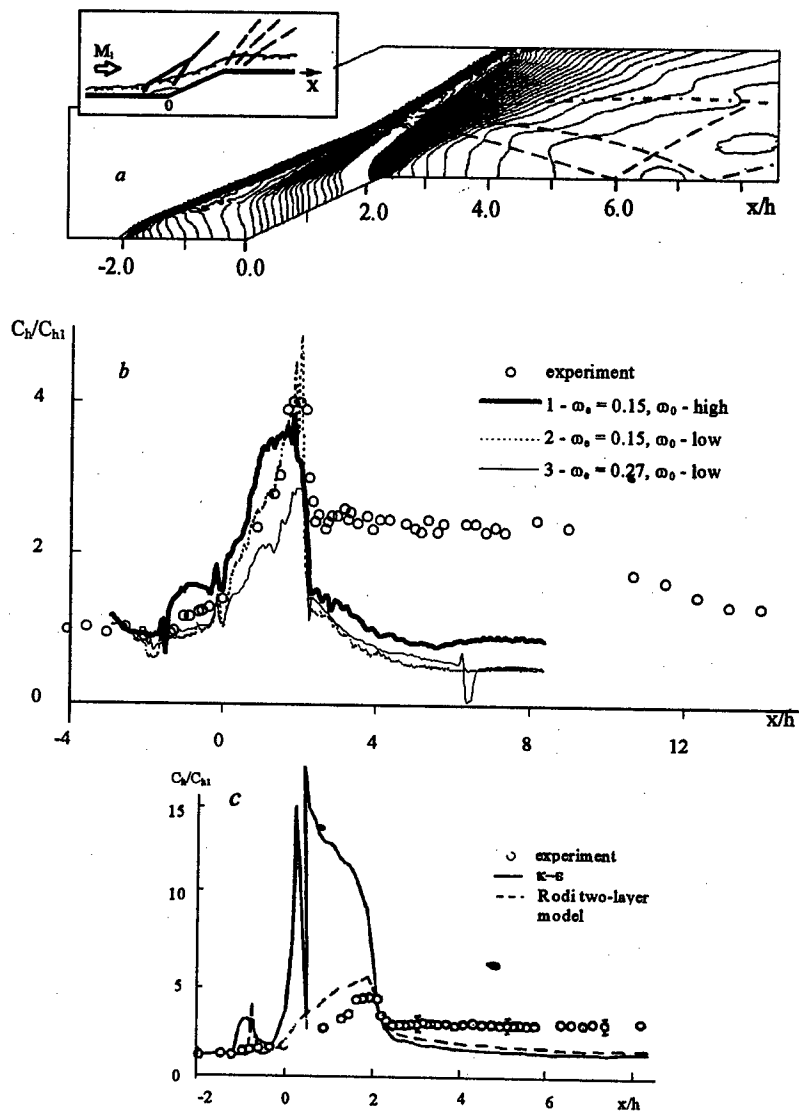


Fig. 5. Flowfield features (a) and heat transfer distribution (b, c) in the vicinity of forward facing step with $\beta = 25^\circ$, $h = 6$ mm at $M = 4$

experimental one. This can be caused by an excessive turbulent viscosity decreasing in the computations immediately after the boundary layer interaction with the expansion fan spreading from the step top to the external flow which results in heat transfer underprediction. Such a conclusion is in agreement with previous heat transfer computations downstream of backward facing steps [1, 17] with the lee side surface angle $\beta = -25^\circ$ where the heat transfer underprediction has been also obtained downstream of the expansion fan.

Thus, further improvement of the heat transfer prediction for considered complex flows requires additional studies of modeling possibilities of different delicate physical phenomena in the framework of two equation turbulence models.

This work has been supported by the Russian Foundation for Basic Research (project codes 96-01-01777 and 97-01-00885).

REFERENCES

1. Zheltovodov A.A., Borisov A.V., Knight D.D., Horstman C.C., Settles G.S. The possibilities of numerical simulation of shock waves/boundary layer interaction in supersonic and hypersonic flows // Int. Conf. on the Methods of Aerophys. Research: Proc. Pt. 1. Novosibirsk, 1992. P. 164-170.
2. Zheltovodov A.A. Shock waves/turbulent boundary layer interactions - fundamental studies and applications. AIAA Pap. 96-1977.-1996.-27 p.
3. Knight D.D. Numerical solution of compressible turbulent flows using the Reynolds-averaged Navier-Stokes equations: Turbulence in Compressible Flows. AGARD Rep.-1997.- № 819. -P. 5-1-5-52.
4. Graur I.A., Elizarova T.G., Chetverushkin B.N. Numerical simulation of a turbulent flow near the right step // Mathematical Modelling. 1990.-Vol. 3.-№ 11.- P. 31-44.
5. Zheltovodov A.A. Analysis of 2-D separated flows properties at supersonic speeds conditions // The studies of near-wall flows of viscous gas. Novosibirsk, 1979. P. 59-94.
6. Borisov A.V., Zheltovodov A.A., Maksimov A.I., Fedorova N.N., Shpak S.I. Verification of turbulence models and computational methods of supersonic separated flows // Int. Conf. on the Methods of Aerophys. Research: Proc. Pt. 1. Novosibirsk. 1996. P. 54-61.
7. Zheltovodov A.A. Regimes and properties of three-dimensional separated flows initiated by swept shock waves // J. of Appl. Mech. and Techn. Physics. 1982.-№ 3.-P. 116-123.
8. Zheltovodov A.A., Maksimov A.I., Schuelein E. Development of turbulent separated flows in the vicinity of swept shock waves // The Interactions of Complex 3-D Flows. Novosibirsk, 1987. P. 67-91.
9. Panaras A.G. The effect of the structure of swept-shock wave/turbulent-boundary-layer interactions on turbulence modeling // J. Fluid. Mech. 1997.-Vol. 338.-P. 203-230.
10. Panaras A.G. Algebraic turbulence modeling for swept shock-wave/turbulent-boundary-layer interactions // AIAA J. 1997.-Vol. 35.-№ 3.-P. 456-463.
11. Zheltovodov A.A., Bedarev I.A., Borisov A.V., Volkov V.F., Mazhul I.I., Maksimov A.I., Fedorova N.N., Shpak S.I. Development and verification of computational methods with application to the supersonic aerodynamics problems. Novosibirsk, 1997. 52 p. (Preprint / ITAM SD RAS; N 7 - 97).
12. Wilcox D.C. Reassessment of the scale determining equation for advanced turbulence models // AIAA J. 1988.-Vol. 32.-No. 11.-P. 1299-1310.
13. Borisov A.V., Fedorova N.N. Numerical simulation of turbulent flows near the forward-facing steps // Thermophysics and Aeromechanics. 1996.-Vol. 3.-№ 1.-P. 69-82.
14. Chapman D.R., Kuehn D.M., Larson H.K. Investigation of a separated flows in supersonic and subsonic streams with emphasis on the effect of transition. NACA Rep. 1958.-N 1356.-40 p.
15. Zheltovodov A.A., Zaulichniy E.G., Trofimov V.M., Yakovlev V.N. Heat transfer and turbulence study in compressible separated flows. Novosibirsk, 1987. 47 p. (Preprint / ITAM SD Acad. Sci. USSR; N 22 - 87).
16. Zheltovodov A.A., Zaulichniy E.G., Trofimov V.M. Development of the models for heat transfer computation at supersonic turbulent separated flows conditions // J. of Appl. Mech. and Techn. Physics. 1990.-№ 4.-P. 96-104.
17. Zheltovodov A.A., Horstman C.C. Experimental and numerical investigation of 2-D expansion/shock wave-turbulent boundary layer interactions. Novosibirsk, 1993. 25 p. (Preprint / ITAM SD RAS; N 2 - 93).

CARS-MEASUREMENTS IN RANQUE-HILSCH'S VORTEX TUBE.

B.F. Boyarshinov, S. Yu. Fedorov, and A.A. Volkov

Institute of Thermophysics SB RAS,
630090, Novosibirsk, Russia

The Ranque-Hilsch's vortex tube is widely used as a device for the temperature separation of gases, as well as in cooling and conditioning systems [1]. The compressed air intensively rotates in the limited volume and gains a lower temperature near to the chamber axis and a higher temperature at the periphery relative to the temperature of the inlet air. The temperature difference between outlet "hot" and "cold" flows is about 20÷40°K. The similar devices can be used for the gas mixture separation on its content. From the times of their discovery, these effects attract the attention of numerous investigators; however, there is no indisputable explanation of these effect to the present time. This situation is partially caused by the difficulties in application of conventional methods for measuring of the local gas flow parameters.

The CARS method is an effective tool for the measurement of the local temperature and gas component concentrations in a gaseous mixture which does not disturbs the investigated flow. For example, it was successfully used for investigation of flames [2], gas discharge [3], etc. This method was not still used for investigation of a swirl flow, although the method allows us to obtain also the information about the gas pressure. This paper describes the elaboration of the CARS method for simultaneous measurements of temperature, composition and pressure of a gas mixture (air) in application to the separation processes in the Ranque-Hilsch's tube.

Measurements were carry out on a serial counterflow vortex tube VC-1 with optical windows. The internal diameter of a channel was 20 mm, and its length was 350 mm. The inlet flow rate to the four-slit (30 mm²) swirling apparatus was 16 g/sec; the flow rate through the diaphragm with the diameter of 10 mm was 6.5 g/sec (the "cold" outlet).

INSTRUMENTATION AND DATA PROCESSING

It is usual to record the CARS spectra generated by transitions between the vibrational levels of molecules. It is more convenient to use a low-frequency (with a Raman shift ≤ 200 cm⁻¹) spectra for no-combustion conditions. This spectrum corresponds to the transition between pure rotational levels belonging to the lowest vibrational level. The temperature dependence of their shape is stronger in range up to 1000°K, that is convinient for measurements. Such a rotational spectrum of a pure gas consists of equidistant lines. The integral intensity of an isolated rotational line is as follows:

$$I_4(j) = A_j I_1 I_2 I_3 \left\{ b_{j,j'} \frac{g_j(2j+1)}{Q_{rot}} \exp\left(-\frac{E_j hc}{kT}\right) \left[1 - \exp\left(-\frac{\omega_j hc}{kT}\right) \right] \right\}^2 \frac{N^2}{\Gamma_j}, \quad (1)$$

where A_j is the constant depending on experimental conditions, $I_1 \neq I_3$ are the intensities of the laser radiation, $b_{j,j'}$ is the Plachek-Teller coefficient, g_j is the nuclear spin weight, Q_{rot} is the rotational partition function, E_j is the energy of the initial level, ω_j is the frequency shift of

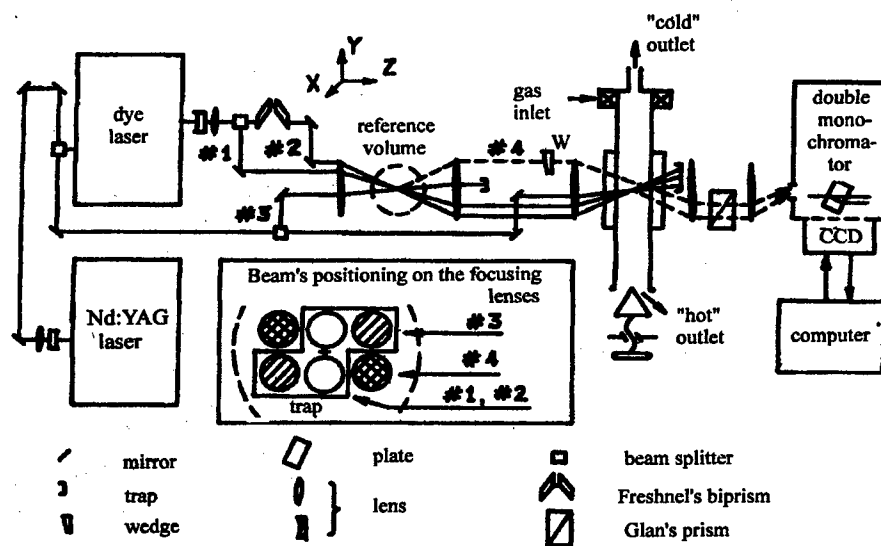


Fig. 1. Schematic diagram of the experimental setup.

these line, h is Planck's constant, c is the light speed, k is Boltzman's constant, T is the temperature, N is the concentration of molecules of this species, and Γ_j is the half-width of the line.

The gas mixture spectrum is a result of the superposition of the components' spectra. Some spectra become unresolvable, because of overlapping of adjacent pressure-broadened lines. For further calculations only six isolated lines of nitrogen (4,7,8,10,11,14) and two lines of oxygen (7,11) were selected from the whole spectrum.

The CARS spectrometer on rotational transitions of molecules was based on the dual broadband pumping scheme (Fig.1). Some part of frequency-doubled radiation of Nd:YAG laser (532 nm, 100 mJ, $2 \cdot 10^{-8}$ sec) was converged in the broadband dye laser (600÷620 nm, 30 mJ, $1.5 \cdot 10^{-8}$ sec), and the remaining part was a probing beam. Two pumping beams, obtained by splitting of the dye laser radiation, and one probing beam were focused by lenses ($F=180$ mm) with their crossing according to the *boxcars* scheme (in the reference and the measuring volumes with the sizes of $0.1 \cdot 0.1 \cdot 2$ mm³). Adjusting the beam polarization and positioning them on the focusing lenses, we made them to interact on cubic non-linear susceptibility: $\chi_{yyx}^{(3)}$ (in the reference) and $\chi_{xyy}^{(3)}$ (in the measuring). The scattered light beams were passed through the Glan's prism and fed to the entrance slit of a double monochromator ($F=820$ mm). Two spectra appeared in its exit focal plane (the first was from the reference volume, and another — from the measuring volume). They were separated in the vertical direction due to optical wedge W .

Each spectrum consisted of S - and O -branch lines corresponding to the transitions $\Delta j=+2$ and $\Delta j=-2$. The plane-parallel plate was installed in the intermediate focal plane. This plate was used to make S -branch (measuring volume) coincide with O -branch (from the reference volume) on the one-dimensional CCD-camera (0.15·25 mm, 1024 element diode

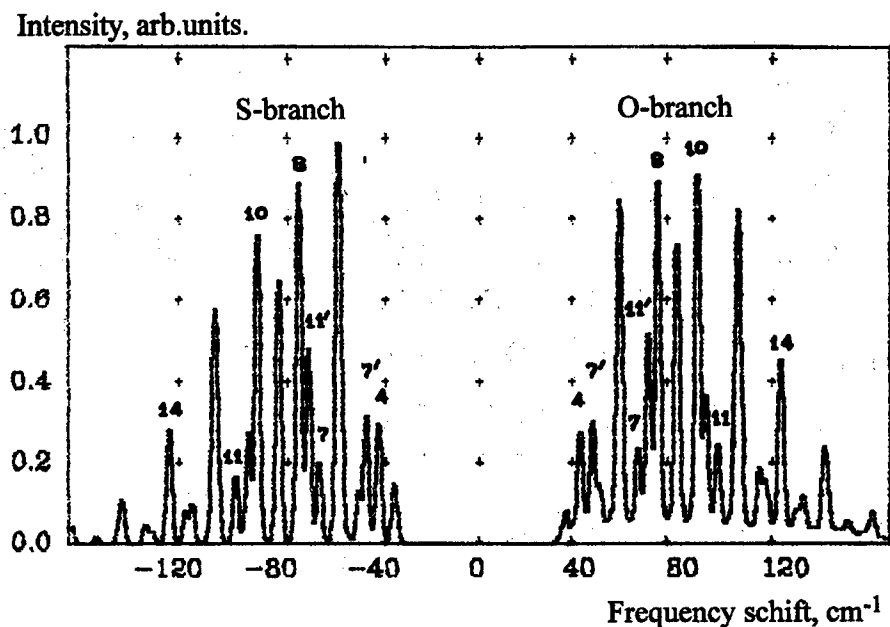


Fig.2. Rotational spectrum for pure air.

array). As shown in [4], the symmetrical lines in this combined spectrum (Fig.2) are generated by the common spectral components of the laser radiation. This fact allows us to use the branch from the reference volume for calibration and for increase in the accuracy of our measurements.

Firstly, the background spectrum was accumulated from 200 laser pulses (one broadband beam was absent). Then this background spectrum was stored in the computer memory and automatically subtracted from all other spectra. Secondly, the spectrum of uniform lighted diode array was recorded (to calculate the sensitivity of diodes).

The experimental data was stored into separate files which was 101 rows of 1024 numbers. The "calibration" spectrum was stored to the first row, accumulated from 200 laser pulses in the measurement volume (this spectrum corresponds to the room conditions: $T_0=293^{\circ}\text{K}$ and $P_0=1\text{ atm}$). This spectrum was used for calculation of coefficient A in formula (1). Then 100 "instantaneous" spectra from one laser pulse were recorded (under conditions of the unknown temperature and concentration).

The data pre-processing software calculated the integral intensities of all spectral lines. This procedure reduced the length of each row from 1024 to 8 numbers. The main software transformed them into files with the "instantaneous" temperature T , the volume concentration of nitrogen $C(\text{N}_2)$, and the pressure P . The program discarded all "instantaneous" spectra with a negative magnitude in any of spectral lines. The same was done if an obviously false magnitude of temperature was reported. Usually the percentage of discarded spectra was less than 5%.

The resulting files were used for calculation of the average values of \bar{T} , $\bar{C}(\text{N}_2)$ and \bar{P} , and other statistical characteristics of these variables.

RESULTS AND DISCUSSION

Figure 3a shows the graphs of the measurements in still compressed air. Here the average values of \bar{T} , $\bar{C}(\text{N}_2)$ and \bar{P} are plotted as a function of the air pressure. It is obviously that the measured parameters correspond to their real numbers within the experimental error (for the range up to 3 atm). Figure 3b shows the axial profiles of these parameters in several cross sections of the Ranque-Hilsh's tube. As it was expected, the values of \bar{T} and \bar{P} increase from the center to the periphery. The profiles of $\bar{C}(\text{N}_2)$ demonstrate that the mixture components are not separated (within the measurement error).

Preliminary measurements in pure gases of N_2 and O_2 in range 1-7 atm demonstrated the linear dependence of the line's intensity on the pressure (as it was expected). The experiments with air revealed the deviation from the initial linear dependency for the pressure

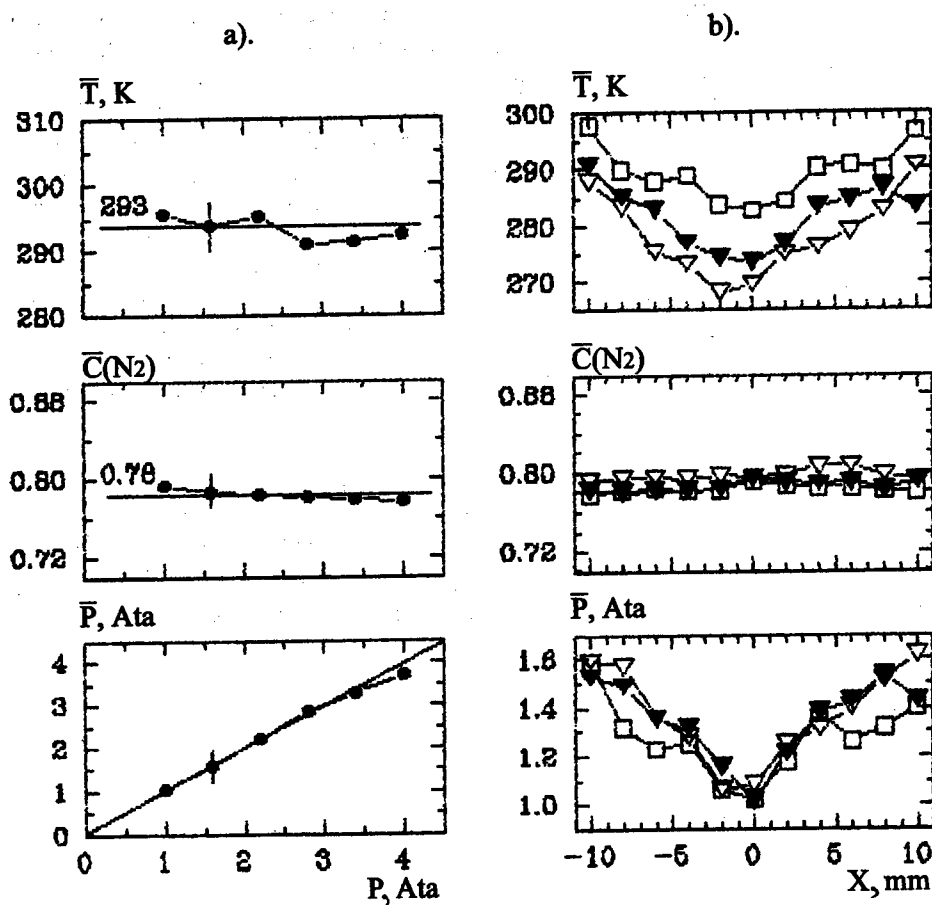


Fig.3. Experimental profiles for T, $\bar{C}(\text{N}_2)$ and \bar{P} for:
 a) still pressured air (\bullet);
 b) Ranque-Hilsh's tube at several distance from the swirler (∇ - 50 mm, \blacktriangledown - 100 mm, \square - 150 mm).

above 3 atm. It is explained by the overlapping of spectral lines due to their broadening. Thus, the upper limit on the gas pressure was found for our method. However, the low pressure limit (the collision broadening becomes less than Doppler's broadening) still was not obtained in our experiments.

The temperature was calculated from intensities of six lines of nitrogen, disregarding the line broadening. At first, the theoretical intensities were calculated for the temperature range from 200°K up to 1000°K with the step of 1°K. Then the instantaneous experimental intensities were compared with the theoretical by the "least-squares" method. The best coincidence gave us the temperature magnitude.

It was noted in preliminary experiments that the intensities of 10-th line of nitrogen and 7-th line of oxygen vary with pressure in a similar way. As it was shown in [5], the pressure broadening coefficients for both lines are equal $80 \cdot 10^{-3} \text{ cm}^{-1}/\text{atm}$. We calculated the ratio of component's concentrations in the mixture from the ratio of lines intensities (for the calculated temperature). Obviously, this ratio does not depend on the pressure, because the close values of Γ_j are reduced. For the convenience of analysis we present here not the ratio of concentrations, but the volumetric concentration of one component — nitrogen.

Substituting in (1) the concentration from the ideal gas equation $N = P/kT$ and the line width $\Gamma_j = \alpha_j P$ (where α_j is the pressure broadening coefficient), we received the formula for the pressure calculation. The pressure was calculated as an average value from all 8 lines with their normalization to the reference branch. The standard deviations of instantaneous values in our experiments were as follows: for the temperature — 10 %, for the volumetric concentration — 15 %, and for the pressure — 40%. They could be considerably smaller for a higher laser power; so the normalization method suggested in [4] could be applied at the stage of the temperature calculation. The standard errors of mean values are shown in figures.

The obtained data confirm the applicability of the developed measurement technique based on CARS-spectroscopy for the study of separation effects in the Ranque-Hilsh's tube.

REFERENCES

1. Kusnetzov W.I., The Theory and Calculation of Ranque's Effect. - Omsk: OmGTU, 1994. (in Russian).
2. Williams D.R., McKeown D., Porter F.M., et al., Coherent anti-Stokes Raman spectroscopy (CARS) and laser-induced fluorescence (LIF) measurements in a Rocket engine plume// Comb. and Flame.- 1993.- V.94.- N.1/2.-P.77-90.
3. Smirnov W.W. and Fabelinski W.I., Temperature measurements and spectroscopy of vibrational-rotational levels excited in discharge by CARS technique// Letters in JETP.- 1978.- Vol.28. - N.7.- P.461.
4. Fedorov S.Yu., Alternative phase-matching in CARS// Instruments and Experimental Techniques.- 1996.- Vol.39.- No.1.- P.110-114.
5. Jammu K.S., John G.E.St., Welsh H.L., Pressure broadening of the rotational Raman lines of some simple gases// Can. J. Phys.- 1966. - V.44.- N.4.- P.797-814.

THE EXACT SOLUTIONS OF EQUATIONS FOR DYNAMICS OF VISCOUS HEAT CONDUCTING GAS

V.V.Bublik

Institute of Theoretical and Applied Mechanics SB RAS,
630090, Novosibirsk, Russia

1. Model. The paper is devoted to construction of exact solutions of equations for dynamics of viscous heat conducting perfect gas with use of methods of group analysis of differential equations [1]. The governing equations are

$$\rho(u_t + uu_x + vv_y) = -p_x + \frac{2}{3}(\mu(2u_x - v_y - \nu \frac{u}{x}))_x + (\mu(u_y + v_x))_y + 2\nu \mu \left(\frac{u}{x}\right)_x, \quad (1)$$

$$\rho(v_t + uv_x + vv_y) = -p_y + (\mu(u_y + v_x))_x + \frac{2}{3}(\mu(2v_y - u_x - \nu \frac{u}{x}))_y + \nu \frac{\mu}{x}(u_y + v_x), \quad (2)$$

$$\rho_t + (u\rho)_x + (v\rho)_y + \nu \frac{u\rho}{x} = 0, \quad (3)$$

$$p_t + up_x + vp_y + \gamma p(u_x + v_y) = \frac{\gamma-1}{R} k_0 \left(\left(\mu \left(\frac{p}{\rho} \right)_x \right)_x + \left(\mu \left(\frac{p}{\rho} \right)_y \right)_y + \nu \frac{\mu}{x} \left(\frac{p}{\rho} \right)_x \right) +$$

$$+ (\gamma-1)\mu \left(\frac{4}{3} (u_x^2 + v_y^2 - u_x v_y + \nu \frac{u}{x} \left(\frac{u}{x} - u_x - v_y \right)) + (v_x + u_y)^2 \right). \quad (4)$$

Here, u and v are the velocity components, ρ is the density, p is the pressure, $\mu = (p/\rho)^\omega$ is the viscosity coefficient, $k_0\mu$ is the heat conductivity coefficient, γ is the ratio of specific heats, R is the gas constant. With $\nu = 0$ system (1)–(4) describes plane motion of gas. With $\nu = 1$ it describes the case of axial symmetry.

As shown in [2] system (1)–(4) in the case of plane symmetry admits the Lie algebra of transformations with the following basis

$$X_1 = \partial_x, \quad X_2 = \partial_y, \quad X_3 = t\partial_x + \partial_u, \quad X_4 = t\partial_y + \partial_v, \quad X_5 = y\partial_x - x\partial_y + v\partial_u - u\partial_v,$$

$$X_6 = \partial_t, \quad X_7 = t\partial_t + x\partial_x + y\partial_y - \rho\partial_\rho - p\partial_p, \quad X_8 = x\partial_x + y\partial_y + u\partial_u + v\partial_v + 2(\omega-1)\rho\partial_\rho + 2\omega p\partial_p.$$

In the case of axial symmetry the Lie algebra with basis

$$X_2, \quad X_4, \quad X_6, \quad X_7, \quad X_8$$

is admitted.

In the construction of invariant and partially invariant solutions the optimal systems of subalgebras of Lie algebra from [2, 3] will be used.

2. Invariant solutions of rank 1. All invariant solutions of rank 1 for plane motions of gas is described in [3]. Here axial symmetric motions are discussed. Invariant solutions of rank 1 are built upon a basis of two-dimensional subalgebras. All subalgebras satisfying necessary condition of existence of invariant solution are listed in table 1. For convenience

Table 1

№	H	The form of solution
1	6, 7 + α8 (α ≠ -1)	$u = x^{\alpha/(\alpha+1)}u_1(\xi), v = x^{\alpha/(\alpha+1)}v_1(\xi), \rho = x^{(2\alpha(\omega-1)-1)/(\alpha+1)}\rho_1(\xi),$ $p = x^{(2\alpha\omega-1)/(\alpha+1)}p_1(\xi), \xi = y/x$
2	4, 7 + α8 (α ≠ -1)	$u = t^\alpha u_1(\xi), v = y/x + t^\alpha v_1(\xi), \rho = t^{2\alpha(\omega-1)-1}\rho_1(\xi),$ $p = t^{2\alpha\omega-1}p_1(\xi), \xi = xt^{-\alpha-1}$
3	2, 7 + α8	$u = t^\alpha u_1(\xi), v = t^\alpha v_1(\xi), \rho = t^{2\alpha(\omega-1)-1}\rho_1(\xi),$ $p = t^{2\alpha\omega-1}p_1(\xi), \xi = xt^{-\alpha-1}$
4	7, 8	$u = xt^{-1}u_1(\xi), v = xt^{-1}v_1(\xi), \rho = x^{2(\omega-1)}t^{1-2\omega}\rho_1(\xi),$ $p = x^{2\omega}t^{-1-2\omega}p_1(\xi), \xi = y/x$
5	6, 2 + 7 - 8	$u = e^{-v}u_1(x), v = e^{-v}v_1(x), \rho = e^{(1-2\omega)v}\rho_1(x), p = e^{-(1+2\omega)v}p_1(x)$
6	4, 2 + 7 - 8	$u = u_1(x)/t, v = (y - \ln t + v_1(x))/t, \rho = t^{1-2\omega}\rho_1(x),$ $p = t^{-1-2\omega}p_1(x)$
7	4 + 6, 7 + 8	$u = x^{1/2}u_1(\xi), v = t + x^{1/2}v_1(\xi), \rho = x^{\omega-3/2}\rho_1(\xi),$ $p = x^{\omega-1/2}p_1(\xi), \xi = (t^2 - 2y)/x$
8	2, 4 + 7	$u = u(\xi), v = \ln t + v_1(\xi), \rho = \rho_1(\xi)/t, p = p_1(\xi)/t, \xi = x/t$
9	2, 6 + 8	$u = e^t u_1(\xi), v = e^t v_1(\xi), \rho = e^{2(\omega-1)t}\rho_1(\xi), p = e^{2\omega t}p_1(\xi), \xi = xe^{-t}$
10	2, 6 - 8	$u = e^{-t}u_1(\xi), v = e^{-t}v_1(\xi), \rho = e^{2(1-\omega)t}\rho_1(\xi),$ $p = e^{-2\omega t}p_1(\xi), \xi = xe^t$
11	6, 8	$u = xu_1(\xi), v = xv_1(\xi), \rho = x^{2(\omega-1)}\rho_1(\xi), p = x^{2\omega}p_1(\xi), \xi = y/x$
12	4, 8	$u = xu_1(t), v = (y + xv_1(t))/t, \rho = x^{2(\omega-1)}\rho_1(t), p = x^{2\omega}p_1(t)$
13	2, 8	$u = xu_1(t), v = xv_1(t), \rho = x^{2(\omega-1)}\rho_1(t), p = x^{2\omega}p_1(t)$
14	2, 4 + 6	$u = u(x), v = t + v_1(x), \rho = \rho(x), p = p(x)$
15	1, 4 + 6	$u = u(x), v = v(x), \rho = \rho(x), p = p(x)$

the basis of subalgebra H is denoted by the numbers of respective operators. Substitution of the form of solution into system (1)–(4) yields the reduced system describing the invariant solution. Such a reduced system in our case is a system of ordinary differential equations of second (or, sometimes, first) order. They may be integrated numerically.

3. Reducible partially invariant solutions. Consider now regular partially invariant solutions [4]. The construction of these solutions is essentially harder than construction of invariant ones. Therefore, finding a criteria for reducibility of partially invariant solutions to invariant ones plays important role. The sufficient condition of reducibility of regular partially invariant solutions of rank 1 and defect 1 of equations (1)–(4) is given here.

Theorem. Let H be any subgroup admitted by system (1)–(4). If the universal invariant of the subgroup H can be chosen in the form

$$J = (\xi(t, x, y), A(t, x, y)u + B(t, x, y)v + C(t, x, y), D(t, x, y)\rho, E(t, x, y)p), \quad (5)$$

with some functions $\xi, A, B, C, D,$ and $E,$ then the respective regular partially invariant H -solution of rank 1 and defect 1 of equations (1)–(4) is reduced to invariant solution. In case of $\nu = 1$ condition (5) may be simplified:

$$J = (\xi(t, x), A(t, x)u, D(t, x)\rho, E(t, x)p).$$

Table 2.

№	H	J
1	1, 3, 7 + α 8	$yt^{-\alpha-1}, vt^{-\alpha}, \rho t^{1-2\alpha(\omega-1)}, pt^{1-2\alpha\omega}$
2	1, 3, 4 + 7	$y/t - \ln t, v - \ln t, \rho t, pt$
3	1, 3, 4 + 6	$t^2 - 2y, v - t, \rho, p$
4	1, 3, 6 + 8	$ye^{-t}, ve^{-t}, \rho e^{2(1-\omega)t}, pe^{-2\omega t}$
5	1, 3, 6 - 8	$ye^t, ve^t, \rho e^{2(\omega-1)t}, pe^{2\omega t}$
6	1, 3, 6	y, v, ρ, p
7	1, 3, 8	$t, v/y, \rho y^{2(1-\omega)}, py^{-2\omega}$
8	1, 3, 4	$t, tv - y, \rho, p$
9	1, 2, 3	t, v, ρ, p

The set of subgroups satisfying condition (5) is not empty. In table 2 all such subgroups from optimal system of subgroups for a plane symmetry case are listed. In column J the invariant of subgroup H is presented. The table of this sort for an axial symmetry case consists of five subgroups.

The work was supported by Russian Foundation for Basic Research (the project 96-01-01888).

REFERENCES

1. Ovsiannikov L.V. Group analysis of differential equations. — M.: Nauka, 1978.
2. Bublik V.V. Group classification of two-dimensional equations of motion of viscous heat conducting gas // Russian Journal of Applied Mechanics and Technical Physics. — 1996. — V. 37, No 2. — P. 27-34.
3. Bublik V.V. Invariant solutions of rank 1 of equations for plane motions of viscous heat conducting gas // Russian Journal of Applied Mechanics and Technical Physics. — 1997. — V. 38, No 3. — P. 26-31.
4. Ovsiannikov L.V. Regular and nonregular partially invariant solutions // Dokl. Ross. Akad. Nauk. — 1995. — V. 343, No 2. — P. 156-159.

LATERAL UNSTEADY AERODYNAMICS AND DYNAMIC STABILITY EFFECTS IN HYPERSONIC FLIGHT

T. CVRLJE AND C. BREITSAMTER

Institute of Fluid Dynamics
Technische Universität München,
85747 Garching, Germany

M. HELLER AND G. SACHS

Institute of Flight Mechanics and Flight Control
Technische Universität München,
85747 Garching, Germany

Abstract

Lateral unsteady aerodynamics and dynamic stability effects relating to the hypersonic flight regime up to Mach 7 are considered. The unsteady flowfields of a two-staged hypersonic vehicle during the separation process are investigated. The aerodynamic calculations are based on a finite-volume-method for real-time solutions of the three-dimensional Euler equations. Particularly, the aerodynamic characteristics of the orbital stage performing small yaw and roll oscillations at a certain distance over the lower stage are addressed. The results focus on the pressure distributions as well as on the aerodynamic lateral coefficients. The latter are used as input for the stability and control evaluations discussed in the flight mechanics part.

Key issues of hypersonic lateral dynamics and its significant interdependencies with aerothermodynamics are considered. The inherent dynamic characteristics show specific stability and control deficiencies relating to a partially unstable dutch roll mode with high roll-yaw-coupling in combination with a weak roll damping. Additionally, for certain configurations coupling of the roll and spiral poles appears to form a slow, partly unstable oscillation called lateral phugoid. The decisive reasons and effects concerning the stability deficiencies addressed are identified by analyzing specific approximations for the lateral modes in hypersonic flight.

Introduction

Currently, considerable efforts in the field of hypersonic research are made in order to establish a technology base for innovative, full reusable aerospace planes (Refs. 1-4). There are challenging problems in many technological areas, hence a significant need for fundamental hypersonic research exists.

Two of the main critical key technology areas in the development of novel space planes are represented by specific aerothermodynamics and stability/control problems in hypersonic flight. It is the purpose of this paper to consider key issues of lateral aerothermodynamics and flight dynamics in the hypersonic regime up to Mach 7 together with the substantial interdependencies between these areas.

Especially, the separation process of two-staged space transportation systems occurring at high Mach numbers must be carefully investigated. Extensive numerical simulations have shown that during the separation strong reflecting shock waves occur between the carrier stage and the orbital stage (Refs. 5-7). The propagation of the shock waves depends on the separation speed, the distance between the two stages and the incidence of the stages. Thus, the points of intersection of the shock waves change significantly which causes strong unsteady airloads on the orbital stage.

Beside longitudinal motion small disturbances may also evoke lateral motions. The unsteady aerodynamic forces and moments induced thereby must be analyzed in detail to identify stability and control problems. The calculations of the unsteady flowfields are based on the solution of the

Euler equations. Their application provides a reasonable means to describe the shock wave systems between both stages as well as the body wakes and in turn to determine force and moment coefficients of the separating body (Ref. 7). Considering only small angles of attack as well as small angles of yaw and roll it is assumed that flow separation due to friction does not predominate the flowfield characteristics.

The particular problems of hypersonic flight dynamics are concerned with specific stability and control characteristics of the vehicles relating to the flight in the range of high Mach numbers. Here, specific inherent stability and control deficiencies including instabilities are existing in longitudinal as well as lateral motion. Up to now, nearly all investigations of hypersonic flight dynamics and control are concerned with longitudinal dynamics, e.g. Refs. 8, 9. Therefore, a significant need of fundamental research exists on the field of hypersonic lateral dynamics, stability and control. This paper is aimed to point out the specific problems of lateral aerothermodynamics and flight dynamics in the hypersonic flight regime.

Lateral Unsteady Aerodynamic Effects

CFD Simulation

The numerical simulation is based on a finite-volume approximation for real-time-solutions to the integral form of the unsteady Euler equations. The time-dependent flow vector for multi-dimensional problems is calculated by using the Strang-type of fractional step. The numerical fluxes are calculated by the method of Yee, Roe and Davis (Ref. 10). An additional flux-limiting function is introduced to guarantee the spatial second-order accuracy in smooth regions as well as the TVD-character of the solver. The function involves the vector of wavestrengths and the right eigenvector matrix of the corresponding Jacobian formed by using Roe averaged values in order to solve the approximate Riemann problem. At points of a discontinuous change of the state variables, the function vanishes which results in a switch in accuracy of the method to first order to avoid wiggles. An entropy correction function designed to exclude non-physically solutions of expansion shocks is calculated as the product of an empirical determined constant and the maximum speed at the corresponding cell interface.

On impermeable wall characteristic boundary conditions are applied to evaluate the primitive variables. For hypersonic inflow or outflow at the farfield boundary, the flow variables are either fixed to their freestream values or extrapolated by employing the solution in the computational domain.

Geometry and Grid Generation

The calculations are conducted for a generic orbital stage interfering with a flat plate representing the carrier stage. A side and top view of the orbital stage including all relevant geometric quantities are shown in Fig. 1. The middle section of the orbital stage consists of two partial ellipses, a mainly flat lower side and a flat tail section. The surface of the body is described from a discrete set of points provided by an algebraic grid generator.

The computational mesh was created by a Poisson algorithm. It consists of 16 blocks arranged in a hybrid C-H topology, Fig. 2. The overall mesh consists of 140.000 cells. The surface of the body involves 6.500 cells. For unsteady calculations the separating body is moved for each time step according to the prescribed motion, and the mesh is iterated again. The velocity of the mesh as well as the deformation of the cells are considered in the unsteady transformation of the Euler equations.

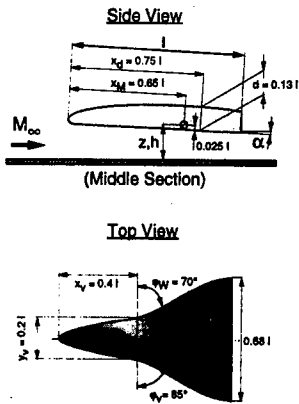


Fig. 1: Geometrie of the generic orbital stage

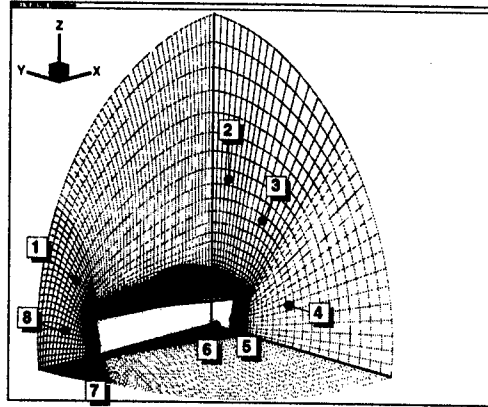


Fig. 2: Computational mesh with block topology

Results of Yaw and Roll Motion

At a given separation distance of $h/l = 0.225$ the orbiter performs harmonically oscillations in yaw and roll. The oscillations are of the form

$$\begin{aligned} \beta(\tau) &= \beta_0 + \Delta\beta \sin(k\tau) & \text{yaw} \\ \Phi(\tau) &= \Phi_0 + \Delta\Phi \sin(k\tau) & \text{roll} \end{aligned} \quad (1)$$

The motions take place at a freestream Mach number of $M_\infty = 6.8$ and a defined reduced frequency of $k = 1.0$. For all calculations the angle of attack is hold constant at $\alpha = 0^\circ$. Both the yaw and roll oscillations are performed at $\beta_0 = 0^\circ$, $\Phi_0 = 0^\circ$ with an amplitude $\Delta\beta = 2^\circ$ and $\Delta\Phi = 2^\circ$, respectively.

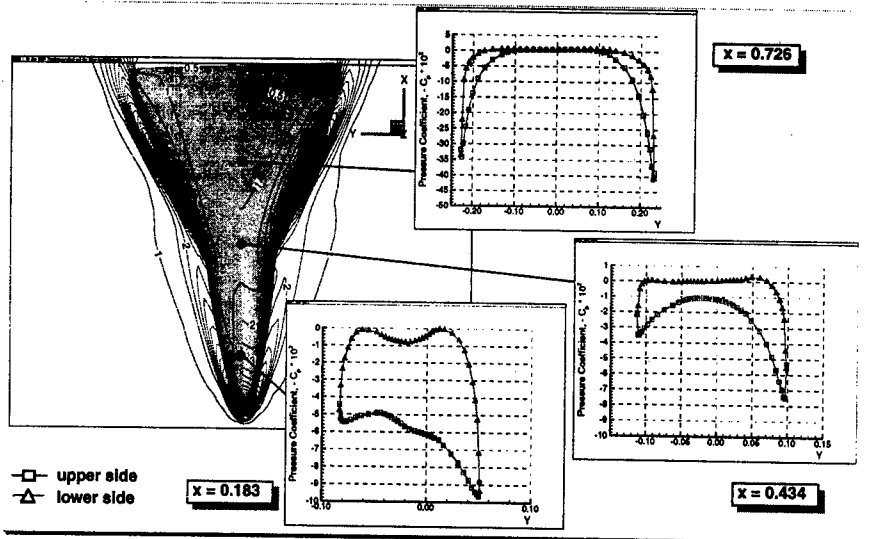


Fig. 3: Pressure distribution at the orbiter at $\beta = 2^\circ$

The results shown herein contain distributions of the pressure coefficients of the orbital stage during the yawing and rolling oscillation as well as of the side force, rolling and yawing moment coefficients.

Fig. 3 shows both the pressure coefficient of the lower and upper side in defined sections of the orbital stage along the x -axis and the isobars at $\beta = 2^\circ$. The distribution of the pressure coefficient indicates that the main changes involve the nose region of the body. The C_p -distribution is bulge and the extrema are located more aside. In streamwise direction the influence of a yaw motion on the pressure coefficient decreases. Thus the rear part of the idealized body is not considerably affected by a yaw angle deflection and the C_p -distribution is nearly the same as for a symmetric flowfield.

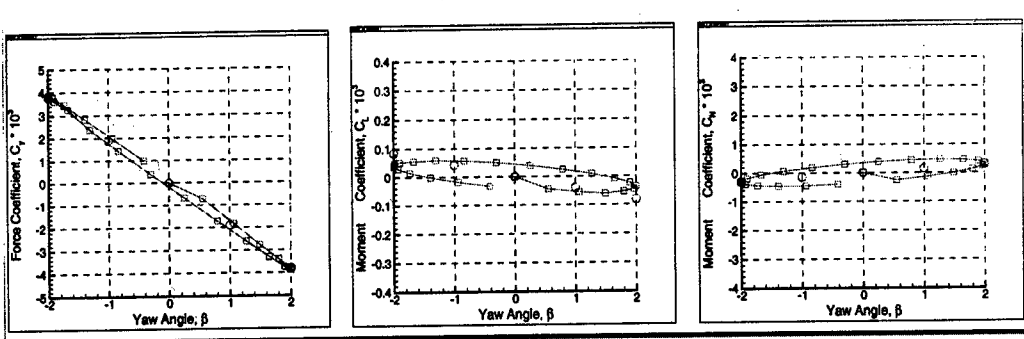


Fig. 4: Side force, roll, and yaw moment coefficients for the yawing motion

The steady and unsteady side force, yaw and roll coefficients are depicted in Fig. 4. A comparison between steady (circle symbols) and unsteady (square symbols) coefficients shows only small differences for the side force. The coefficient is symmetric to the steady initial position at $\beta = 0$ and is within a range of $|C_Y(\beta)| \leq 3.8812 \cdot 10^{-3}$. However, the coefficients do not correspond exactly with an elliptic curve. The higher harmonic components result in an increase of the amplitude at higher deflections (Ref. 11). The coefficients of yaw and roll differ clearly from the linear steady values. The maximum amplitude of the roll coefficient $|C_L|_{\max} = 8.5701 \cdot 10^{-5}$ is considerably higher than the yaw coefficient with $|C_N|_{\max} = 4.6039 \cdot 10^{-5}$.

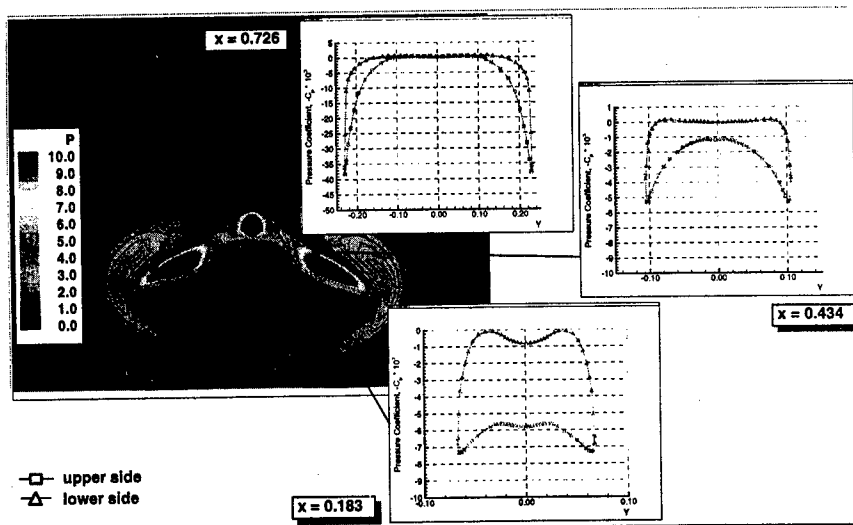


Fig. 5: Pressure distribution at the orbiter at $\Phi = 2^\circ$

Fig. 5 shows the pressure coefficient along the x-axis and the isobars in the wake area of the orbital stage during a roll motion. The corresponding steady and unsteady side force, roll and yaw coefficients are depicted in Fig. 6.

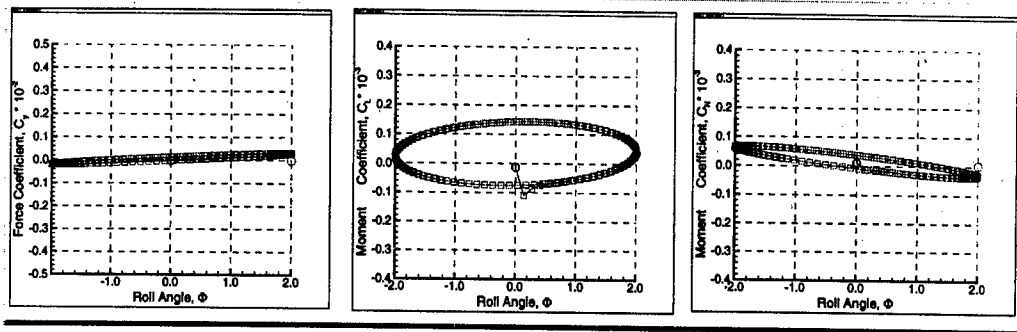


Fig. 6: Side force, roll, and yaw moment coefficients for the rolling motion

Lateral Hypersonic Dynamics and Stability

Basic Flight Dynamics

One of the critical key technology problems in the development of novel space planes are due to specific inherent stability and control deficiencies in hypersonic flight. For the investigations of the dynamic characteristics, a multi-purpose hypersonic test vehicle with ramjet propulsion has been chosen as a reference configuration, Refs. 12, 13. This configuration is considered to be a promising approach for contributing to progress in the hypersonic flight regime up to Mach 7 and therefore has led to a remarkable international collaboration within the program.

To investigate all critical key technology areas, a hypersonic flight test profile was defined according to ramjet propulsion characteristics. The reference profile consists of an acceleration phase from Mach 3.5 (altitude 17.5 km) up to Mach 6.8 (altitude approx. 30 km) followed by a deceleration part with engine off. A representative set of altitude/Mach number combinations was specified along the test profile serving as reference flight conditions for the investigation of test vehicle dynamics and control.

A nonlinear 6 degree-of-freedom aircraft simulation model was developed. Particular emphasis was placed on a realistic modelling of aerothermodynamics and ramjet engine effects. Linearized models for longitudinal and lateral motion are derived from the nonlinear equations of motion. Regarding the reference flight conditions as steady state wings-level climb/descent, the linearized equations of motion can be expressed:

$$\begin{aligned} \dot{x} &= Ax + Bu + Ez \\ y &= Cx + Dz \end{aligned} \quad (2)$$

where for lateral motion the state, control and disturbance vectors are

$$x = [p, r, \beta_K, \Phi, \Psi]^T, \quad u = [\xi, \zeta]^T, \quad z = \beta_W.$$

The corresponding coefficient, control and disturbance matrices are given by

$$A = \begin{bmatrix} L_p & L_r & L_\beta & 0 & 0 \\ N_p & N_r & N_\beta & 0 & 0 \\ Y_p & Y_r - 1 & Y_\beta & \frac{g}{V_0} \cos \theta_0 & 0 \\ \frac{\cos \gamma_0}{\cos \theta_0} & \frac{\sin \gamma_0}{\cos \theta_0} & 0 & 0 & 0 \\ \frac{\sin \alpha_0}{\cos \theta_0} & \frac{\cos \alpha_0}{\cos \theta_0} & 0 & 0 & 0 \end{bmatrix}, \quad B = \begin{bmatrix} L_\xi & L_\zeta \\ N_\xi & N_\zeta \\ Y_\xi & Y_\zeta \\ 0 & 0 \\ 0 & 0 \end{bmatrix}, \quad E = \begin{bmatrix} -L_\beta \\ -N_\beta \\ -Y_\beta \\ 0 \\ 0 \end{bmatrix}.$$

The output vector together with the corresponding output and direct feed matrices read:

$$y = [p, r, \beta, \Phi]^T, \quad C = I_{4 \times 5}, \quad D = [0 \ 0 \ -1 \ 0]^T.$$

Dynamic and control characteristics are investigated for a c.g. range of realistic and reasonable use. The forward limit is specified as $x_{for} = 11.12$ m indicating positive pitch stability. The rearward limit is defined by the minimum trimmed drag configuration $x_{opt} = 12.06$ m at Mach 6.8 yielding inherent instability, Ref. 6. Therefore, a reference position $x_{ref} = 11.22$ m has been chosen as a suitable compromise featuring marginal pitch stability up to Mach 5.5 and slightly aperiodic instability for higher Mach numbers.

Lateral Stability Characteristics

In contrast to longitudinal motion, where short- and long-term dynamics may be discussed separately due to different frequency levels, the lateral modes generally show more coupling and therefore can not be separated quite commonly. Furthermore, the decisive parameters are strongly dependent on the configuration as well as on the flight condition and hence, the lateral modes may be manifold shaped. However, in subsonic as well as hypersonic flight three typical modes of lateral dynamics can be usually identified: the dutch roll oscillation, the roll subsidence and the spiral mode.

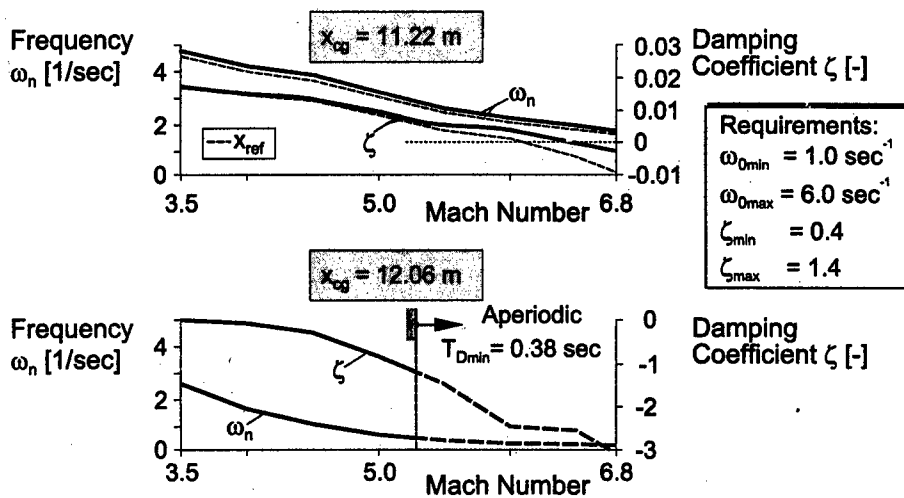


Fig. 7: Inherent dutch roll stability characteristics

An evaluation of inherent dutch roll characteristics of the test vehicle is presented in Fig. 7 and related flying qualities requirements (Ref. 14) are shown. The upper part of Fig. 7 depicts the natural frequency ω_n and the damping coefficient ζ for the forward c.g. position along the test profile. Additionally, the values for the reference c.g. position are plotted as dashed lines. Up to

approx. Mach 6 the dutch roll is stable but has a low damping. Beyond Mach 6 (resp. Mach 6.5 for the forward c.g. position) the dutch roll is unstable with a minimum time to double amplitude $T_D = 46.1$ sec. At the rearward c.g. position x_{opt} the dutch roll is permanently unstable and becomes aperiodic above Mach 5.5 exposing a minimum time to double $T_D = 0.38$ sec, as shown in the lower part of Fig. 7.

Another important flying qualities aspect concerns the roll-yaw-coupling which is illustrated in Fig. 8. As measure for the roll-yaw-coupling, the amplitude ratio of bank angle Φ versus sideslip β in the free dutch roll oscillation is used, and hence $|\Phi/\beta|$ approximately quantifies the roll reaction to a disturbance in sideslip. The roll-yaw-coupling can be determined by the dutch roll eigenvector relationships, for $N_\beta > 0$ the following approximation may be used:

$$\left| \frac{\Phi}{\beta} \right| \approx \left| \frac{L_\beta}{N_\beta} \right| \approx \left| \frac{C_{l\beta}}{C_{n\beta}} \cdot \frac{I_z}{I_x} \right| \quad (3)$$

With reference to flying qualities requirements (Ref. 14) a range for good aircraft behavior concerning $|\Phi/\beta|$ is specified and marked as a grey area in the upper part of Fig. 8. The determined $|\Phi/\beta|$ values are rather high with a maximum ratio $|\Phi/\beta| \approx 14$ or 17 for the forward or the reference c.g. position at Mach 6.8 respectively, and values over 200 for the rearward c.g. position x_{opt} . Since $|\Phi/\beta|$ is approximately proportional to the ratio of inertia I_z/I_x according to Eq. (3), the main reason for this high values is found in the slender configuration of the test vehicle with low moment of inertia I_x . Additionally, the decreasing weather-cock stability $C_{n\beta}$ with c.g. position shifted aft causes the extremely high values for the rearward c.g. position x_{opt} .

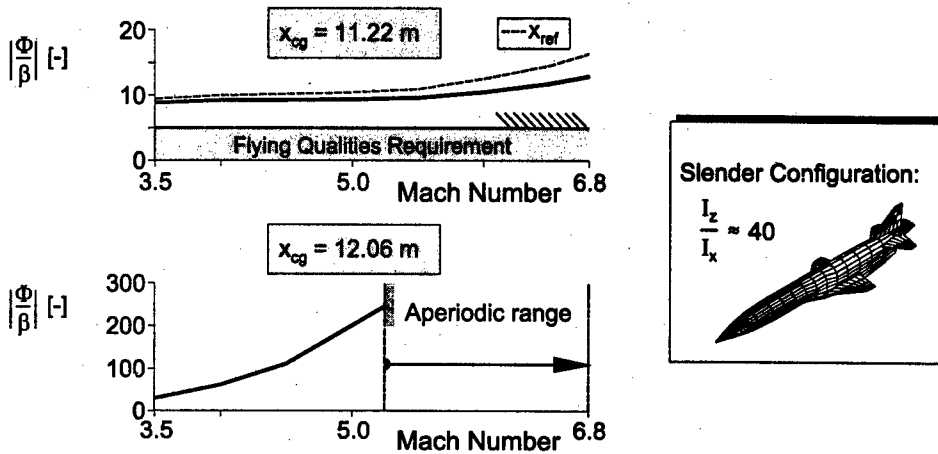


Fig. 8: Roll-Yaw-Coupling $|\Phi/\beta|$ in dutch roll oscillation

To illustrate the influence of the high roll-yaw-coupling on the lateral stability characteristics, the aircraft response to an initial sideslip disturbance ($\Delta\beta = 1$ deg specified, $Ma = 4.5$) is considered. A six degree-of-freedom nonlinear simulation is performed because of the expected large deviations from reference flight condition. Fig. 9 shows the time histories of sideslip β and bank angle Φ together with a pictorial sequence of the three-dimensional motion of the hypersonic vehicle. The dutch roll mode degenerates to an almost pure roll oscillation with small yaw/sideslip involvement.

Stability characteristics of roll subsidence and spiral mode are depicted in Fig. 10 together with related flying quality requirements. The upper part of Fig. 10 shows the roll time constant T_R for the three c.g. positions along the test profile. The roll mode has a weak damping due to the small-sized wing with low aspect ratio and hypersonic aerodynamic characteristics.

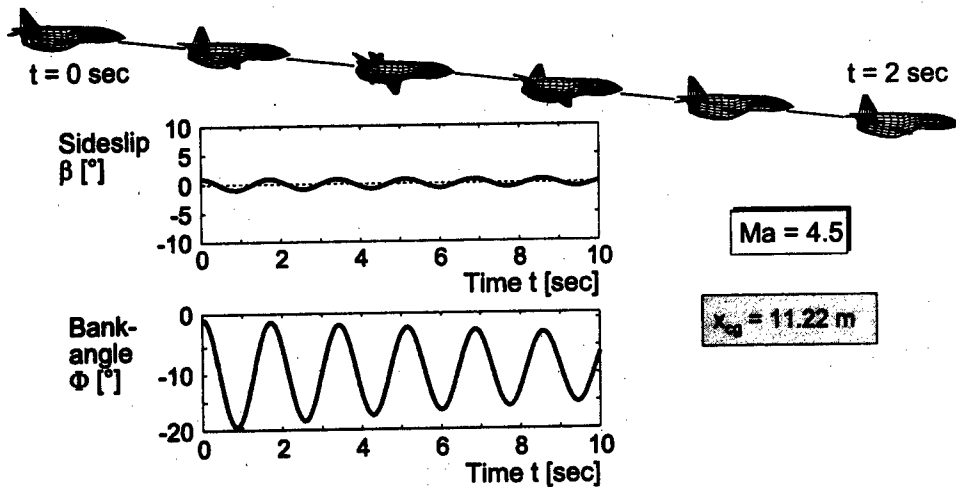


Fig. 9: Aircraft response to an initial sideslip disturbance $\Delta\beta = 1$ deg

The spiral mode, as illustrated in the lower part of Fig. 10, is almost neutral stable and therefore meets the flying quality requirements which allow a slight spiral instability.

Therefore, inherent lateral stability characteristics of the test vehicle in hypersonic flight can present significant flying qualities deficiencies relating to a weak roll damping in combination with a partially unstable dutch roll oscillation with high roll-yaw-coupling.

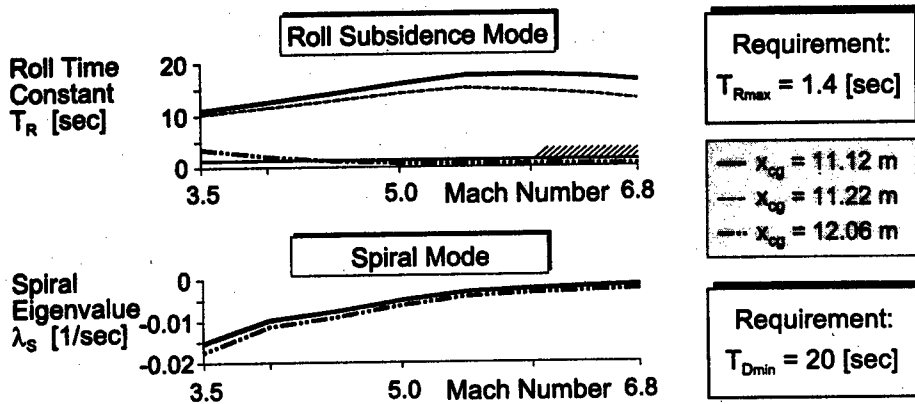


Fig. 10: Inherent stability characteristics of roll subsidence and spiral mode

Coupled Roll-Spiral-Oscillation

Another stability problem of lateral dynamics which was not identifiable with the previous investigation occurs for specific configurations of the hypersonic vehicles. For larger roll dampings the roll and the spiral poles are moving towards each other with a rearward shift of c.g. position. This is shown in Fig. 11 as root loci for the hypersonic test vehicle as well as for the carrier stage of a two-staged space transportation system (Ref. 15), c.g. shift step size $0.5\% l_{ref}$. The frequency of the dutch roll oscillation is decreased while shifting c.g. aft due to the reduced weather-cock stability ($\Delta C_{n\beta} = C_{Y\beta} \cdot \Delta x_{cg} / s_{ref}$). The roll and spiral poles are moving closer and combine to yield a slow coupled roll-spiral-oscillation (phugoid of lateral motion). Since the coupled roll-spiral-oscillation is difficult to control and causes considerable problems in lateral maneuvering it

is undesired and therefore not acceptable for most flight phases (Ref. 14). An unstable lateral phugoid, as seen in the left part of Fig. 11, is generally not allowed and has to be avoided in any case. Therefore, it is necessary to investigate the reasons for the appearance of this unusual mode and to investigate how to resolve this interesting stability problem.

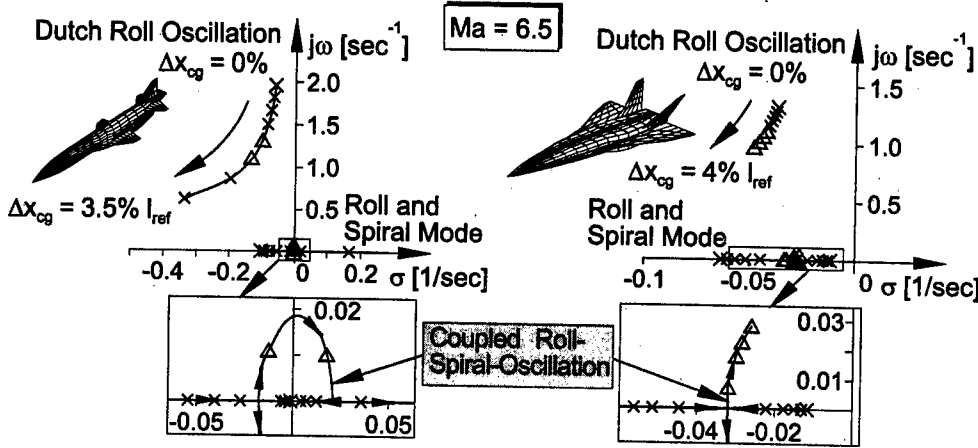


Fig. 11: Effect of a rearward c.g. shift on lateral dynamics for specific configurations

To gain better physical insight into the complex properties of lateral dynamics, it is useful to investigate the different lateral modes by appropriate approximations. Since the hypersonic stability characteristics show substantial differences compared with subsonic flight, specific approximations are needed. The proposed approach to determine suitable approximations for the hypersonic flight regime up to Mach 7 is based on the characteristic determinant of the fourth order state space equations (with the heading Ψ -equation cancelled out):

$$N(s) = \det(sI - A') = s^4 + a_3s^3 + a_2s^2 + a_1s + a_0 = [s^2 - 2\sigma_d s + \omega_{nd}^2] \cdot [s^2 - (s_s + s_r)s + s_s s_r] \quad (4)$$

Concerning the magnitude of the dutch roll and the roll/spiral poles, it can be assumed that $|s_d| \gg |s_{s,r}|$ in the Mach number regime of interest, Figs. 7, 8, 10. Therefore, the trajectory motion modes can be separated from the dutch roll oscillation and a common second order approximation for the roll and spiral mode as well as an approximation for the dutch roll oscillation is obtained. After neglecting minor important parts of Eq. (4), the following approximation for the dutch roll oscillation results:

$$\begin{aligned} \omega_{nd} &\approx \sqrt{N_\beta} \\ 2\sigma_d &\approx N_r + Y_\beta - \left(\frac{g}{V_0} - N_p \right) \frac{L_\beta}{N_\beta} \end{aligned} \quad (5)$$

For the spiral and roll modes, an approximation can be developed which holds also for coupling of the spiral and roll poles forming the lateral phugoid:

$$2s_{s,r} \approx L_p + \left(\frac{g}{V_0} - N_p \right) \frac{L_\beta}{N_\beta} \pm \sqrt{\left[L_p + \left(\frac{g}{V_0} - N_p \right) \frac{L_\beta}{N_\beta} \right]^2 - 4N_r \frac{g}{V_0} \frac{L_\beta}{N_\beta}} \quad (6)$$

In Fig. 12 the approximations are shown together with the exact solutions of the fourth order polynomial for the hypersonic test vehicle. Instead of varying the c.g. position, the weather-cock stability $C_{n\beta}$ is decreased because this yields the same effect, as shown before. The approximations show good agreement with the exact solutions and, especially, the coupled roll-spiral oscil-

lation could be identified well. Comparable good results are obtained for the carrier and orbital stage of a space transportation system in the Mach number range of concern.

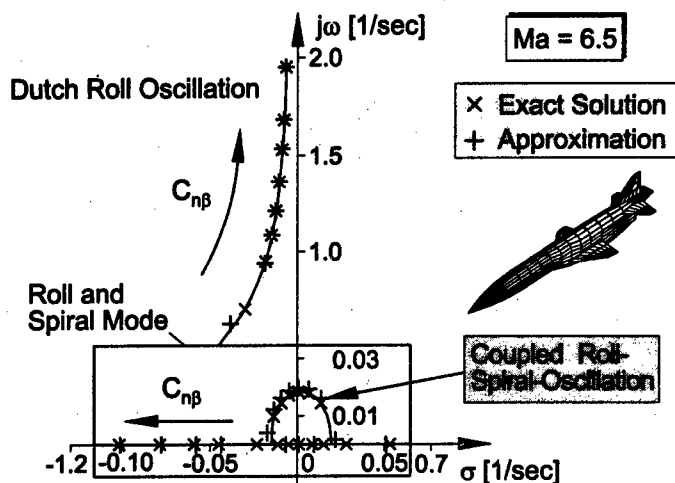


Fig. 12: Approximations and exact solutions for hypersonic test vehicle

The damping exponent σ_d includes besides the usual derivatives N_r and Y_β an additional dominant expression which is nearly proportional to the roll-yaw-coupling:

$$\left(\frac{g}{V_0} - N_p \right) \left| \frac{L_\beta}{N_\beta} \right| \approx \left(\frac{g}{V_0} - N_p \right) \left| \frac{\Phi}{\beta} \right| \quad (7)$$

This expression may show a positive or negative sign dependent on the configuration and flight condition and represent decisive contributions due to a high roll-yaw-coupling. The second order approximation for spiral and roll mode differs basically from the classical first order approximations valid in subsonic flight. Because of the small aerodynamic dampings in hypersonic flight, the usually dominant stability derivatives L_p , N_r , N_p are less important and the expression Eq.(7) which was also found in the dutch roll approximation is of great importance.

Now, analyzing the sign of the square root of Eq. (6) yields a criterion for the existence of the coupled roll-spiral oscillation:

$$\left[L_p + \left(\frac{g}{V_0} - N_p \right) \frac{L_\beta}{N_\beta} \right]^2 < 4N_r \frac{g}{V_0} \frac{L_\beta}{N_\beta} \quad (8)$$

From this relation, simple conditions can be derived indicating a possible existence of the lateral phugoid oscillation:

- $L_\beta / N_\beta < 0$; necessary for Eq. (8) since $N_r < 0$
- $(g/V_0 - N_p) < 0$; hence the two addends in left hand side brackets are opposed to each other
- High roll-yaw-coupling $|\Phi/\beta| \approx |L_\beta/N_\beta|$ for small $|g/V_0 - N_p|$

Summarizing the results of the investigations above, a high roll-yaw-coupling in combination with weak aerodynamic damping derivatives can be the main reasons for the stability deficiencies of lateral dynamics in hypersonic flight. The effects described by Eq. (7) are of considerable importance for dutch roll as well as roll/spiral characteristics. Based on this conclusions, requirements concerning configuration modifications and/or controller design may be specified related to the tasks of hypersonic flight.

Conclusions

Lateral dynamic characteristics and unsteady aerodynamic effects in hypersonic flight up to Mach 7 are considered.

Oscillations in yaw and roll of the second stage of a two-staged hypersonic vehicle are studied. The related unsteady flowfields are calculated using a finite-volume-method to solve the three-dimensional Euler equations. Surface pressure distributions and lateral aerodynamic coefficients are analyzed. For both the yawing and rolling motion the unsteady moment coefficients differs from the steady state calculations. Thus, unsteady calculations are needed to evaluate the associated stability derivatives in order to prescribe the separation process.

Inherent lateral dynamics in hypersonic flight show considerable stability and control deficiencies. Beside a partially unstable dutch roll mode with high roll-yaw-coupling and a weak roll damping, coupling of the roll and spiral poles appears for certain configurations. Since this so called lateral phugoid oscillation causes control problems and is additionally partly unstable, it has to be avoided. By use of specific approximations, the decisive reasons and effects concerning the stability deficiencies are analyzed and following requirements on a suitable control system structure could be identified.

Acknowledgement

The subject of this paper is part of the research of collaborative research center 255 'Transatmospheric Flight Systems' of the Deutsche Forschungsgemeinschaft DFG at Technische Universität München.

References

- 1 Kuczera, H.; Sacher, P. W.; Dujarric, Ch.: FESTIP System Study – An Overview. AIAA 7th International Space Planes and Hypersonic Systems and Technologies Conference, Norfolk, Virginia, Nov. 1996.
- 2 Freeman, D.; Reubusch, D.; McClinton, C.; Rausch, V.; Crawford, L.: The NASA Hyper-X Program. IAF-97-V.4.07, 48th International Astronautical Congress, Turin, Italy, Oct. 1997
- 3 Sancho, M.: The French Hypersonic Research Program: Progress Review. AIAA-95-6004, 6th International Aerospace Planes and Hypersonics Technologies Conference, Chattanooga, TN, April 1995.
- 4 Kobayashi, S.; Maita, M.: Japanese Spaceplane Program overview. AIAA-95-6002, AIAA 6th International Aerospace Planes and Hypersonics Technologies Conference, Chattanooga, TN, April 1995.
- 5 Rochholz, H.; Huber, Th.; Matyas, F.: Unsteady airloads during the separation of an idealized two-stage hypersonic vehicle. , ZFW, Zeitschrift für Flugwissenschaften und Weltraumforschung. Vol. 19, No. 1, pp. 2-9., 1995
- 6 Rochholz, H.; Schoder, W.: Separation of Two-Stage Hypersonic Vehicles. 2nd Space Course on Low Earth Orbit Transportation, Technische Universität München, 11th - 22nd Oct., Vol. 2, pp. 36-1 - 36-22, 1993.
- 7 Rochholz, H.: Eulerlösungen für den Separationsvorgang von Träger-Orbiter-Systemen im Hyperschall. Dissertation, Technische Universität München, DM 16120, 1994.
- 8 Sachs, G., Heller, M., Wahlberg, L.: Robust Control of a Hypersonic Experimental Vehicle with Ramjet Engines, AIAA 96-3728, San Diego, California, Juli 1996.
- 9 Sachs, G.: Flugeigenschaftskriterien und Langzeit-Dynamik im Überschall- und Hyperschallflug, ZFW, Zeitschrift für Flugwissenschaften und Weltraumforschung, Vol. 15, No. 4, S. 243-251, Germany 1991.
- 10 Yee, H. C.: Upwind and Symmetric Shock-Capturing Schemes. NASA TM 89464, 1987.
- 11 Heller, G.: Aerodynamik von Deltaflügelkonfigurationen bei Schieben und Gieren. Dissertation, Technische Universität München, DM 18259, 1997.
- 12 Sacher, P.W.: Flight Testing Vehicles for Verification and Validation of Hypersonics Technology. AGARD FVP, Symposium on Space Systems Design and Development Testing, Cannes, France, Oct. 3-6, 1994.
- 13 Sacher, P. W.; Zellner, B.: Flight testing objectives for small hypersonic flight test vehicles featuring a ramjet engine. AIAA-95-6014, AIAA 6th International Aerospace Planes and Hypersonics Technologies Conference, Chattanooga, TN, April 1995.
- 14 MIL-F-8785C: Military Specification - Flying Qualities of Piloted Airplanes. MIL Standard and Handbook, Washington, September 1991.
- 15 Kuczera, H., Hauck, H., Krammer, P., Sacher, P.: The German Hypersonics Technology Programme, IAF-93-V.4.629, Graz, Austria, 1993.

EVALUATION OF EFFECTIVENESS OF THE AIRDRYER CONSISTED OF COOLED ROTATING DISKS

S.V. Dolgushev

Institute of Theoretical and Applied Mechanics, SB RAS, 630090
Novosibirsk, Russia

The development of high-efficiency devices for ventilation, purification, and drying of air in production sites rooms represents one of the important problems in applied aerodynamics. In this connection, the facilities having as a principal element the system of rotating disks are of great interest. The last ones have simultaneously two functions: pumping air through device and air-drying due to vapour condensation on cooled surfaces.

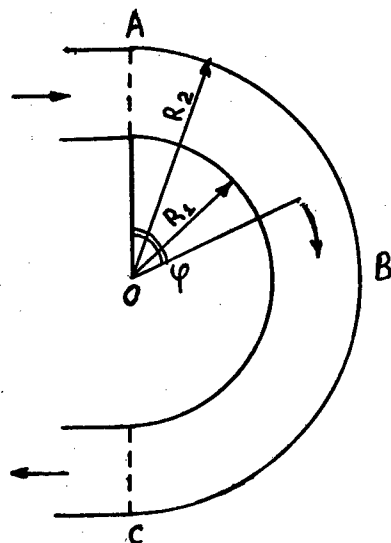


Fig. 1

In this report, approximate estimates are presented for such an air-dryer. Because of complicated flow patterns in device, that were not investigated earlier theoretically or experimentally, a simplified picture is used for flow field between disks and for water vapor condensation on cooled moving surfaces. Shown in Fig. 1 is a simplified flow picture in element of disk air-dryer (the description of the facility is given in paper [1] submitted to this conference). Air flows in a channel of rectangular cross section

© S.V. Dolgushev, 1998

bending through 180 degrees (circular path ABC). The upper and bottom walls of ABC portion of the channel have the same constant angular velocities of rotation equal to disks rotation velocity. The location of a fluid particle moving in a gap between disks is determined by an angle φ reckoned from line OA , where O is disks center, A is a point of junction of semicylindrical enclosure and rectangular entry part. The semicircular stripe ABC of width $(R_2 - R_1)$ ($0 \leq \varphi \leq \pi$) is an active part where the main process of water vapour deposition onto cooled disks surfaces takes place. Here, R_2 is a disk radius, R_1 is a radius of a cylindrical hub on which disks are hold. Effects of secondary circular flows [2,3] appearing in rotating fluid are not taken into account. This flow model is based, in essence, on results of computations presented in papers [2,3] (we suppose some analogy of our flow and that in enclosed configuration), and those of measurements performed by authors of report [1]. According to this model, the main part of fluid flows with a constant linear velocity $0,6\Omega R_2$ along the arc ABC (Ω is circular frequency of disks rotation), thus, breaking away from channel walls. Regarding condensation process, a number of usual simplifying assumptions is made, such as absence of influence of condensation on the flow picture, vapour concentration at the disk surfaces corresponds to saturation conditions at surface temperature, that is constant, absence of the longitudinal diffusion etc. Most of them are quite justified at atmospheric pressure and air temperature 20–30°C. Possibility of condensation onto the surfaces of hub and shell surfaces is ignored. Two cases were considered: 1) the flow is laminar, and vapour transfer to disks is controlled by molecular diffusion throughout all the space between disks: 2) the flow is turbulent, in its major part an effective mixing takes place resulting in an uniform distribution of vapour concentration throughout this portion of the flow field, all the resistance to the mass transport is concentrated in a thin wall viscous sublayer.

1. **Laminar flow.** In this case an uniform velocity profile is assumed (plug flow) everywhere along an effective channel, and mass transport to the wall is driven by molecular diffusion throughout all the space between disks. The problem is reduced to the solution of the equation in dimensionless form

$$\frac{\partial n}{\partial \varphi} = \gamma \frac{\partial^2 n}{\partial z^2},$$

that describes water molecules diffusion in air between disks. The solution should be found in a region $0 \leq \varphi \leq \pi$, $0 \leq z \leq 1$, where z is a distance from symmetry plane(located between disks) scaled on the semihight of the channel d , n is water molecular concentration, divided on

its entry value, $\gamma = D/(0.6\Omega d^2)$. Molecular diffusion coefficient for water in air D is expressed by formula: $D = 2,16 \cdot 10^{-5}(T/273)^{1,8}$ m/s², T is air temperature. Boundary conditions are taken in the form: 1) $n = 1$ at $\varphi = 0$ - distribution uniformity for vapour concentration in entry plane; 2) $\partial n/\partial z = 0$ at $\varphi > 0$, $z = 0$ - symmetry about the middle plane in a gap between disks 3) $\partial n/\partial z = -\alpha(n - \beta n_s)$ - condition of matching of two expressions for molecular flow to a solid surface, one defined by Fick's law and another by kinetic Hertz - Knudsen formula. $\alpha = (K_c/D)[RT/(2\pi\mu)]^{1/2}$, $\beta = K_e n_s \sqrt{T_s/T/K_c}$, where K_c and K_e are condensation and evaporation coefficients, respectively, taken equal to 0.9 and 0.8, T_s is a disk temperature, R is an universal gas constant, μ is molecular weight of water. Using method of variables separation [4], we find the solution in a form:

$$n = \beta n_s + (1 - \beta n_s) \sum_{i=1}^{\infty} A_i \exp(-\gamma \lambda_i^2 \varphi) \cos(\lambda_i z),$$

λ_i are eigenvalues, determined by an equation $\tan \lambda_i = \alpha/\lambda_i$. For the conditions considered here α is about 100 and greater, so a number of first eigenvalues and coefficients A_i can be evaluated by formulae [4]:

$$\lambda_i \simeq \frac{2i-1}{2} \pi, \quad A_i = \frac{(-1)^{i+1} 4}{(2i-1) \pi}, \quad i = 1, 2, \dots$$

Averaging of vapour concentration across the spacing between disks gives an expression for dependence of average vapour concentration on angle φ :

$$\bar{n} = \beta n_s + \frac{(1 - \beta n_s)}{2} \sum_{i=1}^{\infty} A_i^2 \exp(-\gamma \lambda_i^2 \varphi).$$

The degree of cleaning of air from water vapour at the exit essentially depends on the disks rotation frequency because of $\gamma \sim \Omega^{-1}$.

2. Turbulent flow. To estimate drying effectiveness of a humid air in this case, as a basic model was taken that presented in paper [5]. It gives good predictions of experimental data for an amount of condensed water in narrow, right, metallic pipes of circular cross section for, approximately, the same range of flow parameters as we use. The major contribution to the resistance to diffusive mass transport in a direction of channel walls supposed to be concentrated in a thin (\sim some percents of the channel width) viscous sublayer with a width $\delta = 127d / \text{Re}_{ref}^{0,875}$, where $\text{Re}_{ref} = dR_2\Delta\Omega/\nu$, ν is kinematic viscosity of air, $\Delta\Omega$ is a difference between average circular frequencies of disk surfaces in the arc path ABC and that of fluid, it was taken to be equal $0,15\Omega$. This estimation was

derived from the fact that, according to [2,3], in a range $0,6R_2 < r < R_2$ gas possess an average velocity nearly $0,65R_2\Omega$, and for disks an average linear velocity here is about $0,8R_2\Omega$ (for a case of flow in an enclosure). Test estimates have show a good agreement of values of δ calculated in such a way with width of zones of sharp asimuthal velocity changing near disk surfaces shown on graphics of [2,3] (order of magnitude and better). Modification of the model [4] for our situation leads to the following problem: to determine the vapour concentration in turbulent core we should solve an ordinary differential equation in dimensionless form:

$$\frac{\partial \bar{n}}{\partial \varphi} = -\theta(\bar{n} - n_s)$$

with boundary condition $\bar{n}(0) = 1$. Here $\theta = D/(0,6\Delta\Omega(d - \delta)\delta)$. The solution is

$$\frac{\bar{n} - n_s}{1 - n_s} = \exp(-\theta\varphi).$$

Note, that in this case we have a weak dependence of \bar{n} on Ω because of $\theta \sim \Omega^{-0,125}$.

3. Results and conclusions. Calculations were performed for the following conditions in production room and parameters of drying facility: the pressure equals to 1 atm, air temperature equals to 25°C, relative air humidity equals to 95%, the distance between disks equals to 4 mm, radius of disks is 1 m. Disk temperature was varied in a range $0 \div 16^\circ\text{C}$, speed of disks rotations - in a range $100 \div 1500$ rpm.

In Figs. 2 and 3, dependences of relative humidity on angle φ are illustrated for the following conditions: speed of disks rotation equals to: 100 (solid lines), 250 (dashed lines), and 1000 (puncture) rpm. The ciphers denote the temperature ($^\circ\text{C}$) of disks: 1 - $T_s = 0$, 2 - 8, 3 - 16°C . Graphics on Fig. 2 correspond to laminar model, on Fig. 3 - to turbulent model. One can make the following conclusions.

1. The system of cooled rotating disks presents an effective tool for air dehumidification in rooms with a high content of water vapor.

2. If the flow regime between disks is laminar, then air humidity at the exit of facility functioning at relatively high values of T_s (for example, 16°C) depends essentially on residence time of gas portion in a space between disks, that is on rotation frequency. At moderate cooling of disks in laminar regime of air drying, one should determine an optimum rotation frequency providing desired degree of exit humidity at required volume throughpumping. If an intensive cooling of disks is used ($T_s = 0 \div 8^\circ\text{C}$),

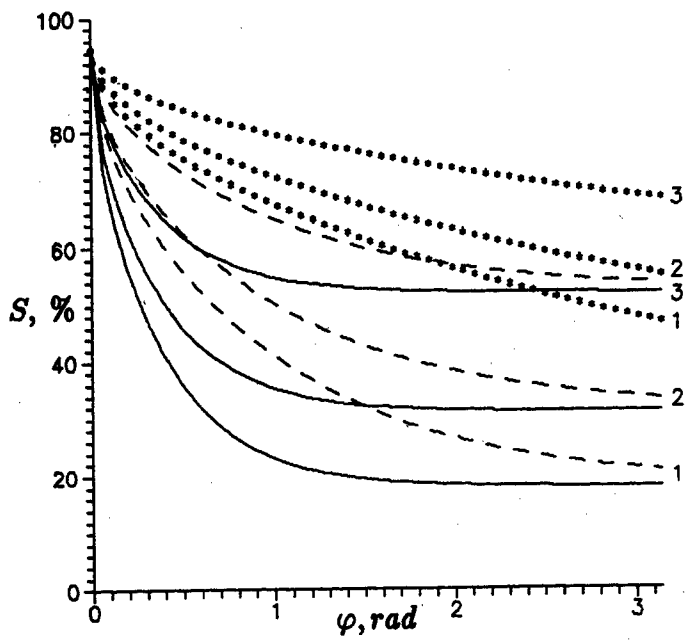


Fig. 2

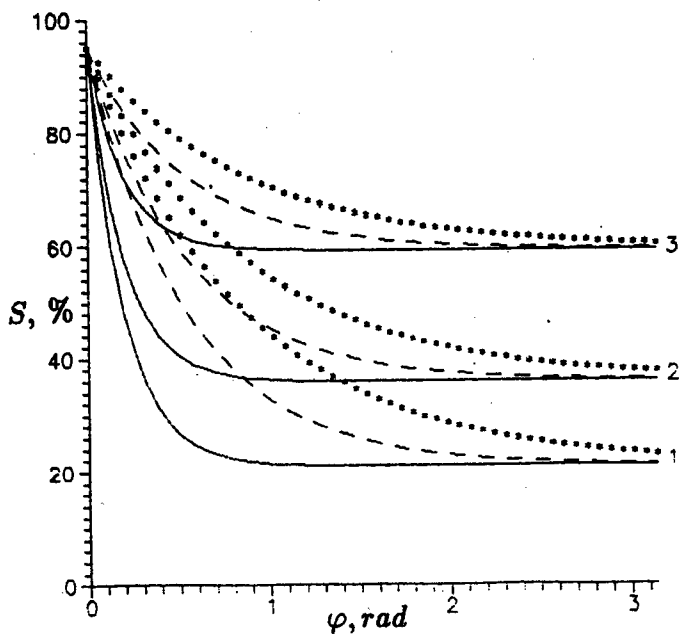


Fig. 3

then device productivity can be risen considerably through an increasing of disks rotation frequency.

3. If the flow regime between disks is turbulent, then dependence of air dehumidification on rotation frequency is expressed rather weaker than in laminar case for a wide range of T_s values. As a sequel, when requirements to the degree of dehumidification are not very high, the productivity of the airdryer can be risen through an increasing of rotation frequency at moderate disk cooling.

REFERENCES

1. Fomichev V.P., Khaidarov S.V., Kovrizhina V.N., Pravdin S.S., Zharkova G.M. The study of special gasdynamic features of the flow in a diameter disk pump by means of liquid crystal thermography // Int. Conf. on the Methods of Aerophys. Research: Proc. Pt II. - Novosibirsk, 1998.
2. Chang C.J., Humphrey J.A.C., and Greif R. Calculation of turbulent convection between co-rotating disks in axisymmetric enclosures // Int. J. Heat and Mass Transfer. - 1990. - Vol.33. - P.2701.
3. Schuler C.A., Usry W., Weber B., Humphrey J.A.C., and Greif R. On the flow in the unobstructed space between shrouded co-rotating disks // Phys. Fluids. - 1990. - Vol.A2. - P.1760.
4. Luikov A.V. The theory of heat conduction. - Moscow: Nauka, 1967.
5. Vizel Ya.M., Mostinskii I.L. Mass exchange by vapour condensation from vapour-gas mixture // Izv. AN SSSR. Ser.: Energetika i transport. - 1968. - N 3. - P.122.

PROPAGATION AND REFLECTION OF NONEQUILIBRIUM SHOCK WAVES IN TWO-COMPONENTS MEDIA

A. V. Fedorov and A. A. Zhilin

Institute of Theoretical and Applied Mechanics SB RAS, 630090, Novosibirsk, Russia

The structures of shock waves (SW) in the mixture of two solids are described in [1-3] taking into account the pressure and velocity difference of the components. It was established that SWs can be of four types: completely dispersion, frozen-dispersion, dispersion-frozen and frozen two-front configuration. For a mixture of two compressible media it was shown in [4] that at SW reflection from a rigid wall its type is retained. The SW reflection from a rigid wall in a mixture of gas and small solid particles was investigated in [5] in the two-velocity two-temperature approximation. It was shown that three types of transition from incident SWs (frozen and dispersed structure) to reflected ones were available depending on the pressure difference on the incident SW. The processes of propagation, initiation and reflection of shock waves of various types from a rigid border in a mixture of liquid and solid particles are considered below.

PHYSICO-MATHEMATICAL FORMULATION OF THE PROBLEM

To describe the process of propagation of unsteady shock waves over a heterogeneous mixture of condensed media with different pressures and velocities of components, we involve the equations of mechanics of heterogeneous media. The mass and momentum conservation laws for each component of the mixture, complemented by the equation of m_2 - transfer and equations of state, are written in the following nondimensional form:

$$\begin{aligned} \frac{\partial \rho_1}{\partial t} + \frac{\partial \rho_1 u_1}{\partial x} = 0, \quad \frac{\partial \rho_2}{\partial t} + \frac{\partial \rho_2 u_2}{\partial x} = 0, \quad \frac{\partial \rho_1 u_1}{\partial t} + \frac{\partial \rho_1 u_1^2}{\partial x} = -m_1 \frac{\partial R}{\partial x} + F_S, \\ \frac{\partial \rho_2 u_2}{\partial t} + \frac{\partial \rho_2 u_2^2}{\partial x} = -m_2 \frac{\partial P_2}{\partial x} - (P_2 - R) \frac{\partial m_2}{\partial x} - F_S, \quad \frac{\partial m_2}{\partial t} + u_2 \frac{\partial m_2}{\partial x} = R, \end{aligned} \quad (1)$$

$$m_1 = 1 - m_2, \quad R_1 = \rho_1 / m_1 - 1, \quad P_2 = a^2 (\rho_2 / m_2 - \bar{\rho}), \quad \rho_i = m_i \rho_{ii},$$

where m_i are the volume concentration of the i -th component of the mixture; $F_S = m_1 \rho_2 (u_2 - u_1) / \tau_S$ is the Stokes force; $\tau_S = 2\bar{\rho} / (9\mu_1)$ is the time of the Stokes velocity relaxation; $R = m_1 m_2 (P_2 - R_1) / \tau_{m_2}$ is a function that describes the solid phase transfer process; $\tau_{m_2} = \mu_2 / (\rho_{1,0} a_1^2)$ is the pressure relaxation time for the mixture components; $a = a_2 / a_1$; $\bar{\rho} = \rho_{2,0} / \rho_{1,0}$. Velocities are nondimensionalized to a_1 , densities - to $\rho_{1,0}$, pressures - to $a_1^2 \rho_{1,0}$, x - to the radius of solid particles, t - to $t_0 = r / a_1$, μ_i - to $a_1 \rho_{1,0} r$.

A correct problem for system (1) is the Cauchy problem for the solution vector $\Phi(\rho_1, \rho_2, u_1, u_2, m_2)$

$$t = 0: \quad \Phi = \Phi_1 \quad (2)$$

where Φ_1 is the vector of flow parameters at the initial time moment.

Problem 1. Stability of SW propagation. A steady SW described by a solution of the boundary-value problem for a system of ordinary differential equations (ODE) [1 - 3] is considered as the initial data. In this case, Φ_1 can be: continuous functions for fully dispersed SW; discontinuous functions in the first (light) component and continuous functions in the second (heavy) component for frozen-dispersed SW; continuous functions in the first component and discontinuous functions in the second component

for dispersed-frozen SW; discontinuous functions in the both components for frozen SW. Such initial data contain small perturbations of all wavelengths caused by the use of the numerical method of solving the boundary-value problem for an ODE system. The results of calculating this problem are often treated in the literature as the study of stability of steady SW propagation with respect to infinitesimal perturbations.

Problem 2. Initiation of a steady SW. The function φ_1 is assumed to be a constant solution ahead of the SW front propagating with velocity D (initial state φ_0) and behind the front (final state φ_K). The initial and final states belong to the equilibrium Hugoniot's adiabat.

Problem 3. SW reflection on a rigid wall. The initial-boundary conditions for the problem under consideration are presented as

$$\varphi = \varphi_1(x), \quad x \geq 0, \quad t = 0, \quad u_1 = u_2 = 0, \quad x = 0, \quad t \geq 0.$$

The solution vector $\varphi_1(x)$ describes here steady SW.

REFLECTED SW PARAMETERS IN EQUILIBRIUM APPROXIMATION

Let an SW propagate from the left to the right in a medium at rest with initial parameters $\rho_i = \rho_{i0}$, $u_i = 0$, $P_i = 0$, behind its front the mixture parameters acquire finite equilibrium values. For an equilibrium state behind the reflected SW $u_i = u_r = 0$ and $P_i = P_r$. From the conservation laws of mass and momentum for incident and reflected SW we obtain a cubic equation for determining are velocities of the reflected SW D_r , that has a trivial solution $D_r = D$ corresponding to the incident SW velocity, and two real roots

$$D_r^\pm = \frac{2 - C + u_K \rho_K D - C_{ef}^2 \rho_K \pm \sqrt{(C - u_K \rho_K D + C_{ef}^2 \rho_K)^2 + 4 \rho_K (u_K^2 \rho_K C_{ef}^2 - C_{ef}^2 + u_K D)}}{2 u_K \rho_K}$$

One can easily see that the radicant is always positive, the lower branch (corresponding to the minus sign) where $D_r^- > 0$ is physically meaningful. The behavior of reflected SW velocity, relative phase velocities behind its front, equilibrium speeds of sound are shown in Fig. 1 versus m_{10} for an incident SW velocity $D = -1.5$.

DISCUSSION OF NUMERICAL RESULTS

The posed problems 1, 2 and 3 are solved using the "coarse particles" method of the first-order approximation [6], modified to take into account the equations of compacting kinetics.

Stability of propagation of SW of various types (problem 1). Let us consider the propagation of various types of SW obtained in [3] for a self-similar flow of the mixture within the framework of unsteady approximation.

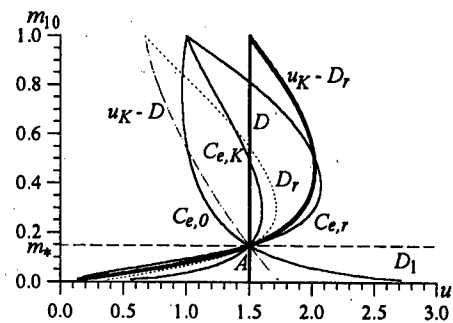


Fig. 1. Behavior of characteristic velocities of the mixture versus m_{10} for $D = -1.5$.

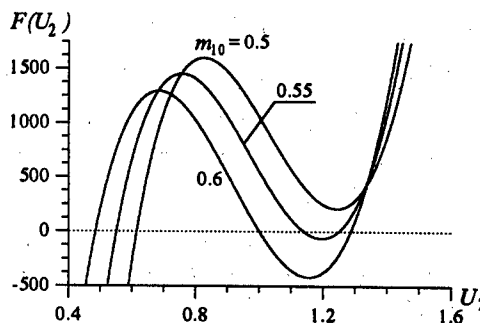


Fig. 3. Behavior of the function $F(U_2)$ versus m_{10} for $U_0 = 25$.

1. For $D = -1.5$ and small values of m_{10} the steady-state formulation yields a fully dispersed flow for the both components of the mixture. Constant equilibrium values of the mixture parameters are sustained in problem 1 at the right boundary of the flow region, and a steady leftward propagation of a dispersed SW with monotonic velocity and pressure profiles of components is observed. In computations, these profiles move steadily with a constant velocity and remain monotonic at later instants $t = 100, 300$ and 500 .

It was shown that the increase of the volume concentration of the light component causes the change of the flow type from fully dispersed to frozen-dispersed flow. Steady state is violated here in the beginning of computations, but then the flow with the previous profile is established again. The time of flow stabilization is $t < 10$. Afterwards, the propagating wave retains a constant configuration of a frozen-dispersed SW.

2. As the SW velocity increases ($D = -2.5$), the flow is at first a fully dispersed SW with a monotonic (for $m_{10} = 0.1$) or nonmonotonic (for $m_{10} = 0.3$ and 0.5) velocity profile in the light component. The velocity profile in the first component is nonmonotonic. With increasing the water content in the mixture, the flow structure is changed; an SW arises in the first phase. It was found that for $D = -2.5$, $m_{10} = 0.7$ and 0.9 the SW propagates steadily with a constant velocity. The shock is slightly smeared because of the solution technique.

3. Let us increase the SW velocity $D = -3.3$. Analysis of the pressure profile of the second component showed that the front shock is also smeared a little because of the solution technique, and the wave propagates steadily with velocity $D = -3.3$.

Increasing the volume concentration $m_{10} = 0.7; 0.9$ with the same value $D = -3.3$, we pass to the region of existence of a frozen SW with a two-wave structure. In this case, a stable steady propagation of a two-wave configuration in the initial form is observed.

Initiation of shock waves (problem 2).

1. A dispersed SW with velocity $D = -1.5$ is formed from stepwise initial data at $m_{10} = 0.2$. The formation process of such an SW continues from $t = 0$ to 300 . With increasing m_{10} , the duration of SW formation decreases, and at $m_{10} = 0.5$ the stabilization period is reduced to $t = 100$. An increase of m_{10} up to 0.6 leads to the flow restructuring: an internal SW appears in the light component. The amplitude of arising SW is very small; thus, it was difficult to determine its position in the steady-state problem. At the initial stage of stabilization, there is a peak in pressure of the second component over its equilibrium value, which is gradually resolved with time. At $m_{10} = 0.7$ the pressure in the heavy component has a nonmonotonic behavior, and one should take into account singularities of steady-state solutions to distinguish nonmonotonicity caused by numerical integration (like, for instance, at $m_{10} = 0.6$). With further increase of m_{10} up to 0.85 and 0.95 , the SW amplitude increases, the velocity profiles of components become more and more different. For these values of m_{10} , the flows are formed by $t = 30$.

2. When D is increased up to -2.5 , a steady flow is formed faster than at $D = -1.5$. The analysis of results of computing the flow with different values of m_{10} ($0.1, 0.3, 0.5, 0.6, 0.7, 0.9$) showed that they are completely coincident with those obtained previously in problem 1. This allows one to state that initiating the flow from stepwise initial data, it is always possible in due time to obtain the velocity and pressure profiles of components of the same structure as in solving a self-similar problem. Moreover, on the basis of solving the initiation problem one can obtain flows whose steady-state calculation was difficult because of internal singularities. Figure 2 shows the velocity and pressure profiles for a mixture with $m_{10} = 0.6$. The solution in a self-similar approximation was complicated because of necessity

of a smooth transition through the speed of sound in the first component. Analyzing the profiles at $t = 20$ and 30 one can conclude that the transition from a supersonic state into a subsonic one in the first component is performed by means of a low-amplitude internal SW. Behind the SW, the liquid is accelerated, and its velocity profile approaches smoothly the sonic point, which is an unstable singular point and through which the flow passes continuously to a supersonic state.

Let us analyze the picture of transition in a transonic flow type in the first phase with a singular point mentioned above. The variation of the first phase velocity is described by an ordinary differential equation $dU_1/d\zeta = U_1(F_S - \rho_1 R/m_1)/\rho_1(U_1^2 - 1)$. As the first component velocity approaches the speed of sound of the first phase, a gradient catastrophe occurs. Equating the numerator in \dot{U}_1 to zero at $U_1 = 1$, we obtain that the value of velocity U_2 in the heavy component satisfies the equation of the fifth order $F(U_2) = 0$. The resultant equation has one real root which lies within the interval from 0 to 1. It is physically meaningless and will not be further considered. Behavior of the function $F(U_2)$ is presented in fig. 3 as a function of the parameter m_{10} . We can trace the process of appearance of two new roots of equation. Thus, at $m_{10} = 0.5$ a U-shaped branch of $F(U_2)$ is located above the abscissa axis that goes down with increasing m_{10} and touches this axis at $m_{10} \approx 0.5396$. Two multiple roots appear thereat. A further increase of volume concentration of the light component leads to appearance of two different roots. With the growth of m_{10} , one solution shifts towards a smaller value of U_2 , and the other increases.

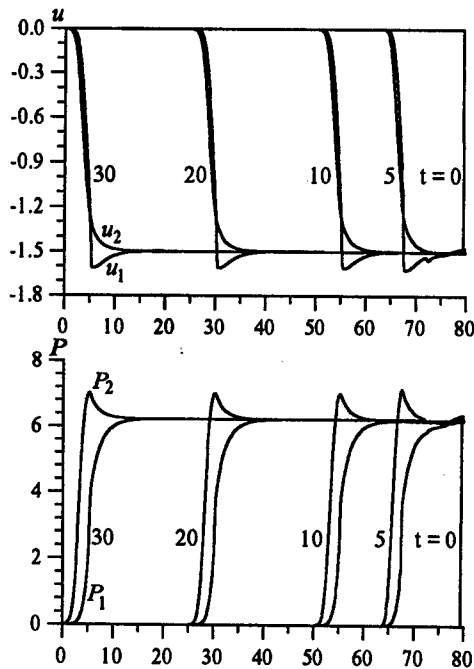


Fig. 2. Velocity and pressure distributions of components for $D = -2.5$ and $m_{10} = 0.6$.

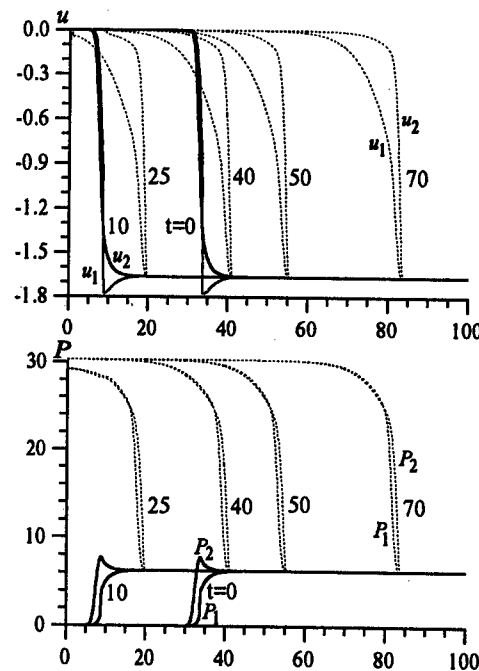


Fig. 4. Velocity and pressure profiles for shock wave reflection with $D = -2.5$ and $m_{10} = 0.7$.

Thus, for an initial velocity $U_0 = 2.5$ the transonic flow region begins at $m_{10} \approx 0.53$ and ends at $m_{10} \approx 0.6005$. It should be noted that after the formation of the flow with a sonic final state in the first phase $U_1 = U_2 = U_K = 1$, the subsequent motion of the mixture with increasing m_{10} have a subsonic final state in the both components. The analysis validates that a continuous transition from subsonic to supersonic branch of solution is possible.

3. With increasing D up to -3.3 , the flow is complemented with a bow SW in the second component for all m_{10} . The process of establishment for $m_{10} = 0.2$ and 0.4 can trace the formation of a bow SW whose amplitude fluctuates slightly at the initial stage of flow stabilization. It should be also noted that a monotonically decreasing velocity profile u_2 in the flow with a bow SW is formed faster than nonmonotonic velocity profile in the first component. A flow entering the transonic region is formed at $m_{10} = 0.5$. For an SW with the propagation velocity $D = -3.3$, the width of the region of existence of transonic flow with varied m_{10} increases. The computations showed that the transonic region begins at $m_{10} \approx 0.43$ and ends at $m_{10} \approx 0.6063$. If $m_{10} = 0.7$ or 0.9 , a flow with a two-front SW is formed: with a bow SW in the second component and with an internal SW in the first one. As in the previously considered problem of stabilization, the flow with a front discontinuity in the second phase is formed faster than the flow with an internal discontinuity in the first phase.

SW reflection on a rigid wall (problem 3).

1. For $D = -1.5$ and small m_{10} , the incident SW of a fully dispersed configuration is reflected as an SW of similar type (the mixture parameters are such that the phases have close values of velocities and pressures). The reflected wave is rapidly formed and stabilized. It is seen from fig. 1 that the reflected SW velocity ($D_r = 1.636$) is slightly higher than the modulus of the incident SW velocity ($D = -1.5$). The reflected wave width is smaller than that of the incident wave. This is caused by amplification of the reflected SW. Let us consider now the reflection of a frozen-dispersed SW with $m_{10} = 0.85$. The SW, incident with equal velocity, has an internal discontinuity here in flow parameters of the first component and is continuous for the second component. The reflected SW belongs to the same class, but is characterized by a nonmonotonic behavior of water velocity.

2. Let $D = -2.5$. If $m_{10} = 0.3$, the flow is continuous in the both components. The velocity is decreasing monotonically in the second component and having a minimum in the first one. When a shock wave of this structure is reflected, the type of the wave configuration is changed. The reflected SW has a bow wave in the second component and a monotonically increasing velocity profile in the first one; i.e., it is dispersed-frozen. The pressures in components of the mixture increase monotonically. Note that there appears an internal equilibrium point for the pressures of components. The pressure amplitude in the reflected SW is nearly twice as high as the incident SW amplitude. At $m_{10} = 0.7$ the incident frozen-dispersed SW has an internal SW in the first phase and a continuous flow in the second one. The reflected wave in a dispersed-frozen SW with a bow discontinuity is the second component of the flow and continuous in the first one (Fig. 4). For the case of $m_{10} = 0.9$ the reflected SW is continuous in the second component, since $|\mu_K - D_r| = -2.809 < a_2 = 3$. The monotonic velocity profile of the second component has a maximum whose value is higher than the mixture parameters in the equilibrium state behind the reflected SW front.

3. If $D = -3.3$, then at small values of m_{10} the incident and reflected shock waves belong to the dispersed-frozen flow type. When the SW is reflected, a flow of the same type is formed with a nonmonotonic velocity profile in the first component. The width of the

relaxation zone in a reflected SW increases nearly twice at $m_{10} = 0.2$ and thrice at $m_{10} = 0.4$. This effect is caused by a drastic reduction (by nearly 6.7 times at $m_{10} = 0.2$ and by 5.7 times at $m_{10} = 0.4$) of the volume content of liquid behind the incident SW because of inertial properties of the mixture materials. Note that the shock amplitude in the second component increases after reflection.

With increasing the initial volume concentration of the light component, the incident SW is a frozen SW of a two-front configuration, and the reflected SW is either dispersed-frozen at $m_{10} < m_1^*$, or frozen of a two-wave configuration at $m_{10} > m_1^*$.

CONCLUSIONS

- On the basis of numerical simulation of unsteady problems of SW propagation in a heterogeneous mixture of condensed media with different pressures and velocities it is shown that all possible types of SW are stable with respect to infinitesimal disturbances and are developed in time from stepwise initial data which is the initial and final steady states on the equilibrium Hugoniot's adiabat.
- Are proved that exists a transonic motion of the mixture in the form of a frozen-dispersed SW with a continuous transition through the speed of sound in the first phase.
- Specific features of SW reflection of different structure on a rigid wall are established numerically and analytically. It is shown, in particular, that: a) an incident SW of a dispersed type can be reflected either as a dispersed or as a dispersed-frozen SW; b) a frozen-dispersed SW with a monotonically decreasing velocity profile is reflected as a frozen-dispersed SW with either monotonically decreasing or nonmonotonic velocity profile in the first component. A frozen-dispersion wave with a nonmonotonic velocity profile in the first component can be reflected as a dispersed-frozen SW with monotonic velocity profiles of components or as a dispersed SW with nonmonotonic velocity profile in the second component; c) a dispersed-frozen SW with a minimum in the first component velocity is reflected as a dispersed-frozen SW with nonmonotonic velocity profiles; d) a frozen SW of a two-front configuration can be reflected either as a dispersed-frozen SW with monotonic velocity profiles or as a frozen SW of a two-front configuration.

REFERENCES

1. Zhilin A.A., Fedorov A.V. and Fomin V.M. A traveling wave in a two-velocity mixture of compressible media with different pressures // *Doklady AN.* - 1996. - Vol. 350, No. 2. - P. 201 - 205.
2. Zhilin A.A. and Fedorov A.V. The shock wave structure in a two-velocity mixture of compressible media with two pressures // *Int. Conf. on Methods of Aerophys. Research: Proc. Pt 2.* - Novosibirsk, 1996, P. 237-242.
3. Zhilin A.A. and Fedorov A.V. The structure of shock wave in a two-velocity mixture of compressible media with different pressures // *Prikl. Mekh. Tekh. Fiz.* - 1998. - No. 2. - P.10 - 19.
4. Fedorov A.V. and Fedorova N.N. Structure, propagation and reflection of shock waves in a mixture of two solids (hydrodynamic approximation) // *Prikl. Mekh. Tekh. Fiz.* - 1992. - No. 4. - P.10 - 18.
5. Miura H., Saito T. and Glass I.I. Shock-wave reflection from a rigid wall in a dusty gas // *Proc. R. Soc. Lond.* 1986. A 404. P. 55 - 67.
6. Gubaidulin A.A., Ivandaev A.I. and Nigmatulin R.I. A modified "coarse particles" method for calculating unsteady wave processes in multiphase dispersed media // *Zh. vychisl. matem. i matem. fiz.* - 1977. - Vol. 17, No. 6. - P. 1531 - 1544.

PARAMETRIC INVESTIGATION OF FLOWFIELD STRUCTURE AND VALIDATION ISSUES IN 3-D CROSSING-SHOCK WAVE/TURBULENT BOUNDARY LAYER INTERACTIONS

Datta V. Gaitonde, M.R. Visbal & J.S. Shang
Air Vehicles Directorate, Air Force Research Laboratory
Wright-Patterson AFB, Ohio, USA

A.A. Zheltovodov & A.I. Maksimov
Institute of Theoretical and Applied Mechanics
Novosibirsk, Russia

Abstract

This paper presents some insights gained from a computational study of the three-dimensional interaction caused by the turbulent crossing-shock interaction. The accuracy of the scheme in reproducing the features of the flowfield is first established by comparisons with a variety of strong interaction experimental data. The four primary regimes in the flowfield are summarized and the model is then extended to describe the evolution with increasing asymmetry. The sidewall/shock-vortex interaction, characteristic of highly asymmetric situations, is investigated in detail. The baseline turbulence model fails to predict some of the primary features observed in the experiment. However, a modification which controls the development of the fin boundary layer by limiting the production of turbulence kinetic energy rectifies this discrepancy. The sidewall interaction is shown to cause the ejection of the corner vortex in a direction parallel to the sidewall and generally normal to the plate. The improved understanding of flowfield is utilized to comment on observed quantitative discrepancies and several areas of future computational research are identified.

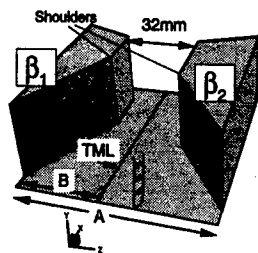
§1 Introduction

The interaction of shock waves with boundary layers results in a complex variety of phenomena including three-dimensional separation and the formation of vortical structures. In inlets of propulsion systems, these flow features degrade performance or limit operation envelopes because of the associated reduction in pressure recovery and increase in distortion. A clear understanding of the fundamental physics is thus a critical component in efforts directed towards improving inlet design.

Basic studies of shock wave/turbulent boundary layer interactions (STBLI) are generally performed in geometrically simple configurations which nevertheless retain the pertinent fluid dynamic mechanisms and provide an ideal testbed for computational investigations. Typically, shock generators are mounted a plate which provides a platform for the turbulent boundary layer. Space constraints do not permit a detailed literature survey: some review articles include Refs. 1-3. The present work focuses on the double-fin (or crossing-shock) configuration shown in Fig. 1. The principal flow parameters determining the details of the interaction are the Mach and Reynolds numbers, the properties of the incoming boundary layer, the fin angles, the distance between the fins and the wall thermal conditions.

One of the earliest studies on the double-fin configuration discussed a control aspect of the problem: in Ref. 4 it was noted that for a specified incoming boundary layer, sep-

This paper is declared a work of the U.S. Government and is not subject to copyright protection in the United States



β_1	β_2	A	B
7	7	71.5	35.7
7	11	73.5	35.7
7	15	75.4	35.9
11	11	75.6	37.6
11	15	77.5	38.0
15	15	79.1	39.5

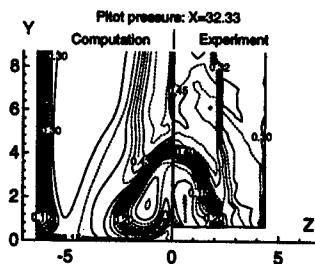


Fig. 1: Double-fin configuration and test matrix

Fig. 2: Crossflow comparison of pitot pressure in 15x15 interaction. Experiment of Garrison and Settles (see Ref.[14])

aration could be inhibited by achieving the desired pressure rise with weaker intersecting shocks instead of the single stronger shock alternative. However, this interaction can also be studied from more fundamental viewpoints. One aspect is concerned with the "interaction" between the individual vortical structures generated by each fin. In this context it is important to note that vortex lines in the flow traverse downward in the boundary layer associated with the right fin (looking downstream), cross the channel between the two fins where they are distorted (but are nevertheless smooth) and then upward in the left fin boundary layer.⁵ A second issue is specific to symmetric situations where the substantial differences between two- and three-dimensional separation can be elucidated.⁵

This paper focuses on the computational simulation of the mean flowfield of the crossing-shock interaction as obtained with the theoretical model outlined in §2. We address in turn, the two primary thrusts of numerical simulation i) investigation of flow structure and ii) assessment of turbulence modeling accuracy. Experimental investigations play a critical role in these investigations by providing a framework for validation. Most of the computations described here are modeled after the comprehensive test matrix of Refs. 6,7 consisting of all six combinations of 7, 11 and 15 degree fins at Mach 3.95, $P_t = 1.492MPa$, $T_t = 260.4K$ and $Re = 87.5$ million per meter (Fig. 1). Although all the six configurations have been computed, for brevity, the results will be presented on a selective basis to illustrate the points under discussion. We follow the convention of denoting the interaction as $\beta_1 \times \beta_2$ where, viewing downstream, β_1 and β_2 denote left and right fin angles respectively.

Computational fluid dynamics has achieved a great degree of success in reproducing the features of the overall flow structure. In §3, we first show several comparisons which together demonstrate that both primary and secondary features are reproduced with reasonable fidelity. The simulations are then employed to develop a model for strong interactions i.e., where the incoming boundary layer is fully separated. New simulations are employed to characterize the evolution of the fully separated interaction under the influence of asymmetry: these results supplement the evolution with interaction strength presented in Ref. 8.

The issue of turbulence modeling is addressed in §4 with particular emphasis on an aspect which has received relatively little attention in the literature, viz., the flow on the sidewalls. We focus on the sidewall/shock-vortex interaction in the 7×15 case. The analysis contained in §4 indicates that the baseline model does not predict the sidewall surface oil pattern very well. A possible cause of this discrepancy is that the computed fin

boundary layer becomes turbulent immediately downstream of the fin leading edge, a situation which is likely at variance with the experiment. In an effort to delay transition, we investigate the modification consisting of limiting of turbulent kinetic energy production. The improved results are then employed to present a model of the sidewall/shock-vortex interaction.

The performance of numerical studies in a variety of STBLI has been presented in a recent report⁹ which identified turbulence modeling as a primary source of inaccuracy. Unfortunately, most models and various corrections thereto are generally tailored for specific 2-D situations (Ref. 10 for example discusses different modifications for separated flows, favorable pressure gradients etc.). An understanding of the flowfield structure as in §3 affords significant new insight into the cause of discrepancies: these are also discussed in §4. The paper concludes with some thoughts on future areas of computational emphasis.

§2 Theoretical Model

The full 3-D mean compressible Navier-Stokes equations are solved in strong conservation form and mass-averaged variables. The numerical scheme utilizes a transformed plane approach. Details may be found in Ref. 11 and are not repeated here. Briefly, the inviscid fluxes are evaluated to nominal third order accuracy with Roe's flux-difference split scheme combined with a limiter for monotonicity. Viscous terms are differenced to second order accuracy in a centered manner. The effects of turbulence are incorporated through the eddy viscosity, μ_t , assumption and the turbulent Prandtl number is assumed constant at 0.9. The turbulence model employed to derive μ_t is based on the popular $k-\epsilon$ equations¹² with low Reynolds number terms and incorporating a compressibility correction. Additional relevant details are provided in §4 below. The meshes are comprised of a sequence of non-uniform Cartesian planes. A typical mesh consists of $123 \times 88 \times 197$ points and has been shown in Ref. 13 to be adequate subject to the qualifications noted in §4. The upstream profile is generated independently with a 2-D code to match the momentum thickness of the incoming boundary layer at the fin leading edge ($\theta = 0.0128mm$).

§3 Model of flowfield structure

It is important to first characterize the fidelity of the computations in reproducing not only primary but also secondary flow features. Towards this end, Figs. 2, 3 and 4 compare simulated and experimental pitot pressure, shock structure and surface oil flow patterns respectively. A cursory examination of these figures reveals clearly that each of the primary features is reproduced. It is noteworthy however that smaller features are also readily apparent. For example, the shock marked 6 in Fig. 3 is a secondary feature in that it is a consequence of the crossing of the primary λ systems.¹⁶ (Notational gaps in this and other figures to follow arise partly due to the limited number of comparisons presented and partly due to the desire to maintain the same terminology for computational and experimental results). Similarly, the lines of separation denoted S_4 and S_{12} in the computed surface pattern are also secondary in nature and in fact correspond to secondary separation. The differences between computation and experiment in Fig. 4 can be considered as inferential rather than physical (see also Ref. 8 in this regard).

Of the various modes of describing a flowfield, we choose here the approach utilizing streamribbons. Fig. 5 presents a compendium of results from symmetric as well as asymmetric strong interaction cases. Note that an aspect ratio has been applied for clarity. Fig. 5, frame (a) depicts the flowfield of a symmetric 15×15 interaction while prominent features in its surface streamline pattern are shown in frame (b). The special lines of coalescence and divergence marked in the latter have been observed in the experiments of Ref 6, 15 and indeed, constitute the symmetric counterparts of those depicted previously

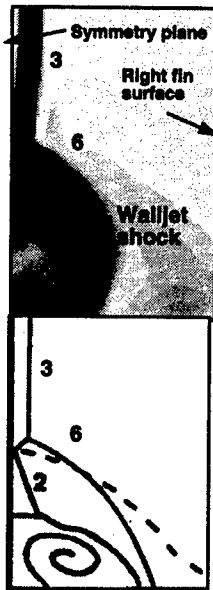


Fig. 3: Shock structure comparison on crossflow plane of 15x15 interaction: computed results (top) and Planar Laser Scattering inference of Ref. [15] (bottom). 2=Primary rear shock, 3=Primary inviscid shock, 6=Secondary separation shock.

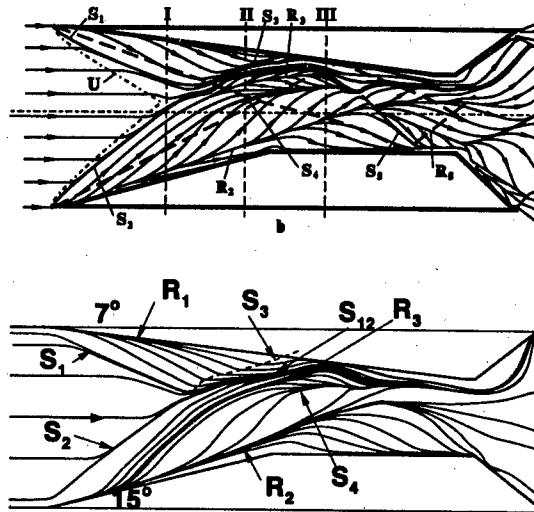


Fig. 4: Surface oil-flow comparison for 7x15 interaction. Top: Experimental inference by Zheltovodov et al (Ref. 7); bottom: simulated.

in Fig. 4 as elucidated later. From Fig. 5(a), it is evident that the incoming boundary layer (*BL*) separates at the line of coalescence S_1 and at its symmetric counterpart S_2 (not marked). This regime does not reattach thus setting up an open structure with no "trapped" fluid. Flow attaching near the fin-plate corners at R_1 and R_2 (not marked) can be categorized into several regimes, the first of which is a vortex interaction (VI), characterized by off-surface stagnation points^{5,8} and which separates from the downstream side of S_1 . Fluid attaching further downstream forms the entrainment flow (*EF*) which brings high speed fluid near the plate. This regime separates prior to reaching the symmetry plane, and two centerline vortices (*CV*) are formed as shown. In Ref. 5, it has been shown that the same coherent features are discernible in a Mach 8 flow as well.

A close examination of the surface patterns in Fig. 4 and Fig. 5 (b) reveals a correspondence between the features of symmetric and asymmetric interactions. Specifically, S_1 and S_2 (R_1 and R_2) denote the primary lines of separation (attachment). Further downstream, each pattern shows two lines of separation (S_{12} and S_4 in Fig. 4 and S_3 , S_4 in Fig. 5 (b)) which are separated by a line of divergence (R_3 in both figures). Because of this similarity, asymmetric interactions can be described with the same four regimes. Fig. 5 (c) and 5 (d) show some of the coherent features for the 11×15 and the highly asymmetric 7×15 interaction respectively. The vortex interaction flow is omitted in each figure to better provide a view of the structure beneath the separated boundary layer. The surface of separation in the 7×15 interaction is shallow near the 15 degree side due to the 3-D relief effect but rises steeply away from the plate in the downstream region. For the weak interaction side, there is some ambiguity in the classification of primary and secondary separation since the line of primary coalescence S_1 is not as well-formed and asymptotically approaches S_2 to form S_{12} . Fluid separating from S_{12} essentially envelops the core formed by *BL*. The sideward inclination of the flow towards the 7 deg fin causes

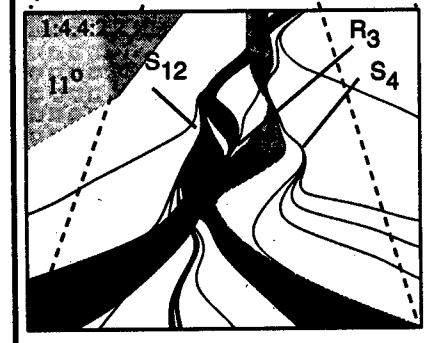
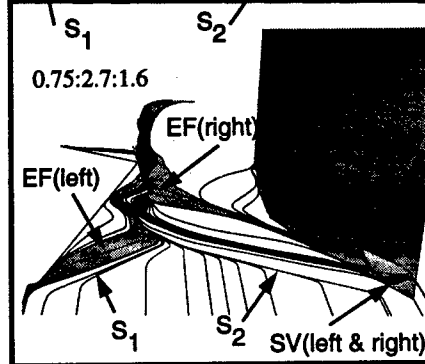
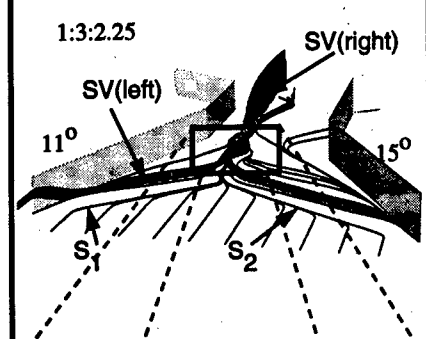
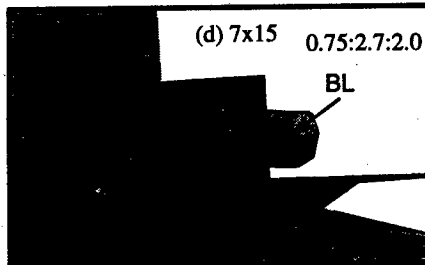
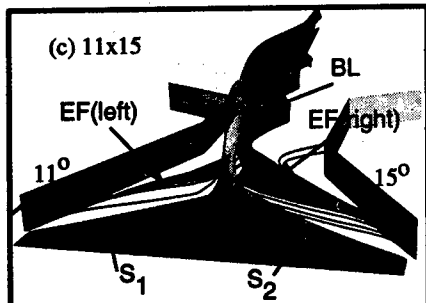
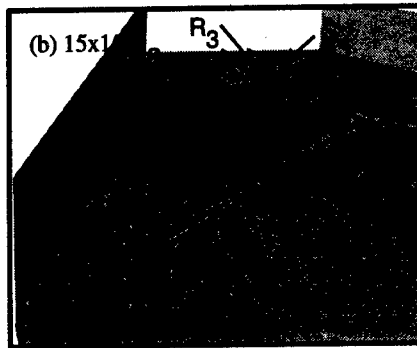
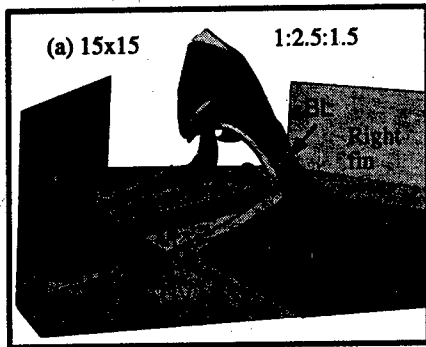


Fig. 5: Compendium of simulated flow visualization results at Mach 4: a) 15x15 interaction b) surface pattern for 15x15 interaction, c) 11x15 interaction, d) 7x15 interaction. BL=Boundary layer, VI=Vortex interaction, SV=Secondary vortex, EF=Entrainment flow, S=separation line, R=attachment line. Note: vertical extent of fins is truncated for clarity

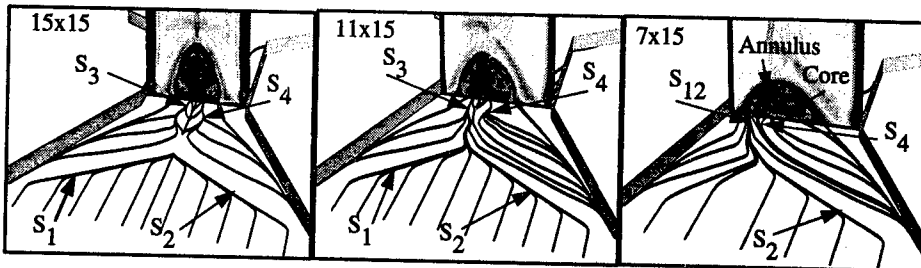


Fig. 6: Variation of vorticity magnitude map on crossflow plane with degree of asymmetry.

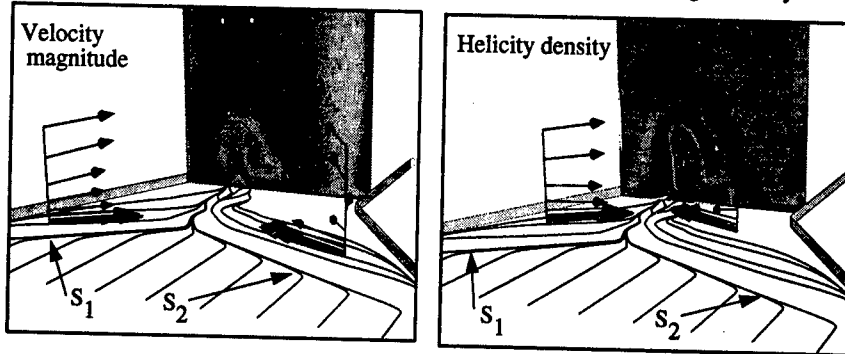


Fig. 7: Velocity and helicity maps on crossflow plane for 11x15 interaction together with velocity vectors exhibiting development of wall-jet-like structure

a sidewall/shock-vortex interaction which is discussed in greater detail below. The secondary vortices are relatively weak compared to the 15×15 case and, interestingly, the fluid in the centerline vortices originates exclusively from near the strong interaction side. The 11×15 flow shown in Fig. 5 (c) represents an intermediate situation. *BL* is clearly defined near each fin as for the 15×15 case. However, the entrainment regimes envelop *BL* after secondary separation as for the 7×15 case. The detail shown in Fig. 5 c reveals further that fluid in the initial segment of both secondary vortices is formed from fluid in the strong interaction side. Downstream however, fluid from both sides attaches at the line of divergence, R_3 .

The regimes shown in Fig. 5 can be correlated to other field quantities. For example, Fig. 6 explores the vorticity field for various degrees of asymmetry at a typical cross-flow station. The surface pattern has been superposed to provide some degree of orientation. Then 15×15 interaction exhibits two regions of high vorticity: an arch-like structure due to primary separation which caps the fluid experiencing secondary separation. The 7×15 interaction on the other hand divides the incoming boundary layer into an inner core and an outer annulus which demarcate the fluid from the strong and weak interaction sides respectively. The 11×15 interaction again represents an interesting intermediate map in that both entrainment regimes now wrap around the separated boundary layer core.

Further insight into the interaction is provided in Figs. 7 which display velocity magnitude and helicity density maps in a crossflow plane together with select velocity vectors. These latter reveal an important component of the flow: the development of the entrainment regime on each side into two wall-jet-like structures which introduce high velocity fluid near the surface. This encompasses the low velocity region of the vortical core to create the classic "mushroom" portrait. The helicity map delineates the two regions within

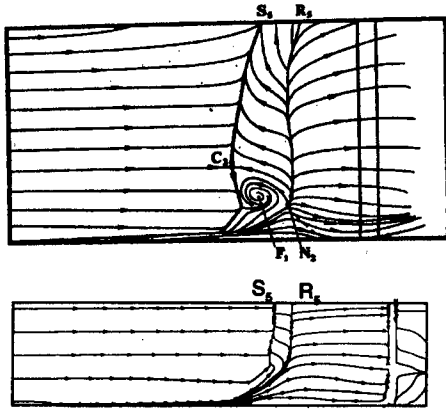


Fig. 8: Comparison of experimental inference of Zheltovodov et al with computation (baseline $k-\epsilon$ model) for sidewall surface pattern on 7 deg fin of 7x15 interaction

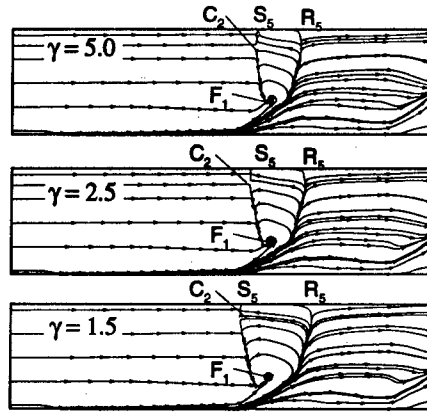


Fig. 9: Effect of limiting of turbulence energy production in the prediction of sidewall surface pattern. C=Saddle point, F=Focus, S=Separation, R=Attachment

the mushroom, the outer entrained fluid and the separated boundary layer core. Since the axial component of velocity is positive, the opposite direction of turning (along the local streamline) in the two regions is a consequence of the reversal of the axial vorticity component as discussed Ref. 8. The wall-jet-like regimes are deflected downstream first partially through the separation shock which is marked component 6 in Fig. 3 and then finally by the wall-jet shock. This latter interaction is closely correlated with the observed secondary separation.

§4 Turbulence modeling issues

The features described above are independent of turbulence model employed and are observed with algebraic⁵ as well as with several variations of the two equation $k-\epsilon$ models.¹⁷ The model does not however address the flow on the fins (or sidewalls). To investigate this issue, we focus on the 7×15 interaction, specifically on the 7 degree sidewall which is subject to a vortical impingement.

Fig. 8 displays the sidewall surface pattern as obtained in experiment and in the computation (note: the height of the fin is roughly double in experiment as in computation. Further, these figures are only approximately to the same scale because of artificial aspect ratios introduced in the plotting procedure – the comparison is thus only qualitative. Although the separation and attachment lines, S_5 and R_5 respectively, are observed in the computations, significant discrepancies are evident in the size of the reversed flow region. Most importantly, the prominent focus denoted F_1 is absent as such in the computations. A possible explanation for this dissimilarity is based on the state of the fin boundary layer. In the computation, the fin boundary layer becomes turbulent forthwith at the fin leading edge, a situation which may not mirror the actual situation in the experiment where transition may occur some distance downstream.

An elegant technique to restrain the development of a turbulent boundary layer is to limit the production of turbulent kinetic energy as discussed in Refs. 18. The production term, P_k , of the $k-\epsilon$ model of Ref. 12 may be written as:

$$P_k = \frac{1}{Re} \tau_{t_{ij}} \frac{\partial \xi_k}{\partial x_j} \frac{\partial u_i}{\partial \xi_k} \quad (1)$$

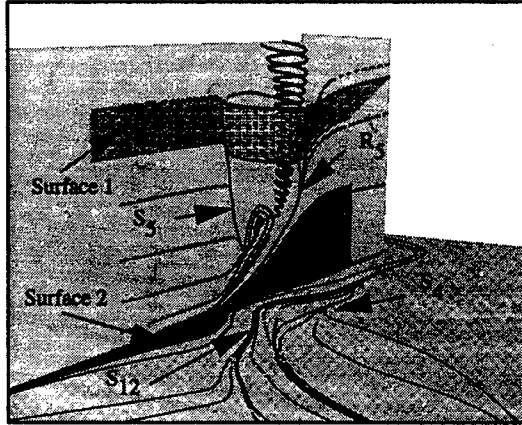


Fig. 10: Flowfield structure caused by vortex/sidewall interaction in 7x15 case.

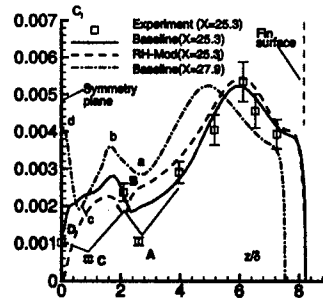


Fig 11: Skin-friction coefficient on plate along spanwise line at streamwise location $X=x/\delta=25.3$. Experiments of Garrison et al. (see Ref. [14]). RH-Mod = Length scale modification of Rodi-Horstman (see Ref. [17]).

where τ is the shear stress tensor, $\frac{\partial \xi_k}{\partial x_j}$ denote coordinate metrics and u_i are Cartesian components of velocity. The limiting procedure is enforced by replacing P_k by P'_k where

$$P'_k = \min(P_k, \gamma \rho \epsilon) \quad (2)$$

and ρ and ϵ denote the density and turbulence energy dissipation respectively. Three different values of γ , 5, 2.5 and 1.5 respectively, are investigated.

The impact of this modification on the sidewall surface pattern is shown in Fig. 9. It is apparent that at $\gamma = 5.0$, there is a drastic improvement in the comparison with experiment. Note particularly the increased reversed flow region between S_5 and R_5 and the appearance of the focus-saddle combination, F_1-C_2 , which satisfies the local rules of topological bifurcation. Reducing γ to 2.5 and then to 1.5 results in an increase in the size of the reversed flow region but has no additional topological impact. Further reduction in γ was not investigated since at such values, the upstream plate boundary layer is perturbed and alters the momentum thickness of the boundary layer entering the interaction. However, we note that at $\gamma = 1.5$, eddy viscosity values in the sidewall boundary layer are extremely low. This observation suggests that additional local reduction in γ is unlikely to result in large surface pattern variation. Finally, these modifications have no significant impact on the plate surface pattern (not shown).

The improved prediction of the sidewall/shock-vortex interaction permits an investigation of the flowfield details which are depicted in Fig. 10. The fin boundary layer separates at S_5 , the surface of separation is identified as Surface 1. For the computational height of the fin, this surface does not reattach to the fin. Rather, the fluid attaching at R_5 originates near the fin/plate corner. A truncated version of this regime is depicted as Surface 2 which spans the entire region downstream of R_5 beneath Surface 1. The significance of the focus is also clearly evident from Fig. 10: this represents the lift off of the corner vortex which traverses vertically parallel to the fin. The interaction can be expected to evolve into the common quasi-two-dimensional situation at distances far from the fin/plate corner.

A comparison of several turbulence models in their ability to predict experimental data has been compiled recently in Ref. 9. An insightful discussion of the impact of unsteadiness on such studies may be found in Ref. 19. Before concluding, we employ our

understanding of the flowfield to comment on some aspects of the quantitative comparison of computed data with experiment. The previous discussions have clearly highlighted the existence of high gradients and three-dimensionality in the vicinity of the secondary structures where shock induced separation occurs. In such regions, the performance of numerical schemes suffers for several reasons. Most schemes degrade to lower accuracy near shocks: this is a severe problem for viscous computations. Additionally, for gradient related quantities such as skin-friction and heat transfer, local mesh resolution criteria are turbulence model dependent and are extremely stringent.¹⁷ Finally, common turbulence models are straightforward extensions of their 2-D counterparts and can be expected to fail in regions of large three-dimensional effects. A related effect of the high gradients associated with the secondary features is that a small "mismatch" between computation and experiment can result in large errors in the comparison of pointwise quantities. It is thus not surprising that comparisons near these features is generally poorer than in relatively benign regions of the flow. This point is illustrated in Fig. 11 which displays spanwise (z) variation of skin-friction coefficient in a 15×15 interaction with two different turbulence models. At the proper streamwise location ($X = 25.3$, the data are in good agreement in the entrained flow region ($4 < z/\delta < 8$) but show large quantitative discrepancies near the symmetry plane ($z/\delta < 4$). More significantly, even the trends are inaccurate since the 'W' feature (A-B-C-D) observed experimentally is completely absent. Given that all of the surface oil flow features are reproduced in the computation, this is initially a surprising observation. However, further examination of the computed flow reveals the same 'W' structure but at a downstream location ($X/\delta = 27.9$) as shown in Fig. 11. Some of the computational discrepancies are thus associated with the displaced development of coherent features.

§5 Conclusion and Future Work

It is evident that primary and secondary features of the interaction are reproduced to sufficient accuracy with proper analysis combined with adequate mesh resolution and numerical schemes. The computations have been employed successfully to propose a model which is valid under a wide range of interaction strengths and asymmetries. The various regimes identified previously for symmetric interactions have been shown to persist in asymmetric interactions and provide a unified understanding of the flowfield. The prediction of the sidewall/shock-vortex interaction has been improved through the use of a modification which inhibits transition of the sidewall boundary layer. An understanding of the flow structure is shown to be an important component of quantitative turbulence model evaluation.

Several areas of future research may be identified. From an engineering standpoint, a proper calibration of turbulence model may be feasible for a wide range of flow parameters. Such calibration must however account for the basic three-dimensionality of the secondary features. On a more fundamental level, the dynamics of compressible turbulence remain an issue of present research. Given the daunting nature of the task, this is a long term endeavor requiring advances in numerical algorithms, physical modeling and computational technology. Finally, it is known that such interactions are highly unsteady. This is an important issue of both engineering and scientific importance, but has so far not been explored computationally.

Acknowledgments

The authors would like to acknowledge the assistance of A.M. Shevchenko and M.S. Maurice. The support of several agencies is also gratefully acknowledged. Authors based in the United States were supported by AFOSR (monitor: Dr. Len Sakell) and by the

Major Shared Resource Centers at CEWES, NAVOCEANO and ASC. Authors affiliated with ITAM were supported by the Russian Foundation for Basic Research (project codes 96-01-01777 and 97-01-00885) and EOARD Contract F61708-97-W0136 (monitor: Dr. C.Raffoul).

References

- [1] A.G. Panaras. Review of the Physics of Swept-Shock/Boundary Layer Interactions. *Prog. Aerospace Sci.*, 31:173-244, 1995.
- [2] A.A. Zheltovodov. Shock Waves/Turbulent Boundary-Layer Interactions - Fundamental Studies and Applications. *AIAA Paper 96-1977*, June 1996.
- [3] G.S. Settles and D.S. Dolling. *Tactical Missile Aerodynamics: General Topics*, volume I, chapter Swept Shock Wave/Boundary-Layer Interactions. AIAA, 1997.
- [4] D. Mee and R. Stalker. Investigation of Weak Shock-Shock and Shock-Expansion Intersection in the Presence of a Turbulent Boundary Layer. *AIAA Paper 87-0549*, 1987.
- [5] D. Gaitonde, J.S. Shang, and M.R. Visbal. Structure of a Double-Fin Turbulent Interaction at High Speed. *AIAA Journal*, 33(2):193-200, Feb. 1995.
- [6] A.A. Zheltovodov, A.I. Maksimov, and A.M. Shevchenko. 3-D Separation topology in symmetric crossing shock waves and expansion fans/turbulent boundary layer interaction conditions. *Thermophysics and Aeromechanics*, V.4 (to be published), 1998.
- [7] A.A. Zheltovodov, Maksimov A.I., Shevchenko A.M., and Knight D.D. 3-D Separation topology in asymmetric crossing shock waves and expansion fans/turbulent boundary layer interaction conditions. *Thermophysics and Aeromechanics*, V.4 (to be published), 1998.
- [8] D. Gaitonde, J.S. Shang, T.J. Garrison, A.A. Zheltovodov, and A.I. Maksimov. Evolution of the Separated Flowfield in a 3-D Shock Wave/Turbulent Boundary Layer Interaction. *AIAA Paper 97-1837*, June 1997.
- [9] D.D. Knight and G. Degrez. Shock Wave Boundary Layer Interactions in High Mach Number Flows - A Critical Survey of Current CFD Prediction Capabilities. Technical report, AGARD, 1997 (to appear).
- [10] T.J. Coakley and P.G. Huang. Turbulence Modeling For High Speed Flows. *AIAA Paper 92-0436*, Jan. 1992.
- [11] D. Gaitonde, J.R. Edwards, and J.S. Shang. The Computed Structure of a 3-D Turbulent Interaction Caused by a Cylinder/Offset Flare Juncture. *AIAA Paper 95-0230*, 1995.
- [12] B.E. Launder and B. I. Sharma. Application of the Energy Dissipation Model of Turbulence to the Calculation of Flows near a Spinning Disk. *Letters in Heat and Mass Transfer*, 1:131-138, 1974.
- [13] D. Gaitonde and J.S. Shang. Skin-Friction Predictions in a Crossing-Shock Turbulent Interaction. *J. Prop. Power*, 13(3):342-348, 1997.
- [14] G.S. Settles and L.J. Dodson. Supersonic and Hypersonic Shock/Boundary-Layer Interaction Database. *AIAA Journal*, 32(7):1377-1383, July 1994.
- [15] T.J. Garrison and G.S. Settles. Interaction Strength and Model Geometry Effects on the Structure of Crossing-Shock Wave/Turbulent Boundary-Layer Interactions. *AIAA Paper 93-0780*, 1993.
- [16] D. Gaitonde and J.S. Shang. The Structure of a Double-Fin Turbulent Interaction at Mach 4. *AIAA J.*, 33(12):2250-2258, Dec. 1995.
- [17] D.V. Gaitonde and J.S. Shang. On 3-D Shock-Wave/Turbulent Boundary Layer Interactions at Mach 4. *AIAA Paper 96-0043*, January 1996.
- [18] F.R. Menter. Zonal Two Equation k-w Turbulence Models for Aerodynamic Flows. *AIAA Paper 93-2906*, July 1993.
- [19] D.S. Dolling. Problems in the Validation of CFD Codes Through Comparison with Experiment. In *AGARD Symposium on Theoretical and Experimental Methods in Hypersonic Flows*. Turin, Italy, 1992.

ABOUT NONLINEAR INFLUENCE OF EXTERNAL ACOUSTIC FIELD ON SUPERSONIC BOUNDARY LAYER FLUCTUATIONS

S.A. Gaponov, I.I. Maslennikova, V.Yu. Tyushin

Institute of Theoretical and Applied Mechanics SB RAS
600090, Novosibirsk, Russia

The problem of nonlinear interaction between acoustic waves and supersonic boundary layer eigenmodes has the direct relation to the problem of stationary flow receptivity to an external disturbance influence. Solution of linear receptivity problem give acoustic wave amplitude for a given wave length of external influence. We should emphasize that when the basic flow is parallel, the external monochromatic waves do not give rise to eigenoscillations [1]. The linear problem of the excitation of eigenmodes by monochromatic acoustic wave has been considered in [2].

On the nonlinear level an external wave can be considered as the basic wave, in the field of which the eigenmodes develop. The example of such process is a disturbance development in the boundary layer of a model in supersonic wind tunnel. In this case an external acoustic field is generated by the turbulent layer on the wind tunnel walls. That puts a problem about the principal possibility of experiments on linear stability theory because of lack of any estimates for the allowable level of external disturbances. At the same time a great number of experiments on the supersonic boundary layer stability have been performed in T-325 wind tunnel in ITAM SB RAS [3]. Although achieved results are consistent with linear stability theory, a possible influence of acoustic waves on the development of unstable hydrodynamic waves may be a problem. Therefore a question about nonlinear interaction of external acoustics and boundary layer eigenmodes is of practical significance connected with the possibility of modeling of non-stationary phenomena, let alone its scientific importance.

The problem of nonlinear development of disturbances in the supersonic boundary layer came to be regarded rather recently and the number of work is modest. A good review of these works can be found in [4].

This paper is concerned with the resonant interaction between the hydrodynamic waves (which are damping out at infinity) and the external acoustic wave in the frame of weakly nonlinear theory. The method described in [4] has been applied for this problem. This work differs from [4] in that the basic acoustic wave does not damp out at infinity.

This work takes a step further in comparison with the work [5], where the interaction parameters are determined for the case when acoustic wavevector is aligned with the external flow. Here the more general case of arbitrary oriented acoustic wave is considered. A detailed setting up of mathematical problem is found in [4] and [5]. As shown there, the amplitude equations, based on weakly nonlinear

theory, for a three-wave resonant triad are as follows:

$$\begin{aligned}
 \frac{da_1}{dX} &= k_1 a_2 a_3 \exp(i\Delta\phi_1), \\
 \frac{da_2}{dX} &= k_2 a_1 a_3^* \exp(i\Delta\phi_2), \\
 \frac{da_3}{dX} &= k_3 a_1 a_2^* \exp(i\Delta\phi_3), \\
 k_j &= \int_0^\infty (\vec{M}_j \cdot \vec{W}^{oj}) dy / \int_0^\infty (B \vec{z}^{oj} \cdot \vec{W}^{oj}) dy.
 \end{aligned}
 \tag{1}$$

where the indexes 1 and 2 correspond to the hydrodynamic waves and index 3 — to the external acoustic wave. Here a_j and $\Delta\phi_j$ ($j=1, 2, 3$) represent amplitudes and streamwise wave number detuning, respectively, k_j ($j=1, 2$) are interaction coefficients (in this work at parametrical stage for hydrodynamic waves we do not take into account coefficient k_3).

Expressions for \vec{W}^{oj} , \vec{M}_j and B are reported in [6].

Resonance condition should be met for disturbance frequencies and spanwise wave numbers b_i (it is defined in [4]):

$$\omega_1 = \omega_2 + \omega_3, \quad b_1 = b_2 + b_3
 \tag{2}$$

In this work the nonlinear interaction coefficients are calculated for the resonant triad of the type under discussion in supersonic boundary layer. The flow parameters correspond to the wind tunnel conditions and are the following: $T_0=310^\circ\text{K}$, $\gamma=1.4$, $\text{Pr}=0.72$.

The stability equations (direct and adjoint problems) were solved with IV-th order Runge-Kutta method. A Newton - Raphson scheme was used for eigenvalue search. For linear independent solutions the orthonormalization procedure was used [6]. Linear problem eigenfunctions for Tollmien - Schlichting waves were normalized by the maximum streamwise disturbance velocity inside the boundary layer. Linear problem functions for an acoustic wave were normalized by streamwise disturbance velocity in the falling wave.

Numerical calculations were carried out for the Mach number $M=2$, Reynolds numbers $\text{Re}=400, 425, 450$, the first hydrodynamic wave frequency $F_1=0.5 \cdot 10^{-4}$; acoustic wave frequency $F_3=0.5 \cdot 10^{-5}$ (where $F=\omega/\text{Re}$), acoustic wave phase velocities $c_{\beta 3} = 0.35, 0.40, 0.45$. The Z-direction wave numbers were varied holding valid the second condition (2). Numerical results are displayed in Figs 1-4. Hydrodynamic wave interaction coefficient dependences on the acoustic spanwise wave number for the various Reynolds numbers (Fig. 1) and acoustic wave phase velocities in

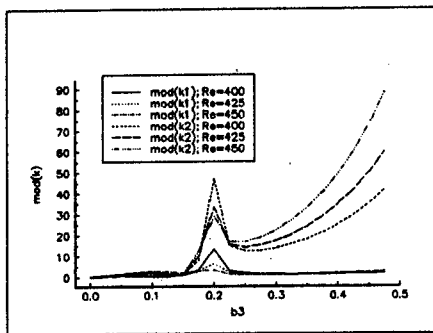


Fig. 1. Interaction coefficient modules versus acoustic spanwise wave numbers b_3 for various Re ($c_{\beta}=0.35$, $b_1=0.1$)

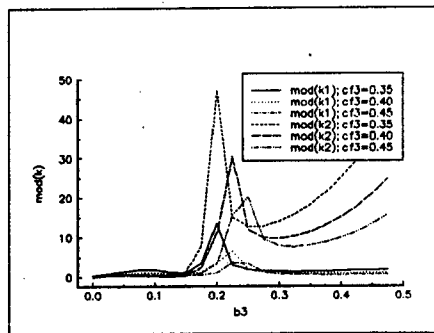


Fig. 2. Interaction coefficient modules versus acoustic spanwise wave numbers b_3 for various c_{β} ($Re = 400$, $b_1 = 0.1$).

x-direction (Fig. 2) are shown. Here the detuning is small ($\Delta\phi \cdot Re < 1$) only for $b_3 < 0.3$. These figures show that maxima are located in the vicinity $b_3 = 0.2$ and this location poorly depends on the phase velocity and practically does not depend on Reynolds number.

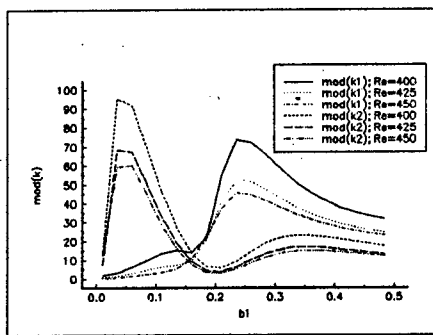


Fig. 3 The interaction coefficients modules versus b_1 for Re is various ($c_{\beta}=0.35$, $b_3=0.2$).

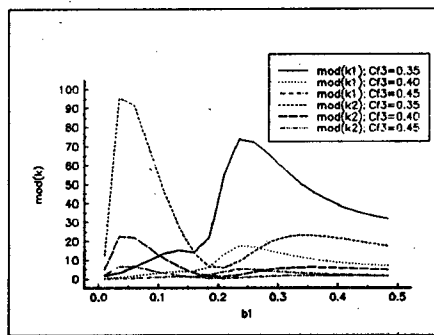


Fig. 4 The interaction coefficients modules versus b_1 for c_{β} is various ($Re = 400$, $b_3 = 0.2$)

Fig. 3 and Fig. 4 show interaction coefficients versus spanwise wave number b_1 at constant value $b_3=0.2$. From these figures a conclusion can be made that there are two wave groups which have the maximal increase. The first group corresponds to the case when the first wave is practically aligned with external flow and then the second wave interaction coefficient achieves a maximal value. The second case takes place when the second wave is practically aligned with external flow and then the first wave has the greatest

amplification. From Fig. 4 we also notice that the interaction coefficients quickly decrease when the acoustic wave phase velocity increases in x -direction.

In summary it is necessary to note that interaction coefficient values obtained in this work are much higher than in work [5]. It is possible to make a conclusion that the external acoustic field can have a distinct influence on the boundary layer at certain wave parameters. This fact should be taken into account while performing experiments in the wind tunnels.

This work was supported by RFFI, grant № 96-01-01580.

REFERENCES

1. Gaponov S.A. On the mathematical simulation of disturbance development in the compressible flows near walls//*Thermophysics and Aeromechanics*, 1994 . V. 1. N 1, P. 75 - 88.
2. Gaponov S.A. Tollmien - Schlichting waves excitation by sound in the supersonic boundary layer//*Izv. AN USSR. MZhG*. 1983 . N 3.
3. Kosinov A.D., Semionov N.V., Shevelkov S.G. and Zinin O.I. Experiments on the nonlinear instability of supersonic boundary layers//*Nonlinear Instability of nonparallel flows*/Eds. Valentine D.T., Lin S.P., Philips W.R.C. Springer-Verlag, 1994. P. 196 - 205.
4. Gaponov S.A., Maslennikova I.I. Subharmonic instability of supersonic boundary layer // *Thermophysics and aeromechanic*. 1997. V. 4, N1. P. 1 - 10.
5. Gaponov S.A., Maslennikova I.I., Tyushin V.Yu. Nonlinear influence of the external low-frequency acoustics on the supersonic boundary layer eigenfluctuations// *App.Mech.Tech.Phys*. 1998 . V. 39, to be published.
6. Gaponov S.A., Maslov A.A. Disturbances development in compressed flows. Novosibirsk: Nauka, 1980.

HIGH-LIFTING WAVERIDERS DERIVED FROM SUPERSONIC AXISYMMETRIC COMPRESSION FLOWS

Yu.P. Goon'ko, I.I. Mazhul, G.N. Markelov

Institute of Theoretical and Applied Mechanics SB RAS,
630090, Novosibirsk, Russia

INTRODUCTION

Waveriders are known to be lifting configurations aerodynamically designed using streamlines of supersonic flows behind shock waves. These flows are determined analytically or can be computed numerically. Waveriders are usually designed on the base of the simplest flows behind plane and conical shock waves, axisymmetric shocks whose shape is described by a power function, as well as some other, mainly two-dimensional flows. A particular flow type should be chosen reasoning from a specific purpose of designed waveriders. Such an aerodynamic design are used to construct both the simple lifting bodies and more complicated configurations with inlets and ducts, corresponding to those of vehicles powered by air-breathing engines.

The present paper deals with waveriders derived from internal axisymmetric flows in constricting conical ducts (funnels of a circular cross-section with the radius linearly decreasing downstream). The designed waveriders have smooth transverse-concave lower compression surfaces. An initial funnel-shaped shock wave forms in such a duct beginning from the leading edge, the basic design flow is locally two-dimensional near this edge, and there is a longitudinal pressure gradient downstream along the duct surface and streamlines behind the shock. This should provide a noticeably larger flow compression near designed surfaces, as compared with that for waveriders based on uniform flows behind oblique shock waves and axisymmetric flows behind conical shock waves for the same angles of compression surface inclination. These waveriders, therefore, can have better lifting properties. In this aspect, the waveriders under study can be of interest as applied to hypersonic reentry vehicles where configurations with a high lifting ability are necessary to ensure appropriate maneuverability.

On the other hand, a high level of flow compression provided by the lower surface on these waveriders can be also a favorable factor increasing the propulsion efficiency of promising hypersonic vehicles powered by air-breathing engines. In this connection so-called convergent inlets should be noted, wherein supersonic flow is compressed in directions converging in space [1, 2]. Such inlets, in particular, provide a compact shape of duct cross-section in the throat region. This can facilitate the problem of heat protection of hypersonic air-breathing engines due to a smaller wetted area of duct surface of convergent inlets, as compared with 2D or axisymmetric ones. Besides, convergent inlets ensure a larger compression of the flow at equal wall inclination angles. A class of convergent inlets was aerodynamically designed in [1, 2] using the streamlines of compression flows in axisymmetric constricting conical ducts. There are inlets of this type, which can be called shovel-type, they have an arc-shaped leading edge and a transverse-concave compression surface of a ramp. Similar construction principles were used in [3] for aerodynamic design of more general lifting configurations, also with transverse-concave surfaces, that form three-dimensional convergent compression flows. The assignment of the transverse contour of the lower surface of examined waveriders as an arc of a circle makes their integration with shovel-type convergent inlets rather simple.

The results of the study of lifting properties, lift-to-drag ratio as an aerodynamic efficiency parameter and integral heat flux to the surface of waveriders involved are presented below, the waveriders being mainly considered from the viewpoint of their use as lifting configurations. The geometry of waveriders are specified by an arc-shaped transverse contour of the lower surface in the rear cross-section. The aerodynamic characteristics of these waveriders are compared with those of Nonweiler caret wings, waveriders designed using uniform flows behind plane oblique shocks, and waveriders derived from the axisymmetric flows around circular cones at zero incidence.

DESIGN OF CONVERGENT WAVERIDERS

An example of waverider design definition using the flow in a constricting conical duct is shown in Fig.1. A basic axisymmetric flow with a funnel-shaped shock wave S forms in such a duct. The duct geometry is defined with radius R_0 in the initial cross-section $X = 0$ and angle δ of the wall inclination to the flow axis. In a certain cross-section X_b , which is regarded as the rear cross-section or the base face of the waverider, a transverse-concave contour C of the lower surface is specified. The lower surface is constructed upstream of this cross-section along the basic flow streamlines passing through the contour C , and the leading edge of a waverider is the line E of intersection of the lower surface and the shock wave S . The constructed lower transverse-concave surface ensures the flow compression along converging streamlines. Following [3], where some characteristics of convergent waveriders for an inviscid flow are also considered, we will use the term "convergent" for waveriders with such surfaces. The upper surface of constructed waveriders is a cylindrical surface with generatrices parallel to the flow axis.

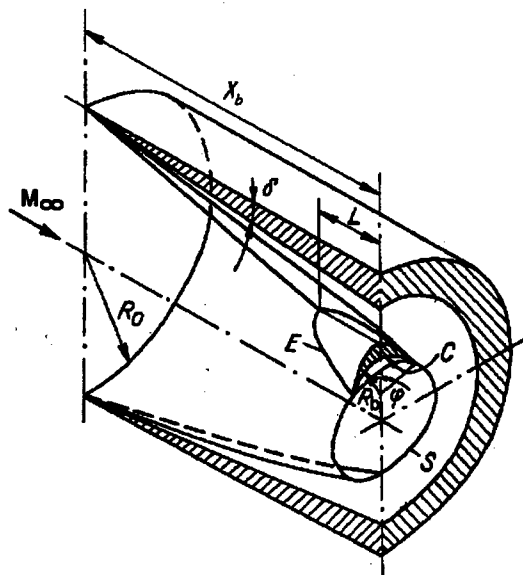


Fig. 1. Design of convergent waverider from the flow in a constricting conical duct.

Waveriders, whose lower surface transverse contour in the rear cross-section is an arc of a circle of radius R_b , were considered. Along with the prescribed values of M_∞ and δ determining the basic inviscid flow field, the relative radius of the lower surface $\bar{R}_b = R_b/R_0$ and the half-angle φ of the arc in the rear cross-section were taken as independent parameters for describing waverider geometry (see Fig.1). It should be noted here that for $\bar{R}_b = 0$ or $\bar{R}_b = R_0$, the waverider length is $L = 0$. Hence, the waverider has a maximum of length L depending on \bar{R}_b . Besides, because of converging streamlines and longitudinal pressure gradients, the geometric and aerodynamic characteristics of these waveriders should also depend on their position in the basic flow field along the curved

shock wave S . Since these waveriders are constructed upstream from the rear cross-section, this position is determined by the relative longitudinal coordinate of this cross-section $\bar{X}_b = X_b / R_o$. In coordinates normalized to R_o , an inviscid flow field in a constricting conical duct is independent of initial radius R_o , though we used $R_o = 10$ m for determining viscous effects.

A basic inviscid supersonic flow in a constricting conical duct was calculated by the method of characteristics [4]. The friction forces and heat fluxes on the lower and upper surfaces of a waverider were determined assuming a local two-dimensional flow for a fully turbulent boundary layer development along the streamlines. The integral boundary layer characteristics, including the skin friction and heat flux coefficients, were determined by the method [5] and using an "effective" length to take into account the longitudinal gradients of flow parameters [6]. The total heat flux Q to be removed by the cooling system to ensure a specified body surface temperature $T_w = \text{const}$ was determined as the difference between convective and radiation heat fluxes. The value of Q was obtained by integration along the streamlines on the surface and normalized to the total enthalpy $H_{o,\infty}$ of the free stream with a unit cross-section area, i.e., the quantity $\bar{Q} = Q/H_{o,\infty}$ was determined. The pressure at the waverider base face was assumed equal to the free-stream pressure. All the results presented refer only to waverider design conditions. The free-stream Mach number $M_\infty = 6$ and duct wall inclination angle $\delta = 10^\circ$ were chosen for an example. Viscous flow conditions correspond to the dynamic pressure $q_\infty = 7 \cdot 10^4$ Pa and wall temperature $T_w = 800$ K.

CHARACTERISTICS OF CONVERGENT WAVERIDERS

An example of calculated data for $\varphi = 45^\circ$ is shown in Fig.2. It is seen that the lift coefficient C_L (Fig.2a) of waveriders under consideration is almost independent of the relative radius of the lower surface in the rear cross-section. The same figure shows the C_L value for a simple Nonweiler caret wing which equals the pressure coefficient for a flow behind an oblique shock generated by a flat wedge. This value, in fact, determines the lower limit of possible C_L values of examined waveriders when they are located in the flow region close to the leading edge of the internal cone, i.e., at $\bar{X}_b \rightarrow 0$. Furthermore, as it could be expected in accordance with the basic flow feature related to the presence of longitudinal pressure gradients, an increase of the parameter \bar{X}_b , i.e., a more downstream displacement of configurations in the basic flow, leads to a noticeable growth of the lift coefficient. For example, the values of C_L in this case are higher than the corresponding values for a simple caret wing approximately by a factor of 1.2, 1.4, and 1.6 for $\bar{X}_b = 1.17, 1.7$, and 2.04 , respectively. Thus, for equal values of the free-stream Mach number M_∞ and surface inclination angle δ , the examined waveriders based on the flow in a constricting

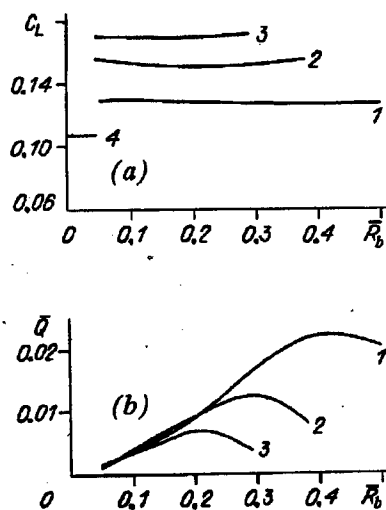


Fig. 2. Waverider lift force coefficient (a) and integral heat flux (b).

$\bar{X}_b = 1.17$ (1), 1.78 (2), 2.04 (3), caret wing (4).

conical duct can ensure considerable advantages in the lift coefficient over waveriders generated from the flow behind plane shock waves.

As for the lift force, the level of the lift-to-drag ratio C_L/C_D is mainly affected by the parameter \bar{X}_b , i.e., the waverider position in the basic flow field, and yet an increase in \bar{X}_b related to a more downstream waverider displacement in this field decreases the aerodynamic efficiency. The decrease is caused both by a larger flow compression on the surface, i.e., a higher surface pressure coefficient, and by an increase of the relative base face area $\bar{S}_b = S_b/S_{pl}$, where S_{pl} is the waverider projected planform area. The presence of a gently sloping maximum of the lift-to-drag ratio versus the arc radius \bar{R}_b should be also noted. As \bar{X}_b decreases, the optimal \bar{R}_b values shift to a higher level, and inversely, as \bar{X}_b increases, the waverider is moved to a more compressed region of the basic flow, the optimal values of this arc radius are decreasing.

Figure 2b shows the relative heat flux \bar{Q} , calculated in accordance with the above assumptions, as a function of the relative radius of the lower surface \bar{R}_b and relative coordinate of the rear cross-section \bar{X}_b . The curve $\bar{Q} = f(\bar{R}_b)$ at given $\bar{X}_b = \text{const}$ has a maximum caused by corresponding changes in configuration length and, hence, the total wetted area which is one of the governing factors of integral heat flux level. As the waveriders are located farther from the conical duct leading edge, i.e., with an increase of \bar{X}_b , their length decreases due to specific features of the basic flow related to an increase of shock inclination angle downstream. In addition, with increasing \bar{X}_b , i.e., when the designed configuration shifts to the region of more compressed flow, the heat transfer intensity also increases; nevertheless, the governing factor here is the corresponding change of the relative wetted area, which decreases the level of \bar{Q} as a whole.

The data presented correspond to a half-angle of the arc of the lower surface in the rear cross-section $\varphi = 45^\circ$. The calculations show that the drag coefficient C_D and lift coefficient C_L decrease slightly with increasing φ , and the lift-to-drag ratio versus φ has a gently sloping maximum. By and large, aerodynamic characteristics vary little in a fairly wide range $30^\circ < \varphi < 90^\circ$ which is of practical interest.

Thus, a parametric analysis of the influence of independent variables determining the examined waverider geometry shows that, for such aerodynamic characteristics as C_D , C_L , and C_L/C_D , the governing factor is the waverider position in the basic flow field, i.e., the value of \bar{X}_b , rather than the relative radius of the lower surface \bar{R}_b or arc half-angle φ . At the same time, all independent geometric variables mentioned above affect noticeably the heat flux value \bar{Q} .

COMPARISON OF CONVERGENT AND DIVERGENT WAVERIDERS

In parallel with the examined convergent waveriders were considered waveriders, whose transverse-concave compression surface was generated from an axisymmetric flow around a circular cone at zero incidence (Fig.3).

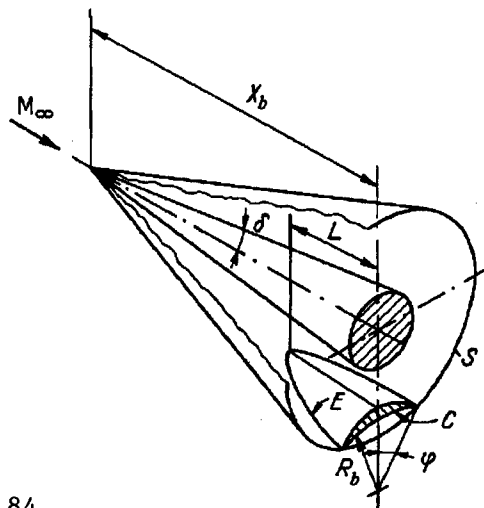


Fig.3. Design of cone-derived waveriders.

The basic conical flow was determined through numerical solution of known ordinary differential equations, the designing procedure and restrictions being similar to those described above. In particular, the transverse surface contour in the rear cross-section was also specified as an arc of a circle of radius R_b . A principal difference of the cone-derived waveriders is that their aerodynamic characteristics are independent of the longitudinal coordinate of the rear cross-section in the basic flow field, contrary to convergent waveriders for which this body position is a determining factor for their aerodynamic characteristics. Besides, the basic flow around a circular cone is divergent, i.e., the streamlines on the compression surface of designed waveriders are also divergent. Therefore, we will also call these waveriders divergent conical ones.

Comparison of aerodynamic efficiency, i.e., the dependencies of the lift coefficient C_L and lift-to-drag ratio C_L/C_D versus volume coefficient $\tau = V^{2/3}/S_{pl}$ of the considered

different waverider types are presented in Fig.4. Note that an increase of τ for divergent conical waveriders is associated with the increase of the lower surface radius R_b in the rear cross-section and the body length, while for convergent waveriders — with the decrease of R_b . The data obtained show that convergent waveriders ensure significantly better lifting properties at given $\tau = \text{const}$ (Fig. 4, a) than divergent conical waveriders or simple caret wings. At the same time, divergent conical waveriders have a higher aerodynamic efficiency with respect to the lift-to-drag ratio (Fig.4, b) within the entire range of the volume coefficient τ under consideration.

CONCLUSION

On the whole, the considered class of convergent waveriders derived from compression flows in constricting conical ducts has noticeable advantages in the lifting properties, as compared with waveriders designed on the basis of flows over flat wedges or circular cones. By varying the waverider position in the basic flow field, it is possible to achieve some compromise between possible high lift coefficients and appropriate lift-to-drag ratios reached in this case. On the other hand, uprated flow compression by the lower surface of these waveriders can be effectively used for improving the propulsion operation of an air-breathing engine in case of its integration with the considered type of waveriders. The latter is, however, a subject for another study lying outside the scope of the present paper.

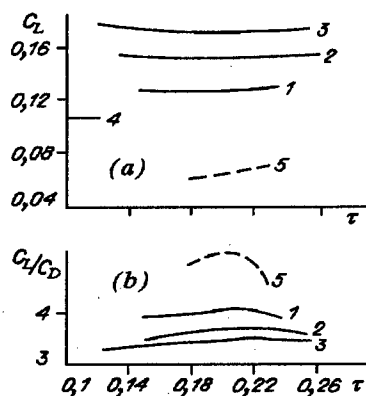


Fig. 4 Comparison of lift coefficient (a) and lift-to-drag ratio (b) of different waveriders.

$$M_\infty = 6, \delta = 10^\circ, \varphi = 45^\circ$$

Convergent waverider:

$$\bar{X}_b = 1.17 (1), 1.78 (2), 2.04 (3);$$

caret wing (4); cone-derived waverider (5).

REFERENCES

1. Blokhin A.M., Gutov B.I., Zatuloka V.V., et al. Convergent inlet diffusers and supersonic axisymmetric conical Busemann compression flows, in: *Aerophysical Studies, Inst. Theor. Appl. Mech.* -Novosibirsk. -1972. - P. 105-108.
2. Gutov B.I., Zatuloka V.V. Convergent diffusers with the initial shock and additional external compression, in: *Aerophysical Studies, Inst. Theor. Appl. Mech.* -Novosibirsk. -1973. -P. 64-66.
3. Goon'ko Yu.P., Markelov G.N., Shashkin A.P. Aerodynamic design of waveriders with convergent compression surfaces and inlets // *Sib. Fiz.-Tekh. Zh. (Izv. SO RAN)*. -1993. -Iss. 4. - P. 47-55.
4. Katskova O.N., Naumova I.N., Shmyglevsky Yu.D., Shushilina N.P. Experience of calculating two-dimensional and axisymmetric supersonic gas flows by the method of characteristics, *Computer Center of AN SSSR, Moscow.* - 1961.
5. Kovalenko V.M. Calculation of friction and heat transfer coefficients of a plate at supersonic speeds and in the presence of heat exchange // *Proceedings of TsAGI*, - 1967.- Iss. 1084.
6. Repik E.U. Approximate calculation of a turbulent boundary layer in compressible flow in the presence of pressure gradients // *Ibid.* -1960.- Iss. 167.
7. Mazhul I.I. Aerodynamics of lifting waveriders derived from axisymmetric conical flows // *Thermophysics and Aeromechanics.* - 1996. - Vol. 3. - No. 4.- P. 327-332.

THE MODEL OF MOMENTUM AND HEAT TURBULENT TRANSPORT IN THE CONVECTIVE PBL

B.B.Ilyushin, A.F.Kurbatskii

Institute of Theoretical and Applied Mechanics SB RAS
630090, Novosibirsk, Russia

INTRODUCTION

In modeling pollutant dispersion in the convective PBL it is necessary to describe correctly the skewness factor of turbulent vertical velocity fluctuations [1]. The third-order moment models [2-4] used at present can not describe in agreement with experimental data behavior of both the skewness factor $S_w = \langle w^3 \rangle / \langle w^2 \rangle^{3/2}$ (w is a vertical velocity fluctuation) and the vertical flux of the turbulent kinetic energy (TKE) $\langle wE' \rangle$ ($E' = 1/2(u^2 + v^2 + w^2)$ and u, v are turbulent fluctuations of horizontal wind velocity components) across the whole width of the PBL, from the ground up to the upper boundary. Moreover, in the surface layer the calculated skewness factor is negative in contrast with the observed data [5]. In the new suggested model, turbulent vertical momentum transport emphasizes. The turbulent vertical velocity variance $\langle w^2 \rangle$ and the triple correlations $\langle w^3 \rangle$, $\langle w^2 \theta \rangle$, $\langle we'_h \rangle$ ($e'_h = 1/2(u^2 + v^2)$) are calculated from the differential transport equations, whereas other triple correlations necessary for closure are found from algebraical expressions. In the transport equations for the triple correlations $\langle w^3 \rangle$ and $\langle w^2 \theta \rangle$, the cumulants $C_{4w} = \langle w^4 \rangle - 3\langle w^2 \rangle^2$ and $C_{4\theta} = \langle w^3 \theta \rangle - 3\langle w^2 \rangle \langle w \theta \rangle$ are not equal zero as it follows from Millionshchikov's quasinormality hypothesis, but found from the algebraical equations.

BASIC EQUATIONS FOR VERTICAL TURBULENT TRANSPORT

The model of turbulent transport in the PBL homogeneous in the horizontal plates includes equations for the mean wind components U and V , mean potential temperature θ , its dispersion $\langle \theta^2 \rangle$, vertical $\langle w^2 \rangle$ and horizontal e_h components of the TKE, and its dissipation ε [2]. The shear components of the Reynolds stress tensor $\langle u_i u_j \rangle$, horizontal components of the TKE $\langle u^2 \rangle$ and $\langle v^2 \rangle$ as well as heat flux $\langle u_i \theta \rangle$ are calculated by the gradient transport models (GTM) [2] taking into account both anisotropy of turbulent transport and dependence of the turbulence time scale on the Brunt-Väisälä frequency N ($N^2 = \beta g \partial \theta / \partial z$). The use of the GTM for moments $\langle w^3 \rangle$ and $\langle wE' \rangle$ results, as it is shown in [2], in their qualitatively incorrect behavior in the surface layer,

whereas for the correlation $\langle w\theta^2 \rangle$ it gives adequate results [2,5,6]. In the new model there are used for calculating the correlations $\langle w\theta^2 \rangle$ and $\langle \theta^3 \rangle$ the GTMs derived from the corresponding differential transport equations in the stationary case:

$$\langle w\theta^2 \rangle = -\frac{\tau}{c_7} \left[\langle w^2 \rangle \frac{\partial \langle \theta^2 \rangle}{\partial z} + 2 \langle w\theta \rangle \frac{\partial \langle w\theta \rangle}{\partial z} + 2 \langle w^2\theta \rangle \frac{\partial \Theta}{\partial z} - \beta g \langle \theta^3 \rangle \right], \quad (1)$$

$$\langle \theta^3 \rangle = -\frac{3\tau}{c_{10}} \left[\langle w\theta \rangle \frac{\partial \langle \theta^2 \rangle}{\partial z} + \langle w\theta^2 \rangle \frac{\partial \Theta}{\partial z} \right]$$

where $\tau = E/\varepsilon$ is the turbulence (decay) time scale, β is the mean coefficient of thermal expansion, g is the acceleration of gravity, c_7 and c_{10} are the model constants. Eliminating $\langle \theta^3 \rangle$ from set (1), the equation for $\langle w\theta^2 \rangle$ can be written as

$$\langle w\theta^2 \rangle = -\frac{\tilde{\tau}_3}{c_7} \left[\left(\langle w^2 \rangle + \frac{3}{c_{10}} \beta g \tau \langle w\theta \rangle \right) \frac{\partial \langle \theta^2 \rangle}{\partial z} + 2 \langle w\theta \rangle \frac{\partial \langle w\theta \rangle}{\partial z} + 2 \langle w^2\theta \rangle \frac{\partial \Theta}{\partial z} \right]$$

$$\tilde{\tau}_3 = \frac{\tau}{1 + 3\tau^2 N^2 / (c_7 c_{10})}. \quad (2)$$

The time scale τ_3 in (2) takes account of turbulent fluctuation damping in the stable stratified area of the PBL [7]. The correlations $\langle e'_h w \rangle$, $\langle w^3 \rangle$, and $\langle w^2 \theta \rangle$ are calculated from the transport equations:

$$\frac{\partial \langle e'_h w \rangle}{\partial t} = -\langle uw^2 \rangle \frac{\partial U}{\partial z} - \langle vw^2 \rangle \frac{\partial V}{\partial z} - \langle w^2 \rangle \frac{\partial \alpha_h}{\partial z} - \langle uw \rangle \frac{\partial \langle uw \rangle}{\partial z} - \langle vw \rangle \frac{\partial \langle vw \rangle}{\partial z} + \beta g \langle e'_h \theta \rangle - c_7 \frac{\langle e'_h w \rangle}{\tau_3},$$

$$\frac{\partial \langle w^3 \rangle}{\partial t} = -\frac{\partial \mathcal{C}_{4w}}{\partial z} - 3 \langle w^2 \rangle \frac{\partial \langle w^2 \rangle}{\partial z} + 3 \beta g \langle w^2 \theta \rangle - c_7 \frac{\langle w^3 \rangle}{\tau_3}, \quad (3)$$

$$\frac{\partial \langle w^2 \theta \rangle}{\partial t} = -\frac{\partial \mathcal{C}_{4\theta}}{\partial z} - 2 \langle w^2 \rangle \frac{\partial \langle w\theta \rangle}{\partial z} - \langle w\theta \rangle \frac{\partial \langle w^2 \rangle}{\partial z} - \langle w^3 \rangle \frac{\partial \Theta}{\partial z} + 2 \beta g \langle w\theta^2 \rangle - c_7 \frac{\langle w^2 \theta \rangle}{\tau_3},$$

where τ_3 is the "return-to-isotropy" time scale. The triple pressure containing correlations are modeled as "return-to-isotropy" terms. The equation for $\langle e'_h w \rangle$ is written with using Millionshchikov's quasnormality hypothesis to express the fourth-order moments through the second-order ones. The correlations $\langle uw^2 \rangle$, $\langle vw^2 \rangle$, $\langle e'_h w \rangle$, $\langle uw\theta \rangle$, and $\langle vw\theta \rangle$ are calculated by the GTM:

$$\langle uw^2 \rangle = -\frac{\tau}{c_7} \left[\langle w^3 \rangle \frac{\partial U}{\partial z} + \langle uw \rangle \frac{\partial \langle w^2 \rangle}{\partial z} + 2 \langle w^2 \rangle \frac{\partial \langle uw \rangle}{\partial z} \right],$$

$$\langle vw^2 \rangle = -\frac{\tau}{c_7} \left[\langle w^3 \rangle \frac{\partial N}{\partial z} + \langle vw \rangle \frac{\partial \langle w^2 \rangle}{\partial z} + 2 \langle w^2 \rangle \frac{\partial \langle vw \rangle}{\partial z} \right], \quad (4)$$

$$\langle e_h \theta \rangle = -\frac{\tau}{c_7} \left[\langle e_h w \rangle \frac{\partial \theta}{\partial z} + \langle w \theta \rangle \frac{\partial e_h}{\partial z} + \langle uw \theta \rangle \frac{\partial U}{\partial z} + \langle vw \theta \rangle \frac{\partial V}{\partial z} + \langle uw \rangle \frac{\partial \langle u \theta \rangle}{\partial z} + \langle vw \rangle \frac{\partial \langle v \theta \rangle}{\partial z} \right],$$

$$\langle uw \theta \rangle = -\frac{\tau}{c_7} \left[\langle uw^2 \rangle \frac{\partial \theta}{\partial z} + \langle w^2 \theta \rangle \frac{\partial U}{\partial z} + \langle uw \rangle \frac{\partial \langle w \theta \rangle}{\partial z} + \langle w \theta \rangle \frac{\partial \langle uw \rangle}{\partial z} + \langle w^2 \rangle \frac{\partial \langle u \theta \rangle}{\partial z} \right],$$

$$\langle vw \theta \rangle = -\frac{\tau}{c_7} \left[\langle vw^2 \rangle \frac{\partial \theta}{\partial z} + \langle w^2 \theta \rangle \frac{\partial V}{\partial z} + \langle vw \rangle \frac{\partial \langle w \theta \rangle}{\partial z} + \langle w \theta \rangle \frac{\partial \langle vw \rangle}{\partial z} + \langle w^2 \rangle \frac{\partial \langle v \theta \rangle}{\partial z} \right].$$

In correct description of the triple correlation behavior in the stable stratified area of the PBL, the relaxation time scale τ_3 calculated taking into account the Kolmogorov spectra of turbulent fluctuations depends, as it is shown in [7], on the Brunt - Väisälä frequency as:

$$\tau_3 = \frac{\tau}{1 + H(N^2) \frac{\pi}{18} \tau^2 N^2}, \quad \text{where } H(N^2) = \begin{cases} 0 & \text{when } N^2 < 0 \\ 1 & \text{when } N^2 \geq 0 \end{cases} \quad (5)$$

For co-ordinated triple correlations damping in the stable stratified area of the PBL, the condition $\tau_3 = \tau$ at $N^2 \geq 0$ must be satisfied. From this condition, the relation $c_{10} = 54/(\pi c_7)$ between the coefficients follows. The value of coefficient c_7 used in papers of different authors changes from 5 to 12. In the present work, it is taken $c_7 = 6,5$ as the result of numerical optimization of the model: the profiles of $\langle E'w \rangle$ and $\langle w^3 \rangle$ calculated by the new model (Figs.1-2) were compared with the observed data. The use of Millionshchikov's quasinormality hypothesis for closing the triple correlation transport equations does not yield physically correct description of the correlation behavior in the PBL as well as in modeling the pollutant dispersion from the point sources in homogeneous turbulence [9]. To develop necessary mechanism for the triple correlations damping, it was suggested in [9] to modify the cumulantless approximation by adding the diffusion term "to down gradient" to the common model quasinormal expression for the quadruple correlation. That idea was used in this work also, with the differential transport equations for $\langle w^2 \rangle$ and $\langle w^4 \rangle$ being solved. In the transport equation for $\langle w^4 \rangle$, the fifth-order moment is expressed through the second- and third-order ones by the relation $\langle w^5 \rangle = 10 \langle w^3 \rangle \langle w^2 \rangle$ following from Gram-Charlier series expansion of the probability density function of the turbulent velocity field and their following truncation on the fourth-order terms. The series convergence for the probability density function of the turbulent velocity field in the boundary layer under a plane was shown in [10]. Thus, the equation for the cumulant C_{4w} in the high Reynolds number approximation and buoyancy effect disregard can be written as

$$\frac{\partial C_{4w}}{\partial t} = \frac{4}{\rho} \left\{ \left\langle w^3 \frac{\partial p}{\partial z} \right\rangle - 3 \langle w^2 \rangle \left\langle w \frac{\partial p}{\partial z} \right\rangle \right\} - 4 \langle w^2 \rangle \frac{\partial \langle w^3 \rangle}{\partial z} - 6 \langle w^3 \rangle \frac{\partial \langle w^2 \rangle}{\partial z}. \quad (6)$$

With the relaxation model applying to the cumulant of the pressure containing correlation (the terms in the braces), it is possible to derive from (6) the algebraical model for the cumulant C_{4w} in the stationary case:

$$C_{4w} = -\frac{\tau}{c_k} \left[6 \langle w^3 \rangle \frac{\partial \langle w^2 \rangle}{\partial z} + 4 \langle w^2 \rangle \frac{\partial \langle w^3 \rangle}{\partial z} \right] \quad (7)$$

In the same way, the model for the mixed cumulant $C_{4\theta}$ is derived:

$$C_{4\theta} = -\frac{\tau}{c_k} \left[3 \langle w^3 \rangle \frac{\partial \langle w\theta \rangle}{\partial z} + \langle w\theta \rangle \frac{\partial \langle w^3 \rangle}{\partial z} + 3 \langle w^2\theta \rangle \frac{\partial \langle w^2 \rangle}{\partial z} + 3 \langle w^2 \rangle \frac{\partial \langle w^2\theta \rangle}{\partial z} \right] \quad (8)$$

Equations (7) and (8) close set (3). Testing models (7) and (8) showed that buoyancy effects do not influence noticeably on the calculated profiles of the correlations $\langle w^3 \rangle$ and $\langle w^2\theta \rangle$ if the correlations $\langle w\theta^2 \rangle$ and $\langle \theta^3 \rangle$ are calculated from the differential transport equations and the correlations $\langle w^3 \rangle$ and $\langle w^2\theta \rangle$ are found by the GTM, as it is suggested in the new triple correlation model.

The realizability conditions derived from generalized Schwarz' inequalities for the triple covariance of the vertical turbulent velocity is the following [11]:

$$\langle w^4 \rangle \geq \langle w^3 \rangle^2 / \langle w^2 \rangle + \langle w^2 \rangle^2. \quad (9)$$

Necessary relaxation of the correlation $\langle w^3 \rangle$ in [3,11] is achieved by clipping its value ("clipping approximation") with the use of inequality (9) in which $\langle w^4 \rangle = 3 \langle w^2 \rangle^2$ (the quasnormality hypothesis) is assumed. It is possible to note, that such procedure is not physically correct. Taking into account (9), more strong the inequality for the cumulant can be written:

$$C_{4w} \geq \langle w^3 \rangle^2 / \langle w^2 \rangle \quad (10)$$

Condition (10) is used to estimate the value of the coefficient c_k in (7) and (8). For this, there is considered decay of homogeneous turbulence satisfying the following relations:

$$\begin{aligned} \langle w^2 \rangle &= \langle w^2 \rangle_0 \exp(-t^*) \\ \langle w^3 \rangle &= \langle w^3 \rangle_0 \exp(-c_7 t^*), \\ C_{4w} &= C_{4w0} \exp(-c_k t^*), \end{aligned} \quad (11)$$

where t^* is transformed time ($dt^* = dt/\tau$). Then, it follows from (10) taking into account (11) that $c_k \leq 2c_7 - 1$. From the Gram-Charlier series convergence, the additional condition for the coefficients run out $1 < c_7 < c_k$. Estimate for c_k is

written as $c_7 < c_k \leq 2c_7 - 1$. In calculations the upper value of this estimate $c_k = 2c_7 - 1$ is used. Decreasing the coefficient c_k value causes decreasing maximum values of the correlations $\langle w^3 \rangle$ and $\langle wE' \rangle$.

RESULTS OF CALCULATION

The calculated profiles of the vertical turbulence energy flux $\langle E'w \rangle$ and the triple velocity correlation $\langle w^3 \rangle$ ($w_* = (\beta g z_i Q_0)^{1/3}$ - is the velocity scale in the PBL, Q_0 is turbulent heat flux on the surface, z_i is the height of the inversion layer) across the whole width of the PBL are shown in Fig. 1-2 by solid lines. Calculations correspond to 4 p.m. (the developed the PBL). The dots of different configurations show the observed data as well as the experimental ones. Moreover, the vertical profile of $\langle E'w \rangle$ calculated in [3] is given by dashed line. It is seen, that the triple correlation profiles calculated by the new model are positive across the whole PBL including the surface layer. The observed data [5] lie in large range and the experimental data [12] correspond to the PBL without mean wind. Differences between the profiles of $\langle E'w \rangle$ calculated by the new model and the one suggested in [3], when all correlations up to the triple ones were found from the prognostic differential transport equations, are negligible. The profiles of the triple correlations $\langle w^2 \theta \rangle$ and $\langle w \theta^2 \rangle$ across the layer height which were calculated by models (2) and (3) as well as the observed data

[5] are shown in Figs. 3-4. It is possible to note that in the lower part of the mixed layer behavior of $\langle w^2 \theta \rangle$ calculated by the new model correspond qualitatively correctly to the observed data, because in the equation for $\langle w \theta^2 \rangle$ in (3) there is the term $\langle w^3 \rangle \partial \theta / \partial z$. To ignore this term in model [13] leads to qualitatively incorrect behavior of $\langle w^2 \theta \rangle$ in the lower part of the PBL (dot-and-dash line in Fig. 3).

Thus, the new model for the triple correlations gives the profiles $\langle w^3 \rangle$ and $\langle E'w \rangle$ positive in the whole width of the CBL including the surface layer without using physically incorrect procedure of "clipping approximation" [3] for the triple correlation values. Computing efficiency of the new model is achieved by means of minimized calculation of the triple correlations from the differential transport equations. To physically correct description of vertical

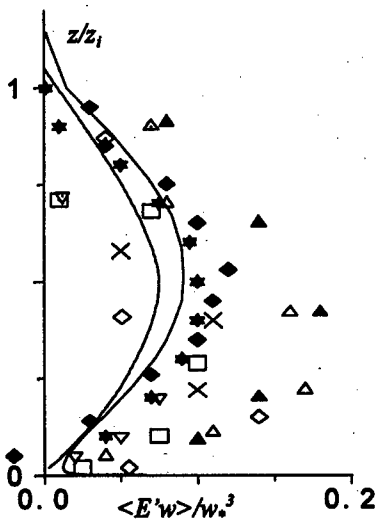


Fig.1. The profiles of TKE vertical flux: solid line - calculated by the model presented in this work, dashed line - calculated by model [3], \square - experimental data [12], \star , \blacktriangle , \times , \square , \diamond , ∇ , \triangle - observed data [5].

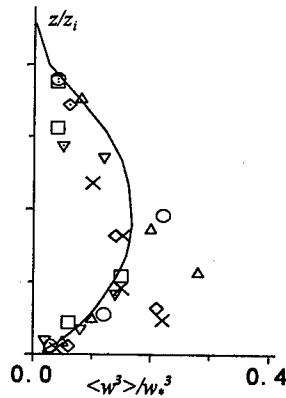


Fig.2. The profile of correlation $\langle w^3 \rangle$, line and symbols as fig. 1.

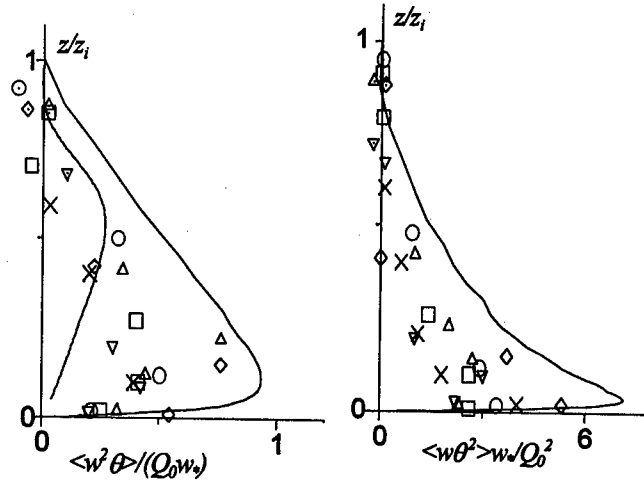


Fig.3. Profile of the vertical flux of turbulent convective flux. Dashed line: calculated by model [13], solid line and symbols as fig.1.

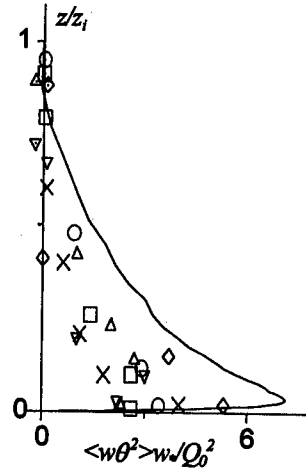


Fig.4. The profile of correlation $\langle w \theta \rangle$, line and symbols as fig. 1.

transport, it is necessary to solve three transport equations for the triple correlations $\langle w^3 \rangle$, $\langle w^2 \theta \rangle$, and $\langle e'_h w \rangle$. All other triple correlations necessary to closure are calculated by the GTM.

This work was financially supported by the Russian Foundation for Basic Research (Grant N 98-01-00719)

1. Atmospheric Turbulence and Air Pollution Modelling/Eds. F.T.M. Nieuwstadt, H.Van Dop. Dordrecht: Holland, et al. 1981.
2. Ilyushin B.B., Kurbatskii A.F. Modeling of Contaminant Dispersion in the Atmospheric Convective Boundary Layer// Izv. RAN. Fizika Atmos. i Okeana.- 1996.-Vol. 32.- P. 307-322.
3. Andre J.C., De Moor G., Lacarrere P., Thery G., du Vachat R. Modeling the 24-hour evolution of the mean and temperature structures of the planetary boundary layer// J. Atmos. Sci.- 1978.- Vol. 35.- P.1861-1883.
4. Canuto V.M., Minotti F., Ronchi C., Ypma R.M., Zeman, O. Second-order closure PBL model with new third-order moments: comparison with LES data// J.Atmos.Sci.- 1994.- Vol. 51.- P.1605-1618.
5. Lenschow D.H.,Wyngaard J.C., Pennel W.T. Mean-field and second-moment budgets in a baroclinic, convective boundary layer// J.Atmos.Sci. 1980.- Vol. 37.- P.1313-1326.
6. Chin-Hoh Moeng and Wyngaard J. C. Evaluation of turbulent transport and dissipation closures in Second-order modeling//American Meteorological Society.- 1989.- Vol. 46.- P.2311-2330.
7. Weinstock J. A theory of turbulent transport// J.Fluid Mech. 1989.- Vol. 202.- P.319-338.
8. Moeng C.-H.,Randall D.A. Problem in simulating the stratocumulus-topped boundary layer with a therd-order closure model// J. Atmos. Sci. 1984.- Vol. 41.- P.1588-1600.
9. Deardorff, J.W. Closure of second- and third-moment rate equations for diffusion in homogeneous turbulence// Phys.Fluids. 1978.- Vol.21.- P.525-530.
10. Jovanovic J., Durst F. Statistical analysis of dynamic equations for higher-order moments in turbulent wall bounded flows// Phys.Fluids A. -1993.- Vol.5.- P.2886-2900.
11. Andre J.C., De Moor G., Lacarrere P and Du Vachat R. Turbulence approximation for ingomogeneous flow: Part 1. The clipping approximation// J.Atmos.Sci. 1976.- Vol.33.- P.476-481.
12. Willis G.E., Deardorff, J.W. A laboratory model of the unstable planetary boundary layer// J.Atmos.Sci.- 1974.- Vol.31.- P.1297-1307.
13. Wen-Yin Sun and Ogura Y. Modeling the evolution of the convective planetary boundary layer // J.Atmos.Sci.- 1980.- Vol.37.- P.1558-1572.

RECEPTIVITY OF THE BLASIUS BOUNDARY LAYER TO SURFACE VIBRATIONS. COMPARISON OF THEORY AND EXPERIMENT

A.V. Ivanov¹, Y.S. Kachanov¹, T.G. Obolentseva¹, **A. Michalke**²

¹) Institute of Theoretical and Applied Mechanics, Novosibirsk, Russia

²) Hermann-Föttinger Institut, Berlin Technical University, Berlin, Germany

1. INTRODUCTION

During past years the problem of the boundary layer receptivity has been extensively investigated both experimentally and theoretically (see for review [1,2]). Most of these studies deal with the two-dimensional receptivity mechanisms rather than with the three-dimensional ones (see for example [3,4]). In particular, the role of the 3D surface vibrations at the initial stages of the laminar-turbulent transition is not well known, especially in the case of the two-dimensional boundary layer. At the same time, in many practical situations the surface vibrations can have rather high amplitudes (as compared to the boundary-layer displacement thickness) and, therefore, can produce fairly intensive instability waves. In particular it was shown in experiments [5], conducted in the 3D boundary layer, that even microscopic surface vibrations (like ten microns, for example) can produce rather intensive 3D instability waves. However the quantitative experimental data about the Blasius boundary layer receptivity with respect to three-dimensional disturbances is practically absent today. First quantitative experimental results on this problem were obtained very recently in [6].

The purpose of the present work is to perform a *combined experimental and theoretical* investigation of the Blasius boundary layer receptivity with respect to three-dimensional non-stationary localized surface non-uniformities using the experimental data obtained in [6] and calculations by Professor A. Michalke, who started our joint work very actively but, unfortunately, was not able to complete it together with us.

2. METHODS OF STUDY AND MEAN-FLOW CHARACTERISTICS

The experimental part of the study was conducted at low-turbulence wind-tunnel of the ITAM (Novosibirsk), at a free-stream velocity $U_0 = 9.05$ m/s with the turbulence level less than 0.02% (measured at frequencies higher than 1 Hz). A flat plate having a chord length of 1.2 m, a span 1.0 m, a thickness of 10 mm, and elliptic leading edge was used. The plate was mounted in the test section under zero attack angle. The experiments were performed at controlled conditions: the wave-trains of instability waves (harmonic in time) were excited within the laminar boundary layer by means of a special disturbances source (surface vibrator) mounted flush with the wall at a distance $x = 287$ mm from the leading edge of the plate.

All main measurements discussed in the present paper were conducted by means of a hot-wire anemometer, with probe positioned on a constant nondimensional distance to the wall $y/\delta_1 = 0.77$. This distance is very close to a position of the main disturbance maxima in y -profiles (Fig. 1) and corresponds to nondimensional velocity $U/U_0 = 0.435$.

The region of measurement was the following: the streamwise coordinate from $x = 287$ to 750 mm and the spanwise coordinate from $z = -100$ to +100 mm. The local Reynolds numbers $Re = U_0 \delta_1 / \nu$ varied in this region from approximately 730 to 1100. The measurements were conducted at three different frequencies of excitation $f = 55.0, 81.4,$ and 109.1 Hz that corresponded to the nondimensional frequency parameters $F = 2\pi f \nu / U_0^2 \cdot 10^6 = 64.1, 94.9,$ and 127.2 respectively (where ν is the kinematic viscosity of the air).

Some of the normal-to-wall profiles of the mean flow velocity measured at various streamwise and spanwise positions are shown in Fig. 2 in comparison with the Blasius profile. It is seen that the agreement is very good. A comparison of the experimental downstream dependence of the boundary-layer displacement thickness δ_1 with corresponding dependence for the Blasius flow (taken into account a virtual position of the flat-plate leading edge) showed

also very well agreement with the Blasius law. The average experimental value of the shape factor $H = \delta_1/\delta_2$ (where δ_2 is the boundary-layer momentum thickness) was found to be also very close to the Blasius value. Thus, in the present experiments the structure of the mean flow corresponds locally to the Blasius boundary layer with very high accuracy.

The theoretical part of the study was performed in the Hermann-Foettinger-Institute for Fluid Mechanics of the Technical University of Berlin for the Blasius boundary layer on a basis of a linear receptivity theory described in [7,8].

In the theory the following approach was used. For parallel basic flow the excitation by a source at the wall can be investigated by using a Fourier transform with respect to the streamwise and the spanwise coordinate, leading to the Orr-Sommerfeld equation. The solution satisfying the boundary condition yields to the inverse Fourier integral, which is evaluated for the unstable Tollmien-Schlichting waves by means of the residuum-theory. The calculations were carried out for the specific conditions of the present experiments and used the same definition of the receptivity function as in the experimental part of this work and in previous experiments [5] (devoted to the swept-wing boundary-layer receptivity).

3. SURFACE VIBRATIONS

In order to obtain in the experiment a controlled and measurable surface vibration for exaction of the instability waves a special disturbance source (vibrator) was used. The construction of the vibrator is shown in Fig 3. A thin plastic membrane with a thickness of

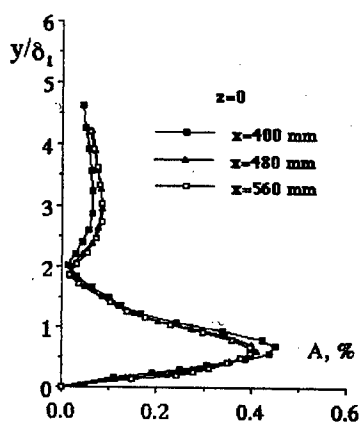


Fig. 1. Typical normal-to-wall profiles of disturbances

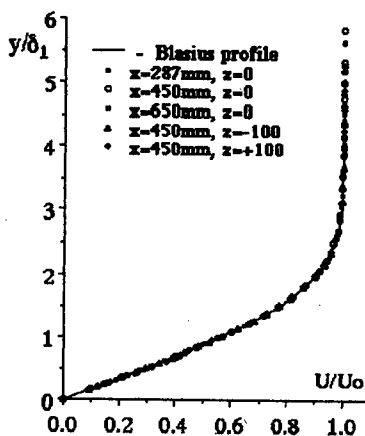


Fig. 2. Comparison of measured profiles with the Blasius profile

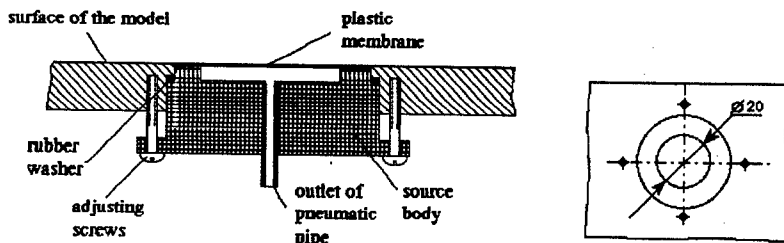


Fig. 3. Design of the surface vibrator

around 0.2 mm (diameter of 20 mm) oscillates under the influence of a pressure fluctuations produced by a closed loudspeaker positioned outside the wind-tunnel test section. The loudspeaker was connected with the source by means of a plastic pipe. Adjusting screws gave possibility to set up the membrane flush with the model surface.

The shape of the membrane displacement from an equilibrium position (during oscillation) was investigated by means of two different methods: (a) the laser-beam technique, for measurements of the amplitude and shape of the membrane oscillations at various frequencies and amplitudes of the oscillation, and (b) the hot-wire method used for the phase measurements. It is found that the shape of oscillations (after normalization by a maximum value) is independent of frequency and amplitude of the oscillations.

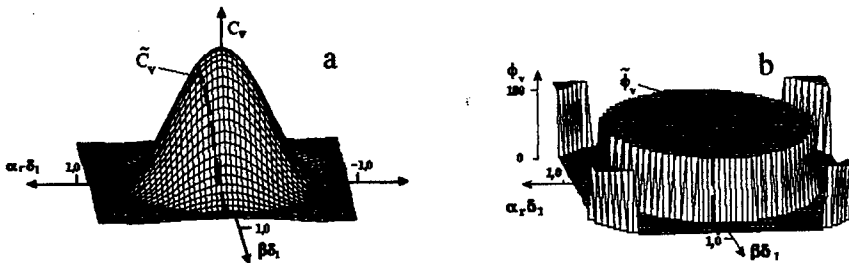


Fig. 4. Amplitude (a) and phase (b) parts of spatial spectrum of surface vibrations and "resonant" vibrational spectrum

To obtain a wavenumber spectrum of the surface vibrations, the measured shape of the oscillating membrane was subjected to the spatial double Fourier transform. Shown in Fig. 4 is a qualitative picture of the 2D wavenumber spectrum of the shape of vibrations. It is seen that the spectrum has a central cupola and ring-like side maxima (having much smaller amplitudes). The phase of the spectral components remains constant within each local maximum and jumps by π on junctions between the maxima where the amplitude tends to zero.

4. DISPERSION FUNCTIONS

For determining the receptivity coefficients it is necessary to know the dispersion functions for the 3D instability modes, namely the dependencies of the streamwise wavenumber α_r on the spanwise wavenumber β for every fixed disturbance frequency. These dispersion curves

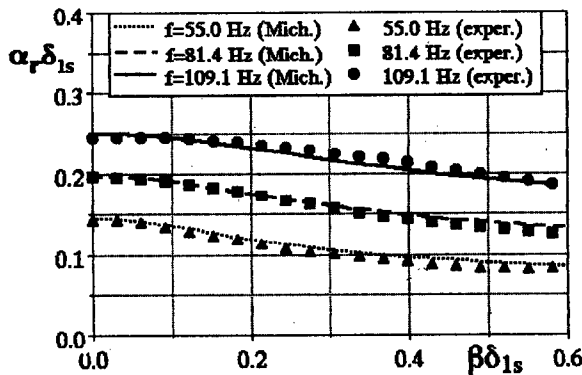


Fig. 5. Theoretically and experimentally determined dispersion curves for 3D instability waves.

have to be determined for the streamwise position of the source and are used for a selection of the 'resonant' modes in the 2D wavenumber spectrum of the shape of the membrane oscillations (Fig. 4). By the resonant modes we mean those modes of the wavenumber spectrum which have the same streamwise wavenumbers (for a given spanwise wavenumber and frequency) as the instability modes in the flow. The non-dimensional dispersion curves $\alpha_r \delta_{1s}(\beta \delta_{1s})$ (where δ_{1s} is the boundary layer displacement thickness at the position of the source) obtained in the theory and experiment are presented in Fig. 5 for all three disturbance frequencies studied. The figure demonstrates a very good agreement of theoretical and experimental results despite the experimental one are obtained by an upstream extrapolation of the measurement results of to the position of the source center.

The resonant modes selected in the amplitude $C_v(\alpha_r \beta)$ and phase $\phi_v(\alpha_r \beta)$ spectra of vibrations with the help of the dispersion curves are designated as $\tilde{C}_v(\beta)$ and $\tilde{\phi}_v(\beta)$ respectively and shown on the surface of the spectrum with bold dashed lines (Fig. 4).

5. INITIAL VALUES OF INSTABILITY WAVES

For determination of the complex receptivity functions it is also necessary to know the complex initial (i.e. at the source position) amplitudes of the instability waves, which can not be measured in an experiment directly. The initial values were obtained by means of an extrapolation of the complex spectral amplitudes measured downstream the vibrator. An example of distributions of the spectral disturbance amplitudes and phases for 7 downstream x -positions is shown in Fig. 6 for the disturbance frequency $f = 81.4$ Hz. The results of extrapolation (initial amplitudes and phases) are shown in the same figure by solid circles.

6. COMPLEX RECEPTIVITY FUNCTIONS

For a fixed frequency of excitation the *complex receptivity function*

$$G_{rC}(\beta) = G_r(\beta) \exp[i\varphi_r(\beta)]$$

is defined as the following ratio:

$$G_{rC}(\beta) = B_{inc}(\beta) / \tilde{C}_{vC}(\beta),$$

where

$$B_{inc}(\beta) = B_{in}(\beta) \exp[i\phi_{in}(\beta)]$$

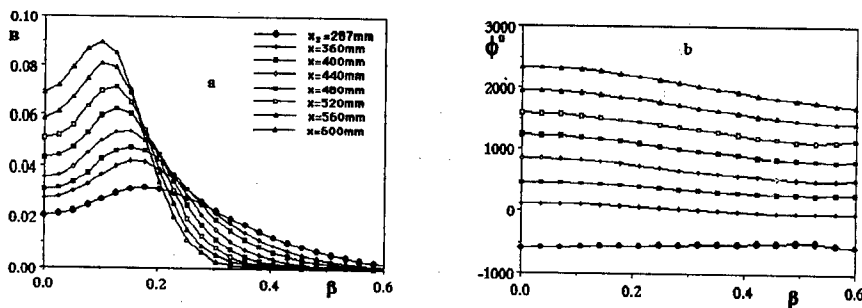


Fig. 6. Amplitude (a) and phase (b) of spectra of instability waves and their initial values at $f = 81.4$ Hz.

is the complex initial spectrum of instability waves (see section 5), and

$$\tilde{C}_{vc}(\beta) = \tilde{C}_v(\beta) \exp[i\tilde{\phi}_v(\beta)]$$

is the complex spectrum of the surface vibration determined for resonant wavenumbers (see section 4). This definition means that

$$G_r(\beta) = B_{in}(\beta) / \tilde{C}_v(\beta) \quad \text{and} \quad \varphi_r(\beta) = \phi_{in}(\beta) - \tilde{\phi}_v(\beta).$$

According to the given definition, the complex receptivity functions were found both theoretically and experimentally for all three frequencies investigated. The main results of the present study are shown in the next two figures. Fig. 7 demonstrates the theoretically obtained receptivity functions versus the nondimensional spanwise wavenumber. The corresponding experimental results are shown in Fig. 8.

It is seen that the experimental and theoretical results are in a very good qualitative agreement with which other, including a behavior of the receptivity functions with both the frequency and the spanwise wavenumber (or wave propagation angle). The smallest receptivity amplitudes are observed for the 2D waves with $\beta\delta_{1s} = 0$. Then the receptivity amplitudes grow with the spanwise wavenumber. Maximum values of the receptivity coefficient amplitudes are observed for $\beta\delta_{1s} > 0.25$, at least, i.e. for 3D waves with propagation angles greater than $45^\circ - 50^\circ$. The receptivity amplitudes grow also significantly with the excitation frequency for all fixed values of the spanwise wavenumber (or the wave propagation angle).

Quantitative comparison of the receptivity coefficient amplitudes (Figs. 7a and 8a) shows that in averaged the theory yields somewhat higher values of the receptivity amplitudes which are greater than the experimental ones by a factor of $\sqrt{2}$. After multiplying the experimental

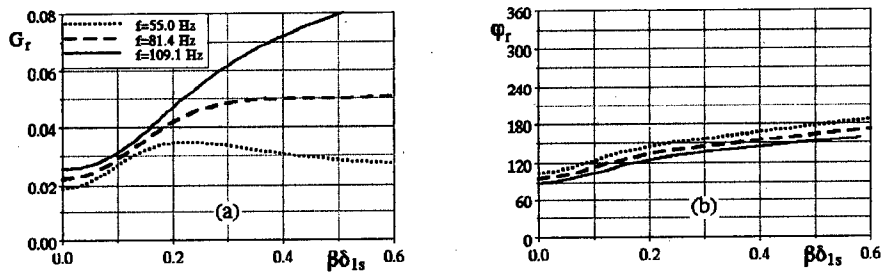


Fig. 7. Theoretically determined amplitudes (a) and phases (b) of the receptivity functions.

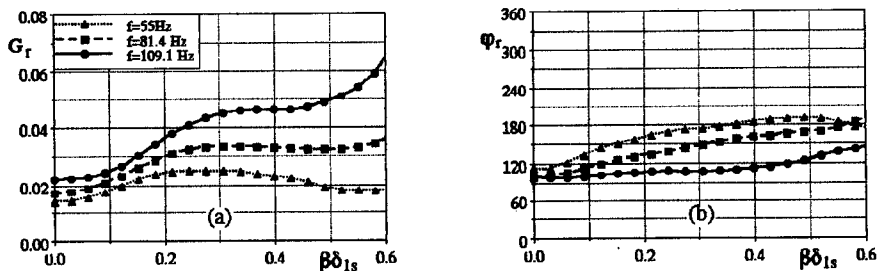


Fig. 8. Experimentally determined amplitudes (a) and phases (b) of the receptivity functions.

coefficients by this factor, or dividing the theoretical values by this factor (not shown), the receptivity coefficient amplitudes become very close to each other for all values of the spanwise wavenumber. The authors presume that the difference by $\sqrt{2}$ appears due to a different normalization of one of many quantities used in a procedure of determining the receptivity coefficients.

The receptivity coefficient phases (Figs. 7b and 8b) have very similar behaviour (with β and f) in the experiment and theory and display a quite good quantitative agreement with each other (especially for the frequency 81.4 Hz). Some distortions of the experimental phase curves in Fig. 8b is mainly explained by an experimental error conditioned by an uncertainty of the procedure of upstream approximation of the experimental data for the functions growing very rapidly downstream.

Conclusions

The developed methods of experimental and theoretical study of the Blasius boundary-layer receptivity to the surface vibrations are shown to provide possibility to obtain the receptivity functions. As the result of the present combined study, the complex receptivity coefficients (amplitudes and phases) for various normal modes of the frequency-wavenumber spectrum were determined experimentally and theoretically. As a result of the comparison of the receptivity functions experimentally and theoretically obtained it is found a very good qualitative agreement and satisfactory quantitative fit.

Experimental part of this work was supported by Russian Foundation for Basic Research (RFBR), grant № 94-01-00062-a.

References

1. Kozlov V.V., Ryzhov O.S. Receptivity of boundary layers: asymptotic theory and experiment // *Proc. Roy. Soc. London.* - 1990. - A 429. P. 341-373.
2. Kachanov Y.S. Laminar-turbulent transition in 3D boundary layers on swept wings. // *Proc. of 14th International Symposium on Continuum Mechanics Models* / V.N. Zhigulyov ed. - Moscow: Moscow Phys.-Tech. Inst., 1997, P. 79-88.
3. Gilyov V.M., Kozlov V.V. Excitation of Tollmien-Schlichting waves in the boundary layer on a vibrator / *Preprint No 19-83.* - Novosibirsk: Inst. Theor. & Appl. Mech., 1983.
4. Terentyev E.D. Linear problem on a vibrator in subsonic boundary layer // *PMM.* - 1981. - T. 45, No 6. - P. 1049-1055 (in Russian).
5. Gaponenko V.R., Ivanov A.V., Kachanov Y.S. Experimental study of 3D boundary-layer receptivity to surface vibrations // *Nonlinear Instability and Transition in Three-Dimensional Boundary Layers* / P.W. Duck & P. Hall, eds. - Dordrecht: Kluwer Academic Publishers, 1996, P. 389-398.
6. Ivanov A.V., Kachanov Y. S., Obolentseva T.G. Experimental investigation of flat-plate boundary-layer receptivity to 3D surface vibrations. // *Stability and Transition of Boundary-Layer Flows. EUROMECH Colloquium 359. Collection of Abstracts.* - Stuttgart: Universität Stuttgart, March 10-13, 1997, Abst. No 4.
7. Michalke A. and Al-Maaitan A.A. On the receptivity of the unstable wall boundary layer along a surface hump excited by 2-D Dirac source at the wall // *European Journal of Mechanics, B/Fluids* 11, 1992, P.521-542.
8. Michalke A. Excitation of small disturbances by a Dirac line source at the wall and their growth in a decelerated laminar boundary layer // *European Journal of Mechanics, B/Fluids.* - 1997 - V. 16, No 1.

BOUNDARY LAYER LONGITUDINAL LOCALIZED STRUCTURES CONTROL BY MEANS OF RIBLETS AND SPANWISE-WALL OSCILLATION

M. M. Katasonov, V. V. Kozlov

Institute of Theoretical and Applied Mechanics, Russian Academy of Sciences, Siberian
Branch, 630090 Novosibirsk, Russia

INTRODUCTION

In last time a great attention paid to investigations of streamwise oriented structures (streaky structures-"puff"-structures, longitudinal localized structures) in a laminar-turbulent transition. One of such examples is a boundary layer flow at high free stream turbulence (FST). The free stream disturbances give rise to streamwise oriented streaky structures inside the boundary layer. These structures, which appear randomly in the spanwise direction, consists of regions of high and low streamwise velocity. In downstream direction their intensity increases and results in boundary layer turbulence. The breakdown of the streaks into turbulence seems to originate from the development of a high frequency secondary traveling wave instability which results in the formation of turbulent spots [1].

In present work, two means of streaky structures control are considered both the spanwise-wall oscillations [2] and riblets. The longitudinal structures investigated in our experiments are so-called "puff"-structures which model the boundary layer streaky structures at high FST.

EXPERIMENTAL SET-UP AND MEASUREMENT TECHNIQUE

The experiments were performed in the low-turbulence wind tunnel MT-324 at the Institute of Theoretical and Applied Mechanics of the Siberian Branch of the Russian Academy of Sciences (Novosibirsk) at the free-stream velocity equaled to 6.6 ms^{-1} . The amplitude of spanwise-wall oscillations was 15 mm, frequency varied in limits 0-18 Hz, experimental set-up 1, figure 1. The riblets, experimental set-up 2, figure 2, is a longitudinal micro roughness with triangular cross section. Scale of riblets was adjusted to produce a maximum effect on the longitudinal structures figure 3. It placed at the distance of 160 mm from the leading edge and sticks out from the flat plate surface.

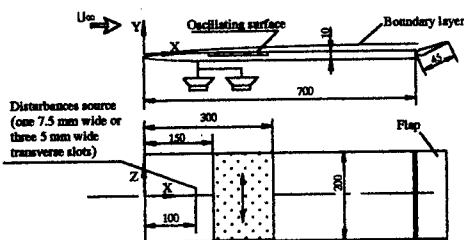


Figure 1. Experimental set-up 1.

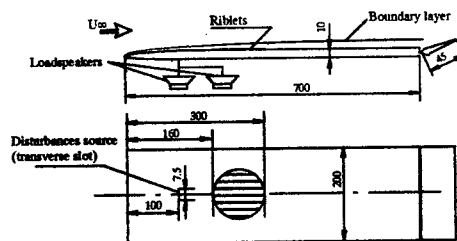


Figure 2. Experimental set-up 2.

Localized longitudinal disturbances ("puff"-structures, streaky-structures) were introduced into the boundary layer by means of suction-injection technique through a narrow (0.4 mm) transverse slot at the plate surface, Bakchinov *et al* (1997). It is make a possible to save a phase information, because processes introduction and collection were synchronized.

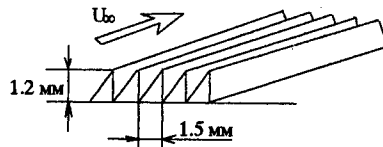


Figure 3. Sketch of riblets.

The slot was connected with a dynamic loudspeaker, which produced pressure fluctuations. In experiments two dynamic loudspeakers had been applied, one of them generated the streaky-structures ("puffs") and the other produced high-frequency (200-300 Hz) fluctuations. The localized disturbance amplification was conducted by means of high frequency disturbance, which was generated simultaneously with "puff"-structures from the same source [1]. Without the "puff"-structures the high frequency disturbance is TS-wave, which decrease downstream.

A hot-wire anemometer of constant temperature was used for measurements of the longitudinal components of the mean velocity (\bar{u}) and the fluctuations of the flow velocity (u'). The data had been collected at the maximum level of disturbances in normal direction (Y) at a distance of 321 mm from leading edge. A local boundary layer thickness (δ) was 4 mm. The probe calibration, data acquisition and data reduction were conducted by means of a MacADIOS-ADIO analog-to-digital converter (GW instruments) connected to a personal computer Macintosh LCII. The data were presented in contour diagrams of constant velocity fluctuations in $Z/\delta - t$ plane (Z/δ - transversal coordinate, normalized with local boundary layer thickness, t - time, measured in milliseconds). Also a Fourier-transform on transversal wave numbers β has been made.

EXPERIMENTAL RESULTS

1. Spanwise-wall oscillations effects on longitudinal structures

From the previous investigations should be mentioned a turbulent boundary layer control by means of spanwise-wall oscillations by K.-S. Choi *et al* (1996). In its experiments the skin-friction reduction up to 40% is observed. The experiments showed that skin-friction reduction due to a loss of longitudinal structures intensity.

The purpose of the present experiments is to investigate the spanwise-wall oscillations effects on streaky structures which is appearing in boundary layer at high FST. The experimental data indicate that the spanwise-wall oscillations decrease the streaky structure intensity, figure 4. By various of oscillations parameters (frequency and/or amplitude) showed that the spanwise-wall oscillation effects on longitudinal disturbances was larger if the amplitude of spanwise-wall oscillations was compared with transverse scale of disturbance (≈ 15 mm). It is hypothesized that the spanwise motion influenced the gradient dU/dZ and thereby the secondary instability which result in breakdown of "puff"-structure. Figure 5 demonstrated influence spanwise-wall oscillations on several streaky-structures, introduced from three transverse slots. One can see, with decreasing of intensity, several streaks coalesce into a single streak, thereby increasing the streak spacing (reducing dU/dZ) with wall oscillations. The optimum frequency of spanwise oscillations is 12-18 Hz, when a maximum decrease of intensity "puff"-structures was reached at present conditions.

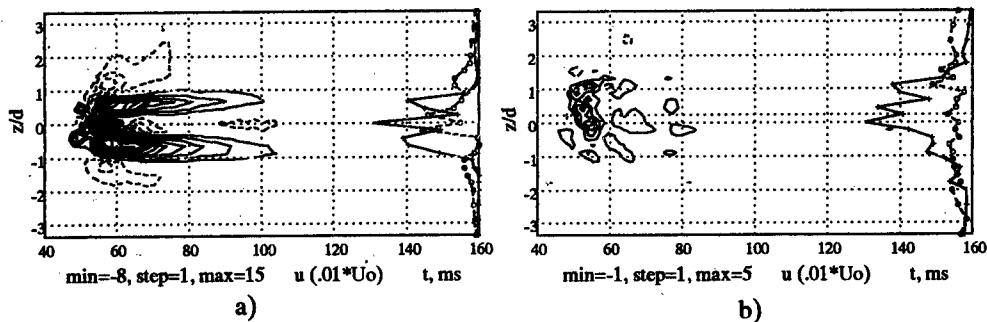


Figure 4. Contour diagrams of constant velocity fluctuations of "puff"-structure with secondary instability (incipient spot) in (Z-t) plane at X=320 mm from leading edge, introduced from single transverse slot; a) without spanwise wall oscillations, intensity of disturbance A=23% from U₀; b) 18 Hz spanwise wall oscillations, intensity of disturbance A=7% from U₀.

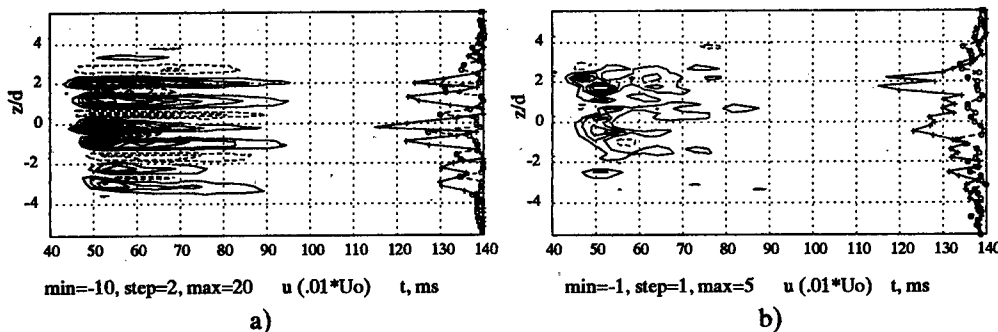


Figure 5. Contour diagrams of constant velocity fluctuations of "puff"-structures with secondary instability (incipient spots) in (Z-t) plane at X=320 mm from leading edge, introduced from three transverse slot; a) without spanwise-wall oscillations, intensity of disturbance A=30% U₀; b) 18 Hz spanwise-wall oscillations, intensity of disturbance A=8% U₀.

2. Control by means of riblets

There are many studies connected with riblets have been carried both for a laminar and a turbulent boundary layer. Some of earliest results for the turbulent boundary layer were obtained by Walsh (1979, 1983) and Walsh & Linderman (1984). They had 7-8% drag reduction. In other case the studies of the influence of riblets on laminar-turbulent transition have been presented by G.R.Grek *et al* (1996). They experimentally studied the effects of riblets on three-dimensional nonlinear structures, so-called Λ -vortices, on the laminar-turbulent transition. It is shown, that riblets delay the transformation of the Λ -vortices into turbulent spots and shift the point of transition downstream.

In our experiments the riblets effects on "puff"-structures (streaky structures) were investigated. Both the moderates intensity disturbances ("puffs") and high-intensity "puff"-structures (up to its transformation into incipient spots) had been considered. The result of effect of riblets on the moderate intensity "puff"-structure is a total intensity decrease of disturbance by 60%, see figure 6. From the Fourier-transform on transversal wave number β , the three different disturbances with the scale of periodically along spanwise direction were

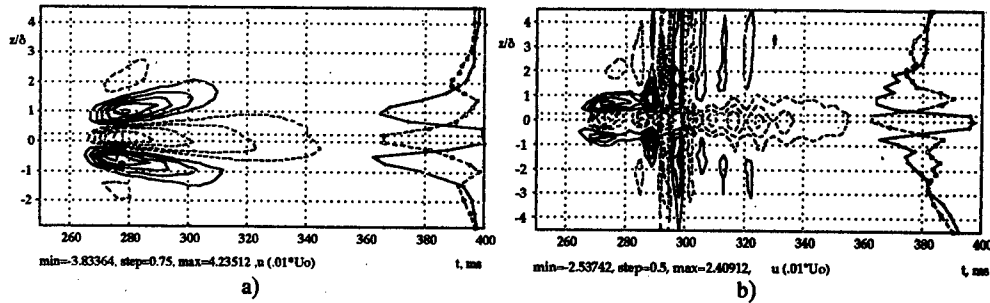


Figure 6. Contour diagrams of constant velocity fluctuations of moderate amplitude "puff"-structures, $U_0=6.6$ m/s, $X_{probe}=321$ mm; a) "puff"-structure, intensity of disturbance $A=8\%$ from U_0 ; b) "puff"-structure with riblets, $A=5\%$.

detected, $\beta/\delta=0.5$ - longitudinal localized disturbances, $\beta/\delta=0.2$ - corresponds an oblique Tollmien-Schlichting (TS) waves, $\beta/\delta=0$ -two-dimensional TS waves. Figure 7(a) shows the largest riblets effect both for $\beta/\delta=0.5$ (disturbance intensity decrease in three times), and $\beta/\delta=0$ (intensity increases more than in three times). The riblets effect on the oblique TS-waves ($\beta/\delta=0.2$) was not observed. At spanwise wave number versus frequency amplitude spectra, one can see two peaks at frequencies of 92 and 125 Hz, see figure 8(b). As showed by G.R.Grek *at all* (1996) the riblets can give rise of two-dimensional TS-waves. However, in the flow with FST the primary role in laminar-turbulent transition lead by longitudinal localized structures. One can see from present experiments its intensity is decreased with riblets.

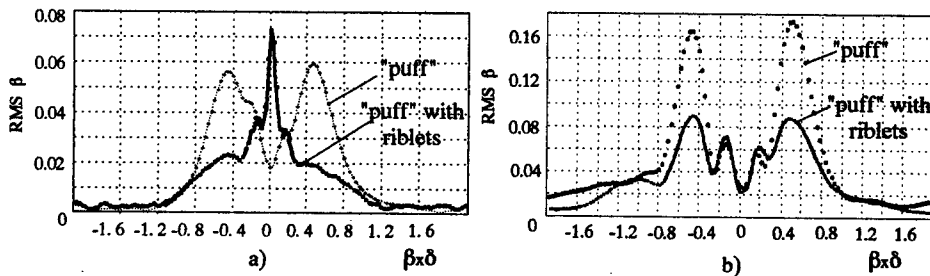


Figure 7. Levels of β -harmonics (transversal wave numbers); a) moderate amplitude "puff"-structure; b) high-amplitude "puff"-structure.

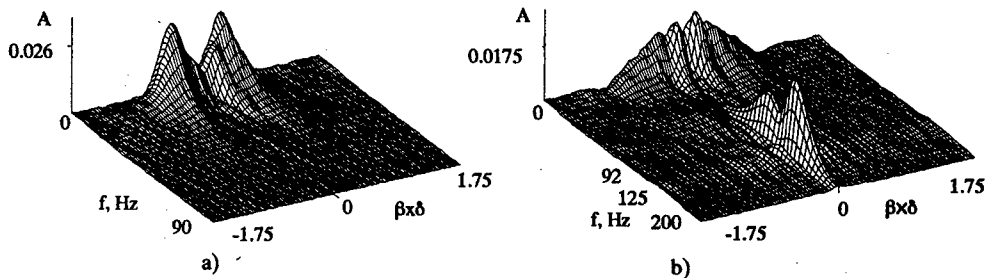


Figure 8. Two-dimensional (spanwise wave number versus frequency) amplitude spectra for moderate amplitude "puff"-structure; a) without riblets; b) with riblets.

Figure 9 shows the effect of riblets on high-intensity "puff"-structures. In that case, as with moderate intensity "puff"-structure, a total intensity decrease of longitudinal structure by 60% is detected.

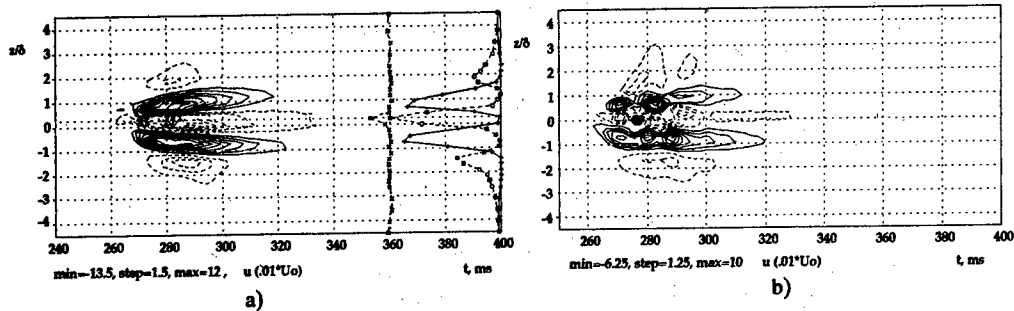


Figure 9. Contour diagrams of constant velocity fluctuations of high-amplitude "puff"-structures $U_0=6.6$ m/s, $X_{probe}=321$ mm; a) "puff"-structure, intensity of disturbance $A=26\%$ from U_0 ; b) "puff"-structure with riblets, $A=16\%$.

Fourier-transform on transversal wave number β shows the intensity of disturbance with $\beta/\delta=0.5$ decrease more than in two times. As before, the oblique TS-waves ($\beta/\delta=0.2$) are not has affected by riblets, see figure 7(b). In contrary with the previous case the two-dimensional wave amplitude ($\beta/\delta=0$) remains constant, however, one can see a small peak at the frequency of 120 Hz on spanwise wave number versus frequency amplitude spectra, see figure 10(b).

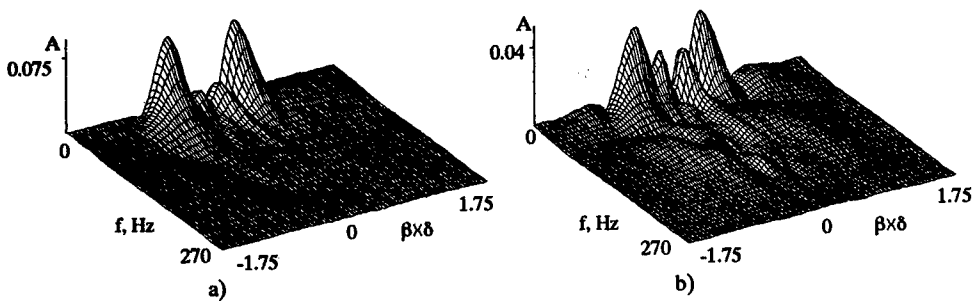


Figure 10. Two-dimensional (spanwise wave number versus frequency) amplitude spectra for high-amplitude "puff"-structure; a) without riblets; b) with riblets.

CONCLUSIONS

The observations from the present measurements can be summarized as follows:

- (i) The spanwise-wall oscillations decrease the streaky structure intensity.
- (ii) The experimental data indicate that the riblets reduce intensity both of moderate level "puff"-structures and high-intensity "puff"-structures.

These experiments were made possible by the financial support of the Russian Foundation for Fundamental Researches under Grants 96-01-01892 and 96-15-96310.

REFERENCES

1. Bakchinov, A.A., Grek, G.R., Katasonov, M.M. & Kozlov, V.V., Experimental study of the interaction between streaky structures and high-frequency disturbances // Proceedings of the 3rd Int. Conf. on Experimental Fluid Mechanics, Moscow, Russia, 1997.
2. Katasonov, M.M. , Kozlov, V.V., 1997a. Boundary layer longitudinal localized structures control by means of spanwisewall oscillations. Preprint No. 5-97, ITAM, Russian Academy of Sciences, Novosibirsk, Russia. (in Russian).
3. Bakchinov, A.A., Grek, G.R., Katasonov, M.M. & Kozlov, V.V., 1997a. Experimental study of localized disturbances and their development in a flat plate boundary layer. Preprint No. 1-97, ITAM, Russian Academy of Sciences, Novosibirsk, Russia. (in Russian).
4. Kwing-So Choi, Jean-Robert De Bisschop and Brian R. Clayton. Turbulent boundary-layer control by spanwise-wall oscillation // Theoretical and applied mechanics: XIXth INTERNATIONAL Congress, Kyoto, Japan, August 25-31, 1996. -P. 376.
5. Walsh, M.S. Drag characteristics of V-groove and transverse curvature riblets.//Viscouse Flow and Drag Reduction. Progress in Astronautics and aeronautics /Ed.G.R.Hough, -1979.-Vol.72.
6. Walsh, M.S. Riblets as a viscous drag reduction technique. //AIAA J. -1983.-Vol. 21.
7. Walsh, M.S. & Linderman, A.M. Optimization and application of riblets for turbulent drag reduction. //AIAA Paper 84-0347.-1984.
8. Grek, G.R., Kozlov, V.V. & Titarenko, S.V., An experimental study on the influence of riblets on transition. // J. Fluid Mech.-1996. -Vol. 315. -p. 31-49.

TWO-DIMENSIONAL ASYMMETRICAL TURBULENT WAKE/AIRFOIL-BOUNDARY LAYER INTERACTION

V. I. Kornilov

Institute of Theoretical and Applied Mechanics SB RAS,
630090, Novosibirsk, Russia

1. Introduction

The problem of interaction between a turbulent wake produced by a flow around a body and a boundary layer formed on a surface immediately downstream (especially, curved surface) is one of the most important and at the same time poorly studied problems of viscous fluid dynamics. In a special case, this problem is a part of a more complicated problem that under certain conditions the turbulent wake can produce a number of adverse phenomena on a downstream surface, up to the buffet-like phenomenon [1]. From the practical point of view, such a wake can lead to a loss of lifting properties of the said surface, considerable spanwise loads, and thus present a significant danger for flying vehicles which are in the wake influence region.

The modeling of interacting flows which develop under the conditions of an increased turbulence of the wake and its significant asymmetry involves certain difficulties caused by several reasons. The main reason is that the process under study is strongly nonlinear which is primarily caused by a nonequilibrium (according to Clauser) character of initial flow produced by the upstream surface. Initially, such a flow is usually formed under the conditions of a streamwise pressure gradient existence which, as is shown by experiments of [2, 3], decreases intensely along the wake itself. This flow relaxes gradually to a state of full hydrodynamic equilibrium which, depending on specific conditions, is achieved at a distance from several tens to several hundreds and even thousands of reference lengths of the body. Because of these reasons, the character of interaction of the system "nonequilibrium wake/boundary layer" becomes much more complicated.

Another aspect of the problem has a direct relationship to the development of effective numerical methods and generation of a suitable physical model of the flow. This is a necessity of improving the calculation procedures for the flow around a curved surface with regard for the turbulent wake effect. Despite a long-time history, this problem has no proper theoretical justification. Though the Navier-Stokes equations that describe such a flow are known in principle, their solution faces certain difficulties, even taking into account the latest achievements in the field of computational aerohydrodynamics. In this case, an explicit approximation of all terms of the transport equations for the Reynolds stresses is needed to solve the closure problem. This, in turn, complicates significantly the turbulence model itself which is based to a large extent on experimental data. Thus, the development and improvement of the flow modeling process and the development of effective methods for calculating this class of flows require accurate information on the structure, transport mechanisms, and regularities of flow evolution in a wide range of varied conditions.

The studies carried out during the last two decades [4-8] allowed one to understand and verify some details of such flows for certain values of determining parameters. A strong

influence of the turbulence level in the wake on the process of its interaction with the boundary layer of a flat surface was found in [9, 10]. It was shown that from the computational viewpoint, the most severe problems arise at the initial section of interaction, where the flow regions with negative turbulent viscosity are formed.

Unlike the above cited papers, the initial flows (wake and boundary layer) in the present study are formed in the flow around fully identical, comparatively thin symmetric airfoils located in tandem, which can change their positions both in the streamwise and crosswise directions. Thus, it is possible to study the structure and properties of an interacting flow in the framework of a simple model approach, when the relative positions of the wake and boundary layer are changed. This is of vital importance because these changes lead to a significant amplification or attenuation of the interaction intensity up to a complete vanishing of the interaction process itself. However, in actual practice this process can be complicated by vortices shed from the wing tip. In the approach used here, this influence is deliberately eliminated so that not to complicate the problem by additional effects.

2. Experimental conditions and procedure

The wind tunnel used for these experiments was the closed-return low-turbulence wind tunnel T-324 of the ITAM RAS. The tunnel is driven by an axial fan and powered by a 0.6 MW d.c. motor. The settling chamber contains ten screens and a special filter mounted onto the first screen. The contraction reduces the octahedral cross-section of the settling chamber to a square cross-section of the test section with the fillets in the corners and has a contraction ratio 17:1. The test section has a cross-section of $1 \times 1 \text{ m}^2$ and a length of 4 m. The streamwise velocity fluctuations are less than 0.06 % at a velocity \bar{u}_∞ of 25 m/s for the present experiments.

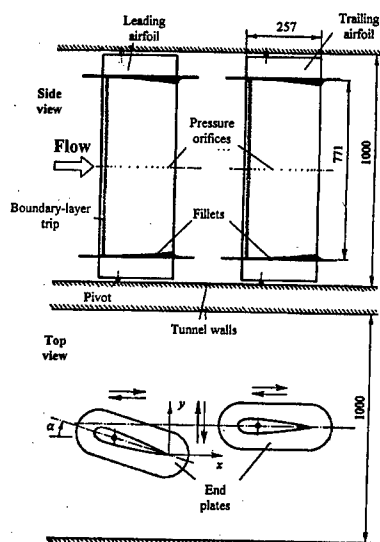


Fig. 1. Schematic of the model. Not to scale. All dimensions in mm.

The model under study consists of two identical unswept rectangular airfoils (upstream and downstream) located in tandem in the test section (Fig. 1). The construction allows one to change smoothly the wing positions in the streamwise (x) and crosswise (y) directions, and change the angle of attack α within $\alpha = \pm 40^\circ$. Each of the wings had a Joukowski-type symmetrical airfoil section with a chord $c = 257 \text{ mm}$, whole span 970 mm , and relative thickness $t = t/c = 0.07$. The static pressure orifices 0.35 mm in diameter were located at the both sides of the wing along its central chord. To reduce the tip vortex intensity and increase the effective aspect ratio of the wing AR_{eff} , the model is equipped with aerodynamic end plates made as ellipses whose major axis is 1.5 of the wing chord. The distance l between the end plates in the wing span direction is 771 mm , which corresponds to the actual wing aspect ratio $AR_{\text{eff}} = 3.83$.

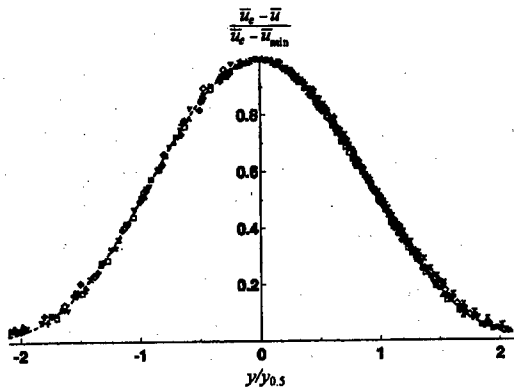


Fig. 2. The shape of self-similar streamwise mean velocity profile in the wing wake at $\alpha=7.5^\circ$. Values of chordwise location, x/c : 1.196 (Δ), 1.391 (\wedge), 1.586 (\square), 1.780 (\blacksquare), 1.897 (∇), 2.014 (∇), 2.130 (\circ), 2.247 (\otimes), 2.364 (\times), 2.480 (\ast), 2.543 (\diamond); ---exponential function according to [11]: $(\bar{u}_e - \bar{u}) / (\bar{u}_e - \bar{u}_{\min}) = \exp[-0.637(y/y_{0.5})^2 - 0.056(y/y_{0.5})^4]$.

of the signal corresponding to the root-mean-square value of the streamwise velocity component $\sqrt{u'^2}$ was filtered by a 55D25 Auxiliary Unit and measured by a 55D35 RMS Voltmeter. As a primary-measuring-transducer, we used a miniature hot-wire probe with a single sensor made of tungsten wire with diameter of $5 \mu\text{m}$ and active length 1.2 mm.

The main measurements were performed in 14 stations along the wake in the range from $x/c=1.004$ (near the leading wing trailing edge) to $x/c=2.54$ (far wake) and in 8 cross-sections in the boundary layer of the trailing (downstream) wing within $x/c=(0.195 \div 0.962)$.

The random measurement error for variables C_p , T_∞ , q_∞ , \bar{u} , \bar{u}_∞ , $\sqrt{u'^2}$ normalized to their maximum values observed in experiments is equal $\pm 0.3\%$, $\pm 1\%$, $\pm 0.25\%$, $\pm 0.5\%$, $\pm 0.5\%$, $\pm 2\%$, respectively.

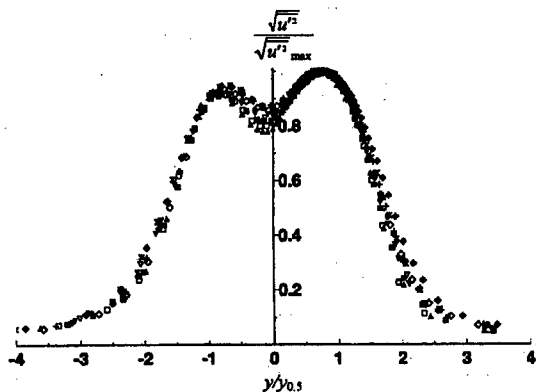


Fig. 3. The normalized streamwise turbulent normal stresses distribution across the wake at $\alpha=7.5^\circ$. Values of chordwise location, x/c : 1.391 (\wedge), 1.586 (\square), 1.780 (\blacksquare), 1.897 (∇), 2.014 (∇), 2.130 (\circ), 2.247 (\otimes), 2.364 (\times), 2.480 (\ast), 2.543 (\diamond).

The freestream velocity upstream of the model was kept constant at $\bar{u}_\infty=25 \text{ m/s}$, which yielded a Reynolds number based on airfoil chord $Re_c=4.28 \times 10^5$ ($Re_l=1.66 \times 10^6 \text{ m}^{-1}$).

The mean velocity and the streamwise component of velocity fluctuations in an examined point of the flow field were measured using a DISA 55M hot wire constant temperature anemometer. The scheme of measurements included a 55M01 hot-wire Bridge with a 55D10 Linearizer connected to its output. The constant component of the linearized signal corresponding to the mean flow velocity \bar{u} was measured by a 55D31 Digital DC Voltmeter. The variable component

3. Results and discussion

Of certain interest is the analysis of regularities of the mean velocity evolution across the isolated wake. For this purpose, let us use self-similar coordinates that are often used to describe the normalized velocity defect $(\bar{u}_e - \bar{u}) / (\bar{u}_e - \bar{u}_{\min})$ in the wake produced by a transverse positioned cylinder. The results of this approach are illustrated in Fig. 2. It is seen that the profiles measured in a clearly asymmetric wake have a self-similar character (except for the near wake region) and are readily approximated by the exponential function

$$(\bar{u}_e - \bar{u}) / (\bar{u}_e - \bar{u}_{\min}) = \exp[-0.637(y / y_{0.5})^2 - 0.056(y / y_{0.5})^4]$$

suggested by Wagnanski *et al.* [11] (dashed line) for a wake flow behind a circular cylinder.

Wagnanski *et al.* [11] showed also that through the distribution of turbulent velocity fluctuations in the wake behind this or that symmetric generator is close to a self-similar one, it depends on generator geometry. In this connection, it is of interest to consider analogous distributions in self-similar coordinates for a considerably asymmetric wake behind an airfoil (Fig. 3). Here, $\sqrt{u'^2}_{\max}$ is the maximum value of the streamwise component of velocity

fluctuations in the profile. It is seen that though the scatter of the values of $\sqrt{u'^2} / \sqrt{u'^2}_{\max}$ is rather large (see the region $-0.8 \leq y/y_{0.5} \leq 0.1$) and it has a systematic rather than random character, one can argue that the profiles presented have a form close to a self-similar one. Thus, apart from some specific features, an asymmetric turbulent wake behind an airfoil has a

certain similarity with the known types of the flow.

As characteristics of the isolated airfoil boundary layer is concern, the data presented have nothing unexpected and correlate with the known concepts of the flow around a wing at incidence.

The flow characteristics under the conditions of interaction of a turbulent wake with a boundary layer were measured in the same cross-sections as for isolated flow around the wing. The following measurement procedure was used. The downstream wing was mounted at a certain distance y_a across the wake, after that all necessary measurements were performed in 8 cross-sections along the wing. (Here y_a is the distance from the wake axis to the wing chord in an examined cross-section x/c). Naturally, depending on the y_a coordinate, the wing was in different flow regions with mean and fluctuating characteristics either strongly changing in the streamwise direction, or weakly changing, or even not changing at all.

As an example, Figs 4 and 5 show the distributions of the mean velocity \bar{u} / \bar{u}_{pw} and the streamwise component of velocity fluctuations $\sqrt{u'^2} / \bar{u}_{pw}$ in the cross-section $x/c = 0.962$ for varied y_a .

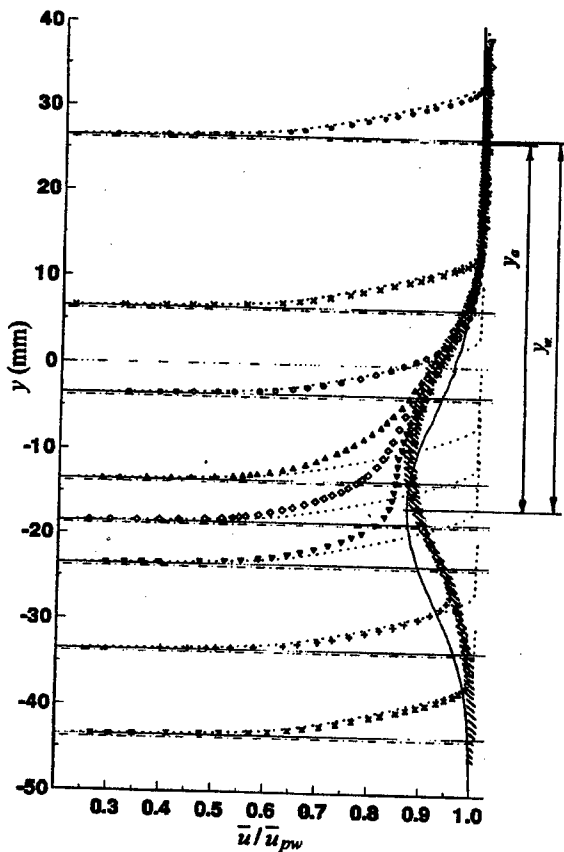


Fig. 4. Streamwise mean velocity profiles at $x/c = 0.962$ and various position of the wing across the wake (symbols) as compared with corresponding boundary-layer profiles for isolated wing (dotted lines) and wake (solid line). y_a denotes chordwise wing position; y_w denotes surface wing coordinate at a given x station. The dash-dotted line shows the wing trailing edge position. The shaded region indicates the "generic" profile.

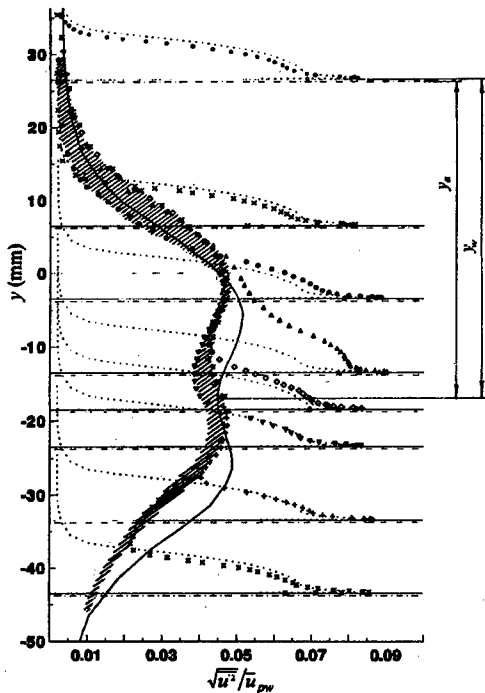


Fig. 5. Streamwise RMS velocity fluctuation profiles at $x/c=0.962$ and various position of the wing across the wake (symbols) as compared with corresponding boundary-layer profiles for isolated wing (dotted lines) and wake (solid line). Other designations are the same as in Fig. 4.

The following typical features of the flow under study should be noted.

(i) If the wing is located at the wake periphery ($y=26.2$ mm, 6.2 mm, -43.8 mm), a certain increase in mean velocity is observed simultaneously with a decrease in the level of turbulent fluctuations, as compared with the case of an isolated flow. It means that when the wing is located near the upper or lower wake boundary, flow regions with favorable interference prevail (the difference $[(\sqrt{u'^2}/\bar{u}_{pw}) - (\sqrt{u'^2}/\bar{u}_{pw})_{is}]$ is negative). It seems that this fact is caused by the interaction of turbulent scales of initial flows, i.e., the wake and the boundary layer.

(ii) For any value of y_a , the profile of the mean velocity and, hence, the streamwise component of velocity fluctuations in the outer region of the interacting flow follows the isolated wake profile. Within a certain uncertainty band (dashed band), it is possible to identify in this region a typical profile which is unifying for all values of y_a . We conventionally called this profile a "generic" one. This "generic" profile is shifted with respect to the isolated wake profile towards the positive values of y at a distance Δy . The

value of Δy remains practically constant for all cross-sections x/c and equal to 6.5 ± 0.3 mm.

(iii) The distribution of the analyzed quantities in the intermediate flow region has a more complicated character. When approaching the wake axis, the profiles of both the mean velocity and turbulent fluctuations more and more deviate from the corresponding distributions typical of an isolated boundary layer and acquire gradually the features of an isolated wake profile. It is worth noting that the level of turbulent fluctuations in the "generic" profile somewhat decreases in comparison with the corresponding values in an isolated wake.

These features are observed for all values of the x/c coordinate. When approaching the leading edge of the wing, the difference in the level of turbulent fluctuations of $\sqrt{u'^2}/\bar{u}_{pw}$ in the "generic" profile and isolated wake increases noticeably.

The above features laid the basis for generalizing the data on the mean velocity distribution in the outer flow region in self-similar coordinates. The results obtained are presented in Fig. 6. The results of measurement in 8 cross-sections along the wing for its 7 positions y_a across the wake are shown here.

It is seen that though the scatter of experimental data is rather large, all the data are generalized by a single dependence (dashed line) used to describe the normalized profile of velocity defect in the wake behind a transverse positioned cylinder [11]. This means that the outer region of the interacting flow under study can be approximately described in the framework of the known model.

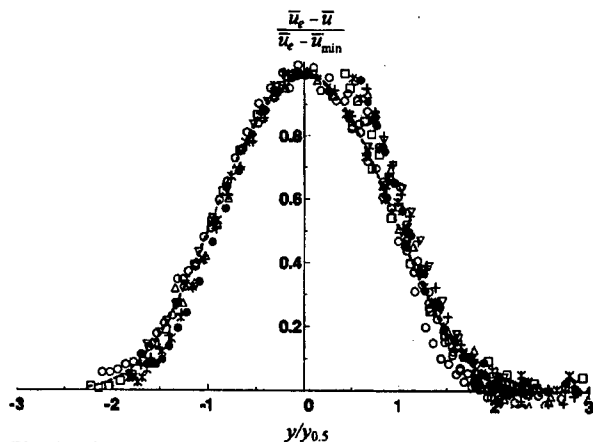


Fig. 6. The shape of self-similar mean velocity profile in the external part of interacting shear flow. Values of chordwise location, x/c : 0.311 (\square), 0.428 ($*$), 0.545 (\bullet), 0.661 (∇), 0.778 ($+$), 0.895 (Δ), 0.962 (\circ).

was also registered in the outer region of the interacting flow when the airfoil is located in the central part of the wake. Moreover the reduction in the level of the turbulent velocity fluctuations, in comparison with the corresponding values in an isolated wake, progresses when approaching the leading edge of the wing. The reasons for these features are to be additionally studied. It is shown that nearly for all examined values of x/c and y_0 , the normalized profiles of velocity defect in the outer region of the interacting flow can be roughly described by simple correlations traditionally used for a wake flow behind a transverse positioned circular cylinder.

REFERENCES

1. Mabey D.G. Beyond the buffet boundary// *The Aero. J.* -1973. -77, 748. -P.201-215.
2. Cousteix J., Pailhas G. Measurement of mean velocity and Reynolds stress tensor within a wake of swept wing// Rapport Technique ONERA CERT, OA 41/2259 AYD. -1980.
3. Cousteix J., Pailhas G., Aupeix B. Three-dimensional wake of a swept wing// Proc. 2nd Symp. on Numerical and Physical Aspects of Aerodynamic Flows, Long Beach (Calif.), 17-20 January, 1983. - 1983.
4. Pot P.J. Measurement in two-dimensional wake and in a two-dimensional wake merging into a boundary layer// Data Report NLR TR, 79063L. - 1979.
5. Andreopoulos J., Bradshaw P. Measurements of interacting turbulent shear layers in the near wake of a flat plate// *J. Fluid Mech.* -1980. - 100, 3. -P.639-668.
6. Savill A.M., Zhou M.D. Wake/boundary layer and wake/wake interactions: smoke flow visualization and modeling// Proc. 2nd Asian Congr. of Fluid Mechanics. - 1983. - P.743-752.
7. Bario F., Charnay G., Papailiou K.D. An experiment concerning the confluence of a wake and a boundary layer// *Trans. ASME. J. of Fluids Engin.* -1982. -104, 1. -P.18-24.
8. Agoropoulos D., Squire L.C. Interactions between turbulent wakes and boundary layers// *AIAA J.* -1988. -26, 10. - P.1194-1200.
9. Zhou M.D., Squire L.C. The interaction of a wake with a boundary layer// Proc. Intern. Symp. on Structure of Complex Turbulent Shear Flow, Marseille, August-September 1982. -1983. -P.376-387.
10. Zhou M.D., Squire L.C. The interaction of a wake with a turbulent boundary layer// *The Aeron. J.* -1985. - 89, 882. -P.72-81.
11. Wagnanski I., Champagne F., Marasli, B. On the large-scale structures in two-dimensional, small-deficit, turbulent wakes// *J. Fluid Mech.* -1986. - 168. -P.31-71.

4. Conclusions

An experimental study of the interaction of an asymmetric two-dimensional wake produced by a symmetric airfoil at incidence with a boundary layer formed on a similar airfoil immediately downstream was carried out under the conditions of incompressible flow.

Some increase of the mean velocity was observed simultaneously with suppression of turbulent velocity fluctuations in the interacting flow, as compared with an isolated flow, when the airfoil is located in the peripheral part of the wake. A similar effect

THE EFFECT OF A LOCAL ENERGY SOURCE ON THE AERODYNAMIC CHARACTERISTICS OF POINTED BODIES AT SUPERSONIC FLOW

T.A.Korotaeva, V.M.Fomin and A.P.Shashkin
Institute of Theoretical and Applied Mechanics SB RAS,
630090, Novosibirsk, Russia

Much interest is paid now to the study of a supersonic nonuniform flow around various bodies. The nonuniformity of the distribution of flow parameters can be caused by various reasons, including the presence of a local energy source. It is shown in the literature [1-7 and others] that an energy impact on the free stream can alter the flow regimes and affect the aerodynamic characteristics of bodies located in the wake behind the energy supply region. Two approaches are used for numerical simulation of this phenomenon:

- 1) the volume-distributed energy sources are specified, the source power being considered as a known function of coordinates and time, in particular [1-3], the energy can be supplied in accordance with the Gaussian distribution;
- 2) the flow nonuniformity is specified as a local area with lowered density, which is equivalent to temperature increase at constant pressure [4-6].

In the both cases, the research was performed under the assumption of an ideal nonconducting gas for axisymmetric and plane flows. A complex three-dimensional flow structure was not studied in these papers. This blank is partly filled in the present paper. The flow around an ogival body is studied for the same method of energy supply as in [1-3]. Contrary to the cited papers, the source position is changed not only along the body centerline but also normal to it. In this case, the flow has an essentially three-dimensional character, and the local source affects not only the drag, but also the lift and moment characteristics.

1. Let us consider a supersonic inviscid nonconducting flow around an ogival body located in the wake behind the energy supply region.

The power of the energy source \dot{Q} (amount of heat supplied to a unit mass of the gas per unit time) is assumed to be a known function of coordinates and time [1-3]:

$$\dot{Q} = q_0 \left(\frac{p_\infty}{\rho_\infty} \right)^{3/2} \frac{1}{R_s} \exp \left(-\frac{\Delta r^2}{R_s^2} \right), \quad (1)$$

where $\dot{Q} = dQ/dt$; R_s is the effective radius of the heat spot; Δr is the distance from the current point to the energy source; p_∞, ρ_∞ are the free-stream pressure and density; q_0 is the parameter describing the energy supply intensity. The equations of gas motion, ignoring heat conduction, viscosity, and mass forces, are written as

$$\dot{\rho} + \rho \operatorname{div} \vec{V} = 0$$

$$\vec{V} + \frac{1}{\rho} \operatorname{grad} p = 0$$

$$\dot{f}_s = \frac{\kappa - 1}{p} \rho \dot{Q}$$

Here f_s is the entropy function which takes the following form, taking into account the equa-

tion of state for an ideal gas: $f_s = \ln(p/\rho^\kappa)$; κ is the ratio of specific heats; the dot denotes the total derivative with respect to time. The first of these equations is the mass conservation law, the second one is the momentum conservation law, and the third equation is the conservation law for entropy balance.

A uniform free stream at infinity and no-slip condition on the body surface are used as the boundary conditions, the free-stream parameters are used as the initial conditions. The values of the flow parameters are normalized: density to ρ_∞ , velocity to $|V_\infty|$, pressure to $\rho_\infty V_\infty^2$, entropy function to $f_{s\infty}$, and energy to V_∞^2 .

The numerical study was performed using the method of finite volumes without capturing the bow shock. The marching method was used for flow calculations (the flow is supersonic everywhere). The computational algorithm was described in [7]. The algorithm was verified by wind-tunnel experimental data without regard for the energy source.

2. A numerical analysis was performed for a supersonic flow around an ogival body located in the wake behind a local energy source. A uniform (at infinity) flow with the Mach number equal to 3 hits the body at zero incidence. The ogive aspect ratio is $\lambda = l/2R_M = 2.5$. (l is the body length, R_M is the mid-section radius). The source power, following [1-3], is supposed constant in time and depending only on the coordinates (1), $q_0 = 20$, since it is shown in [1] that an "effect of stabilization with heat supply" is observed, i.e., for $q_0 > 20$ the efficiency of increasing energy supply is small from the viewpoint of its effect on aerodynamic characteristics.

The calculations were performed for various distances between the source and the body tip, and various heights from the symmetry axis, the axial distance from the body tip being equal to $l_s = 4R_s$, where $R_s = 1/q_0$ is the effective radius of the source.

The most typical calculated results of distributions of the fields of the entropy function $f_s = \ln(p/\rho^\kappa)$, the pressure in the symmetry plane and in one of cross-sections ($X=\text{const}$) far from the body tip for various heights of the source are presented in Figs. 1-2.

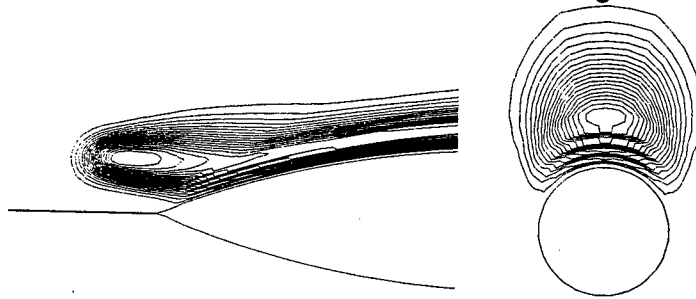


Fig.1. Entropy core behavior with the source deflected from the axis for $h/R_s = 3$

The calculations showed that the presence of a source affects considerably the character of the flow around the body. It was found that a local energy source positioned in the flow changes the flow field in the wake behind it and forms a divergent axisymmetric flow. Near the axis of the region disturbed by the source, the inclination angle of the velocity vector to the free stream is close to zero. On the bow shock wave formed by the source, this angle is rather large and then decreases with increasing distance from the source in accordance with a decrease in

intensity and wave inclination angle. A high-entropy region is formed near the energy source. This region extends behind the source and has the form of almost cylindrical high-entropy core (Fig. 1). The position of this core with respect to the body changes depending on the distance between the source and the body axis. Thus, when the source is located at the body axis, the core flows uniformly around the surface. When the source is shifted from the body axis, this core transforms and becomes thicker at the upper part of the body. At large distances from the axis, the core hangs above the body and forms a high-entropy region in the upper part of the flow around the body (see Fig. 1). The entropy value is almost constant along the streamlines. The typical feature of the wake flow immediately behind the source is that the local Mach number dramatically decreases near the source and rapidly grows when moving away from it. A normal compression wave is formed ahead of the source, which rapidly decays at the periphery, like behind a blunted body. The pressure attains the highest value in the source core. As the distance from the source increases, the pressure and density decrease to values considerably lower than in the free stream.

Thus, an ogival body located in the flow at the same symmetry line with the source is exposed to a rarefied high-entropy gas with a lower local angle of attack of the forebody. This results in a decrease of the total drag coefficient. It is possible to find a distance between the source and the body, such that the averaged local angle of attack has the least value. In case the source located at the symmetry axis is at the distance $l_s = R_s$ from the body tip, the drag increases. The bow shock waves from the source and the body merge near the tip to form a single wave of large strength and create a flow with elevated pressure between the body and the shock wave. The body tip is affected by the high pressure immediately from the source. The flow pattern is considerably changed by changing the source position with respect to the body axis (Fig. 3).

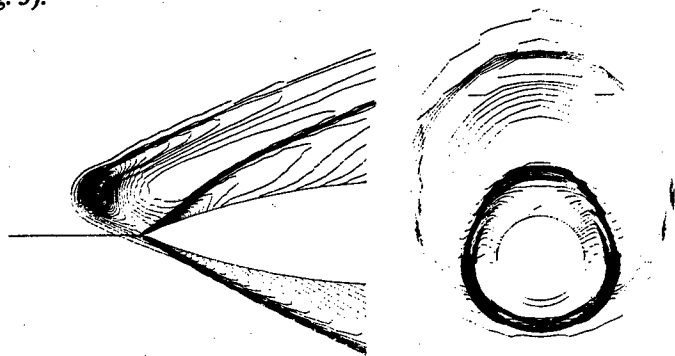


Fig.2. Equal pressure field with the source deflected from the axis for $M/R_s=3$

On one hand, a redistribution of the local angles of attack occurs with increasing the distance between the source and the body axis, and, hence, the drag, lift, and pitching moment with respect to the body tip change. Both an increase of drag, lift, and moment, and a certain decrease of drag coefficient and reduction of lift and pitching moment down to negative values are possible. On the other hand, as is seen from Fig. 1, as the source height increases, the high-entropy core flow becomes nonuniform, which leads to protruding of the bow shock from the body and lower pressure at the ogive surface. The pressure difference between the lower and upper surfaces changes the direction of the lift force and pitching moment to the opposite one. As the height of the energy source above the symmetry axis increases, either the

first type of action, or the second one prevails.

In case the distance between the source and the axis from the lower body surface is small, the shock waves from the source and the body merge to form an elevated pressure region under the body and a rarefaction region above it, which results in increasing the lift force of the body. With further changes in the source position with respect to the body axis, a weakly compressed but rather extended region is formed on the upper part of the body. On the lower part, behind the forebody, the pressure drops down and the lift force increases. A further increase of the distance between the source and the body axis leads to a flow, in which the compression wave from the source is incident into the forebody and then, turning around it, can generate a considerable compression below (see Fig. 2), thus increasing the lift force and pitching moment.

Figure 3 shows the influence of a local energy source on the total aerodynamic characteristics and its possible effect on the flight trajectory.

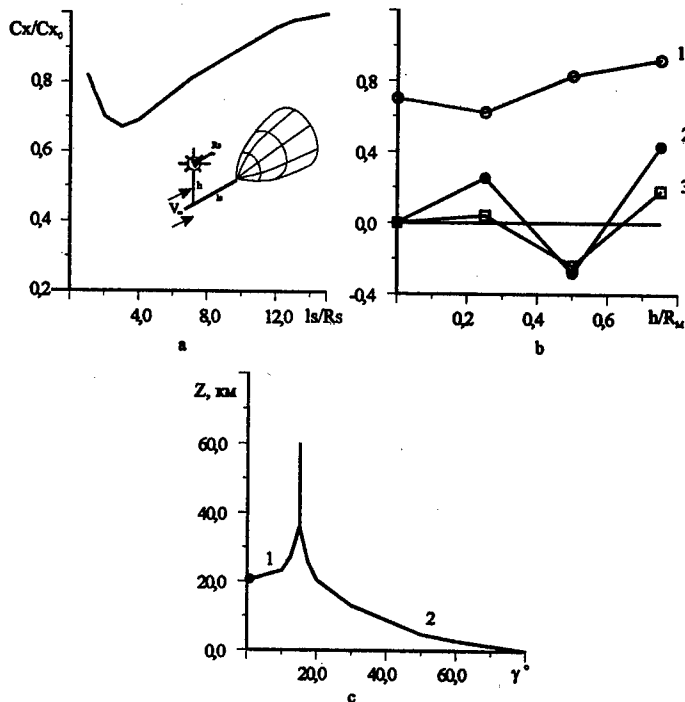


Fig.3. Energy source influence on aerodynamic (a,b) and ballistic (c) characteristics of the body: b: 1 - C_x/C_{x0} ; 2 - C_y/C_x ; 3 - $m_2 \times 10$; c: 1 - $K=0.3$; 2 - $K=-0.3$.

The total values of the wave drag of the ogive versus the distance between the source and the body in an axisymmetric flow are shown in Fig. 3,a. Here C_x is the wave drag coefficient of the body in the presence of the source, C_{x0} is the same without the source, the distance is given in effective radii of the source ($l_s = R_s$). It is seen that for $l_s = R_s$, the body drag is lower than without the source, but appreciably higher than for $l_s = 4R_s$. As l_s increases up to values of about $l_s \sim 14R_s$, the ratio C_x/C_{x0} of the body increases, approaching unity.

Figure 3,b shows the values of C_x/C_{x0} , lift-to-drag ratio $K = C_y/C_x$, and pitching mo-

ments with respect to the body tip as functions of the source height relative to the symmetry axis of the body normalized to the mid-section radius (h/R_M) for $l_s = 4R_s$. It is seen that this dependence is nonmonotonic because of changes in the flow regime and can yield some scatter in the lift-to-drag ratio ($K \approx \pm 0.3$). The source effect on the flight trajectory can be evaluated from Fig. 3,c borrowed from [8]. For a body with the ballistic coefficient $\sigma = m/C_x S = 48.8 \text{ kg/m}^2$, the atmosphere reentry velocity $V = V_E$ and the reentry angle $\gamma_E = 15^\circ$, the influence of the lift-to-drag ratio on the trajectory angle is shown as a function of the flight altitude Z . The dots on the curves mark the altitude where the flight becomes gliding, i.e., the lift force equals the gravitational force. It is seen from the graphs that a scatter of the lift-to-drag ratio within $K \approx \pm 0.3$ can lead to considerable changes in the flight trajectory of a flying vehicle.

Further computations were performed for elliptic cones with half-axes ratio $a/b = 0.25, 0.125$. A wing at zero incidence was studied in a supersonic flow with the Mach number $M = 6$. The energy supply distance is located above the upper surface, at a distance $Yz = 2Rz$. Several sequential positions of the source were considered as it was moved along the longitudinal axis: $l/L = 0, 0.25, 0.5, 0.75$.

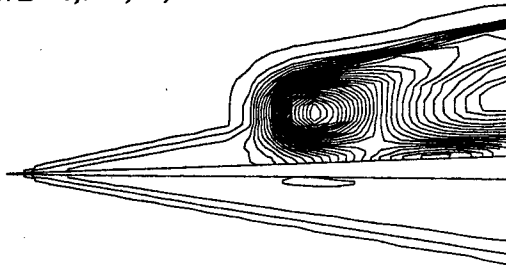


Fig.4 An example of streamlines distribution in the symmetry plane ($l/L = 0.5, a/b=0.125$).

It is seen from Fig. 4 that the streamlines become more dense, which corresponds to a pressure increase in the region of energy source. Another high-pressure region is observed on the body surface and in its vicinity. The pressure decreases inside this region when moving away from the source. One can also notice a single shock wave front (common for the body and energy source) above the upper surface of the configuration and a high-pressure region on the lower body surface directly under the source, which is a consequence of the overflow of compressed gas from the upper surface to the lower one. A picture typical of an undisturbed flow around such a configuration is observed in the flow field in the cross-section ahead of the energy supply region. One can see here the formation of the bow shock wave, the pressure increase, and the classical behavior of velocity vectors near the wing edge. In the cross-section passing through the energy source core, the typical pattern of the flow around an airfoil is complemented by a region of elevated pressure and "smearing" of velocity vectors in the "heat spot". The interaction of shock waves from the body and from the source is weak because of low strength of the bow shock from a slender body. In the cross-section far from the energy supply region, one can see the interaction between the body and the shock wave from the local energy source, as well as a rarefaction zone in the wake behind it.

For an elliptic cone with half-axes ratio $a/b = 0.25$ the bow shock strength is higher and its interaction with the high-pressure region in the source core is more pronounced. There is a rarefaction zone behind the energy supply region, and a strong compression region arises near

the wing surface, like in the previous case. A region with alternating compression waves in the wake periphery, expansion in the central part of the wake, compression in the shock wave reflected on the body surface, and expansion in the flow behind it is formed.

The effect of the energy source position on the total aerodynamic characteristics of the bodies under consideration are shown in Fig. 5. It is seen that the lift-to-drag ratio decreases ($\Delta K \approx -10$) when moving the source from the trailing edge towards the body tip. The energy source effect decreases near the wing tip due to the overflow of compressed gas to the lower surface because the effective radius of the energy source is larger than the wing width. For a thicker body, the influence of the energy source on the lift-to-drag ratio is considerably smaller.

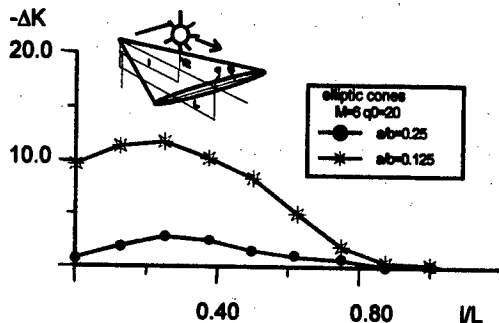


Fig.5 Effect of the energy source position on the total aerodynamic characteristics

It can be concluded from the presented results that a local energy source placed upstream of a supersonic vehicle can have a considerable effect on its total aerodynamic characteristics and flight trajectory. This yields a possibility of controlling both the vehicle velocity and flight direction by introducing a local energy source into the flow.

It is found that when studying the influence of the source of flow disturbances on the lift force and moment characteristics one cannot ignore the factors of transverse overflow of compression and rarefaction waves. The influence of this factor is particularly noticeable at moderate Mach numbers.

REFERENCES

1. Georgievsky P.Yu. and Levin V.A., Supersonic flow around a body with heat supply upstream of it// *Modern Problems of Mechanics and their Applications (Papers of Mathematical Institute of USSR Acad. Sci.)*. -1989. - Vol. 186. -P.197-201.
2. Georgievsky P.Yu. and Levin V.A., Supersonic flow around bodies with external heat sources// *Pis'ma v ZhTF*. -1988. -Vol. 14. -Iss. 8. -P. 684-687.
3. Georgievsky P.Yu. and Levin V.A., Supersonic flow around volume sources of energy// *Mechanics: Modern Problems*. Moscow, 1987. -P.93-99.
4. Artem'ev V.I., Bergelson V.I., Nemchinov I.V., et al., Changes in the supersonic flow around an obstacle with a slender rarefied channel ahead of it// *Izv. AN SSSR. Ser. MZG*. -1989.No. 5. -P.146-151.
5. Bergelson V.I., Medvedyuk S.A., Nemchinov I.V., Orlova T.I., Hazins V.M., Aerodynamic characteristics of a body with different location of the heat spike// *Mat. Modelirovanie*. -1996. -Vol. 6. -No. 1. -P. 3-9.
6. Borzov V.Yu., Rybka I.V., and Yur'ev A.S., The influence of local heat supply into hypersonic flow on the drag of bodies with various bluntness// *Inzh.-Fiz. Zhurn*. -1994. -Vol. 47. -No. 5-6. -P. 355-361.
7. Korotaeva T.A., Fomin V.M., and Shashkin A.P., Numerical study of the influence of a local energy source on the flow around pointed bodies. -Novosibirsk, 1996.-36 p. -(Preprint /Sib. Branch, Russian Acad. Sci. ITAM; No. 1-96).
8. Martin J., *Atmospheric Reentry*. -New York: Prentice-Hall, Inc., Englewood Cliffs, 1966.

A MARCHING PROCEDURE OF NUMERICAL SOLUTION OF TWO-DIMENSIONAL AND THREE-DIMENSIONAL STEADY EULER EQUATIONS USING SHOCK-CAPTURING SCHEMES

A.N.Kudryavtsev and R.D.Rakhimov

Institute of Theoretical and Applied Mechanics SB RAS,
Novosibirsk 630090, Russia

INTRODUCTION

Rapid development of computational equipment and numerical simulation methods has made quite possible the computation of the inviscid flow field around complex-shaped three-dimensional bodies. Nevertheless, such computations, especially those with high resolution, impose rather severe requirements to computer memory and need considerable time. The latter becomes particularly important in those cases when it is necessary to calculate a great number of variants, as, for instance, in solving optimization problems. If the flow is fully supersonic, great computational resources can be saved by using marching algorithms for the steady Euler equations [1,2]. The approach used in the present paper for constructing those is based on the high-order TVD schemes, which were primarily suggested for solving unsteady problems. Examples of calculations are presented, which were performed for a number of two-dimensional (plane and axisymmetric) and three-dimensional flows, including complex configurations of shock waves.

DESCRIPTION OF THE METHOD

Let us describe the proposed numerical method for the case of 2D steady fully supersonic flow of perfect gas. The Euler equations that govern such a flow have the form

$$\frac{\partial \mathbf{E}}{\partial x} + \frac{\partial \mathbf{F}}{\partial y} = \mathbf{S}, \quad \mathbf{E} = \begin{pmatrix} \rho u \\ \rho u^2 + p \\ \rho uv \\ \rho uH \end{pmatrix}, \quad \mathbf{F} = \begin{pmatrix} \rho v \\ \rho uv \\ \rho v^2 + p \\ \rho vH \end{pmatrix}, \quad \mathbf{S} = \frac{\nu}{y} \begin{pmatrix} \rho v \\ \rho uv \\ \rho v^2 \\ \rho vH \end{pmatrix} \quad (1)$$

The x axis is assumed to coincide with the marching direction; u, v are the velocity components along x and y ; p is the pressure; ρ is the density; H is the total gas enthalpy related to p and ρ through the equation of state

$$H = \frac{\gamma p}{(\gamma - 1)\rho} + \frac{u^2 + v^2}{2}; \quad (2)$$

γ is the ratio of specific heats; $\nu = 0$ and 1 in the plane and axisymmetric cases, respectively. When solving (1-2) numerically, the cross-sections $x = \text{const}$ are divided into cells $[y_{j-1/2}, y_{j+1/2}]$ of length $\Delta y_j = y_{j+1/2} - y_{j-1/2}$ with centers at points y_j . (Fig. 1).

The fluxes along x averaged over the cells

$$E_j = \frac{1}{\Delta y_j} \int_{y_{j-1/2}}^{y_{j+1/2}} E(y) dy \quad (3)$$

coincide with their values in the cell centers up to the second-order accuracy. From known values of E the values of primitive variables u, v, p, ρ can be easily decoded [1,2]. Integrating equation (1) over a trapezium with infinitesimal height dx (see Fig. 1) we obtain the following semi-discrete equation:

$$\frac{d}{dx} (\Delta y_j E_j) = - (\hat{F}_{j+1/2} - \hat{F}_{j-1/2}) + \Delta y_j S_j, \quad (4)$$

where $\hat{F}_{j+1/2} = F_{j+1/2} - (dy_{j+1/2}/dx) \cdot E_{j+1/2}$, and, similarly, for $\hat{F}_{j-1/2}$. The quantities $\hat{F}_{j-1/2}, \hat{F}_{j+1/2}$ are the fluxes normal to the lateral sides of the trapezium.

Gas dynamic quantities in the cross-section $x = x^n$ being known, the calculation of E_j^{n+1} in the next cross-section $x^{n+1} = x^n + \Delta x^n$ consists of the following stages: 1) reconstruction of gas dynamic quantities at the boundaries between the cells; 2) calculation of the fluxes $\hat{F}_{j+1/2}^n$; and 3) numerical integration of ODE (4).

The van Leer k -formula is used for reconstruction [3]:

$$\begin{aligned} q_{j+1/2}^L &= q_j + \frac{1-k}{4} \Phi(\Delta q_{j-1/2}, \Delta q_{j+1/2}) + \frac{1+k}{4} \Phi(\Delta q_{j+1/2}, \Delta q_{j-1/2}), \\ q_{j-1/2}^R &= q_j - \frac{1-k}{4} \Phi(\Delta q_{j+1/2}, \Delta q_{j-1/2}) - \frac{1+k}{4} \Phi(\Delta q_{j-1/2}, \Delta q_{j+1/2}), \\ \Delta q_{j-1/2} &= q_j - q_{j-1}, \quad \Delta q_{j+1/2} = q_{j+1} - q_j \end{aligned} \quad (5)$$

Here the superscripts L and R refer to the states at two sides of the boundary, $\Phi(a, b)$ is a nonlinear function limiting the slope of the solution near discontinuities (a limiter). The use of slope limiters is necessary for obtaining a solution free of oscillations. If the condition $\Phi(a, a) = a$ is satisfied, then the formulas in (5) have the second-order accuracy (on a grid close to uniform) for any arbitrary value of the parameter $-1 \leq k \leq 1$. For $k = 1/3$ the unlimited form ($\Phi(a, b) \equiv a$) of formulas (5) has the third-order accuracy. It is known that the quality of the solution can substantially depend on the form of Φ . The functions suggested by Chakravarthy and Osher (MINMOD) and by van Albada [4] were used in various computations in the present work.

Various choices of the set of reconstructed variables is also possible. Below we reconstruct either primitive variables $q = (u, v, p, \rho)$, or a set in which p is substituted by T , or, finally, the variables $q = (M, \theta, p, \rho)$, where M is the Mach number, and θ is the angle between the velocity vector and the marching direction.

The calculation of the fluxes $\hat{F}_{j+1/2}$ is performed by solving the Riemann problem for the states $q_{j+1/2}^L, q_{j+1/2}^R$. Both an exact solution of the problem of interaction of two steady supersonic flows [1,2] and any approximate solver can be used. Moreover, it is obvious that the desired fluxes have to coincide with those obtained in the asymptotic steady state from the solution of an unsteady problem. Hence, an arbitrary method of flux calculation among those used in algorithms for solving 2D unsteady Euler equations can be used. In practice, we used either an exact (iterative) solution of the steady Riemann problem or an approximate solution obtained by two-wave approximation, or, finally, the flux vector

splitting for unsteady problem, which was suggested by van Leer [5]. The two-wave approximation is widely used for the approximate solution of unsteady equations (Harten - Lax- van Leer - Einfeldt, HLLC solver [6]). This is a simple and robust, but sometimes too diffusive method of flux calculation. Taking into account that its implementation in a 3D problem requires some modifications, a brief derivation of the corresponding formula is presented below.

Let the interaction between the states E_L and E_R forms two shock waves with slopes b_L, b_R (Fig. 2). Integrating equation (1) (without the source term) over the quadrangles $ABCD$ and $CDEF$, we find from two resultant equations the values of E^*, F^* in the region between the waves. Hence, the flux through the side $y_{j+1/2}$ is

$$\hat{F}_{j+1/2} = a_L(F_L - b_L E_L) + a_R(F_R - b_R E_R), \quad (6)$$

$$\text{where } a_L = \frac{b_R - s}{b_R - b_L}, \quad a_R = \frac{s - b_L}{b_R - b_L}, \quad s \equiv \frac{dy_{j+1/2}}{dx}$$

When estimating the slopes, we use the eigenvalues of the matrix $\partial F / \partial E$:

$$b_L = \min(\lambda_-^L, \tilde{\lambda}_-, s), \quad b_R = \max(\lambda_+^R, \tilde{\lambda}_+, s), \quad (7)$$

$$\lambda_{\pm} = \frac{uv \pm a\sqrt{u^2 + v^2 - a^2}}{u^2 - a^2}, \quad a = \sqrt{\frac{\gamma p}{\rho}}$$

Here λ^L and λ^R are calculated from the values of gas dynamic variables in the states q^L and q^R , and $\tilde{\lambda}$ from their values in the Roe-averaged state [7].

The system of equations (4) can be written as

$$\frac{\partial Q}{\partial x} = \mathcal{L}(x, Q) \quad (8)$$

Since the position of boundaries between the cells $y_{j+1/2}(x)$ depends on the marching coordinate, the right-hand side of this system is explicitly dependent on x . Explicit TVD Runge-Kutta schemes [8] are used for its integration, which allows one to reach a high-order accuracy for the marching coordinate with retaining monotonicity of the solution. For a non-autonomous system (8) the second- and third-order schemes have the following form:

$$\text{2nd order } \begin{cases} Q^{(1)} &= Q^n + \Delta x \mathcal{L}(x^n, Q^n), \\ Q^{n+1} &= \frac{1}{2} (Q^n + Q^{(1)}) + \frac{\Delta x}{2} \mathcal{L}(x + \Delta x, Q^{(1)}) \end{cases} \quad (9)$$

$$\text{3rd order } \begin{cases} Q^{(1)} &= Q^n + \Delta x \mathcal{L}(x^n, Q^n), \\ Q^{(2)} &= \frac{1}{4} (3Q^n + Q^{(1)}) + \frac{\Delta x}{4} \mathcal{L}(x + \Delta x, Q^{(1)}), \\ Q^{n+1} &= \frac{1}{3} (Q^n + 2Q^{(2)}) + \frac{2\Delta x}{3} \mathcal{L}(x + \frac{\Delta x}{2}, Q^{(2)}) \end{cases} \quad (10)$$

The above described algorithm for solving the steady Euler equations is naturally generalized to 3D supersonic flows.

NUMERICAL RESULTS

To evaluate the accuracy and effectiveness of the proposed numerical algorithm, we used it for calculating the plane, axisymmetric, and three-dimensional flows. In calculations considered below, we used a scheme of the third-order accuracy in all

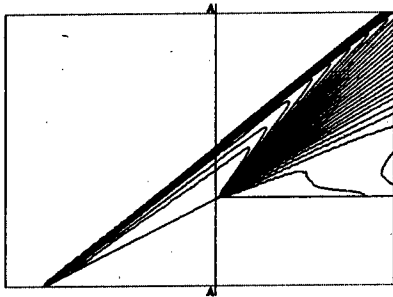


Fig.5. Density isolines for an axisymmetric flow around a cone-cylinder body.

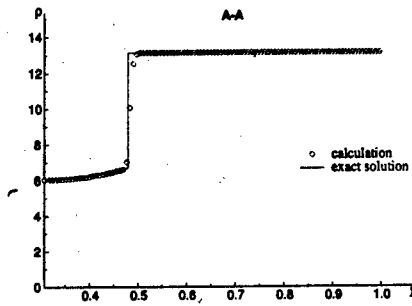


Fig.6. Density distribution in the cross-section A - A, as compared with an exact solution.



Fig.7. Pressure isolines for a flow around a cone at incidence.



Fig.8. Isolines of velocity component along z in the flow around a cone at incidence.

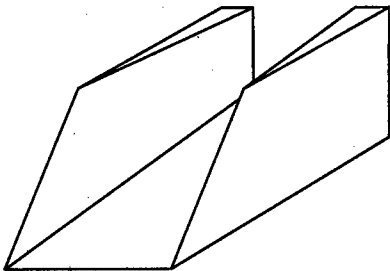


Fig.9. A schematic of the forebody of a hypersonic inlet.

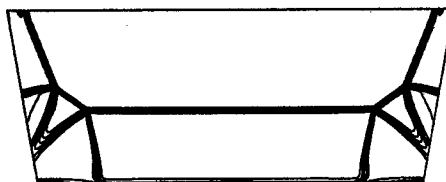


Fig.10. Isolines of streamwise velocity in one of the cross-sections.

directions except for the flow in a 3D channel, for which the second-order scheme was used in the marching direction.

Figs. 3,4 shows the results of flow calculation in a plane converging channel for the inflow Mach number $M=10$ and inclination angles of the upper and lower walls 10° and 20° , respectively. The number of grid points in the cross-streamwise direction is $N_y = 150$. Figs. 5,6 shows the calculated results of an axisymmetric flow around a cone-cylinder body with a 20° cone half-angle at $M=3$, $N_y = 100$. The variables u, v, T, ρ were reconstructed in the first case, M, θ, p, ρ in the second case. The Riemann problem was solved using the HLL solver. A high accuracy of the obtained solution should be noted, including the region near the solid wall, where the accuracy often decreases because of so-called numerical boundary layer. Contrary to [2], we did not use any special procedure near the wall slope discontinuity and the cone tip.

Figs. 7-10 show the results of calculation of three-dimensional flows: the flow with $M = 2$ around a cone with a 10° half-angle at a 25° angle of attack and the flow around a forebody of hypersonic inlet. When calculating the flow around the cone, we used the van Leer flux vector splitting, the number of points in the cross-section was 80×50 . A shock wave and a vortex formed at the leeward side are clearly seen (see Fig. 8 where the isolines with negative values of velocity along z are shown by gray color).

The forebody, whose sketch is shown in Fig. 9, is formed by three wedges: the lower one with an angle of 12.5° and two lateral wedges with an angle of 10° . The lateral wedges are inclined at an angle of 10° in the YZ plane, and their leading edges form a 45° angle with the hypersonic ($M = 6$) free stream. The Godunov scheme was used here for solving the Riemann problem, $N_y = 120$, $N_z = 150$. The interaction of shock waves from the lower and lateral wedges result in the formation of a bridge-like shock and two contact discontinuities emanating from triple points (Fig. 10). A good resolution of this method for so complicated wave structure simulation with no procedure of grid adaptation should be noted.

REFERENCES

1. Godunov S.K., Zabrodin A.V., Ivanov M.Ya., Kraiko A.N. Numerical Solution of Multi-dimensional Problems of Gas Dynamics.- Moscow: Nauka, 1976.
2. Glaz H.M., Wardlaw A.B. A high-order Godunov scheme for steady supersonic gas dynamics // J. Comput. Phys. - 1985. - Vol.58.- No.2.- P.157-187.
3. Anderson W.K., Thomas J.L., van Leer B. Comparison of finite volume flux vector splitting for the Euler equations // AIAA Journ. - 1986. - Vol.24.- No.9.- P.1453-1460.
4. Sweeby P.K. High resolution schemes using flux limiters for hyperbolic conservation laws. // SIAM J. Numer. Anal. - 1984. - Vol.21.- No.5.- P.995-1011.
5. Van Leer B. Flux-vector splitting for the Euler equations. // Lect. Notes in Phys. - 1982. - Vol.170.- P.507-512.
6. Einfeldt B., Munz C.D., Roe P.L., Sjogreen B. On Godunov-type methods near low densities // J. Comput. Phys. - 1991. - Vol.92.- No.2.- P.273-295.
7. Roe P.L. Approximate Riemann solvers, parameter vectors, and difference schemes. // J. Comput. Phys. - 1981. - Vol.43.- No.2.- P.357-372.
8. Shu C.-W., Osher S. Efficient implementation of essentially non-oscillatory shock-capturing schemes. // J. Comput. Phys. - 1988. - Vol.77.- No.2.- P.439-471.

VERIFICATION OF TURBULENCE SECOND-ORDER MODELS IN DIFFERENT REGIONS OF A ROTATING CYLINDRICAL PIPE FLOW

A.F. Kurbatskii, S.V. Poroseva

Institute of Theoretical and Applied Mechanics SB RAS
630090, Novosibirsk, Russia

INTRODUCTION

As experimental data show, swirl of a turbulent flow in a cylindrical pipe rotating around its longitudinal axis, influences essentially on the turbulence structure. This influence is determined, in particular, by the pipe length and the degree of swirl. In the flow, it is possible to distinguish two regions with the different structure of turbulence: the "short pipe" area ($x/D \leq 30$, x is axial distance from the entrance of a rotating pipe, D is the pipe diameter) and the "long pipe" one ($x/D = 68 + 168$). In the former region, strong suppression of turbulent intensities in both radial and longitudinal directions is observed [1-3], In the later one, the profiles of statistical characteristics reach their limit shapes [4-7]. So, profiles of the longitudinal component U of the mean flow velocity become similar, but the limit profile at $N = 1$ ($N = W_0 / U_m$ is a swirl parameter, W_0 is the rotating pipe wall velocity; U_m is the mean axial velocity) is still far from to be parabolic as the one in a laminar flow. Profiles of the circumferential component W of the mean flow velocity have the parabolic limit shape ($W/W_0 = (r/R)^2$, r is the radial coordinate, R is the pipe radius), whereas it is known that for a forced rotational flow, this function should be linear. Also experiments show that both limit profiles U and W are not affected, in fact, by the Reynolds number (Re), and the profile W does not depend on the value of N . Turbulent friction decreases along a pipe as well as with the swirl parameter increasing down to its limit value. In transition area, from one region to another one, increase of kinetic turbulence energy is observed. A correct model of turbulence should describe these phenomena.

The mathematical modeling of turbulence structure of a flow in a rotating cylindrical pipe with $k - \epsilon$ models does not give satisfactory results. In particular, a model for a developed pipe flow gives a linear limit profile for the circumferential velocity W , as it would be in the case of solid body rotation, that is in contradiction with experimental data.

The aim of the present research was to consider possibilities of some known Reynolds stress transport models (RSTM) to describe the turbulence structure of both regions in an isothermal rotating pipe flow as well as the transition area between them.

GOVERNING EQUATIONS

The set of exact transport equations for the mean velocity vector and the turbulent stress tensor in the case of stationary incompressible flow is written in the general tensor form as:

$$U_{,i}^i = 0; \quad U^j U_{i,j} = \nu g^{jk} U_{i,jk} - \langle u_i u^j \rangle_{,j} - \hat{P}_{,i} / \rho; \quad (1)$$

$$U^k \langle u_i u_j \rangle_{,k} = D_{ij} + P_{ij} + \Pi_{ij} - \varepsilon_{ij}, \quad (2)$$

where $\varepsilon_{ij} = 2\nu g^{km} \langle u_{i,m} u_{j,k} \rangle$ is the dissipation tensor;

$D_{ij} = -\langle u_i u_j u^m \rangle_{,m} - (\langle p u_i \rangle_{,j} + \langle p u_j \rangle_{,i}) / \rho + \nu (g^{km} \langle u_i u_j \rangle_{,k})_{,m}$ is the diffusion term;

$P_{ij} = -\langle u_j u^k \rangle U_{i,k} - \langle u_i u^k \rangle U_{j,k}$ is the production term;

$\Pi_{ij} = \langle p(u_{i,j} + u_{j,i}) \rangle / \rho$ is the pressure - strain correlation;

U_i and u_i are covariant components of mean and fluctuating velocities; $f_{,i}$ denotes the differential operator defined by $\partial f / \partial x_i$ (x_i is coordinates), g^{ij} is the metric tensor, $\langle \dots \rangle$ means ensemble averaging, \hat{P} is mean pressure, p is pressure fluctuation, ρ is flow density, ν is kinematic viscosity.

To close set (1) - (2), terms D_{ij} , Π_{ij} , and ε_{ij} should be modeled.

REYNOLDS STRESS TRANSPORT MODELS

In the present research in each tested RSTM, the simple gradient diffusion model suggested for D_{ij} by Daly-Harlow [8] was used.

The dissipation tensor ε_{ij} is modeled by the isotropic expression with correction on low Reynolds numbers near a solid wall [9], and the equation for the kinetic turbulence energy dissipation rate is used in the following form [9,10]:

$$U^k \varepsilon_{,k} = \left[g^{km} (\nu \varepsilon_{,k} + C_e \frac{k}{\varepsilon} \langle u_k u^l \rangle_{,l}) \right]_{,m} + (C_{e1} P - C_{e2}^* \varepsilon) \frac{\varepsilon}{k} - \frac{2\nu \varepsilon}{x_n^2} f_1, \quad (3)$$

where $k = 1/2 \langle u_i^2 \rangle$ is the kinetic turbulence energy, x_n is normal distance to a pipe wall, $P = 1/2 \cdot P_{ii} = -\langle u_i u^k \rangle U_{i,k}$; C_e , C_{e1} , C_{e2} , C_{e3} are empirical model constants, f_1 and f_2 are damping functions [9], $C_{e2}^* = \max(1, 4, C_{e2} f_2 / (1 - C_{e3} Ri))$ [10], The Richardson number Ri characterizes influence of streamline curvature on turbulence like there of medium stratification on turbulent transport. Equation (3) at $Ri = 0$ transforms into "standard" equation for the turbulent dissipation rate which we denote by (3a).

There were considered two model expressions [11,12] for the pressure - strain correlation Π_{ij} .

In [11] the correlation Π_{ij} is considered as a sum of three terms:

$$\Pi_{ij} = \Pi_{ij}^{(1)} + \Pi_{ij}^{(2)} + (\Pi'_{ij}^{(1)} + \Pi'_{ij}^{(2)}) f(x_n), \quad (4)$$

$$\text{where } \Pi_{ij}^{(1)} = -C_1 \frac{\varepsilon}{k} (\langle u_i u_j \rangle - \frac{2}{3} \delta_{ij} k), \quad (C_1 = 1,5), \quad (5)$$

$$\Pi_{ij}^{(2)} = -C_2 (P_{ij} - \frac{2}{3} \delta_{ij} P), \quad (C_2 = 0,6), \quad (6)$$

$$\Pi'_{ij}^{(1)} = C_1' \frac{\varepsilon}{k} \left[\langle u_n^2 \rangle g_{nn} \delta_{ij} - \frac{3}{2} (\langle u_n u_j \rangle g_{in} + \langle u_n u_i \rangle g_{jn}) \right], \quad (7)$$

$$\Pi'_{ij}(2) = C_2' \frac{\varepsilon}{k} \left[\Pi_{nn}^{(2)} g_{nn} \delta_{ij} - \frac{3}{2} \left(\Pi_{nj}^{(2)} g_{in} + \Pi_{ni}^{(2)} g_{jn} \right) \right], \quad (8)$$

$f = (1/5)k^{3/2}/(\varepsilon x_n)$ is a damping function, $C_1' = C_2' = 0,3$.

It is shown in [12] that in the case of an axisymmetric swirl flow, the convective transport tensor can be inserted in expression (6) to get better result:

$$C_{ij} = \frac{\partial}{\partial x_k} (U_k \langle u_i u_j \rangle) : \Pi_{ij}^{(2)} = -C_2 (P_{ij} - C_{ij} - \frac{1}{3} \delta_{ij} (P_{kk} - C_{kk})), \quad (9)$$

Verification of three RSTMs was carried out. Model 1 (denoted further by M1) which was suggested in [10], includes equation (3) and model expressions (4)-(8) to close set (1)-(2). In the second model (M2) there is used equation (3a) instead of (3). At present, this model is considered as the "standard" one and some its properties have been analyzed for a turbulent flow in a long cylindrical rotating pipe in [13]. Model 3 (M3) is similar to M2, but instead of expression (6) there is used its modification (9).

In each model, the set of the closed equations for required functions such as mean velocity vector, turbulent stresses, and kinetic turbulence energy dissipation rate was written in the axisymmetric cylindrical frame of references in the boundary layer approximation and solved by the control volume method. Details of used numerical procedure and boundary conditions can be found in [10].

DISCUSSION

Results of calculations were compared with experimental data [1-7]. In experiments [1-3], statistical characteristics of a turbulent flow (the first- and second-order moments of the velocity field) were measured in the exit section of a short rotating pipe at $x/D = 25$, $Re_m = 37000$ ($Re_m = U_m D/\nu$), $N \leq 0,6$. In [4-7] behavior of the mean flow velocity components (longitudinal and circumferential) as well as the longitudinal turbulence intensity was studied in the rotating long section of a cylindrical pipe ($x/D \leq 168$) at $Re_m = 0,5 + 3 \cdot 10^4$ and $N = 0,5 + 3$. Because experiments were carried out under different conditions, quantitative comparison of the data is difficult.

M1 reproduces satisfactorily transformation of the longitudinal U and circumferential W components of the mean flow velocity, as well as there of Reynolds stresses under moderate flow swirl ($N \leq 0,6$) in a short rotating pipe ($x/D = 25$) [10]. Here efficiency of this model for the case of a long pipe flow is considered.

The results of calculation of the damping coefficient of the longitudinal kinetic turbulence energy component $Ku = \langle u^2 \rangle (N > 0) / \langle u^2 \rangle (N = 0)$ at three values of the swirl parameter ($N = 0,34; 0,62; 1,0$) is shown on Fig.1 depending on a distance along the pipe axis. To make qualitative comparison, experimental points from [6] are given also at $N = 0,5; 1,0$ in sections $x/D = 11, 36, 68$, and 168 . It is seen, that at $N = 1$ the model predicts almost total suppression of turbulence intensity in the section $x/D = 168$. It is necessary to note that experimental data [1-3] give more strong suppression of turbulence in the initial section of a rotating pipe ($x/D = 25$) than the data [6] do. It is possible to conclude that M1 reproduces correctly transformation of the longitudinal kinetic turbulence energy component in a short pipe and qualitatively correct behavior of Ku with increasing a distance along the axis of a rotating long pipe under moderate swirl ($N = 0,34$). At strong swirl ($N = 1$) the model does not describe turbulence structure adequately. Influence of the Reynolds number on behavior of Ku along a pipe calculated by M1 is shown on Fig. 2.

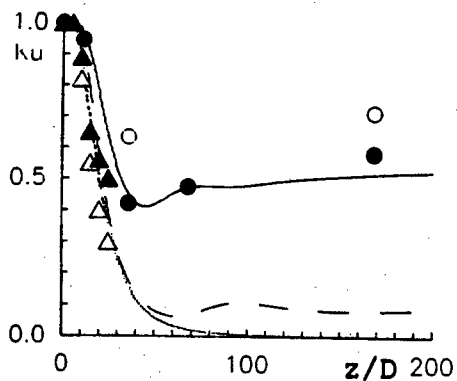


Fig. 1 Behavior of the damping coefficient Ku along a pipe axis ($r/R = 0$) calculated by M1 at different swirl parameters. Calculations: (—) - $N = 0,34$, (---) - $N = 0,62$, (····) - $N = 1$; experiments: [1-3] ($Re_m = 37000$): (Δ) - $N = 0,34$, (Δ) - $N = 0,62$; [6] ($Re_m = 30000$): (o) - $N = 0,5$, (e) - $N = 1$.

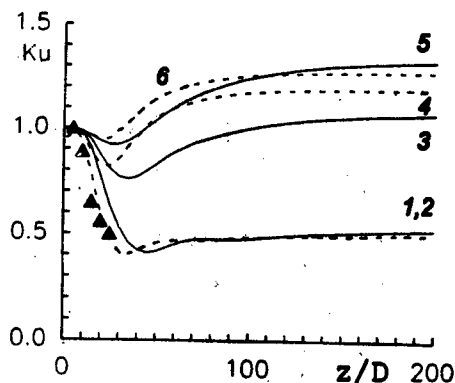
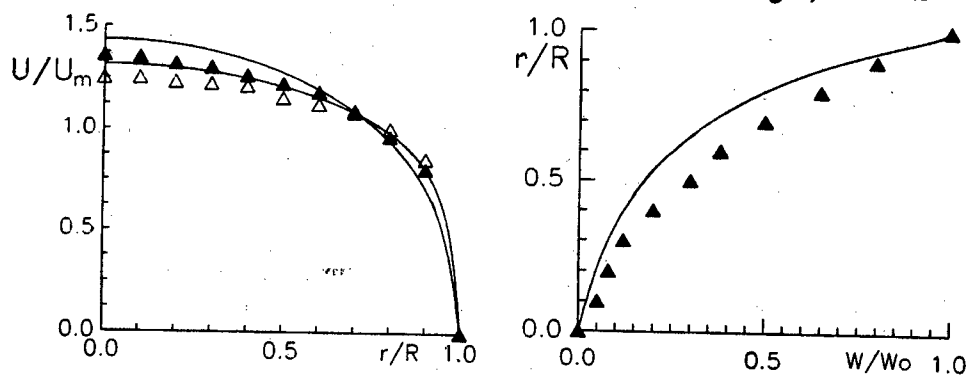


Fig. 2 Behavior of the damping coefficient Ku along a pipe axis, ($r/R = 0$, $N = 0,34$) at different Re . Calculations: (—) - $Re_m = 37000$, (---) - $Re_m = 10000$ (curves 1,2 - M1; 3,4 - M2; 5,6 - M3). Experiments: [1-3].

Note also, that the model describes the friction coefficient decreasing in consequence of "laminarization" of the longitudinal velocity profile (more exactly, its parabolization) and anisotropy of kinetic turbulence energy components as well as tendency of the profiles of the longitudinal and circumferential velocity components to their limit shapes of stabilization regime [4-7]. However, these profiles are not in quantitative agreement with the experimental ones. Moreover, their dependence on both the Reynolds number and the swirl parameter is observed, and stabilization regime is reached on distances much larger from the entrance of a rotating pipe than it was obtained in experiments [4-7].

Some results of calculations by M2 are given on Figs. 2-4. The model does not describe behavior of the damping coefficient Ku , as it is seen from Fig. 2, and other



Figs.3,4 Experimental data for $Re_m = 10000$ [5]: ($\Delta\Delta\Delta$) - $N = 0$., ($\blacktriangle\blacktriangle\blacktriangle$) - $N = 0,5$; (—) - calculations by M2.

statistical characteristics (figures for which are not shown in this paper) in a short pipe flow, though increase of turbulence intensities in the section $68 \leq x/D \leq 168$ of a rotating pipe, which was observed in [6], is reproduced qualitative correctly. Dependence of Ku on the Reynolds number is observed at different pipe lengths and swirl parameters in contradiction with experimental data.

The model describes transformation of the components of the mean flow velocity to their limit shapes at $Re_m = 10000$, $N = 0.5$ (Figs.3,4; see also Fig.2, curve 3). However, it is observed much earlier than in experiments and the limit profile of W (Fig. 4) does not coincide with the experimental one. At high Reynolds numbers (Fig.2), stabilization regime is not reached.

Thus, the most known and simple variant of RSTM does not describe correctly neither "short pipe" region, no "long pipe" one.

The calculation results obtained by M3 are presented on Figs. 2,5,6. The profiles of the longitudinal and circumferential components of the mean flow velocity are shown at sections $x/D = 160$ [5], 120 [7] at different swirl parameters. At moderate swirls, the model reproduces correctly transformation of the profile U along a pipe under applied rotation on a flow and gives its correct limit shape (Fig. 5). It is seen, that dependence of U on the Reynolds number is weak in stabilization regime in accordance with experimental data [4-7]. The profile of the circumferential velocity component (Fig. 6) reaches also its limit parabolic dependence on the radial coordinate at $N \leq 1$ not depending on Re . Other statistical characteristics reaches their limit profiles either, but their behavior along a pipe is described only qualitatively as, for instance, behavior of the longitudinal kinetic turbulence energy component (Fig.2). For this characteristic of turbulence structure, there is observed in calculations weak dependence on the Reynolds number, but it remains along the whole pipe length.

The results of calculations let us conclude the following. The structure of a turbulent flow in a cylindrical pipe is transformed in a complicated way along the whole length of a rotating pipe. Data of calculations and experiments show, in particular, that although the longitudinal component of the mean flow velocity is tending to the profile

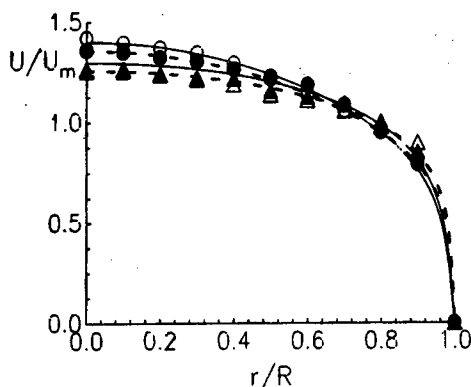


Fig. 5. Calculations by M3: (—) - $Re_m = 10^4$, (- -) - $Re_m = 37000$. Experiments: [5] ($Re_m = 10^4$): (▲) - $N = 0$, (●) - $N = 0,5$; [7] ($Re_m = 2 \cdot 10^4$): (Δ) - $N = 0$, (○) - $N = 0,5$.

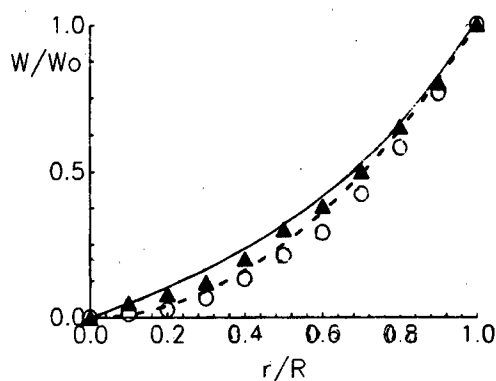


Fig. 6. Calculations: by M3 (—); parabolic profile (- -). Experiments: (▲) - [5] ($Re_m = 10^4, 3 \cdot 10^4$); (○) - [7] ($Re_m = 2 \cdot 10^4$).

typical for a laminar flow, kinetic turbulence energy is suppressed strongly only in the initial section of a pipe, but then, its increase is observed. RSTMs, even those which were developed specially for a swirl flow, can not describe structure of both regions of a flow, transition area between them, as well as there of a flow under strong swirl. Possible ways to solve this problem are to further development of model expressions for physically correct describing turbulent diffusion and influence of rotation on spectral expenditure of turbulence energy.

REFERENCES

1. Zaets P.G., Safarov N.A., Safarov R.A. Experimental study of turbulence characteristics behavior under rotating a pipe around its longitudinal axis (in Russian) // Modern problems of continuous medium mechanics. - Moscow: Moscow Physics and Technics Institute (MFTI), 1985. - P.136 - 142.
2. Pilipchuk M.I. Study of statistical characteristics of the longitudinal velocity component in a turbulent flow in a rotating pipe (in Russian): Ph.D. Thesis. - Moscow: Moscow Physics and Technics Institute (MFTI), 1986.
3. Safarov N.A. Behavior of parameters of a developed turbulent flow in a straight cylindrical channel rotated around the longitudinal axis: Ph.D. Thesis. - Moscow: Moscow Physics and Technics Institute (MFTI), 1986.
4. Murakami M., Kikuyama K. Turbulent flow in axially rotating pipes // Trans. ASME J. Fluids Eng. - 1980. - Vol.10 2, N 1. - P. 97 - 103.
5. Kikuyama K. et al. Flow in an axially rotating pipe (a calculation of flow in the saturated region) // Bull. JSME. - 1983. - Vol.26, N 214. - P. 506 - 513.
6. Nishibori K., Kikuyama K., Murakami M. Laminarization of turbulent flow in the inlet region of an axially rotating pipe // Bull. JSME. - 1987. - Vol. 30, N 260. - P. 255 - 262.
7. Imao S., Itoh M., and Harada T. Turbulent characteristics of the flow in an axially rotating pipe // Int. J. Heat and Fluid Flow. - 1996. - Vol.17, N 5. - P. 444 - 451.
8. Daly B.J., Harlow F.H. Transport equations in turbulence // Phys. Fluids. - 1970. - Vol.13 (11). - P. 2634 - 2649.
9. So R.M.C., Yoo G.J. On the modeling of low-Reynolds-number turbulence. - NASA Contractor Report 3994, 1986.
10. Kurbatskii A.F., Poroseva S.V., Yakovenko S.N. Calculation of statistical characteristics of a turbulent flow in a rotated cylindrical pipe // High Temperature. - 1995. - Vol. 133, N 5. - P. 738 - 748.
11. Launder B.E., Reece G.J., Rodi W. Progress in the development of a Reynolds stress turbulent model // J. Fluid. Mech. - 1973. - Vol.68. - P. 537 - 566.
12. Launder B.E. Second-moment closure and its use in modeling turbulent industrial flows // Int.J. for Numer. Meth. in Fluids. - 1989. Vol.9. - P. 963 - 985.
13. Hirai S., Takagi T., Matsumoto M. Contribution towards a Reynolds - stress closure for low - Reynolds - number turbulence // Trans. JSME. - 1989. - Vol.52 (476 B). - P. 1608 - 1616.

MODELING A TURBULENT FLOW IN THE PLANE CHANNEL WITH A QUADRATIC CROSS-SECTION RIB

A.F.Kurbatskii, S.N.Yakovenko

Institute of Theoretical and Applied Mechanics SB RAS

Aerophysics and Gasdynamics Chair, Novosibirsk State University

630090 Novosibirsk, Russia

Results of modeling a flow around a two-dimensional surface-placed obstacle of square cross-section in the closed plane channel have been presented. Possibilities of algebraic and differential Reynolds-stress models (RSM) have been investigated.

Reynolds-stress models. The differential model (DM) containing the transport equations for components of the Reynolds stress tensor $\langle u_i u_j \rangle$ can be written for two-dimensional flow as

$$\partial U / \partial x + \partial V / \partial y = 0; \quad (1)$$

$$\frac{\partial U}{\partial t} + \frac{\partial U^2}{\partial x} + \frac{\partial UV}{\partial y} = \frac{\partial}{\partial x} \left[\nu \frac{\partial U}{\partial x} - \langle u^2 \rangle \right] + \frac{\partial}{\partial y} \left[\nu \frac{\partial U}{\partial y} - \langle uv \rangle \right] - \frac{1}{\rho} \frac{\partial p}{\partial x}; \quad (2)$$

$$\frac{\partial V}{\partial t} + \frac{\partial UV}{\partial x} + \frac{\partial V^2}{\partial y} = \frac{\partial}{\partial y} \left[\nu \frac{\partial V}{\partial y} - \langle v^2 \rangle \right] + \frac{\partial}{\partial x} \left[\nu \frac{\partial V}{\partial x} - \langle uv \rangle \right] - \frac{1}{\rho} \frac{\partial p}{\partial y}; \quad (3)$$

$$\frac{\partial k}{\partial t} + \frac{\partial kU}{\partial x} + \frac{\partial kV}{\partial y} = \frac{\partial}{\partial x} \left[(\nu + \nu_t) \frac{\partial k}{\partial x} \right] + \frac{\partial}{\partial y} \left[(\nu + \nu_t) \frac{\partial k}{\partial y} \right] + P - \varepsilon; \quad (4)$$

$$\frac{\partial \varepsilon}{\partial t} + \frac{\partial \varepsilon U}{\partial x} + \frac{\partial \varepsilon V}{\partial y} = \frac{\partial}{\partial x} \left[\left(\nu + \frac{\nu_t}{\sigma_\varepsilon} \right) \frac{\partial \varepsilon}{\partial x} \right] + \frac{\partial}{\partial y} \left[\left(\nu + \frac{\nu_t}{\sigma_\varepsilon} \right) \frac{\partial \varepsilon}{\partial y} \right] + (C_{\varepsilon 1} P - C_{\varepsilon 2} \varepsilon) \frac{\varepsilon}{k}; \quad (5)$$

$$\frac{\partial \langle u^2 \rangle}{\partial t} + \frac{\partial \langle u^2 \rangle U}{\partial x} + \frac{\partial \langle u^2 \rangle V}{\partial y} = \frac{\partial}{\partial x} \left[(\nu + \nu_t) \frac{\partial \langle u^2 \rangle}{\partial x} \right] + \frac{\partial}{\partial y} \left[(\nu + \nu_t) \frac{\partial \langle u^2 \rangle}{\partial y} \right] - \frac{2}{3} \varepsilon + P_{11} + \Pi_{11}; \quad (6)$$

$$\frac{\partial \langle v^2 \rangle}{\partial t} + \frac{\partial \langle v^2 \rangle U}{\partial x} + \frac{\partial \langle v^2 \rangle V}{\partial y} = \frac{\partial}{\partial x} \left[(\nu + \nu_t) \frac{\partial \langle v^2 \rangle}{\partial x} \right] + \frac{\partial}{\partial y} \left[(\nu + \nu_t) \frac{\partial \langle v^2 \rangle}{\partial y} \right] - \frac{2}{3} \varepsilon + P_{22} + \Pi_{22}; \quad (7)$$

$$\frac{\partial \langle uv \rangle}{\partial t} + \frac{\partial \langle uv \rangle U}{\partial x} + \frac{\partial \langle uv \rangle V}{\partial y} = \frac{\partial}{\partial x} \left[(\nu + \nu_t) \frac{\partial \langle uv \rangle}{\partial x} \right] + \frac{\partial}{\partial y} \left[(\nu + \nu_t) \frac{\partial \langle uv \rangle}{\partial y} \right] + P_{12} + \Pi_{12}, \quad (8)$$

where ν and $\nu_t = C_\mu k^2 / \varepsilon$ are coefficients of molecular and turbulent viscosity; ε and $P = \sum_{i=1}^2 P_{ii} / 2 = (P_{11} + P_{22}) / 2$ are dissipation and production of the turbulence energy k ;

$$P_{11} = -2 \left(\langle u^2 \rangle \frac{\partial U}{\partial x} + \langle uv \rangle \frac{\partial U}{\partial y} \right), \quad P_{22} = -2 \left(\langle v^2 \rangle \frac{\partial V}{\partial y} + \langle uv \rangle \frac{\partial V}{\partial x} \right), \quad P_{12} = -\langle u^2 \rangle \frac{\partial V}{\partial x} - \langle v^2 \rangle \frac{\partial U}{\partial y}$$

are components of the tensor of turbulence production by the mean velocity shear; U and V are horizontal and vertical components of the mean velocity vector; u and v are the corresponding fluctuation velocity components; t is time; p is mean pressure; ρ is density; $\langle \dots \rangle$ means Reynolds averaging; $C_{\varepsilon 1} = 1.44$; $C_{\varepsilon 2} = 1.92$; $\sigma_\varepsilon = 1.3$; $C_\mu = 0.09$.

Processes of turbulent diffusion (first terms in the right sides of (4)–(8)) are described by the isotropic gradient model using the turbulent viscosity coefficient ν_t .

The pressure-strain terms Π_{ij} are expressed as in [1] with $C_1 = 1.5$; $C_2 = 0.4$:

$$\begin{aligned} \Pi_{11} = & -C_1 \varepsilon \left(\frac{\langle u^2 \rangle}{k} - \frac{2}{3} \right) - \frac{C_2 + 8}{11} \left(P_{11} - \frac{2}{3} P \right) - \frac{30C_2 - 2}{55} k \cdot 2 \frac{\partial U}{\partial x} - \\ & - \frac{8C_2 - 2}{11} \left(-2\langle u^2 \rangle \frac{\partial U}{\partial x} - 2\langle uv \rangle \frac{\partial V}{\partial x} - \frac{2}{3} P \right); \end{aligned} \quad (9)$$

$$\begin{aligned} \Pi_{22} = & -C_1 \varepsilon \left(\frac{\langle v^2 \rangle}{k} - \frac{2}{3} \right) - \frac{C_2 + 8}{11} \left(P_{22} - \frac{2}{3} P \right) - \frac{30C_2 - 2}{55} k \cdot 2 \frac{\partial V}{\partial y} - \\ & - \frac{8C_2 - 2}{11} \left(-2\langle v^2 \rangle \frac{\partial V}{\partial y} - 2\langle uv \rangle \frac{\partial U}{\partial y} - \frac{2}{3} P \right); \end{aligned} \quad (10)$$

$$\Pi_{12} = -C_1 \varepsilon \frac{\langle uv \rangle}{k} - \frac{C_2 + 8}{11} P_{12} - \frac{30C_2 - 2}{55} k \left(\frac{\partial U}{\partial y} + \frac{\partial V}{\partial x} \right) - u^2 \frac{\partial U}{\partial y} - \langle v^2 \rangle \frac{\partial V}{\partial x}. \quad (11)$$

The non-linear explicit algebraic model (AM) can be reduced [2] from DM as

$$\langle u^2 \rangle = \frac{2}{3} k - 2G \frac{k^2}{\varepsilon} \frac{\partial U}{\partial x} + \frac{Gk}{C_1 - 1 + 2G\{S^2\}} \left[b_3 \frac{k^2}{\varepsilon^2} \left\{ \left(\frac{\partial U}{\partial y} \right)^2 - \left(\frac{\partial V}{\partial x} \right)^2 \right\} + \frac{2}{3} b_2 \{S^2\} \right]; \quad (12)$$

$$\langle v^2 \rangle = \frac{2}{3} k - 2G \frac{k^2}{\varepsilon} \frac{\partial V}{\partial y} - \frac{Gk}{C_1 - 1 + 2G\{S^2\}} \left[b_3 \frac{k^2}{\varepsilon^2} \left\{ \left(\frac{\partial U}{\partial y} \right)^2 - \left(\frac{\partial V}{\partial x} \right)^2 \right\} - \frac{2}{3} b_2 \{S^2\} \right]; \quad (13)$$

$$\langle uv \rangle = -G \frac{k^2}{\varepsilon} \left(\frac{\partial U}{\partial y} + \frac{\partial V}{\partial x} \right) + \frac{Gk}{C_1 - 1 + 2G\{S^2\}} \left[b_3 \frac{k^2}{\varepsilon^2} \left(\frac{\partial U}{\partial y} - \frac{\partial V}{\partial x} \right) \left(\frac{\partial U}{\partial x} - \frac{\partial V}{\partial y} \right) \right], \quad (14)$$

$G = G(k, \varepsilon, \partial U_k / \partial x_m)$ is defined from the cubic equation $G^3 + aG^2 + bG + c = 0$, where

$$a = \frac{C_1 - 1}{\{S^2\}}, \quad b = \frac{(C_1 - 1)^2 - 2b_3^2 W_{ik} W_{ki} - (b_1 + 2b_2^2/3)\{S^2\}}{4\{S^2\}^2}, \quad c = -\frac{b_1(C_1 - 1)}{8\{S^2\}^2},$$

$$\{S^2\} = \frac{1}{2} \frac{k^2}{\varepsilon^2} \left[\left(\frac{\partial U}{\partial y} + \frac{\partial V}{\partial x} \right)^2 + 2 \left(\frac{\partial U}{\partial x} \right)^2 + 2 \left(\frac{\partial V}{\partial y} \right)^2 \right], \quad W_{ik} W_{ki} = -\frac{1}{2} \frac{k^2}{\varepsilon^2} \left(\frac{\partial U}{\partial y} - \frac{\partial V}{\partial x} \right)^2,$$

$$b_1 = 8/15, \quad b_2 = (5 - 9C_2)/11, \quad b_3 = (7C_2 + 1)/11,$$

The linear Boussinesq model (BM) of gradient type for the Reynolds stress tensor

$$\langle u^2 \rangle = (2/3)k - 2C_\mu (k^2/\varepsilon) (\partial U/\partial x), \quad \langle v^2 \rangle = (2/3)k - 2C_\mu (k^2/\varepsilon) (\partial V/\partial y), \quad (15)$$

$$\langle uv \rangle = -C_\mu (E^2/\varepsilon) [(\partial U/\partial y) + (\partial V/\partial x)] \quad (16)$$

contains constant C_μ instead of complex function G in expressions (12)-(14) of AM.

Plane-channel flow has been chosen to examine applicability of the turbulence models because of presence of the measurements data [3] (denoted by points \circ in Fig.1-4). The velocity and length scales in calculations are as in [3]. The Reynolds number Re_H [3] based on the rib height H and inflow velocity U_H at this height is sufficiently high and the viscous sublayer influence on the model assumptions and boundary conditions is neglected. So the first near-wall computational node is placed outside the viscous sublayer and the wall boundary conditions are taken as "wall law" [4]. The developed turbulent inflow is set at the upstream boundary with the vertical profiles of velocity U and turbulence energy k from experiments [3]. Normal gradients of all sought quantities except the pressure are set to zero at the downstream boundary. Details of initial distributions, pressure boundary conditions, equations discretization and computation procedure are given in [4].

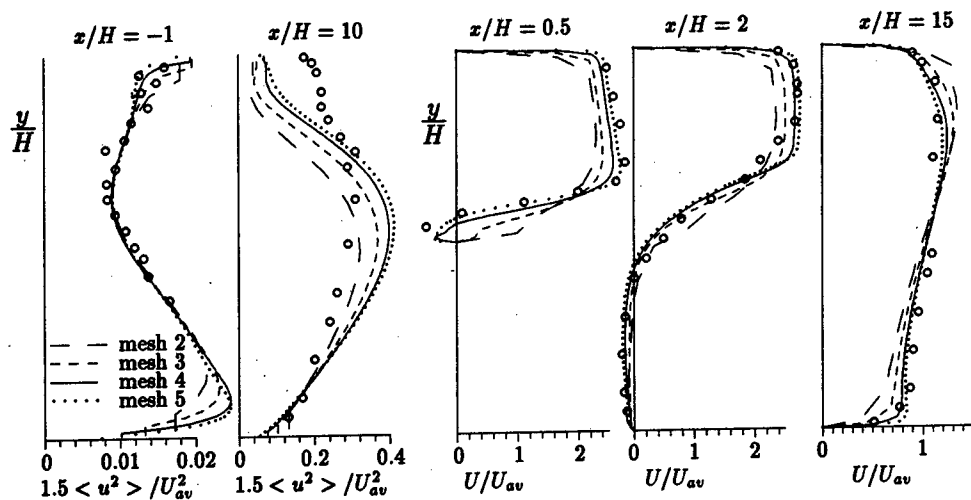


Fig.1. Vertical profiles of horizontal components of turbulence kinetic energy and mean velocity calculated at mesh 2-5 by means of DM.

Computation results. The series of calculations has been performed to obtain the approximation convergence of solutions of difference equations to exact ones with refinement of non-uniform grid and to clear up the detail structure of turbulent flow around an obstacle. The mesh interval δ near obstacle surfaces was taken in successive runs to be equal to $H/6$, $H/12$, $H/24$, $H/48$, $H/96$ (meshes 1-5, respectively). The differences between the results of computations used mesh 1, 2, 3, 4 and 5 are decreased continuously with grid refinement (Fig.1) and localized near the top where the third recirculation region forms in calculations at mesh 4, 5. The further grid refinement must take into account the flow structure in the viscous sublayer by means of corrections of turbulence model and near-wall boundary conditions. It can be seen from Fig.1 that mesh 4 with $\delta = H/48$ provides the satisfactory approximation convergence. The deviations between the results computed by DM at mesh 4 and 5 (Fig.1) are much less than differences between the results obtained by means of different RSM at mesh 4 (Fig.2) or 5.

Possibilities of algebraic and differential RSM have been studied. The linear on mean velocity derivatives BM model (1)-(5),(15)-(16) (long dashed line in Fig.2) gives large quantitative discrepancies with experiments data and even negative non-physical values of horizontal component $\langle u^2 \rangle$ of turbulence kinetic energy. The non-linear algebraic model AMN (1)-(5),(12)-(13),(16) for normal Reynolds stresses (short dashed line in Fig.2) is able to reproduce their anisotropy and to correct the shortcoming of the linear model. The differential model DMN (1)-(7),(9)-(10),(16) with transport equations for $\langle u^2 \rangle, \langle v^2 \rangle$ and linear gradient expression for $\langle uv \rangle$ (dotted line in Fig.2) describes behavior of $\langle u^2 \rangle$ in front of an obstacle (where the convection and diffusion processes are essential) better than AMN. The complete DM model (1)-(11) (solid lines in Fig.2) with transport equations for all components of $\langle u_i u_j \rangle$ gives most exact prediction of the mean velocity field in front of the obstacle, above it and in the recovery region behind it. This model describes (Fig.3d,e) also the joint of recirculation zones above and behind the rib at mesh 4, 5.

The problem of using of difference schemes for convective terms in the transport equations for calculations of flows around sharp-edged obstacles at the high Reynolds

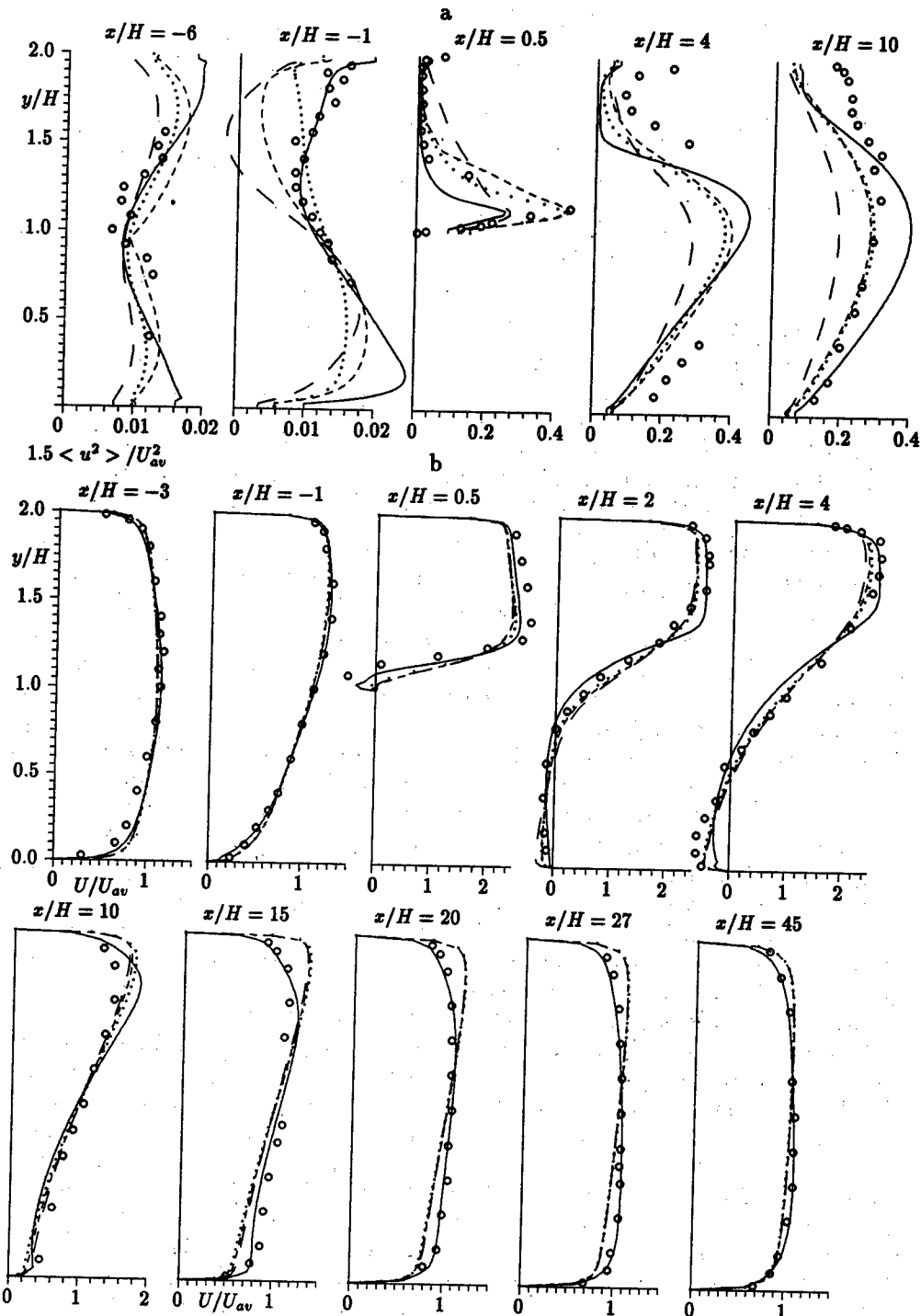


Fig.2. Results of computations by different models and of measurements at $\delta = H/48$.

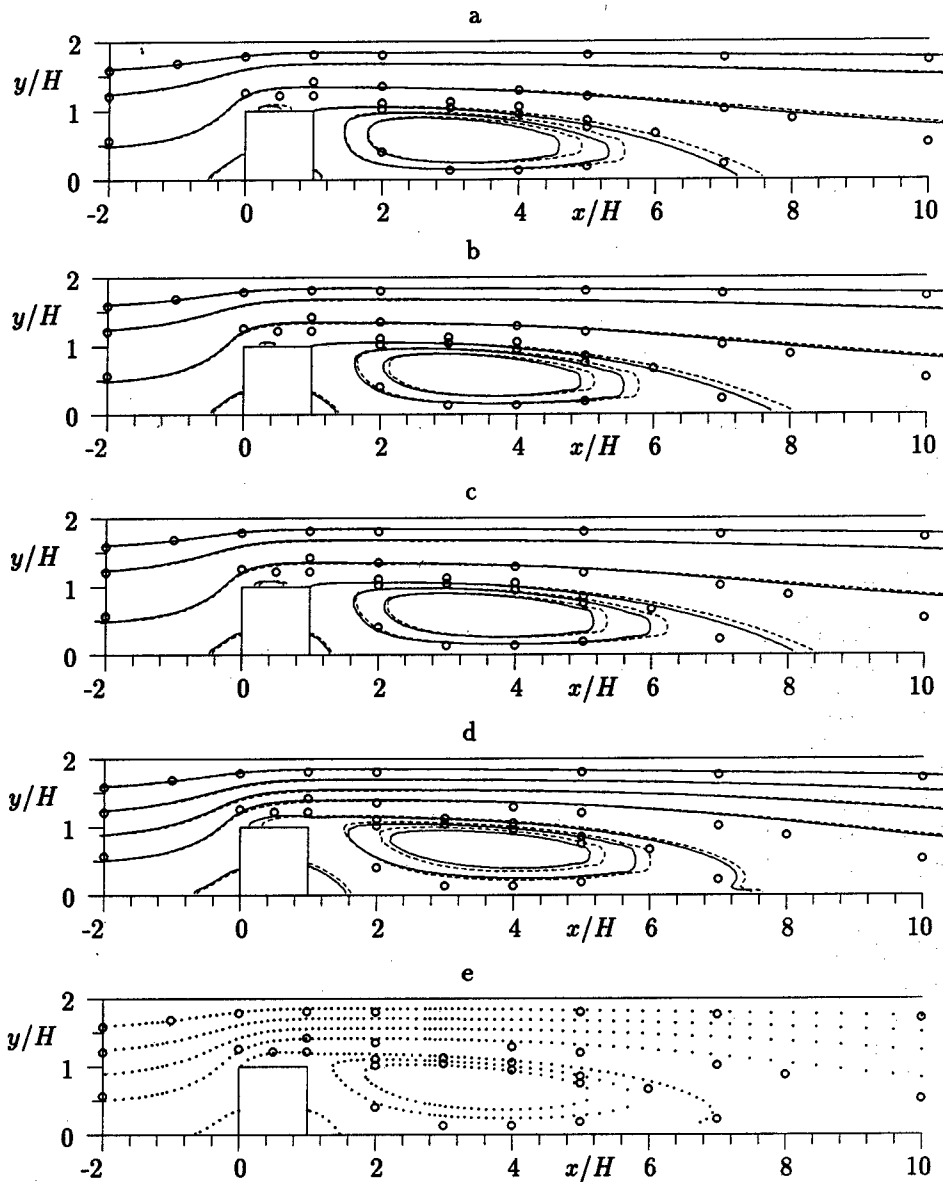


Fig.3. Streamlines of flow near an obstacle. Computations with $\delta = H/48$ by models: (a) BM, (b) AMN, (c) DMN, (d) DM; solid lines correspond to calculations with upwind scheme for convective terms in equations for all sought quantities, dashed lines correspond to calculations with second-order scheme for convective terms in equations for U and V ; (e) calculation by DM at grid with $\delta = H/96$ (dotted lines).

numbers is until discussed in science papers. However, it has been obtained that differences between curves computed by means of the same model (Fig.3a-d,4) with different schemes (in particular, first-order upwind scheme and QUICK one) at the refined grid with

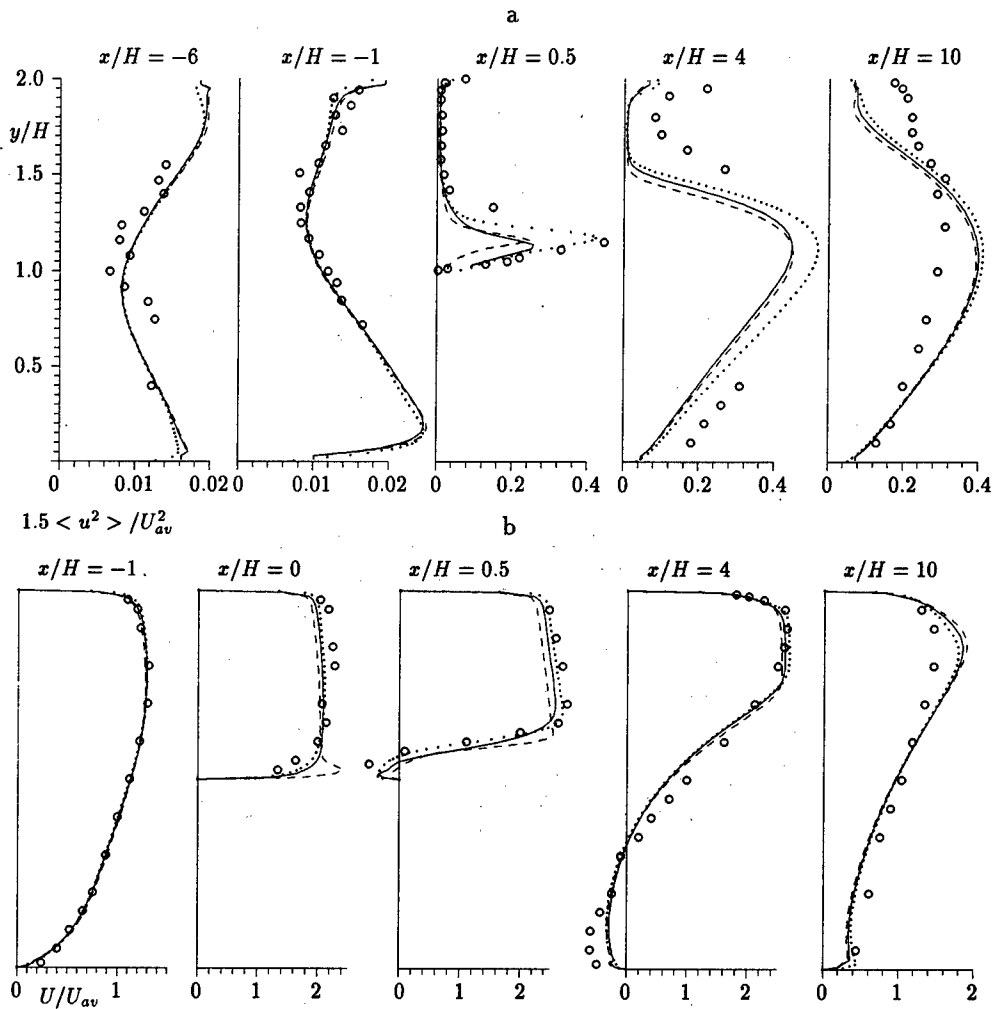


Fig.4. Results of computations by DM (lines correspond to the same cases as in Fig.3).

$\delta = H/48$ are much less than discrepancies of sought functions and streamlines calculated by means of different turbulence models (Fig.2,3) but with the same convective scheme. Refinement of the grid up to $\delta = H/96$ allows to obtain better agreement with measurements data (Fig.3e,4) in the top separation region especially.

This work is supported by Russian Foundation (grants No.96-05-64007, 96-15-96310).

REFERENCES

1. Hanjalic K., Launder B.E. A Reynolds stress model of turbulence and its application to thin shear flows // J.Fluid Mech. - 1972. - Vol. 52. - P.609.
2. Pope S.B. A more general effective viscosity hypothesis // J.Fluid Mech. - 1975. - Vol.72. - P.331.
3. Durst F., Rastogi A.K. Theoretical and experimental investigations of turbulent flows with separation // Turbulent Shear Flows 1. - Berlin: Springer-Verlag, 1979, P.208.
4. Kurbatskii A.F., Yakovenko S.N. Numerical investigation of turbulent flow around two-dimensional obstacle in the boundary layer // Thermophysics and Aeromechanics. - 1996. - Vol.3, No.2. - P.137.

COMPARISON OF CHARACTERISTICS OF ANEMOMETERS OF DIFFERENT TYPES

V.A.Lebiga*, A.Yu.Pak†

*Institute of Theoretical and Applied Mechanics, 630090 Novosibirsk, Russia

†Novosibirsk State Technical University, 630092 Novosibirsk, Russia

Hot wire anemometer is one of the most frequently used tools for investigation of fine structure of laminar and turbulent incompressible flows. Peculiarities of hot wire application at high velocities (the presence of several sorts of fluctuations, large aerodynamic loads, high pulsation frequency etc.) lead to using the top possibilities of equipment, whose characteristics depend on the type of anemometer. When a choice has to be done, attention is paid to comparison of sensitivities, frequency ranges and noises of different anemometers.

Two types of equipment have been used until recently: constant temperature anemometer (CTA) and constant current anemometer (CCA). Their advantages and disadvantages are well known. Information on a new type of anemometer has appeared lately. This anemometer has a scheme, where the probe is maintained at a constant voltage [1]. Possibly, it can provide new properties of anemometers. Therefore, it is interesting to compare principal characteristics of constant voltage anemometer (CVA) with previous types.

The block diagram of CVA (see Fig. 1) consists of the probe R_p , resistors R_1 and R_2 , a source of stable voltage E , a high gain operational amplifier OA , impedance Z maintaining zero voltage at the input of OA . There are no any Wheatstone bridges in this scheme.

It is possible to write for loops I and II, respectively,

$$E + iR_1 + e_{IN} = 0$$

$$\text{and } e + iR_2 + e_{IN} = 0.$$

Taking into account that $e_{IN} = 0$, the voltage e across the probe is

$$e = -E \frac{R_2}{R_1} = \text{const}, \quad I = \frac{E}{R_1} = \text{const}.$$

The output of the amplifier corresponds to flow fluctuations.

To analyze and compare the characteristics of anemometers of different systems we shall consider the heat transfer equation for a probe. In the general case it can be written [2]

$$ei = \pi \lambda_0 (T_w - T_e) (A_* + B_* \sqrt{Re_0}) (1 - ka_w) + C_w \frac{dT_w}{dt} \quad (1)$$

where l is the wire length, λ is the thermal conductivity of the gas, T_e , T_w and R_e , R_w are the temperature and resistance of "cold" and heated wire respectively, Re and Nu are the Reynolds and Nusselt numbers, C_w is the thermal capacity of the sensor, $a_w = (R_w - R_e)/R_e$ is the overheating, k is the coefficient to correct a linear dependence of heat losses on the overheating [2].

According to Kovaznay [3], it is necessary to determine λ and Re in (1) for parameters behind the normal shock: $Re_0 = md/\mu_0$, where d is the probe wire diameter, $m = \rho u$.

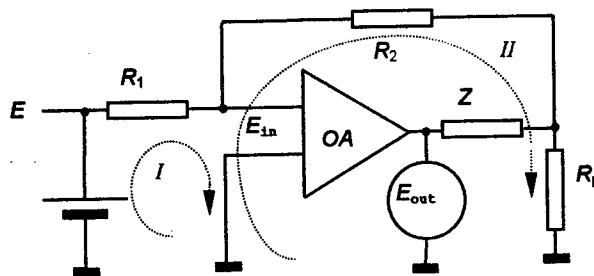


Fig. 1

Power relationships are used for thermal conductivity and dynamic viscosity dependences on temperature:

$$\mu_0 = \mu_* \left(\frac{T_0}{T_*} \right)^{\alpha}, \quad \lambda_0 = \lambda_* \left(\frac{T_0}{T_*} \right)^{\beta}, \quad (2)$$

and the linear one for the probe resistance dependence on temperature:

$$R = R_* [1 + \alpha_* (T - T_*)], \quad (3)$$

where α_* is the thermal coefficient of resistance.

Using the above mentioned equations we can find relations for the coefficients of probe sensitivities.

1. Analytical Relationships for Sensitivity Coefficients

1. Constant temperature anemometer. Both the probe temperature and resistance are constant ($T_w = \text{const}$, $R_w = \text{const}$). Therefore, the non-stationary term in Eq. (1) vanishes, and it is more convenient to write the equation as:

$$\frac{e^2}{R_w} = \pi \lambda_0 (T_w - T_*) (A + B\sqrt{\text{Re}})(1 - ka_w). \quad (4)$$

After logarithmic differentiation of Eq. (4) taking into account (2),(3), it is possible to write the equation connecting the voltage deviation e with mass flow m and total temperature T_0 deviations:

$$\frac{\Delta e}{e} = \frac{\Delta m}{m} \left[\frac{B\sqrt{\text{Re}}}{4(A+B\sqrt{\text{Re}})} - \frac{ka_w}{2(1-ka_w)} \frac{\partial \ln k}{\partial \ln \text{Re}} \right] + \frac{\Delta T_0}{T_0} \left\{ \omega \left[1 - \frac{B\sqrt{\text{Re}}}{2(A+B\sqrt{\text{Re}})} + \frac{ka_w}{1-ka_w} \frac{\partial \ln k}{\partial \ln \text{Re}} \right] - \frac{\alpha_* R_* \eta T_0 [1 - ka_w (a_w + 2)]}{R_* 2a_w (1 - ka_w)} \right\}$$

or
$$\frac{\Delta e}{e} = F_{\text{cra}} \frac{\Delta m}{m} - G_{\text{cra}} \frac{\Delta T_0}{T_0}, \quad (5)$$

where
$$F_{\text{cra}} = \frac{B\sqrt{\text{Re}}}{4(A+B\sqrt{\text{Re}})} - \frac{ka_w}{2(1-ka_w)} \frac{\partial \ln k}{\partial \ln \text{Re}}, \quad (6)$$

$$G_{\text{cra}} = \frac{\alpha_* R_* \eta T_0 [1 - ka_w (a_w + 2)]}{R_* 2a_w (1 - ka_w)} \frac{\omega}{2} (1 - 2F_{\text{cra}}). \quad (7)$$

2. Constant current anemometer. ($i = \text{const}$). Similarly, after transformations we obtain an equation connecting voltage deviations with the mass flux and total temperature at a constant current through the probe:

$$\begin{aligned} \frac{\Delta e}{e} + C_w \frac{(a_w + 1)}{\pi \lambda_0 (A + B\sqrt{\text{Re}}) [1 - ka_w (a_w + 2)]} \frac{d}{dt} \left(\frac{\Delta e}{e} \right) = \\ = - \frac{a_w (1 - ka_w)}{1 - ka_w (a_w + 2)} \left\{ \left[\frac{B\sqrt{\text{Re}}}{2(A+B\sqrt{\text{Re}})} - \frac{ka_w}{1-ka_w} \frac{\partial \ln k}{\partial \ln \text{Re}} \right] \frac{\Delta m}{m} + \right. \\ \left. + \left[\omega \left(1 - \frac{B\sqrt{\text{Re}}}{2(A+B\sqrt{\text{Re}})} + \frac{ka_w}{1-ka_w} \frac{\partial \ln k}{\partial \ln \text{Re}} \right) - \frac{\alpha_* R_* \eta T_0 [1 - ka_w (a_w + 2)]}{R_* a_w (1 - ka_w)} \right] \frac{\Delta T_0}{T_0} \right\} \end{aligned}$$

or
$$\frac{\Delta e}{e} + \tau \frac{d}{dt} \left(\frac{\Delta e}{e} \right) = F_{\text{cca}} \frac{\Delta m}{m} - G_{\text{cca}} \frac{\Delta T_0}{T_0}, \quad (8)$$

where
$$F_{cca} = \frac{a_w(1-ka_w)}{1-ka_w(a_w+2)} \left(\frac{B\sqrt{Re}}{2(A+B\sqrt{Re})} - \frac{ka_w}{1-ka_w} \frac{\partial \ln k}{\partial \ln Re} \right) \quad (9)$$

$$G_{cca} = \frac{\alpha_w R_s \eta T_0}{R_s} - \frac{\alpha_w a_w(1-ka_w)}{1-ka_w(a_w+2)} \left(1 - \frac{B\sqrt{Re}}{2(A+B\sqrt{Re})} + \frac{ka_w}{1-ka_w} \frac{\partial \ln k}{\partial \ln Re} \right) \quad (10)$$

$$\tau_{cca} = \frac{C_w(a_w+1)}{\pi \lambda_0 (A+B\sqrt{Re}) [1-ka_w(a_w+2)]} \quad (11)$$

Since the total probe thermal capacity is determined by the expression $C_w (\pi^2/4) l \rho_w c_w$, where ρ_w , c_w are the density and specific thermal capacity of the wire material, the dependence of the time constant on the overheating coefficient can be written as

$$\tau_{cca} = \tau_0 \frac{(a_w+1)}{1-ka_w(a_w+2)} \quad (12)$$

where
$$\tau_0 = \frac{\rho_w c_w d^2}{4 \lambda_0 Nu} \quad (13)$$

3. *Constant voltage anemometer*, ($e = \text{const}$). The voltage E_{out} is a measure of flow fluctuations at constant voltage across the probe (see Fig 1). Since $E_{out} = R \cdot i_1$ and $R = \text{const}$, fluctuations of E_{out} are determined by fluctuations of the current i_1 , which are equal to fluctuations of a current through the probe, because of the current $i = \text{const}$. Therefore, it is necessary to determine how changes of current i_1 depend on flow fluctuations in this case.

After transformations similar to the first two cases we obtain:

$$\begin{aligned} & \frac{\Delta i}{i} + C_w \frac{(a_w+1)}{\pi \lambda_0 (A+B\sqrt{Re}) [1+2a_w-2ka_w-3ka_w^2]} \frac{d}{dt} \left(\frac{\Delta i}{i} \right) = \\ & = \frac{a_w(1-ka_w)}{1+2a_w-2ka_w-3ka_w^2} \left\{ \left[\frac{B\sqrt{Re}}{2(A+B\sqrt{Re})} - \frac{ka_w}{1-ka_w} \frac{\partial \ln k}{\partial \ln Re} \right] \frac{\Delta m}{m} + \right. \\ & \left. + \left[\omega \left(1 - \frac{B\sqrt{Re}}{2(A+B\sqrt{Re})} + \frac{ka_w}{1-ka_w} \frac{\partial \ln k}{\partial \ln Re} \right) - \frac{\alpha_w R_s \eta T_0 [1-ka_w(a_w+2)]}{R_s a_w(1-ka_w)} \right] \frac{\Delta T_0}{T_0} \right\} \end{aligned}$$

or
$$\frac{\Delta i}{i} + \tau \frac{d}{dt} \left(\frac{\Delta i}{i} \right) = F_{cva} \frac{\Delta m}{m} - G_{cva} \frac{\Delta T_0}{T_0} \quad (14)$$

where
$$F_{cva} = \frac{a_w(1-ka_w)}{1+2a_w-2ka_w-3ka_w^2} \left(\frac{B\sqrt{Re}}{2(A+B\sqrt{Re})} - \frac{ka_w}{1-ka_w} \frac{\partial \ln k}{\partial \ln Re} \right) \quad (15)$$

$$G_{cva} = \frac{1-ka_w(a_w+2)}{1+2a_w-2ka_w-3ka_w^2} \frac{\alpha_w R_s \eta T_0}{R_s} \quad (16)$$

$$\tau_{cva} = \tau_0 \frac{(a_w+1)}{1+2a_w-2ka_w-3ka_w^2} \quad (17)$$

Comparing (6), (7) and (9), (10); (15), (16), we obtain:

$$F_{cca} = \varphi F_{cta}, \quad G_{cca} = \varphi G_{cta} \quad (18)$$

$$F_{cva} = \psi F_{cta}, \quad G_{cva} = \psi G_{cta} \quad (19)$$

where
$$\varphi = \frac{2a_w(1-ka_w)}{1-ka_w(a_w+2)}, \quad (20)$$

$$\psi = \frac{2a_w(1-ka_w)}{1+2a_w-2ka_w-3ka_w^2}. \quad (21)$$

Taking into account Eqs (9), (12) and (18), it is possible to rewrite the last expressions in a more compact form:

$$G_{cca} = \frac{\alpha_w R_w \eta T_0}{\varphi R_s} - \frac{\omega}{2} (1 - 2F_{cca}), \quad (22)$$

$$G_{cca} = \frac{\alpha_w R_w \eta T_0}{R_s} - \frac{\omega}{2} (\varphi - 2F_{cca}), \quad (23)$$

$$G_{cva} = \frac{\psi \alpha_w R_w \eta T_0}{\varphi R_s} - \frac{\omega}{2} (\psi - 2F_{cva}). \quad (24)$$

The sensitivity coefficients F, G for different types of anemometers systems are shown in Fig. 2 as functions of the overheating coefficient.

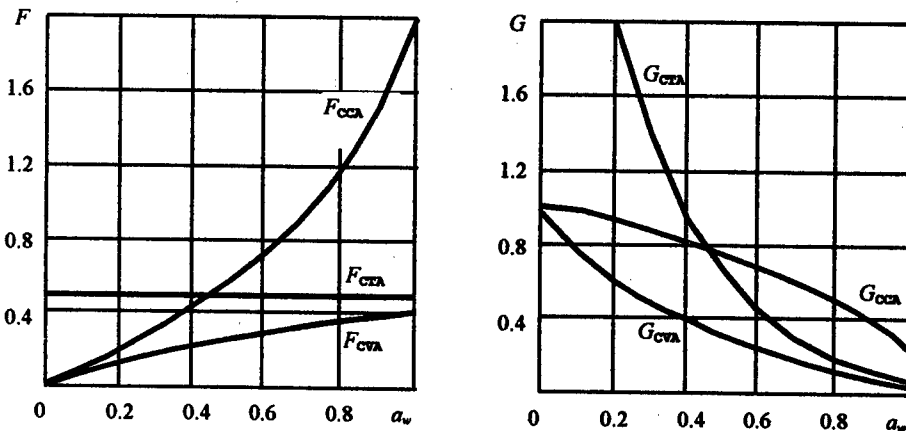


Fig. 2

As is clear from these plots, the CVA sensitivity coefficients to the mass flux and total temperature have the smallest values at any overheatings.

2. Probe Sensitivity to Mechanical and Aerodynamical Loading

The main idea of any hot wire/film anemometer is based on the change of resistance of a thin sensor under the flow action. Therefore, it is important to reduce or eliminate influences which can also cause a change of the probe resistance, for example, the strain gage effect due to vibration of prongs resulting in vibration of the wire which can vibrate themselves. The frequencies of prong and wire vibrations can be estimated by relationship proposed in [4]:

$$f_i = \frac{\nu_i^2}{8\pi} \sqrt{\frac{E_w d}{\rho_w l^2}}, \quad (25)$$

where E_w, ρ_w are the elasticity modulus and density of a wire or a prong; ν is the coefficient of harmonics:

$$\nu_i = \frac{2(i+1) \pm 1}{2} \pi, \quad i > 1.$$

The values $\nu_0 = 4.73$, $\nu_1 = 7.85$ and (+) correspond to wires, and $\nu_0 = 1.875$, $\nu_1 = 4.694$ and (-) correspond to prongs.

It is easy to estimate that frequencies of vibrations for a typical hot-wire probe (6 microns, 1,5 mm length tungsten wires supported with steel prongs 0,4 mm in diameter and 5 mm length) are $f_1 = 16$ kHz, $f_2 = 44$ kHz for the wire, and $f_1 = 11,2$ kHz, $f_2 = 75$ kHz for the prongs. These values correspond to frequencies for typical flow fluctuation range, therefore a possibility exists that a distortion of spectrum of the hot-wire output can take place and errors can appear.

There are some ways for the transformation of vibrations into electrical signal, therefore various can be ways to avoid or reduce vibrations. Strain gage effect is, of course, the main source of false signals. A small deflection h of a wire, about 20 % of its length l , is an effective way to avoid or, at least, reduce the strain gage effect, see Fig.3 where the dependence of the total RMS anemometer output on wire deflection is shown [5].

The place of joining of the wire (platinum, tungsten) with prongs (steel, nickel) is represented as a thermocouple, whose electromotive force (EMF) depends not only on materials of the junction and temperature difference, but also on other conditions, there are mechanical stresses and microstructure of the junction among those.

The preliminary deflection does not eliminate this kind of interference completely. It is necessary to select appropriate wire and prong materials so that to reduce the thermocouple effect. The combination of "tungsten - nickel" is more "noisy" comparing with "tungsten - stainless steel".

It is possible to supplement the expression for fluctuations of electrical voltage across the hot-wire probe, see, for example (5), by two terms:

$$\frac{de}{e} = \pm \left(F \frac{dm}{m} - G \frac{dT_0}{T_0} \mp H \frac{dl}{l} + \frac{d\varepsilon}{e} \right), \quad (26)$$

where H is the probe strain gage sensitivity; ε is the EMF arising at the probe.

To estimate the contribution of additional terms in Eq. 26 to the hot-wire output, let us determine the value of H .

The change of wire resistance due to strain gage effect corresponds to the change of wire length as [6]

$$\frac{dR}{R} = (1 + 2\mu) \frac{dl}{l}; \quad (27)$$

To find the sensitivity coefficients to strain gage stresses, it is necessary to differentiate Eq.1 with constant m and T_0 , taking into account that the wire temperature T_w changes for all types of anemometer (CTA, CCA, CVA) due to strain gage effect.

If the current is constant, the sensitivity is

$$H_{cca} = 1 + 2\mu + \frac{\varphi}{2} \left(2 + \frac{B\sqrt{Re}}{2(A + B\sqrt{Re})} \right) \mu, \quad (28)$$

here μ is the Poisson coefficient. (For tungsten $\mu = 0,29$.)

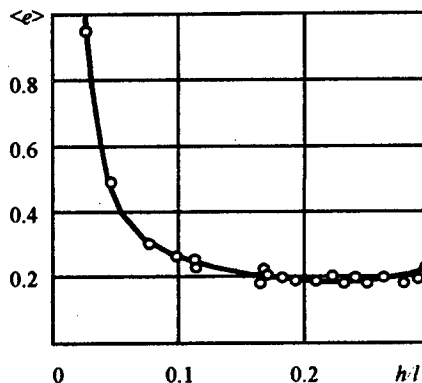


Fig. 3.

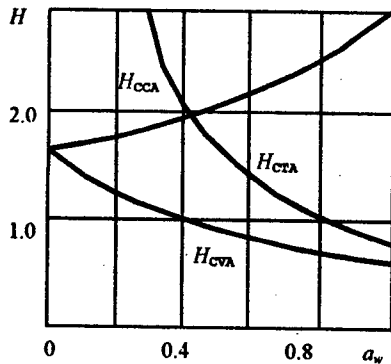


Fig. 4

For CVA:

$$H_{CVA} = 1 + 2\mu - \frac{\psi}{2} \left[2 + \left(2 - \frac{B\sqrt{Re}}{2(A+B\sqrt{Re})} \right) \mu \right] \quad (29)$$

And for CTA:

$$H_{CTA} = \frac{1-2ka_w}{1-ka_w} \frac{a_w+1}{2a_w} (1+2\mu) - \frac{1}{2} + \frac{\mu}{4} \frac{B\sqrt{Re}}{A+B\sqrt{Re}} \quad (30)$$

The calculated values of H_{CTA} , H_{CCA} , H_{CVA} for typical probes are shown in Fig.4. As it is clear from the figure, the CVA has the least sensitivity to strain gage at all overheatings and $H_{CTA} > H_{CCA}$ at small overheatings, while $H_{CTA} < H_{CCA}$ at high overheatings.

3. Frequency Response of the Hot-Wire Probes

A decrease of the probe signal amplitude against frequency due to the wire lag is determined by the relation

$$N = \varepsilon_f / \varepsilon_{f \rightarrow 0} = \left(\sqrt{1 + (2\pi f \tau)^2} \right)^{-1} \quad (31)$$

Therefore, the probe frequency range can be determined as $f = (2\pi\tau)^{-1}$, where τ depends both on probe overheating and on anemometer type (see Eqs.12 and 17). It is clear that the difference of frequency ranges for minimum overheatings is not significant due to small τ difference. (The constant temperature anemometer is not used at minimum overheatings.) At high overheatings $\tau_{CTA} \ll \tau_{CCA}$, τ_{CVA} , and advantages of the CTA are indisputable, however the CCA can be improved considerably using the compensation circuits. An advantage of the CVA is a possibility of some expansion of the frequency range (as comparing to the CCA) without any compensation circuits.

CONCLUSIONS

The constant voltage anemometer has the worst values of sensitivity coefficients to mass flux and total temperature at any overheatings. The constant voltage anemometer had the lowest sensitivity coefficients to strain gage effect at all overheatings. However mutual ratios of the same name sensitivity coefficients (F/G , F/H , G/H) do not depend on the type of anemometer.

The CVA frequency band is the intermediate one between those for the CTA (at the highest overheatings) and CCA (without compensation). However, the CCA frequency range can be improved by using the compensation circuits.

This work is carried out in the frame of Project № 98-01-00723 supported by the Russian Foundation for Basic Research.

REFERENCES

1. Mangalam S.M., Sarma G.R., Kuppa S., Kubendran L.R. A New Approach to High-Speed Flow Measurements Using Constant Voltage Anemometry, AIAA 92-3957: AIAA 17th Aerospace Ground Testing Conf., 1992.
2. Lebiga V.A. Turbulence Measurement in Compressible Flows // Methods and Technique of Aerophysical Investigations. - Novosibirsk: ITAM. - 1978. - P. 44-56. (In Russian.)
3. Kovaszny L.S.G. The Hot-Wire Anemometer in Supersonic Flow // J.A.S.-1950. - Vol.17.-N 9.
4. Timoshenko S.P. Oscillations in Engineering. - Moscow: Fizmatgiz, 1967. (In Russian.)
5. Lebiga V.A. Peculiarities of Hot-Wire Application in Supersonic Flows // Experimental Methods and Apparatuses for Turbulence Study. - Novosibirsk: ITAM, 1976. (In Russian.)
6. Preobrazhensky V.P. Heat Power Measurements and Devices. Moscow: Energiya, 1978. (In Russian.)

COMBINED STUDY OF MECHANISMS OF EVOLUTION AND BREAKDOWN OF COHERENT STRUCTURES IN TRANSITIONAL BOUNDARY LAYER AT CONTROLLED CONDITIONS

C.B. Lee¹, X.D. Du², Q.X. Lian³, V.I. Borodulin⁴, V.R. Gaponenko⁴, Y.S. Kachanov⁴

1) Institute of Atmospheric Physics, Chinese Academy of Sciences, Beijing, China

2) Peking University, Beijing, China

3) Beijing University of Aeronautics and Astronautics, Beijing, China

4) Institute of Theoretical and Applied Mechanics, Novosibirsk, Russia

1. INTRODUCTION

The paper is devoted to an experimental study of late nonlinear stages of the laminar-turbulent transition in the Blasius boundary layer by means of the hydrogen-bubble flow visualization, the hot-film anemometry, and the laser-Doppler velocimetry (LDV). The processes of development and breakdown of the coherent structures, formed in the transitional flow, are investigated under controlled experimental conditions.

It was shown in previous studies that at nonlinear stages of the transition the Λ -structures are formed which consists mainly of the Λ -vortex [1] and the Λ -shaped layer of a high share of the streamwise component of the flow velocity [2]. Further downstream, in a vicinity of the Λ -vortex tip it is observed an appearance of some very intensive localized velocity fluctuations called the "spikes" [3] which represent themselves another kind of the coherent structures, called the CS-solitons [4-7]. In space the appearance of the "developed" spikes corresponds to formation of ring-like vortices [8,9]. Originally this sequence of events was observed only in the so-called K -regime of transition. However, it was shown later in [10] that a very similar behaviour of the coherent structures (starting with the stage of appearance of the Λ -vortices) is observed in the other known regime of transition — in the N -regime (see for review [8]). It was also found [8,11,12] that this scenario of development of the coherent structures is very similar to that observed in the developed turbulent boundary layer and, consequently, this scenario represents a rather universal mechanism of the turbulence production.

A number of very important questions, however, are still not clear in this scenario and need additional study. The present experiment was carried out in order to clarify some of these questions.

2. EXPERIMENTAL PROCEDURE AND BASIC-FLOW STRUCTURE

2.1. Experimental procedure. The experiments were conducted in the boundary layer on a flat plate in a low-turbulence water-channel of the State Key Laboratory for Turbulent Research of Peking University at the free-stream velocity $U_0 = 16.8$ cm/s and the turbulence level about 0.06%. A sketch of the measurements is shown in Fig. 1. The plate was mounted vertically in the test-section of the channel under the zero angle of attack. It had a flap that gave possibility to control the position of the attachment line at the plate nose.

The instability waves, having controlled frequency and spanwise-wavenumber spectrum, were excited in the flat-plate boundary layer by means of a new generator (see Fig. 1) created on a basis of a slit source designed in [13] and used later in different air flows (for example in [10]). The source was positioned at a distance $x = x_s = 200$ mm from the plate leading edge. It represented an insert in a form of a parallelepiped mounted flush with the plate wall. The inner volume of the insert was separated into several chambers by means of a semi-permeable baffles. With the help of the plastic pipes the chambers were connected to loudspeakers which produced the pressure fluctuations inside the chambers. In the cover of the insert (from the working side of the plate) a narrow slit was made which provided a communication of the fluid in the chamber and in the boundary layer. The signals of the loudspeakers were harmonic in time and generated by a computer with the help of an analog-to-digital converter and a power amplifier. During the experiment the parameters of the source were varied and optimized in order to obtain some required regimes of the disturbance generation (see below).

The main studies of the flow structures were performed by means of the hydrogen-bubble visualization technique. The bubbles were introduced into the flow with the help of a thing

tungsten wire (about 40 microns in diameter) positioned in the boundary layer at various distances from the wall and from the disturbance source. The flow patterns were documented by means of a CCD video-camera and a high-speed cinecamera. The hot-film anemometer was used for measurements of the streamwise component of the mean flow velocity and the velocity fluctuations inside the boundary layer. The LDV system was employed for measurements of the mean-velocity distributions outside the boundary layer. The LDV was used also for the hot-film probe calibration.

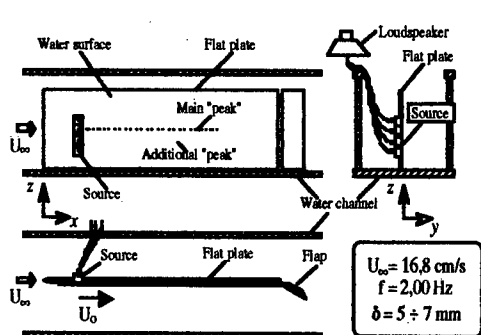


Fig. 1. Sketch of water channel, experimental model, and disturbance source

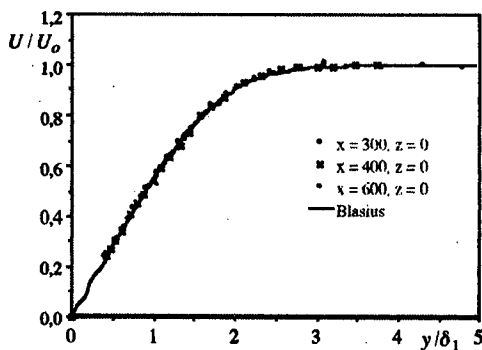


Fig. 2. Mean velocity profiles without excitation.

2.2. Basic-flow structure. The measurements performed in the free stream had shown that the mean flow velocity over the plate was independent of the spatial coordinates with a high accuracy, i.e. the potential flow was 2D and had a zero pressure gradient.

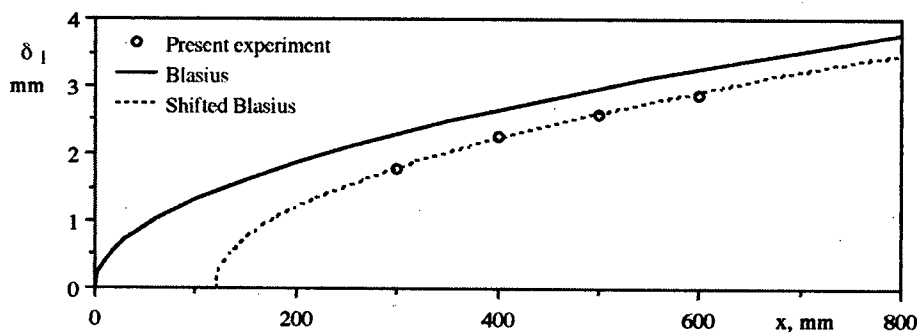


Fig. 3. Boundary-layer displacement thickness versus streamwise coordinate without excitation.

Shown in Fig. 2 are the mean velocity profiles measured by the hot-film at several downstream distances in the absence of the disturbance excitation and presented in the non-dimensional coordinates, where δ_1 is the boundary-layer displacement thickness. The theoretical Blasius profile is also shown in Fig. 2 for comparison. It is seen that under the conditions of the present experiment the flow corresponds with a high accuracy to the Blasius boundary layer. The streamwise distributions of δ_1 (Fig. 3) corroborates this conclusion. The experimental distribution agree very well with the theoretical one if to take into account a virtual position of the plate leading edge displaced downstream by $\Delta x = 120$ mm.

2.3. Regime of main measurements. The main regime of the disturbance excitation was chosen in a way that it would be close to the regimes studied in the previous experiments in air (see for instance [4,5]). The primary instability wave generated by the source was almost two-dimensional, harmonic in time, and weakly modulated in the spanwise direction. The frequency of excitation was 2.0 Hz and the initial amplitude of the instability wave was about 2% in the first streamwise position studied $x = 250$ mm ($x - x_s = 50$ mm). As a result, the transition scenario observed in the boundary layer corresponded to the K-regime of breakdown.

In vicinities of the local (in span) maxima of the disturbance amplitude (the so-called 'peak' positions [3]) a formation of the Λ -structures was observed as usually. Their subsequent development, an appearance of new structures, and a beginning of the flow randomization were studied in detail by means of the hydrogen-bubble flow visualization.

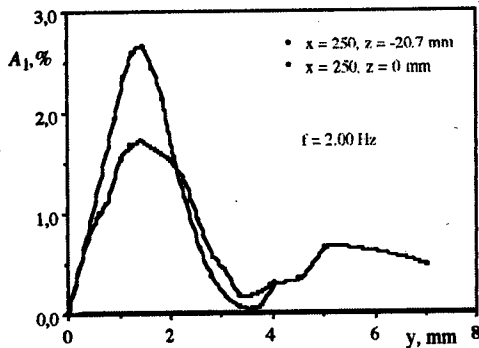


Fig. 4. Amplitude profiles for fundamental mode at "initial" downstream position.

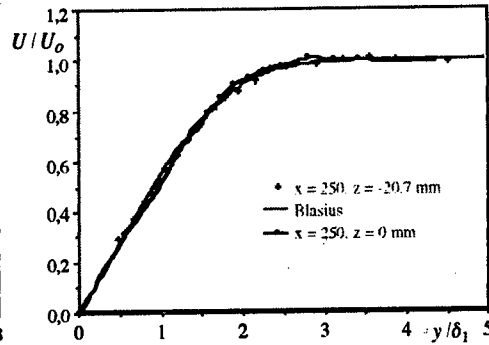


Fig. 5. Mean velocity profiles measured at "initial" downstream position in presence of excitation.

3. MAIN RESULTS OF STUDY

3.1. Flow in "initial" section. Shown in Fig. 4 are the normal-to-wall profiles of the fundamental wave amplitude measured by the hot-film anemometer at in an "initial" downstream section ($x = 250$ mm) in the peak position ($z = 0$) and outside of it ($z = -20.7$ mm). In the "initial" section the disturbances are almost harmonic in time and weakly disturbed by the second and third frequency harmonics. The profiles have a shape typical for a nearly two-dimensional linear Tollmien-Schlichting wave. However, the disturbance amplitude is already so large here (about 2.7% at $z = 0$) that the non-linearity is quite significant. In particular, the presence of the perturbations results in a distortion of the mean velocity profile in the vicinity of the peak position (Fig. 5). Although outside of this region the mean velocity profiles remain in the "initial" section very close to the Blasius one (Fig. 5) despite the disturbance amplitude is also rather large here (about 1.7%). The spatial distributions of the mean and instantaneous flow velocities, the shape of the time-traces, and the disturbance amplitudes and phases were studied in detail for the K -regime of breakdown in previous experiments (see for instance [14,15]). In the present study the main attention was concentrated on the flow visualization.

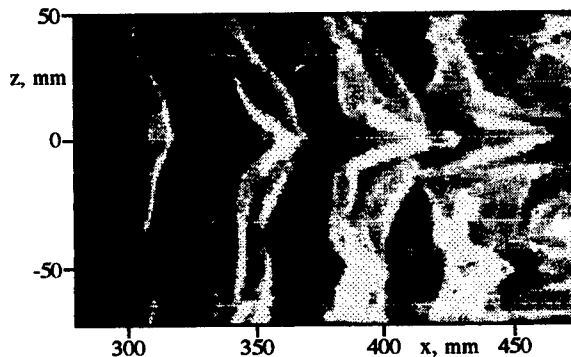


Fig. 6. Formation of Λ -structures from initial quasi-2D instability wave.

3.2. Formation of Λ -structures. The initial stage of the disturbance development is characterized by a process of formation of the Λ -structures typical for the boundary layer-transition at all and for the K -regime in particular. This process is illustrated in Fig. 6 obtained by means of the flow visualization in the (x, z) -plane with the cathode-wire positioned parallel to

the wall at $x = x_w = 250$ mm and $y = y_w = 1.0$ mm. The picture demonstrates visually the process of an appearance of the Λ -structures from the primary (almost two-dimensional) instability wave. The light regions correspond to the places of concentration of the hydrogen bubbles which are accumulated (at the initial stages) mainly inside the nonlinear critical layer visualizing the instability wave front that starts to warp (see for example [16]).

3.3. Appearance of ring-like vortices. In the present experiment a process of multiple (at least $7 \div 8$ times or more) reconnection of the Λ -vortex "legs" in a vicinity of its tip was clearly observed and documented for the first time. It is found that this process results in formation of a series of ring-like vortices with a new eigen spatial (and temporal) scale that is very close to a characteristic local scale of the boundary layer, i.e. to δ_1 . The whole process is very visually seen in the video film that will be shown at the conference during the talk.

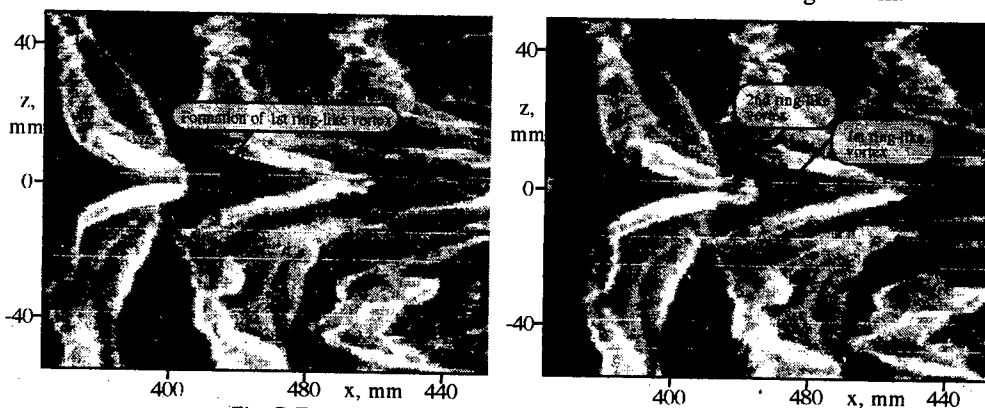


Fig. 7. Formation of first (a) and second (b) ring-like vortex.

The beginning of formation of the ring-like vortices (appearance of the first 2 vortices) is illustrated in Fig. 7. The pictures are obtained at two consecutive time moments with the cathode-wire positioned parallel to the wall at $x_w = 250$ mm and $y_w = 1.0$ mm. The appearance of the first and second vortices is very well seen in Fig. 7a and 7b respectively. The ring-like vortices displace very quickly towards the external edge of the boundary layer and represent very stable formations (the coherent structures), called in [5] CS-solitons (see also introduction). At the same time, it is necessary to note that in the previous studies the spatial shape of the ring-like vortices was observed only in the results of the direct numerical simulation obtained in the Stuttgart-University group, meanwhile in experiment an information about them was obtained in the peak plane only (at $z = 0$) where a pair of contra-rotating vortices (corresponded to a section of the ring-like vortices by this plane) was observed.

It is found in the present experiments that the process of quasi-periodic reconnection of the Λ -vortex "legs" continues for a rather long time. The first ring-like vortices start to appear in the region $x \approx 450$ mm and their generation proceeds almost to the end of the region studied (at least up to $x = 650$ mm), i.e. for a more than 100 boundary-layer displacement thicknesses.

3.4. Appearance of steady streamwise structures. Another very interesting phenomenon detected and investigated in the present experiment is a process of formation of a system of steady streamwise structures. This process is displayed in a deep stationary modulation of the streamwise component of the flow velocity observed near the wall at late stages of development of the Λ -vortices. The formation of the steady streamwise structures is illustrated in Fig. 8a obtained with the cathode-wire positioned at $x_w = 350$ mm and $y_w = 0.5$ mm. The structures appear in a vicinity of the peak position ($z = 0$) but, in contrast to the ring-like vortices, they are formed very near the wall. On the flow visualization pictures the structures are displayed as a very narrow strip of a low-speed fluid in the peak position with a high concentration of the hydrogen bubbles. At the sides of this strip two wide streaks of a high-speed fluid are formed with a rather low concentration of the bubbles (Fig. 8a). Farther from the peak position the flow velocity decreases again and the concentration of the bubbles increases. These structures are weakly modulated in time with the fundamental frequency.

Formation of very similar vortices was found at late stages of the K -regime of transition in some DNS calculations of the Stuttgart group. The steady streamwise structures found in the

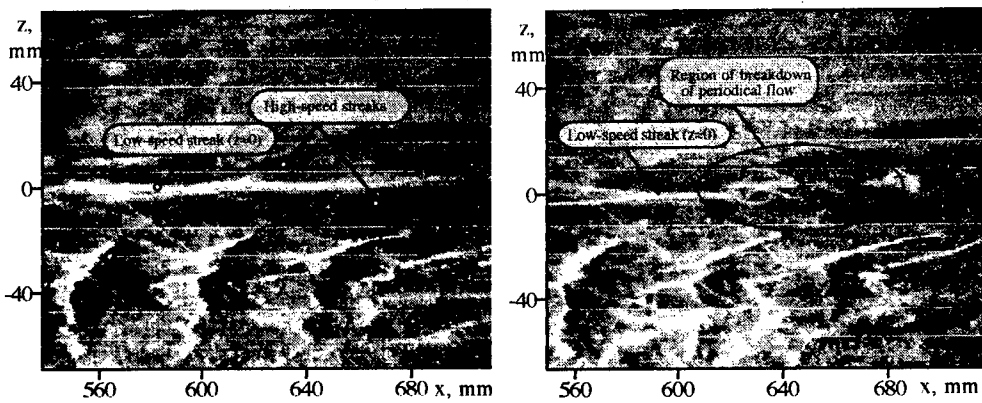


Fig. 8. Appearance of streaky structures in near-wall region (a) and beginning of their breakdown (b).

present experiment look also very similar to the 'streaky structures' investigated in previous experiments devoted to the 'bypass' transition at high levels of the free-stream turbulence (see for example [17,18]). At the same time, these structures have never been observed in the two known "normal" regimes of the boundary-layer transition, neither in the K -regime nor in the N -regime. The observation of formation of the near-wall streaky structures at late stages of the K -regime of transition is an additional evidence of a similarity between the physical mechanisms of the turbulence production in different transitional boundary layers, as well as between these mechanisms in the transitional and the developed turbulent near-wall flows. [In the turbulent boundary layers the streamwise streaky structures are also observed in the near-wall region in numerous experiments, as well as in the direct numerical simulations.]

3.5. Beginning of the flow randomization. The visualization gives possibility to obtain a very important additional information about the ways of breakdown of the periodic stationary structures occurred at final stages of the K -regime of transition. In the previous studies several possible mechanisms of amplification of some non-periodic (i.e. non-coherent with the primary instability wave) perturbations were suggested. In particular: (a) a breakdown of the Ω -vortices [1] found in a vicinity of the Λ -vortex tip; (b) a local "secondary" instability of the high-shear layer leading to formation and "multiplication" of the spikes [3]; (c) a "secondary" instability of the Λ -vortex "legs" [19], (d) a low-frequency breakdown of the deterministic flow in a near-wall region at the peak position under the Λ -vortex [14], and (e) a growth of low-frequency background perturbations with a continuous frequency spectrum due to their resonant interaction with the deterministic disturbances [20]. In the present experiment it is clearly shown that the mechanisms (a), (b), and (c) are not observed in the transition studied. The Λ -structures are found to develop downstream in a deterministic way. During this development in the near-wall region they are transformed into a system of streamwise quasi-stationary structures, while in the outer part of the boundary layer they produce a series of the ring-like vortices associated with the CS -solitons. The Ω -vortex, described in [1], represents just an initial stage of formation of the first CS -soliton after which the second, third, and others appear in a similar way due to a multiple reconnection of the Λ -vortex "legs". All ring-like vortices are very stable and conserve their main properties until very late stages of the transition process, including the stages of formation of the developed turbulent flow.

In the present experiments a growth of non-periodic perturbations was found at rather late stages in the near-wall region at the peak position under the CS -solitons. This fact is illustrated in Fig. 8b that was obtained at the same conditions as Fig. 8a but at another time moment. First non-periodic perturbations look like waves which are *asymmetric* with respect to the plane of symmetry of the Λ -structure and have a characteristic streamwise scale close to a streamwise distance between the ring-like vortices. These perturbations appear in a low-speed fluid streak (around $z = 0$) and are amplified with portions in an intermittent way. Such intermittent character of these disturbances testifies, most probably, to their origin from some

background perturbations of the water channel. The visualized non-periodic disturbances have a shape of meanders or spirals (Fig. 8a). These observations are in consistence with the results of experiments [14] (way (d) of the randomization) and provide an additional information on the mechanisms of the turbulence production at late stages of the transition.

Conclusions

Thus, the results obtained in the present experimental study help to advance significantly in understanding the physical mechanisms of the turbulence production at late nonlinear stages of the laminar-turbulent transition and testify to a similarity of these mechanisms in different regimes of the transition, as well as in the developed turbulent boundary layer.

This study was supported by the Russian Foundation for Basic Research (Grant No 96-01-00001c) and Chinese Natural Science Foundation."

References

1. Hama F.R., Nutant J. Detailed flow-field observations in the transition process in a thick boundary layer // Proc. 1963 Heat Transfer & Fluid Mech. Inst. - Palo Alto, Calif.: Stanford Univ. Press, 1963, P. 77-93.
2. Kovasznay L.S., Komoda H., Vasudeva B.R. 1962. Detailed flow field in transition // Proc. 1963 Heat Transfer & Fluid Mech. Inst. - Palo Alto, Calif.: Stanford Univ. Press, 1963, P. 1-26.
3. Klebanoff P.S., Tidstrom K.D., Sargent L.M. The three-dimensional nature of boundary-layer instability // J. Fluid Mech. - 1962. - Vol. 12. - P.1-34.
4. Borodulin, V.I. & Kachanov, Y.S. Role of the mechanism of local secondary instability in K-breakdown of boundary layer // Izv. Sib. Otd. Akad. Nauk SSSR, Ser. Tekh. Nauk. - 1988. - Vol. 5, No 18. - P. 65-77.
5. Borodulin V.I., Kachanov Y.S. Experimental study of soliton-like coherent structures in boundary layer // Proceedings of Scientific & Methodological Seminar on Ship Hydrodynamics, 19th Session. Vol. 2. - Varna: Bulgarian Ship Hydrodyn. Center, 1990, P. 99-1 - 99-10.
6. Kachanov Y.S., Ryzhov O.S., Smith F.T. Formation of solitons in transitional boundary layers: theory and experiments // J. Fluid Mech. - 1993. - Vol. 251. - P. 273-297.
7. Lee C.B., Lian Q.X. Combined CS-solitons, CS-solitons and wave resonant concept // IUTAM Symp. on Nonlinear Instability and Transition in Three-Dimensional Boundary Layers / P.W. Duck & P. Hall. - Dordrecht: Kluwer, 1995.
8. Kachanov Y.S. Physical mechanisms of laminar-boundary-layer transition // Annu. Rev. Fluid Mech. - 1994. Vol. 26. - P. 411-482.
9. Rist U., Kachanov Y.S. Numerical and experimental investigation of the K-regime of boundary-layer transition // Laminar-Turbulent Transition / R. Kobayashi - Berlin: Springer, 1995, P. 405-412.
10. Bake S., Kachanov Y.S., Fernholz H.H. Subharmonic K-regime of boundary-layer breakdown // Transitional Boundary Layers in Aeronautics. - Amsterdam: North-Holland, 1996, P. 81-88.
11. Blackwelder R.F. Analogies between transitional and turbulent boundary layers // Phys. Fluids. - 1983. - Vol. 26, N 10. - P. 2807-2815.
12. Lian Q.X. A visual study of the coherent structure of the turbulent boundary layer in flow with adverse pressure gradient // J. Fluid Mech. - 1990. - Vol. 215. - P. 101-214.
13. Gaponenko V.R., Kachanov Y.S. New method of generation of controlled spectrum instability waves in the boundary layer // Proc. of Int. Conference on Methods of Aerophysical Research. Part 1. - Novosibirsk: Inst. Theor. & Appl. Mech., 1994, P. 90-97.
14. Kachanov Y.S., Kozlov V.V., Levchenko V.Y., Ramazanov M.P. The nature of K-breakdown of laminar boundary layer // Proc. Siberian Div. USSR Acad. Sci., Ser. Tech. Sci. - 1989. - No 2. - P. 124-158
15. Borodulin V.I., Kachanov Y.S. Formation and development of coherent structures in transitional boundary layer // Applied Mechanics & Technical Physics. - 1995. - Vol. 36, No 4. - P. 60-97.
16. Rist U., Fasel H. Direct numerical simulation of controlled transition in a flat-plate boundary layer // J. Fluid Mech. - 1995. - Vol. 298. - P. 211-248.
17. Kendall J.M. Experimental study of disturbances produced in a pre-transitional laminar boundary layer by weak freestream turbulence // AIAA Paper 85-1695, 1985.
18. Gulyaev A.N., Kozlov V.E., Kuznetsov V.R., Mineev B.I., Sekundov A.N. Interaction of a laminar boundary layer with external turbulence // Fluid Dyn. - 1990. - Vol. 24, N 5. - P. 700-710.
19. Knapp, C.F., Roache, P.J. A combined visual and hot-wire anemometer investigation of boundary-layer transition // AIAA J. - 1968. - Vol. - 6. - P. 29-36.
20. Dryganets S.V., Kachanov Y.S., Levchenko V.Y., Ramazanov M.P. Resonant flow randomization in K-regime of boundary layer transition // Zhurnal Prikladnoy Mekhaniki i Tekhnicheskoy Fiziki. - 1990. - No 2. - P. 83-94.

AN EXPERIMENTAL STUDY OF HYPERSONIC FLOW STABILITY

A.A.Maslov

Institute of Theoretical and Applied Mechanics SB RAS,
630090, Novosibirsk, Russia

INTRODUCTION

The studies of stability of hypersonic flows attract researchers' attention primarily in connection with creation of hypersonic flying vehicles. Along with applied interest, these studies have a fundamental significance because they are directly related to the problem of turbulence origin. The wave processes that change the flow regimes at hypersonic speeds are much more versatile than for sub- and supersonic speeds. In fact, all characteristic features of sub- and supersonic instability are inherent in hypersonic flows, along with specific phenomena typical of only hypersonic flows. There are few experimental studies of instability at high Mach numbers, probably, because they are complicated and expensive.

In the present review we deal with the study of stability of boundary layers. The major work in this direction has been performed in the USA. The research has been conducted for more than three decades. The latest achievements are published in [1,2]. Recently the first experiments have been performed in Germany and in Russia [3,4]. The evolution of natural disturbances has been studied in all these works, i.e., the disturbances arising in the boundary layer without any interference of the researcher.

More informative is the simulation of unsteady wave processes using artificially introduced disturbances. A point source is often used to generate the disturbances. This source introduces a wave packet of specified frequency into the boundary layer. Such a packet (which is commonly called a wave train) consists of many inclined waves. The development of this wave train in the boundary layer is usually registered by a hot-wire anemometer. As a result, three-dimensional distributions of pulsations are obtained, which are decomposed into a Fourier series. The resultant wave spectra are used for stability analysis. This approach is frequently used at ITAM SB RAS for sub- and supersonic velocities [5,6].

Let us consider in more detail the prospects of instability simulation at hypersonic flow speeds.

STABILITY OF HYPERSONIC BOUNDARY LAYER

Flat plate. The first successful application of wave trains for the study of linear stability of the boundary layer on a flat plate for $M=6$ is presented in [7,8]. The measurements were taken in the hypersonic wind tunnel T-326 of ITAM SB RAS. These measurements did not reveal any unexpected results. The hot-wire measurements of eigenfunctions of the mass flow fluctuations showed that the main portion of fluctuations is concentrated near the outer edge of the boundary layer. Besides, the eigenfunctions of artificial disturbances coincided with the measurements of natural disturbances. The phase velocity was determined from the phase measurements; it turned out to be $C=0.85$, which was in good agreement with theoretical concepts. The measurements were taken only for low-frequency disturbances of the first mode,

and a comprehensive spectral analysis of these results could not be performed because of a large wavelength of these disturbances.

The first studied revealed also the difficulties related to this approach. Firstly, it is difficult to organize a point source of artificial disturbances. Because of low static pressure, a spark electric discharge transforms into a glow discharge and occupies an extended region. Some difficulties are also involved by modeling of high-frequency (hundreds of kHz) disturbances, whereas they are of special interest because they determine the second, most unstable mode in a hypersonic boundary layer.

Cone with a flare. Artificial disturbances were more successfully used to study the boundary layer stability on a cone model with a flare, also for $M=6$ in the same wind tunnel T-326 [9]. Prior to experiments, the mean flow was carefully studied, the separation region was determined, the development of natural disturbances in the boundary layer in the separation region was examined, and the eigenfunctions and pulsation spectra were obtained. It was shown that the main fluctuations are concentrated in a narrow region near the upper edge of the boundary layer. From the changes in disturbance spectra downstream, three typical regions (low-frequency, medium-frequency and high-frequency ones) are identified. Low-frequency disturbances in the separation region increase slowly (by approximately 1.5 times). Disturbances in the medium-frequency region are neutral. High-frequency pulsations in the separation region increase strongly (by about a factor of 5). After the reattachment, disturbances of all frequencies increase, which indicates the beginning of the boundary layer turbulization.

Artificial disturbances were introduced by a high-voltage point discharge located on the conical part of the model. The evolution of artificial disturbances in the boundary layer of the cone and in the separation region was studied. Artificial pulsations were introduced with the frequency of 40 kHz, which corresponds to the region of medium frequencies from the measurements of natural disturbances. Wave spectra were obtained, and wave vector inclination angles were estimated. Upstream of the separation region, in the cone boundary layer, the behavior of the wave spectra was in line with traditional notions. Inclined waves with about 60 degree inclination angle of the wave vector to the main flow were identified in the wave train. The onset of two-dimensional disturbances in the separation region was shown, which was apparently related to a high receptivity of the boundary layer in the inhomogeneous region. Phase velocities of disturbances were estimated, which showed that acoustic disturbances prevail at small wave vector inclination angles <55 degrees, and Tollmien-Schlichting waves prevail at high angles.

The analysis of wave spectra of artificial disturbances allows one to suppose that nonlinear processes with the formation of asymmetric wave triplets begin for the examined flow regime downstream of the reattachment region. Special experiments are required, however, to verify this assumption. It is necessary to watch not only the fundamental harmonic, as it was done in [9], but also the subharmonics.

A possibility of determining the mechanisms of flow turbulization is another merit of the method of artificial disturbances.

RECEPTIVITY OF HYPERSONIC BOUNDARY LAYERS

Artificial disturbances were successfully used in the study of the boundary layer receptivity near the leading edge of a flat plate to external acoustic disturbances for $M=6$ in the tests in the wind tunnel T-326 [10].

The receptivity to waves incident onto the leading edge from below was studied. A source plate with a generator of artificial disturbances was used to create determined acoustic waves. The generation of these disturbances is accompanied by the irradiation of acoustic waves into the external flow. The source plate was located upstream of the examined plate in such a way that the generated acoustic disturbances were incident onto the leading edge of the examined plate from below. The disturbances incident onto the leading edge induced waves in the boundary layer of the examined plate, which were coherent with the generator of the source plate. The measurements were taken upstream of the leading edge of the examined plate and in its boundary layer. The measurements allowed for calculating the transfer functions: the ratio of the signal amplitude in the boundary layer to the amplitude of the signal, that invoked it, near the leading edge. Such an approach makes it possible to determine the initial conditions for the development of boundary layer instability.

Two different source plates were used in the experiments. The first plate had a point generator. A small orifice was made in the surface of the source plate, with a periodic high-voltage discharge being ignited in the chamber beneath this orifice. This generator created a complicated field of disturbances in the free stream, due to a wave train developed in the boundary layer of the source plate. Careful investigations of the radiation field showed that these waves are acoustic and propagate along the Mach contours, and the wave vector of these disturbances is mainly directed normal to the flow. The absolute value of the receptivity coefficient to these disturbances was about 0.6 and depended on the orientation of generated waves. The waves excited in the boundary layer of the examined plate with the maximum amplitude had the wave vectors with about 60 degree inclination to the main flow in the model plane.

The second source plate had a two-dimensional generator. It consisted of two flat electrodes flush-mounted with the surface of the source plate. This generator produced two-dimensional waves both in the boundary layer of the source plate and in the external field. Their wave vectors were mainly directed in the streamwise direction. Two-dimensional disturbances were also generated in the boundary layer of the examined plate. The absolute value of the receptivity coefficient to these waves was much higher than in the first case and roughly amounted to 3. These results are in agreement with the conclusions of the theoretical paper [11], in which it was shown that the maximum receptivity coefficient is observed to acoustic disturbances with zero angle between the wave vector and the flow direction. In this case, the waves penetrate completely into the boundary layer, thus, causing the resonance phenomena and exciting the vortex disturbances, whereas only a part of the wave penetrates into the boundary layer because of diffraction.

The presented results are pioneering and refer only to one special case of the receptivity problem. Natural disturbance, involving the change in the flow regime, can be excited by roughness elements, steps, and other inhomogeneities of the flow. The receptivity of hypersonic flow has not yet been studied for these conditions.

STABILITY OF HYPERSONIC SHOCK LAYER

Low Reynolds number flows are formed in usual wind tunnels at high Mach numbers ($M \sim 20$), and the flow instability can be hardly expected in these conditions. However, it makes sense to study experimentally the wave processes in such flows, because the theory often deals with the limit cases of infinite M , and it is desirable to verify these results.

The gas density in test sections of hypersonic wind tunnels is usually low, and the use of hot-wire anemometry for pulsation measurements is problematic. New diagnostic methods are

needed. All this appreciably hampers the measurements. Nevertheless, there are some favorable moments. The use of artificial disturbances can be avoided in stability research. The correlation length is rather large, and the wave characteristics can be obtained from the measurement of spatial correlation.

A cycle of measurements of characteristics of density fluctuations in a hypersonic shock layer on a flat plate was carried out for $M=21$ and temperature factor $T_w/T_0=0.26$ in the hypersonic nitrogen wind tunnel T-327 based at ITAM SB RAS. The measurements were performed using the electron beam fluorescence method. For the purposes of investigation, the equipment and techniques for measurement and data processing were developed. They were adapted for two-dimensional flows under the conditions of low fluorescence intensity [12,13]. The techniques allowed one to obtain the mean density profiles and spectral distributions of fluctuations across the shock layer, to determine the wave increments, to measure the phase velocities, and to estimate the spatial scales of correlation of density disturbances in the x , y , and z directions.

Natural disturbances. The data of measurements showed that for natural disturbances the major portion of fluctuations is localized in a narrow region directly below the shock wave. The spectra of fluctuations across the shock layer were similar. The measurements of phase velocities in the x and z directions showed that waves with the wave vector inclination angle less than 20 degrees and high values of the streamwise phase velocity ($C_x < 0.92$) are formed in the shock layer for all measured values of examined parameters.

The values of the streamwise phase velocity of density waves in the external flow lie within the same range. However, the wave vector inclination angle in the external flow depends substantially on frequency, reaching 80 degrees in the low-frequency region. The wave vector inclination angle decreases suddenly when the measurement point passes through the shock wave. On the whole, the phase characteristics of density waves correspond to the acoustic mode of pulsations. The data on the growth rates in the region of maximum fluctuations in the shock layer was measured. A considerable growth of disturbances in the high-frequency region can be noted with increasing of the Reynolds number. The streamwise and spanwise correlation measurements in the shock layer and in the external flow revealed close spatial scales of correlation in the both directions, which testifies to an isotropic character of the correlations scales of density disturbances. Their values amount to 0.2-0.25 of the reference spanwise flow size.

Artificial disturbances. A gasdynamic whistle was used to generate artificial disturbances of density in the shock layer on the plate. The whistle is a closed cylinder with an oblique front face. A gage for pressure fluctuations was placed at the end face of the cylinder, its signal being used as a reference signal for identification of the artificial disturbances.

When the whistle is positioned in a hypersonic flow, intense pressure fluctuations arise in its cavity, which are accompanied by fluctuations of the bow shock wave position. The characteristics of fluctuations and the flow behind the whistle were studied by the electron beam fluorescence method mentioned above [13]. Artificial disturbances were generated in the shock layer on the plate at the moment of interaction of the shock wave from the whistle with the plate leading edge. The whistle was located under the plate and slightly upstream of its leading edge [14].

The measurements showed that two-dimensional wave fronts with intensity of $(4-40) \times 10^{-3}$ of the free-stream density are formed in the shock layer, their spanwise width determined from their half-height varies from 10 to 30 mm depending on disturbance intensity. The

streamwise phase velocity of disturbances lies within $C_x=0.84-0.28$ for all frequencies, which indicates an acoustic nature of all the introduced disturbances. The main front is accompanied by plane fronts with much smaller intensity and spanwise size, which are adjacent to it on both sides. When the measurement point passes from the main front region to the regions of side fronts, the phase of fluctuations experiences a 180 degree jump.

In the y direction, the maximum of fluctuations is in the region lying immediately under the shock wave on the plate, which is in qualitative agreement with the measurements of natural disturbances.

It should be noted that the use of gasdynamic whistle distorted the mean flow field. When shock wave from the whistle crossed the leading edge of the examined plate, a low-pressure region was formed, which possibly led to formation of a vortex flow. The stability of a complicated object was actually studied rather than the shock layer stability on a flat plate.

CONCLUSIONS

The considered examples show that the use of artificial disturbances in the study of stability of hypersonic boundary layers is possible and rather informative. However, there are only few works in this direction. Let us enumerate some problems that can be solved using this approach. Firstly, this is the study of various modes typical of hypersonic flows. This problem is not clear yet, we can recall the contradictions which was mentioned in the paper [3]. The use of artificial disturbances could elucidate the mechanisms of nonlinear interaction of the waves. There are no such works at all. The study of receptivity is in its infancy and refers to only one special case. This problem being solved, the amplitude method, for example, could be reasonably used for predicting the transition. The study of the surface roughness effect on the behavior of disturbances can be of practical importance.

ACKNOWLEDGEMENT

The author is thankful to the Russian Foundation for Basic Research (grant 98-01-00735, 98-01-00462) for supporting this work.

REFERENCES

1. Stetson K.F., Kimmel R.L. On hypersonic boundary layer stability. -- AIAA Paper 92-0737, 1992.
2. Lachowicz J.T., Chokani N. Hypersonic boundary layer stability over a flared cone in a quiet tunnel. -- AIAA Paper 96-0782, 1996.
3. Wendt V., Simen M., Hanifi A. An experimental and theoretical investigation of instabilities in hypersonic flat plate boundary layer flow // *Phys. Fluids* - 1995.-Vol. 7.- No. 4.- P.877 - 887.
4. Maslov A.A., Sidorenko A.A., Shipluk A.N. An experimental investigation of natural disturbances in a hypersonic boundary layer on a flat plate // *J. Appl. Mech. Tech. Phys.*-1997.- Vol.38.-No. 1.- P.71 - 75.
5. Gilev V.M., Kachanov Yu.S., Kozlov V.V. Space wave packet development in the boundary layer // *Izv. SO AN SSSR. Ser. Techn. Nauk.* - 1983.- Vol. 3.- No. 13.- P.27 - 37.
6. Kosinov, A.D., Maslov, A.A., Shevelkov, S.G. Experiments on the stability of supersonic boundary layers // *J. Fluid Mech.* -1990.-Vol. 219.- P. 621 - 633.
7. Maslov A.A., Sidorenko A.A., Shipluk A.N. The use of artificial disturbances for the study of hypersonic boundary layer stability // *Thermophys. and Aeromech.*- 1997.- Vol. 4.- No. 4.- P.397 - 400.

-
8. Maslov, A.A., Sidorenko, A.A., Shpiyuk, A.N. On an experimental technique for the study of hypersonic boundary layer stability // Int. Conf. on the Methods of Aerophys. Research: Proc. Pt 2. — Novosibirsk, 1996, P.175 - 179.
 9. Maslov A.A., Shpiyuk A.N., Sidorenko A.A., Tran Ph. Study related to hypersonic boundary layer stability on a cone with a flare.— Novosibirsk, 1997.- Preprint / SB RAS. ITAM; No. 2-97.
 10. Maslov A.A., Shpiyuk A.N., Sidorenko A.A., Arnal D. Leading edge receptivity of the hypersonic boundary layer on a flat plate.— Novosibirsk, 1998.- Preprint / SB RAS. ITAM; No. 1-98.
 11. Fedorov A.V., Khohlov A.P. Supersonic boundary layer receptivity to the acoustic disturbances // Izv. RAN. Ser. Mech. Zhidk. G.— 1992.— No. 1.— P. 40 - 47.
 12. Maslov, A.A., Mironov, S.G., Shpiyuk, A.N. Experimental study of density pulsations in the hypersonic shock layer on a flat plate // J. Appl. Mech. Tech. Phys.—1996.— Vol.37.—No. 6.— P.51 - 60.
 13. Maslov, A.A., Mironov S.G. Experimental study of interaction of semi-opened cylindrical cavity with hypersonic flow // Izv. RAN. Ser. Mech. Zhidk. G.— 1996.— No. 6.— P. 165 - 170.
 14. Maslov, A.A., Mironov, S.G., Shpiyuk, A.N. An experimental electron-beam study of perturbations in a hypersonic shock layer on a plate // Int. Conf. on the Methods of Aerophys. Research: Proc. Pt 3. — Novosibirsk, 1996. P.212 - 215.

AN EXPERIMENTAL AND THEORETICAL STUDY OF AERODYNAMIC HEATING OF A PLATE IN VISCOUS HYPERSONIC FLOW

A.A.Maslov, S.G.Mironov, T.V.Poplavskaya, A.N.Shiplyuk, and V.N.Vetlutsky

Institute of Theoretical and Applied Mechanics SB RAS,
630090, Novosibirsk, Russia

Hypersonic motion of a flying vehicle is accompanied by considerable heating of its surface. Thus, the problem of constructing numerical algorithms for thermal loads acquires much significance. Numerical studies in hypersonic flows are especially important, since none of existing facilities simulates real flight conditions.

The heat transfer coefficients calculated using the Full Viscous Shock Layer (FVSL) theory are compared in the present paper with those measured by calorimetric gages and infra-red imaging system.

NUMERICAL STUDY

The objective of the present work is to study the aerodynamic heating on a plate within the framework of the FVSL theory in a wide range of governing parameters. The FVSL model [1] is an intermediate level of asymptotic approximation between the boundary layer and full Navier-Stokes equations. Apart from all terms of the boundary layer equations, the FVSL equations contain the momentum equation in projection onto the normal to the plate and all terms of the Euler equations. The FVSL equations, therefore, describe well the entire disturbed viscous flow region between the shock wave and the body surface.

The FVSL equations written in Cartesian coordinate system (x, y) , where the x coordinate is directed along the plate surface and y is normal to it, can be found in [2-6].

The slip and temperature drop conditions are used on the plate surface [7] (the subscript "w" indicates the surface parameters). The shock wave is assumed thin, and the generalized Rankine-Hugoniot conditions are set on it [8] taking into account the angle of attack α [3, 6] (the subscript "s" corresponds to parameters behind the shock wave). The shock wave position is determined by two methods:

- 1) from experiment (experimental values of y_s are interpolated by a bicubic spline);
- 2) from the condition of constant flow rate when passing through the shock wave

$$\int_0^{y_s(x)} \rho u dy \Big|_x = \int_0^{y_s(x)} \rho u dy \Big|_{x=x_0} + \int_{x_0}^x \frac{\sin(\beta + \alpha)}{\cos \beta} dx \quad (1)$$

(here $y_s = y_s(x)$ is the shock wave equation, u is the x -component of velocity vector, ρ - is the density, α and β are the angle of attack and the shock wave inclination angle, respectively).

It is assumed that the flow in the initial cross-section x_0 is described by the boundary layer equations and the shock wave has a constant inclination between the leading edge of the plate and cross-section $x = x_0$. The viscous shock layer equations are solved by the marching method with respect to the x coordinate using the algorithm described in [3].

The profiles of velocity, temperature, density and pressure in the entire shock layer are obtained while solving the problem. The skin friction coefficient

$C_f = \mu \frac{\partial u}{\partial y} \Big|_{y=0} / 0.5 \rho_\infty U_\infty^2$ and the heat transfer coefficient St (Stanton number) are

calculated on the plate surface. For the slipping boundary conditions, the Stanton number takes into account the energy transfer by "friction with slipping" [9]:

$St = \left(k \frac{\partial T}{\partial y} + u \mu \frac{\partial u}{\partial y} \right) \Big|_{y=0} / \rho_\infty U_\infty (H_\infty - H_w)$. Here μ , k , T are the viscosity, heat

conductivity and temperature, respectively; H is the total enthalpy, the subscript " ∞ " corresponds to the free-stream parameters.

The FVSL computations were performed on a difference grid with 400 points along the normal, the step in the x direction was 0.0001. The Prandtl number was $Pr = \mu_\infty c_{p\infty} / k_\infty = 0.7$, the ratio of specific heats was $\gamma = 1.4$. Viscosity was approximated by Sutherland's law.

EXPERIMENTAL TECHNIQUE

The measurements were performed in the hypersonic nitrogen wind tunnel T-327 of ITAM SB RAS for the Mach number $M_\infty = 21$ and unit Reynolds number calculated from the free-stream parameters $Re_1 = 6 \times 10^5 \text{ m}^{-1}$. The stagnation pressure was $P_0 = 8 \text{ MPa}$, the stagnation temperature was $T_0 = 1100 \text{ K}$, the uniform flow core diameter was 0.1 m. The flow visualization was performed using the electron-beam fluorescence [3]. The heat fluxes to the plate surface were measured by calorimetric gages and infra-red imaging system.

A steel plate with 0.01 m thickness, 0.34 m length, 0.08 m leading edge width, and 0.05 m trailing edge width was used for heat flux measurements. The leading and side edges of the plate had an angle of 11° , and the leading edge bluntness was 0.05 mm. An insert made of heat insulator AG-4V with 0.307 m length, 0.012 m width, and 0.006 m thickness was placed at the model axis for heat flux measurements. Five calorimetric gages were installed at the axis of this insert at a distance of 0.03, 0.06, 0.09, 0.15, and 0.27 m from the leading edge of the plate. The calorimetric gages were copper cylinders 1.9 mm in diameter and 1.7 mm high, flushed with the heat insulator surface and containing a thermocouple inside. The plate model was fixed on a rotating device that ensured the variation of the angle of attack within $0 \dots +5^\circ$.

A modular optical-mechanical scanning infra-red imaging system TV-M3 developed and manufactured at ITAM SB RAS was used for temperature measurements on the model surface [10]. The results obtained were processed using the technique described in [11]. The method is based on the finite-difference calculation of one-dimensional unsteady differential equations of heat

conductivity in the model-fitted coordinate system. The results of infra-red imaging are used as the boundary and initial conditions for computations.

RESULTS AND DISCUSSION

The calculated and experimental values of the Stanton number for the angles of attack $\alpha = 0^\circ$ (a) and 5° (b) are compared in Fig. 1. Curves 1 correspond to computations based on the FVSL equations with the shock wave position specified by experimental points, curves 2 show the FVSL computations with the shock wave detachment which is calculated from the condition of constant flow rate (1). The triangles describe experimental data obtained by infra-red imaging, and the circles indicate experimental data obtained by calorimetric gages. The error in determining the Stanton number by infra-red imaging is mainly determined by the error of model surface temperature measurement and uncertainty of heat insulator material characteristics. It is shown in the figure as a confidence interval ($\pm 28\%$). This and other figures show the x coordinate related to the model length L .

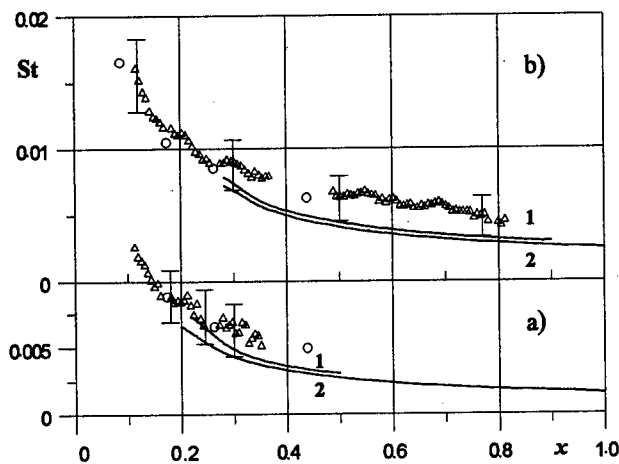


Fig. 1. Comparison of calculated and experimental Stanton numbers

for $M_\infty = 21$, $Re_L = 1,93 \times 10^5$, $T_o = 1100$ K, $T_w = 291$ K,
a) $\alpha = 0^\circ$ and b) $\alpha = 5^\circ$: solid line - FVSL computations,
 Δ - St (infra-red imaging), O - St (calorimetric gages).

It is seen that setting the shock wave position on the basis of experimental points yields more accurate results when calculating the Stanton number, while the FVSL equations with the shock wave detachment give slightly underrated values of St.

Using the above algorithm of the FVSL equations with determining the shock wave position from the condition of constant flow rate [6], we performed parametric calculations in a wide range of governing parameters: $15 \leq M_\infty \leq 25$, $Re_x = 10^4 - 10^6$, $\alpha = 0^\circ - 15^\circ$, $0.05 \leq T_w/T_o \leq 0.26$.

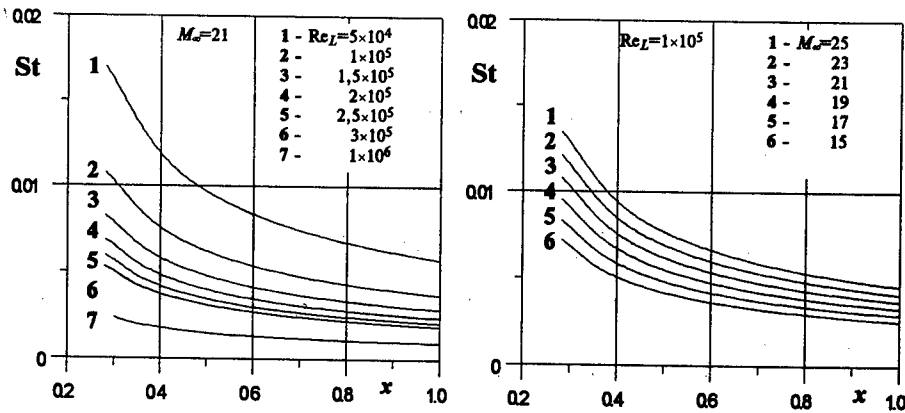


Fig. 2. Stanton number versus Reynolds and Mach numbers for $T_o = 1100$ K, $T_w = 291$ K, $\alpha = 5^\circ$.

Figure 2 shows the Stanton number versus the Reynolds and Mach numbers for $\alpha = 5^\circ$. As predicted by the strong interaction theory [12], the calculated values of St are proportional to $(M_\infty)^{3/2}$ and inversely proportional to $(Re_x)^{3/4}$, i.e., St is related to the rarefaction parameter $V = M_\infty \sqrt{C/Re_x}$ by a power law: $St \sim V^{3/2}$. Figure 3 demonstrates this dependence for various angles of attack $\alpha = 0^\circ$ to 15° . The parametric FVSL calculations yield almost linear dependence of the heat transfer coefficient on the angle of attack varied from 0° to 15° .

When studying the surface temperature T_w effect, it was found that the Stanton number changes weakly (within 5%) in the temperature range $T_w = 80$ - 300 K typical of wind tunnel experiments conditions (fig.4). At the same time, its dependence on stagnation temperature T_o is rather significant, which is shown in Fig. 5.

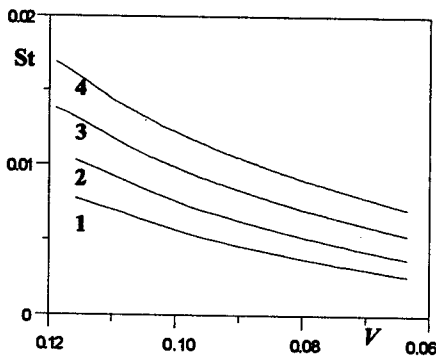


Fig. 3. St versus the rarefaction parameter $V = M_\infty \sqrt{C/Re_x}$:
 1,2,3,4 - $\alpha = 0, 5, 10, 15^\circ$,
 $M_\infty = 21$, $T_o = 1100$ K, $T_w = 291$ K,
 $Re_L = 1 \times 10^5$.

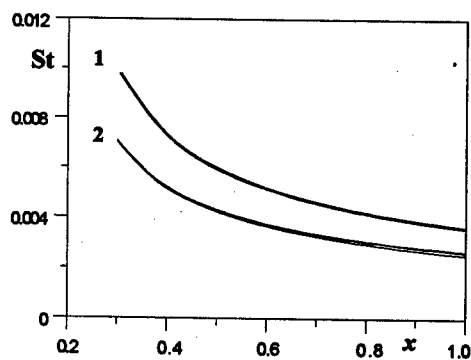


Fig. 4. Distribution of St for different values of surface temperature T_w :
 $M_\infty = 21$, $Re_L = 1 \times 10^5$, $\alpha = 5^\circ$,
 1 - $T_o = 1100$ K, $T_w = 80, 160, 300$ K,
 2 - $T_o = 5800$ K, $T_w = 80, 160, 300$ K.

When analyzing the parametric FVSL computations, we obtained an empirical function approximating the results for the heat transfer coefficient:

$$St_{FVSL} = (0.016\alpha + 0.16) \left[M_\infty \sqrt{C} / \sqrt{Re_x} \right]^3 \quad (2)$$

(α is taken in degrees). When constructing the approximation function (2), the goal was to obtain a unified simplest relationship for the entire range of applicability of the FVSL model ($15 \leq M_\infty \leq 25$, $Re_x = 10^4 + 10^6$, $\alpha = 0^\circ + 15^\circ$, $0.05 \leq T_w/T_o \leq 0.26$). The accuracy of approximation of the heat transfer coefficient reaches 10% on the most part of the plate with $V < 0.12$ and 20% with $V > 0.12$.

At first sight, formula (2) is independent of the temperature factor T_w/T_o . It should be noted that like in [13], the Chapman-Rubezin constant C is calculated in the present work in terms of the characteristic temperature $T_* = T_o(1+3$

$$T_w/T_o)/6: \quad C = \frac{\mu_* T_\infty}{\mu_\infty T_*}$$

(with the power dependence of viscosity on temperature). Thus, it is C in formula (2) that depends on T_w/T_o and varies from 0.5 to 1.1 in the present computations.

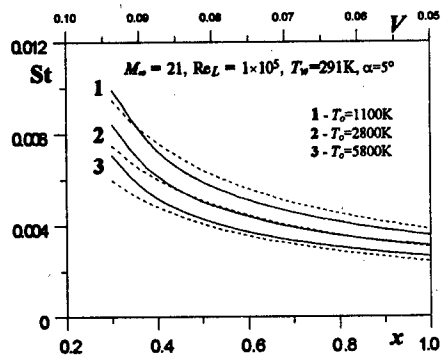


Fig. 5.

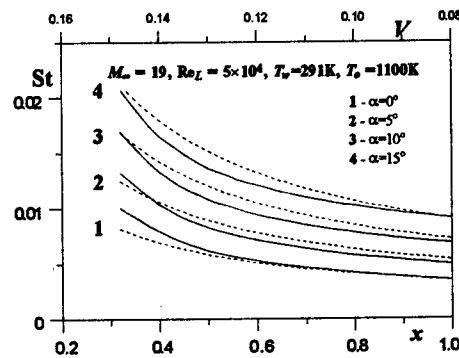


Fig. 6.

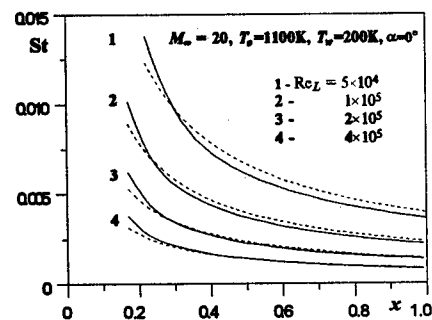


Fig. 7.

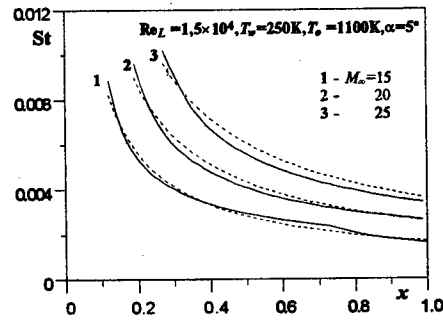


Fig. 8.

The Stanton numbers calculated using the FVSL model (solid lines) are compared in Fig. 5 - 8 with the FVSL approximation function (2) (dashed lines) for various stagnation temperature $T_o = 5800, 2800, 1100$ K (for various temperature factors $T_w/T_o = 0.05, 0.1, 0.26$ - curves 3, 2, 1, respectively, fig.5) and for various angles of attack $\alpha = 0^\circ, +15^\circ$ (curves 1-4, respectively, fig.6), for various Reynolds numbers (fig.7) and Mach numbers (fig.8). It is seen that the discrepancy lies within the above mentioned limits.

The work was supported by the Russian Foundation for Basic Research (grant 98-01-00735).

REFERENCES

1. Davis R.T. Numerical solution of the hypersonic viscous shock-layer-equations // AIAA J. 1970.- V. 8.- N. 5.- P. 843-851.
2. Vetlutsky V.N., Maslov A.A., Mironov S.G., Poplavskaya T.V. and A.N.Shiplyuk A.N. Hypersonic flow on a flat plate. Experimental results and numerical simulation // J. Appl. Mech. Tech. Phys. - 1995.- Vol. 36.- No. 6.- P. 60-67.
3. Vetlutsky V.N., Mironov S.G., Poplavskaya T.V. Hypersonic flow on a plate at incidence within the frames of the viscous shock layer model // Int. Conf. on the Methods of Aerophys.l Research: Proc. Pt 2.- Novosibirsk, 1996, P.221-226.
4. Vetlutsky V.N., Mironov S.G., Poplavskaya T.V. Hypersonic flow over a plate at incidence // Thermophysics and Aeromechanics. -1997.- Vol. 4.- No. 1.- P. 33-39.
5. Poplavskaya T.V. and Vetlutsky V.N. Calculation of viscous shock layer on a plate // J. Appl. Mech. Tech. Phys.- 1997.- Vol. 38.- No. 2.- P. 91-100.
6. Maslov A.A., Mironov S.G., Poplavskaya T.V. and Vetlutsky V.N. On the incidence angle effect on the flow over a plate // High Temp. -1998.- No. 4.
7. Loitsyansky L.G.. Fluid Mechanics.- Moscow: Nauka, 1973.
8. Tirsky G.A. On the theory of the viscous chemically reacting gas flow over plane and axisymmetric blunted bodies with injection // Trudy Mosk. Gos. Univ. - 1975.- No. 39.- P. 5-38.
9. Rudman S., Rubin S.G. Hypersonic viscous flow over slender bodies with sharp leading edges // AIAA J. - 1968.- V.6.- N.10.- P.1883-1890.
10. Bashurov V.V., Boichuk L.N., Vorontsov S.S. and Vyshenkov Yu.I. Modular measurement infra-red imaging system TV-M // Teplovidenie.- Iss. 6, Moscow, 1986 (Trudy Mosk. Instit. Radio Ingenerii, Elektroniki i Avtomatiki).
11. Maslov A.A., Sapogov B.A., and Shipliyuk A.N. A technique for the heat flux determination in an aerodynamic experiment // Thermophysics and Aeromechanics.- 1996.- Vol. 3.- No. 2.- P. 157-166.
12. Pan Y.S., Probst Ronald F. Rarefied-flow transition at a leading edge // Fundamental phenomena in hypersonic flow: Proc. of Intern. Symp./ed. J. Gordon Hall. -1966.- P.259-306.
13. Cheng H.K., Gordon H.K., Golian T.C. and Hertzberg A. Boundary-layer displacement and leading edge bluntness effects in high-temperature hypersonic flow // J.Aerospace Sciences.- 1961.- Vol. 28.- No. 5.- P.353-381.

AN ANALYTICAL STUDY OF HYSTERESIS AT PLANE SHOCK WAVE REFLECTION IN A SLENDER CHANNEL

A.E. Medvedev, V.M. Fomin

Institute of Theoretical and Applied Mechanics SB RAS,
630090, Novosibirsk, Russia

Let us consider a steady supersonic gas flow which enters a plane channel formed by two symmetrically positioned wedges (Figure 1 shows only the upper half-plane of the channel). Within a certain range of angles β ($\beta_N \leq \beta \leq \beta_D$) of the converging channel, both the regular (RR) and irregular (Mach) (MR) reflections of the incident shock wave are possible, this is a so-called dual solution domain. The hysteresis phenomenon consists in the following: as the angle β increases from β_0 ($\beta_0 < \beta_N$) up to β_1 ($\beta_N \leq \beta_1 \leq \beta_D$), an RR reflection is formed, and when the angle β decreases from β_2 ($\beta_2 > \beta_D$) down to β_1 , an MR reflection is observed. This means that both the RR and MR configurations of the shock waves are possible for the same value of the angle β , depending on the history of variation of the wedge inclination angle.

A possibility of existence of the hysteresis phenomenon of the RR \leftrightarrow MR transition was discussed in [1] for angles β within $\beta_N < \beta < \beta_D$. An attempt to verify experimentally the existence of hysteresis was made in [2]. Finally, the hysteresis of the RR \leftrightarrow MR transition was obtained numerically in the papers [3-5] and experimentally in [6]. Nevertheless, there are still many open questions in this problem. The experimental results of [6] were not supported by the papers of other authors. Numerous experimental results conducted earlier [7] yielded only one solution in the dual solution domain, i.e., rejected the hysteresis. The main difficulty in experimental verification of the hysteresis phenomenon is the obtaining of regular reflection for angles β lying within $\beta_N < \beta < \beta_D$, i.e., in the dual solution domain. The failure in experimental obtaining of the hysteresis can be explained by three-dimensional effects in the shock tube [8]. Hornung [9] suggests to increase the wedge angle more rapidly (with a higher wedge rotation velocity) to obtain an RR configuration in the dual solution domain. Experimental instability of the RR configuration in the dual solution domain was the reason for studying the stability of regular reflection. It is known [10] that the regular solution is stable to linear unsteady perturbations. Stability of the RR and MR configurations is physically grounded in [9], and it is shown in [11] that the RR \leftrightarrow MR transition satisfies the principle of the minimum entropy production. Thus, the existence of hysteresis of the RR \leftrightarrow MR transition has not been analytically proved yet; there are no criteria (for example, the wedge rotation velocity) of realization of hysteresis of the RR \leftrightarrow MR transition; the unsteady problem of gas flow between the wedges with varied wedge inclination angle has not been solved (the steady problem has been solved numerically in [3-5]).

Let us consider the flow in a plane channel formed by two symmetrically positioned wedges (Figure 1 shows the upper half-plane of the flow). The following parameters are assumed known: wedge parameters – length w of the side AG and angle θ ; half-width of the entrance cross-section of the channel Y_1 ; free-stream parameters – pressure P_1 , velocity U_1 , density ρ_1 , and the Mach number $M_1 > 1$; the gas is polytropic with the ratio of specific heats γ .

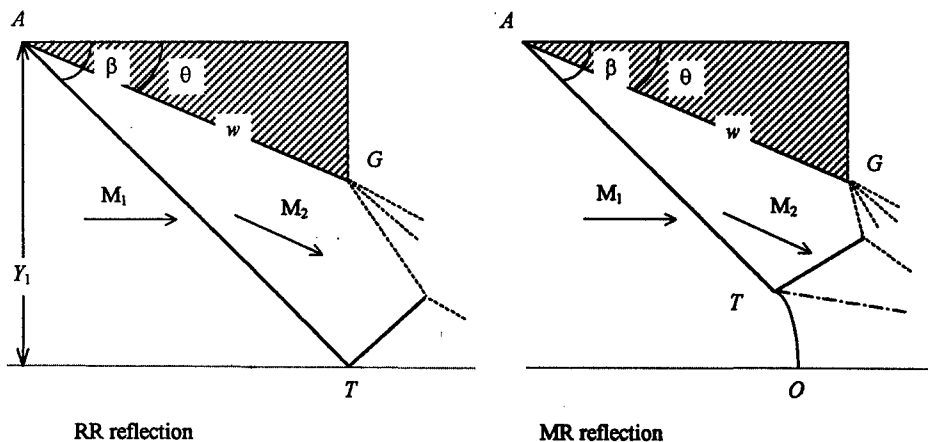


Fig. 1.

It is known [7,12] that for an angle $\beta > \beta_*$ the RR reflection transforms into the MR reflection (β_* is the critical angle of the RR \leftrightarrow MR transition). There are two criteria for the angle β_* :

1) double-shock criterion [7] or von Neumann criterion [12] - $\beta_* = \beta_N$; 2) triple-shock criterion [7] or detachment criterion [12] - $\beta_* = \beta_D$. In both cases $\beta_D > \beta_N$.

Let us choose a nondimensional length l as a quantity characterizing the flow with varied angle β , l is the length of the shock wave AT related to w (Fig. 1). Let us consider (Fig. 2) the function $l = l_{eq}(\beta)$ - the steady value of the length l when the wedge is rotated around the point A . The function $l = l_{eq}(\beta)$ is calculated by the formula

$$l_{eq}(\beta) = \begin{cases} l_{eq(RR)}(\beta) & \text{for RR reflection;} \\ l_{eq(MR)}(\beta) & \text{for MR reflection;} \end{cases} \quad (1)$$

where $l_{eq(RR)}(\beta) = (Y_1/w)/\sin \beta$, $l_{eq(MR)}(\beta)$ is determined using the approximate-analytical model [13,14] or the less accurate model [15].

Let us consider the unsteady process of wedge rotation around the point A with almost constant angular velocity $\omega = d\theta/dt$ ($\omega > 0$ denotes the clockwise rotation), i.e., $d\omega/dt \ll 1$. The angle β (the inclination angle of the shock wave AT at the point A) is uniquely determined from the wedge angle θ using the formula [12]

$$\text{ctg } \theta = \left[\frac{(\gamma+1)M_1^2}{2(M_1^2 \sin^2 \beta - 1)} - 1 \right] \text{tg } \beta. \quad (2)$$

The wedge rotation velocity ω given, we can then determine the functions

$$\theta = \theta(t; \omega), \quad \beta = \beta(t; \omega). \quad (3)$$

When the wedge is rotated around the point A with velocity ω , the length of the shock wave AT does not depend directly on time t , i.e.,

$$l = l(\beta; \omega), \quad (4)$$

since t can be excluded from the right-hand part of (4) using (2) and (3).

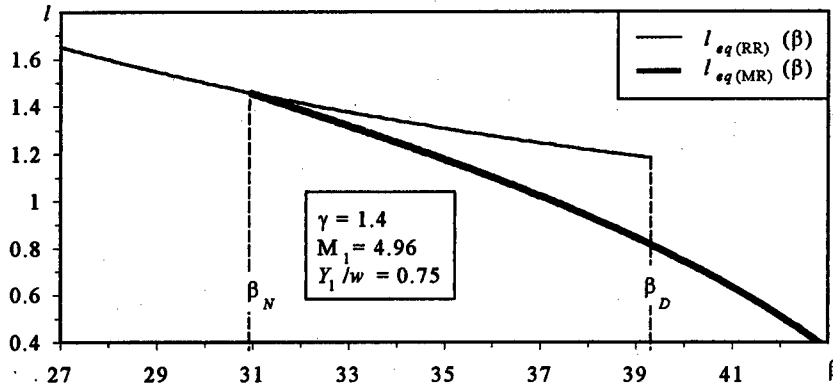


Fig. 2. Steady value of the length of the shock wave AT .

The function $l = l(\beta; \omega)$ should satisfy the differential equation

$$dl/dt = F(l, \beta). \quad (5)$$

The time dependence can be excluded from the right-hand part of (5) using relations (2) and (3). An explicit parametric dependence of the function F on the rotation velocity ω can be excluded using (4). The parametric dependence on the wedge rotation velocity ω implicitly enters the right-hand part of (5) via the function $\beta = \beta(l; \omega)$, which can be obtained by inversion of the function (4). To determine the function F , one has to solve the problem about the wedge rotation with the angular velocity ω – this will be done below. Prior to solving the problem, however, we can draw some useful conclusions based on the properties of the function F . Since the problem of wedge rotation has only two steady-state solutions to (1) – regular and Mach reflection, the function F is larger than zero everywhere except for the steady-state solutions – curve $l = l_{eq}(\beta)$:

$$F(l, \beta) = 0, \text{ for } l = l_{eq}(\beta);$$

$$F(l, \beta) \neq 0, \text{ for } l \neq l_{eq}(\beta);$$

Let us consider possible trajectories of the function $l = l(\beta)$ in the plane (l, β) when the wedge is rotated around the point A . Let us represent the left-hand part of equation (5) in the form

$$\frac{dl}{dt} = \frac{\partial l}{\partial \beta} \frac{d\beta}{d\theta} \omega(t) + \frac{\partial l}{\partial \omega} \frac{d\omega}{dt}. \quad (6)$$

For the first term in the right-hand part of (6): the first multiplier is the trajectory of variation of the shock wave length l in the plane (l, β) ; the second multiplier is determined from (2), it is positive within the considered range of angles β and θ ; the third multiplier is the wedge rota-

tion velocity. The second term in the right-hand part of (6) can be neglected because it is very small: the first multiplier, as it will be shown below for the RR reflection, is small, i.e., the length of the shock wave AT changes only weakly with changing the wedge rotation velocity; the second multiplier is small due to almost constant velocity of wedge rotation. If the wedge rotation velocity is $\omega(t) \neq 0$, then the trajectory $l = l(\beta)$ has steady points (points where $\partial l / \partial \beta = 0$) only on the equilibrium curve $l = l_{eq}(\beta)$.

Let us consider possible trajectories in the plane (l, β) with rotating wedge (Fig. 3: thin curve - $l = l_{eq(RR)}(\beta)$; thick curve - $l = l_{eq(MR)}(\beta)$).

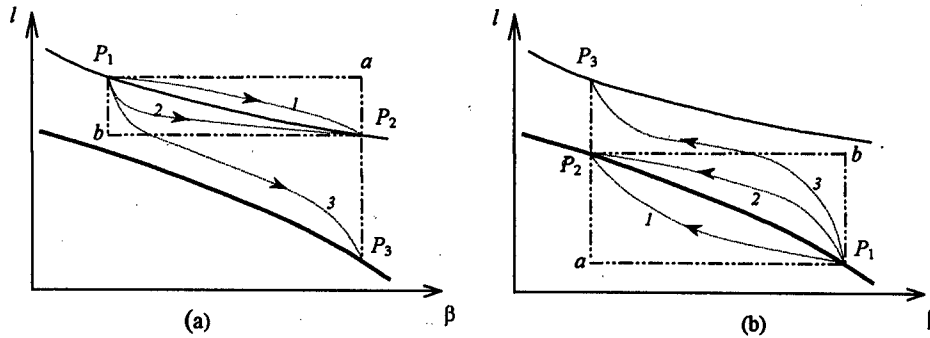


Fig. 3.

Let the point P_1 lie on the RR branch of solution (Fig. 3a). Rotating the wedge anticlockwise ($\omega > 0$), we try to reach the point P_2 which is also located on the RR branch of solution. Possible trajectories in this unsteady process are trajectories 1 and 2 (Fig. 3a). There exists a critical rotation velocity $\omega_k(\beta)$ that ensures the motion in the triangle P_1bP_2 for the RR reflection - $\omega_{k(RR)}(\beta)$. If the rotation velocity is $\omega < \omega_{k(RR)}$, then the motion occurs from the point P_1 to the point P_2 along curve 2 lying in the upper triangle P_1bP_2 (Fig. 3a). If the wedge rotation velocity is $\omega > \omega_{k(RR)}$, the motion trajectory leaves the triangle P_1bP_2 (curve 3 in Fig. 3a), and further motion follows curve 3, the point P_2 is not reached, and the motion is finished at the point P_3 on the equilibrium curve of the MR reflection (Fig. 3a).

Let the point P_1 lie on the MR branch of solution (Fig. 3b). Rotating the wedge anticlockwise ($\omega < 0$), we try to reach the point P_2 which is also located on the MR branch of solution. Possible trajectories in this unsteady process are trajectories 1 and 2 (Fig. 3b). There exists a critical rotation velocity $\omega_k(\beta)$ that ensures the motion in the triangle P_1bP_2 for the MR reflection - $\omega_{k(MR)}(\beta)$. If the rotation velocity is $\omega > \omega_{k(MR)}$, then the motion occurs from the point P_1 to the point P_2 along curve 2 lying in the upper triangle P_1bP_2 (Fig. 3b). If the wedge rotation velocity is $\omega < \omega_{k(MR)}$, the motion trajectory leaves the triangle P_1bP_2 (curve 3 in Fig. 3b), and further motion follows curve 3, the point P_2 is not reached, and the motion is finished at the point P_3 on the equilibrium curve of the RR reflection (Fig. 3b).

Thus, the hysteresis of the $RR \leftrightarrow MR$ transition is realized if the wedge rotation velocity satisfies the condition $|\omega(t)| \leq |\omega_k(\beta)|$, i.e., there exists a limiting velocity of wedge rotation $\omega_k(\beta)$ for hysteresis realization.

The qualitative pattern of transformation of the shock wave AT is presented in Fig. 4 for wedge rotation around the tip. The numerals 1, 2 and 3 denote sequential stages of the wedge rotation. If the wedge rotation velocity is $\omega > 0$, then the shock wave of steady RR reflection (Fig. 4a - 1) begins to bend (Fig. 4a - 2), and the angle $\tilde{\beta}$ increases. For angles higher than the critical angle $\tilde{\beta} > \beta_D$ the regular reflection is not possible, and a triple configuration is formed (Fig. 4a - 3). Inversely, if the rotation begins from the MR reflection with negative velocity $\omega < 0$, the shock wave AT bends to the opposite side (the angle $\tilde{\beta}$ decreases - Fig. 4b - 2). With further rotation of the wedge, the angle $\tilde{\beta}$ becomes smaller than the critical angle $\tilde{\beta} < \beta_N$, and the Mach reflection transforms into regular reflection (Fig. 4b - 3). The motion along curve 1 (Fig. 3) is not observed when the wedge is rotated with almost constant velocity. Since on curve 1 the shock wave length is $l > l_{eq(RR)}$ for the RR reflection and, inversely, for the MR reflection $l < l_{eq(MR)}$, this is in contradiction with the variation of the length of the shock wave AT in Fig. 4. Thus, when the wedge is rotated around its tip, a continuous transition of the shock wave configuration from RR to MR and back is observed in the dual solution domain.

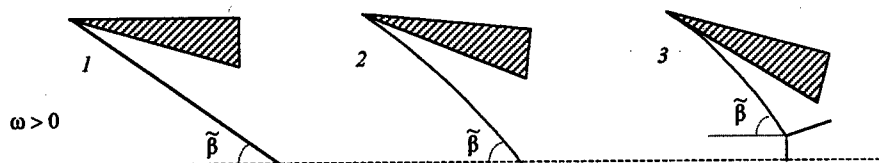


Fig. 4a.

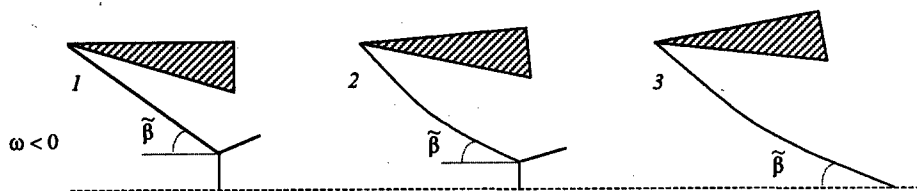


Fig. 4b.

Let the wedge be rotated (Fig. 5a) around the tip (point A) with velocity $\omega(t) > 0$. The Hayes similarity in aerodynamics is known [16]: a supersonic flow around a thin body with thickness $y_w < 1$ is mathematically identical to the problem of an unsteady one-dimensional flow with accuracy to magnitudes of the order $O(y_w^2)$. This motion is observed ahead of a piston moving with velocity proportional to the inclination of the aerodynamic surface. Let us use this aerodynamic analogy for the mathematical transition from a rotating wedge (Fig. 5a) to a curvilinear wedge (Fig. 5b). The value of wedge curvature y_w (in the local coordinate system (x,y) - Fig. 5b) is proportional to the wedge rotation velocity $y_w(x) = d_1 x^2$, where $d_1 = \omega / (2U_2)$, U_2 is the velocity behind the shock wave AT (Fig. 5a).

Let us consider a uniform supersonic flow around a curvilinear wedge. The attached shock wave AT becomes curved (the shock wave $A\tilde{T}$ in Fig. 5b), and a vortex flow arises behind it. Since the curved surface of the wedge differs insignificantly from the flat surface ($d_1^2 \ll 1$), we can use the linearized theory of vortex flow. The linearized problem for a supersonic flow around a curvilinear wedge (ogive) was solved in [16].

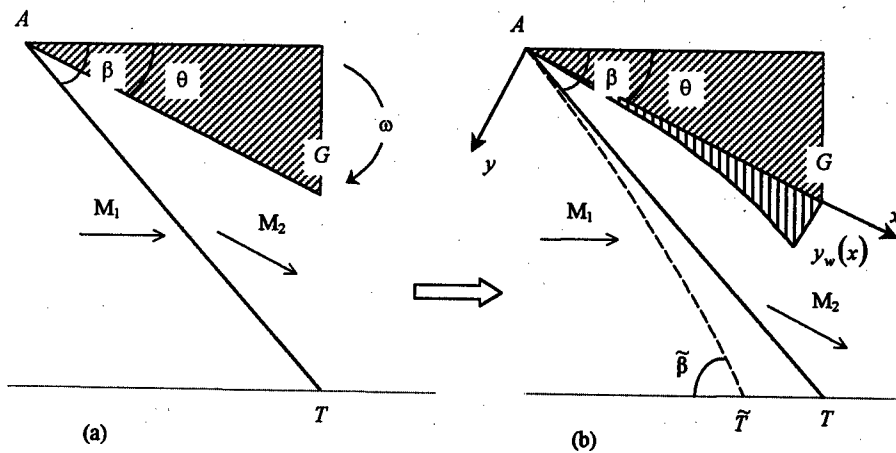


Fig. 5.

Applying the solution of [16] to a curved wedge (Fig. 5b), we find the length of the shock wave $A\tilde{T}$

$$l = l(\beta; \omega) \quad (7)$$

and the incidence angle of the shock wave $A\tilde{T}$ onto the symmetry plane

$$\tilde{\beta} = \tilde{\beta}(\beta; \omega). \quad (8)$$

The found solution (7), (8) has the following property: the inclination angle $\tilde{\beta}$ of the shock wave $A\tilde{T}$ at the point \tilde{T} (Fig. 5b) is larger than the angle β and $l(\beta; \omega) < l_{eq(RR)}(\beta)$ for $\omega > 0$.

For experiments [6], when the wedge was rotated with velocity $\omega = 0.57 \text{ s}^{-1}$ and the angle was $\beta = 35^\circ$, the shock wave length l decreases only by 0.00085% in comparison with the equilibrium length, and the angle is $\tilde{\beta} = 35.00005^\circ$. This is related to the fact that the wedge rotation velocity is small in comparison with the main flow velocity (the parameter $d_1 = 3.824 \times 10^{-7}$).

The proposed model allows one to estimate the value of the critical velocity $\omega_{k(RR)}(\beta)$, i.e., the maximum velocity with which the wedge can be rotated to pass from the point P_1 to the point P_2 . The critical velocity $\omega_{k(RR)}(\beta)$ depends on the distance between the points P_1 and P_2 (Fig. 3a). The function $\omega_{k(RR)}(\beta)$ for the data of [6] for two arbitrary points P_1 and P_2 lying at a distance no less than $\Delta\beta = 0.001^\circ$ – curve 1, $\Delta\beta = 0.01^\circ$ – curve 2, $\Delta\beta = 0.1^\circ$ – curve 3 is plotted in Fig. 6. An increase of the distance between the points P_1 and P_2 increases the criti-

cal velocity (curves 1, 2 and 3 in Fig. 6). A typical feature of behavior of the critical velocity is a monotonic decrease down to zero as the angle β is increased. This explains why it is not possible to obtain regular reflection with $\beta \rightarrow \beta_D$ in computations [3-5] and experiments [6], since even a small wedge rotation velocity leads to transition from regular to Mach reflection. An overrated value of the critical rotation velocity is due to the fact that the proposed model (Fig. 5) is valid only for a low velocity of wedge rotation.

It is seen from the computation results obtained using the proposed model that an RR configuration is obtained for wedge rotation velocities $\omega < \omega_{k(RR)}$. The critical velocity of wedge rotation drop down to zero with increasing the angle β , and for any finite velocity $\omega > 0$ the transition to Mach reflection occurs at $\beta < \beta_D$. The following statement is valid for Mach reflection: an MR configuration is obtained in the dual solution domain when the wedge rotation velocity (anticlockwise) is $|\omega| < |\omega_{k(MR)}|$. If the wedge rotation velocity is $|\omega| > |\omega_{k(MR)}|$, the transition from MR to RR configuration (curve 3 in Fig. 4b) in the dual solution domain is possible. The transition was not observed experimentally. This is explained by the fact that the model ignores the external disturbances of the flow and three-dimensionality of the real flow obtained in wind tunnels [8]. Thus, the critical velocity is also overrated.

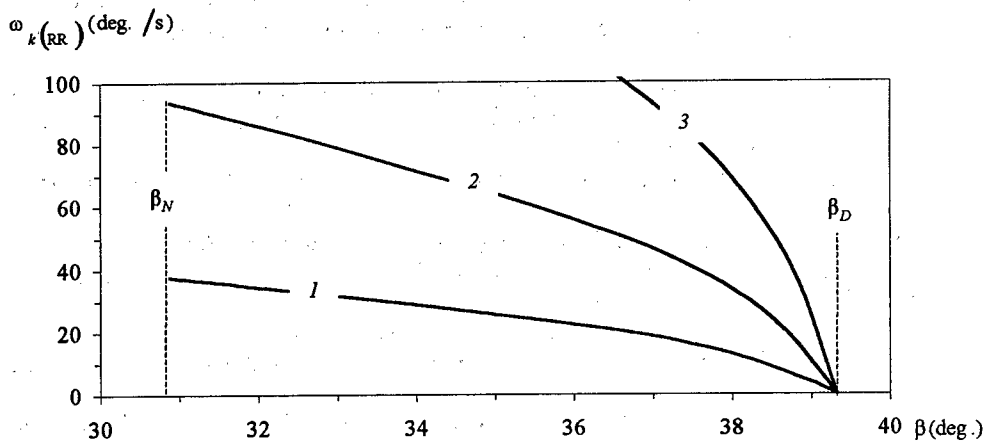


Fig. 6.

A model of the RR \leftrightarrow MR transition for a wedge rotated around its tip is proposed in the paper. It is shown that there exists a critical velocity of wedge rotation: if the wedge rotation velocity is smaller than the critical value, the hysteresis of the RR \leftrightarrow MR transition exists.

REFERENCES

1. Henderson L.F., Lozzi A. Further experiments on transition to Mach reflection // J. Fluid Mech. - 1979. - Vol. 94. - P. 541-559.
2. Hornung H.B., Robinson M.L. Transition from regular to Mach reflection of shock waves. Part 2. The steady-flow criterion // J. Fluid Mech. - 1982. - Vol. 123. - P. 155-164.

3. Ivanov M.S., Gimelshein S.F., Beylich A.E. Hysteresis effect in stationary reflection of shock waves // *Phys. Fluids*. – 1995. – Vol.7. – P. 685-687.
4. Chpoun A., Ben-Dor G. Numerical confirmation of the hysteresis phenomenon in the regular to the Mach reflection transition in steady flows // *Shock Waves*. – 1995. – Vol. 5. – P. 199-203.
5. Ivanov M., Zeitoun D., Vuillon J., Gimelshein S., Markelov G. Investigation of the hysteresis phenomena in steady shock reflection using kinetic and continuum methods // *Shock Waves*. – 1996. – Vol. 5. – P. 341-346.
6. Chpoun A., Passerel D., Li H., Ben-Dor G. Reconsideration of oblique shock wave reflections in steady flows. Part I. Experimental investigation // *J. Fluid Mech.* – 1995. – Vol. 301. – P. 19-36.
7. Bazhenova G.V. et al., *Unsteady Interactions of Shock and Detonation Waves in Gases* // Nauka: Moscow, 1986, 208 p.
8. Fomin V.M., Ivanov M.S., Kharitonov A.M., Gimelshein S.F., Klemenkov G.P., Kudryavtsev A.N., Markelov G.N., Pavlov A.A., Hornung H.G. Analysis of hysteresis phenomenon in steady interaction of strong shock waves // *Int. Conf. On the Methods of Aerophys. Research: Proc. Pt 3*. – Novosibirsk, 1996. – P. 53-61.
9. Hornung H.G. On the stability of steady-flow regular and Mach reflection // *Shock Wave*. – 1997. – Vol. 7. – P. 123-125.
10. Teshukov V.M. Unsteady disturbances of a supersonic flow behind the reflected shock wave // *Computational Methods of Applied Hydrodynamics*, Novosibirsk, 1998, Iss. 84, P. 116-134.
11. Li H., Ben-Dor G. Application of the principle of minimum entropy production to the regular-to-Mach-reflection transition in steady flows // *20th Int. Symp. on Shock Waves: Proc. Pt 1*. – Pasadena, 1995, P. 447-452.
12. Courant R., Friedrichs K. *Supersonic flow and shock waves*. – New York: Interscience, 1948.
13. Medvedev A.E., Fomin V.M. Numerical-analytical solution for Mach configuration of steady shock waves in a 2D slender // *Int. Conf. On the Methods of Aerophys. Research: Proc. Pt 3*. – Novosibirsk, 1996. – P. 216-220.
14. Medvedev A.E., Fomin V.M. Approximate-analytical calculation of the Mach configuration of steady shock waves in a plane convergent channel // *J. Appl. Mech. Tech. Phys.*, 1998, No. 3.
15. Azevedo D.J., Liu C.S. Engineering approach to the prediction of shock patterns in bounded high-speed flows // *AIAA Journal*. – 1993. – Vol. 31. – P. 83-90.
16. Pai S.I. *Introduction to the theory of compressible flow*. – New York: D. Van Nostrand, 1960.

DEVELOPEMENT OF THE OIL FILM METHOD OF SKIN FRICTION MEASUREMENT FOR CURVED AND ARBITRARY ORIENTED SURFACES

R.V. Nestoulia, S.B. Nikiforov, A.A. Pavlov

Institute of Theoretical and Applied Mechanics SB RAS, Novosibirsk 630090, Russia

INTRODUCTION

This paper describes a further development of the optical skin friction measurement technique for curved and arbitrary oriented surfaces. Fundamentals of the method formulated by Tanner and Blows [1] were further developed in [2-4]. The method is based on the registration changes of an oil droplet shape in time. An oil droplet placed on the surface under investigation is deformed under the action of a skin friction force defined as

$$\tau(\xi) = \frac{2\rho\nu}{\Delta S(\xi) \cdot L^2(\xi)} \frac{d \int_0^{\xi} \Delta S(\xi) \cdot L(\xi) d\xi}{dt} \quad (1)$$

where ξ is the coordinate along a surface streamline, L is the oil droplet thickness, ρ and ν are oil density and kinematic viscosity, respectively, ΔS is the stream filament width which can be presented as

$$\Delta S(\xi) = \Delta S(0) \cdot e^{\int_0^{\xi} \frac{d\varphi}{ds} d\xi}$$

where $d\varphi/ds$ is the derivative of the streamline inclination angle φ with respect to the coordinate S orthogonal to ξ .

The papers [1-2] contain estimates of the method accuracy of about 10%, which is fairly acceptable for this parameter.

In the previous works, the oil droplet shape was registered using specular reflection optical schemes, thus limiting the technique implementation to flat surfaces. Besides, in this case, the surface orientation must ensure the registration of the light specular reflected from the surface. In this work, a new technique based on a diffuse light interference is presented. Its implementation allows one to avoid the constraints of specular reflection optical schemes dealing with surface orientation and curvature.

As follows from eq.(1), to obtain skin friction force, both the registration of changes of the oil droplet shape change in time and the detection of surface streamline direction are required. A possibility of detecting the surface streamline direction by means of analysing the oil visualisation pictures is also discussed in this work.

1. THEORETICAL JUSTIFICATION OF THIN FILM SHAPE REGISTRATION WITH THE USE OF DIFFUSE LIGHT

The scheme of interference utilising diffuse light is presented in fig. 1. An interrogation area of the model surface coated with an oil film is illuminated using radiation 1 spreading from diffuser 2. A collecting optics combines lens 3 and stop 4 placed in the lens focal plane. The image is collected by a CCD camera 5. A V1005 CCD camera was used to grab fringe-image patterns. A video frame grabber developed at ITAM was used to feed the TV frames directly into an AT 486/66Mhz personal computer. The number of pictures collected depends

on the computer RAM. Eight pictures sized 512 by 256 pixels require 1Mb of the computer RAM.

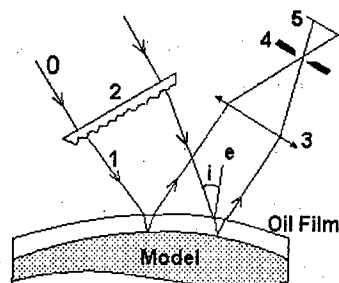


Fig.1. The scheme of interference utilizing diffuse light.

It is well known that any light wave consists of a number of plane waves spreading at different angles (external diffuse lighting). In case of the infinitesimal beam limiting aperture, the radiation of only one plane wave spreading from the model surface can pass through the stop. This wave will spread from the area under consideration at an angle equal to i . Such a plane wave will form fringe patterns with an interference path difference $\Delta L = 2nD \cos(r)$, where D is the oil film thickness; n is the oil refractive index, r is the refraction angle. For curved surfaces, the angle i corresponding to the incident beam of the specular reflection scheme is changed in accordance to surface orientation. In general, i is equal to the angle between a wave vector and a normal to the surface under investigation at a corresponding point.

Indeed, the beam limiting aperture is not set to zero, thus the CCD camera registers a number of fringe patterns formed by plane waves, whose wave vectors lay inside a solid angle Ω defined by the beam limiting aperture radius R and the lens focal length F . The main difference between the axial plane wave direction and any other plane wave direction is defined as: $\Delta l \approx R/F$. It is obvious that each plane wave forms its own fringe patterns, but in case of thin films and small i angle changes, all fringe patterns will agree, and fringe patterns of equal thickness will be successfully registered. In our experiments, reliable results were obtained by means of "HELIOS -44-2" lens ($F=44$ mm, relative aperture is equal to 2). A setup used to register the fringe patterns of equal thickness is presented in fig. 2. When external diffuse lighting tests were performed, both the light source position and the diffuser position were changed in dependence of the β angle. In case of internal lighting, the CCD camera position was not changed.

Although the external diffuse lighting provides fringe patterns for curved and arbitrary oriented surfaces, the technique implementation requires for the incident light to contain plane waves which are specularly reflected to the collecting aperture from each point of the surface. It significantly complicates the experiment. However, the model surface itself can be used as a diffuse light source (internal diffuse lighting). If the model surface reflects a fraction of the collimated incident light and diffuses the rest of the incoming beam (thus providing internal diffuse lighting), the same fringe patterns can be registered. The interference path difference is the same, too. A diffuse coating on the model surface creates an impression of internal model glowing due to incident light scattered on the surface. Therefore, it is pertinent to use the term "internal" diffuse lighting.

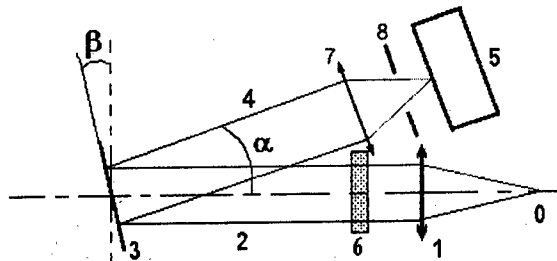


Fig. 2. A setup used to register the fringe patterns of equal thickness

Figure 3abc contrasts the differences between the specular reflection scheme, external diffuse lighting, and internal diffuse lighting.

Figure 3a) shows a setup operating in specular reflected light. It can be used only for flat surfaces. The collecting optics 4 should be positioned so that to register light 3 specularly reflected on the surface, which restricts the applicability area of the method.

Figure 3b) shows a scheme for external diffuse lighting. In this case, the model surface 1 can have an arbitrary curvature, but since the light is specularly reflected on it, the measurements can be taken only for those surface portions for which the entrapment of specularly reflected light 3 from diffuser 5 by the detecting optics 4 is ensured. This allows one to take measurements on curved surfaces but restricts the surface orientation.

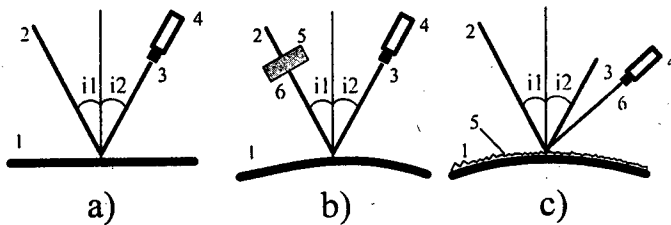


Fig. 3. The differences between the specular reflection scheme, external diffuse lighting, and internal diffuse lighting.

In fig. 4 the oil droplet fringe patterns obtained using a common specular reflection scheme (fig. 4b) and by means of external diffuse lighting (fig. 4a) are presented. It is clear that both patterns are the same, but in case of the external diffuse lighting, there are no distortions typical of specular reflection schemes. Thus, if a facility allows the use of specular reflection schemes, diffuse lighting should be preferred to light up the model.

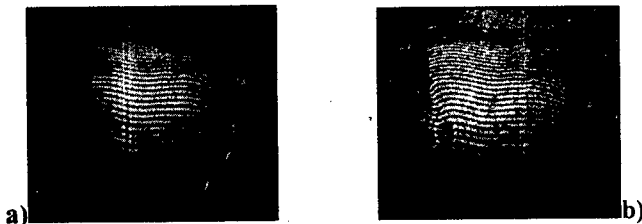


Fig. 4. Oil drop interference fringes. a)- diffuse lighting; b)- specular reflection scheme.

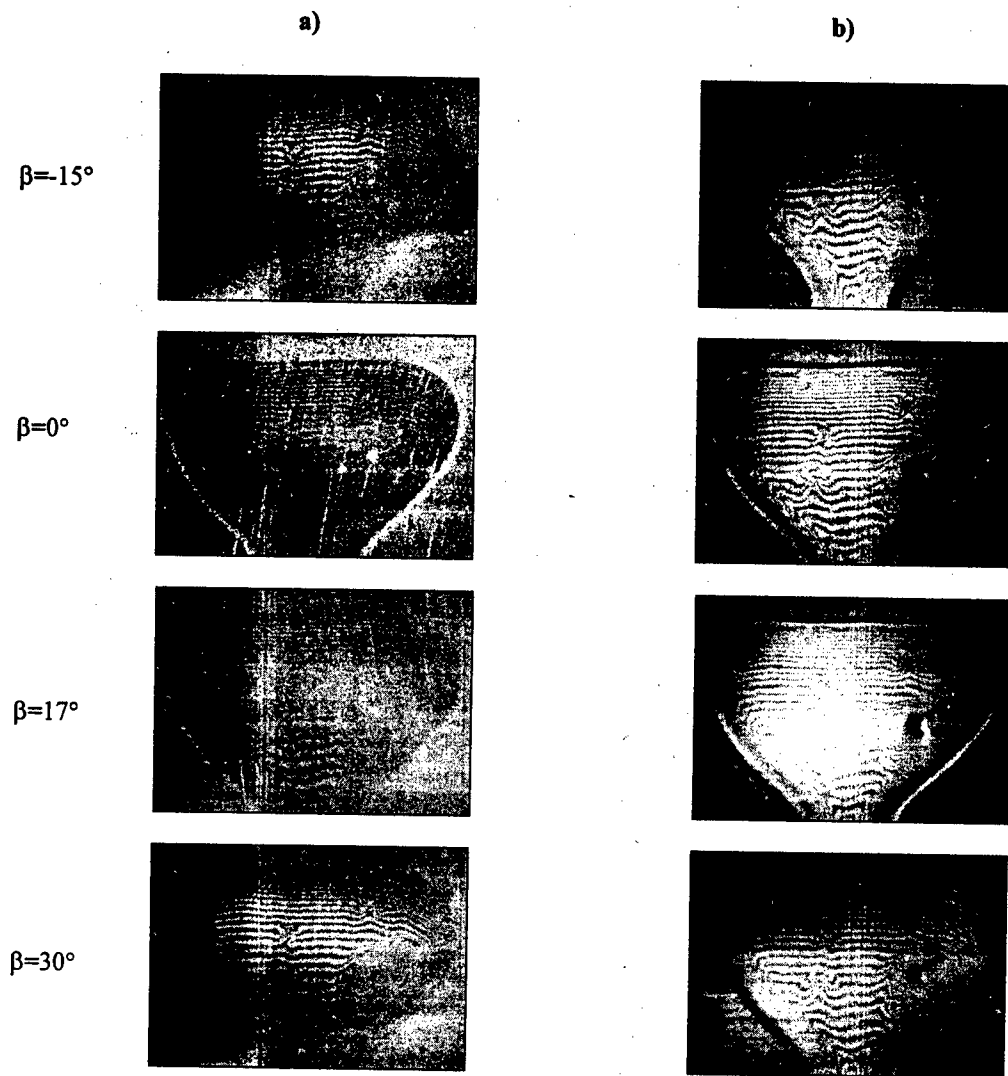


Fig. 5. The images of the oil drop modulated by equal thickness interference fringes. a)- internal diffuse lighting; b)- external diffuse lighting.

Figure 3c) shows a scheme for internal diffuse light. It allows an arbitrary surface curvature and an arbitrary position of detecting optics 4. However, the scattered light 6 has a lower intensity than specular reflected light, thus providing a weaker signal at the photodetector (a CCD camera in our case)

Figure 5 presents the fringe patterns of an oil droplet placed on a copper plate previously used for skin friction measurements with the use of specular reflection optical scheme Kornilov (1992). In the case of internal diffuse lighting (fig. 5a), the light diffusion was provided by cupric oxide arised on the model surface. It can be seen that the type of fringe patterns does not depend on the type of lighting: internal (fig. 5a) or external (fig. 5b).

When using the internal lighting, the setup was not changed except for the angle β . It proved a possibility of obtaining fringe patterns on arbitrarily oriented and curved surfaces; but due to a weaker signal at the CCD camera, the quality of the images obtained is worse than in case 5b. Although a good quality can be obtained with the use of external diffuse lighting, its implementation is more laborious, because each model reorientation requires the optical scheme adjustment: changing the angle β requires changing the angle α to provide specular reflection. Thus, only the internal diffuse lighting can be used if the facility does not allow one to ensure specular reflection (high β angles, curved surfaces).

The results obtained provide conclusive evidence that it is possible to obtain fringe patterns on curved and arbitrary oriented surfaces using both the external and internal diffuse lighting.

2.SKIN FRICTION REGISTRATION AT HIGH SPEEDS

A possibility of skin friction registration on curved and arbitrarily oriented surfaces at supersonic speeds was shown experimentally. The measurements were taken on cone and cylinder models. Since these models are bodies of revolution and they were tested at zero incidence, there was no need to have the oil-film visualisation of the limiting streamlines. Their positions were determined from the model geometry.

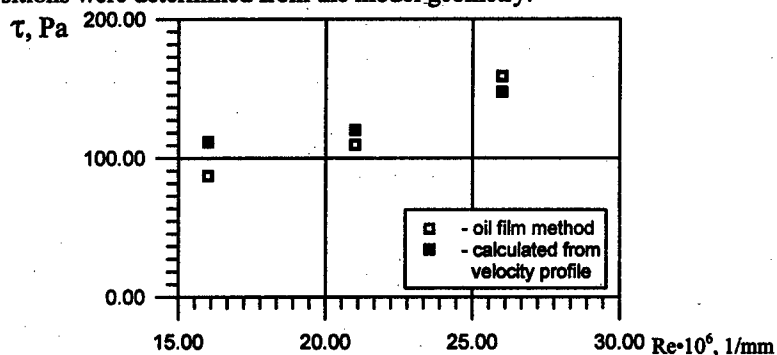


Fig. 6. The results of skin friction measurements on a cone ($q=15^\circ$) for different values of the Reynolds number.

Figure 6 shows the results of skin friction measurements on a cone ($q=15^\circ$) for different values of the Reynolds number. The boundary layer was turbulent in the region of measurements. For comparison, the same figure shows the values calculated from the velocity profile. The q is the angle between the axis of the cone and cone outline. The greater difference in the skin friction values at the $Re=16 \cdot 10^6 M^{-1}$ results from the boundary layer was not completely turbulent.

The results of skin friction measurements ($Re=21 \cdot 10^6 M^{-1}$) by the optical method and those calculated from velocity profiles on a cylinder in the region of laminar-turbulent transition are presented in figure 7. The values obtained by the optical method are in agreement with the typical skin friction distribution in the region of transition of a laminar boundary layer to a turbulent state. This region is of interest because the calculation based on velocity profiles is not always valid, since it requires some preliminary information about the boundary layer state. However, the both methods yield similar results in the region where the boundary layer state is known in advance.

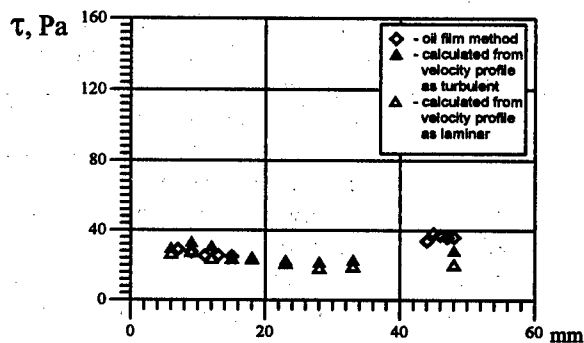


Fig. 7. The results of skin friction measurements ($Re=21 \cdot 10^6 M^{-1}$) by the optical method and those calculated from velocity profiles on a cylinder in the region of laminar-turbulent transition

CONCLUSION

The experiments made showed that it is possible to use diffuse light for skin friction registration on curved at arbitrarily oriented surfaces. The use of external diffuse light allows one to take measurements on curved surfaces but restricts the surface orientation. The use of internal diffuse light allow one to take measurements on surfaces with arbitrary orientation and curvature, which considerably extends the area of application of the optical method of skin friction registration.

REFERENCES

1. Tanner L.H., Blows L.G. A Study of the motion of oil films on surfaces in air flow, with application to the measurement of skin friction // *J. of Physics E., Scientific Instruments*, 1976, No. 9. P. 194-202.
2. Monson D. A nonintrusive laser Interferometer method for measurement of skin friction // *Experiments in Fluids*. 1983. No. 1. P. 15-22.
3. Kornilov V.I., Pavlov A.A., Shpak S.I. On the techniques of skin friction measurement using optical method // *Int. Conf. on the Methods of Aerophysical Research: Proc. Pt 1. Novosibirsk*, 1992.
4. Maksimov A.I., Pavlov A.A., Shevchenko A.M. Development of the skin friction measurement technique for supersonic gradient flows // *Int. Conf. on the Methods of Aerophysical Research: Proc. Pt 2. Novosibirsk*, 1994.

THE RESULTS OF ANALYTICAL AND EXPERIMENTAL INVESTIGATION OF SWIRLING GAS FLOWS

V.S.Politov

Chelyabinsk State University,
454021, Chelyabinsk, Russia.

This work gives a treatment of swirling (rotationally symmetric), steady, potential flow of perfect gas. The given model presents well swirling flow properties with already specified rotary motion of particles about the flow symmetry axis. The cylindrical coordinate system (r, φ, z) with an axis $r = 0$, coinciding with the flow symmetry axis, is used. The set of the Euler of differential and continuity equations on condition that $g \ll V_\varphi^2/r$ forms the basis of the given investigations[1]:

$$\begin{aligned} V_r \frac{\partial V_r}{\partial r} + V_\varphi \frac{\partial V_r}{r \partial \varphi} + V_z \frac{\partial V_r}{\partial z} - \frac{V_\varphi^2}{r} &= -\frac{1}{\rho} \frac{\partial P}{\partial r}, \\ V_r \frac{\partial V_\varphi}{\partial r} + V_\varphi \frac{\partial V_\varphi}{r \partial \varphi} + V_z \frac{\partial V_\varphi}{\partial z} + \frac{V_r V_\varphi}{r} &= -\frac{1}{\rho} \frac{\partial P}{r \partial \varphi}, \\ V_r \frac{\partial V_z}{\partial r} + V_\varphi \frac{\partial V_z}{r \partial \varphi} + V_z \frac{\partial V_z}{\partial z} &= -\frac{1}{\rho} \frac{\partial P}{\partial z}, \\ \frac{1}{r} \frac{\partial(r \rho V_r)}{\partial r} + \frac{\partial(\rho V_\varphi)}{r \partial \varphi} + \frac{\partial(\rho V_z)}{\partial z} &= 0. \end{aligned} \tag{1}$$

Here V_r, V_φ, V_z – velocity projections on the coordinate axes, P – pressure, ρ – mass density, g – acceleration of gravity, V_φ^2/r – centrifugal acceleration.

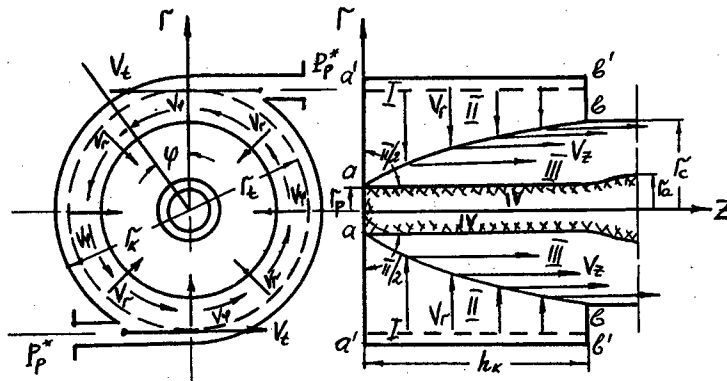


Fig. 1

The kinematic model of the flow under investigation is schematically shown in Fig.1. The rotary motion of gas particles about the flow symmetry axis is organized at the expense of tangential gas inlet into the cylindrical chamber. Its end faces are completely perpendicular to the flow symmetry axis and set a limit to the linear dimension on an altitude h_x . Area I is an annular space, in which axisymmetric rotary and radial motions of particles are formed. This

work fails to give a treatment of the problems of gas flow through tangential channels and area I, because it is generally known in gasdynamics. Further areas II and III follow, in which the axisymmetric rotary motion of gas particles goes well with their radial (V_r) and axial (V_z) motions respectively. The swirling flow through an outlet cylindrical channel of radius r_c is accompanied by conversion of the part of a kinetic energy of axisymmetric rotary motion of gas particles to a kinetic energy of their axial motion [2]. In consequence, cross - section area decreases (Fig.1). It is common knowledge that in the core of swirling incompressible flow there is a gas space (i. e. area IV), which is connected with the gaseous environment [3]. The numerous experiments in see-through models, which are similar to the schematically shown in Fig.1, under various combinations of geometrical parameters, including h_k , have shown that the angle of the end wall a'-a' with the boundary cylindrical surface of swirling incompressible flow is constantly equal to π_2 . This is established by experiment, that ingress of driven flow from the gaseous environment into area IV constantly occurs. It should be noted that swirling flow of area III acts as a driving gas flow. This work fails to give a treatment of the ejection process. By experiment it have been achieved by substitution of area IV for the central body of dimensions, corresponding to geometrical parameters of area IV [4].

By rearranging, we reduce the Euler equations (1) to the Gromeka - Lamb equations obviously involving the rotation components $\omega_r = \frac{\partial V_z}{r \partial \varphi} - \frac{\partial V_\varphi}{\partial z}$, $\omega_\varphi = \frac{\partial V_r}{\partial z} - \frac{\partial V_z}{\partial r}$,

$\omega_z = \frac{1}{r} \frac{\partial(V_\varphi r)}{\partial r} - \frac{\partial V_r}{r \partial \varphi}$. It is known that $\omega_r = \omega_\varphi = \omega_z = 0$ holds true for potential flows.

Besides, by virtue of the condition that $\partial / \partial \varphi = 0$ for the axisymmetric flow, we have

$\frac{\partial V_r}{r \partial \varphi} = \frac{\partial V_\varphi}{r \partial \varphi} = \frac{\partial V_z}{r \partial \varphi} = 0$. In consequence, $V_r(\varphi) = \text{Const}$, $V_\varphi(\varphi) = \text{Const}$, $V_z(\varphi) = \text{Const}$. In

so doing from the first and the third equalities we get $\partial(V_\varphi r) / \partial r = 0$ and $\partial V_\varphi / \partial z = 0$.

From this it follows that $V_\varphi(z) = \text{Const}$ and $\Gamma / 2\pi = V_\varphi r = \text{Const}$. The latter is generally

known in hydrodynamics of swirling flows as a relation which defines the rotary motion of particles about the flow symmetry axis by law of constant velocity circulation. The given relationships were verified by experiment [4]. The equality for ω_φ is noteworthy and presents

one of the generalities of swirling flow. In projection on the meridian plane rz (Fig.1), swirling flow may be considered as an analogue of clean flow inside the right angle, which is characterized by decrease in $V_r(z)$ and increase in $V_z(r)$ [1]. If $\partial V_r / \partial z = \partial V_z / \partial r \neq 0$, then the

signs on the derivatives are the same and swirling flow under desired condition will not be realized. The second variant of the equality of the same derivatives $\partial V_r / \partial z = \partial V_z / \partial r = 0$ is

satisfied, if $V_r(z) = \text{Const}$ and $V_z(r) = \text{Const}$. It holds true, when $V_{z2} = 0$ in area II and

$V_{r3} = 0$ in area III. From this it follows that in potential swirling liquid and gas flows the

change from the radial (V_r) motion of particles to their axial (V_z) motion takes place at conjugation points of the given flows on condition that $V_z \perp V_r$ (Fig.1). As follows from the

continuity equation (1) in swirling incompressible flow $V_r = \text{Const} / r$ and $V_z(z) = \text{Const}$. One

may assume that the given relationships hold true for swirling gas flows, too. Thus, the velocity components $V_r = f(r)$ and $V_\varphi = f(r)$ increase towards the core of flow hyperbolically.

In all other respects the velocity components V_r, V_ϕ, V_z as the coordinate functions are constant.

As follows from the flow line differential equation $dr / V_r = r d\phi / V_\phi = dz / V_z$ the flow lines are logarithmic spirals ($dr / r = V_r d\phi / V_\phi$) in area II and helical lines ($dz = V_z r d\phi / V_\phi$) in area III. The given swirling potential flows are known in mechanics of fluids [5]. The equation $dz = V_z dr / V_r$ is a differential equation for conjugation line in the plane of rz . It is shown as the line a'-b' in Fig.1. In space of swirling flow they form the parabolic surface of revolution. It needs to be considered as a conjugation surface of radial (V_r) and axial (V_z) swirling flows. It is a locus of singular points, which are among areas II and III.

Basically, the gasdynamic model of swirling flow reduces to the differential equation system, which we have obtained from (1) subject to the kinematic conditions cited above:

$$\begin{array}{l}
 \text{Area II} \\
 V_r \frac{\partial V_r}{\partial r} - \frac{V_\phi^2}{r} = -\frac{1}{\rho} \frac{\partial P}{\partial r}, \\
 \frac{\partial V_\phi}{\partial r} + \frac{V_\phi}{r} = 0, \\
 \frac{\partial \rho}{\rho} + \frac{\partial V_r}{V_r} + \frac{\partial r}{r} = 0.
 \end{array}
 \qquad
 \begin{array}{l}
 \text{Area III} \\
 \frac{V_\phi^2}{r} = \frac{1}{\rho} \frac{\partial P}{\partial r}, \\
 \frac{\partial V_\phi}{\partial r} + \frac{V_\phi}{r} = 0, \\
 V_z \frac{\partial V_z}{\partial z} = -\frac{1}{\rho} \frac{\partial P}{\partial z}, \\
 \rho \frac{\partial V_z}{\partial z} + V_z \frac{\partial \rho}{\partial z} = 0
 \end{array}
 \quad (2)$$

Multiplying the first equation for area II through by dr and using the second equation, we get the Bernoulli equation in differential form $dP / \rho + V_r dV_r + V_\phi dV_\phi = 0$. And multiplying the first equation for area III by dr and the third equation by dz and subtracting one from other, we get the following equality $V_z dV_z - V_\phi^2 dr / r = -dP / \rho$. Considering it in the planes which are orthogonal to the z - axis and for which the change only in V_ϕ with the r -coordinate is characteristic, we get the radial equilibrium equation of gas particles in area III: $dP = \rho V_\phi^2 dr / r$. In so doing from the last equality it follows that $dV_z = 0$ and $V_z(z) = \text{Const}$. Using the second equation in the given equality, we get $dP / \rho + V_z dV_z + V_\phi dV_\phi = 0$ - the Bernoulli equation in differential form for area III.

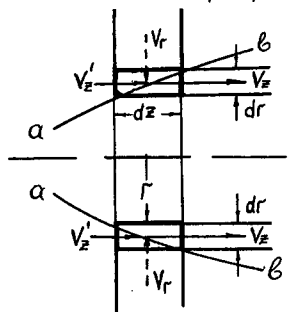


Fig.2

In area II we put emphasis on the flat annular stream filament of altitude dz . It is bounded by two flat stream surfaces which are orthogonal to the z - axis and are formed by flow lines - logarithmic spirals (Fig.2). During motion of gas particles in area II towards the core of flow they cannot pass through the conjugation surface in the r - direction. In accordance with condition of radial equilibrium of particles and $V_r = 0$ for area III they can pass through the conjugation surface only in the z - direction. In consequence, in area III the annular cylindrical stream filament of thickness dr , to the flat annular stream filament of area II corresponds. It is bounded by two cylindrical stream surfaces of

radii r and $r + dr$, which are formed by helical flow lines (Fig.2). During conjugation of the foregoing stream filaments the annular cylindrical filament of altitude dz and with $dF = 2\pi r dr$ as constant normal-section area is formed. One may assume that in passing through the conjugation surface gas particles constituting the given filament are characterized by three components of velocity V_r, V_ϕ, V_z on condition that $V_\phi(z) = Const$. The momentum equation in hydrodynamic form may not be applied to the similar filament, the finite dimensions of which are $2\pi r \Delta r \Delta z$. The condition $V_z \perp V_r$ is the cause of it. The momentum equation may be applied only on condition that the filament shrinks to the sizes of gas particles and on the assumption that the velocity component V_r is transformed in the process into the perpendicular to V_r and equal to it in absolute value velocity component $V_z', V_z' \perp V_r$ and $|V_z'| = |V_r|$ (Fig.2 and Fig.3). Here the centres of mass of particles of the given filament lie at

singular points which constitute the conjugation surface and are among areas II and III. Thus, by analogy with the application of the momentum equation for the rectilinear filament with uniform section at the infinitesimal distance dz between control surfaces, to the problem in question the application of the momentum equation in differential form is legitimate. The last is easily transformed to the Bernoulli equation in differential form. The given transformation is expedient to do in view of the condition $V_\phi(z) = Const$. In the final analysis, as applied to the annular cylindrical filament $2\pi r dr dz$ we get the following Bernoulli equation in differential form $dP / \rho + d(V^2 / 2) = 0$. Here V^2 in areas II and III has the calculated values for $V_2^2 = V_r^2 + V_\phi^2 = V_z'^2 + V_\phi^2$ and

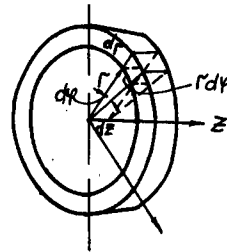


Fig.3

$V_3^2 = V_z^2 + V_\phi^2$ respectively. In consequence, come to the conclusion that gaseous state variables in passing through the conjugation surface by its particles vary as the ideal adiabat $P / \rho^k = Const$, $P_r / P_z = (\rho_r / \rho_z)^k$. Here P_r and P_z - pressures, ρ_r and ρ_z - densities in the areas II and III respectively, k - adiabatic exponent. Under condition that $P / \rho^k = Const$ the last differential equation integrates between the limits from P_r to P_z and between V_2 and V_3 respectively to the Bernoulli equation (the energy equation in mechanical form) for swirling perfect gas flow

$$\frac{k}{k-1} \frac{P_r}{\rho_r} + \frac{V_r^2}{2} + \frac{V_\phi^2}{2} = \frac{k}{k-1} \frac{P_z}{\rho_z} + \frac{V_z^2}{2} + \frac{V_\phi^2}{2} = C, \quad (3)$$

Here the constant C has one and only one value at all points of swirling flow. If $V_r = V_\phi = V_z = 0$, then $C = \frac{k}{k-1} \frac{P_p^*}{\rho_p^*} = \frac{k}{k-1} RT_p^*$. Here P_p^* - Pitot pressure. ρ_p^* - stagnation

density, T_p^* - potential stagnation temperature, R - gas constant.

Solving the equation (3) for state variables in view of expressions for reduced velocities $\lambda_r^* = V_r / a_{kp}^*$, $\lambda_\phi^* = V_\phi / a_{kp}^*$, $\lambda_z^* = V_z / a_{kp}^*$ and for critical sonic speed

$a_{kp}^* = \sqrt{k \frac{2}{k+1} RT_p^*}$, the equations of state $P_r / \rho_r = RT_r$, $P_z / \rho_z = RT_z$, $P_p^* / \rho_p^* = RT_p^*$,

and the following adiabatic relations $\frac{P_r}{P} = \left(\frac{T^*}{T}\right)^{\frac{k}{k-1}}$ and $\frac{\rho^*}{\rho} = \left(\frac{T^*}{T}\right)^{\frac{1}{k-1}}$, by a number of

simple manipulations, we get the following equalities for swirling gas flow through areas II and III:

$$\begin{aligned} T_r &= T_p^* \left(1 - \frac{k-1}{k+1} \lambda_r^{*2} - \frac{k-1}{k+1} \lambda_\phi^{*2}\right), & T_z &= T_p^* \left(1 - \frac{k-1}{k+1} \lambda_z^{*2} - \frac{k-1}{k+1} \lambda_\phi^{*2}\right), \\ \rho_r &= \rho_p^* \left(1 - \frac{k-1}{k+1} \lambda_r^{*2} - \frac{k-1}{k+1} \lambda_\phi^{*2}\right)^{\frac{1}{k-1}}, & \rho_z &= \rho_p^* \left(1 - \frac{k-1}{k+1} \lambda_z^{*2} - \frac{k-1}{k+1} \lambda_\phi^{*2}\right)^{\frac{1}{k-1}}, \\ P_r &= P_p^* \left(1 - \frac{k-1}{k+1} \lambda_r^{*2} - \frac{k-1}{k+1} \lambda_\phi^{*2}\right)^{\frac{k}{k-1}}, & P_z &= P_p^* \left(1 - \frac{k-1}{k+1} \lambda_z^{*2} - \frac{k-1}{k+1} \lambda_\phi^{*2}\right)^{\frac{k}{k-1}}. \end{aligned} \quad (4)$$

From the results of investigations of discharge characteristics of swirling liquid and gas flows [6] on condition that $h_k > (r_c^2 - r_p^2) / 2r_p$ it follows that, $V_r < V_z$ at all points of the conjugation surface, including points of the circle of radius r_p in section a-a (Fig.1). In the final analysis, we come to the conclusion that velocity variable of motion and gaseous state variable as functions of space points, in which swirling flow occurs, have a discontinuity at points of the conjugation surface. In the process velocity abruptly increases while pressure, density and temperature abruptly decrease. By analogy with the gas supersonic shock the conjugation surface of subsonic swirling gas flows should be considered an expansion - shock surface. It is evident that by the given analogy the expansion - shock-front thickness is com-

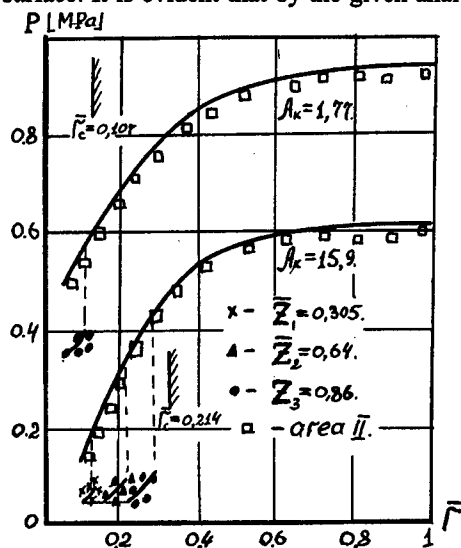


Fig.4

measurable with free path length of molecules. Unlike shock, in passing through an expansion - shock front by gas particles the entropy remains constant $S = C_v \ln(P / \rho^k) = \text{Const}$ (C_v - heat capacity at constant volume). It is advisable to evaluate the expansion - shock intensity in Pl numbers: $Pl_v = V_2 / V_3$, $Pl_{v_{rz}} = V_r / V_z$, $Pl_p = P_r / P_z$, $Pl_\rho = \rho_r / \rho_z$, $Pl_T = T_r / T_z$.

The formation of expansion shock in subsonic swirling gas flows is verified by experiment. The accompanying calculation and experimental data (Fig.4) are a distribution in static pressure (P_r and P_z) across swirling air flow. The experimental results were obtained by air blow of model chambers, which are similar to the shown one in Fig.1.[7]. Pressures and velocity components are indicated by a 6-hole Pitot probe [8]. At the points of areas II and III

the pressures have been determined at different values of $\bar{r} = r / r_t$, $\bar{z} = z / h_k$ and a geometrical chamber parameter $A_k = F_c / F_t$. Here r and z — current position of points, at which the static pressures were determined; r_t — reference radius of swirling flow; F_c —outlet channel area, F_t — total area of tangential channels. The calculated values for P_r and P_z have been determined by means of the system of equations (4). As follows from plots the experimental data check with calculations well enough. The curve denoting the firm line represents the calculated values for P_r in area II. As follows from the experimental data for $\bar{r}_p < \bar{r} < \bar{r}_c$ and defined values of z , static pressure decreases abruptly, $P_r > P_z$ (lower test points and dot lines fall in area III). The limiting left points of the curves correspond to the values for P_r and P_z ($P_r > P_z$) on the end wall, $\bar{z} = 0$.

References

1. Kochin N.Ye., Kibel I.A., Rose N.V. Theoretical hydromechanics. – Moscow, 1963.
2. Politov V.S. Kinetic energy conversion due to axisymmetric rotation of liquid and gas flows to a dynamic head due to translation // Theses of papers of All- Union seminar school on microscopic kinetics, chemical and magnetogas dynamics. – Tomsk–Krasnoyarsk, 1991 – p.p.51– 52.
3. Abramovich G.N. Applied gas dynamics. – Moscow, 1953.
4. Golovin A.G., Politov V.S. Some questions in swirling flow gas dynamics // Some questions of vortex effect investigation and its industrial application. –Kuibyshev, 1974 – p.p. 197–200.
5. Milovich A.Ya. The principles of fluid dynamics. – Moscow – Leningrad, 1933
6. Politov V.S. Discharge of swirling incompressible flow from cylindrical channel// Dynamics of three - dimensional and non- equilibrium liquid and gas flows – Chelyabinsk– Miass, 1992 p.p.248 – 258.
7. Gorshenin V.F., Zaikovski V.N., Zaulichny Ye.G., Politov V.S. Experimental investigation concerning the gas dynamics of high-speed vortex chambers // Wall jet flows. –Academy of sciences of the USSR. Siberian branch, Thermophysics Institute. 1984 – p.p.59 – 65.
8. Gorshenin V.F., Zaikovski V.N. Six- hole Pitot probe for investigation of high-speed three- dimensional flows // Mechanics of high-speed process. Tomsk University, 1989– p.3 –9.

TURBULENT CHEMICAL REACTING GASES FLOWS THROUGH CURVED SMOOTH WALL CHANNELS

B.V. Rogov *, I.A. Sokolova **

* Institute for High Temperatures of Russian Academy of Science
127412, Moscow, Russia

** Institute for Mathematical Modeling of Russian Academy of Science
127047, Moscow, Russia

1. Introduction

One of the important problem of computational gasdynamic is the numerical calculation of turbulent chemical-reacting viscous flows on the base of full system of Navier-Stokes (NS) equations. Numerical methods for such flows are very complicated and require very much resources, especially in the case of 3D and 2D geometry of channel. The well-known numerical procedures consume a large amount of computer time, which is growing up immensely as the number of chemical nonequilibrium reactions increases [1]. For efficient solving the problem it is necessary to derive accurate simplified gasdynamic equations and work out fast algorithms with controlled accuracy. The objects of this work are: (1) the simplification of the full NS equations for internal turbulent burning viscous flows to 2D parabolic form by neglecting all the small terms of order $1/Re$ and keeping all the terms of higher order. This is in case of the variable cross section channel and the curved wall; (2) the improvement of algorithm and numerical methods providing fast calculation for both subsonic and supersonic flow regimes in nozzle; (3) derivation of the controlled accuracy in numerical computation of the critical mass flow; (4) the numerical investigations of burning mixture in turbulent flow through Laval Nozzle.

2. Simplification of NS in the Adapted Coordinates

We will assume turbulent chemical reacting viscous gas flows through channel with a smooth curve wall without large-scale vorticity .

The progressive simplification of the full NS equations is possible in relevant system of coordinates fitted to the boundaries of channel. The simplified equations for laminar flow through channel with variable cross section (Smooth Channel Approximation (SmC)) have been proposed in works [2,3]. The model is based on the curvilinear orthogonal system of coordinates

$$\xi = \xi(x, y), \quad \eta = y/y_w(x), \quad \zeta = \varphi,$$

adapted to the wall shape and then simplifying the whole sistem of NS gasdynamic equations in the adapted coordinates.

The curvilinear co-ordinates are derived from the differential equation of partial derivatives of first order, which is consequence of the orthogonality condition. The main feature of the curvilinear co-ordinates is that the lines are closed to the streamlines of

The work is supported by RFBR, project No. 97-01-00005.

flow, and in the simplest cases they coincide with them (we assume the wall shape of channel as a smooth curve without breaks); parameter v/u is a small one (v is the transversal velocity, u is the longitudinal velocity in curvilinear coordinates). For all that the transformation from the Cartesian coordinates to curvilinear ones and back can be performed before the whole gasdynamic equations calculation.

The hydrodynamic equations in adapted coordinates system are simplified by neglecting all small terms of order $1/Re$ and keeping on all the terms of higher order. They are fitted asymptotically in the two cases: (1) $Re_l \gg 1$, $r_0/l_0 \sim v_0/u_0 \sim \text{tg}\alpha_w \ll 1$; and (2) $Re_r \gg 1$, $r_0/l_0 \sim \text{tg}\alpha_w \sim 1$, $v_0/u_0 \ll 1$, where $Re_l = \rho_0 u_0 l_0 / \mu_0$ is the Reynolds number constructed by a longitudinal specific size l_0 , $Re_r = \rho_0 u_0 r_0 / \mu_0$ is the Reynolds number constructed by a transversal specific size r_0 , u and v are the velocity projections on the ξ and η axis correspondingly, ρ is the mass density, μ is the dynamic molecular viscosity of mixture. Subscript "o" refers to the specific dimensional values. (The intrinsic condition $v_0/u_0 \ll 1$ due to adapted curvilinear coordinates, means that the streamlines are closed to the coordinate lines $\xi = \text{const}$)

3. The Simplified Equations System

Taking into account the dimensionless streamline function Ψ the resulted simplified equations SmC for averaged gasdynamic characteristic are the following (the bar of mean is omitted).

The equation for impulse

$$\frac{\partial}{\partial \xi} \left(u \frac{\partial \Psi}{\partial \eta} \right) - \frac{\partial}{\partial \eta} \left(u \frac{\partial \Psi}{\partial \xi} \right) - \frac{1}{Re_r} \left\{ \frac{\partial}{\partial \eta} \left[y^\nu H_\xi \frac{\mu_{eff}}{H_\eta} \left(\frac{\partial u}{\partial \eta} + \beta u \right) \right] - \beta y^\nu H_\xi \frac{\mu_{eff}}{H_\eta} \left(\frac{\partial u}{\partial \eta} + \beta u \right) \right\} + \beta u \frac{\partial \Psi}{\partial \xi} + \frac{1}{\gamma} y^\nu H_\eta \frac{\partial p}{\partial \xi} = 0, \quad \Psi = \int_0^\eta \rho u y^\nu H_\eta d\eta_b \quad (1)$$

The equation of pressure

$$\frac{\partial p}{\partial \eta} + \beta \gamma \rho u^2 = 0, \quad (2)$$

The equation of energy

$$\frac{\partial}{\partial \xi} \left(H \frac{\partial \Psi}{\partial \eta} \right) - \frac{\partial}{\partial \eta} \left(H \frac{\partial \Psi}{\partial \xi} \right) - \frac{1}{Re_r} \frac{\partial}{\partial \eta} \left\{ y^\nu H_\xi \left[\frac{1}{Pr} \frac{\lambda_{eff}}{H_\eta} \frac{\partial T}{\partial \eta} - \sum_{j=1}^N \frac{1}{Sc_j} h_j J_{j\eta} + (\gamma - 1) \frac{\mu_{eff}}{H_\eta} u \left(\frac{\partial u}{\partial \eta} + \beta u \right) \right] \right\} = 0, \quad (3)$$

$$H = h/m + (\gamma - 1)u^2/2, \quad h = \sum_{j=1}^N x_j h_j, \quad m = \sum_{j=1}^N x_j m_j$$

The equation for molar fractions ($x_i, i=1, \dots, N$):

$$\frac{\partial}{\partial \xi} \left(\frac{x_j}{m} \frac{\partial \Psi}{\partial \eta} \right) - \frac{\partial}{\partial \eta} \left(\frac{x_j}{m} \frac{\partial \Psi}{\partial \xi} \right) + \frac{1}{\text{Re}_r \text{Sc}_j} \frac{\partial}{\partial \eta} (y^\nu H_\xi J_{jn}) - y^\nu H_\xi H_\eta \sum_{s=1}^K (v''_{sj} - v'_{sj}) \text{Da}_s k'_s n^{v_s} \left(\prod_{k=1}^N x_k^{v_k} - p^{v_s - v'_s} K_{ps} \prod_{k=1}^N x_k^{v'_k} \right) = 0, \quad (4)$$

$$v'_s = \sum_{j=1}^N v'_{sj}, \quad v''_s = \sum_{j=1}^N v''_{sj}$$

where Ψ complies with the following equations

$$\frac{\partial \Psi}{\partial \eta} = y^\nu H_\eta \rho u, \quad \frac{\partial \Psi}{\partial \xi} = -y^\nu H_\xi \rho v. \quad (5)$$

Here H_ξ, H_η, H_ζ are the Lamé coefficients; H is the whole specific enthalpy of mixture; p is the pressure; x_i is the molar fraction of the i th component; Pr is Prandtl number; Sc_j is the Schmidt number; K_{ps} is the constant of chemical equilibrium; Da_s is the Damköhler number; k_r is the chemical reaction constant; \tilde{J}_η is the physical component of diffusion flow vector \tilde{J} ; $v'_{s,i}$ and $v''_{s,i}$ are the stoichiometric coefficients. β is the parameter of geometry

$$\beta = H_\eta / R_\eta,$$

where R_η is the curvature radius of transversal co-ordinate line $\eta = \text{const}$. R_η coincides with the curvature radius of wall R_w on the wall of channel and with the curvature radius of axis R_{sl} on the axis of channel.

For turbulent transport the Sebis-Smith model is taken. In the interior domain of boundary layer the turbulent viscosity μ_t is calculated in dimensionless form as follows

$$\mu_{t,i} = \text{Re}_r \rho l^2 \frac{\eta}{H_\eta} \left| \frac{\partial u}{\partial \eta} \right|, \quad l = \kappa n \left[1 - \exp \left(- \frac{n^+}{A^+} \sqrt{\frac{\rho_w}{\rho}} \right) \right], \quad (6)$$

$$n = \int_\eta^1 H_\eta d\eta, \quad n^+ = n \sqrt{\text{Re}_r} \frac{\rho}{\mu} \left(\frac{\mu}{\rho} \frac{1}{H_\eta} \left| \frac{\partial u}{\partial \eta} \right| \right)_w^{1/2}, \quad \kappa = 0.4, \quad A^+ = 26$$

and in the exterior domain as

$$\mu_{t,o} = \alpha_i \text{Re}_r \rho \left| \int_0^1 (u_{sl} - u) \eta H_\eta d\eta \right|, \quad \alpha_i = 0.0168. \quad (7)$$

Here index i and o refers to interior and exterior domains of boundary layer; w refers to values on the wall ($\eta = 1$) and sl to the value on the axis of nozzle ($\eta = 0$). And we had transformed the integral in Eq. (7), taking the displacement width of boundary layer as the following

$$\mu_{t,o} = \alpha_i \text{Re}_r \rho \int_\eta^1 (u_e - u) \eta H_\eta d\eta,$$

where η_e and u_e are the values of η and u on the exterior line of boundary layer. They can be derived from condition of the proximity of two terms of equation (1), which responsible for convective and viscous impulse transfer, or from the condition of proximity of the local Reynolds Re_{loc} to the unity

$$Re_{loc} = Re_r \frac{\rho v}{\mu_{ro}} \left(\frac{1}{H_\eta} \frac{\partial \ln u}{\partial \eta} \right)^{-1} \cong 1. \quad (8)$$

The numerical calculations show identical results of using the two equations in the case of monotonous profile of velocity (in the area of throat of nozzle).

The turbulent thermoconductivity is calculated in the same manner.

4. Direct Task of Laval Nozzle

We consider a steady-state turbulent flow of viscous, thermal conducting chemical reacting gases through axially symmetric nozzle (see fig.1, where the solid line is the dimensionless profile of nozzle, 0 is the axis of nozzle). As well known, the critical mass consumption while computing viscous flow through Laval nozzle is a specific difficulty of numerical calculations [2]. At the present time the theorems of uniqueness and existence had been proof for simplified equations of parabolic type (such as SmC equations). Principally, the critical mass consumption may be computed. Here the new algorithm and numerical method is offered.

As assumed axial symmetric flow in Laval nozzle, the system of gasdynamic equations for numerical calculation is added by the conditions on the symmetry line $\eta = 0$. The boundary conditions of first genus $u = 0$ and $T = T_w$ are taken on the wall. The flow field calculations is confined by the solid wall, the symmetry line and the line of channel entrance. The velocity and temperature profiles u/u_{s1} and T/T_{s1} are taken at $\xi=0$. The boundary conditions defined by the such manner are correct.

The gasdynamic equations are closed by equation of state $p=nkT$ and equation of mass consumption through channel

$$\frac{\partial \Psi(\xi,1)}{\partial \xi} = 0 \quad \text{or} \quad \Psi_w = \frac{1}{2} Q = const.$$

Here Q is the dimensionless mass consumption with scale number $\pi r_o^2 \rho_o u_o$.

The object of direct problem of Laval nozzle is the computation of critical mass flow.

5. Numerical Method

5.1. Marching Method I

The ordinary used marching methods to computing internal steady-state flows as parabolic type equations face with obstacle due to a singularity in transonic area. To provide calculation of the critical mass consumption Q_{cr} with control accuracy we modify the finite-difference scheme of Petukhov [4], which is fourth order approximation over lateral coordinate η , and second order over longitudinal coordinate ξ . The longitudinal velocity, temperature and pressure gradient are calculated simultaneously at the very characteristic $\xi = const$. The main difference from the Petukhov's scheme [4] is the other approximation of derivatives with respect to longitudinal coordinate. As Petukhov's scheme: $\hat{\xi} = (\xi^+ + \xi^-) / 2$; our is as follows

$$(\partial a / \partial \xi)^+ = 2(a^+ - \tilde{a}^-) / \Delta \xi, \quad \tilde{a}^- = a^- + 1/2(\partial a / \partial \xi)^- \Delta \xi.$$

The finite difference equations for u , T and molar fractions of species are calculated by vector sweep method. In order to provide convergence while calculating the finite difference equations, the special equations for pressure and its gradient are deduced.

The dimensional pressure distribution $p=p(\xi, \eta)$ is derived in terms of the longitudinal axis pressure $p_{sl}(\xi)$

$$p = p_{sl}(\xi)\alpha(\xi, \eta), \quad \alpha = \exp\left(-\gamma \int_0^\eta \beta m \frac{u^2}{T} d\eta\right)$$

and equation for axial pressure is written in terms of Q (mass consumption)

$$p_{sl} = \frac{1}{2} Q / \int_0^1 \alpha m \frac{u}{T} y H_\eta d\eta.$$

In the transonic area the pressure and the wall friction coefficient is very sensitive to the value of the critical mass consumption. Our numerical calculation shows the branching of axial pressure, its gradient and wall friction coefficient over corresponding limiting mass consumption Q_{lim} . This branching allows to derive value of the critical mass consumption with controlled accuracy in those numerical grid. In its own turn, the value of the limiting mass flow tends to that of critical mass flow Q_{cr} , as the width of finite-difference grid tends to zero (fig.2)

The marching method I provides calculation the critical mass consumption Q_{cr} with high accuracy. In our case it is of 0.01%.

5.2. Marching Method II

Marching method II is derived for computing flow after the critical cross section of nozzle ($x=0$, fig.1). Now, the prefer-defined critical mass consumption Q_{cr} , and the known profiles u_- , T_- and molar fractions x_{j-} are taken on the preceding characteristic. The global iterations over pressure is added. The initial pressure distribution is taken by special procedure of extrapolation. Then the finite-difference equations for velocity u , temperature T and molar fractions x_j are calculated by marching method I.

6. Numerical Results

The gasdynamic flow of burning hydrogen-oxygen turbulised gas mixture through Laval Nozzle is calculated. Combustion of hydrogen in oxygen is represented by 7 chemical products H_2O , H_2 , H , OH , O_2 , O , HO_2 of 11 chemical nonequilibrium kinetic reactions. On the entrance of nozzle the chemical-equilibrium calculation of combustion in combustion chamber at $p_0 = 210$ bar and $T_0 = 3603$ K are taken. The excess coefficient of oxidation is $\alpha_{ox}=0.756$; the mass density $\rho_0=10.73\text{kg/m}^3$; the molar mass of mixture $m_0=14.61\text{kg/kmol}$; the thermal conductivity at constant pressure $c_{po}=53.34\text{J/mol K}$; the isentropic exponent $\gamma_0=1.185$; the sound velocity $a_0=1558$ m/s; the molecular viscosity $\mu_0=6.53 \times 10^{-5}$ Ps; the molecular thermal conductivity $\lambda_0=0.505\text{W/m K}$; $Pr=0.472$. The chemical frozen compound of mixture (volume fractions) is: H_2O -69.1136%; H_2 -24.6382%; H -2.4881%; OH -3.3530%; O_2 -0.2075%; O -0.1949%; HO_2 -0.0047%. The corresponding Reynolds number $Re_r = 3.162 \times 10^7$.

The resulting critical mass consumption is 0.5476. The Mach number, the heat flux on the wall and the wall friction coefficient are shown in fig.1: solid line (1) is the shape of nozzle,

dotted line (2) is the Mach number, dotted line (3) is the wall friction coefficient and dotted line (4) is the heat flux.

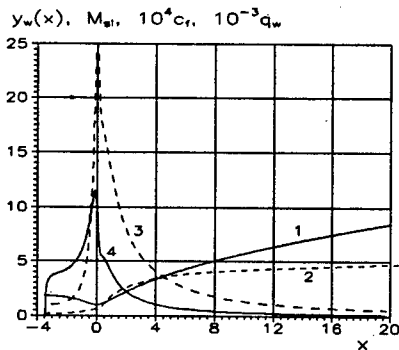


Fig.1

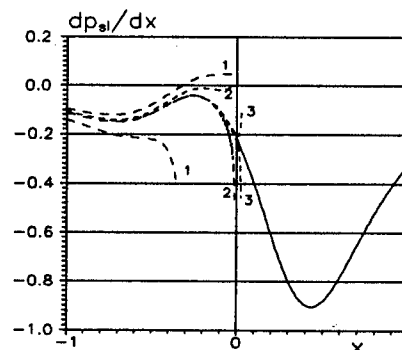


Fig.2

Fig.1. 1 is the shape of nozzle; 2 is the Mach number; 3 is the C_f ; 4 is the q_w .

Fig. 2. The axis pressure gradient dp_{ax}/dx at different Q . Dotted lines are the calculations by the direct marching method I: the lines (1) correspond to values Q which differ in second figure; the lines (2) correspond to values Q which differ in third figure; and so on. The upper lines correspond to the less values of the Q as compared with Q_{crit} ; the lower to the higher ones. The solid line is calculated by the second method II and corresponds to Q_{crit} . $x=0$ refers to the critical cross section

The axis temperature near the critical cross section in two cases of chemical equilibrium and chemical frozen flow is shown in fig.3. As one can see the approach of chemical frozen flow lower the temperature significantly. In the case of chemical frozen the critical flow increases of 2% and equal 0.5587.

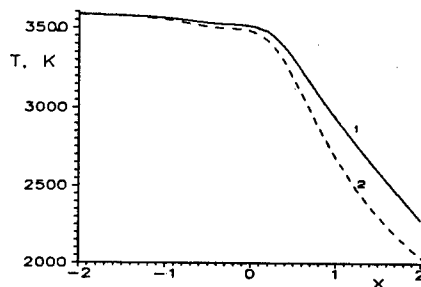


Fig.3.

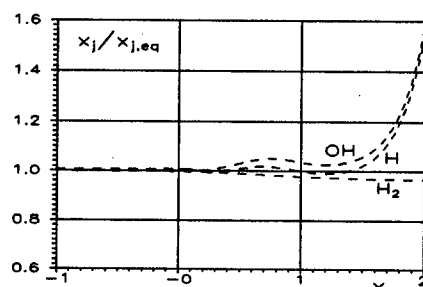


Fig.4.

Fig3. Axis temperature. 1: chemical reacting flow; 2: chemical frozen flow (without heat expulsion)

Fig.4. Mole fractions (on the axis of channel) of species in chemical reacting mixture, referred to the frozen compound mole fractions

The after-burning of hydrogen fuel in supersonic part of the nozzle is shown in and fig. 4. The process of after-burning of hydrogen fuel becomes the best in supersonic part of nozzle.

References

1. Lapin, Yu. V., Streletz, M.H. Internal Flows of gas mixtures. Moscow : Nauka, 1989. 368p.
2. Rogov, B.V., Sokolova, I.A. //Physics-Doklady V.40, N12, 1995. p. 654-657.
3. Rogov, B.V., Sokolova, I.A. Smooth Channel Approximation for Viscous Flows Through Nozzles // Proceedings of ICMAR'96, 1996, part 1, p.180-185.
4. Petuhov, I.B. /Numerical methods of solution of differential and integral equations and quadrature formulae. Moscow Nauka, 1964, p. 304-325

DIRECT MEASUREMENTS OF SKIN FRICTION IN COMPLEX, HIGH-SPEED FLOWS

Joseph A. Schetz

*Aerospace and Ocean Engineering Department
Virginia Polytechnic Institute and State University
Blacksburg, VA 24061*

SUMMARY

This paper describes methods for direct measurement of skin friction in fluid flows under a very wide variety of conditions. The emphasis is on high-speed, high-enthalpy cases. The challenges involved in different flow situations are highlighted, and representative instrument designs and measurement results are presented. The test conditions considered span the range from incompressible to hypersonic speeds; ambient to very high temperature including combusting flows; smooth, rough and porous surfaces with and without injection and test times from 10^{-6} to essentially continuous runs. Our latest efforts involve the use of fiber-optic devices to replace conventional strain gages. Techniques for simultaneous measurements of skin friction, heat flux, surface pressure and surface temperature with the same gage are also discussed.

INTRODUCTION

Accurate measurements of skin friction in fluid flows are important for both assessing the performance of fluid machinery systems or components and building understanding of basic fluid physics phenomena. For example, the so-called "friction velocity" $u_* = (\tau_w/\rho)^{1/2}$ where τ_w is the wall shear and ρ is the density, is the basic scaling quantity for correlating turbulent boundary layer data. These correlations are central to the development of all turbulent transport models.

Before the work of Dhawan [1] reliable skin friction data was obtained in pipe flows where the wall shear can be directly related to the pressure drop, which is easy to measure accurately. Dhawan was the first to successfully measure the small frictional force exerted on a movable element of the surface. A scheme of this type yields what are called "direct" measurements of skin friction. There are also numerous methods for "indirect" measurements of skin friction, but these presuppose some knowledge of the flow such as a correlation or some associating principle. Such methods work for cases where the flows of interest are already well understood, but they are not reliable for complex flows such as 3D and/or unsteady cases, cases with rough walls, curved wall cases, cases with injection or suction, mixing with foreign fluid injection or high-speed flows especially those with high enthalpies or combustion. A good discussion of the available indirect methods can be found in Nitsche *et al* [2]. They will not be considered further here. It is worth noting that the moving wall element, direct methods work equally well for laminar, transitional and turbulent flows; indeed, it is not necessary to know the state of the flow beforehand.

Following Dhawan's initial work, there have been many developments in moving wall element (also called floating head), direct shear measurement devices. A review of work through the mid-70's is given in Winter [3]. Dhawan's device and many of the ones that followed it were quite complicated, and they often required a floating wall element of a rather large size to get sufficient accuracy. We started our work at Virginia Tech [4] using a highly developed design of this type from the Naval Ordnance Lab. That unit had a floating head about 2.5 cm. diameter mounted on a moment arm about 25 cm. long. It featured a weak flexure formed of a wheel with very thin spokes and a feedback system to bring the floating head back to the no-load position

after the wall shear load was applied during the test. It, therefore, had a slow response time on the order of seconds. This kind of arrangement is called a "nulling" type, since the floating head returns to its null position before a measurement is made. In principle, this is important to remove any errors due to tilting of the floating head when the balance is under load and the beam or flexure supporting the head deflects. The whole matter of the errors introduced by tilting, protrusion and/or recession of the floating head has been the subject of careful systematic study, most notably by Allen [5], [6]. He also considered the influence of the size of the gap between the floating head and the surrounding wall. The main result is that these errors can all be kept under reasonable limits by careful design. For reference, under low-speed, laboratory conditions, skin friction values can be measured to about $\pm 3-5\%$. Calibration is usually performed by simply hanging small weights from the head on a thread attached with tape.

For flows with strong streamwise pressure gradients, the gap around the floating head and the whole interior of the gage housing is filled with a liquid, which is contained in place by the strong capillary forces in the small gap. The idea here is to minimize any forces on the floating head or the support arm by a pressure difference. The liquid internal to the gage will simply shift to relieve any pressure difference. The liquid also provides some useful damping of vibrations.

A "non-nulling" type of balance would have obvious advantages of simplicity and improved time response if the deflections could be kept small enough to minimize the tilting of the floating head and still have sufficient strain in the support to yield a measurable output. We were able to develop successful units of the non-nulling type starting in the mid-70's [7] by utilizing semi-conductor strain gages that have an output of about 100 times that of conventional strain gages. For low-speed wind tunnel tests, we used a floating head on the order of 2.5 cm. diameter on a 25 cm. arm, and the streamwise deflection of the head could be limited to a fraction of 1/100 mm. Under these conditions, the tilting of the head is negligible.

We have successfully employed this type of non-nulling gage for complex, low-speed flows on smooth and rough surfaces, curved surfaces and porous surfaces with and without injection [8]-[10]. Injection through the floating head with a porous surface was accomplished by using a support arm made from a tube and feeding the injectant into that tube through rubber tubes that entered from the two sides perpendicular to the external flow direction. This introduced no force component in the direction of the skin friction force as confirmed by experiment.

GAGES FOR HIGH-SPEED FLOWS

Early work on supersonic flows at Virginia Tech [4], [11], [12] was limited to unheated cases, but in the 80's, we turned our attention to hot, high-speed flows for two reasons. First, as the Mach number range increases, one necessarily encounters hot flows. Also, we became interested in supersonic flows with injection of combustible gases such as hydrogen.

Hot flows with attendant high wall heat fluxes immediately raise new issues in the design of skin friction gages. First, one has to be concerned with the simple physical integrity of the gage. Second, the strain gages must be thermally protected to avoid large thermal "drift," especially for semiconductor strain gages. Third, the floating head of the skin friction gage must be maintained at a temperature close to that of the surrounding wall, or the instrument will no longer be non-intrusive to the flow. At the same time, high-speed flows usually have higher wall shears, so the floating head can be made considerably smaller. A design successfully used in a Mach 3 flow with an air total temperature of 1667 K and hydrogen injection and burning from Ref. [13] is shown in Fig. 1. The floating head is made of the same material and thickness as the surrounding wall to match the thermal behavior, and the unit is thermally protected by water cooling around the housing. The liquid filling the housing now plays the important additional role of an efficient heat

transfer medium. The fins on the support arm are for the same purpose. Finally, it is important to note that this gage can measure two, orthogonal components of the wall shear for 3D flows. Designs of this type have proven to be adequate for heat flux values up to about 1000 kW/m².

For very high heat flux values cases, one needs to go to the added complexity of active cooling of the floating head to maintain its temperature near that of the surrounding wall, which is necessarily strongly cooled itself. A gage with such a design from Ref. [14] is shown in Fig. 2; it was successfully employed in tests fully simulating a supersonic combustor at a flight Mach number of about 10-12 ($T_t \approx 4500$ K). The local heat flux was of the order of 2000 kW/m². A typical output is shown in Fig. 3.

Another item of great interest is time response of the skin friction gages, especially for application in so-called "impulse" test facilities like shock tunnels where the test times are 0.5 - 5 msec. This places severe constraints on the gage design problem. One issue, however, becomes less severe - namely thermal protection and surface temperature matching. For such short run times, the surfaces hardly have time to respond to the heat flux, even for surprisingly high heat flux values. The main challenges are first, of course, frequency response itself and second the effects of acceleration loads. We have developed [15] the conceptually simple design shown in Fig. 4 that meets the needs of this kind of testing. The idea is to use a light material (a high-temperature plastic) so that the mass of the system is very low, and the acceleration forces are negligible compared to those from the wall shear. Also, the plastic material has favorable mechanical properties that permit designing a gage with both a high natural frequency (~ 10 's kHz) and a measurable strain resulting from the wall shear. Finally, the plastic has a low thermal conductivity which protects the strain gages from the heat.

We have tried replacing the liquid in the gage housing with a silicone rubber compound to ease the practical problem of frequent checking and refilling of the liquid. The results to date have been generally favorable. The positive result is that useful skin friction data can be obtained free of the oil checking and refilling matter. On the other hand, the rubber fill carries some of the load, so the gage must be redesigned to maintain the same sensitivity. Also, the gap size has to be increased substantially, or the loss in sensitivity is severe. This leads to a situation where some of the surface shear force acting on the exposed rubber is transmitted to the gage beam. In that case, the gage cannot be calibrated by simply hanging a weight from the head. One needs a flow facility producing a known shear force. We have been using a rig with fully-developed flow of glycerine through a narrow, 2D gap. The design of rubber-filled gages requires the use of detailed finite-element method analyses. Also, we have begun to investigate the use of gels to replace oil or rubber as a fill material.

The direct measurement of wall heat flux is of great engineering interest in its own right, and we have been working on gages which combine skin friction and heat flux measurements to be made simultaneously at the same location using a single gage. To date, we have successfully demonstrated such a gage in an unheated supersonic flow at Mach 2.4 [16]. The heat flux gage consists of two, thin layers of thermocouples separated by a very thin layer of insulation to form a thermal resistance all sputtered directly on to the floating head of a skin friction balance. That arrangement has worked well, and we intend to extend these methods to hot, high-speed flows.

At this point, we are concentrating on applying fiber optics to replace the strain gages in our earlier skin friction gage designs. In general, optical fibers offer several advantages: 1) immunity to electromagnetic interference, 2) avoidance of ground loops, 3) the capability to respond to different measurands, 4) excellent resolution, 5) avoidance of sparks, and 6) operation at temperatures of 800 C for silica waveguides and 1900 C for sapphire waveguides. The basic fiber-optic strain sensor is based on the extrinsic Fabry-Perot interferometer (EFPI) which was first proposed and demonstrated as a strain sensor by Murphy and co-workers [17]. Figure 5 shows

a single-mode silica fiber transmitting light from a laser diode to the sensor element. At the opposite end of the input fiber, the laser light is partially reflected off the polished end and partially transmitted across a small gap separating the input fiber and an output fiber which serves only as a reflector. The two signals R_1 and R_2 interfere and propagate back to a photodiode detector. Very small changes in the separation distance, s , between the surfaces of the two fibers produce a modulation of the output signal current.

The basic idea behind the EFPI sensor has been applied to the skin friction gage shown in Fig. 6. This gage has been successfully tested in the Virginia Tech supersonic wind tunnel at Mach 3.0. Predicted values of the skin friction coefficient from the Schultz-Grunow correlation and measurements with a strain gage skin friction unit were $C_f = 0.0014$ and 0.0015 , respectively. We obtained $C_f = 0.0012$ with the fiber-optic based gage. We are pursuing further refinement of that unit, and the goal is to miniaturize it with MEMS technology. In addition, efforts are underway to make a single unit for simultaneous measurements of skin friction, heat flux, surface pressure and surface temperature using fiber optic techniques. Some suggestions can be found in Ref. [18].

REFERENCES

1. Dhawan, S., "Direct Measurements of Skin Friction," NACA Rept. 1121, 1953
2. Nitsche, W., Haberland, C. and Thunker, R., "Comparative Investigations of the Friction Drag Measuring Techniques in Experimental Aerodynamics," ICAS -84-2.4.1, 14th ICAS Congress, 1984
3. Winter, K.G., "An Outline of the Techniques Available for the Measurement of Skin Friction in Turbulent Boundary Layers," Progress in Aerospace Sci., Vol. 18, pp. 1-57, 1977
4. Waltrup, P. J. and Schetz, J.A., "Supersonic Boundary Layer Subjected to Adverse Pressure Gradients, AIAA J., Vol. 11, No. 1, pp. 50-57, 1973
5. Allen, J.M., "Systematic Study of Error Sources in Supersonic Skin-Friction Balance Measurements," NASA TN D-8291, 1976
6. Allen, J.M., "Improved Sensing Element for Skin-Friction Balance Measurements," AIAA J., Vol. 18, No. 10, pp. 1342-1345, 1980
7. Schetz, J.A. and Nerney, B., "Turbulent Boundary Layer with Injection and Surface Roughness, AIAA J., Vol. 15, No. 9, pp. 1268-1274, 1977
8. Kong, F. and Schetz, J.A., "Turbulent Boundary Layer over Solid and Porous Surfaces with Small Roughness," AIAA 81-0418, 1981
9. Kong, F. and Schetz, J.A., "Turbulent Boundary Layer over Porous Surfaces with Different Geometries," AIAA 82-0030, 1982
10. Collier, F.S. and Schetz, J.A., "Injection into a Turbulent Boundary Layer through Different Porous Surfaces," AIAA J., Vol. 22, No. 6, pp. 839-841, 1984
11. Kenworthy, M. and Schetz, J.A., "Experimental Study of Slot Injection into a Supersonic Stream," AIAA J., Vol. 11, No. 5, pp. 585-586, 1973
12. Schetz, J.A. and Van Overeem, J., "Skin Friction Reduction by Injection through Combinations of Slots and Porous Sections," AIAA J., Vol. 13, No. 8, pp. 971-972, 1975
13. DeTurris, D., Schetz, J.A. and Hellbaum, R., "Direct Measurement of Skin Friction in a Scramjet Combustor," AIAA 90-2342, 1990
14. Chadwick, K., DeTurris, D.J. and Schetz, J.A., "Direct Measurements of Skin Friction in Supersonic Combustion Flowfields," J. Eng. Gas Turbines and Power, Vol. 115, No. 3, pp. 507-514, 1993
15. Bowersox, R.D.W., Schetz, J.A., Chadwick, K. and Deiwert, S., "Technique for Direct Measurement of Skin Friction in High Enthalpy Impulsive Scramjet Flowfields," AIAA J., Vol.

33, No. 7, pp. 1286-1291, 1995

16. Paik, S.W. and Schetz, J.A., "Simultaneous Direct Measurements of Skin Friction and Heat Transfer in a Supersonic Flow," *Proc. Sixth Asian Congress of Fluid Mechanics*, Y.T. Chew and C.P. Tso (Eds.) Nanyang Tech. Univ., Singapore, 1995

17. Murphy, K., Gunther, M., Vengarkar, A. and Claus, R., "Quadrature Phase-shifted, Extrinsic Fabry-Perot Optical Sensors," *Optical Letters*, Vol. 16, No. 4, pp. 173-275, 1991

18. Pulliam, W., Jones, M., Schetz, J. and Murphy, K., "Fiber Optic Pressure/Skin Friction Gage for Supersonic Flow Applications," 17th Int. Congress on Instrumentation in Aerospace Simulation Facilities, IEEE Congress Record, Sept. 1997.

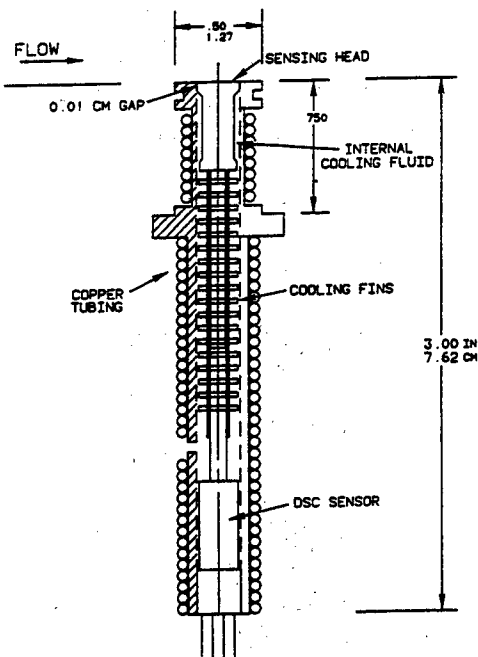


Figure 1. Skin Friction Gage for Hot, High-Speed Flows (Ref. [13])

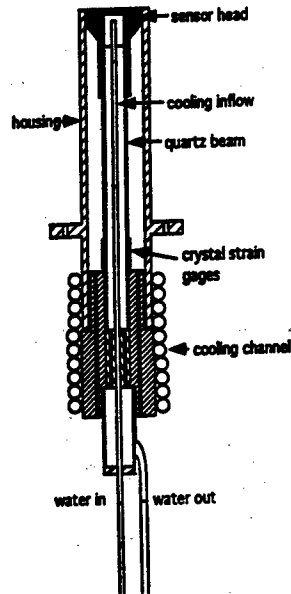


Figure 2. Cooled-Head Skin Friction Gage for Very Hot Flows (Ref. [14])

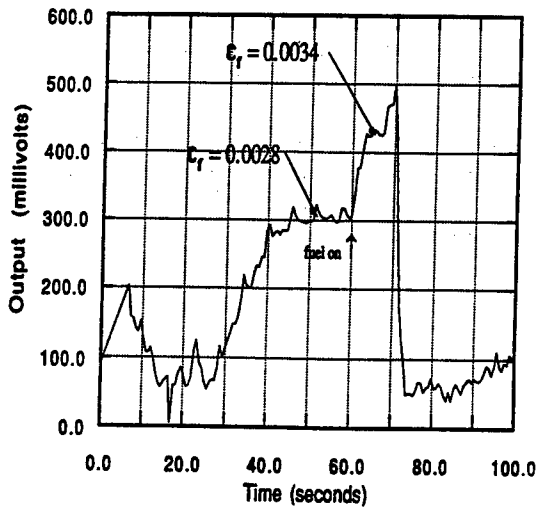


Figure 3. Typical Skin Friction Measurement in a Combusting, Supersonic Flow (Ref. [14])

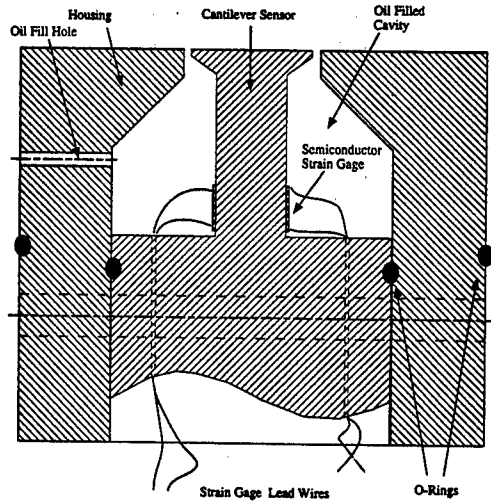


Figure 4. Fast Response Skin Friction Gage for Short Duration Tests (Ref. [15])

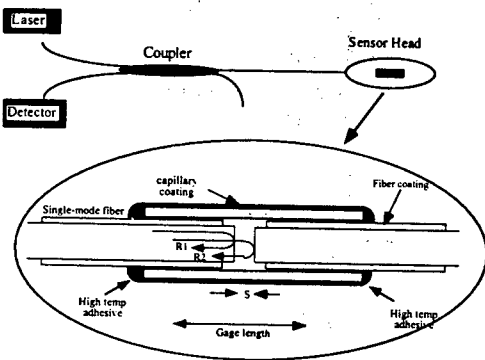


Figure 5. The EFPI Displacement Sensor

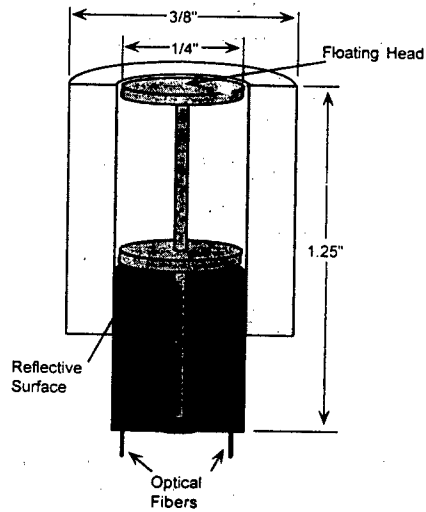


Figure 6. Schematic of the Fiber Optic Skin Friction Gage (Ref. [18])

DEVELOPMENT OF EXPERIMENTAL METHODS FOR THE HYPERSONIC FLOWS STUDIES IN LUDWIEG TUBE

E.Schuelein

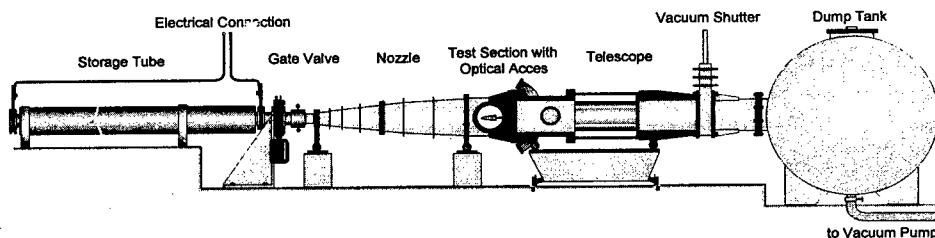
DLR Institute of Fluid Mechanics,
37073 Goettingen, Germany

A.A.Zheltevodov

Institute of Theoretical and Applied Mechanics
SD RAS, 630090 Novosibirsk, Russia

Development of the modern aerospace vehicles requires a unity of experimental and computational studies. Flowfields around vehicles must be generated numerically and studied on a basis of experiments to help understand flow features and determine performance trends. The accuracy of the numerical solutions is often uncertain because of numerical techniques and flow modeling assumptions. Experiment plays a prominent role in the validation of computational fluid dynamics (CFD) code. The stages of code development and the corresponding role of experiments are considered in [1, 2]. Experiments are required at each such stage. In accordance with [3] the experimental database lacked sufficient information namely at hypersonic Mach numbers. Development of the experimental studies to improve our knowledge about different types of hypersonic flows, including shock wave/turbulent boundary layer interaction processes, turbulent separated flows, laminar-turbulent transition phenomena etc is important today.

Our attention herein is focused on the development of some experimental methods with application to the studies of various complex hypersonic flows in the supersonic/hypersonic Ludwig-Tube (RWG) of DLR at Goettingen. This facility (Fig. 1) covers a Mach number range of $3 \leq M \leq 7$ and a unit Reynolds number range of $5 \cdot 10^6 \text{ m}^{-1} \leq Re \leq 80 \cdot 10^6 \text{ m}^{-1}$. The facility consists of an 80-meter long tube used as pressure reservoir which is separated from the nozzles and the test section by a fast-response gate valve. The tunnel is started by opening this valve. The test section for the Mach numbers $M = 3$ and 4 has a cross section $0,5 \times 0,5 \text{ m}^2$, while those for high



Performance	Tube A	Tube B
Max. Stag. Pressure, bar	15	40
Max. Stag. Temperature, °C	20	400
Mach Number	2.79 to 4.65	5.0 to 6.9
Unit Reynolds Number, 10^6 m^{-1}	5 to 80	5 to 50
Run Time, s	0.4	0.3
Test Section	$0.5 \times 0.5 \text{ m}^2$	$\varnothing 0.5 \text{ m}$

Fig. 1. Super- and Hypersonic Ludwig-Tube Goettingen (RWG)

Mach numbers have circular sections of 0,5 m diameter. Additional details of the design and the operation of the RWG are given in [4].

The short run times of the facility (0,3-0,4 s) require the development of new and adaptation of standard measurement techniques. In accordance with the modern requirements to the CFD validation, wide and comprehensive experimental studies on a basis of different methods are important. The optical visualization of 2-D and 3-D hypersonic flows, the measurements of different surface and flowfield variables have been developed and used. Some of the advances showing an application of these measurements to the analysis of various turbulent flows as well as to the study of laminar-turbulent transition at $M = 5$ are considered below.

Various measurements have been used for a study of 2-D hypersonic impinging shock wave/turbulent boundary layer interaction flows in the range of shock generator angles $\beta = 6^\circ - 14^\circ$ [5]. A quantitative flowfield scheme (Fig. 2, *a*) for the case with separation at $\beta = 14^\circ$, $M = 5$, $Re = 40 \cdot 10^6 \text{ m}^{-1}$, $T_w/T_r = 0,782$ has been obtained from the shadowgraphs as well as by analysis of pitot, static pressure and velocity profiles surveys in the specific sections 2-9. Such a scheme together with the surface pressure (Fig. 2, *b*), skin friction distributions (Fig. 2, *c*) and velocity profiles (Fig. 2, *d*) is a good basis for the CFD validation. Nevertheless, it is necessary to note the limited data for the skin friction (Fig. 2, *c*) obtained from the measured mean velocity profiles by an application of the combined wall-wake law with the Van Driest mixing-length damping function for the viscous sublayer to the corresponding transformed "incompressible" flow [5, 6]. Such C_f data are, of course, approximate after the interaction region because this technique can only fit the velocity profiles, when they have a wall-wake-law form (Fig. 2, *d*). Another limitation of such technique is impossibility of the measurements in the vicinity of separation (*S*) and reattachment (*R*) points as well as in the reversed flow region between these points.

The oil film interferometer technique proposed in [7] overcomes many well known limitations of other existing methods, since it provides non-intrusive skin friction measurements. It is based on the relationship between the thinning of an oil film, placed on the test surface exposed to the flow, and the local surface shear. The rate of thinning of the oil film is determined using optical interference arising when an incident light beam is partially reflected from the oil and test surface. The surveys of different realizations of such a technique are presented in [6, 8]. The Global Interferometer Skin Friction (GISF) meter, firstly developed and applied in [9, 10] for the C_f measurements on the flat plate test model in subsonic and supersonic long run duration wind tunnels, has been considered as a perspective one for a short duration facility such as the Ludwig-Tube. Global shear stress distributions in 2-D and 3-D flows can be obtained with this instrument during a single run of this facility.

The first skin friction measurements on the flat plates in the RWG with an application of the GISF meter are described in [6]. The beam from a 2 mW, 633 nm wavelength He-Ne laser was widened by the lenses and sent with a mirror to the test surface with the thin oil film. In some cases the interference pattern was produced simply by illuminating the oil film directly without mirror. Because of very short test times in the facility, the images were recorded during a run by Sony VO-9600P video recorder and digitized thereafter by a full frame video capture card Hauppauge Win/Motion 60 and stored on a PC's hard disk at up to 30 frames per second. Various Wacker silicon oils AK-10, AK-0.65 and Shell mineral oil S.5585 with corresponding nominal viscosity of $10 \text{ mm}^2/\text{s}$, $0,65 \text{ mm}^2/\text{s}$ and $5,4 \text{ mm}^2/\text{s}$ at 25°C have been used. Typically, 4 to 5 high quality images were captured 40 ms apart at an image resolution of 768×576 pixels. The skin friction coefficient C_f was calculated by the integral method, described in [8, 11].

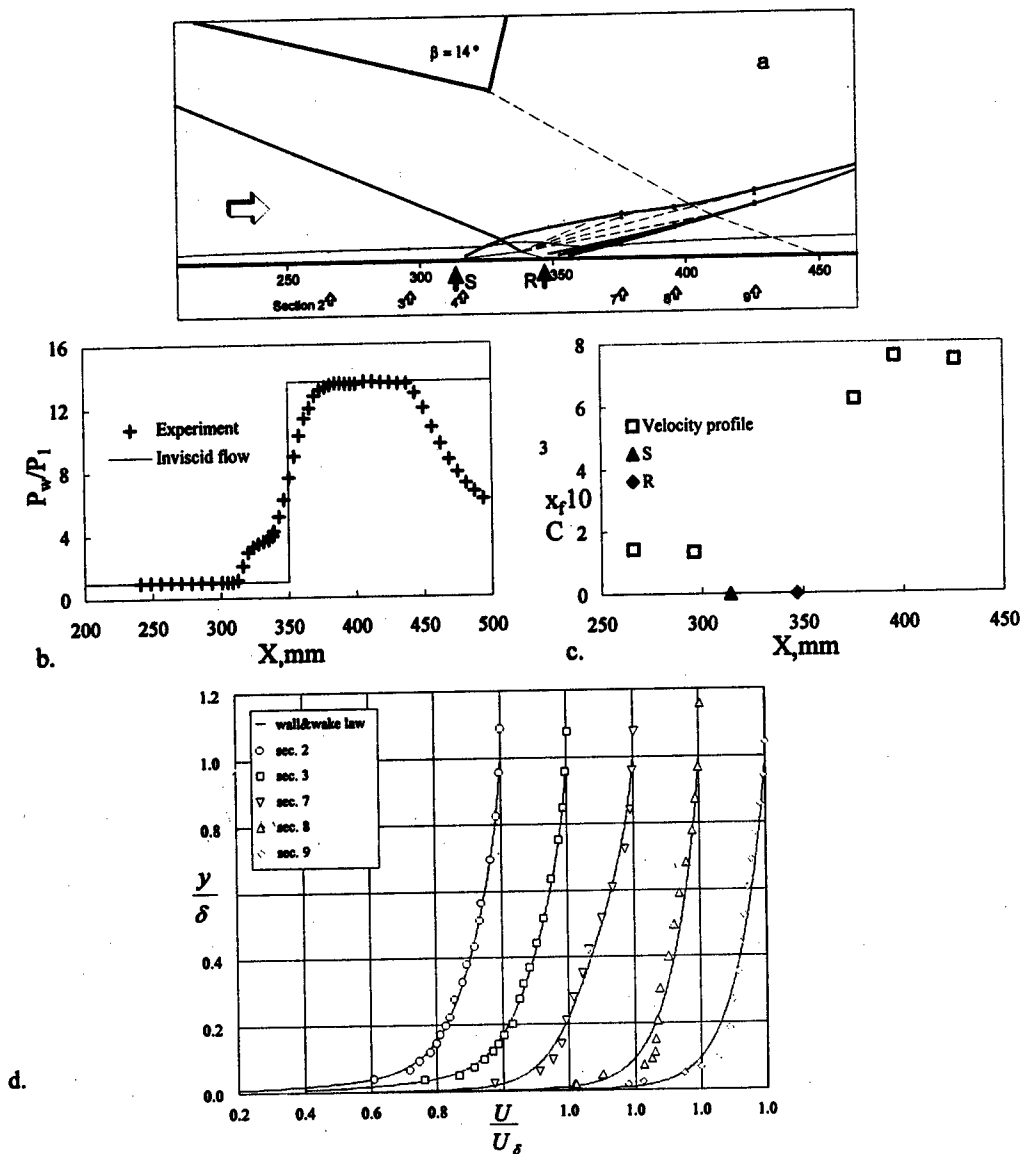


Fig. 2. Incident shock/boundary layer interaction flow at $\beta = 14^\circ$ and $M = 5$

The results of the C_f measurements [6] on the flat plate models of different length L at $M = 5$ used for validation of the GISF meter in the RWG are shown in Fig. 3. The C_f values, extracted from the GISF measurements (Fig. 3, a, open symbols), show an adequate distribution and good agreement with the data obtained from the velocity profile measurements (black symbols) and at $x > 150 - 200$ mm agree with the well-known Van Driest II correlation for the turbulent boundary layer. At $x < 150 - 200$ mm (depending of the L values) the skin friction distributions show a transitional and laminar boundary layer. The curve for laminar boundary layers corresponds to the empirical Young correlation [12]. An increase of the plate length led to early transition with the

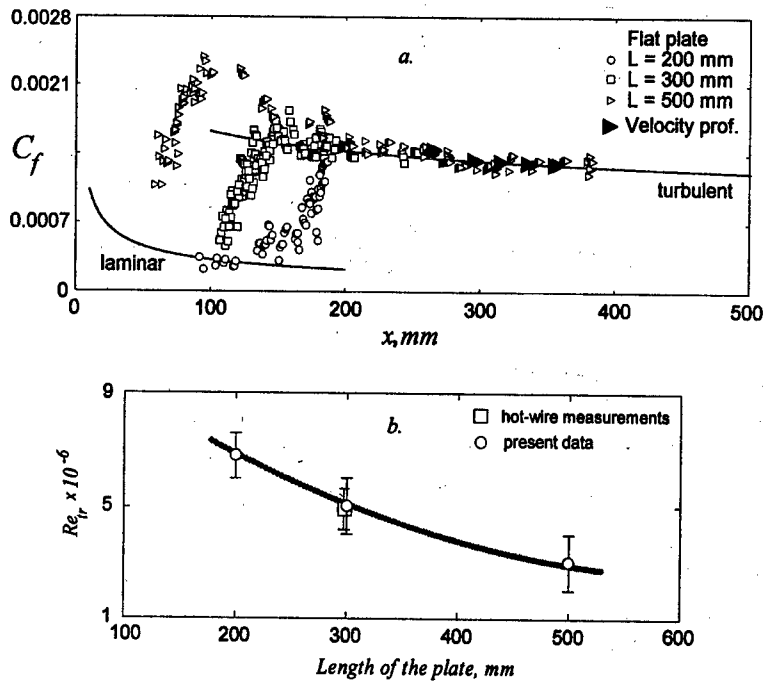


Fig. 3. The measurements of the laminar-turbulent boundary layer transition on a flat plate in the RWG.

corresponding value of the Reynolds number essentially decreasing (Fig. 3, b). The credibility of GISF measurements is also confirmed by a comparison with the hot-wire transition measurements on a plate of $L = 300$ mm [13]. The flat plate length influence on the boundary layer transition position can be explained by the existing relation between the test model dimensions and the level of its vibration during a run [6]. The support of the plates was such that the longer plates exhibit stronger vibrations, partly provoked by the start-up process of the impulse-type Ludwig-Tube facility. It is very conceivable, that high model vibration can lead to early laminar-turbulent transition and additional vibration measurements are necessary to confirm a qualitative dependence of the transitional Reynolds number, Re_{tr} .

The GISF meter has been applied for the new studies of hypersonic turbulent separated flows performed in the RWG. The shadowgraph of 2-D turbulent separated flow in the vicinity of the forward-facing step with the height $h = 15$ mm at $M = 5$, $Re = 40 \cdot 10^6 \text{ m}^{-1}$, $T_w/T_r = 0,8$ is presented in Fig. 4, a. The step was mounted on a flat plate at the distance $L_o = 340$ mm downstream of its leading edge. A high value of the plate width to step height ratio $b/h = 26,6$ excluded the test model sides influence on the separated flow which has been close to two dimensional one in accordance with the surface flow pattern visualization. The surface P/P_1 and C_f distributions along the plate symmetry axis are presented in Figs. 4, b and 4, c. It is important that the optical C_f measurements obtain very detailed data in the vicinity of the separation point (S) and in the region of the reversed flow which are necessary for the modern CFD validation. Considered data are in good qualitative agreement with the similar measurements of [14] performed in a supersonic long run duration wind tunnel at $M = 3$.

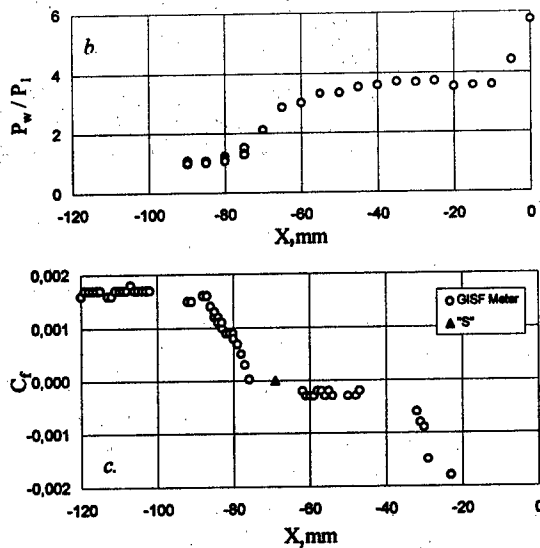
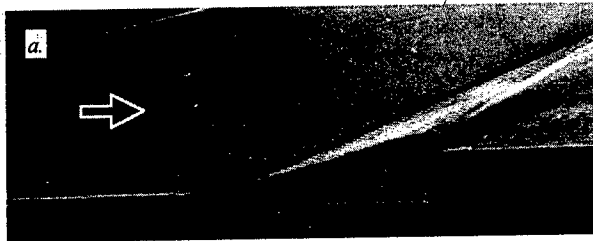


Fig. 4. Turbulent separated flow in the vicinity of the forward-facing step.

The surface reflective visualization (SRV) technique has been developed and used in the RWG parallel with the surface flow pattern visualization by the oil-lamp black and C_f measurements by the GISF meter for the 3-D shock waves/turbulent boundary layer interactions in the vicinity of one and two fins mounted on a flat plate. This technique is similar in some details with one described in [15]. The SRV system is a derivative of a double-pass shadowgraph system in which the model surface itself is a mirror and a component of the optical system (Fig. 5, a). A parallel bundle of light was directed into the test section along a path perpendicular to the surface of the model. The light is reflected back along nominally the same path and brought to focus on the image plane of CCD camera. Such an optical system produces a two-dimensional image of a component of the density gradient existing perpendicular to a parallel light bundle integrated over its path. The crossing shock wave structure and the oil-lamp black surface flow visualization in the vicinity of two symmetric ($\beta = 18$ deg.) chamfered fins mounted on the plate at $M = 5$, $Re = 40 \cdot 10^6 \text{ m}^{-1}$, $T_w/T_r = 0,8$ are presented in Fig. 5, b. The fins mounted 269 mm downstream of the plate leading edge with the distance between their tips $A = 139$ mm and the throat width of the channel $B = 43,2$ mm. The appearance of a 3-D separated zone around the crossing shock waves is seen distinctly.

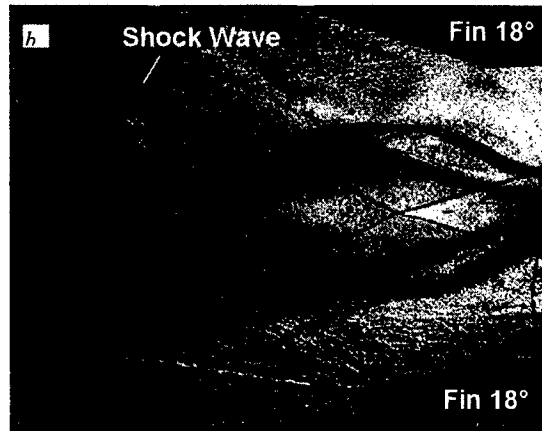
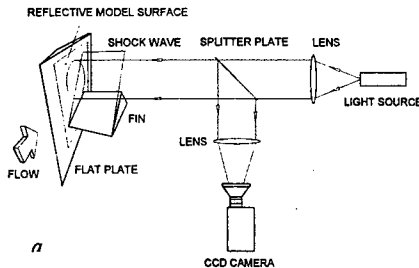


Fig.5. Surface reflective visualization shadowgraph and surface flow pattern for the double fin configuration $\beta = 18^\circ$ at Mach 5

Increased fragments of the surface flow pattern and their corresponding schemes in the vicinity of the central separated zone "apex" specify the stages of the flow topology development for considered configuration at different fins inclination angles in the range of $\beta = 16^\circ$ – 18° (Fig. 6). A very liquid mixture of the Shell mineral oil S.5585 with the lamp black or oil-paint has been used for this visualization. The time approximately 20–40 ms was necessary to achieve the stable surface flow pattern properties which existed for the next 260–280 ms of the RWG facility run time without any significant changes. The movement of the mixture particles along the limiting streamlines was recorded during a run by the Sony VO-9600P video recorder. This gave a possibility of analyzing the dynamics of the topology development.

The formation of two coalescence (separation) lines S_1 and S'_1 , two secondary coalescence lines S_2 and S'_2 and one divergence line R_1 has been fixed for the $\beta = 16^\circ$ case (Fig. 6, a). It can be only supposed that a saddle–node singular points combination exists upstream of the line R_1 in the region shaded in the sketch. The appearance of the local separated zone has been registered after the separation line S_2 at $\beta = 17^\circ$ (Fig. 6, b). This local zone is limited upstream and downstream by two saddle points. It is seen from the scheme for $\beta = 17,5^\circ$ (Fig. 6, c) that two focuses also exist in this separation zone. The next scheme for $\beta = 18^\circ$ (Fig. 6, d) displays the appearance of the long reversed flow from the downstream located node to the saddle point in the center of the separation line S_2 . The scale of this figure is decreased approximately twice comparing with the previous ones to show the main features. It is important to note the appearance of two additional saddle points in the last scheme in the regions of the divergent side flows after the focuses. Two shaded regions in the scheme show the supposed position of these saddle points by their upstream parts. The interpretation of the flow pattern in these shaded regions is difficult. A possibility of the appearance of such two symmetric saddle points as well as downstream node has been predicted at $M = 4$ by computations [16]. Nevertheless, the computation predicts the appearance of the node but not saddle and two focuses in the upstream part of the considered separated flow fixed in this experiment. The next stage of the CFD code validation is necessary.

The GISF meter has been applied to obtain an information about the C_f distribution for the 3-D flows. An example of the oil interferogram is presented in Fig. 7, a for the region shown in the corresponding scheme in Fig. 7, b in the vicinity of two fins configuration at $\beta = 23^\circ$, $M = 5$. The panoramic image (Fig. 7, a) demonstrates the C_f field features in the downstream and the reversed flows. The distance decreasing between the interference fringes corresponds to the regions of the C_f decreasing.

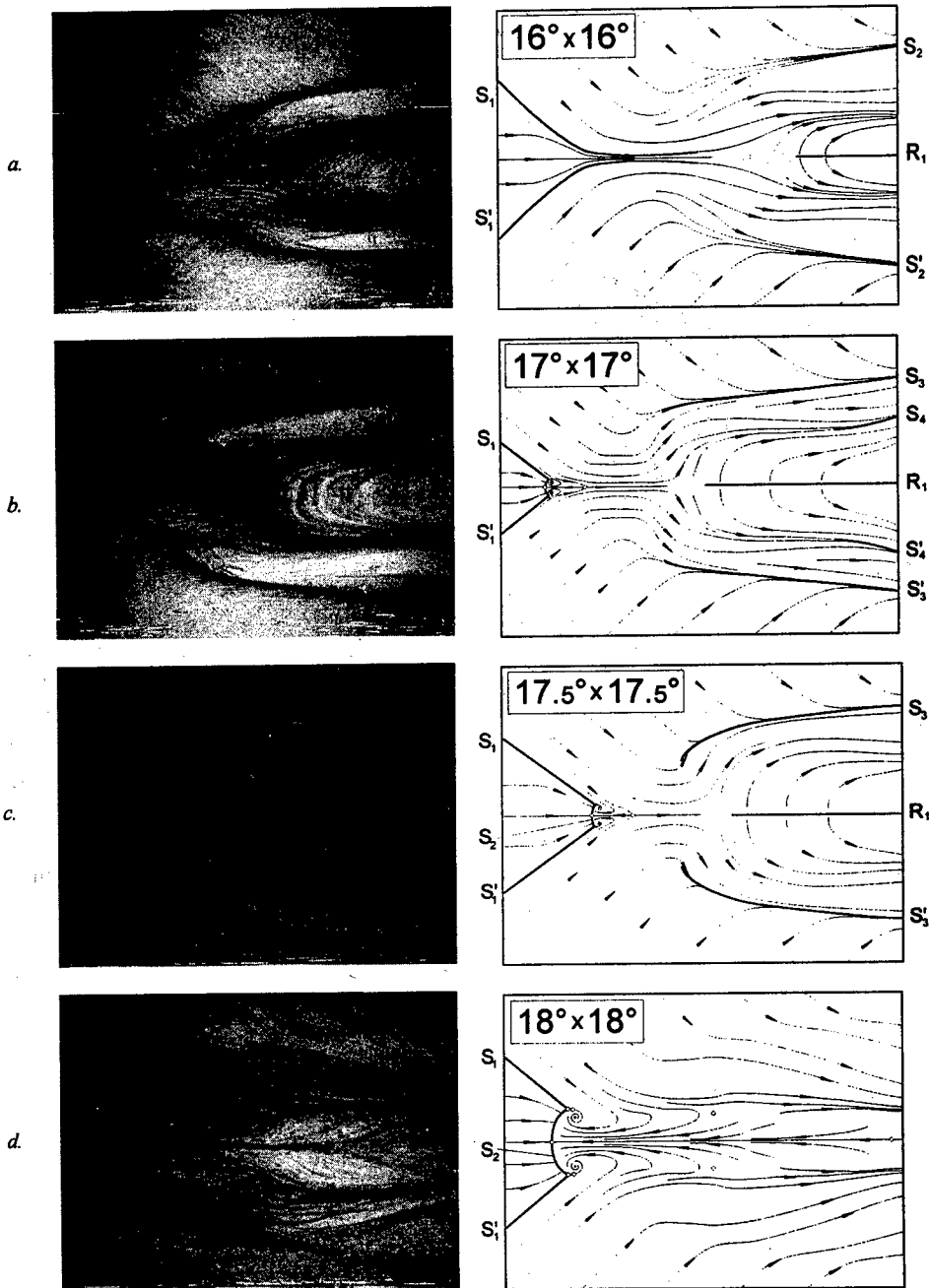


Fig. 6. Surface flow pattern in the vicinity of the double fin configuration at $M = 5$, $Re = 40 \cdot 10^6 \text{ m}^{-1}$, $B = 100 \text{ mm}$: $A/B = 1.85$ (*a*); $A/B = 1.9105$ (*b*); $A/B = 1.93$ (*c*); $A/B = 1.96$ (*d*)

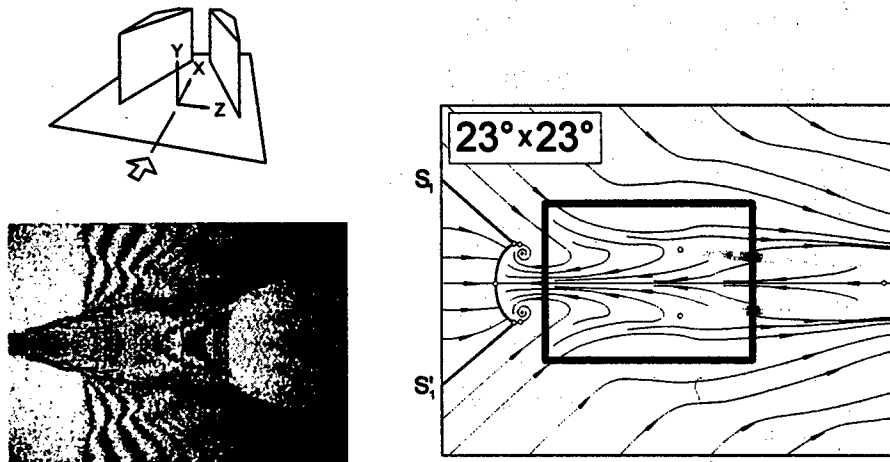


Fig. 7. The oil interferogram and surface flow scheme for a double fin configuration:
 $\beta = 23^\circ$, $A = 307$ mm, $B = 100$ mm.

Some results of the study of 3-D shock wave/turbulent boundary layer interaction in the vicinity of one fin configuration at $M = 5$ are shown in Fig. 8. The fins with different inclination angles β_1 (Fig. 8, a) were mounted on a plate in a similar position as two fins and investigated at the same flow conditions. The angles of the separation angle φ_1 fixed on a basis of the surface flow pattern in the range of the fin angle $\beta_1 = 1^\circ - 28^\circ$ are in good agreement with the proposed in [17] correlation for the lower values of the Mach numbers: $\varphi_1 - \varphi_1^* = 2,15(\varepsilon - \varepsilon^*) - 0,0144(\varepsilon - \varepsilon^*)^2$, where φ_1 - the separation line angle; ε - the shock wave angle; $\varphi_1^* = \varepsilon^* = 14,3^\circ$ - the critical (incipient separation) experimental values of these angles. This comparison shows a possibility of the correlation application at $M = 5$ for a wide range of β_1 and specifies the conclusion and the data of [18]. An application of developed in [17] engineering computational method for surface pressure prediction in the interaction region at $M = 5$, $\beta_1 = 18^\circ$ for two conical cross sections

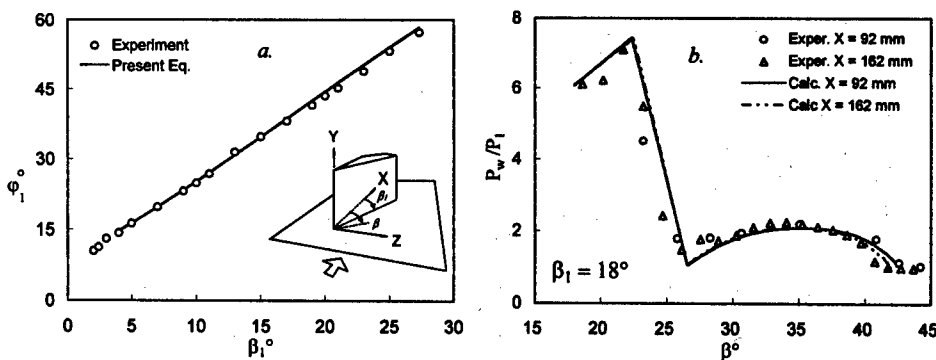


Fig.8. Experimental data for one fin configuration at $M = 5$.

($x = 92\text{mm}$ and 162 mm) is demonstrated in Fig. 8, *d*. The pressure maximum and minimum positions have been corrected ($1,6^\circ$ decreased) in accordance with the new data generalizations comparing with the previous correlation to improve predictions at the hypersonic Mach number.

The considered development and applications of different experimental methods to the short-duration supersonic/hypersonic Ludwig-Tube (RWG) of DLR have demonstrated a possibility of performing wide hypersonic flows studies in the facility. Some results of such studies have been considered, including 2-D and 3-D shock wave/turbulent boundary layer interactions, turbulent separated flows, laminar-turbulent transition phenomena. The new data can be recommended for the CFD validation.

The authors would like to acknowledge the assistance of Dr. P.Krogmann in preparation of this study.

REFERENCES

1. Marvin J.G. Turbulence modeling for computational aerodynamics // AIAA J. 1983. Vol. 21, N 7. P. 941 - 955.
2. Marvin J.G. Perspective on computational fluid dynamics validation. // AIAA J. 1995. Vol. 33, N 10. P. 1778 - 1787.
3. Settles G.S., Dodson L.J. Supersonic and hypersonic shock/boundary layer interaction database // AIAA J. 1994. Vol. 32, N 7. P. 1377 - 1383.
4. Ludwig H., Hottner Th., Grauer-Garson H. Der Rohrwindkanal der Aerodynamischen Versuchsanstalt Göttingen // Jahrbuch 1969 der DGLR. 1970. P. 52-58.
5. Schuelein E., Krogmann P., Stanewsky E. Documentation of two-dimensional impinging shock/turbulent boundary layer interaction flow. - DLR Forschungsbericht. IB 223 - 96 A 49. October, 1996. 69 p.
6. Schuelein E., Koch S., Rosemann H. Skin friction measurement and transition detection techniques for the Ludwig-Tubes at DLR // Proc. RTO/AGARD Fluid Dynamic Measurement Technology, Seattle, USA, September 22-25. 1997. P. 23-1-23-9.
7. Tanner L., Blows L. A study of the motion of oil films on surfaces in an air flow, with application to the measurement of skin friction // J.Phys. E.: Sci. Instrum. 1976. Vol. 9. P. 194-202.
8. Borisov A.V., Vorontsov S.S., Zheltovodov A.A., Pavlov A.A., Shpak S.I. Development of experimental and computational methods of studies of supersonic separated flows. Novosibirsk, 1993. 45 p. (Preprint / ITAM SD RAS; N 9 - 93).
9. Kornilov V.I., Mekler D.K., Pavlov A.A. On the technique of skin friction measurement using one beam laser interferometry // The Methods of Aerophysical Research (V School on the Methods Aerophysical Research, 7-16 July, Abakan): Proc. Novosibirsk, 1990. P. 145-151.
10. Kornilov V.I., Pavlov A.A., Shpak S.I. On the technique of the optical surface skin friction measurement in supersonic flow // Siberian Phys.-Techn. J., 1991. Vol. 6. P.47-51.
11. Maksimov A.I., Pavlov A.A., Shevchenko A.M. Development of the optical skin friction measurement technique for supersonic gradient flows // Int. Conf. on the Methods of Aerophys. Research: Proc. Pt. 2. Novosibirsk, 1994. P. 172-177.
12. Young A.D. High speed flow // Modern developments in fluid mechanics. Vol. 1. / Ed. L. Howard. Oxford: Clarendon Press, 1953. P. 375-475.
13. Wendt V. Experimental investigation of instability in planar and conical hypersonic laminar boundary layers. DLR Forschungsbericht FB 93-56, DLR. 1993.
14. Borisov A.V., Zheltovodov A.A., Maksimov A.I., Fedorova N.N., Shpak S.I. Verification of turbulence models and computational methods of supersonic separated flows.// Int. Conf. on the Methods of Aerophys. Research. Proc. Pt. 1. Novosibirsk. 1996. P. 54-61.
15. Donohoe S.R., Bannik W.J. Surface reflective visualization of shock-wave/vortex interactions above a delta wing // AIAA J. 1997. Vol. 35, N 10. P. 1568-1573.
16. Gaitonde D.V., Shang J.S., Garrison T.J., Zheltovodov A.A., Maksimov A.I. Evolution of the separated flowfield in a 3-D shock wave/turbulent boundary layer interaction // AIAA 97-1837, 1997. 14 p.
17. Zheltovodov A.A., Maksimov A.I., Schuelein E. Development of turbulent separated flows in the vicinity of swept shock waves // The Interactions of Complex 3-D Flows. Novosibirsk, 1987. P. 67-91.
18. Schmisser J.D., Dolling D.S. Fluctuating wall pressure near separation in highly swept turbulent interactions // AIAA J. 1994. Vol. 32, N 6. P. 1151-1157.

ON INTERACTION BETWEEN CROSS-FLOW AND STREAMLINE-CURVATURE MODES IN ROTATING-DISK FLOW

Shohei TAKAGI and Nobutake ITOH

National Aerospace Laboratory, Chofu, Tokyo 182-8522, JAPAN

Abstract

An experimental observation of rotating-disk flow is made to investigate nonlinear interaction between cross-flow instability and streamline-curvature instability. The latter instability of the centrifugal type having a very low critical Reynolds number is excited by acoustic forcing with various strength through an annular slit on the disk, where the crossflow instability is subcritical. Experimental results show that even weak excitation of S-C mode is effective on the suppression of cross-flow stationary disturbances, and that ensuingly the end of transition location moves downwards when the excitation is strengthened.

1. Introduction

The subject of three-dimensional boundary-layer instability and transition on swept wings has attracted fluid dynamists over half a century, because of its practical application to wing design and laminar-flow-control technology. It is well known that cross flow in three-dimensional (henceafter referred to as 3-D) boundary layers invites a strong instability of the inflection-point type. Characteristic features of the cross-flow instability in transition process of 3-D flows have been investigated in both experimental and theoretical studies. On the other hand, recent linear stability analyses^{1,2} have revealed the existence of a new instability due to the curvature of inviscid external streamline in 3-D boundary layers. Subsequent experimental investigations by Takagi & Itoh^{3,4} in a yawed cylinder boundary layer, which simulates the flow near the leading-edge region of swept wing, have confirmed unsteady disturbances arising from the new instability. This instability was newly labeled the streamline-curvature (referred to as S-C) instability after the main cause.

Besides such swept-wing flows, a number of investigations have been made in Ekman layer and rotating-disk flow, because these belong to a simplest class of 3-D boundary layers. A common feature in experiments and stability calculations for the rotating flows⁵⁻⁷ is the traveling waves due to the instability called "parallel", "Type II" or "viscous" mode, which are usually observed at a certain Reynolds number much lower than the critical value of the C-F instability. Recently, Itoh^{2,8} has applied the linear stability theory including curvature of external streamlines to rotating-disk flow and showed the existence of a corresponding instability caused by streamline curvature also in this flow. Takagi et al.⁹⁻¹¹ in a parallel study attempted an artificial excitation of S-C disturbances by a loud speaker through the annular slit or a pin hole on the disk, and identified growing disturbances in good agreement with linear stability calculations. This implies that Itoh's new instability is identical to Type II, parallel or viscous instability previously observed in rotating flows.

In the Ekman-layer experiment of Faller & Kaylor⁵, the Type II mode was observed to be very sensitive to external fluctuations in the surrounding fluid and to lead to directly turbulent state in the case that a large initial amplitude of Type II or S-C mode was given by some reason. This sensitivity of S-C mode to external fluctuations implies that S-C instability may play an important role in transition process when environmental disturbances are not negligibly small. To our knowledge, however, little have been investigated about the role in transition or the influence of S-C mode on C-F mode in rotating flows.

The primary objective of the present paper is to investigate nonlinear interaction between

C-F mode and S-C mode in rotating-disk flow with various initial amplitudes of S-C mode given by a loud speaker through an annular slit. This situation may be considered to simulate environmental disturbances like turbulent patch, gust or high turbulent environment.

2. Experimental apparatus and procedure

Figure 1 shows a flat disk with a diameter of 0.8m and a thickness of 30mm and a loud speaker installed beneath it, both of which rotate together in a counter-clockwise direction as viewed from above. Local Reynolds number is a function of the radius r and defined as $Re = r\sqrt{2\pi N/\nu}$, where N and ν are the revolution per second and the kinematic viscosity, respectively. In order to introduce artificial disturbances into the boundary layer, the disk was annularly slitted at 80 mm from the center with the gap of evenly 0.5 mm. Its annular gap of the slit is evenly 0.5mm. It has been shown in our previous experimental results^{10,11} that the slit facilitates growth of the annular mode of S-C instability with zero wavenumber in the azimuthal direction and that this mode has the critical Reynolds number approximately 120 in consistence with the theoretical prediction¹¹, although the critical Reynolds number of the whole S-C instability is about 65 as obtained by Itoh⁸ and Balakumar and Malik¹². As the laminar-to-turbulent transition occurs at $Re \approx 550$ in many earlier experiments, the disk rotation speed is chosen $N=5.5$, which allows $Re \approx 560$ at $r=380$ mm and $Re \approx 118$ at the slit and therefore is appropriate to realize the turbulent state on the disk as well as to excite the S-C annular mode at the slit.

Since surface roughness and its waviness favor steady mode of C-F instability as documented in earlier experiments, the disk was carefully buffed after machining and chromium-plating, so that the surface was mirror-finished with the flatness less than 0.01mm. It is obvious that the slit has no serious effect on development of C-F instability, because its critical Reynolds number ($Re \approx 290$) is much larger than the slit Reynolds number mentioned above.

A single hot-wire anemometers can measure mean and fluctuating velocities in either fixed or moving frame. In most measurements, a hot-wire sensor is mounted on a three-dimensional traversing mechanism, which moves in the radial, vertical directions and rotates the sensor body held normal to the disk with the individual stepping motors. For a hot-wire measurement fixed to the disk and speaker forcing, a low-noise rotary connector is attached to the lower end of the rotating shaft. A stereo amplifier powers the speaker with a pure sinusoidal wave supplied from a function generator. The disk rotation speed is measured by a photo interrupter, which generates a TTL pulse when a flat bar fixed to the rotating shaft passes the interrupter.

A multi-purpose spectrum analyzer with dual channel inputs acquires and analyzes all data such as waveforms, spectra, cross-correlation functions between hot-wire and speaker input. A microcomputer is occasionally used for off-line analysis of all the data stored on diskettes.

3. Experimental results and discussion

3.1 Natural transition

Linear stability theory shows that 3-D boundary layer on a rotating disk is exposed first to S-C instability at low Reynolds number near the rotation center, then to C-F instability and consequently the two modes coexist downstream of $Re \approx 300$. Figure 2 is a typical spectrum of the most unstable flow under a very weak forcing, which may be considered to give little effect on natural transition. This spectrum was obtained at $Re=460$ from a hot-wire sensor on the traversing mechanism in the laboratory frame and indicates two kinds of growing disturbances arising from the aforementioned instabilities. The broad frequency components peaked at 50 Hz are due to S-C instability and have the same characteristics as identified in the previous experiments^{10,11}. Several bumps at higher frequencies than 100 Hz with many spiky

components are found to be the stationary modes due to C-F instability, because such components disappear in the hot-wire measurements fixed to the disk, while the spiky components seem come from fluctuations induced by disk imperfection. The number of stationary vortices is obtained as about 32 from the center frequency (approximately 180 Hz) of the fundamental and the revolution of the disk ($N=5.5$), in consistence with earlier experimental observations. Traveling mode of C-F instability has not been detected in this series of experiments. Results of similar measurements and spectral analyses repeated along the radial direction are summarized in Figure 3, which shows the amplitudes of S-C disturbances and the fundamental of C-F mode plotted against Re . The S-C mode appears at lower Reynolds number in accordance with theory, while the first appearance of C-F mode is discernible at $Re=350$.

Both modes grow with similar growth rates and coexist as far as $Re=480$. After the amplitude of C-F mode exceeds that of S-C mode, the S-C mode seems to decrease but the C-F mode keeps growing and obviously dominates the transition process. Downstream of $Re=540$, the amplitude of C-F vortices suddenly decreases, probably because the high shear layer produced by C-F vortices breaks down and periodical components abruptly decrease with increasing irregularity¹³. Finally, fully turbulent state with no more regularity and periodicity is accomplished at $Re=560$. This transition location gives very good agreement with earlier observations¹⁴.

3.2 Weak forcing

Various state of interaction between C-F mode and S-C mode can be observed by varying initial amplitudes of S-C mode with speaker input voltage under a constant frequency 45Hz, which is close to the most unstable frequency of S-C mode but is slightly shifted from the power-line frequency (50 Hz). Several spectra measured under the same conditions as Figure 2 are compared in Figure 4, from which the amplitude variation of the forced component is obtained as shown in Figure 5. The fundamental amplitude of forced S-C disturbances grows first exponentially with input voltage but the growth rate becomes smaller above 3 mV and finally the amplitude tends to saturation when forcing exceeds 9 mV. Such a complex response of S-C disturbance to forcing seems to be related to interaction between C-F mode and S-C mode, because C-F stationary vortices and their harmonics decrease as forcing voltage increases. Simultaneously, C-F harmonic components modulated by disturbances due to surface imperfection are suppressed with the increase of speaker input. This is consistent with decrease of the higher harmonics of 5.5 Hz, which is itself invariable to forcing level. On the other hand, higher harmonics of S-C mode appear when the speaker input exceeds 3 mV, although such nonlinear development of S-C mode is hardly observed in natural transition process, where S-C instability is very weak. Ensuingly, the second and higher harmonics of S-C mode seem to overwhelm C-F mode and to reduce continuous components in higher frequency range above 300 Hz in spectral evolution. Such a strong interaction suggests that the transition process with more predominant S-C mode than C-F mode is different from the case of natural forcing given in Figure 3. It can be expected, therefore, that laminar-turbulent transition may be delayed by this kind of forcing, because S-C mode inherently has smaller growth rate than C-F mode.

3.3 Delay of transition

According to the above speculation, the speaker input was varied in order that C-F mode did not exceed S-C mode in the whole transition process and finally 4 mV is chosen as an effective forcing. A series of spectral evolutions with 4 mV forcing is compared with the case of 0.2mV in Figure 6, which is equivalent to the natural forcing as found in Figure 5. An important difference in spectra between with and without forcing appears downstream of $Re=460$, where the growth of C-F mode is alleviated in the presence of S-C mode with larger amplitude than C-F mode. It is remarkable that higher frequency components than 0.5kHz are significantly increased between $Re=460$ and 500 perhaps due to the breakdown of high-shear layer in both cases. Downstream of $Re=520$, no notable difference is discernible in spectra except for the forcing component. At $Re=560$, the flow with the natural forcing seems to reach turbulent state, while the fundamental of S-C mode is still present in the case of 4 mV forcing.

A quantitative expression of different stages of transition to turbulent state can be made by introducing a randomization factor γ , which is defined as unity minus the ratio of the fundamental amplitude of S-C mode to the rms value of the overall fluctuation¹⁵. For example, the flow with $\gamma=0$ includes very low background turbulence, while $\gamma=1$ shows fully turbulent flow. The spectra at $Re=560$ in Figure 6 show $\gamma=1$ for 0.2 mV forcing but $\gamma=0.94$ for 4 mV forcing, indicating that the boundary layer is not fully turbulent and the end of transition is located further downstream in the latter case. It is evident that laminar-to-turbulent transition is consequently delayed by an artificial excitation of S-C mode.

4. Conclusions

Nonlinear interaction between cross-flow mode and streamline-curvature mode has been investigated with acoustic forcing through an annular slit in rotating-disk flow. Spectral evolutions of unsteady fluctuations due to both streamline-curvature and cross-flow instabilities in the radial direction clearly show the fundamental difference between the cases with and without forcing. An optimal forcing induces higher harmonics of the streamline-curvature mode with the magnitude competitive to the cross-flow mode, and then the cross-flow stationary vortices are overwhelmed and, as a result, the transition location moves downstream. It may be concluded that acoustic forcing of streamline-curvature instability gives direct influence on the growth and evolution of cross-flow mode and is effective to control the transition process.

Acknowledgements

The authors would like to express their appreciation to Mr. T. Kuratsu, who conducted part of the experiment for his Bachelor thesis at the University of Electro-Communications.

References

- ¹ Itoh, N. : Instability of three-dimensional boundary layers due to streamline curvature. *Fluid Dyn. Res.*, **14**, 1994, pp. 353-366.
- ² Itoh, N. : Simple cases of the streamline-curvature instability in three-dimensional boundary layers. *J. Fluid Mech.*, **317**, 1996, pp.129-154.
- ³ Takagi, S. and Itoh, N. : Dispersive evolution of crossflow disturbances excited by an airjet column in a three-dimensional boundary layer. *Fluid Dyn. Res.*, **22**, 1998, pp.25-42.
- ⁴ Takagi, S., Itoh, N. and Tokugawa, N.: Dispersive development of unsteady disturbances due to cross-flow and streamline-curvature instabilities in a 3-D boundary layer on a yawed cylinder. to appear.
- ⁵ Faller, A.J. and Kaylor, R.E.: Investigations of stability and transition in rotating boundary layers. In *Dyn. of Fluid and Plasma* (ed. S.I.Pai). (Academic, New York) 1966, pp.309-329.
- ⁶ Lilly, D.K. : On the instability of Ekman boundary flow. *J. Atmos. Sci.*, **23**, 1966, pp.481-494.
- ⁷ Malik, M.R.: Instability and transition in rotating disk flow. *AIAA J.*, **19**, 1981, pp.1131-1138.
- ⁸ Itoh, N. : Theoretical description of instability waves in the flow on a rotating disk. Part 2. Development of wedge-shaped disturbances. *Trans. Japan Soc. Aeron. and Space Sci.*, **40**, no.130, 1998, pp.280-291.
- ⁹ Buck, G.A. and Takagi, S. : Observations of traveling disturbances from a point source in rotating disk flow. *AIAA Pap.* 97-2299, 1997.
- ¹⁰ Takagi, S. and Itoh, N. : Characteristics of unsteady disturbances due to streamline-curvature in stability in a rotating-disk flow. *Proc. the Seventh Asian Cong. Fluid Mech.* Dec. 8-12, 1997, Madras, India.
- ¹¹ Takagi, S., Itoh, N. and Tokugawa, N.: Characteristics of streamline-curvature disturbances in a rotating-disk flow. *AIAA Paper* 98-0341, 1998.
- ¹² Balakumar, P. and Malik, M.R : Traveling disturbances in rotating-disk flow. *Theoret. Comput. Fluid Dyn.* **2**, 1990, pp.125-137.
- ¹³ Kohama, Y., Onodera, T. and Egami, Y.: Design and control of crossflow instability field. *Proc. of the IUTAM Symposium On Nonlinear Instability and Transition in Three Dimensional Boundary Layers*, Manchester.

Kluwer, 1996.

¹⁴ Kobayashi, R., Kohama, Y. and Takamada, C.: Spiral vortices in boundary layer transition regime on a rotating disk, *Acta Mech.* 35, 1980, 71-82.

¹⁵ Sato, H. and Saito, H.: Artificial control of the laminar-turbulent transition of a two-dimensional wake by external sound. *J. Fluid Mech.*, 84, 1978, pp.657-672.

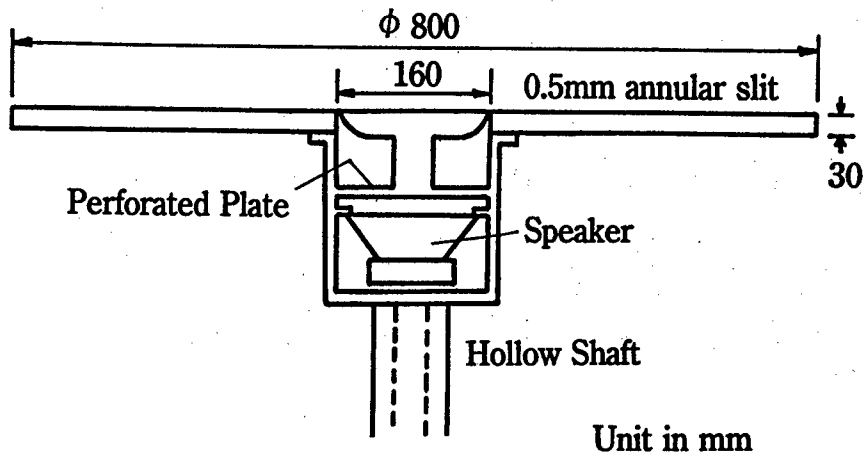


Figure 1. Schematic drawing of the disk apparatus.

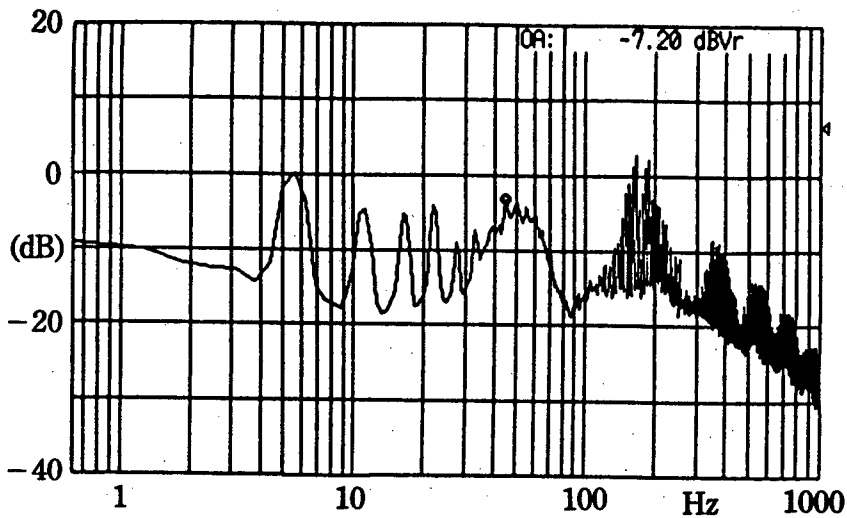


Figure 2. Power spectrum at $Re=480$ with very weak forcing voltage (0.2 mV) at a forcing frequency 45 Hz denoted by an open circle.

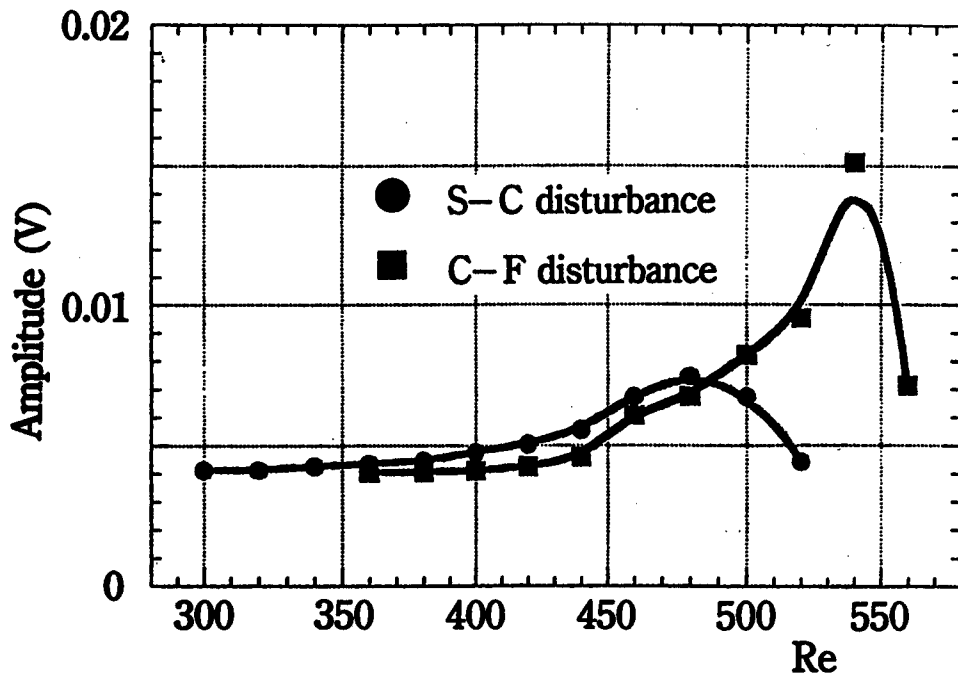


Figure 3. Amplitude variations of S-C mode and C-F mode in the downstream direction in the natural transition.

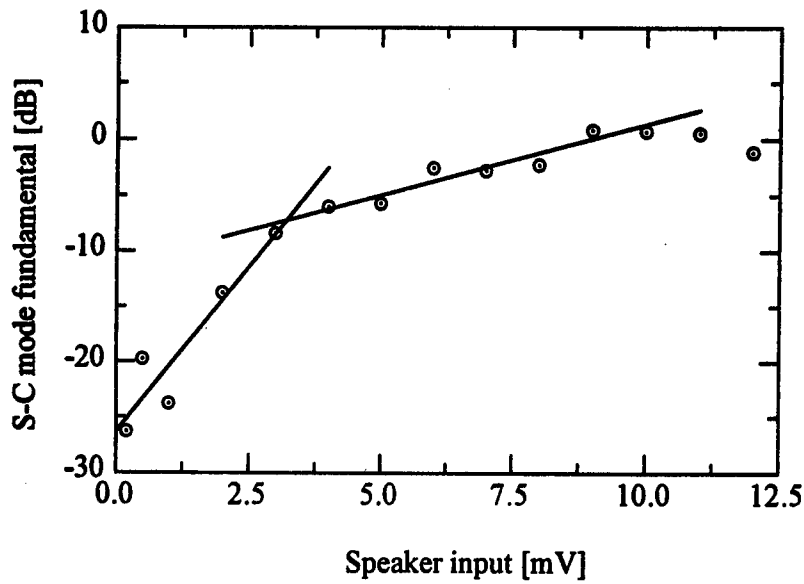
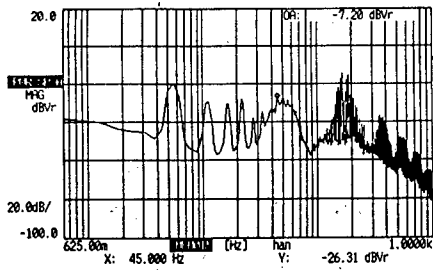
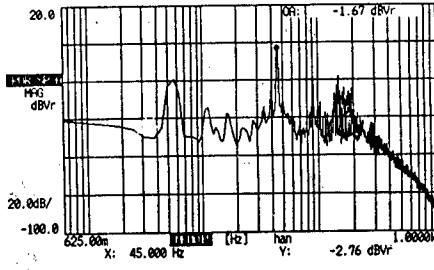


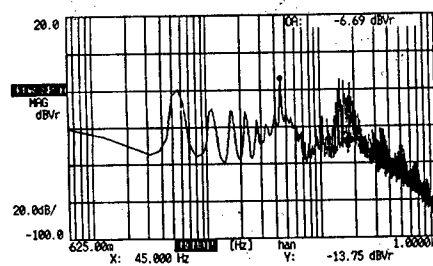
Figure 5. Amplitude variation of the fundamental of S-C mode against the speaker input.



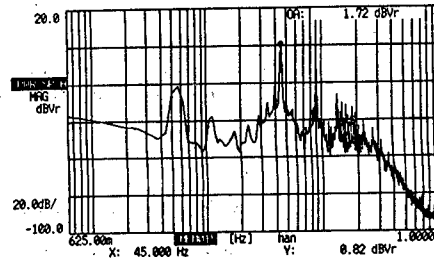
Speaker input 0.2mV



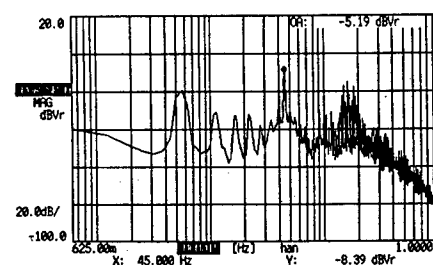
7mV



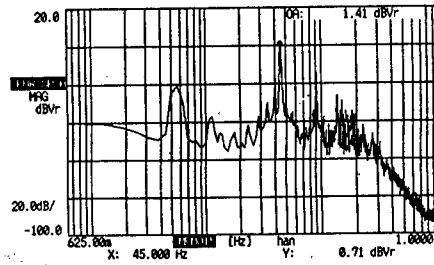
2mV



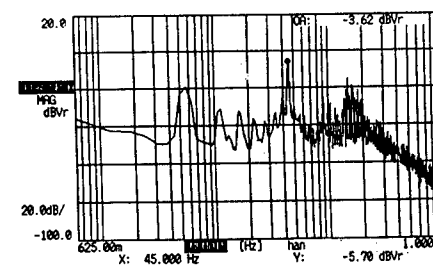
9mV



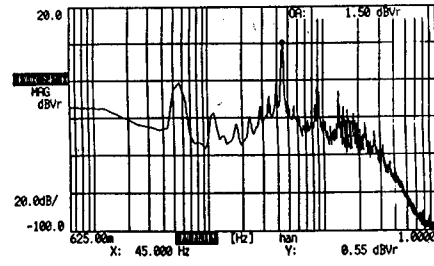
3mV



10mV

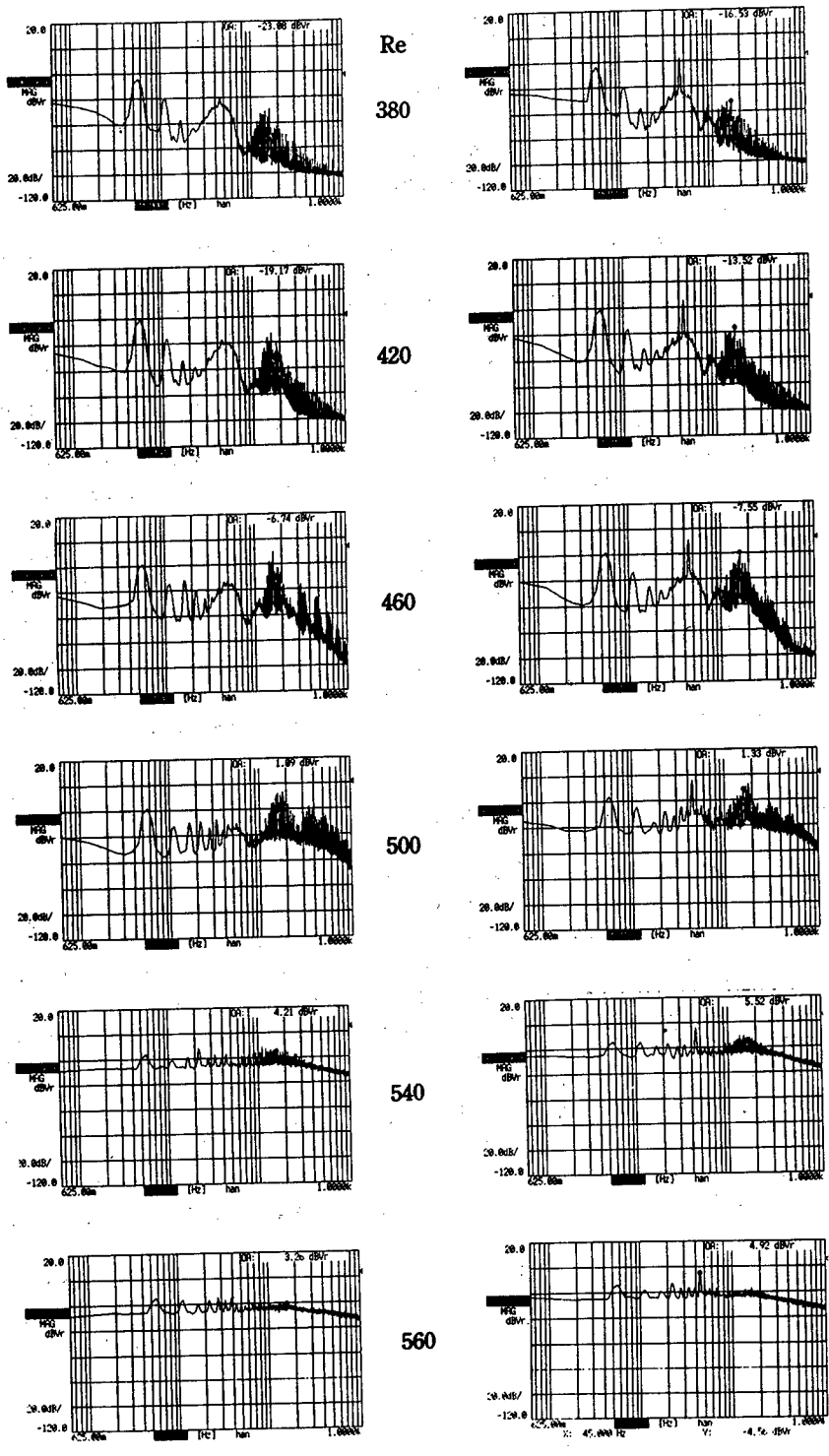


5mV



11mV

Figure 4. Power spectrum of unsteady fluctuations observed at Re=480 versus the speaker input voltage under a forcing frequency 45 Hz.



(a) Natural(0.2mV)

(b) 4mV forcing

Figure 6. Spectral evolutions in the downstream direction (a) with very weak forcing voltage 0.2 mV, and with forcing voltage 4 mV at a forcing frequency.

HYDRODYNAMIC DISTURBANCES IN SUPERSONIC JET

N.M. Terekhova

Institute of Theoretical and Applied Mechanics SB RAS,
630090, Novosibirsk, Russia

In supersonic axisymmetric jets two basic types of unstable disturbances are known which determine the processes of mixing and generation of noise by a free flow. The first is Kelvin-Helmholtz (K-H) shear instability, connected with the hydrodynamic instability of mean profile, and the second - rotational instability habitually called now as Taylor-Goertler (T-G) instability. This type of disturbances arises in jets at nonisobaric regimes of the expiration. Theoretically the simulation of the both instability types were studied on the basis of numerical integration of linearized motion equations for an inviscid compressible gas (the investigations of the professor Tam' school in USA and of the corresponding member RAS Zheltukhin' school in Russia).

The necessity of viscous effects consideration stems from a number of reasons. For the case of K-H instability it would allow to receive yet unknown critical values of Reynolds numbers for a free supersonic jet and also to study the damping disturbances. Just one paper is available on the verification of viscous effects for K-H waves [1], but a more limited problem about disturbances on the basic section of jet is considered, though an initial section is more important because this is the region where the disturbances arise and pass the basic stages of the development.

The expansion of theoretical frame is of basic significance for T-G instability. The rotational instability is investigated sufficiently well by inviscid approach [2]. But there are a number of effects which are not adequate to experiments [3]. The main effect is the rapid decrease of small-scale waves for the higher azimuthal numbers in an expanding supersonic jet. At the same time the inviscid approximation specifies that the increment of small-scale component grows more intensively.

It is possible to improve the theory by taking into account the increment reduction as the thickness of a mixing layer increases and the vortex pattern reconstructs. It is shown in [4]. But yet it does not allow to describe the real process of decrease of higher-order modes (small-scale waves). Thus in this case a viscous form of stability analysis is necessary.

We shall state some reasons about the role of viscosity in free mixing layers. It is common knowledge that the main profile $U(r)$ is of typical inflection character $(\rho_0 U')/r = 0$ and can be classified as inviscidly unstable. In this case the viscosity suppresses disturbances and represents itself appreciable for the small values of Reynolds numbers ($Re = U_0 \bar{r}_0 / \nu$) only.

Obviously, it is possible to restrict analysis to the first physical viscosity only and not to introduce the second viscosity. This restricts the analysis to the case of moderate Mach numbers and flows with little variation in the mean static temperature ($1 < M_0 < 2$).

Then the viscous terms in the momentum equations can be taken the same as in incompressible flows, and energy equation can be replaced by the entropy equation on a line of flux like in inviscid case.

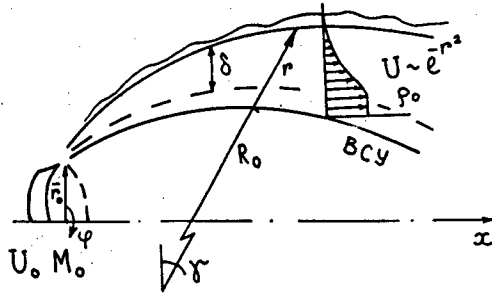


Fig.1 The scheme of flow on an initial site

The system R, φ, γ is chosen as the orthogonal coordinate system within the first "barrel" of the underexpanded jet (fig.1). Here $R=R_0+r$, r is the variable radial coordinate, and R_0 is the radius of curvature of the gas trajectories, φ and γ are angular coordinates ($dx=Rd\varphi$).

The field of velocities is given as $\bar{u} = |v', w', U(r) + u'|$, where the wave components are $u' = u(r)e^{i(\alpha x - \omega t + n\varphi)}$. Here α^r and n are the longitudinal and azimuthal wave numbers, α^i is a coefficient of longitudinal amplification, ω is the real radian frequency. For T-G waves α^r and $\omega \rightarrow 0$ and $v', u' = (v, u)(r)e^{-\alpha^i x} \cos n\varphi$, and $w' = iw(r)e^{-\alpha^i} \sin n\varphi$.

A system of linearized equations for disturbances in the distorted cylindrical system of coordinate have the form

$$iFv + p' / \rho_0 - 2Uu / R_0 = [Dv + v / r^2 - 2inw / r^2 + (v' - v / R_0 - 2i\alpha u) / R_0] / \text{Re}$$

$$iFw + inp / (\rho_0 r) = [Dw + w / r^2 + 2inv / r^2 + w' / R_0] / \text{Re}$$

$$iFu + Uv + i\alpha p / \rho_0 + Uv / R_0 = [Du + (u' - u / R_0 + 2i\alpha v) / R_0] / \text{Re}$$

$$iF M_0^2 p + v' + v / r + inw / r + i\alpha u + v / R_0 = 0$$

$$F = \alpha U - \omega, Dv = v'' + v' / r - (\alpha^2 + n^2 / r^2)v.$$

Outside the mixing layer $v, w, u, p \rightarrow 0$ at $r \rightarrow 0$ and $r \rightarrow \infty$. Hereafter (') means derivative in r . For isobarical jets the curvature $1/R_0$ is equal to zero.

The solutions of the system was obtained by a method [5]. Outside of δ the solutions of this expression can be presented in terms of modified Bessel functions Z of the first (at $r \rightarrow 0$) and second (at $r \rightarrow \infty$) kind [1]

$$u = C_1 Z_n(\lambda_1 r) + C_2 Z_n(\lambda_1 r) + C_2 Z_n(\lambda_2 r)$$

$$v = -C_1 i / \alpha Z_n'(\lambda_1 r) - C_2 \alpha / \lambda_2 Z_{n+1}(\lambda_2 r) C_3 in / r Z_n(\lambda_2 r)$$

$$w = C_1 n / (\alpha r) Z_n(\lambda_1 r) + C_2 i \alpha / \lambda_2 Z_{n+1}(\lambda_2 r) C_3 Z_n'(\lambda_2 r)$$

$$p = -C_1 \rho_0 F \text{Re} Z_n(\lambda_1 r) / (\alpha (\text{Re} + i M_0^2 F)),$$

where $\lambda_1^2 = (\alpha^2 \text{Re} + i \alpha^2 M_0^2 F) / (\text{Re} + i M_0^2 F)$; $\lambda_2^2 = \alpha^2 + i \rho_0 F \text{Re}$. The first vector corresponds to inviscid approximation, and $\lambda_1 = \lambda_{\text{inv}}$ at $\text{Re} \rightarrow \infty$.

Here we have a boundary-value problem for determining multifunctional connections $\alpha = \alpha(\omega, Re, M_0, R_0, \delta, n)$ and for searching the critical Reynolds numbers which separate unstable ($\alpha^i < 0$) stable regions ($\alpha^i > 0$) for waves. The dimensionless frequency is given by the acoustic Strouhal number ($Sh = 2\pi\omega r_0/a_0$).

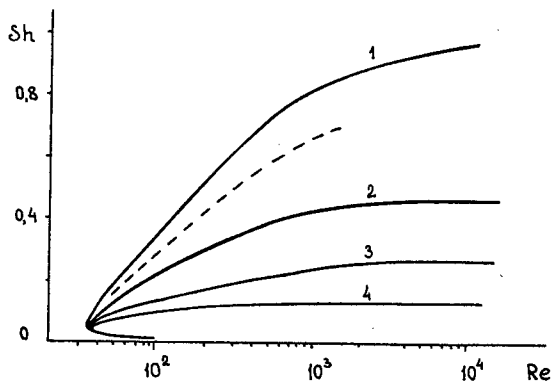


Fig. 2 The curves of neutral stability for K-H waves $\delta=0.3; 0.7; 1.2; 1.6$ (1 - 4)

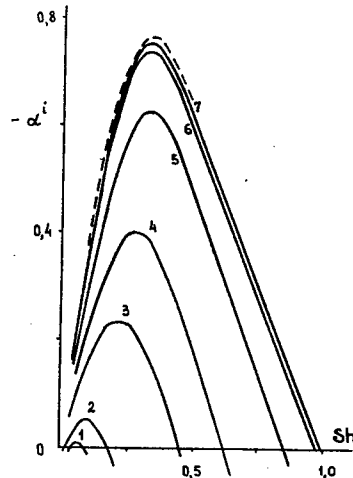


Fig. 3 The dependences $\alpha^i(Sh, Re)$ for K-H waves $Re=35; 50; 150; 300; 10^4; 510^4; 10^5$ (1 - 7) for $\delta=0.3$

The main results for viscous instability of K-H wave (the azimuthal mode $n=1$) in initial section of isobaric jet are shown for $M_0=1.5$ in fig. 2 and 3. Neutral stability curves (fig. 2) are given for the different thickness of the mixing layers (the near-root region, middle of an initial section and transitive area). It was shown that the critical Reynolds number is rather insignificant $Re_c \sim 32$. The region of unstable frequencies decreases as the thickness of a mixing layer increases, thus the bottom branch of a neutral curve lies close to zero. The resulted values $\alpha^i(Sh)$ in fig. 3 shows that the increments takes maximal values in the region of higher frequencies as Re increases. Here the dashed lines shows the values of increments for inviscid case. As the Max number increases, so the maximum growth rate decreases and the range of amplifying frequencies decreases (the dashed line for $M_0=2$ in fig. 2). As it was expected, the viscosity suppresses the oscillations reducing the increments for moderate Re .

It is necessary to begin a discussion of the results for T-G instability with fig. 4, where the dependences $\alpha^i(Re)$ are shown for $R_0=25$, $\delta=0.15$ and $M_0=1.5$. From this figure we notice (the critical of Reynolds numbers Re_c are given on an axis $\alpha^i=0$) that the large-scale vortices (small n) lose the stability at lower Re . There is the range of values Re in which they have considerably higher increments than the small-scale vortexes. The lines $\alpha^i = \text{const}$ characterize the achievement of limit α^i when the increments correspond to inviscid approximation.

For small n this occurs rather quickly but the growth n delays the process. For example, for $n=30$ it corresponds to rather high Reynolds number $\sim 10^5$. This result is rather important for a treatment of experimental data.

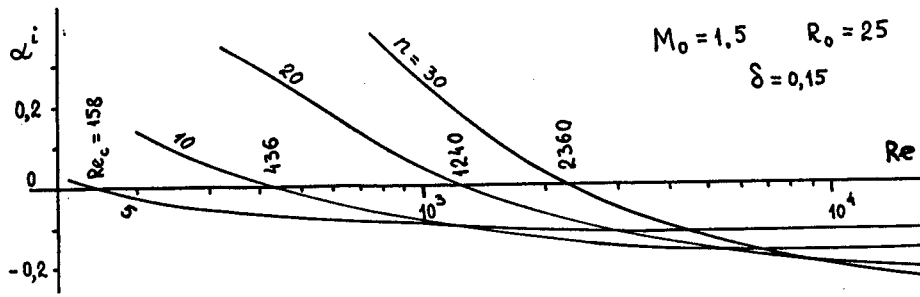


Fig.4. The influence of Re on increments α^i for T-G waves.

The classical neutral curves and the lines of equal amplification are given in fig.5. The area of stability is situated above neutral curve $\alpha^i=0$, the area of instability - below it. It was found that the mode $n=3$ is been boundary and the modes $n=1$ and 2 are unstable at any parameters of the expiration.

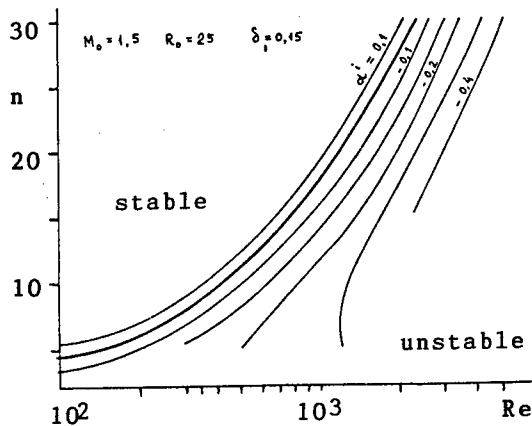


Fig.5 The curves of neutral stability for T-G waves

The generalized results are given in fig.6. It is known that the Goertler number $G^2=Re/R_0$ was introduced for the consideration of T-G instability. This parameter is described a ratio of viscous and centrifugal effects. The curves $Re_c(G)$ for $n=const$ separate stability regions (to the left and below of the lines Re_c) from instability regions (to the right and above them). These curves designed at small thickness δ for the most characteristic values R_0 , they give the basical critical values practically for all possible parameters inherent for jets.

The results of investigations show that the account of viscosity allows to clear the most inconsistent place of the inviscid analysis. They prove that the small-scale wave components have the higher increments in comparison with the large-scale waves at moderate Reynolds numbers. Besides, in accordance with attached jet case, the latter increments decrease much faster and the small-scale vortices are generated much earlier than the large-scale vortices in fluctuation spectra.

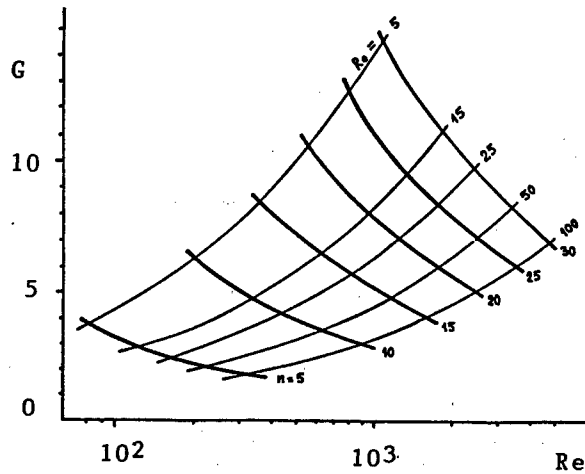


Fig.6 The Re_c family for T-G waves.

REFERENCES

1. Morris P.J. Viscous Stability of Compressible Axisymmetric Jets// AIAA J.-1983.- Vol. 21. - No 4.
2. Zheltukhin N.A., Terekhova N.M. Taylor-Goertler instability in supersonic jet// J. Appl. Mech. and Techn. Phys.-1993.-Vol.34. - N 5 (in Russian).
3. Zapryagaev V.I., Mironov S.G., Solotchin A.V. Spectral structure of wave numbers and peculiarities of structure of jet flow// J. Appl. Mech. and Techn.Phys.-1993.-Vol.34. - N 5 (in Russian).
4. Terekhova N.M. Streamwise vortexes in supersonic jets// J. Appl. Mech. and Techn. Phys. -1996. - Vol.37. - N 3 (in Russian).
5. Gaponov S.A., Maslov A.A. Development of disturbances in compressed flows. - Novosibirsk: Nauka, 1980 (in Russian).

GASDYNAMICS OF THE RADIAL SLOT JET IN CYLINDRICAL CHANNEL.

V.I.Terekhov, Yu.M.Mshvidobadze, and V.A.Sukharev.

Institute of Thermophysics, SB RAS
Novosibirsk, Russia

1. INTRODUCTION

The jet flows in channels are widely used in power plants and combustion chambers of aircraft and rocket engines. The study of gasdynamic interaction and mixing of radial slot jets injected into a channel normally to its axis is of considerable scientific interest and practical significance.

Up to now, a considerable body of information on jet dynamics and heat transfer in crossflows has been accumulated [1 - 3]. The studies, however, were carried out mainly for plane jets or a system of round jets in rectangular channels. For the fan-shaped plane jets injected at an angle to the main stream, studies [4, 5] are worth noting. In these studies, the emphasis was placed primarily on the heat-shielding properties of such jets.

The mixing behaviour of fan-shaped jets, especially in channels of finite sizes, when the slot width becomes comparable with the channel radius, $S/R \rightarrow 1$, possesses some peculiarities as compared to the case of plane jets in unbounded streams.

In this paper, results are presented of an experimental study of pressure and velocity fields in a cylindrical channel into which a fan-shaped jet injected normally to the main stream. In the experiments, aerodynamic losses on the jet injection section were determined as well, including those in the flow separation and reattachment region, at varying injection parameter and channel geometry.

2. EXPERIMENTAL SETUP AND MEASUREMENT PROCEDURE

The scheme of the experimental setup is shown in Fig.1. The diameter of the cylindrical channel D_k was 34 mm, while the width of the radial slot $S=2.2$ and 4.5 mm. As the main and injected gas, room-temperature air was used, with mass-flow rates measured with measuring orifices.

The experiments were conducted at varying mass-flow rate of the main stream G_1 which was 0 to 60 g/s ($Re_1 = \rho_1 w_1 D_k / \mu_0 \leq 1.5 \times 10^5$) and that of the injected jet $G_s = 0$ to 95 g/s ($Re_s = \rho_s w_s S / \mu_s \leq 5 \times 10^4$).

In this way, the experiments covered the whole range of injection parameter $m = \rho_s w_s / \rho_0 w_0 = 0 \rightarrow \infty$, the near-sonic outflow regime at the slot exit being realized

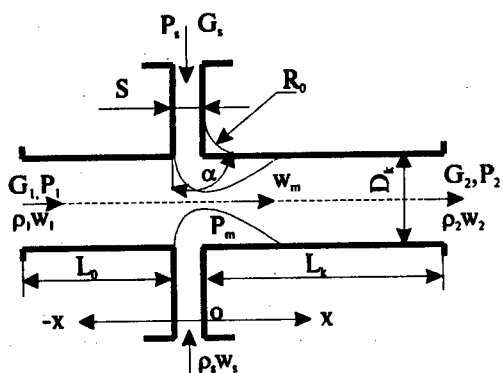


Fig.1. Scheme of the experimental setup.

at maximum mass-flow rates of the injected gas. The flow regime of both the main stream and jet was turbulent. Measurements have shown that the velocity profile across the cylindrical channel at the cross-section just in front of slot was near the same as that of the stabilized flow, with the power exponent $n = 1/7$ in the power velocity law. The length of the outlet section of the cylindrical channel L was 160 mm ($L_k/D_k \sim 5$); in a number of experiments, in order to determine the effect of outlet conditions on the formation of separated flow, the length of the outlet section of the channel was increased up to $L_k/D_k \sim 15$.

In the work, effect of the geometry of radial slot on the mixing of jet with stream was studied. The radius R_o of the rounding of the downstream edge of slot was either 0 (sharp edge) or 20 mm (round edge). The mass-flow proportions in these two series of experiments were the same.

In the experiments, the wall static pressure was measured as well as distributions of total and static pressure along channel axis. Besides, pressure and velocity profiles at channel inlet and outlet were measured, which allowed to determine integrals of total pressure and Coriolis coefficients required for finding aerodynamic losses. In a number of tests, distributions of pressure across the channel in their different cross-sections were measured with the help of micropneumatic comb Pitot.

3. EXPERIMENTAL RESULTS AND THEIR DISCUSSION

3.1. Pressure and velocity distributions.

The distribution of static pressure at the channel wall at different injection parameters is shown in Fig.2.

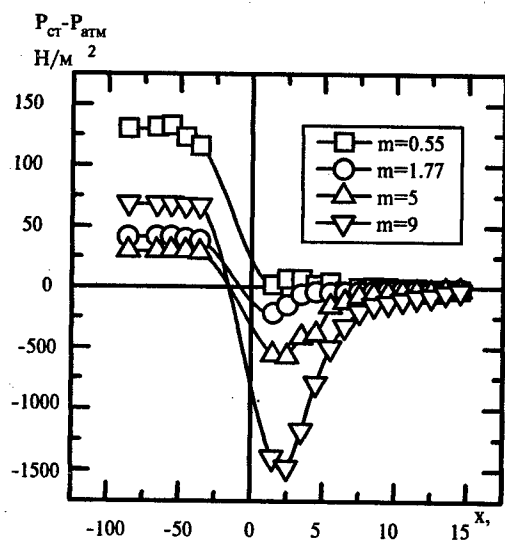


Fig.2. Distribution of static pressure over the channel wall channels ($L_k/D_k \approx 15$).

These experiments were carried out at fixed mass-flow rate of jet ($G_s = 22$ g/s) and at fixed slot width $S = 2.2$ mm. The pressure curves are seen to have similar shapes: a plateau of excess pressure in front of the fan-shaped jet, then an abrupt fall in the separation region, and gradual restoration up to the atmospheric level at the channel exit. The specificity of the interaction of a fan-shaped jet with the crossflow in a restricted channel as compared to plane jets [1, 2] consists in that in this case no clearly defined reattachment region of separated stream with a local pressure maximum is observed. The latter is evidenced by the experiments performed in longer

Measurements of static pressure at the axis for all the regimes studied yielded practically the same results as at the wall. No radial changes in pressure were

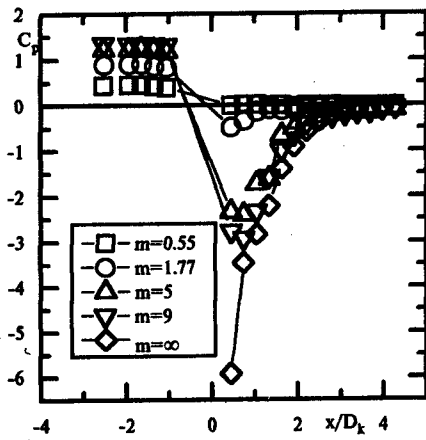


Fig. 3. Variation of pressure coefficient at different injection parameters.

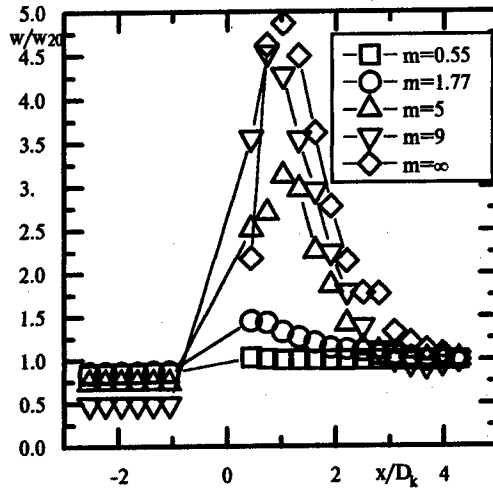


Fig. 4. Velocity distribution along the axis of the cylindrical channel

observed as well. The only exception was the flow without the cross-stream ($m \rightarrow \infty$), when the rarefaction region exceeded that at the axis by 50%.

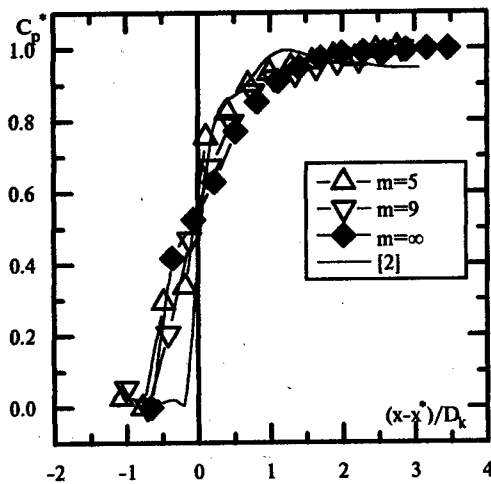


Fig. 5. Modified pressure coefficient in the separated-flow region

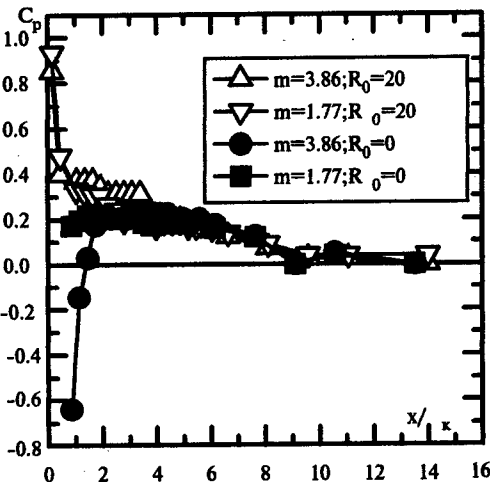


Fig. 6. Comparison of the distributions of wall pressure for round (light dots) and sharp (dark dots) edges of slot

Figure 3 illustrates variation of pressure coefficients along the channel length. Their value here and in what follows was calculated from the dynamic head at the channel outlet $C_p = 2(P_w - P_{atm})/\rho_2 w_2^2$, where w_2 is the mean outlet velocity. With increasing injection parameter, the pressure in the region in front of jet also raises. The value of rarefaction in the separation region increases as well, being the highest at $m \rightarrow \infty$. The extension of the disturbed region also increases from $x/D_k = 0.5$ at $m = 0.55$ up to $x/D_k = 3-4$ at $m = 9 \rightarrow \infty$. All the characteristic features of the development of fan-shaped jet illustrated by Figs. 2 and 3 reflect on the velocity distribution along the channel axis. These data are shown in Fig. 4. Contraction of the stream by the separation toroidal bubble results in a substantial acceleration of the stream, the ratio $(w/w_{20})_{max}$ increasing with increasing injection parameter and the value w_{mo} exceeding the outlet velocity by a factor of five. Thus, analysis of data of Figs. 2 - 4 gives an evidence that the stream deforms mainly due to separation at maximum injection ratios ($m \rightarrow \infty$), the extension of the disturbed-flow zone increasing as well. This conclusion is confirmed by measurements of longitudinal velocity at the channel outlet: the velocity profile at high injection parameters is of the jet character.

Figure 5 presents distributions of modified pressure coefficient $C_p^* = (C_p - C_{pmin}) / (C_{pmax} - C_{pmin})$ in the zone lying in immediate vicinity to the separation region. The experimental data in this form are seen to be generalizable, which is indicative of the universal character of the pressure distribution at different intensities of flow separation. The same conclusion is supported also by the experimental data [2] for a plane jet in crossflow which are also plotted in Fig. 5.

Rounding the downstream edge of the slot results in a drastically changed pressure variation. It follows from Fig. 6, which compares experimental data for slots with sharp and rounded edges, the mass-flow rates of the main and injected streams being the same. For the round edge, instead of rarefaction zone, in the injection region a peak of pressure is observed. In this case, throughout the whole region, the level of static pressure is higher as well in the channel with the rounded edge.

3.2. Maximum rarefaction behind the jet

One of the characteristic parameters determining the intensity of the separation flow is the maximum rarefaction behind the jet. Considerable attention in the literature has been paid to determining this parameter [1, 6, 7]. For radial fan-shaped jets in channels, such data are lacking.

The calculation analysis presented below is based on the model [1, 6] devised for the non-viscous gas flow. The main assumption made when developing the model, that the static pressure remains unchanged along the channel radius at the point of maximum flow contraction has been approved by special tests. From the set of equations for conservation of mass and momentum at the inlet and outlet cross-sections, and at maximum contraction ratio, the following transcendental equation has been obtained for rarefaction behind jet:

$$C_{pm}(1 + 2Sm / R_k)^2 + 2 + 4m^2 S \cos \alpha / R_k - 2\sqrt{1 + C_{pm}(1 + 2Sm / R_k)^2} - 4mS / R_k \sqrt{\frac{C_{pm}}{2}(1 + 2Sm / R_k)^2 + m^2 + 1/2} = 0 \quad (1)$$

where $C_{pm} = 2(P_1 - P_m) / \rho u_2^2$ is the rarefaction coefficient in the separation region.

The calculation data on maximum rarefaction upon varying jet injection parameter and angle for different ratios S/R_k is presented in Fig.7. The value $\alpha = 0$ corresponds to the cocurrent flow of stream and jet, where the rarefaction is absent and $C_{pm} = 0$. At counter-injection ($\alpha = \pi$), the rarefaction is maximal. With increasing injection parameter, as was stated above, the rarefaction also increases and at $m \rightarrow \infty$ it attains its highest. Upon increasing the slot width at a fixed injection parameter, the C_{pm} value decreases.

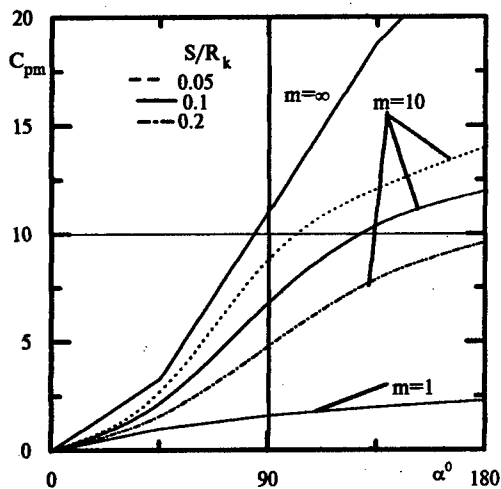


Fig.7. Effect of the injection parameter and angle of the fan-shaped jet on the rarefaction in the separation region.

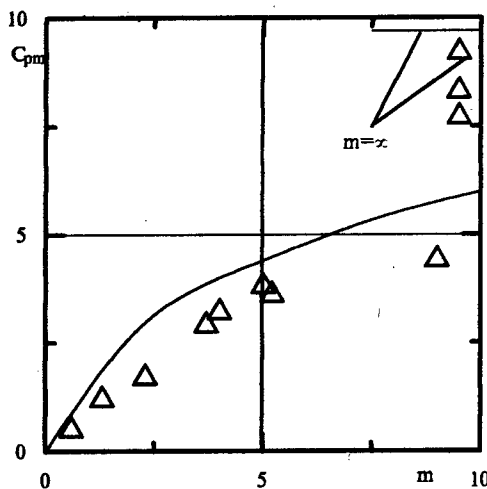


Fig.8. Comparison between the experimental data on the rarefaction behind the fan-shaped jet and calculation results obtained according to formula (1).

Comparison between the calculation results according to formula (1) with the experimental data for normal injection at $S/R_k = 0.13$ is presented in Fig.8. On the whole, in spite of the model's roughness ignoring the presence of boundary layers, complex structure of both the separation region and interaction between the jet and the flow, etc., formula (1) qualitatively agrees with the experiment.

3.3. Hydraulic resistance of channel

The hydraulic-resistance coefficient for a channel with fan-shaped jet was determined from the difference between total pressures at its inlet and outlet:

$$\xi_2 = 2(P_1^* - P_2^*) / \rho_2 w_2^2 \quad (2)$$

where $P_{1,2} = P_{1,2} + N_{1,2} \rho_{1,2} w_{1,2}^2 / 2$ is the total pressure, and $N_{1,2} = \frac{1}{F_{1,2}} \int_{F_{1,2}} (w / \bar{w})^3 dF$

are the Coriolis coefficients accounting for the contribution to kinetic energy made by real distribution of the velocity w as compared to the mean-mass-flow one $\bar{w}_{1,2}$. The values $N_{1,2}$, according to data [8], may run well above unity, so that the nonuniformity in the velocity profile should be taken into account. In our experiments, the Coriolis coefficients were determined from the measured velocity profiles at the channel inlet and outlet.

For the problem under consideration, the value of the minimum energy losses for turning around and dissipation of the injected gas can be theoretically estimated. From the set of equations for conservation of mass and momenta in cross-sections 1 - 2 (Fig.1) at $N_1 = N_2 = 1$ we obtain:

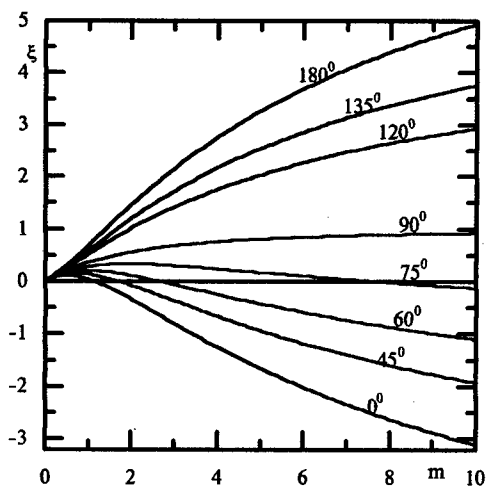


Fig.9. Hydraulic resistance coefficient of the channel with fan-shaped jet. ($S/R_k = 0.13$).

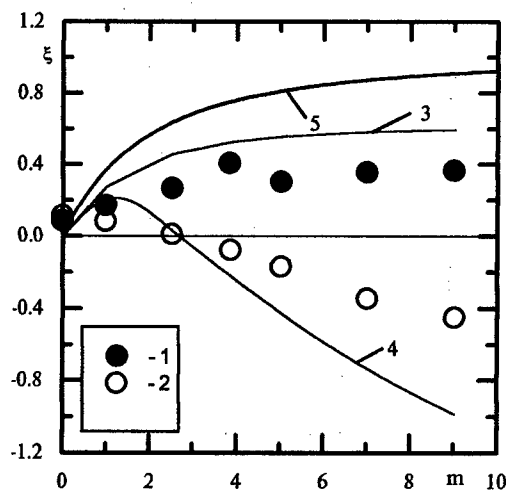


Fig.10. Comparison between the experimental and calculation data on hydraulic losses. 1,2 - experiments of the present authors for sharp and round slot edges, respectively; 3,4 - experiments [9] for T-joints with $\alpha = 90^\circ$ and 60° ; 5 - calculation according to formula (5) for $\alpha = 90^\circ$.

$$\rho_1 w_1 F_1 + \rho_s w_s F_s = \rho_2 w_2 F_2, \quad (3)$$

$$(P_1 + \rho_1 w_1^2) F_1 + \rho_s w_s^2 F_s \cos \alpha = (P_2 + \rho_2 w_2^2) F_2 \quad (4)$$

at $F_1 = F_2$

$$\xi = 1 - \frac{1 + 4(S/R_k)m^2 \cos \alpha}{(1 + 2(S/R_k)m)^2} \quad (5)$$

Since the coefficient ξ in Eq.(5) takes no account of losses for friction and vortex

formation which take place in real flows, it represents the lower bound of hydraulic losses. Fig. 9 shows the calculated dependences of ξ on injection parameter for different injection angles. As is seen, changes in the inclination angle of jet to the channel axis strongly influence the value and shape of the distribution of ξ . The highest value of ξ is observed at counter-injection ($\alpha = 180^\circ$), while at the cocurrent injection ($\alpha = 0^\circ$) $\xi < 0$, which is indicative of the upgrowing of the total energy at the cost of mass inflow. At some intermediate injection angles, depending on the slot geometry (S/R_0) and m -parameter, the channel resistance reduces to zero.

Fig. 10 compares the experimental data of this study for sharp and rounded edges with the calculations according to formula (5). The experimental data were expected to yield higher values than those being predicted by the ideal-mixing theory. However, as evidenced from Fig.10, the situation is quite an opposite one, and experimental dots for $\alpha = 90^\circ$ falls to the region situated approximately twice below the calculated line. For the round edge, the behavior of the experimentally determined value changes drastically, and at $m > 3$, ξ becomes negative. At the same time, the experimental data reported in [9] for the transverse mass inflow (T-joints) agree qualitatively with the results of our study, in spite of obvious differences in the way the gas injection was organized. The reasons for such a dramatic discrepancy between the experimental and calculation data remain still unrevealed up to date. Possible reasons for such behaviour of ξ is gasdynamical instability of jet near its mouth and deviation of jet from the direction normal to axis caused by the crossflow. However, in order to justify this assumption more detailed experimental investigations are required.

This work has been carried out under partial financial support from Russian Fund for Fundamental Research (grant 97-02-18497).

REFERENCES

1. Girshovich T.A. Turbulent jets in crossflows. M.: Mashinostroenie, 1993, 251 p.
2. Wittig S., Scherer V. Heat transfer measurements downstream of a two-dimensional jet entering a crossflow. Journal of Turbomachinery, 1987, No 4, p. 572-578.
3. Foster R., Hadjee-Shceih A. Experimental investigation of boundary layer and heat transfer in the separated zone after normal slot injection. J. of Heat transfer, Trans ASME, ser. C, 1975, N 2, p. 108 - 113.
4. Ktalkherman M.G. and Solovova E.A. Effectiveness of gas screen in a tube at the slot injection normal to air stream, in: Combustion Gasdynamics in Supersonic Flow. Novosibirsk, 1979, p.90 - 101.
5. Repukhov V.M. Thermal protection of walls with gas blowing, Kiev: Naukova Dumka, 1977, 216 p.
6. Abramovich G.N., Girshovich T.A, and Grishin A.M. On the calculation of rarefaction behind a plane jet and a system of round jets injected at an angle into the bounded cross-stream, Izd. VUZov, 1985, N 2, p. 3 - 7.
7. G.N.Abramovich and T.A.Girshovich. On the rarefaction behind a plane jet extending in a crossflow, Izd. AN SSSR, Energetika i Transport, 1984, N 6, p.113-117.
8. Lebedev V.P., Lemanov V.V., Mar'yash V.I, ets. Hydraulic resistance in a tube at interaction of stream with a wall counter jet, Sib. Fiz.-Tekhn. Zhurn., 1993, V. 2, p.41 - 47.
9. Idel'chik I.E., Handbook on hydraulic resistances, M.:Mashinostroenie, 1975, 559 p.

THE STRUCTURE OF THE SEPARATED FLOW BEHIND OBSTACLES AT HIGH EXTERNAL TURBULENCE

V. I. Terekhov, N. I. Yarygina, R. F. Zhdanov

Institute of Thermophysics SB RAS,
630090, Novosibirsk, Russia

1. INTRODUCTION

The separated flow as a means to intensify heat transfer can be successfully used in many types of heat exchangers.

Studies of the separated flow [1] have revealed a particular contribution of large-scale structures to pressure pulsations and to maximum turbulent shears inside the core of the separated shear layer. As the recirculation flow interacts with the main stream along the outer boundary, not only the self-induced turbulence running into 30%, but also the external one becomes an important factor which determines the strength of the interaction, position of the reattachment point and downstream behaviour of the flow. Under the presence of high external turbulence, the integral scale across stream in the reattachment region changes substantially, while in the low-turbulent regime it remains practically unchanged [2, 3].

By now the question on the interaction of a high-turbulent external stream with a separated flow in the reattachment, recirculation and relaxation regions remains open for further investigations and discussions. The present work is aimed at the elucidation of the effect of high external turbulence on dynamic and thermal characteristics of the two-dimensional separation caused by an isolated rib or downward step.

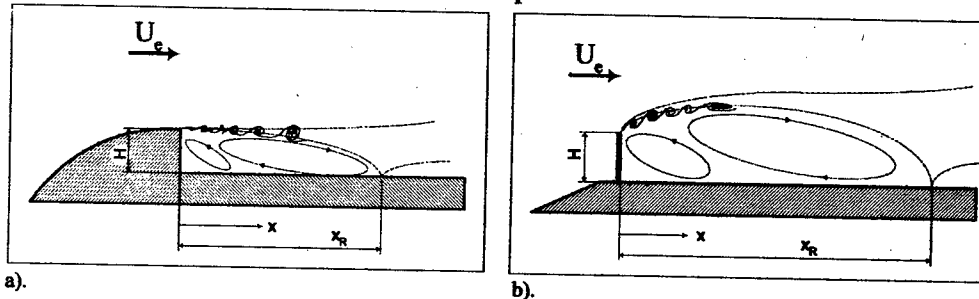


Fig. 1. Flow configuration and coordinates behind a downward step (a) and a rib (b).

Analysis of relevant data reported in the literature has shown that turbulization of the free stream makes it possible to intensify heat transfer over a ribbed surface due to its influence exerted both on the structure of flow around obstacles and on the heat transfer in the recirculation zone situated behind them. However, no quantitative estimations are possible because of lack of experimental results and difficulties arising in modelling separated flows. When evaluating heat transfer in a separated flow according to the κ - ϵ model of turbulence [4], it was assumed that the thickness of the viscous sublayer is self-adjusted as a known function of turbulent energy of the free stream. However, this type of assumption so far was given no experimental verification even for the low-turbulent stream, experimental heat transfer studies in the separation regions being less numerous than those dealing with the hydrodynamic aspects of the problem.

The present work places primary emphasis on the comparative analysis of high-turbulent flows over an isolated rib and a downward step at the same heights of the obstacles and on the comparison between their dynamic and thermal characteristics, in particular, their pressure and heat-transfer coefficients.

2. EXPERIMENTAL EQUIPMENT AND PROCEDURE

The studies were carried out in a subsonic wind tunnel with a 600 mm-long rectangular working channel having the cross-sectional area $200 \times 200 \text{ mm}^2$. The experiments were conducted at the velocity U_e of the free stream over obstacle of 20 m/s at corresponding Reynolds numbers $Re_x = xU_e/\nu = 5 \times 10^3 \div 5 \times 10^5$.

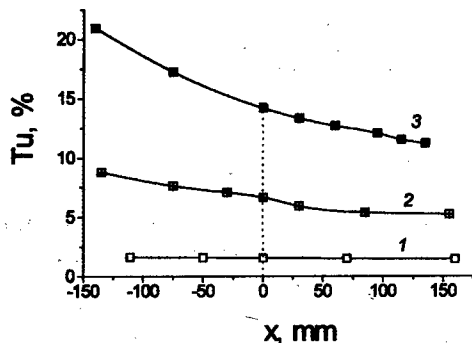


Fig. 2. Longitudinal velocity pulsation of free stream. 1 - without turbulizator; 2 - with «perforated» turbulizator; 3 - with «flag» generator.

mm^2 ensured a uniformly distributed heat flux. Heat-transfer characteristics were measured using 40 Chromel-Alumel thermocouples built-in along the plate axis and spaced about 10 mm apart. The heat leaks due to thermal conductivity of the model were determined from the temperature difference between its sides. In the work, also the static pressure behind the obstacles was determined. In this case, the experimental model was an above-described plate with taps arranged along the working section.

The enhanced external turbulization was introduced by passive «perforated plate»-type and flag-type turbulence generators described in detail elsewhere [5], the velocity pulsations $Tu_e = \sqrt{u'^2}/U_e$ being measured with a DISA 55M one-component hot-wire anemometer. The distributions of Tu_e at the natural level and behind the turbulence generators are shown in Fig. 2.

3. RESULTS AND DISCUSSION

3.1. Effect of turbulence level on some dynamic characteristics of separated streams

The distance x_R between the front edge of the model and the reattachment point is an important characteristic of the recirculation region, the value of x_R coinciding with the coordinate x_{omax} , where the heat-transfer coefficient attains its highest [6, 7]. At the same time, behind the step of a height H being comparable with the thickness δ_0 of the boundary layer in front of it, x_{omax} is shifted with respect to x_R towards the obstacle by one and a half-two gages as compared to H [8].

The test model was a flat textolite plate with an isolated obstacle placed on it. Ribs with the height of 3, 6, 10, 20 and 30 mm, made of an organic glass were anchored in turn to the test model 110 mm from its front edge. In the tests with step, a streamlined 230 mm-long plane packing was fixed onto the plate. The height of the step was varied from 6 to 30 mm by vertically displacing the plate while keeping constant 58 mm. Figures 1a,b show the scheme of the flow behind step and behind rib, respectively, the typical coordinates of the obstacles and those of the separation region being presented as well.

The model equipped with a ribbon heater made of a foil with the total area of 150×400

The length of the recirculation region behind step was evaluated from the profiles of velocity vector (Fig.3a). Although the one-wire sensing element of the hot-wire anemometer used in this study provided data for the reversed and turbulized stream with an inaccuracy being rather substantial, as it is insensitive to the negative direction of the stream, the bend in the

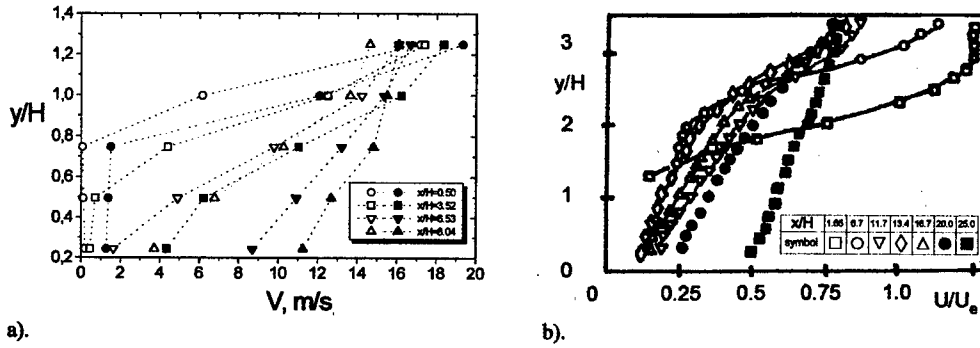


Fig.3. Mean velocity profiles behind a downward step of the height $H=20$ mm (a) and a rib $H=6$ mm (b).

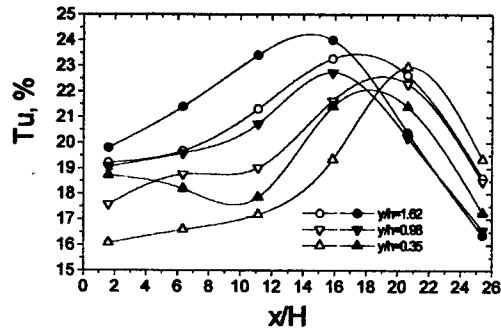


Fig.4. Turbulence intensity distribution behind a rib ($H=6$ mm). Open symbols - $Tu_c=1.5\%$; dark - 14.2% .

profiles correspond to the point with zero velocity. For the negative region, the element generates a stationary signal and, from the reattachment point on, no bend in the velocity profile is observable. According to data shown in Fig.3a, behind the step of the height $H=20$ mm in the low-turbulent stream, the length of the separation region x_R is roughly equal to $8H$, while in the high-turbulent stream ($Tu_c=14.2\%$) $x_R=5H$. This estimate confirms the conclusion made in [2, 3, 7, 9] about marked decreasing of the length of the recirculation region caused by high external turbulence.

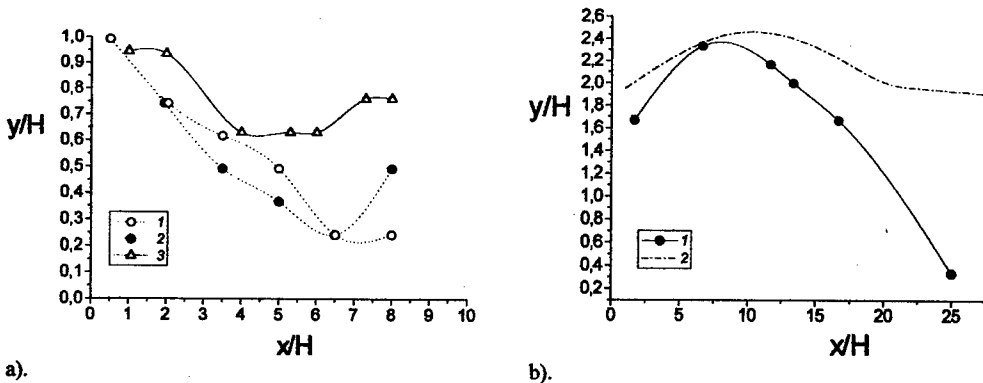


Fig.5. Coordinates of maximum velocity pulsations. a). Step: 1 - $Tu_c=1.5\%$ and 2 - $Tu_c=14.2\%$ ($H=20$ mm); 3 - [10]; b). Rib: 1 - $Tu_c=14.2\%$ ($H=6$ mm); 2 - [8].

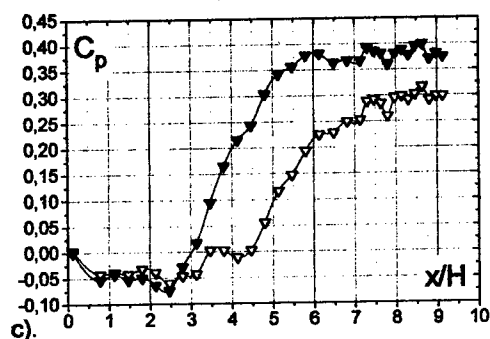
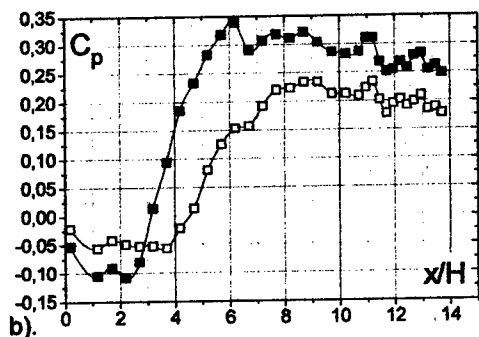
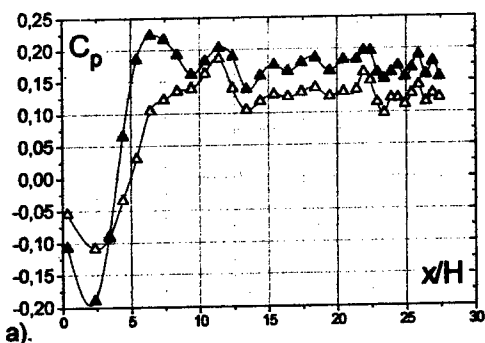


Fig.6. Pressure coefficient distribution in separated and reattached regions formed by a step a). $H=10$ mm; b). 20 mm; c). 30 mm. Open symbols - $Tu_e=1.5\%$; dark - 14.2% .

valid for highly turbulized flows. In Fig.5a at $Tu_e=14.2\%$, turning of points upwards in the reattachment region has occurred at larger distance from the wall than it has at $Tu_e=1.5\%$. Moreover, for the both turbulence levels (see Figs.5a,b) the maxima of pulsational velocity lie close together. Since the position of the maxima approximately coincide with the central line of the mixing layer, in all likelihood, the mixing layer in the turbulized stream gets thick considerably due to increasing vortex-structure scale, and its lower boundary makes the recirculation region shrink.

The distribution of velocity behind rib ($H=6$ mm) at the turbulence level $Tu_e=14.2\%$ (Fig.3b) is very much the same as that behind step, with the only exception that the change in velocity is observable for the heights exceeding the height of rib by more than three times. The latter is due to bending of streamlines in front of rib and due to increasing thickness of shear layer. Behind the reattachment point, over the length of the relaxation region, the velocity profile flattens, the "memory" of the pulsational characteristics being more long. Figure 4 presents the distribution of turbulence intensity over the length of the separation zone in the flow around the 6 mm-long rib for three different distances to the wall, which shows that, as the turbulence level of the approaching stream grows in value, the total level of the pulsational velocity keeps constant, while its maximum moves closer to the obstacle, thus indicating once more that the region of the recirculation zone becomes shorter. Figure 4 also confirms the conclusion made in [8] that no correlation exists between the turbulence energy of the separated flow and that of the outer stream, so that the relationship between them is nonlinear. Figure 5a,b shows in the coordinate x/H and y/H plane the position of the maximum pulsational velocity in the separation region behind a rib and a step at two turbulence levels as compared with the results by other authors. Eaton and Johnston [10] have shown that the closer to the wall the points of the maximum turbulence are situated, the smaller the length of the recirculation-flow region. The values reported by Baker S. for a step [10] are smaller than those for an abrupt expansion of the tube (Eaton J.K. and Johnston J.P. [10]). This conclusion proved to be invalid

3.2. Pressure coefficients

In the experiments, the pressure coefficient was determined as $C_p = 2 \cdot (P_i - P_e) / \rho U_e^2$, where P_i is the static pressure along the separation region, P_e is the pressure in the stream in front of step and over rib. The characteristic velocity U_e over rib was chosen so that the effect due to encumbering H/h of the channel (here h is the height of the working channel) might be neglected. The difference between the velocity in front of rib and that over it at the highest value of H/h , 0.15 ($H=30$ mm), did not exceed 20%.

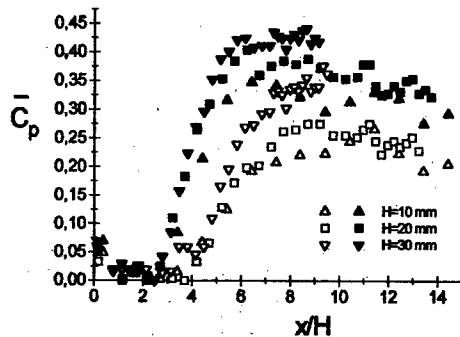


Fig. 7. Reduced pressure coefficient. Open symbols - $Tu_e=1.5\%$; dark - 14.2% .

It is quite reasonable that the pressure coefficient increases with increasing height of obstacle. The shift of the maximum of C_p in the high-turbulent stream points once again to the shortening of the recirculation region. The maximum value of the pressure coefficients increases by a factor of 1.2-1.3, the rarefying in the region adjacent to the step becoming all the more smaller. The total change in the pressure is more clearly illustrated by relative pressure coefficient $\bar{C}_p = (C_p - C_{p\min}) / (1 - C_{p\min})$ first introduced by Roshko A. and Lau j.C. [12],

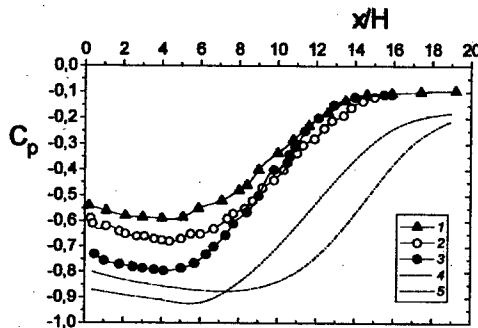


Fig. 8. Pressure coefficient distribution in separated zone formed by a rib. 1 - $Tu_e=14.2\%$ for $H=10$ mm; 2, 3 - $H=20$ mm for $Tu_e=1.5\%$ and 14.2% respectively; 4 - [3] ($H=24$ mm); 5 - with turbulizator [3].

see Fig. 7. The coefficient C_p inside the section where the pressure grows in value is practically independent of the height of the obstacle. For both turbulization levels, stationary values of C_p are attained at the same distances, about $15x/H$. The maximum of C_p increases by 1.3-1.4 times. A completely different type of situation is met when considering the plot of the distribution of pressure coefficient C_p behind rib (Fig. 8). Throughout the whole separation region, the value of the coefficient is negative. Similar results have been obtained in [3, 13, 14]. The relative pressure coefficient $C_p=f(x/H)$ is presented in Fig. 9a showing that the hydraulic resistance of the separation region increases as the level of the external turbulence raises. In the turbulized stream for different rib heights, the values of C_p , unlike in the case of step, do not coincide even in the growth region. Figure 9b shows the dependence of $C_p=f(x/x_R)$, where x_R was assumed equal to the given below values $x_{\alpha\max}$. For the rib with $H=20$ mm, the experimental dependencies at both $Tu_e=1.5$ and 14.2% lie close to the results

Figures 6 show the pressure distribution behind the steps of the height 10 mm (a), 20 mm (b) and 30 mm (c) for two turbulence levels which in the low-turbulent stream has a typical form [11]. Within the zone of the secondary vortex the value C_p is negative, then it increases up to its maximum value at the reattachment point, and, at the point three-four gages downstream it saturates at a constant level.

It is quite reasonable that the pressure coefficient increases with increasing height of obstacle. The shift of the maximum of C_p in the high-turbulent stream points once again to the shortening of the recirculation region. The maximum value of the pressure coefficients increases by a factor of 1.2-1.3, the rarefying in the region adjacent to the step becoming all the more smaller. The total change in the pressure is more clearly illustrated by relative pressure coefficient $\bar{C}_p = (C_p - C_{p\min}) / (1 - C_{p\min})$ first introduced by Roshko A. and Lau j.C. [12],

see Fig. 7. The coefficient C_p inside the section where the pressure grows in value is practically independent of the height of the obstacle. For both turbulization levels, stationary values of C_p are attained at the same distances, about $15x/H$. The maximum of C_p increases by 1.3-1.4 times.

A completely different type of situation is met when considering the plot of the distribution of pressure coefficient C_p behind rib (Fig. 8). Throughout the whole separation region, the value of the coefficient is negative. Similar results have been obtained in [3, 13, 14]. The relative pressure coefficient $C_p=f(x/H)$ is presented in Fig. 9a showing that the hydraulic resistance of the separation region increases as the level of the external turbulence raises. In the turbulized stream for different rib heights, the values of C_p , unlike in the case of step, do not coincide even in the growth region. Figure 9b shows the dependence of $C_p=f(x/x_R)$, where x_R was assumed equal to the given below values $x_{\alpha\max}$. For the rib with $H=20$ mm, the experimental dependencies at both $Tu_e=1.5$ and 14.2% lie close to the results

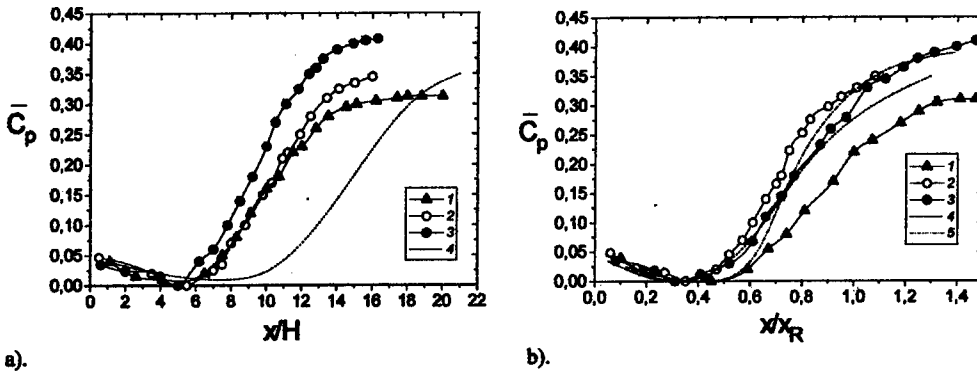


Fig.9. Reduced pressure coefficient. 1, 2, 3 - designations see in fig.8; 4 - [2]; 5 - [12].

of [3, 13] obtained for approximately the same height of obstacles. For smaller height of rib, the dependence $C_p=f(x/x_R)$ turns out to be more gently sloping. The maximum of C_p increases by no more than 1.2 times.

3.3. Heat-transfer coefficients

The heat-transfer coefficients measured up in the low-turbulent stream on a plate without an obstacle are represented by the following standard dependence:

$$St=0.029 \cdot Re_x^{-0.2} \cdot Pr^{-0.6}$$

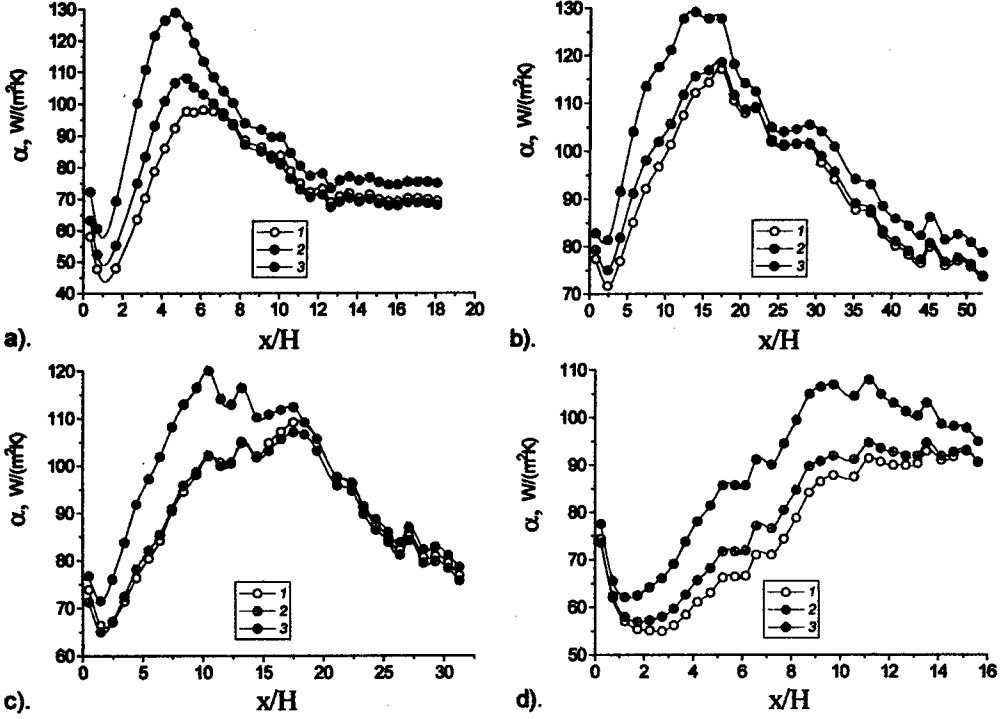


Fig.10. Heat transfer coefficient distribution behind a step $H=20$ mm (a) and a rib: b). $H=6$ mm; c). 10 mm; d). 20 mm. 1 - $Tu_x=1.5\%$; 2 - $Tu_x=6.6\%$; 3 - $Tu_x=14.2\%$.

At smaller distances, the effect due to starting length becomes essential. The effect due to the turbulence generated by the perforated plate on heat transfer was found not to exceed 5%, while that due to the turbulence behind the flag generator increases it by no more than 15%.

The distribution of heat-transfer coefficient at three different turbulence levels behind obstacles is illustrated by fig.10. Behind the step of the height 20 mm (fig.10a), at increasing external turbulence, a shift of $x_{\alpha_{max}}$ from 6 down to 5 and 4.5 gages is observed for $Tu_e=6.6\%$ and 14.2% , respectively, the value of $x_{\alpha_{max}}$ increasing by 10% and by about 30%. Throughout the whole separation region, there takes place a substantial growth of heat transfer. At the beginning of the relaxation region, the difference between α in high and low-turbulent streams gets smaller and over the most part of the relaxation region, heat transfer intensification is approximately the same as on plate. A similar situation is observed also behind ribs of different height (fig.10 b, c, d). On the whole, the heat transfer behind a rib is greater than that behind the step of the same height, and it increases with decreasing height of rib. The length of the recirculation region, and, correspondingly, the distance to the maximum of the heat-transfer coefficient is larger than that behind step. At $H=20$ mm $x_{\alpha_{max}}/H=15$ in the low-turbulent stream, and this ratio increases with decreasing height of rib. In the high-turbulent stream at $Tu_e=14.2\%$, the difference caused by different heights is negligible and $x_{\alpha_{max}}/H=11$, and the largest increase in α_{max} takes place in case of the highest rib, amounting to 22%, i.e., being smaller than that in case of step. Otherwise the behaviour of the dependencies behind ribs is the same as behind steps.

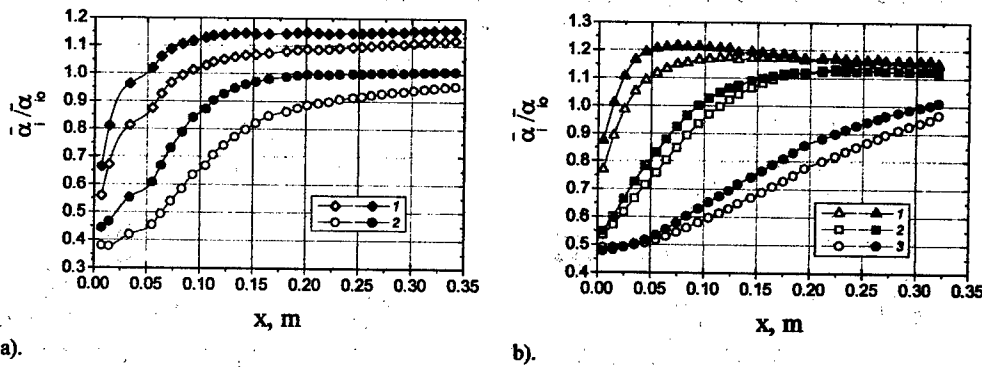


Fig. 11. Average heat transfer coefficient in separated region formed by a step (a): 1 - H=10 mm; 2 - 20 mm and a rib (b): 1 - H=3 mm; 2 - 6 mm; 3 - 20 mm. Open symbols - $Tu_e=1.5\%$; dark symbols 14.2%.

The effectiveness of turbulization in increasing heat transfer can be estimated by considering mean values of $\bar{\alpha}$. Figure 11 present the plot of dependencies $\bar{\alpha}_i/\bar{\alpha}_0 = f(x_i)$ in low- and high-turbulent streams for 10 and 20 mm-high steps and 3, 6, and 20 mm-high ribs. Here $\bar{\alpha}_i$ is the value α averaged over the section stretching from the initial point x_0 to the coordinate x_i , $\bar{\alpha}_0$ is the mean value of heat-transfer coefficient for plate on the interval x_i-x_0 . In the zone of secondary corner vortex, low values of normalised mean heat-transfer coefficient are observed, then up to the reattachment point they grow in value substantially in an abrupt manner and, afterwards, they increase slightly in the relaxation region. While behind steps at $Tu_e=1.5\%$ throughout the heat-transfer section length no increase in $\bar{\alpha}$ is seen, behind ribs there takes place an about 10%-enhanced heat transfer (in case of $H=20$ mm x_R is higher than the heating length). The effect due to external turbulence on mean heat-transfer coefficients is

slightly different behind a rib and behind a step. More clearly pronounced heat-transfer intensification behind steps is seen as compared to the case of ribs, especially for $H=20$ mm, where, over the separation region, $\bar{\alpha}$ increases by a factor of 1.45. The increase in $\bar{\alpha}$ over the relaxation region amounts to 20%. On the whole, ribs proved to be more effective intensifier than steps. However, in highly turbulized streams, step may serve as intensifiers as well, with the effectiveness which can be increased by inclining the side wall [5].

4. CONCLUSIONS

The following conclusions can be drawn from the comparison of flows over isolated steps and ribs at high level of external turbulence.

1. In highly turbulized flow with the turbulence level up to 15% the recirculation region behind a step becomes shorter by a quarter of its initial length, while that behind a rib expands, the extension of the region becoming independent of the obstacle height. **2.** The increased external turbulence has a more pronounced effect on heat transfer than on pressure coefficient.

3. More clearly defined influence of external turbulence behind a step is observed as compared to rib of the same height. For example, for $H=20$ mm the maximum heat-transfer coefficient behind step increases by 1.32 times, while that behind rib only by 1.22 times. **4.** The mean integral quantity $\bar{\alpha}$ gives an indication of a substantially increased heat transfer in turbulized streams both behind a rib and, even to a greater extent, behind a step, thus making it possible to optimise the process on ribbed surfaces.

The research described in this paper was made possible in part by Grant № 97-02-18497 from the Russian Foundation for Fundamental Research.

REFERENCES

1. Simpson R. L. Turbulent boundary-layer separation // *Ann. Review of Fluid Mech.* - 1989. - Vol. 21, P. 205-234.
2. Castro I. P., Haque A. The structure of a turbulent shear layer bounding a separation region. // *J. Fluid Mech.* - 1987. - Vol. 179. - P. 439-468.
3. Castro I. P., Haque A. The structure of a turbulent shear layer bounding a separation region. Part 2. Effects of free-stream turbulence // *J. Fluid Mech.* - 1988. - Vol. 192. - P. 577-595.
4. Durst R., Tropea C. Turbulent, backward-facing step flows in two-dimensional ducts and channels // *Proc. of 3rd Int. Symp. on Turbulent shear flows.* - Davis, CA. - 1981.
5. Terekhov V. I., Yarygina N. I., Zhdanov R. F. Heat transfer behind inclined backward-facing step in the presence external flow turbulization // *J. Thermophysics and Aeromechanics* - 1998. - (to be published).
6. Vogel J. C., Eaton J. K. Combined heat transfer and fluid dynamic measurements downstream of a backward-facing step // *ASME. J. Heat Transfer.* - 1985. - Vol. 107. - № 4 - P. 922-929.
7. Dyban E. P., Epik E. Ya., Yushina L. E. Heat transfer on the surface of longitudinally streamlined bodies in the presence of closed separation and external flow turbulization // *Proc. of Tenth Int. Heat Transfer Conf.*
8. Ota T., Sugawara Y. Turbulent heat transfer on the separated and reattached flow around an inclined downward step // *Proc. of Tenth Int. Heat Transfer Conf.* - Brighton, UK. - 1994. - Vol. 3. - P. 113-118.
9. Kiya M., Sasaki K., Arie M. Free-stream turbulence effects on a separation bubble // *Trans. JSME.* - 1984. - Vol. 50. - № 432. - P. 967-972.
10. Eaton J. K., Johnston J. P. A review of research on subsonic turbulent flow reattachment // *AIAA J.* - 1981. - Vol. 19. - № 9. - P. 1093-1100.
11. Chang P. K. Separation of flow. - M: *Mir* - 1972.
12. Roshko A., Lau J. C. Some observations on transition and reattachment of free shear layer in incompressible flow // *Proc. Heat Trans. and Fl. Mech.* - Stanford Univ. Press. - 1965. - P. 157-167.
13. Ruderich R., Fernholz H. H. An experimental investigation of a turbulent shear flow with separation, reverse flow, and reattachment // *J. Fluid Mech.* - 1986. - Vol. 163. - P. 283-322.
14. Vlasov E. V., Jinevski A. S., Karavosov R. K., Frankfurt M. O. Nearwall pressure pulsations in separation region behind twodimensional obstacles // *Proc. LAJI.* - 1982. - iss. 2137. - P. 3-29.

**DEVELOPMENT OF NUMERICAL METHODS ON THE BASIS OF
EULER EQUATIONS
AS APPLIED TO SUPERSONIC AERODYNAMICS PROBLEMS**

V.F.Volkov

Institute of Theoretical and Applied Mechanics SB RAS,
630090, Novosibirsk, Russia

Along with the development of principally new numerical methods and corresponding software designed for solving applied problems of aerogasdynamics, it is also important to modify the existing software systems in order to extend their capabilities, increase their accuracy and reduce computational costs. The user's utilization of software systems often reveals their drawbacks and the need for their modification. Thus, the previously designed software [1, 2] was aimed at numerical calculations of three-dimensional supersonic flow over bodies of revolution and similar configurations in the framework of Euler equations. Its modification [3-6] was necessitated by extending the class of problems being solved (supersonic interaction of two bodies, the flow over lifting surfaces, etc.) and by the need in parametric numerical studies of various configurations. The extension of the class of problems required adaptation of the boundary conditions for more complicated boundaries of the computational domain [3-5]. The use of the one-step pseudo-transient scheme within the framework of existing algorithm for computational time reduction required its further improvement and also conduction of numerical experiments for verification of the modified algorithm properties.

The developed algorithm, which allows one to solve a wide class of problems of today's aerodynamics, is based on solving the Euler equations in an integral form [4, 6]. The computational domain boundaries are the bow shock wave surface, where the shock conditions are satisfied, the body surface, where no-slip conditions are set, the symmetry plane of the body, where the flow symmetry is assumed. The computational domain is split into finite non-intersecting volumes. The computational grid is adapted to the computational domain boundaries. The initial equations are approximated in each elementary volume, the values of gasdynamic parameters at the cell boundaries are additionally determined linearly from their values in the node points. The changes of parameters in the nodes of a finite-difference grid are determined from the relations taking into account their changes in the neighboring finite volumes. Such an approach ensures the second-order approximation with respect to spatial coordinates [4]. A solution is sought under the condition that the flow is supersonic everywhere around the body. This condition allows one to use the marching method in the longitudinal direction. A steady-state solution of the problem of the flow with prescribed initial parameters is found by the pseudo-transient method with the first-order time (one-step scheme) in each longitudinal cross-section. The flow parameters in the first marching cross-section are calculated from the condition of conical flow near the body tip. The bow shock wave position is corrected in the course of solution convergence.

The efficiency of numerical calculations based on the developed scheme for various classes of three-dimensional supersonic flows was tested by comparing

the solution obtained for the flow over conical configurations with the tabulated numerical results from [7]. For various configurations, a comparison is also made with multiple data of physical experiments.

1. Supersonic flow over lifting configurations with sharp leading edges

The method of determining the normal to the edges described in [3] is used in the problems of three-dimensional flow over various bodies to ensure the no-slip condition. The proposed realization of the boundary conditions on the body surface does not require special procedures for calculating the parameters at the leading edge and makes the numerical algorithm uniform.

The calculated and experimental data are compared in [7] for the flow over a lifting configuration (delta wing with a symmetric hexagonal cross-section and leading edge sweep $\chi=75^\circ$) for $M_\infty=4$ and angle of attack $\alpha=8.3^\circ$.

The numerical and experimental results [8] on the flow over a thin delta wing with a sweep angle $\chi=70.67^\circ$, angle of attack $\alpha=14.5^\circ$ and Mach number $M_\infty=4.05$ are shown in Fig. 1. The wing has sharp leading edges and symmetric rhombic profile with relative thickness $C_{\max}=3.3\%$. The leading edge is supersonic in the considered conditions.

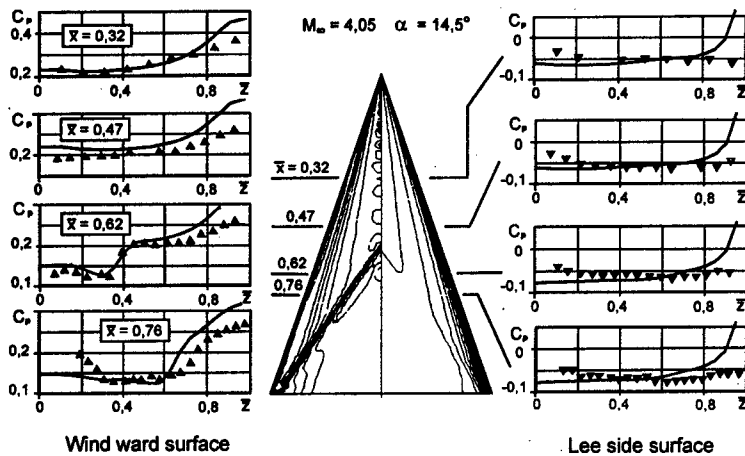


Fig. 1. The flow over a delta wing with rhombic profile.

A good qualitative agreement in the character of variation of the pressure coefficient at the leeward and windward wing surfaces is observed between the computations and experiments. The difference of C_p near the leading edges is caused by the fact that when the shock wave is attached to the leading edge, the boundary conditions disagree with a local plane flow in this region. To eliminate this disagreement, it is necessary to take into account the flow character near a sharp supersonic leading edge, which is similar to a beveled wedge and determines the real shock wave configuration. The disagreement observed in the region $0 < z < 0.3$ in cross-section $\bar{x}=0.76$ at the windward side is explained by the sting influence in experiment [8]. The calculated isolines of the pressure coefficient at the windward and leeward sides of the wing are shown in the central part of Fig. 1 (left and right parts, respectively). It is seen that a conical flow is observed only up to the lines of surface inflection.

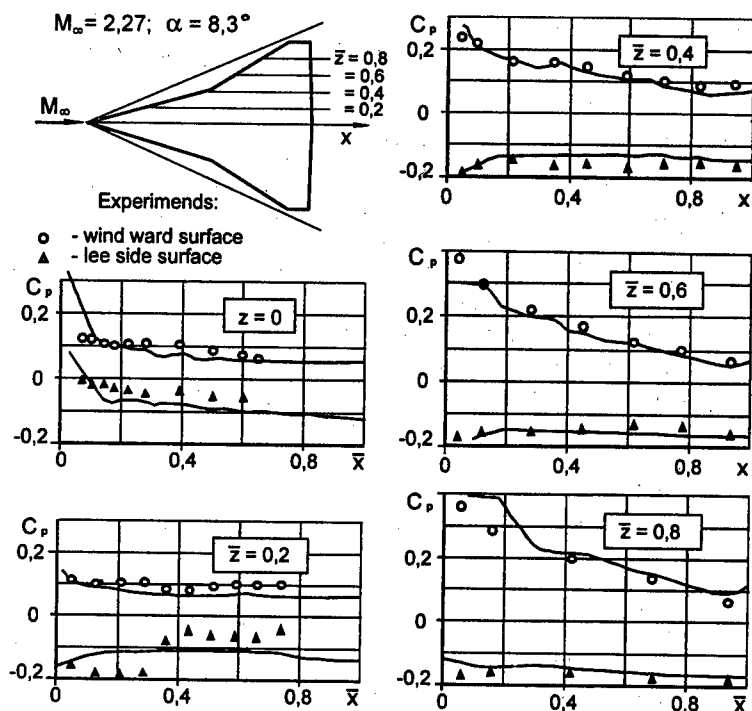


Fig. 2. The flow over a TU-144 wing.

The calculated results (lines) and experiments [9, 10] for a wing of TU-144 are compared in Fig. 2 for $M_\infty=2.27$ and angle of attack $\alpha=8.3^\circ$. This wing with a flat mid-surface has a parabolic profile along the local chord with variable spanwise relative thickness, whose maximum value is $C_{max}=3\%$. On the whole, the calculated results are in good agreement with the experiment. The maximum difference is observed at the leeward side in cross-section $\bar{z}=0.2$, near the leading edge at $0 < \bar{x} < 0.2$ (see Fig. 2), and also in the root part of the local chord ($\bar{x} > 0.7$) where the local characteristics were affected by the sting. The calculated value of the lift force coefficient $C_y=0.227$ is by 6% lower than that obtained experimentally on the basis of pressure measurements.

2. Supersonic flow over the body in the presence of a surface

When the flow over the body with a closely positioned surface is calculated (Fig. 3,a), the no-slip conditions at the interaction surface are added to the Rankine-Hugoniot conditions at the external boundary of the computational domain [4]. We consider situations of regular interaction between the bow shock waves and the shock waves in the disturbed region. A specific feature of the numerical algorithm used for solving this problem is the determination of the points of the bow shock wave intersection with the surface in a cylindrical coordinate system r^* , φ^* , and the satisfaction of the boundary conditions (reflection) near this line.

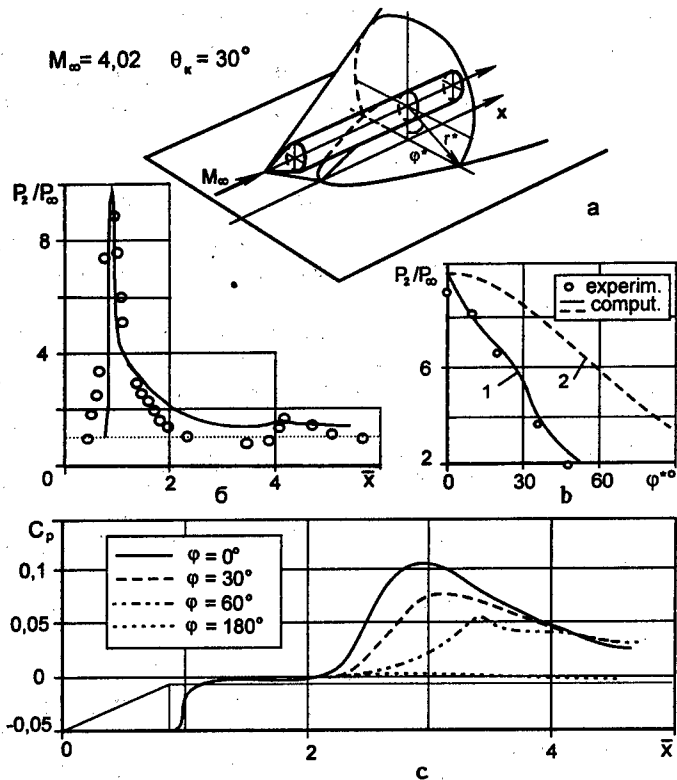


Fig. 3. Interference of the body of revolution with a plate.

Experimental data from [11] were used to test the algorithm. The flow over a body of revolution that has a conical forebody with half-angle $\theta_k=30^\circ$ was studied in this work for $M_\infty=4$. The cylindrical part of the body had an aspect ratio $\lambda=5$. The relative distance from the body axis to the surface was $\bar{R}=R/L_k=1.1$ where L_k is the cone length. Figure 3, c shows the calculated distribution of relative pressure P_2/P_∞ versus ϕ^* along the surface trace of the shock wave induced by the body (line 1), as compared with experimental data and calculations for the shock induced by a purely conical body (line 2). A more intense decay of pressure in comparison with a purely conical shock is caused by the influence of expansion wave propagating from the hinge of the body generatrix. The computation is in good agreement with the experiment, except for the point $\phi^*=0$, where the shock wave/boundary layer interaction effects are observed in experiment.

Figure 3, b shows a comparison of pressure distributions $P_2/P_\infty(\bar{x})$ on the plate along the interaction line symmetry axis ($\bar{x}=x/L_k$). A satisfactory agreement between the computation and experiment [11] is seen. A certain difference at $1.5 < \bar{x} < 4$ is explained by effects of the boundary layer separation caused by the bow shock wave. The influence of the shock wave reflected on the plate surface can be estimated from the pressure coefficient distribution on the body along the cylinder generatrix calculated for various ϕ^* (Fig. 3, d). A lower C_p maximum with increasing ϕ^* is related to a smaller angle of flow deflection from the side surface. It should be noted that at the body generatrix, which is

external to the plate ($\varphi=180^\circ$) the shock reflected on the plate does not exert any influence, and the pressure distribution corresponds to the flow over an isolated body. A repulsive force is induced between the plate and the body in this flow. The calculated value of this force coefficient $\Delta C_y=0.1505$ is fairly close to experimental value $\Delta C_y=0.135$ [11].

3. Estimation of sonic boom parameters

To estimate quantitatively the sonic boom affecting the ground-based objects during supersonic flight, we need the methods for calculating the shock wave strength at large distances from the aircraft.

The existing asymptotic methods allow one to estimate the sonic boom at large distances with suitable accuracy only for disturbance sources of simple shape. For a real aircraft, one has to take into account the disturbances initiated by various constructive elements, which makes the problem more complicated. An approach based on determination of the sonic boom intensity in the far field by recalculating the flow parameters on the control surface of the near field was developed in [12] (Fig. 4, a). The flow parameters on this surface are determined by solving numerically the problem for a real configuration or using the results of a physical experiment.

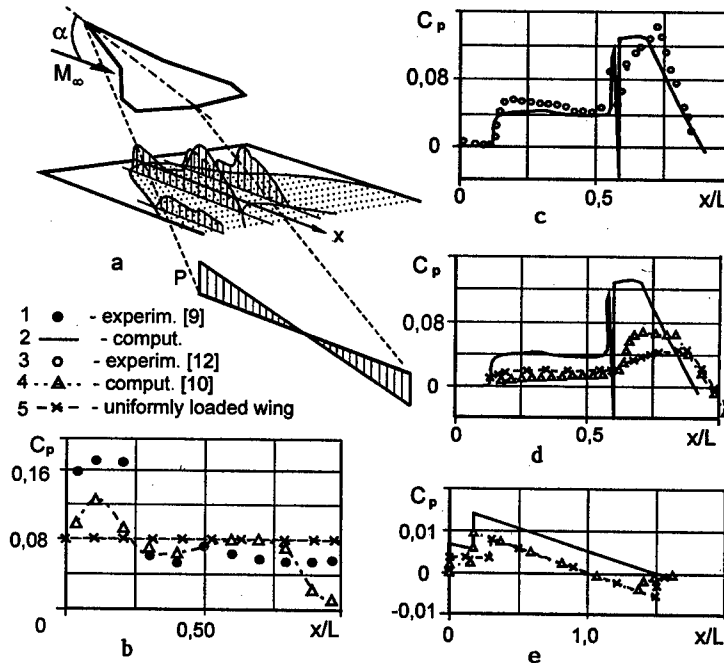


Fig. 4. Calculation of sonic boom parameters.

From the estimates of [13, 14], the sonic boom intensity for heavy transport aircraft at large distances from the source depends on the lift force, wing planform and load distribution over the wing, along with the governing parameters (flight Mach number, distance to the Earth surface). These parameters can be obtained on the basis of pressure distribution over the wing surface obtained numerically or experimentally [9, 10]. The sonic boom

parameters in the near field of the wing of a supersonic passenger aircraft (such as TU-144) calculated for $M_\infty=2.27$ and angle of attack $\alpha=5.6^\circ$ using the experimental load distribution from [9] (Fig. 4, *b*, marked by 1) are presented in Fig. 4, *c* (2) together with the corresponding experimental data (3) from [12]. The longitudinal coordinate x is related to the length L of the root chord of the wing. A good agreement of the calculated pressure distribution with that registered experimentally is seen. Figure 4, *d* shows the calculated pressure distribution in the near field (marked by 2, 4, and 5) for various distributed loads on the wing for the same free-stream parameters and fixed lift force (Fig. 4, *b*) determined experimentally in [9], and also numerical results for the same wing [10] and uniformly loaded wing (marked by 1, 4, 5). The calculations for the medium zone, where an N-wave is formed, for the same cases (the same notations) are shown in Fig. 4, *e*. It is seen that a uniformly loaded wing (marked by 5) ensures the minimum sonic boom intensity.

The work was supported by the Russian Foundation for Basic Research (grant 97-01-00885).

References

1. N.N.Yanenko, V.M.Fomin, V.L.Ganimedov, et al. Applied software system for solving the problems of aerodynamics, hydrodynamics, and continuum mechanics (ARFA). — State Archive of algorithms and codes, Moscow, 1984, No. POO 7481.
2. L.G.Vasenev, V.F.Volkov, V.L.Ganimedov, et al., Software system ARFA. Three-dimensional supersonic flow over bodies of revolution. — Novosibirsk, 1984. — 38 p. — (Preprint / Inst. Theor. Appl. Mech., Sib. Branch, USSR Acad. Sci.; No. 22-84).
3. V.F.Volkov, I.I.Mazhul, and D.V.Shcherbik, Computation of supersonic flow over spatial configurations with sharp leading edges // *Thermophysics and Aeromechanics*, 1995, Vol. 2, No. 3, P. 227-234.
4. V.F.Volkov, An algorithm for solving the problems of spatial supersonic interaction of two bodies. — Novosibirsk, 1987. — 20 p. — (Preprint / Inst. Theor. Appl. Mech., Sib. Branch, USSR Acad. Sci.; No. 29-87).
5. V.F.Volkov, Computation of spatial supersonic inviscid flow over bodies close to prismatic ones // *Modelirovanie v mekhanike*. — 1993. — Vol. 7(24), No. 3. — P. 3-14.
6. A.P.Shashkin and V.F.Volkov, A scheme of numerical calculation of inviscid gasdynamic flows. // *Problems of the Flow over Three-Dimensional Bodies*. — Novosibirsk, 1978.
7. A.A.Zhel'tovodov, I.A.Bedarev, A.V.Borisov, V.F.Volkov, et al., Development and verification of numerical methods for supersonic aerodynamics problems. — Novosibirsk, 1997. — 52 p. — (Preprint / Inst. Theor. Appl. Mech., Sib. Branch, USSR Acad. Sci.; No. 7-97).
8. L.G.Vasenev, Aerodynamic wing/body interference at supersonic speeds: Ph.D. Thesis, Novosibirsk, 1989.
9. M.D.Brodetsky, A.B.Koshcheev, and G.A.Cheremukhin, Experimental study of distributed aerodynamic characteristics of three-dimensional wings at supersonic speeds // *Studies of Three-Dimensional Wing Aerodynamics*. — Novosibirsk, 1977. — P. 144-159.
10. M.D.Brodetsky, Yu.G.Bokovikov, A.B.Koshcheev, and A.M.Makhnin, The study of aerodynamic characteristics of three-dimensional wings at supersonic speeds // *Problems of Gasdynamics*. — Novosibirsk, 1975. — P. 183-186.
11. M.D.Brodetsky and E.K.Derunov, Experimental study of the interference of two bodies of revolution during their separation in the presence of a flat surface: Report No. 1567 / Inst. Theor. Appl. Mech., Sib. Branch, USSR Acad. Sci. — Novosibirsk, 1985.
12. M.D.Brodetsky, V.F.Volkov, E.K.Derunov, and A.B.Koshcheev, The far field sonic bang parameters study on the basis of experimental data in the vicinity of supersonic passenger aircraft model // *Int. Conf. on the Methods of Aerophysical Research: Proc. Pt. 2*. — Novosibirsk, 1994. — P. 19-22.
13. J.Moris, An investigation of lifting effects on the intensity of sonic booms // *J. of Roy. Aeron. Soc.* — 1960. — Vol. 64, No. 598. — P. 610-616.
14. V.F.Volkov, The influence of the pressure distribution over the wing on the sonic boom parameters // *J. Appl. Mech. Tech. Phys.* — 1996. — Vol. 37, No. 2. — 99-102. (In Russian.)

NONLINEAR PROCESSING OF VELOCITY FIELDS CALCULATED WITH PIV - METHOD DATA

Yu.E.Voskoboinikov V.G.Belyavtsev
Novosibirsk State Architectural-Building University
630008 Novosibirsk st.Leningradskay 113

INTRODUCTION

The PIV method (particle - image velocimetry method) [1] have found wide application during the passed ten years in experimental investigation of velocity fields in fluids. The method consists in that one takes moving pictures or makes video records of position of specially introduced marked particles in a flow at precisely given times t and $t+\Delta t$. Then whole observable section is divided into rectangular (most frequently square) fragments of $N_1 \times N_2$ pixels known as spots. For each (j_1, j_2) - spot the maximum value of correlation function is calculated. Then on this values the displacement vectors $h(j_1, j_2)$ are determined. The velocity vectors which must be found in the time moment t , in the point (j_1, j_2) are proportional for this displacement vectors. However, digital processing and random character of initial images cause contradiction between resolution of the method and stability of calculated estimates of the velocity fields.

This contradiction consists in following: at increase of the spot size (i.e. volume of sample) random estimation error of a velocity vector (random distortion of direction and length) is reduced but is worsened the resolution of a method because of replacement all «true» velocity vectors within a spot by one average vector. At decrease of the spot size the return law is observed.

In the given work for reduction of random estimation errors a class of nonlinear vector filters is offered. These filters have better performance than filters, used in [2] for processing separate projections of velocity vectors (scalar filtering).

NONLINEAR VECTOR FILTERS

The shift vector $\tilde{h}(j_1, j_2)$ calculated on correlation function can be presented as

$$\tilde{h}(j_1, j_2) = h(j_1, j_2) + b(j_1, j_2) + \xi(j_1, j_2), \quad (1)$$

where $h(j_1, j_2)$ is the exact shift vector, $b(j_1, j_2)$ is the systematic error, caused by the averaging of vectors in spot area, $\xi(j_1, j_2)$ is the random error, caused by limited volume of data within the spot which is used to calculate correlation function.

Mentioned above contradiction between stability and resolution of PIV method can be solved by reduction of the spot size (reduction of systematic error $b(j_1, j_2)$) with following smoothing of vector field $\tilde{h}(j_1, j_2) = \{\tilde{h}_x(j_1, j_2), \tilde{h}_y(j_1, j_2)\}$ (reduction of random error $\xi(j_1, j_2)$). It is clear, this filter should not cause appreciable increase of a systematic error.

This approach was realized in work [2], in which nonlinear combined filters [3] were used for filtering separate scalar fields $\{\tilde{h}_x(j_1, j_2)\}$ and $\{\tilde{h}_y(j_1, j_2)\}$. As between projection $\{h_x(j_1, j_2)\}$ and $\{h_y(j_1, j_2)\}$ correlation is possible, the processing of vector field (instead its projections) can essentially reduce a random error.

For definition of nonlinear vector filters the following designations will be introduced. Let given a sequence of vectors x_1, x_2, \dots, x_N . The median x^M of this sequence will be identified a vector of this sequence, which satisfies a condition [4]:

$$\sum_{i=1}^N \|x^M - x_i\| \leq \sum_{i=1}^N \|x_j - x_i\| \quad (2)$$

for any vector x_j . The operation of calculation of median will be denoted as

$$med\{x_1, x_2, \dots, x_N\}.$$

The average vector x^{AV} of this sequence will be defined as

$$x^{AV} = \frac{1}{N} sum(x_1, \dots, x_N), \quad (3)$$

where $sum(\bullet)$ denotes a vector summation operation.

The operation of calculation average vector will be denoted as

$$aver\{x_1, x_2, \dots, x_N\}.$$

Using introduced operations we can define local vector filters. These filters process only that vectors $\tilde{h}(j_1, j_2)$, which have fallen into the filter aperture A centered at spot (i_1, i_2) . Hereinafter such vectors will be denoted as

$$\tilde{h}(i_1 + l_1, i_2 + l_2), \quad (l_1, l_2) \in A.$$

So for square window with size 5×5 $l_1 \in [-2, -1, 0, 1, 2]$, $l_2 \in [-2, -1, 0, 1, 2]$.

The output signal of median vector filter is defined by the expression [4]:

$$h^M(i_1, i_2) = med(\tilde{h}(i_1 + l_1, i_2 + l_2)), \quad (l_1, l_2) \in A. \quad (4)$$

Such filters well delete pulsed noise, but not so good smooth the lowamplitude noise. Therefore in analogy with [3] we will introduce combined vector filters.

Filter CF1:

$$h^{CF1}(i_1, i_2) = \text{aver}\{\tilde{h}(i_1 + l_1, i_2 + l_2), (l_1, l_2) \in A: \|\tilde{h}(i_1 + l_1, i_2 + l_2) - h^M(i_1, i_2)\| \leq F\} \quad (5)$$

Filter CF2:

$$h^{CF2}(i_1, i_2) = \text{aver}\{h^M(i_1 + l_1, i_2 + l_2), (l_1, l_2) \in A: \|h^M(i_1 + l_1, i_2 + l_2) - h^M(i_1, i_2)\| \leq F\} \quad (6)$$

Output signal of filter CF1 in a point (i_1, i_2) is defined by averaging of such vectors in filter aperture, which on norm differ from median $h^M(i_1, i_2)$ on value no more than F . Value F is determined from variance of noise ξ , for example $F = 3\sigma_\xi$. Output signal of filter CF2 in a point (i_1, i_2) is defined by averaging of medians h^M in filter aperture, which on norm differ from median $h^M(i_1, i_2)$ on value no more than F . This increases a quality of the filtration under intensive pulsed distortion. For study the offered vector filters (4), (5), (6) was made following computing experiment.

COMPUTING EXPERIMENT AND REAL EXPERIMENT

For "exact" vector field $h(j_1, j_2)$ was accepted field 100×100 spots. The original vector field distorted by the noise with pulsed and lowamplitude components. The level of pulsed component was 100% and the level of lowamplitude component was 5%. Was it changed percentage contents of pulsed noise 0%, 5%, 10%. Noised vector field was processed by filters (4), (5) and (6). In the next table

Pulsed noise %	Median filter \mathcal{E}^F		Filter CF1 \mathcal{E}^F		Filter CF2 \mathcal{E}^F		Relative error \mathcal{E}^h
	Scalar	Vector	Scalar	Vector	Scalar	Vector	
0	0.028	0.026	0.025	0.016	0.023	0.013	0.051
5	0.032	0.028	0.031	0.023	0.029	0.018	0.231
10	0.036	0.033	0.034	0.031	0.031	0.028	0.319

are provided the relative error \mathcal{E}^h of vector field $h(i_1, i_2)$

$$\mathcal{E}^h = \frac{\sum \sum \|\tilde{h}(i_1, i_2) - h(i_1, i_2)\|}{\sum \sum \|h(i_1, i_2)\|} \quad (7)$$

and relative filtering errors ε^F

$$\varepsilon^F = \frac{\sum \sum \|h^F(i_1, i_2) - h(i_1, i_2)\|}{\sum \sum \|h(i_1, i_2)\|}, \quad (8)$$

which was obtained with offered vector filters (4),(5),(6) and scalar filters from [3]. In expression (8) value $h^F(j_1, j_2)$ means vector field after filtering. As can be seen, smaller relative filtration error is provided by filter CF2 defined by expression (6).

As an example of processing of real physical experiment we shall consider the following results. The initial data PIV - method were submitted by two images of particles in a flow, registered at the moment of time t and $t + \Delta t$. The size of the images 512×480 pixels. These images were divided on spot by the size 16×16 . The field of displacement vectors calculated on this initial data is shown on fig. 1. The field contains abnormal displacement vectors. The occurrence of these vectors is caused in small volume of data at calculation correlation functions. For removal of abnormal vectors was used the vector filter CF2. The result of processing is shown on fig. 2. Essential improvement of accuracy of calculation of a displacement vectors field on PIV - method data is visible.

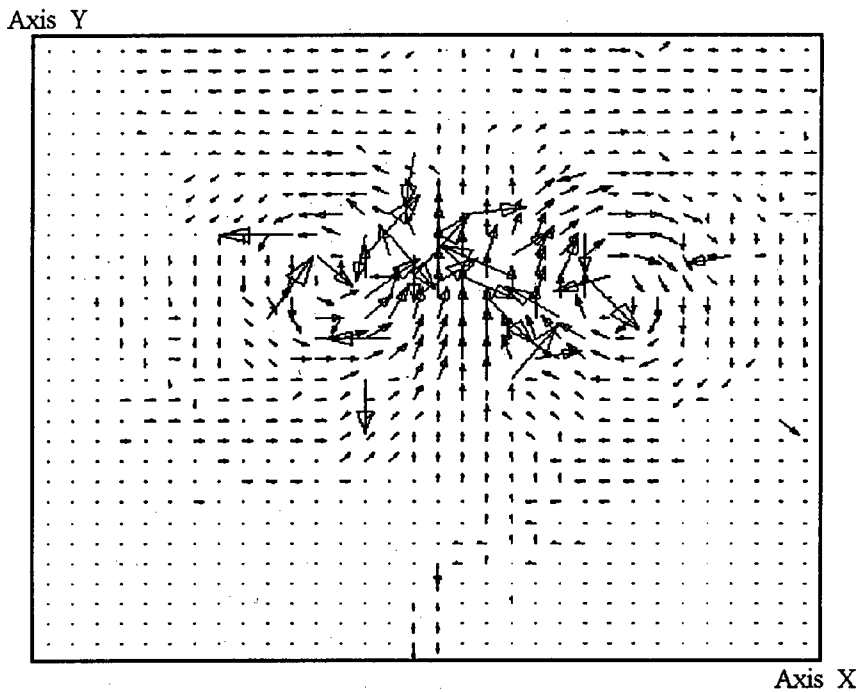


Fig. 1

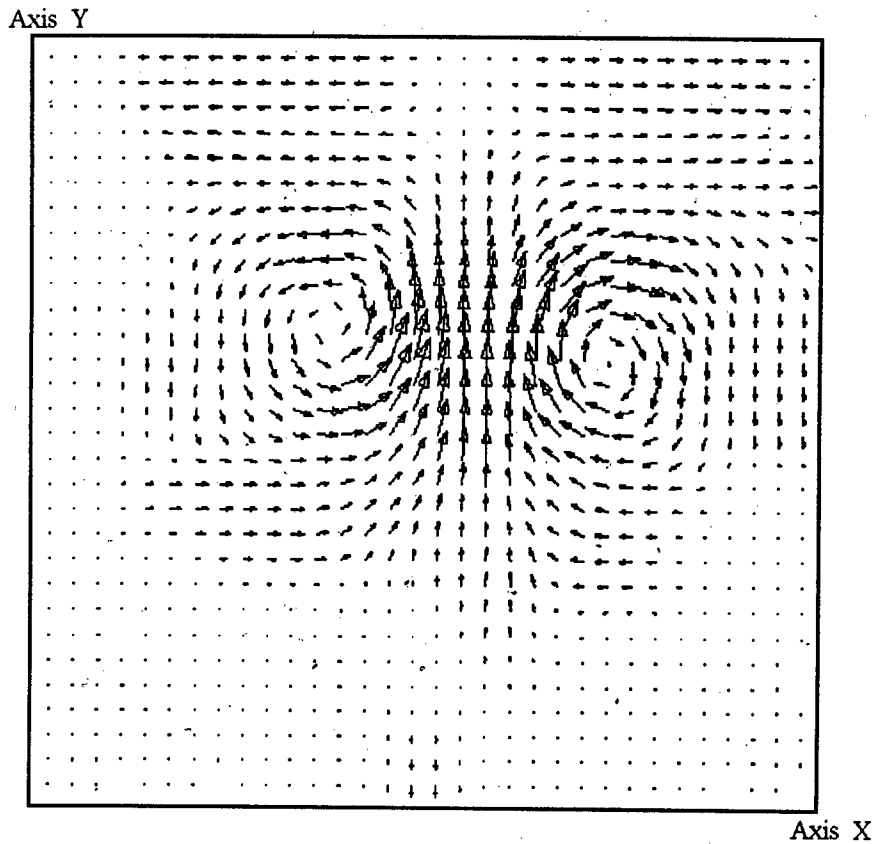


Fig. 2

Thus offered in work nonlinear vector filters allow to remove (in a certain degree) the contradiction of processing of a PIV-method data .

REFERENCES

1. Willert C.E., Gharib M. Digital particle image velocimetry // Experiments in Fluids. – 1991. – Vol.10 – P.181.
2. Voskoboinikov Yu.E., Ivanov M.S., Kislenco N.P., Moseichuk O.N. Efficient algorithms of calculation and processing of velocity fields by particle image in flows // Optoelectronics, Instrumentation and Data Processing. – 1996. --№ 3. – P.32.
3. Bronnikov A.V., Voskoboinikov Yu.E. Composite algorithms for nonlinear filtering of noisy signal and images // Avtometriua. – 1990. – №1. – P. 21.
4. Astova J., Haavisto P. Vector median filter // Proc. IEEE. – 1990. – v. 78. – № 4. – P. 678.

NUMERICAL MODELING OF SUPERSONIC FLOW IN PLANE CHANNEL WITH THE LOCAL SOURCE OF ENERGY

V.P. Zamuraev

Institute of Theoretical and Applied Mechanics SB RAS, Novosibirsk, Russia

The effects related to local action upon supersonic flows are of certain interest. This interest is due to the fact that the flow structure can be sometimes changed by comparatively low energy or substance consumption. The results of [1, 2] can be used as examples.

The effect of a local energy source on a supersonic flow in a plane channel is considered in the present paper. This effect can increase the flow vorticity, which is important for mixing of chemically reacting substances, for the processes of supersonic combustion, etc. [3]. The consideration is confined to the Euler equations of motion of the perfect gas. It is assumed that the size of the energy release region can be by 2-3 or more orders smaller than the channel size. In this case, a specially developed technique is used in the paper. It can be classified as a method of overlapping grids, it differs from the existing grids by the fact that the cell sizes can differ by two orders of magnitude.

PROBLEM FORMULATION

A supersonic flow in a constant-area plane channel with a local energy source near the wall is modeled. The Euler equations are solved in a conservative form with a constant ratio of specific heats γ :

$$\partial U / \partial t + \partial F / \partial x + \partial G / \partial y = 0,$$

$$U = (\rho, \rho u, \rho v, e), \quad F = (\rho u, p + \rho u^2, \rho uv, u(p+e)), \quad G = (\rho v, \rho uv, p + \rho v^2, v(p+e)).$$

The x and y coordinates are directed along and across the channel, respectively, and related to the channel width d ; the time t is related to d/a_0 , the gas velocity components u and v and the sound velocity a - to a_0 , the density ρ - to ρ_0 ; the pressure p and the total energy of unit gas volume e are normalized to $\rho_0 a_0^2$; p_0 and a_0 are dimensional pressure and sound velocity in the flow at the channel entrance (the corresponding gas density is $\gamma\rho_0$). For the gas model under consideration

$$p = (\gamma - 1) \cdot (e - \rho(u^2 + v^2)/2), \quad a^2 = \gamma p / \rho.$$

The non-disturbed flow parameters are set for solving these equations at the channel entrance ($x=0$). Extrapolation is used at the channel exit ($x=l$) for supersonic speeds. The no-slip condition $v=0$ is set at the channel walls ($y=0$ and 1). At the initial time moment, the gas parameters in the entire flow region, except for a small energy release region, are the same as at the channel entrance. The energy source is located near the wall and has a rectangular shape ($l_1 \leq x \leq l_2$, $0 \leq y \leq d_2$). It is assumed that the energy is released very rapidly and the gas density does not change during an appropriate time interval, only local pressure and temperature

change. A higher initial pressure (and temperature) are set in this region. All other parameters (ρ, u, v) are the same as in the remaining part of this region.

NUMERICAL TECHNIQUE

The MacCormack scheme [4, 5] combined with a certain grid procedure is used to solve numerically the posed problem. The overlapping grids are widely used in the literature for solving steady problems [6, 7]. Unsteady problems are solved using two- and three-level adaptive grids with step decreasing by a factor of 2-4 [8-10], and also using the method of unstructured grids [11], where the number of connection of a given node with the neighboring ones is at most doubled. All these approaches, however, require great memory costs for solving the problem considered here. The technique used in the present paper allows one to introduced grids with a smaller step (by an order of magnitude) in certain flow regions. The above approaches do not allow one to do this because of considerable oscillations or nonphysical waves.

In accordance with the present technique, the flow domain, in which the gasdynamics equations are numerically solved, is split into a number of subdomains sequentially surrounding one another. Each of them has its own rectangular grid with the identical directions of cell sides. The most coarse grid is in the external subdomain. The grids become more refined when passing from the external subdomain to the internal one. The most refined grid is in the most internal subdomain, including the energy source region. When passing from one grid to another, the step can be decreased rather considerably, for example, by an order of magnitude, and the step of integration in time decreases correspondingly. Thus, the Courant criterion has the same value for all subdomains, and each of them can be calculated using the same difference scheme.

To merge the solutions, the subdomains are extended to the neighboring ones. For simplicity, hereinafter we will assume that the flow domain is split into two subdomains: with coarse (1) and refined (2) grids. Two layers of the coarse grid nodes are introduced in a subdomain with refined grid near the boundary with the coarse grid subdomain. The values of the flow parameters in these layers at the previous time layer are found from the values of these parameters in the nodes of a refined grid for the same time instant. This is done by linear interpolation. Because of small step, the interpolation error is also small. The resultant parameters are used as boundary conditions for finding a solution in the coarse grid subdomain at a new time layer.

In turn, the refined grid is extended to the coarse grid subdomain for one coarse step (with refinement ratio equal to $r = \Delta t_1 / \Delta t_2$, for r steps of the refined grid). The flow parameters in additional nodes of the refined grid are also calculated by linear interpolation of their values in the coarse grid nodes. The resultant parameters are used as boundary conditions for finding a solution in the refined grid subdomain. Using the same difference scheme (arbitrary scheme using hydrodynamic fluxes), the calculation at a new time step is then performed. Only one time step Δt_1 is made in subdomain (1), whereas r steps are made in subdomain (2), each of them being equal to Δt_2 . The number of nodes in each extended subdomain, where the new parameters are calculated, is reduced on the side of the other subdomain. As a result, the flow parameters at the new time step are known in all nodes of non-extended subdomains. This procedure does not induce oscillations and nonphysical waves.

The MacCormack scheme [4] with spatial splitting was used as a difference scheme. The order of integration with respect to coordinate axes was alternated. To improve the

difference scheme properties, artificial viscosity of the fourth order was applied [5]. It is modified here, taking into account that the grid is refined in a certain subdomain.

TEST COMPUTATIONS

A number of one-dimensional and two-dimensional problems were considered as test computations: propagation of a shock wave, contact discontinuity and rarefaction wave through a subdomain of the refined grid. In the two-dimensional case, the grid was refined in a certain rectangular subdomain near the channel wall. The computations were performed for a perfect gas with the ratio of specific heats equal to 1.4. A ten-fold pressure difference was set for the shock wave and rarefaction wave. The gas density varied by a factor of 10 at the contact discontinuity. The grid step was refined by a factor of 10, 20, 50, and 100. When these disturbances passed through the grid boundaries, no oscillations arise. The test computations verified the efficiency of this numerical technique.

COMPUTATION RESULTS

The influence of a local energy source on the structure of supersonic flow in the channel was calculated for various values of parameters of both the flow itself and the energy source. The main results presented here refer to the following case. At the channel entrance $p=1$, $\rho=1.4$, $u=2$, $v=0$. The channel length is $l=10$. The energy source region is determined by $l_1=3.125$, $l_2=4.025$, $d_2=0.06$. The initial pressure in it equals $p=10$.

Figures 1-4 show the influence of the local energy source on the flow structure at an early stage of disturbance development ($t=0.1170$). These figures show the fields of pressure,

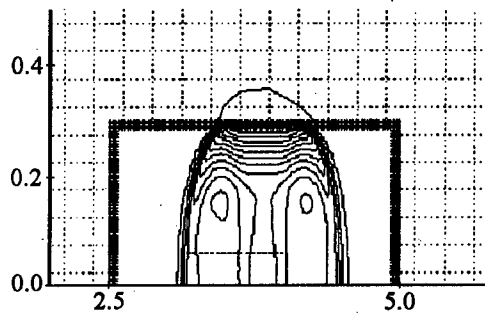


Fig. 1.

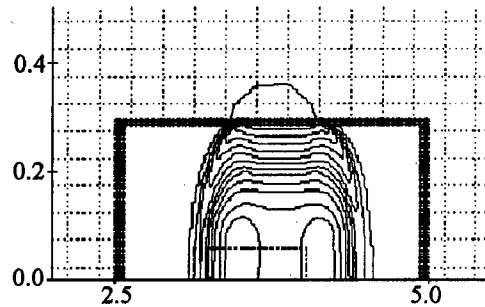


Fig. 2.

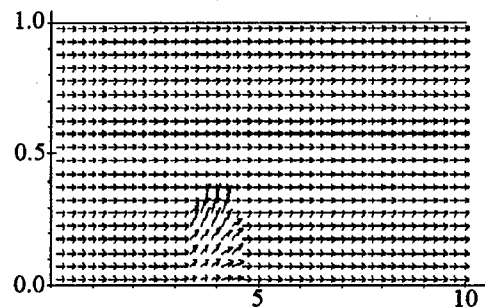


Fig. 3.

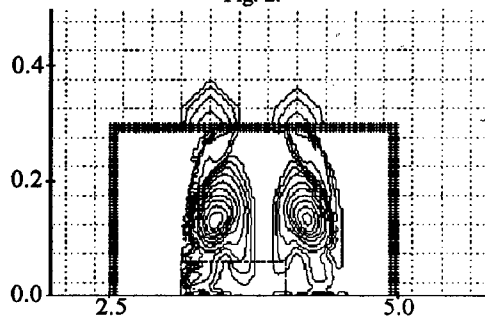


Fig. 4.

density, gas velocity, and flow vorticity, respectively (Figs. 1, 2, and 4 show only a part of the flow domain). The isobars in Fig. 1 are separated by the pressure interval equal to 0.025. The external isobar, which restricts the disturbed flow region, is determined as $p=0.1$ (the pressure is related to the initial value in the energy source region). The dashed lines in the figure represent the coarse grid. The refined grid is only partly shown along the external edge of appropriate subdomain (the refinement ratio is $r=10$). The dashed line in this subdomain shows the energy source region. These comments refer also to Fig. 2, which shows the density levels of 0.3, 0.4 and so on to 2.4 with a 0.2 interval (the density is related to the non-disturbed flow value). The arrows in Fig. 3 indicate in appropriate points the direction of the gas velocity and its value in a certain scale (the solid straight lines with $y=0$ and 1 correspond to the channel walls). The velocities are not shown in all nodes in the refined grid subdomain. Figure 4 shows the lines of constant vorticity which varies from -7 to -1 with an interval equal to 1 (for the left half of the flow domain) and from 1 to 7 with the same interval (for the right half of the domain). Besides, the lines with vorticity equal to -0.5, -0.2, 0.2, and 0.5 are shown.

The decay of an arbitrary discontinuity set at the initial time instant ($t=0$) results in formation of a shock wave. At first, it is straight at some sections. The shock wave is rather strong at the section corresponding to the wave propagation across the channel. The appropriate isobars in Fig. 1 lie close to each other, and the crossflow size of disturbed region increases rapidly. The shock wave strength decreases rapidly at the sections corresponding to the shock wave propagation upstream and downstream. This character of shock wave propagation is related to the energy source geometry ($d_2 \ll l_2 - l_1$).

Rarefaction waves propagate inside the disturbed flow region. The interaction of rarefaction waves propagating upstream and downstream towards each other and the reflection of the rarefaction wave on the channel wall lead to the fact that some regions appear in the disturbed flow, where the pressure is lower than that near the channel wall and in the central part of disturbed flow (see Fig. 1). A similar effect is observed in a plane one-dimensional unsteady case when the centered rarefaction wave is reflected on the wall [12]. When a simple reflected rarefaction wave is formed, the pressure in it becomes lower than near the wall. This effect is complicated here by the problem two-dimensionality, it is caused by the finite size of the energy source region.

The character of mass distribution in the flow validates the mentioned dynamics of initial disturbance evolution. There are also some regions with low density in Fig. 2. The gas mass moves away from the wall. This is also seen from Fig. 3.

Significant vorticity is developed in the disturbed flow region (see Fig. 4). It has negative value in the upstream direction and positive values in the downstream direction (in the right part of the flow domain). By the examined time moment, the disturbance reaches the coarse grid subdomain and enters it. This is also seen from Figs. 1 and 2.

Then the distribution of parameters in the disturbed region is changed. The regions with lower pressures and densities merge. This is illustrated in Fig. 5, which shows isobars for the same pressure values as in Fig. 1 for the time instant $t=0.2048$. The pressure inside the disturbed region decreases but remains still higher than outside it. By the moment $t=0.3633$ (Fig. 6; the dashed lines show the refined grid subdomain and the energy source region) the pressure in the disturbed flow region becomes slightly lower than 0.1. Then the pressure near the wall approaches the non-disturbed flow value, while the gas density is much lower than the non-disturbed flow value because of gas outflow from the wall (see Fig. 7; the above density levels are shown, $t=0.3633$). A certain analogy with strong explosion is observed [13].

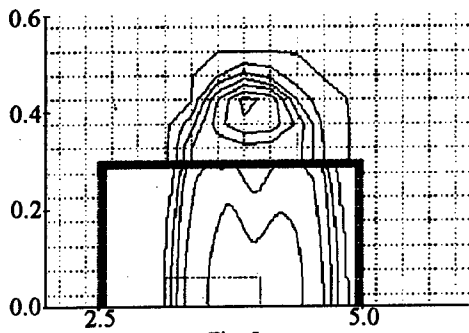


Fig. 5.

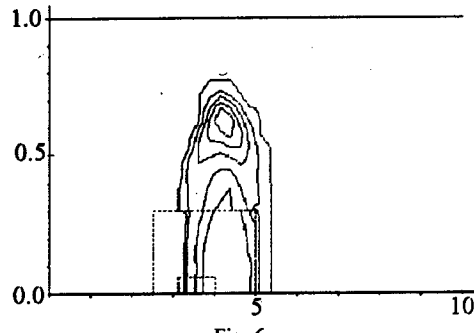


Fig. 6.

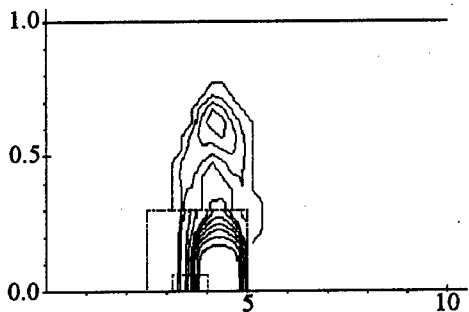


Fig. 7.

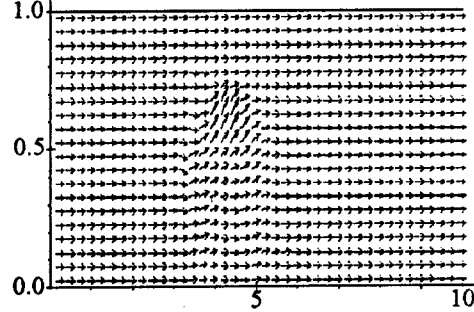


Fig. 8.

It is seen from Fig. 8, which shows the velocity field for $t=0.3633$, that the gas motion acquires a wavy character by this time moment. This testifies to the existence of considerable flow vorticity.

One should also pay attention to comparatively small shift of the disturbed flow region along the channel. This fact and considerable vorticity of the flow are important for mixing of chemically reacting substances.

The case of periodic local energy release was also calculated in the paper. The flow parameters at the channel entrance and the channel dimensions are the same as above. The energy source is located near the lower wall, its longitudinal and transverse sizes are 0.5 % of the length and width of the channel, respectively.

Because of very small size of this region, the grid was refined by a factor of 50. The pressure around the energy source was assumed equal to 10 after a time interval equal to 0.02. Thus, a periodic energy supply to the flow was modeled.

Figure 9 shows the pressure field for the time moment $t=0.1036$ (the refined grid is shown arbitrarily). The isobars are shown for the same pressure values as above. It is seen from the figure that the elevated pressure regions corresponding to earlier energy release are gradually blurred, the pressure in these regions decreases, and the disturbance is already weak in the coarse grid subdomain. The flow vorticity is rather significant for this method of energy supply.

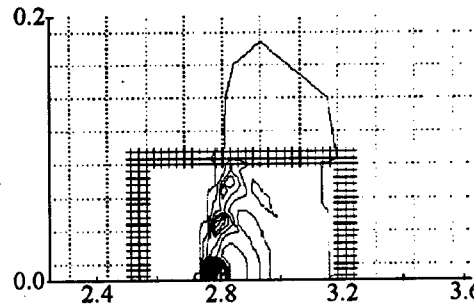


Fig. 9.

Thus, for the examined values of supersonic flow parameters, a local energy source near the channel wall produced favorable conditions for combustion and other chemical reactions: the flow vorticity considerably increases, the initial disturbance is fairly rapidly entrained across the channel. A periodic energy supply is rather effective. The numerical technique used in the present paper allows for successful solution of the problems with different-scale elements.

REFERENCES

1. V.I.Artemiev, V.I.Bergelson, I.V.Nemchinov, et al., Global reconstruction of gasdynamic flows by thin laser beams, *Izv. AN SSSR, Ser. fizich.*, 1991, Vol. 55, No. 6, P. 1184 - 1187.
2. P.K.Tret'yakov, A.F.Garanin, G.N.Grachev, et al., Supersonic flow control using a powerful optical pulsating discharge, *Doklady AN*, 1996, Vol. 351, No. 3, P. 339 - 340.
3. V.K.Baev, V.I.Golovichev, P.K.Tret'yakov, et al., *Combustion in a Supersonic Flow*, Nauka, Novosibirsk, 1984, 304 p.
4. R.W.MacCormack, Numerical solution of the interaction of a shock wave with a laminar boundary layer // *Lecture Notes in Physics*. — Berlin et al.: Springer - Verlag, 1971. — V. 8. — P. 151 - 163.
5. Hung C.M., MacCormack R.W. Numerical solutions of supersonic and hypersonic laminar compression corner flows // *AIAA J.* — 1976. — V. 14, N 4. — P. 475 - 481.
6. Kao K.H., Liou M.S., Chow C.Y. Grid adaptation using Chimera composite overlapping meshes // *AIAA J.* — 1994. — V. 32, N 5. — P. 942 - 949.
7. Wang Z.J. A fully conservative interface algorithm for overlapped grids // *J. Comput. Phys.* — 1995. — V. 122, N 1. — P. 96 - 106.
8. Berger M.J., Colella P. Local adaptive mesh refinement for shock hydrodynamics // *J. Comput. Phys.* — 1989. — V. 82, N 1. — P. 64 - 84.
9. Quirk J.J. A Cartesian grid approach with hierarchical refinement for compressible flows // *Proc. of the 2th European Computational Fluid Dynamics Conf., Stuttgart, Germany.* — 1994. — P. 200 - 209.
10. Ton V.T. Improved shock-capturing methods for multicomponent and reacting flows // *J. Comput. Phys.* — 1996. — V. 128, N 1. — P. 237 - 253.
11. Fursenko A., Sharov D. Efficient algorithms for non-stationary Euler equations // *Proc. of the 2th European Computational Fluid Dynamics Conf., Stuttgart, Germany.* — 1994. — P. 24 - 32.
12. L.D.Landau and E.M.Lifshits, *Continuum Mechanics*, Gos. Izd-vo Tekhniko-teoretich. Lit., Moscow, 1953, 788 p.
13. L.I.Sedov, *Methods of Similarity and Dimension in Mechanics*, Gos. Izd-vo Tekhniko-teoretich. Lit., Moscow, 1957, 376 p.

APPEARANCE OF VORTEX STRUCTURES AT STALL AND TURBULENT SEPARATION ON STRAIGHT WING (REVIEW)

B. Yu. Zanin

Institute of Theoretical and Applied Mechanics SB RAS
630090, Novosibirsk, Russia

INTRODUCTION

The onset of the flow separation regions on the construction elements, primarily, on the wing, refers to phenomena playing the key role in aircraft aerodynamics. The flow separation may be accompanied by radical changes of the mean-time and unsteady aerodynamic loads, affect the aircraft maneuverability and controllability. In this aspect, two types of separated flows are most important: the flow separation near the wing leading edge (called also a global separation or stall) and the turbulent boundary layer separation. In the both cases the separated flow is not reattached to the wing surface, and a vast separation region is formed extending over the entire wing surface from the separation line to the trailing edge.

The literature is abundant with theoretical and experimental results on the subsonic flow separation on airfoils and wings with finite aspect ratio [1-12]. These papers is described in review [13]. The mentioned studies showed that the separated flow over wings of different aspect ratios is not two-dimensional with respect to both mean-time and instantaneous characteristics of the flow, but has a complex three-dimensional vortex structure where correlated large-scale quasi-steady and unsteady vortex structures dominate.

The study of the flow separation in different configurations apart from airfoils and wings showed that the three-dimensionality of velocity field is a universal property of the flow in large-scale separation region. Unsteady and quasi-steady 3D vortex structures were observed by various authors for the flow separation from a cylinder [6,14], from the leading edge of a streamwise plate [15], from a crosswise plate [16,17], ahead of a surface hump and behind it [18,19].

An important problem in the study of separated flows is the search for most effective methods of controlling their structure for improving the wing aerodynamics. One of such methods is the excitation of external low-amplitude acoustic disturbances in a separated flow [20-29]. It is known that the onset of separation is commonly accompanied by some instability modes developed in the separated shear layer; as a result, a weak external action may turn sufficient to change its time-averaged characteristics. In particular, an effective control method for the laminar flow stall is the excitation of disturbances growing in the shear layer of the separating flow that stimulates the transition to turbulence behind the separation point. The properties of hydrodynamic instability and other features of the laminar-turbulent transition in local separated flows involving the mentioned method for the separation control were considered in detail in recent publications [30].

The authors of the papers [25-29] observed a sound-induced effect of irreversible flow reattachment on the global separation in some regimes of the flow over straight and swept wings. After the acoustic excitation was terminated, the flow stall regime was not recovered but the flow remained attached to the wing surface. At the same time, the authors of the papers [20-29] carried out the research in a 2D formulation, i.e., the separated flow

structure was assumed to be two-dimensional with high accuracy, and all quantitative measurements were usually taken in the central cross section of the model.

Another method for the separation control is the use of steady sources of disturbances such as boundary layer tripping, roughnesses, humps of various shape positioned near the wing leading edge.

Next part of the review contains the results of experimental investigations to study the influence of various disturbing factors on the flow over the wing under the leading edge stall and in the case of turbulent separation. The studies were performed in several wind tunnels on the wing models with different profiles and aspect ratios. The sources of both external unsteady (acoustic) and steady (artificially created roughnesses on the wing surface) disturbances were used to affect the separated flow over models. The corresponding materials were included into publications [31-38].

THE INFLUENCE OF EXTERNAL FORCING ON THE 3D STRUCTURE OF SEPARATED FLOWS

The effect of acoustic disturbances on the flow pattern under the stall. The experiments [26-29,31] showed, in particular, the possibility of the use of acoustic effects to control the global separation (stall) of the flow for a new high-lift profile for aerobatics airplanes. The experiments were carried out in the low-turbulent wind tunnel T-324 based at ITAM SB RAS on the model with the aspect ratio $AR=2$ and in the wind tunnel T-203 SibNIA on the model with $AR = 5$ within the chord Reynolds number range from $5 \cdot 10^5$ to 10^6 .

In [31] it was shown that the separated flow on straight wing is characterized by the presence of large-scale 3D vortex structures with an intense reverse flow in the central part of the wing. The increase in intensity of external acoustic disturbances provided the reduction of the separation region dimensions and its complete elimination after reaching a necessary sound level. The lift and drag measurements on the wing model with $AR = 5$ mounted at the angle of attack 12° showed that the lift coefficient increases in this case by about 30 %, whereas the drag coefficient decreases more than by a factor of two [31]. Since the sound effect is related to transformation of external acoustic disturbances into instability waves developed in the separated shear layer, the flow reattachment effect was achieved only at the sound frequencies corresponding to the frequency range of unstable oscillations of the shear layer. No reattachment took place under acoustic forcing with other frequencies. It was found that irreversible reattachment is possible at the hysteresis regimes of the flow over an airfoil.

The measurements of aerodynamic forces acting upon the model with increasing the angle of attack showed that, using acoustic effects, one can slightly increase the critical angle of attack of the model and also considerably increase the lift force and reduce the drag at supercritical angles of attack [31]. Though in this case the acoustic excitation does not provide a complete stall elimination, it exerts an appreciable effect on the flow in the central part of the model where the reverse flow is completely eliminated. A pair of horse-shoe vortices is formed at each wing side.

The detailed study of the influence of acoustic disturbances on the 3D structure of separated flows was carried out when investigating the topology of the separated flow over a finite-span wing with the aspect ratio $AR = 3$ at the chord Reynolds number is 10^6 , the

angle of attack is 25° [32]. The experiments were carried out in the wind tunnel based at DLR, Goettingen. The forcing of spatially-homogeneous and focused acoustic disturbances on the vortex structure of a separated flow was studied. The data obtained testify that large-scale vortex structures formed by the leading edge flow stall are involved in the interaction of disturbances with the separated flow and play an essential role there. The separated flow excitation by a uniform acoustic field from a distant acoustic source with the "optimum" frequencies causes the separated layer reattachment. As a result, the flow stall from the leading edge is changed for the downstream turbulent flow separation. It has a favorable effect on the aerodynamic performance of the wing. When an acoustic beam is used to control the flow stall, the result depends on its focusing on the model surface. The acoustic excitation of the flow in the wing span center yields the same result as a homogeneous acoustic field: the separation region is reduced, retaining its symmetry in the wing plane. The acoustic forcing focused elsewhere proves to be less effective for the stall control of the flow causing its partial reattachment without qualitative effect on the vortex structure of the separation region.

Hysteresis of a separation. It is known that at a sequential increase and decrease of the angle of attack of a wing there are differences in its aerodynamic characteristics, such as lift and drag [7,8], which leads to an ambiguous flow pattern within a certain range of the angles of attack. The authors [28,31] have revealed that the hysteresis phenomena can be observed in the flow about a wing mounted at a constant angle of attack if the flow velocity first increases and then decreases. These papers dealt with global separation (leading-edge stall) on a straight-wing model. The separation was shown in [28,31] to be eliminated by an increase in velocity, whereas it occurs again at a different (lower) velocity, i.e., the hysteresis is observed within a certain range of flow velocities. In this case, the angle of attack was not changed. It was also found that the irreversible flow reattachment to the wing surface can be achieved under the acoustic action on the flow in the hysteresis range of velocities, i.e., the separation is not restored when the sound is switched off. For flow velocities lower than the hysteresis range, the acoustic action leads to reversible reattachment, i.e. the separation is restored after cancelling the sound effect. The contribution of the three-dimensional vortex structure of the separated flow to the appearance of hysteresis has not yet been studied. The goal of the paper [34] is to obtain flow patterns on the wing surface in the hysteresis range of flow velocities and to determine which changes in the three-dimensional structure of the separated flow are caused by a sequential increase and decrease of the flow velocity and how these changes are related to hysteresis. In addition, the effect of the acoustic action on the flow pattern has been studied. The experiments were performed in a T-324 low-turbulence wind tunnel at the Institute of Theoretical and Applied Mechanics. The model with a rectangular shape of the wing in plan and a symmetric profile whose relative thickness is 10% was used. The model span was 945 mm, and the chord length was 196 mm (aspect ratio 4.82). Top plates were installed at the model edges to avoid flow spillage. A angle of attack was 8° and it was kept constant during the experiments. The results were obtained using the oil-film visualization technique. With an increase in the flow velocity from 0 to 22 m/s, a flow stall from the leading edge (global separation) appeared, which was evidenced by a hot-wire anemometer. Upon reaching a velocity of 22 m/s (chord-based Reynolds number $2.9 \cdot 10^5$), flow reattachment occurred. The flow velocity was then decreased. The global flow separation on the model was observed again at a velocity of 16 m/s (chord-based Reynolds number $2.1 \cdot 10^5$). Thus,

there exists a flow hysteresis in the range of 16 – 22 m/s. Visualization of the limiting streamlines using the oil-film technique allowed one to clarify the specific features of the flow pattern under hysteresis conditions. The hysteresis phenomenon is caused by the fact that the flow reattachment occurs gradually as the flow velocity is increased, beginning from the model sides, while the flow remains completely attached as long as it is possible with decreasing velocity, and then the flow separation is restored immediately on the entire wing surface.

Global separation topology on the wing model in the presence of sources of steady disturbances. This part of research was aimed at the study of the flow topology under global separation of the flow above the upper surface of a rectangular wing with roughnesses of different shape mounted near the leading edge.

The experiments [35] were carried out in the low-turbulent wind tunnel using a rectangular wing model with plates positioned at its ends to prevent the overflow. The wing aspect ratio was 4.82; the Reynolds number was 200 000, the angle of attack was 10° . The studies showed that the topology of a 3D flow in the region of global separation can be altered by steady disturbances, i.e., by small-height roughness elements on the surface that induce additional vortex formations in the separation region. It was established that under these conditions the acoustic forcing used for preventing the flow stall may cause its partial rather than complete reattachment on the wing surface between individual humps.

In the paper [36] for the first time it was shown that there are possibilities of controlling the stall (global separation) based on utilization of localized (point-like) sources of disturbances placed behind the separation line, in the reversed flow region, rather than at the leading edge. In this case, additional disturbances are introduced in the three-dimensional flow structure of the separated region, in particular, into large-scale vortices rotating in the wing plane. Such forcing make it possible to control the flow and in some cases completely eliminate the stall.

Turbulent separation structure on a rectangular wing model. The study described in [37,38] was aimed at investigating the flow structure at the turbulent boundary layer separation from the upper surface of a rectangular wing model and its behavior under the flow regime changes and external effects. The experiments were carried out in the low-turbulent wind tunnel T-324 based at ITAM SB RAS. The NACA 63-2-615 rectangular wing model with a laminar profile was used. The model span was 1 m, the chord was 0.27 m, the aspect ratio was 3.7, the Reynolds number was $5.8 \cdot 10^5$. The model mounted in the wind tunnel had its ends seated against the test section walls, i.e., a two-dimensional flow was simulated without end effects caused by the overflow. The model was established at a chosen angle of attack before the experiment, and the angle of attack was not changed during the run.

The results of these studies show that the flow structure at a turbulent separation is somewhat different from that realized at a stall when only two vortices rotating in the model plane are formed on the wing. At a turbulent separation the number of vortex pairs on the wing surface depends on the angle of attack. We failed to affect the turbulent separation with the sound possessing the amplitude sufficient to affect the laminar separation. A vortex pair is also formed in the hump wake at a laminar separation, but the separation line between them has a tendency of deviating from the free stream direction by an angle of $25-30^\circ$, which is not observed at a turbulent separation.

CONCLUSION

On the whole, the results obtained show the existence of both the general property of the flows at a stall and turbulent flow separation (the formation of large-scale vortices rotating in the wing plane) and peculiar features of behavior of these flows under different flow conditions and external effects.

ACKNOWLEDGEMENT

This work was supported by Russian Basic Sciences Foundation (grants N 97-01-00821 and N 96-15-96310).

REFERENCES

1. Winkelmann A.E., Barlow J.B. A flowfield model for a rectangular planform wing beyond stall // AIAA J. - 1980. - Vol.18, No.8. - P. 1006 - 1008.
2. Bippes H., Jacob H., Turk M. Experimental investigations of the separated flow around a rectangular wing. - DFVLR-FB 81-12, 1981 (in German).
3. Tobak M., Peake D.J. Topological structures on three-dimensional separated flows. - AIAA Paper 81-1260, 1981.
4. Neiland V.Ya., Stolyarov G.I. On one type of separated flow on a rectangular wing // Uch. zap. TsAGI. - 1982. - Vol.13, No.1. - P. 83 - 88.
5. Dallman V. Topological structures on three-dimensional vortex flow separation. - AIAA Paper 83-1735, 1983.
6. Weihs D., Katz J. Cellular patterns in poststall flow over unswept wings // AIAA J. - 1983. - Vol.21, No.12. - P. 1757 - 1759.
7. Neiland V.Ya., Stolyarov G.I., Tabachnikov V.G. The influence of the relative thickness of a rectangular wing with low aspect ratio and the Reynolds number effect on regimes of the flow structure reconstruction // Uch. zap. TsAGI. - 1985. - Vol.16, No.3. - P. 1 - 10.
8. Kolmakov Yu.A., Ryzhov Yu.A., Stolyarov G.I., Tabachnikov V.G. An investigation of the structure of the flow over a rectangular wing $AR = 5$ at high angles of attack // Trudy TsAGI. - 1985. - No.2290. - P. 84 - 89.
9. Bastedo Jr.W.G., Mueller T.J. Spanwise variation of laminar separation bubbles on wings at low Reynolds numbers // J. of Aircraft. - 1986. - Vol.23, No.9. - P. 687 - 694.
10. Bippes H. Experimental investigation of topological structures in three-dimensional separated flow // Boundary-Layer Separation / Eds. F.T.Smith, S.N.Brown. - Berlin et al.: Springer, 1987. - P. 379 - 382.
11. Golovkin M.A., Gorban' V.P., Simuseva E.V., Stratonovich A.N. The flow over a rectangular wing at stationary and quasi-stationary external conditions // Uch. zap. TsAGI. - 1987. - Vol.18, No.3. - P. 1 - 12.
12. Winkelmann A.E. Flow field studies behind a wing at low Reynolds number. - AIAA Paper 90-1471, 1990.
13. Boiko A.V., Dovgal A.V., Zanin B.Yu., Kozlov V.V. Three-dimensional structure of separated flow on wings (review) // Thermophysics and Aeromechanics. - 1996. - Vol.3, No.1. - P. 1 - 13.
14. Treschevsky V.N., Volkov L.D., Korotkin A.I. Aerodynamic experiment in ship building. - Leningrad: Sudostroenie, 1976.
15. Kiya M., Sasaki K. Structure of large-scale vortices and unsteady reverse flow in the reattaching zone of a turbulent separation bubble // J. Fluid Mech. - 1985. - Vol.154. - P. 463 - 491.
16. Ruderich R., Fernholz H.H. An experimental investigation of a turbulent shear flow with separation, reverse flow, and reattachment // J. Fluid Mech. - 1986. - Vol.163. - P. 283 - 322.
17. Jaroch M. Oil flow visualisation experiments in the separated and reattachment regions of the flow past a transverse flat plate with a long splitter plate // Z. Flugwiss. Weltraumforsch. - 1987. - Vol.11. - P. 230 - 236.
18. Papadopoulos G., Otugen M.V., Vradis G.C. The three-dimensional separated flow structure in a variable aspect ratio sudden expansion duct. - AIAA Paper 93-0213, 1993.
19. Kozlov A.P. Three-dimensionality manifestation in 2D separated flows // Dokl. RAN. - 1994. - Vol. 338, No.3. - P. 337 - 339.

20. Collins F.G., Zelenevitz J. Influence of sound upon separated flow over wings // *AIAA J.* - 1975. - Vol.13, No.3. - P. 408 - 410.
21. Karovosov R.K., Prozorov A.G. Acoustic effects on the flow over a wing at low Reynolds numbers // *Trudy TsAGI.* - 1976. - No.1790. - P. 12 - 23.
22. Kozlov V.V. Leading edge separation and effect of acoustic disturbances upon it // *J. Appl. Mech. and Techn. Phys.* - 1985. - No.2. - P. 112 - 115.
23. Zaman K.B.M.Q., Bar-Sever A., Mangalam S.M. Effect of acoustic excitation on the flow over a low-Re airfoil // *J. Fluid Mech.* - 1987. - Vol.182. - P. 127 - 148.
24. Nishioka M., Asai M., Yoshida S. Control of flow separation by acoustic excitation // *AIAA J.* - 1990. - Vol.28, No.11. - P. 1909 - 1915.
25. Zhigulev S.V., Fedorov A.V. An investigation of the ultrasonic acoustic field effect on the boundary layer separation on an airfoil // *Uch. zap. TsAGI.* - 1990. - Vol.2, No.6. - P. 58 - 66.
26. Zanin B.Yu., Kozlov V.V., Lushin V.N. The global flow separation control by acoustic effects. - Novosibirsk, 1990. - 15 p. (Preprint/USSR Acad. of sci., Sib. branch., Inst. teor. and appl. mech., No. 2-90).
27. Zanin B.Yu., Kozlov V.V., Lushin V.N. The acoustic field effect on the global separation of the flow from a wing model // *Methods of aerophysical research.* - Novosibirsk, 1990. - P. 132 - 137.
28. Zanin B.Yu., Kozlov V.V., Lushin V.N. The flow separation control on a rectangular wing and swept wing by acoustic excitation // *Sib. phys.-tech. journal.* - 1992. - No. 3. - P. 32 - 36.
29. Kozlov V.V., Lushin V.N., Zanin B.Yu. Separated flow reattachment at an airfoil under sonic effect. // *Separated Flows and Jets: Proc. IUTAM - Symp. / Eds. V.V. Kozlov, A.V. Dovgal.* - Berlin et al.: Springer, 1991. - P.525 - 528.
30. Dovgal A.V., Kozlov V.V., Michalke A. Laminar boundary-layer separation: instability and associated phenomena // *Progr. Aerospace Sci.* - 1994. - Vol.30. - P.61 - 94.
31. Lushin V.N. The flow over a finite-span wing under an external acoustic effect // *Sib. phys.-tech. journal.* - 1992. - No.4. - P. 64 - 68.
32. Kozlov V.V., Grosche F.-R., Dovgal A.V., Bippes H., Kuhn A., Stiewitt H. Control of leading-edge separation by acoustic excitation - DLR-IB 222-93, 1993 (in German).
33. Boiko A.V., Dovgal A.V., Zanin B.Yu., Kozlov V.V., Lushin V.N. On topology of an airfoil flow at global boundary layer separation and external disturbance influence on its behavior // *Int. Conf. on the Methods of Aerophysical Research: Proc. Pt. 2* - Novosibirsk, 1994. - P. 48 - 54.
34. Zanin B.Yu. Hysteresis of a separated variable-velocity flow about a straight wing model // *J. Appl. Mech. and Techn. Phys.* - 1997. - Vol.38, No.5. - P. 80 - 84.
35. Boiko A.V., Dovgal A.V., Zanin B.Yu., et al. On topology of global separation on an airfoil in the presence of stationary disturbance sources // *Thermophysics and Aeromechanics.* - 1995. - Vol.2, No.1. - P. 105 - 112.
36. Zanin B.Yu., Kozlov V.V., Mavrin O.V. On a method of global flow separation control // *Thermophysics and Aeromechanics.* - 1997. - Vol.4, No.5 - P. 355 - 358.
37. Kozlov V.V., Boiko A.V., Dovgal A.V., Zanin B.Yu. Review of visualization of separated flow structure on straight wings // *Fourth Asian symposium on visualization: Proc. / Ed. Q.D. Wey.* - Beijing.: Int. Academic Publishers, 1996. - P. 13 - 18.
38. Boiko A.V., Dovgal A.V., Zanin B.Yu., Kozlov V.V. Visualization of 3-D vortex structure in separation flows // *Int. Conf. on the Methods of Aerophysical Research: Proc. Pt. 2* - Novosibirsk, 1996. - P. 21 - 26.

SURFACE-FLOW VISUALIZATION BY LIQUID CRYSTAL COATINGS AT LOW SUBSONIC VELOCITIES

G.M.Zharkova, A.V.Dovgal, V.N.Kovrizhina, B.Yu.Zanin
Institute of Theoretical and Applied Mechanics SB RAS,
630090, Novosibirsk, Russia

INTRODUCTION

A tool of experimental aerodynamics is the flow visualization using liquid-crystal (LC) coatings. With this method a test model is covered by a thin film of LC changing its color due to temperature variations. In this way one can get the mean flow pattern close to the surface, associated to different heat transfer along the model. Till now the method was used in a number of studies for wide ranges of Mach and Reynolds numbers, first for compressible gas flows [1 - 4] and then at low subsonic velocities [5 - 7]. In those experiments the LC visualization was found to be effective mean of flow diagnostics. The method is nonintrusive contrary to most of classic visualization techniques which use tufts, liquid films or tracing particles. Moreover data processing of the LC color distributions enables to obtain quantitative information about temperature field at the surface of the model indicating details of the surface flow structure.

Previous work of the authors [8, 9] was aimed to adapt the method to aerodynamic researches in the Institute of Theoretical and Applied Mechanics, Novosibirsk at low subsonic velocities. As a result, a particular visualization technique of the boundary-layer structure has been developed to capture local regions of boundary-layer separation, laminar-turbulent transition and fine vortical structure of the near-wall flow. The goal of present study was further elaboration of the LC visualization method applying it to investigation of the flow on the upper surface of unswept wing placed at high angles of attack.

EXPERIMENTAL SET-UP

The experiments were carried out in the subsonic wind tunnel MT-324 of the Institute of Theoretical and Applied Mechanics, Novosibirsk. The experimental model made of wood was a symmetric profile with 228 mm chord, 198 mm span and 16% maximum thickness. It was placed in the open test section of the facility with the nozzle 200 x 200 mm, at the free-stream turbulence level equaled to 0.1%. Two different thermosensitive coatings being mixtures of cholesteric LC and a polymer were used for visualization. One of them had the selective reflection bandwidth between 24.8° and 26.3°C, the other - from 30.0° to 34.0°C changing their colors in the above ranges from red to blue at temperature increase. Flow temperature during the experiments varied between 18.0° to 20.0°C. The LC films were glued onto the wing surface; low thermal conductivity of the experimental model provided the heat flux mainly from the surface to the flow. Then, it was reasonably believed that small thickness of the coatings which was about 25 microns did not affect the heat transfer and, hence, the results of visualization. As far as the flow at low subsonic conditions did not have natural temperature gradients, before starting the visualization the model was artificially overheated above the selective reflection bandwidths of the coatings. It was performed in two manners: the whole

wing was heated or its testing surface only. Afterwards it was exposed to the flow and color variations of the cooling LC film were recorded by a video system. By means of a framegrabber and a PAL decoder the video signal was transformed to the R, G, B components and stored by a computer. Then the RGB signal was converted to more simple for further analysis HSI (Hue, Saturation, Intensity) format; the conversion algorithm is given in [10]. To get quantitative data on temperature distributions a calibration $T(H)$ was obtained. In what follows the linear approximation of $T(H)$ variation was used providing the accuracy about 0.1°C . Then, the H-data were transformed to temperature fields, and their maps were constructed splitting the selective reflection bandwidth of LC coating at eight temperature levels. In addition, absence of heat transfer along the surface of the model was examined.

RESULTS AND DISCUSSION

The visualization was carried out at the free-stream velocity $U_\infty = 16 \text{ m/s}$ corresponding to the chord Reynolds number $Re_c = U_\infty c / \nu = 2.35 \cdot 10^5$ at two angles of attack $\alpha = 27^\circ$ and 18° . Fig.1 shows the results for $\alpha = 27^\circ$ obtained with the LC coating sensitive to temperature variations between 24.8° and 26.3°C .

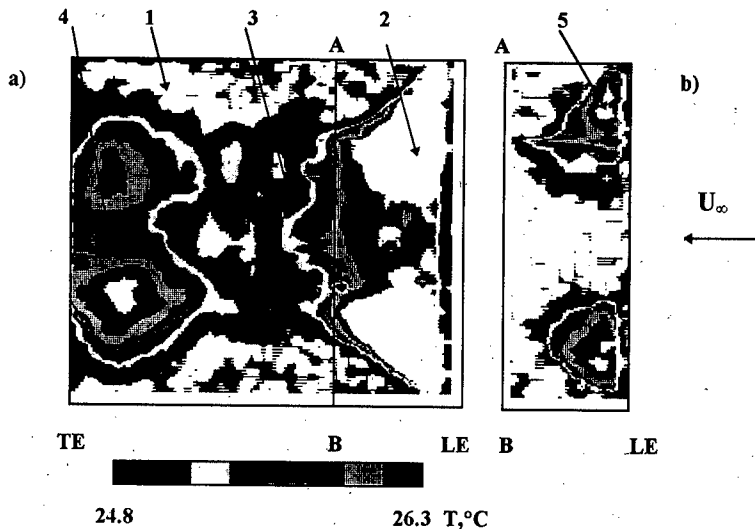


FIG.1. Temperature distribution at the surface of the wing. $\alpha = 27^\circ$. LC sensitivity band: $24.8^\circ - 26.3^\circ\text{C}$. LE and TE - leading and trailing edges of the model, the flow is from right to left. General view (a) and the leading-edge region (b).

Within this range the temperature distribution at the surface of the model is given in eight colors, areas indicated in white are below or above the range of resolution. The data show complex 3-D structure of the flow separating close to the wing leading edge. In Fig.1a the whole view of test surface is given. One can observe cooled regions, $T < 24.8^\circ$ on both sides of the wing affected by tip vortices enhancing the heat transfer (1). Near the leading edge there is a separation region with slow motion close to the surface and its relatively high temperature, $T > 26.3^\circ$ (2). Cooling increases when the flow reattaches to the wall in the middle part of the

wing (3) and further comes down in the turbulent boundary layer (4). Spatial flow structure in the region of separation is visualized by another snapshot of Fig.1b taken at the same exposition of the model five seconds later than the first one as the surface temperature was falling down. It shows a fragment of the wing from the leading edge to section AB in Fig. 1a and resolves a pair of quasi-stationary vortices rotating in the wing plane (5).

Fig.2 shows similar data for the other LC coating changing its color from 30.0° to 34.0°C. The results of visualization are qualitatively the same. In this case, loosing some details due to reduced sensitivity of the coating it is possible to resolve wider panorama of the flow with large temperature gradients on the surface.

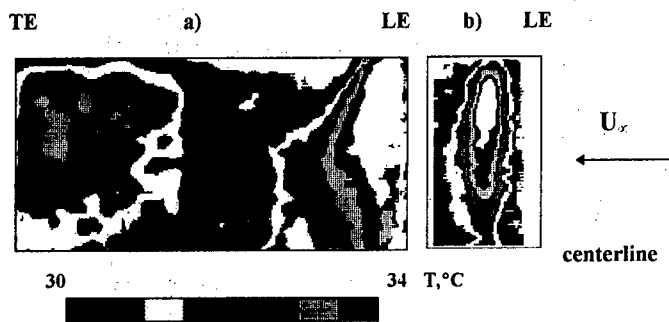


FIG.2. Temperature distribution at the surface of the wing. $\alpha = 27^\circ$. LC sensitivity band: 30.0° - 34.0°C. A half of the model from the centerline (a) and the leading-edge region (b).

LC data obtained at the angle of attack reduced to $\alpha = 18^\circ$ with the coating sensitive at 30.0° - 34.0°C are given in Fig.3.

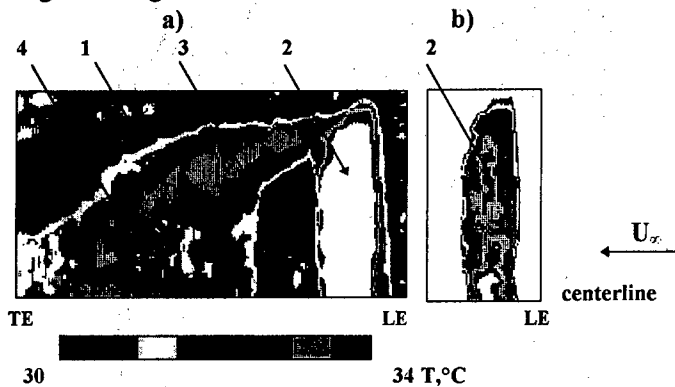


FIG.3. Temperature distribution at the surface of the wing. $\alpha = 18^\circ$. LC sensitivity band: 30.0° - 34.0°C. A half of the model from the centerline (a, b).

As the incidence of the wing gets smaller the large-scale separation region is succeeded by the leading-edge separation bubble. Like that in the previous case one can distinguish in Fig.3a the tip vortices (1), separated flow with $T > 34.0^\circ$ (2), reattachment zone, $T < 30.0^\circ$ (3) and the turbulent boundary layer (4). Then, the separation bubble is resolved in Fig.3b: here the wall

temperature in the "stagnation-flow" region fits to the sensitivity band of the coating while the temperature of the rest surface is below 30.0° (5).

The above data are in general agreement with results on separated flow topology on finite-span wings at high angles of attack obtained by other experimental methods, see for example in [11 - 13]. For direct comparison, Figs. 4 and 5 taken under the experimental conditions of Figs. 1 and 3, respectively, give surface flow visualization by a liquid film, i.e., a mixture of kerosene and the titanium dioxide powder.

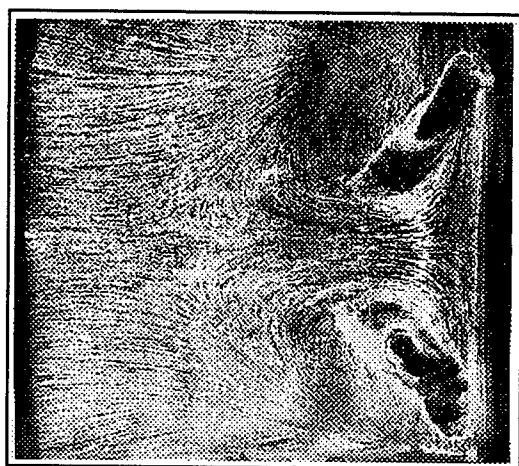


FIG.4. Liquid-film visualization, $\alpha = 27^\circ$.

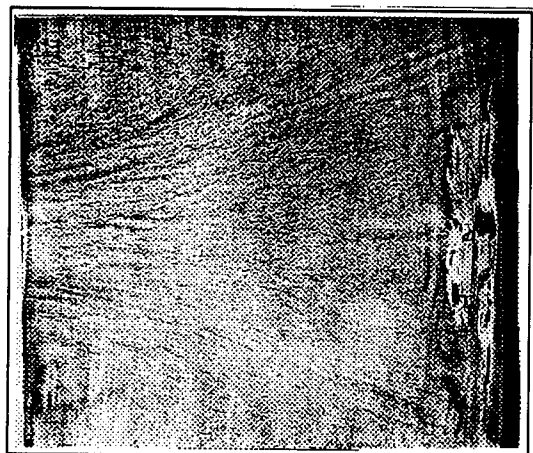


FIG.5. Liquid-film visualization, $\alpha = 18^\circ$.

Both methods show similar 3-D flow structures which, however, somewhat different. Namely, the LC visualization indicates that the liquid film technique does not capture exact positions of the vortices in the separation region at $\alpha = 27^\circ$. Drops of kerosene accumulated in

foci of the vortices distort the flow so that in Fig.4 they are closer to the centerline than in Fig.1. On the same reason, that is, the effect of kerosene film on the flow, the leading-edge separation bubble in Fig.5 seems to have complex internal 3-D structure. At the same time, examination of the flow by nonintrusive LC technique, Fig.3, shows that the bubble is fairly two-dimensional. Then, comparing the LC and liquid-film data of Figs.1 and 4 one can see that the flow patterns are pretty different at the downstream part of the model. The liquid crystals show three-dimensionality of the mean flow - two color spots almost symmetric to the centerline - which is not detected by the other method. To be sure that these spots were not induced by surface imperfections underneath the LC film visualization was performed on another wing model, a twin of the first one. It turned out that under the same experimental conditions the flow pattern of Fig.1 were obtained again. Thus, it is concluded that the LC film indicates the 3-D mean flow structures which do exist being not resolved by the other visualization technique.

CONCLUSIONS AND RECOMMENDATIONS

In present work the LC visualization method was applied to one of classic aerodynamic problems - the flow over a finite-span wing. The obtained results can be resumed in the following way. The visualization technique and the data processing have been developed which make it possible to reconstruct surface temperature fields and temperature gradient distributions in incompressible gas flows. Thus, the method enables to localize accurately regions of strong heat transfer variations induced close to the wall by separation, reattachment, transition to turbulence, and appearance of large-amplitude stationary vortices. The data are in general agreement with those obtained by other experimental methods. The results of the study show how the nonintrusive LC visualization overcomes limitations of experimental techniques which use visualizing substances introduced into the flow affecting the results of observations. It is found that the method is fairly sensitive and resolves flow details which can not be detected by other means of flow visualization. To take a panoramic view of the flow at strong heat transfer variations along the test surface a large selective reflection bandwidth of the LC film is preferable. However it reduces the resolution and details of flow pattern can be extracted increasing sensitivity of the coating. Then, different parts of the flow can be specially focused at suitable stages of the LC cooling. It is found that heating procedure of the experimental model made of low conductive material prior to its aerodynamic cooling in the flow is not crucial for results of visualization. An inference of the study is that reliability of the method requires high quality of the tests surface with minimum local variations of its thermal conductivity.

ACKNOWLEDGEMENTS

The study granted in 1997 by the Basic Researches Initiative of the Institute of Theoretical and Applied Mechanics, Novosibirsk.

REFERENCES

1. Klein E.J. Application of liquid crystals to boundary-layer visualization. — AIAA Paper, 1968, No. 68-386. — 8 p.

2. Zharkova G.M., Khachatryan V.M., Vostokov L.A., Alekseev N.M. Study of liquid crystal. advances in liquid crystal, research and application. (Ed. Bata). Budapest: Pergamon Press, Oxford, Acad. Kiado., 1980, P. 1221-1239.
3. Zharkova G.M. Temperature field visualization using liquid crystal method // *Experimental Heat Transfer*. - 1991. - Vol.4. - P. 85-94.
4. Holmes B.J., Obara C.J., Manuel G.S., Lee C.C. Developments in flow visualization methods for flight research // *Proc. of the Fifth Int. Symp. on Flow Visualization*, Prague, Czechoslovakia, August 21-25, 1989.
5. Stasiek J., Collins M.W. Liquid crystals thermography and image processing in heat and fluid flow experiments // *Proc. of the Sixth Int. Symp. on Flow Visualization*, Yokohama, Japan, October 5-9, 1992. - P. 439-450.
6. Zhou M.D., Liu D.P., Blackwelder R.F. An experimental study of receptivity of acoustic waves in laminar boundary layers // *Experiments in Fluids*. - 1994. - Vol.17. - P. 1-9.
7. Meier H.U., Zhou M.D. The development of acoustic generators and their application as a boundary layer transition control device // *Experiments in Fluids*. - 1991. - Vol.11. - P. 93-104.
8. Dovgal A.V., Kornilov V.I., Kovrizhina V.N., Kozlov V.V., Pavlov A.A., Zharkova G.M. Visualization of boundary-layer structure under the conditions of low subsonic flow velocities using liquid crystal coatings // *Int. Conf. on the Methods of Aerophysical Research: Proc. Pt 2. - Novosibirsk, 1996. - P. 64 - 69*
9. Dovgal A.V., Kozlov V.V., Kovrizhina V.N., Zharkova G.M. Liquid-crystals visualization of the boundary layer in incompressible gas flow // *Proc. of the Seventh Intern. Symp. on Flow Visualization*, Seattle, Washington, September 11-14, 1995. - P. 532-537.
10. Levkowitz H., Herman G.T. GLHS: A generalized lightness, hue and saturation color model // *GVGIP: Graphical Models and Image Processing*. - 1993. - Vol.55. - No.4. - P. 271-285.
11. Neyland V.Ya., Stolyarov G.I. A type of flow separation on a rectangular wing // *Sci. Notes of TsAGI*. - 1982. - Vol.13. - No.1. - P. 83-89 (in Russian).
12. Winkelmann A.E., Barlow J.B. A flowfield model for a rectangular planform wing beyond stall // *AIAA Journ.* - 1980. - Vol.18. - No.8. - P. 1006-1008.
13. Boiko A.V., Dovgal A.V., Zanin B.Yu., Kozlov V.V. Three-dimensional structure of separated flows on wings (review) // *Thermophysics and Aeromechanics*. - 1996. - Vol.3. - No.1. - P. 1-13.

CONTENTS

1. S.M. Aulchenko, A.F. Latypov, V.Yu. Nikulichev. The study of scheme viscosity effect on the stream structure in the particle-in-cell method by the example of the perfect gas flow around a cylinder in a plane channel	5
2. A.A. Bakchinov, G.R. Grek, M.M. Katasonov, V.V. Kozlov. An experimental study of the streaky structures interaction with the high-frequency disturbances	11
3. S. Bake, A.V. Ivanov, Y.S. Kachanov, H.H. Fernholz. A method of experimental study of vibrational receptivity of a boundary layer on a curved wall	17
4. I.A. Bedarev, N.N. Fedorova. Numerical simulation of supersonic turbulent separated flows using various high-resolution schemes	23
5. I.A. Bedarev, A.A. Zheltovodov, N.N. Fedorova. Supersonic turbulent separated flows numerical model verification	30
6. B.F. Boyarshinov, S.Yu. Fedorov, A.A. Volkov. CARS - measurements in Ranque — Hilsch's vortex tube	36
7. V.V. Bublik. The exact solutions of equations for dynamics of viscous heat conducting gas	41
8. T. Cvrlije, C. Breitsamter, M. Heller, G. Sachs. Lateral unsteady aerodynamics and dynamic stability effects in hypersonic flight	44
9. S.V. Dolgushev. Evaluation of effectiveness of the airdryer consisted of cooled rotating disks	55
10. A.V. Fedorov, A.A. Zhilin. Propagation and reflection of nonequilibrium shock waves in two-components media	61
11. D.V. Gaitonde, M.R. Visbal, J.S. Shang, A.A. Zheltovodov, A.I. Maksimov. Parametric investigation of flowfield structure and validation issues in 3-D crossing-shock wave/turbulent boundary layer interactions	67
12. S.A. Gaponov, I.I. Maslennikova, V.Yu. Tyushin. About nonlinear influence of external acoustic field on supersonic boundary layer fluctuations	77
13. Yu. P. Goon'ko, I.I. Mazhul', G.N. Markelov. High-lifting waveriders derived from supersonic axisymmetric compression flows	81
14. B.B. Ilyushin, A.F. Kurbatskii. The model of momentum and heat turbulent transport in the convective PBL	87
15. A.V. Ivanov, Y.S. Kachanov, T.G. Obolentseva, A. Michalke . Receptivity of the Blasius boundary layer to surface vibrations. Comparison of theory and experiment	93
16. M.M. Katasonov, V.V. Kozlov. Boundary layer longitudinal localized structures control by means of riblets and spanwise-wall oscillation	99
17. V.I. Kornilov. Two-dimensional asymmetrical turbulent wake/airfoil-boundary layer interaction	105
18. T.A. Korotaeva, V.M. Fomin, A.P. Shashkin. The effect of a local energy source on the aerodynamic characteristics of pointed bodies at supersonic flow	111
19. A.N. Kudryavtsev, R.D. Rakhimov. A marching procedure of numerical solution of two-dimensional and three-dimensional steady Euler equations using shock-capturing schemes	117
20. A.F. Kurbatskii, S.V. Poroseva. Verification of turbulence second-order models in different regions of a rotating cylindrical pipe flow	123

21. A.F. Kurbatskii, S.N. Yakovenko. Modeling a turbulent flow in the plane channel with a quadratic cross-section rib	129
22. V.A. Lebiga, A.Yu. Pak. Comparison of characteristics of anemometers of different types	135
23. C.B. Lee, X.D. Du, Q.X. Lian, V.I. Borodulin, V.R. Gaponenko, Y.S. Kachanov. Combined study of mechanisms of evolution and breakdown of coherent structures in transitional boundary layer at controlled conditions	141
24. A.A. Maslov. An experimental study of hypersonic flow stability	147
25. A.A. Maslov, S.G. Mironov, T.V. Poplavskaya, A.N. Shipliyuk, V.N. Vetlutsky. An experimental and theoretical study of aerodynamic heating of a plate in viscous hypersonic flow	153
26. A.E. Medvedev, V.M. Fomin. An analytical study of hysteresis at plane shock wave reflection in a slender channel	159
27. R.V. Nestoulia, S.B. Nikiforov, A.A. Pavlov. Development of the oil film method of skin friction measurement for curved and arbitrary oriented surfaces	167
28. V.S. Polotov. The results of analytical and experimental investigation of swirling gas flows	173
29. B.V. Rogov, I. A. Sokolova. Turbulent chemical reacting gases flows through curved smooth wall channels	179
30. J. Schetz. Direct measurements of skin friction in complex, high-speed flows	185
31. E. Schuelein, A.A. Zheltovodov. Development of experimental methods for the hypersonic flows studies in Ludwig tube	191
32. S. Takagi, N. Itoh. On interaction between cross-flow and streamline-curvature modes in rotating-disk flow	200
33. N.M. Terekhova. Hydrodynamic disturbances in supersonic jet	208
34. V.I. Terekhov, Yu.M. Mshvidobadze, V.A. Sukharev. Gasdynamics of the radial slot jet in cylindrical channel	213
35. V.I. Terekhov, N.I. Yarygina, R.F. Zhdanov. The structure of the separated flow behind obstacles at high external turbulence	220
36. V.F. Volkov. Development of numerical methods on the basis of Euler equations as applied to supersonic aerodynamics problems	228
37. Yu.E. Voskoboinikov, V.G. Belyavtsev. Nonlinear processing of velocity fields calculated with PIV-method data	234
38. V.P. Zamuraev. Numerical modeling of supersonic flow in plane channel with the local source of energy	239
39. B.Yu. Zanin. Appearance of vortex structures at stall and turbulent separation on straight wing (review)	245
40. G.M. Zharkova, A.V. Dovgal, V.N. Kovrizhina, B.Yu. Zanin. Surface-flow vizualization by liquid crystal coatings at low subsonic velocities	251
Contents	257